

EISSN 1305-3612

DIR

Diagnostic and Interventional Radiology

TSR
1924
TURKISH SOCIETY
OF RADIOLOGY

dirjournal.org

VOLUME 29
ISSUE 3
MAY 2023

Editor in Chief


Mehmet Ruhi Onur, MD

Department of Radiology, Hacettepe University Faculty of Medicine, Ankara, Turkey

ORCID ID: 0000-0003-1732-7862


Section Editors and Scientific Editorial Board

Abdominal Imaging

İlkay S. İdilman, MD 

Department of Radiology, Hacettepe University Faculty of Medicine, Ankara, Turkey

ORCID ID: 0000-0002-1913-2404

Sonay Aydın, MD 

Department of Radiology, Erzincan Binali Yıldırım University Faculty of Medicine, Erzincan, Turkey

ORCID ID: 0000-0002-3812-6333


Artificial Intelligence and Informatics

Burak Koçak, MD 

Department of Radiology, University of Health Sciences, Başakşehir Çam and Sakura City Hospital, İstanbul, Turkey

ORCID ID: 0000-0002-7307-396X


Breast Imaging

Füsun Taşkın, MD 

Department of Radiology, Acıbadem University Faculty of Medicine, İstanbul, Turkey

ORCID ID: 0000-0001-7985-3660


Chest and Cardiovascular Imaging

Furkan Ufuk, MD 

Department of Radiology, Pamukkale University Faculty of Medicine, Denizli, Turkey

ORCID ID: 0000-0002-8614-5387


Hybrid Imaging and Nuclear Medicine

Evrin Bengi Türkbey, MD 

Radiology and Imaging Sciences, Clinical Center, National Institutes of Health Bethesda, Maryland, United States


ORCID ID: 0000-0002-5216-3528

Interventional Radiology

Barbaros Çil, MD, FCIRES 

Department of Radiology, Koç University School of Medicine, İstanbul, Turkey

ORCID ID: 0000-0003-1079-0088

Bahri Üstünsöz, MD 

Department of Radiology, LSUHSC (Louisiana State University Health Science Center) School of Medicine, New Orleans, United States


ORCID ID: 0000-0003-4308-6708

James Milburn, MD

Department of Radiology, Ochsner Medical System, New Orleans, Louisiana, USA

ORCID ID: 0000-0003-3403-2628


Musculoskeletal Imaging

Zeynep Maraş Özdemir, MD 

Department of Radiology, İnönü University Faculty of Medicine, Malatya, Turkey

ORCID ID: 0000-0003-1085-8978

Neuroradiology

Gülgün Yılmaz Ovalı, MD 

Department of Radiology, Celal Bayar University Faculty of Medicine, Manisa, Turkey


ORCID ID: 0000-0001-8433-5622

Erkan Gökçe, MD 

Department of Radiology, Tokat Gaziosmanpaşa University Faculty of Medicine, Tokat, Turkey


ORCID ID: 0000-0003-3947-2972

Pediatric Radiology

Meltem Ceyhan Bilgici, MD 

Department of Radiology, 19 Mayıs University Faculty of Medicine, Samsun, Turkey

ORCID ID: 0000-0002-0133-0234

Evrin Özmen, MD 

Department of Radiology, Koç University Hospital, İstanbul, Turkey

ORCID ID: 0000-0003-3100-4197

Publication Coordinator

Şükrü Mehmet Ertürk, MD 

Department of Radiology, İstanbul University, İstanbul Faculty of Medicine, İstanbul, Turkey

ORCID ID: 0000-0003-4086-675X

Biostatistical Consultant

İlker Ercan, PhD 

Department of Biostatistics, Uludağ University School of Medicine, Bursa, Turkey

ORCID ID: 0000-0002-2382-290X

Publication Services

Galenos Publishing, İstanbul, TR

Past Editors

Editors in Chief

Mustafa Seçil, MD (2016-2022)

Nevzat Karabulut, MD (2011-2016)

Üstün Aydingöz, MD (2010-2011)

Okan Akhan, MD (2001-2010)

Ferhun Balkancı, MD (1999-2001)

Aytekin Besim, MD (1994-1999)*

* Dr. Aytekin Besim actually served as the General Coordinator. His work in this capacity, however, was in effect that of an Editor in Chief.

Editors

Ayşenur Cila, MD (2001-2002)

Suat Kemal Aytaç, MD (1997-2001)

Erhan Ilgıt, MD (1994-2001)

Okan Akhan, MD (1994-2001)

Ferhun Balkancı, MD (1994-2000)

Serdar Akyar, MD (1994-1997)

Section Editors

Section Editorship was established in 2002 at the tenure of Dr Okan Akhan, Editor in Chief.

Abdominal Imaging

Bengi Gürses, MD (2020-2023)

Mehmet Ruhi Onur, MD (2016-2022)

Bariş Türkbey, MD (2014-2020)

Mustafa N. Özmen, MD (2012-2018)

Murat Acar, MD (2015-2016)

Mustafa Seçil, MD (2011-2016)

Ahmet Tuncay Turgut, MD (2011)

Deniz Akata, MD (2007-2011)

Ayşe Erden, MD (2002-2011)

Okan Akhan, MD (2002-2010)

Hakan Özdemir, MD (2002-2010)

Artificial Intelligence and Informatics

Bariş Türkbey, MD (2020-2023)

Breast Imaging

Mustafa Erkin Arıbal, MD (2016-2023)

Sibel Kul (2015-2018)

Ayşenur Oktay, MD (2009-2014)

Ayşegül Özdemir, MD (2004-2009)

Cardiovascular Imaging

Uğur Bozlar, MD (2016-2023)

Muşturay Karçaaltıncaba, MD (2007-2010)

Mecit Kantarcı (2010-2016)

Chest Imaging

Nevzat Karabulut, MD (2010-2014)

Çetin Atasoy, MD (2007-2010)

Macit Arıyürek, MD (2002-2007)

Figen Demirkazık, MD, (2014-2018)

General Radiology

Ersin Öztürk, MD (2014-2017)

Utku Şenol, MD (2010-2013)

Oğuz Dicle, MD (2007-2010)

Interventional Radiology

Cüneyt Aytekin, MD (2016-2023)

Bora Peynircioğlu, MD (2012-2015)

Levent Oğuzkurt, MD (2011-2014)

Fatih Boyvat, MD (2007-2010)

İsmail Oran, MD (2015-2019)

Musculoskeletal Imaging

Hatice Tuba Sanal, MD (2016-2023)

Fatih Kantarcı, MD (2014-2016)

Ayşenur Oktay, MD (2011-2013)

Üstün Aydıngöz, MD (2002-2011)

Berna Dirim Mete (2016-2017)

Neuroradiology and Head & Neck Imaging

Kubilay Aydın, MD (2016-2023)

Nafi Aygün, MD (2016-2023)

Kader Karlı Oğuz, MD (2011-2015)

Süleyman Men, MD (2007-2013)

Muhteşem Ağıldere, MD (2002-2011)

Nuclear Medicine

A. Cahid Civelek, MD (2016-2023)

Oktay Sarı, MD (2015)

Akın Yıldız, MD (2011-2014)

Pediatric Radiology

Korgün Koral, MD (2016-2023)

Murat Kocaoğlu, MD (2016-2023)

Ensar Yekeler, MD (2014-2016)

Suat Fitöz, MD (2007-2013)

Diagnostic and Interventional Radiology (Diagn Interv Radiol) is a bimonthly periodical of the Turkish Society of Radiology and the content of the journal is available at <https://www.dirjournal.org/>. It is peer-reviewed and adheres to the highest ethical and editorial standards. The editors of the journal endorse the Editorial Policy Statements Approved by the Council of Science Editors Board of Directors (www.councilscienceeditors.org/services/draft_approved.cfm). The journal is in compliance with the Recommendations for the Conduct, Reporting, Editing and Publication of Scholarly Work in Medical Journals published by the International Committee of Medical Journal Editors (updated May 2022, www.icmje.org).

First ten volumes of Diagnostic and Interventional Radiology have been published in Turkish under the name of Tanısal ve Girişimsel Radyoloji (Index Medicus® abbreviation: Tani Girişim Radyol), the current title's exact Turkish translation.

Diagnostic and Interventional Radiology is an open access publication, and the journal's publication model is based on Budapest Open Access Initiative (BOAI) declaration. All published content is available online, free of charge at <https://www.dirjournal.org/>. Authors retain the copyright of their published work in Diagnostic and Interventional Radiology. The journal's content is licensed under a Creative Commons Attribution-NonCommercial (CC BY-NC) 4.0 International License which permits third parties to share and adapt the content for non-commercial purposes by giving the appropriate credit to the original work.

Diagnostic and Interventional Radiology is indexed in **Pubmed/Medline, Pubmed Central, Web of Science, TUBITAK ULAKBIM TR Index, HINARI, EMBASE, CINAHL, Scopus, Gale and CNKI.**

Contact Information

Diagnostic and Interventional Radiology Turkish Society of Radiology

Hoşdere Cad., Güzelkent Sok., Çankaya Evleri, F/2, 06540

Ankara, Turkey

E-mail: info@dirjournal.org

Phone: +90 (312) 442 36 53 Fax: +90 (312) 442 36 54

Publisher Contact

Address: Molla Gürani Mah. Kaçamak Sk.

No: 21/1 34093 İstanbul, Turkey

Phone: +90 (530) 177 30 97

E-mail: info@galenos.com.tr/yayin@galenos.com.tr

Web: www.galenos.com.tr Publisher Certificate Number: 14521

Online Publication Date: May 2023

EISSN 1305-3612

International scientific journal published bimonthly.



Instructions to Authors

Diagnostic and Interventional Radiology (Diagn Interv Radiol) is a medium for disseminating scientific information based on research, clinical experience, and observations pertaining to diagnostic and interventional radiology. The journal is the double-blind peer-reviewed, bimonthly, open-access publication organ of the Turkish Society of Radiology and its publication language is English. Diagnostic and Interventional Radiology is currently indexed by Science Citation Index Expanded, PubMed MEDLINE, PubMed Central, TUBITAK ULAKBIM TR Index, HINARI, EMBASE, CINAHL, Scopus, Gale and CNKI.

The journal is a medium for original articles, reviews, pictorial essays, technical notes related to all fields of diagnostic and interventional radiology.

The editorial and publication process of the Diagnostic and Interventional Radiology are shaped in accordance with the guidelines of the International Committee of Medical Journal Editors (ICMJE), World Association of Medical Editors (WAME), Council of Science Editors (CSE), Committee on Publication Ethics (COPE), European Association of Science Editors (EASE), and National Information Standards Organization (NISO). The journal is in conformity with the Principles of Transparency and Best Practice in Scholarly Publishing.

Authorship

Each individual listed as an author should fulfill the authorship criteria recommended by the International Committee of Medical Journal Editors (ICMJE - www.icmje.org). To be listed as an author, an individual should have made substantial contributions to all four categories established by the ICMJE: (a) conception and design, or acquisition of data, or analysis and interpretation of data, (b) drafting the article or revising it critically for important intellectual content, (c) final approval of the version to be published, and (d) agreement to be accountable for all aspects of the work in ensuring that questions related to the accuracy or integrity of any part of the work are appropriately investigated and resolved. Individuals who contributed to the preparation of the manuscript but do not fulfill the authorship criteria should be acknowledged in an acknowledgements section, which should be included in the title page of the manuscript. If the editorial board suspects a case of "gift authorship", the submission will be rejected without further review.

Ethical standards

For studies involving human or animal participants, the authors should indicate whether the procedures followed were in accordance with the ethical standards of the responsible committee on human and animal experimentation (institutional or regional) and with the Helsinki Declaration). Application or approval number/year of the study should also be provided. The editorial board will act in accordance with COPE guidelines if an ethical misconduct is suspected.

It is the authors' responsibility to carefully protect the patients' anonymity and to verify that any experimental investigation with human subjects reported in the submission was performed with informed consent and following all the guidelines for experimental investigation with human subjects required by the institution(s) with which all the authors are affiliated with. For photographs that may reveal the identity of the patients, signed releases of the patient or of his/her legal representative should be enclosed.

Prospective human studies require both an ethics committee approval and informed consent by participants. Retrospective studies require an ethics committee approval with waiver of informed consent. Authors may be required to document such approval.

All submissions are screened by a similarity detection software (iThenticate by CrossCheck). Manuscripts with an overall similarity index of greater than 20%, or duplication rate at or higher than 5% with a single source are returned back to authors without further evaluation along with the similarity report.

In the event of alleged or suspected research misconduct, e.g., plagiarism, citation manipulation, and data falsification/fabrication, the Editorial Board will follow and act in accordance with COPE guidelines.

Withdrawal Policy

Articles may be withdrawn under certain circumstances.

The article will be withdrawn if it;

- violates professional ethical codes,
- is subject to a legal dispute,
- has multiple submissions,
- includes fake claims of authorship, plagiarism, misleading data, and false data that may pose a severe health risk.

The editorial board will follow the principles set by COPE (Committee on Publication Ethics) in case of an article withdrawal.

Manuscript Preparation

The manuscripts should be prepared in accordance with ICMJE-Recommendations for the Conduct, Reporting, Editing, and Publication of Scholarly Work in Medical Journals (updated in May 2022 - <https://www.icmje.org/recommendations/>).

Original Investigations and Reviews should be presented in accordance with the following guidelines: randomized study – CONSORT, observational study – STROBE, study on diagnostic accuracy – STARD, systematic reviews and meta-analysis PRISMA, nonrandomized behavioral and public health intervention studies – TREND.

Diagnostic and Interventional Radiology will only evaluate manuscripts submitted via the journal's self-explanatory online manuscript submission and evaluation system available at mc04.manuscriptcentral.com/dir. Evaluation process of submitted manuscripts takes 4 weeks on average.

Manuscripts are evaluated and published on the understanding that they are original contributions, and do not contain data that have been published elsewhere or are under consideration by another journal. Authors are required to make a full statement at the time of submission about all prior reports and submissions that might be considered duplicate or redundant publication, and mention any previously published abstracts for meeting presentations that contain partial or similar material in the cover letter. They must reference any similar previous publications in the manuscript.

Authors must obtain written permission from the copyright owner to reproduce previously published figures, tables, or any other material in both print and electronic formats and present it during submission. The original source should be cited within the references and below the reprinted material.

Cover letter: A cover letter must be provided with all manuscripts. This letter may be used to emphasize the importance of the study. The authors should briefly state the existing knowledge relevant to the study and the contributions their study make to the existing knowledge. The correspondent author should also include a statement in the cover letter declaring that he/she accepts to undertake all the responsibility for authorship during the submission and review stages of the manuscript.

Instructions to Authors

Title page: A separate title page should be submitted with all manuscripts and should include the title of the manuscript, name(s), affiliation(s), and major degree(s) of the author(s). The name, address, telephone (including the mobile phone number) and fax numbers and e-mail address of the corresponding author should be clearly listed. Grant information and other sources of support should also be included. Individuals who contributed to the preparation of the manuscript but do not fulfill the authorship criteria should also be acknowledged in the title page. Manuscripts should not be signed by more than 6 authors unless they are multicenter or multidisciplinary studies.

Main document

Abstract: All submissions (except for Letters to the Editor) should be accompanied by an abstract limited to 400 words. A structured abstract is only required with original articles and it should include the following subheadings: PURPOSE, METHODS, RESULTS, CONCLUSION.

Main points: Each submission should be accompanied by 3 to 5 “main points”, which should emphasize the most striking results of the study and highlight the message that is intended to be conveyed to the readers. As these main points would be targeting radiology residents, experts and residents of other fields of medicine, as well as radiology experts, they should be kept as plain and simple as possible. These points should be constructed in a way that provides the readers with a general overview of the article and enables them to have a general idea about the article.

The main points should be listed at the end of the main text, above the reference list.

Example: Liu S, Xu X, Cheng Q, et al. Simple quantitative measurement based on DWI to objectively judge DWI-FLAIR mismatch in a canine stroke model. *Diagn Interv Radiol* 2015; 21:348–354.

- The relative diffusion-weighted imaging signal intensity (rDWI) of ischemic lesions might be helpful to identify the status of fluid attenuated inversion recovery (FLAIR) imaging in acute ischemic stroke.
- The relative apparent diffusion coefficient (rADC) value appears not useful to identify the status of FLAIR imaging in the acute period.
- Based on our embolic canine model, rDWI increased gradually in the acute period, while the rADC kept stable, which might explain why rDWI is helpful to identify the status of FLAIR imaging, while rADC is not.

Main text

Original Articles

Original articles should provide new information based on original research. The main text should be structured with Introduction, Methods, Results, and Discussion subheadings. The number of cited references should not exceed 50 and the main text should be limited to 4500 words. Number of tables included in an original article should be limited to 4 and the number of figures should be limited to 7 (or a total of 15 figure parts).

Introduction

State briefly the nature and purpose of the work, quoting the relevant literature.

Methods

Include the details of clinical and technical procedures.

Research ethics standards compliance

All manuscripts dealing with human subjects must contain a statement indicating that the study was approved by the Institutional Review Board or a comparable formal research ethics review committee. If none is present at your institution, there should be a statement that the research was performed according to the Declaration of Helsinki principles (www.wma.net/e/policy/b3.htm). There should also be a statement about whether informed consent was obtained from research subjects.

Results

Present these clearly, concisely, and without comment. Statistical analysis results should also be provided in this section to support conclusions when available.

Discussion

Explain your results and relate them to those of other authors; define their significance for clinical practice. Limitations, drawbacks, or shortcomings of the study should also be stated in the discussion section before the conclusion paragraph. In the last paragraph, a strong conclusion should be written.

Review Articles

Review articles are scientific analyses of recent developments on a specific topic as reported in the literature. No new information is described, and no opinions or personal experiences are expressed. Reviews include only the highlights on a subject. Main text should be limited to 4000 words and the number of cited references should not exceed 75. Number of tables included in a review article should be limited to 4 and the number of figures should be limited to 15 (or a total of 30 figure parts).

Pictorial Essay

This is a continuing medical education exercise with the teaching message in the figures and their legends. Text should include a brief abstract; there may be as many as 30 figure parts. No new information is included. The value of the paper turns on the quality of the illustrations. Authors can submit dynamic images (e.g. video files) or include supplemental image files for online presentation that further illustrate the educational purpose of the essay. Maximums: Pages of text – 4 (1,500 words); References – 20; Figures – 15 or total of 30 images; No table Main text should be limited to 1500 words and the number of cited references should not exceed 15.

Technical Notes

Technical note is a brief description of a specific technique, procedure, modification of a technique, or new equipment of interest to radiologists. It should include a brief introduction followed by Technique section for case reports or Methods section for case series, and Discussion is limited to the specific message, including the uses of the technique, equipment, or software. Literature reviews and lengthy descriptions of cases are not appropriate.

Main text should be limited to 1500 words and the number of cited references should not exceed 8. Number of tables included in a technical note should be limited to 4 and the number of figures should be limited to 3 (or a total of 6 figure parts).

Letter to the Editor and Reply

Letters to the Editor and Replies should offer objective and constructive criticism of published articles within last 6 months. Letters may also discuss matters of general interest to radiologists and may include images. Material being submitted or published elsewhere should not be duplicated in letters.

Main text should be limited to 500 words and the number of cited references should not exceed 6. No tables should be included and the number of figures should be limited to 2 (or a total of 4 figure parts).

Recommendations for Manuscripts:

| Type of manuscript | Word limit | Abstract word limit | Reference limit | Author limit | Table limit | Figure limit |
|--------------------|------------|---------------------|-----------------|--------------|-------------|--|
| Original Article | 4500 | 400 (Structured) | 50 | 6* | 4 | 7 or total of 15 images |
| Review Article | 4000 | 200 | 75 | 5 | 4 | 15 or total of 24 images |
| Pictorial Essay | 1500 | 400 | 20 | 5 | 1 | 15 figures or total of 30 figure parts |
| Technical Note | 1500 | 200 | 8 | 5 | 2 | 3 figures or total of 6 figure parts |
| Letter | 500 | N/A | 6 | 4 | No tables | 2 figures or total of 4 figure parts |

*Manuscripts should not be signed by more than 6 authors unless they are multicenter or multidisciplinary studies.

**Considering the specific condition of the manuscript, minor flexibilities may be applied for the recommendations upon the decision of Editor-in-Chief or the Section Editors.

References

Both in-text citations and the references must be prepared according to the AMA Manual of style.

While citing publications, preference should be given to the latest, most up-to-date publications. Authors are responsible for the accuracy of references. If an ahead-of-print publication is cited, the DOI number should be provided. Journal titles should be abbreviated in accordance with the journal abbreviations in Index Medicus/MEDLINE/PubMed. When there are six or fewer authors, all authors should be listed. If there are seven or more authors, the first three authors should be listed followed by "et al." In the main text of the manuscript, references should be cited in superscript after punctuation. The reference styles for different types of publications are presented in the following examples.

Journal Article: Economopoulos KJ, Brockmeier SF. Rotator cuff tears in overhead athletes. *Clin Sports Med.* 2012;31(4):675-692.

Book Section: Fikremariam D, Serafini M. Multidisciplinary approach to pain management. In: Vadivelu N, Urman RD, Hines RL, eds. *Essentials of Pain Management.* New York, NY: Springer New York; 2011:17-28.

Books with a Single Author: Patterson JW. *Weedon's Skin Pathology.* 4th ed. Churchill Livingstone; 2016.

Editor(s) as Author: Etzel RA, Balk SJ, eds. *Pediatric Environmental Health.* American Academy of Pediatrics; 2011.

Conference Proceedings: Morales M, Zhou X. Health practices of immigrant women: indigenous knowledge in an urban environment. Paper presented at: 78th Association for Information Science and Technology Annual Meeting; November 6-10; 2015; St Louis, MO. Accessed March 15, 2016. <https://www.asist.org/files/meetings/am15/proceedings/openpage15.html>

Thesis: Maiti N. Association Between Behaviours, Health Characteristics and Injuries Among Adolescents in the United States. Dissertation. Palo Alto University; 2010.

Online Journal Articles: Tamburini S, Shen N, Chih Wu H, Clemente KC. The microbiome in early life: implications for health outcomes. *Nat Med.* Published online July 7, 2016. doi:10.1038/nm4142

Epub Ahead of Print Articles: Websites: International Society for Infectious Diseases. ProMed-mail. Accessed February 10, 2016. <http://www.promedmail.org>

Tables

Tables should be included in the main document and should be presented after the reference list. Tables should be numbered consecutively in the order they are referred to within the main text. A descriptive title should be provided for all tables and the titles should be placed above the tables. Abbreviations used in the tables should be defined below by footnotes (even if they are defined within the main text). Tables should be created using the "insert table" command of the word processing software and they should be arranged clearly to provide an easy reading. Data presented in the tables should not be a repetition of the data presented within the main text but should be supporting the main text.

Figures and figure legends

Figures, graphics, and photographs should be submitted as separate files (in TIFF or JPEG format) through the submission system. The files should not be embedded in a Word document or the main document. When there are figure subunits, the subunits should not be merged to form a single image. Each subunit should be submitted separately through the submission system. Images should not be labelled (a, b, c, etc.) to indicate figure subunits. Thick and thin arrows, arrowheads, stars, asterisks, abbreviations and similar marks can be used on the images to support figure legends. Like the rest of the submission, the figures too should be blind. Any information within the images that may indicate the institution or the patient should be removed.

Figure legends should be listed at the end of the main document.

General

All acronyms and abbreviations used in the manuscript should be defined at first use, both in the abstract and in the main text. The abbreviation should be provided in parenthesis following the definition.

Statistical analysis should be performed in accordance with guidelines on reporting statistics in medical journals (Altman DG, Gore SM, Gardner MJ, Pocock SJ. Statistical guidelines for contributors to medical journals. *Br Med J* 1983; 7; 1489-1493.). Information on the statistical analysis process of the study should be provided within the main text.

When a drug, product, hardware, or software mentioned within the main text product information, the name and producer of the product should be provided in parenthesis in the following format: "Discovery St PET/CT scanner (GE Healthcare)."

Instructions to Authors

All references, tables, and figures should be referred to within the main text and they should be numbered consecutively in the order they are referred to within the main text.

Initial evaluation and Peer review process

Manuscripts submitted to Diagnostic and Interventional Radiology will first go through a technical evaluation process where the editorial office staff will ensure that the manuscript is prepared and submitted in accordance with the journal's guidelines. Submissions that do not conform to the journal's guidelines will be returned to the submitting author with technical correction requests.

All submissions are screened by a similarity detection software (iThenticate by CrossCheck), and those with an overall similarity index of greater than 20%, or duplication rate at or higher than 5% with a single source are returned back to authors without further evaluation along with the similarity report.

Manuscripts meeting the requirements mentioned in journal's guideline will go under the review process. The initial review will be performed by Editor-in-Chief and the Section Editor, which include the evaluation of the manuscript for its originality, importance of the findings, scientific merit, interest to readers and compliance with the policy of the journal in force. Manuscripts with insufficient priority for publication are not sent out for further review and rejected promptly at this level to allow the authors to submit their work elsewhere without delay.

Manuscripts that pass through the initial review are sent to peer review, which is performed in a blinded manner by at least two external and independent reviewers. During the review process, all original articles are evaluated by at least one senior consultant of statistics for proper handling and consistency of data, and use of correct statistical method. The Section Editor and / or Editor-in-Chief are the final authority in the decision-making process for all submissions.

Revisions

When submitting a revised version of a paper, the author must submit a detailed "Response to reviewers" that states point by point how each issue raised by the reviewers has been covered and where it can be found (each reviewer's comment followed by the author's reply and line numbers where the changes have been made) as well as an annotated copy, and a clear copy of the main document.

Revised manuscripts must be submitted within 30 days from the date of the decision letter. If the revised version of the manuscript is not submitted within the allocated time, the revision option will be automatically cancelled by the submission system. If the submitting author(s) believe that additional time is required, they should request an extension before the initial 30-day period is over.

Proofs and DOI Number

Accepted manuscripts are copy-edited for grammar, punctuation, and format by professional language editors. Following the copyediting process, the authors will be asked to review and approve the changes made during the

process. Authors will be contacted for a second time after the layout process and will be asked to review and approve the PDF proof of their article for publication. Once the production process of a manuscript is completed it is published online on the journal's webpage as an ahead-of-print publication before it is included in its scheduled issue.

Publication Fee Policy

Diagnostic and Interventional Radiology (DIR) applies an Article Processing Charge (APCs) for only accepted articles. No fees are requested from the authors during submission and evaluation process. All manuscripts must be submitted via Manuscript Manager.

An APC fee of and local taxes will be applied depending on the article type (see Table 1)

| | |
|------------------|---------|
| Review | \$ 1250 |
| Original Article | \$ 1000 |
| Pictorial Essay | \$ 750 |
| Technical Note | |

Table 1. Article Types and Fees

The APCs will be accepted through the link that will be sent to the corresponding author of each article via the online article system. In the next step, the authors will be receiving a receipt of their payment.

*Please note that the Article Processing Charge (APC) will not affect neither the editorial and peer-review process nor the priority of the manuscripts by no means. All submissions will be evaluated by the Editorial Board and the external reviewers in terms of scientific quality and ethical standards.

Refund Policy:

Returning the article to the author; Diagnostic and Interventional Radiology (DIR) will refund the submission fees with a coupon code if the article is returned to the author. Using this code, authors can use the submission fees of different articles without making a new payment.

Article Retraction:

Infringements of publication/research ethics, such as multiple submissions, bogus claims of authorship, plagiarism, and fraudulent use of data could lead to article retraction.

A retraction statement titled "Retraction: [article title]" must be signed by the authors and/or the editor. The original article is marked as retracted but a PDF version remains available to readers, and the retraction statement is linked to the original published paper.

Contents

ABDOMINAL IMAGING

- 414 Original Article.** Evaluation of abdominal computed tomography findings in patients with COVID-19: a multicenter study. Mehmet Ruhi Onur, Yakup Özbay, İlkey İdilman, Ali Devrim Karasmanoğlu, Selma Uysal Ramadan, Funda Barlık, Sonay Aydın, Hüseyin Odaman, Canan Altay, Işıl Başara Akın, Oğuz Dicle, Özgür Appak, Başak Gülpınar, Ayşe Erden, Sezer Kula, Ayşegül Gürsoy Çoruh, Diğdem Kuru Öz, Melahat Kul, Çağlar Uzun, Erdal Karavaş, Akın Levent, Hakan Artaş, Hasan Eryeşil, Onur Solmaz, Türkan Öztürk Kaygusuz, Mustafa Faraşat, Ahmet Burak Kale, Fatih Düzgün, Gökhan Pekindil, F. Demir Apaydın, Meltem Nass Duce, Yüksel Balcı, Kaan Esen, Ayşegül Sağır Kahraman, Leyla Karaca, Zeynep Maraş Özdemir, Bayram Kahraman, Mesude Tosun, Mehmet Selim Nural, İlkey Çamlıdağ, Mustafa Arda Onar, Kaan Ballı, Ezgi Güler, Mustafa Harman, Nevra Zehra Elmas, Cansu Öztürk, Özlem Güngör, Duygu Herek, Ahmet Baki Yağcı, Cengiz Erol, Mehmet Şeker, İrem İşlek, Yusuf Can, Serdar Aslan, M. Yasemin Karadeniz Bilgili, Alper Göncüoğlu, Hatice Keleş, Pelin Zeynep Bekin Sankaya, Barış Bakır, Merve Gülbiz Dağoğlu Kartal, Görkem Durak, Gülşen Yücel Oğuzdoğan, Fatih Alper, Ahmet Yalçın, Safiye Gürel, Bircan Alan, Elif Gündoğdu, Nevin Aydın, Ayşegül Cansu, Ceyda Civan Kuş, Elif Ofluoğlu Tuncer, Ferhat Can Pişkin, Hale Çolakoğlu Er, Bumin Değirmenci, Mustafa Nasuh Özmen, Mecit Kantarcı, Muşturay Karçaaltıncaba
- 428 Original Article.** Quantitative liver magnetic resonance imaging: correlation between conventional magnetic resonance imaging, laboratory values, and prognostic indices in Budd–Chiari syndrome. Ayşe Erden, Diğdem Kuru Öz, Mehmet Adıgüzel, Funda Seher Özalp Ateş
- 437 Original Article.** LAVA HyperSense and deep-learning reconstruction for near-isotropic (3D) enhanced magnetic resonance enterography in patients with Crohn's disease: utility in noise reduction and image quality improvement. Jung Hee Son, Yedaun Lee, Ho-Joon Lee, Joonsung Lee, Hyunwoong Kim, Marc R. Lebel
- 450 Original Article.** Comparison of quantitative volumetric analysis and linear measurement for predicting the survival of Barcelona Clinic Liver Cancer 0- and A stage hepatocellular carcinoma after radiofrequency ablation. Siwei Yang, Zhiyuan Zhang, Tianhao Su, Qiyang Chen, Haochen Wang, Long Jin

ARTIFICIAL INTELLIGENCE AND INFORMATICS

- 460 Original Article.** Prediction of carcinogenic human papillomavirus types in cervical cancer from multiparametric magnetic resonance images with machine learning-based radiomics models. Okan İnce, Emre Uysal, Görkem Durak, Suzan Önel, Binnur Dönmez Yılmaz, Şükrü Mehmet Ertürk, Hakan Önder

BREAST IMAGING

- 469 Original Article.** Combining primary tumor features derived from conventional and contrast-enhanced ultrasound facilitates the prediction of positive axillary lymph nodes in Breast Imaging Reporting and Data System category 4 malignant breast lesions. Yu Du, Chun-Bei Yi, Li-Wen Du, Hai-Yan Gong, Li-Jun Ling, Xin-Hua Ye, Min Zong, Cui-Ying Li

INTERVENTIONAL RADIOLOGY

- 478 Review.** Risk factors for air embolism following computed tomography-guided percutaneous transthoracic needle biopsy: a systematic review and meta-analysis. Hanfei Zhang, Shan Wang, Feiyang Zhong, Meiyang Liao
- 492 Original Article.** Technical success and associated economic implications of conventional re-entry devices in subintimal recanalization of femoro-popliteal chronic total occlusions. Katharina Rippel, Hannes Ruhnke, Bertram Jehs, Thomas Kroencke, Christian Scheurig-Muenkler
- 500 Review.** Inferior vena cava filter retrievals using advanced techniques: a systematic review. Nikhit Kethidi, Kyrollos Barsoum, Pratik A. Shukla, Abhishek Kumar
- 509 Original Article.** Outcomes of two types of iodine-125 seed delivery with metal stents in treating malignant biliary obstruction: a systematic review and meta-analysis. Xiaobo Fu, Han Qi, Zhenkang Qiu, Weiwei Jiang, Zixiong Chen, Fei Gao

Contents

520 **Original Article.** Inversed albumin-to-globulin ratio and underlying liver disease severity as a prognostic factor for survival in hepatocellular carcinoma patients undergoing transarterial chemoembolization. *Jinlong Li, Zhi Li, Shirui Hao, Jitao Wang, Wei Chen, Shoufang Dai, Zhenguo Hou, Borun Chen, Yewei Zhang, Dengxiang Liu*

529 **Original Article.** The reproducibility of interventional radiology randomized controlled trials and external validation of a classification system. *Assala Aslan, Christopher Stevens, Amro Saad Aldine, Ahmed Mamilly, Luis De Alba, Octavio Arevalo, Chaitanya Ahuja, Hugo H. Cuellar*

535 **Original Article.** Propensity score-matched analysis of six-month outcomes of paclitaxel-coated balloons combined with UltraScore balloons versus conventional scoring balloons for femoropopliteal lesions. *Takuya Haraguchi, Masanaga Tsujimoto, Ryo Otake, Yoshifumi Kashima, Katsuhiko Sato, Tsutomu Fujita*

542 **Original Article.** A comparison of lymphatic embolization and sclerotherapy in the management of iatrogenic abdominopelvic lymphoceles following oncological surgery. *Amgad M. Moussa, Ahmed K. Aly, Majid Maybody, Juan C. Camacho, Fourat Ridouani, Adrian J. Gonzalez-Aguirre, Ernesto Santos*

MODALITY-BASED (UC, CT, MRI, PET-CT) IMAGING

548 **Original Article.** The role of (¹⁸F)-fluoro-D-glucose positron emission tomography/computed tomography in the surveillance of abnormal myocardial energy metabolism and cardiac dysfunction in a rat model of cardiopulmonary resuscitation. *Liming Pan, Fan Zhang, Yingqi Ran, Lei Bi, Hongjun Jin, Lan Yao*

RADIOLOGY PHYSICS

555 **Original Article.** The effect of breast shielding outside the field of view on breast entrance surface dose in axial X-ray examinations: a phantom study. *Lauren Hurley, Yazeed Alashban, Salman Albeshan, Andrew England, Mark F. McEntee*

CHEST IMAGING

561 **Letter to the Editor.** Letter to the Editor: Indeterminate pulmonary subsolid nodules in patients with no history of cancer. *Furkan Ufuk*

ERRATUM

562 **Erratum**



Copyright@Author(s) - Available online at dirjournal.org.
Content of this journal is licensed under a Creative Commons
Attribution-NonCommercial 4.0 International License.

Evaluation of abdominal computed tomography findings in patients with COVID-19: a multicenter study

Mehmet Ruhi Onur , Yakup Özbay , İlkyay İdilman , Ali Devrim Karaosmanoğlu , Selma Uysal Ramadan , Funda Barlık , Sonay Aydın , Hüseyin Odaman , Canan Altay , Işıl Başara Akın , Oğuz Dicle , Özgür Appak , Başak Gülpınar , Ayşe Erden , Sezer Kula , Ayşegül Gürsoy Çoruh , Diğdem Kuru Öz , Melahat Kul , Çağlar Uzun , Erdal Karavaş , Akın Levent , Hakan Artaş , Hasan Eryeşil , Onur Solmaz , Türkkan Öztürk Kaygusuz , Mustafa Faraşat , Ahmet Burak Kale , Fatih Düzgün , Gökhan Pekindil , F. Demir Apaydın , Meltem Nass Duce , Yüksel Balcı , Kaan Esen , Ayşegül Sağır Kahraman , Leyla Karaca , Zeynep Maraş Özdemir , Bayram Kahraman , Mesude Tosun , Mehmet Selim Nural , İlkyay Çamlıdağ , Mustafa Arda Onar , Kaan Ballı , Ezgi Güler , Mustafa Harman , Nevra Zehra Elmas , Cansu Öztürk , Özlem Güngör , Duygu Herek , Ahmet Baki Yağcı , Cengiz Erol , Mehmet Şeker , İrem İşlek , Yusuf Can , Serdar Aslan , M. Yasemin Karadeniz Bilgili , Alper Göncüoğlu , Hatice Keleş , Pelin Zeynep Bekin Sarıkaya , Barış Bakır , Merve Gülbiz Dağoğlu Kartal , Görkem Durak , Gülşen Yücel Oğuzdoğan , Fatih Alper , Ahmet Yalçın , Safiye Gürel , Bircan Alan , Elif Gündoğdu , Nevin Aydın , Ayşegül Cansu , Ceyda Civan Kuş , Elif Ofluoğlu Tuncer , Ferhat Can Pişkin , Hale Çolakoğlu Er , Bumin Değirmenci , Mustafa Nasuh Özmen , Mecit Kantarcı , Muşturay Karçaaltıncaba

From the Department of Radiology (M.R.O. ✉ ruhionur@yahoo.com, Y.Ö., İ.İ., A.D.K., M.N.Ö., M.K. ✉ musturay@yahoo.com), Hacettepe University Faculty of Medicine, Ankara, Turkey; Clinic of Radiology (S.U.R., C.Ö., Ö.G.), University of Health Sciences Turkey, Ankara Atatürk Sanatorium Training and Research Hospital, Ankara, Turkey; Department of Radiology (F.B., H.O., C.A., İ.B.A., O.D.), Dokuz Eylül University Faculty of Medicine, İzmir, Turkey; Department of Radiology (S.A., E.K., A.L., Me.K.), Binali Yıldırım University Faculty of Medicine, Erzincan, Turkey; Department of Medical Microbiology (Ö.A.), Dokuz Eylül University Faculty of Medicine, İzmir, Turkey; Department of Radiology (B.G., A.E., S.K., A.G.Ç., D.K.Ö., Mel.K., Ç.U.), Ankara University Faculty of Medicine, Ankara, Turkey; Department of Radiology (H.A., H.E., O.S.), Fırat University Faculty of Medicine, Elazığ, Turkey; Department of Infectious Diseases and Clinical Microbiology (T.Ö.K.), Fırat University Faculty of Medicine, Elazığ, Turkey; Department of Radiology (M.F., A.B.K., F.D., G.P.), Celal Bayar University Faculty of Medicine, Manisa, Turkey; Department of Radiology (F.D.A., M.N.D., Y.B., K.E.), Mersin University Faculty of Medicine, Mersin, Turkey; Department of Radiology (A.S.K., L.K., Z.M.Ö., İnönü University Faculty of Medicine, Malatya, Turkey; Clinic of Radiology (B.K.), Specialist Doctor Bayram Kahraman Radiology Clinic, Malatya, Turkey; Department of Radiology (M.T.), Kocaeli University Faculty of Medicine, Kocaeli, Turkey; Department of Radiology (M.S.N., İ.Ç., M.A.O.), Ondokuz Mayıs University Faculty of Medicine, Samsun, Turkey; Department of Radiology (K.B., E.G., M.H., N.Z.E.), Ege University Faculty of Medicine, İzmir, Turkey; Department of Radiology (D.H., A.B.Y.), Pamukkale University Faculty of Medicine, Denizli, Turkey; Department of Radiology (C.E., M.Ş., İ.İ., Y.C.), Medipol University Faculty of Medicine, İstanbul, Turkey; Department of Radiology (Se.A.), Giresun University Faculty of Medicine, Giresun, Turkey; Department of Radiology (M.Y.K.B.), Lokman Hekim University Faculty of Medicine, Ankara, Turkey; Department of Radiology (A.G., P.Z.B.S.), Kırıkkale University Faculty of Medicine, Kırıkkale, Turkey; Department of Internal Medicine (H.K.), Kırıkkale University Faculty of Medicine, Kırıkkale, Turkey; Department of Radiology (B.B., M.G.D.K., G.D.), İstanbul University, İstanbul Faculty of Medicine, İstanbul, Turkey; Clinic of Radiology (G.Y.O.), University of Health Sciences Turkey, Başakşehir Çam and Sakura City Hospital, İstanbul, Turkey; Department of Radiology (F.A., A.Y.), Atatürk University Faculty of Medicine, Erzurum, Turkey; Department of Radiology (S.G., B.A.), Bolu Abant İzzet Baysal University Faculty of Medicine, Bolu, Turkey; Department of Radiology (E.G., N.A.), Eskişehir Osmangazi University Faculty of Medicine, Eskişehir, Turkey; Department of Radiology (A.C.), Karadeniz Technical University Faculty of Medicine, Trabzon, Turkey; Clinic of Radiology (C.C.K.), Marmara University Training and Research Hospital, İstanbul, Turkey; Clinic of Radiology (E.O.T.), University of Health Sciences Turkey, Sultan 2. Abdulhamid Han Training and Research Hospital, İstanbul, Turkey; Department of Radiology (F.C.P.), Çukurova University Faculty of Medicine, Adana, Turkey; Department of Radiology (H.Ç.), Ufuk University Faculty of Medicine, Ankara, Turkey; Clinic of Radiology (B.D.), Antalya ASV Life Hospital, Antalya, Turkey.

Received 09 April 2022; revision requested 10 May 2022; last revision received 23 June 2022; accepted 13 July 2022.



Epub: 16.01.2023

Publication date: 30.05.2023

DOI: 10.4274/dir.2022.221575

You may cite this article as: Onur MR, Özbay Y, İdilman İ, et al. Evaluation of abdominal computed tomography findings in patients with COVID-19: a multicenter study. *Diagn Interv Radiol.* 2023;29(3):414-427.

PURPOSE

To evaluate the frequency of abdominal computed tomography (CT) findings in patients with coronavirus disease-2019 (COVID-19) and interrogate the relationship between abdominal CT findings and patient demographic features, clinical findings, and laboratory test results as well as the CT atherosclerosis score in the abdominal aorta.

METHODS

This study was designed as a multicenter retrospective study. The abdominal CT findings of 1,181 patients with positive abdominal symptoms from 26 tertiary medical centers with a positive polymerase chain-reaction test for severe acute respiratory syndrome coronavirus 2 were reviewed. The frequency of ischemic and non-ischemic CT findings as well as the association between CT findings, clinical features, and abdominal aortic calcific atherosclerosis score (AA-CAS) were recorded.

RESULTS

Ischemic and non-ischemic abdominal CT findings were detected in 240 (20.3%) and 328 (27.7%) patients, respectively. In 147 patients (12.4%), intra-abdominal malignancy was present. The most frequent ischemic abdominal CT findings were bowel wall thickening ($n = 120$; 10.2%) and perivascular infiltration ($n = 40$; 3.4%). As for non-ischemic findings, colitis ($n = 91$; 7.7%) and small bowel inflammation ($n = 73$; 6.2%) constituted the most frequent disease processes. The duration of hospital stay was found to be higher in patients with abdominal CT findings than in patients without any positive findings (13.8 ± 13 vs. 10.4 ± 12.8 days, $P < 0.001$). The frequency of abdominal CT findings was significantly higher in patients who did not survive the infection than in patients who were discharged after recovery (41.7% vs. 27.4%, $P < 0.001$). Increased AA-CAS was found to be associated with a higher risk of ischemic conditions in abdominal CT examinations.

CONCLUSION

Abdominal symptoms in patients with COVID-19 are usually associated with positive CT findings. The presence of ischemic findings on CT correlates with poor COVID-19 outcomes. A high AA-CAS is associated with abdominal ischemic findings in patients with COVID-19.

KEYWORDS

COVID-19, abdomen, computed tomography, abdominal aorta, arteriosclerosis

Since the first appearance of severe acute respiratory syndrome-coronavirus 2 (SARS-CoV-2) toward the end of 2019, global scientific interest in the clinical progress and course of patients with this infection has grown rapidly. The disease is typically characterized by pneumonia and severe respiratory distress. Imaging features, both typical and atypical, of coronavirus disease-2019 (COVID-19) pneumonia have been described in detail in several papers.^{1,2} Cough, shortness of breath, fever, myalgia, and generalized fatigue have been frequently observed as the dominant clinical features of infection.

However, with the relentless spread of the disease and rapid increase in the number of patients worldwide, the abdominal, cardiac, neurologic, and musculoskeletal symptoms of these patients have also become clinically recognized.³⁻⁶ With all these newly detected symptoms, the medical community identified the multisystemic disease underlying the virus, even in the relatively early stages of the pandemic.

The multisystemic nature of the COVID-19 virus is mostly attributed to its ability to attach to angiotensin-converting enzyme 2 (ACE-2) receptors in the body. Since ACE-2 receptors are widely disseminated in the body, including in the lungs, vascular endothelium, small intestine, colon, spleen, liver, and kidney, the systemic dissemination of the virus appears to be inevitable.⁷ The virus may exert both cytotoxic and thrombotic effects on the abdominal vascular endothelium, causing widespread vascular dysfunction in the abdomen. Thromboembolism in the abdominal aorta or its branches may occur as early as 12–13 days after the start of the infection.⁸

Since the start of the pandemic, the abdominal manifestations of COVID-19 have been described in detail in several excellent papers.⁹⁻¹¹ However, there is still a gap that needs to be investigated in assessing the relationship between abdominal imaging findings and disease outcomes. In this study,

we aimed to investigate the frequency of abdominal computed tomography (CT) findings in patients with symptomatic COVID-19 and outline the association between abdominal CT findings and patients' clinical progress and outcomes.

Methods

This multicenter retrospective study was conducted in compliance with the Health Insurance Portability and Accountability Act and the Declaration of Helsinki. Approvals were obtained from both the local institutional board and the board of the Ministry of Health. Informed consent was waived due to the retrospective nature of the study (Erzincan Binali Yildirim University Ethics Committee 04/01, Health Ministry of Turkey Ethics Committee 2021-02-23T11_43_57).

Patients: Cohort selection

After reviewing the electronic and written medical charts of the contributing centers, a total of 1,564 patients who had confirmed COVID-19 infection and abdominal symptoms and who had undergone abdominal CT between April and December 2020 were assessed as eligible for this study. The inclusion criteria of the study were as follows: adult patients (>18 years) with a positive real-time reverse transcriptase-polymerase chain-reaction (RT-PCR) test result using throat swabs

Main points

- The coronavirus disease-2019 (COVID-19) virus may give rise to a wide variety of ischemic and non-ischemic abnormalities in the abdomen.
- Patients with COVID-19 and abdominal computed tomography (CT) findings had a longer hospital stay and higher mortality rate than patients without positive findings.
- The detection of positive abdominal CT findings reveals a positive correlation with extended hospital stay and increased mortality.
- Patients with an active COVID-19 infection and high abdominal aortic calcific atherosclerosis score appear to demonstrate more ischemic findings in CT.

for COVID-19 who had undergone abdominal CT studies for various clinical symptoms within 15 days following the positive PCR test. The exclusion criteria were as follows: patients who had undergone abdominal CT 15 days before or after the PCR test; patients who tested as COVID-19 (+) when they were hospitalized following an investigation into abdominal pathologies; patients with insufficient anamnesis and symptom history and with poor CT image quality; patients <18 years; and patients with no positive PCR test. In total, 1,181 adult patients from 26 tertiary medical centers were enrolled in this study (Figure 1).

Clinical data collection

Patient electronic medical records were used to obtain the following data: (1) demographic characteristics of patients (age, sex, smoking habit, and comorbidities); (2) clinical information including the date of the COVID-19 diagnosis; (3) abdominal symptoms including diarrhea, anorexia, nausea, vomiting, epigastric pain, upper gastrointestinal (GI) bleeding, (4) duration of hospital stay, and disease outcome; and (5) laboratory results [PCR and liver function tests such as aspartate transaminase (AST), alanine transaminase (ALT), indirect and direct bilirubin, and D-dimer values]. The COVID-19 period was assessed in terms of days in the hospital and disease outcome (recovery or death). Comorbidities were defined as diabetes mellitus (DM), hypertension (HT), heart failure (HF), chronic renal failure (CRF), and intra-abdominal malignancy.

Computed tomography image acquisition

Abdominal CT scans of patients were performed without ($n = 436$, 36.9%) and with ($n = 745$, 63.1%) intravenous (IV) contrast administration. Contrast-enhanced CT studies were multiphasic in 116 (9.3%) patients. The scanned area was between the dome of the diaphragm and the ischial tuberosity. Contrast-enhanced single-phase CT scans were obtained through the acquisition of abdominopelvic images in the portal venous phase after an IV injection of 80–120 mL of iodinated contrast media (300–350 mg of iodine per mL) with a flow rate of 3–5 mL/sec. The IV contrast injection was followed by a 40 mL saline chaser at the same injection rate as the IV contrast. All CT studies were conducted using various multi-detector CT scanners from different vendors (16–392 detector rows). The CT acquisition parameters varied within a narrow range in accordance with the local institutional protocols: tube voltage: 100–130 kV, tube current: automatic tube current modulation used, collimation thickness: 0.5–2 mm, tube rotation time: 0.5–1 s. Reconstructions were applied to obtain axial images with a section thickness of 2–5 mm and coronal and sagittal images with a section thickness of 3 mm. Multiphasic CT images were obtained using the same CT acquisition parameters as well as an unenhanced phase, and contrast-enhanced images were obtained at arterial and venous phases.

Computed tomography data collection and image analysis

All the evaluated abdominal CT scans were performed within 15 days of confirmation of COVID-19 and were interpreted by radiologists experienced in abdominal radiology. Initially, the dates of the CT scans and information about the IV contrast administration as well as the CT study phases were recorded. Abdominal CT scans were reviewed to detect the presence and frequency of positive ischemic and non-ischemic findings. Positive findings for an ischemic abdominal process were defined as follows: acute mesenteric artery embolism, acute thrombosis of the superior mesenteric vein, non-occlusive mesenteric ischemia (NOMI), perivascular infiltration, bowel wall thickening (single-wall thickness >3 mm in distended loops and >5 mm in collapsed loops), pneumatosis intestinalis, bowel wall necrosis, gas in the portal venous system, hollow viscus perforation, and renal ischemia.

Non-ischemic abdominal CT findings included small and large bowel inflammation, acute pyelonephritis, acute cholecystitis, acute pancreatitis, acute diverticulitis, acute appendicitis, bowel obstruction, and intra-abdominal malignancy.

To investigate the relationship between the severity of atherosclerotic changes in the abdominal aorta and abdominal CT findings, the atherosclerosis score of the abdominal aorta was determined through a quantitative assessment of calcific atheroma plaques in the abdominal aorta. The final scores were designated as the abdominal aortic calcific

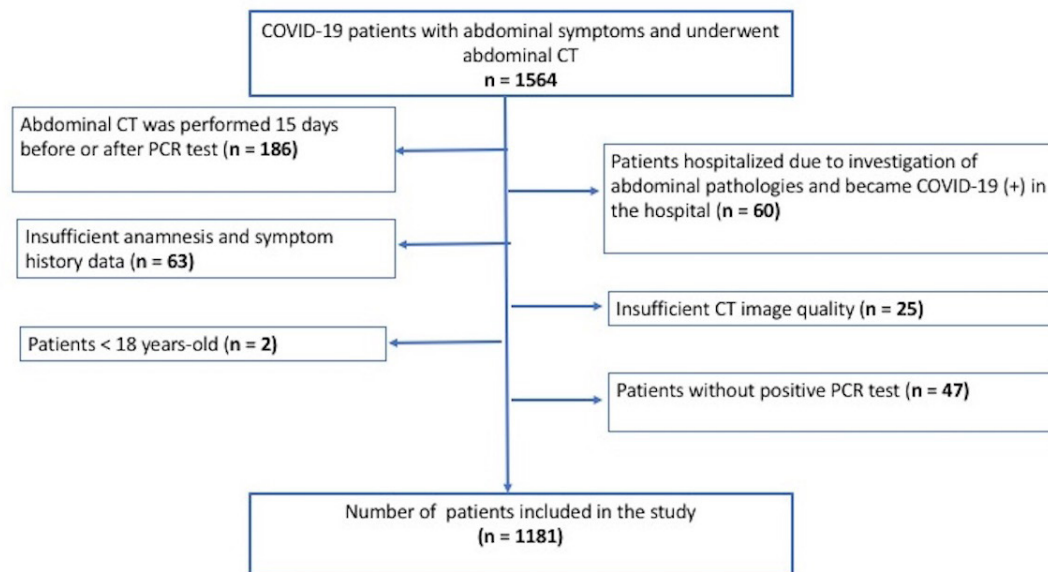


Figure 1. Flowchart of patient selection for the study cohorts. CT, computed tomography; COVID-19, coronavirus disease-2019; PCR, polymerase chain-reaction.

atherosclerosis score (AA-CAS). The AA-CAS was calculated according to a method described in previous reports (Figure 2).¹² The measurements were taken from the aortic wall at a level between the L1 and L4 vertebral bodies. On the sagittal CT images, the affected abdominal aorta length with reciprocal vertebra was scored between 0 and 3 as 0 (no calcification), 1 (1/3 of vertebral length affected), 2 (2/3 of vertebral length affected), and 3 (whole vertebral length affected). An axial CT image of the abdominal aorta at each vertebral level was divided into four quadrants. The total area of the abdominal aorta circle affected by calcific plaques was classified as 1, 2, 3, and 4. For each level, a single-level score was determined by multiplying the scores measured in axial and sagittal image planes. The AA-CAS for each vertebral level ranged from 0 to 12, with a minimum of 0 and a maximum score of 48. The final AA-CAS was concluded as the sum of the AA-CAS from each lumbar vertebral level.

Statistical analysis

All study data were collected from the contributing centers and combined into a single data sheet. Categorical data were presented as numbers (percentages), with continuous variables with normal distribution expressed as mean \pm standard deviation and continuous variables with non-normal distribution as median and 95% confidence interval (95% CI). Categorical data were compared using Pearson's chi-square test or Fisher's exact test, and continuous variables were compared using the Student's t-test or Mann-Whitney U test, depending on the distribution of data. A two-tailed *P* value <0.05 was considered statistically significant. The significance level was established as $\alpha = 0.05$. All statistical analyses were performed using SPSS v22.0 software.

Results

Patient characteristics

The study included 1,181 patients (male/female: 632/549) with a mean age of $61.6 \pm$

17.4 years, ranging from 18 to 97 years. Of all the patients, 274 (23.2%) were smokers, and 597 (50.5%) were non-smokers. Smoking history was obtained from 310 (26.3%) patients. The most common comorbidities of patients were as follows: HT ($n = 483$, 40.89%), DM ($n = 338$, 28.6%), HF ($n = 129$, 10.92%), CRF ($n = 78$, 6.6%), a combination of comorbidities including DM, HT, HF, and CRF ($n = 306$, 25.91%), and intra-abdominal malignancy ($n = 147$, 12.4%). The most frequent symptoms were as follows: epigastric pain (33.3%), nausea (31.2%), vomiting (23.8%), diarrhea (11.9%), and upper GI bleeding (2.6%). The median duration of hospital stay was 8 days (0–142 days). The median and 95% CI of the median for AST, ALT, D-dimer, and the direct and indirect bilirubin levels of the cohort was 30 U/L (29–31), 24 U/L (22–25), 1.03 (0.96–1.10), 0.21 mg/dL (0.20–0.23), and 0.38 mg/dl (0.36–0.40), respectively. A total of 874 patients (74%) were discharged following recovery, whereas 268 patients (22.7%) died secondary to COVID-19 infection. The disease outcome could not be determined from electronic medical charts in 39 (3.3%) patients.

Computed tomography findings

The ischemic and non-ischemic abdominal CT findings detected after a review of CT scans are summarized in Table 1 (Figure 3). The frequency of overall ischemic and non-ischemic CT findings was 20.3% ($n = 240$) and 27.7% ($n = 328$), respectively. The most frequent ischemic abdominal CT findings were bowel wall thickening ($n = 120$, 10.2%) (Figure 4) and perivascular infiltration ($n = 40$, 3.4%) (Figure 5), whereas the most frequent non-ischemic abdominal CT findings were large bowel inflammation, with a frequency of 7.7% ($n = 91$), and small bowel inflammation, with a frequency of 6.2% ($n =$

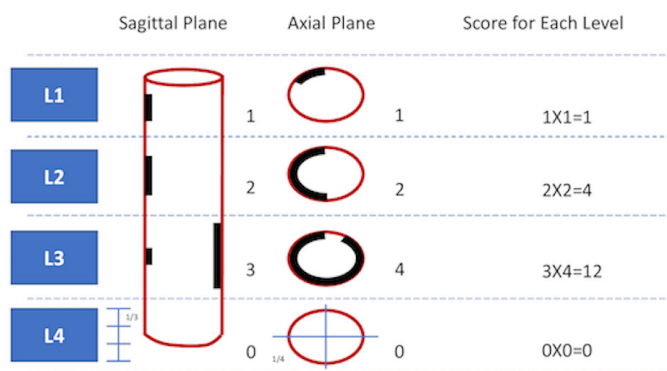


Figure 2. Abdominal aorta calcification score measurement method in the abdominal aorta.

| Table 1. Ischemic and non-ischemic abdominal computed tomography findings in patients with COVID-19 | | | |
|---|------------|------------------------------------|------------|
| Ischemic abdominal CT findings | n (%) | Non-ischemic abdominal CT findings | n (%) |
| Acute superior mesenteric artery embolism | 10 (0.8) | Small bowel inflammation | 73 (6.2) |
| Acute mesenteric vein thrombosis | 6 (0.5) | Large bowel inflammation | 91 (7.7) |
| NOMI | 8 (0.7) | Intestinal obstruction | 42 (3.5) |
| Bowel wall thickening | 120 (10.2) | Acute cholecystitis | 36 (3.04) |
| Perivascular infiltration | 40 (3.4) | Acute pancreatitis | 38 (3.21) |
| Pneumatosis intestinalis | 12 (1) | Acute diverticulitis | 8 (0.67) |
| Portal venous gas | 9 (0.8) | Acute appendicitis | 18 (1.5) |
| Intestinal necrosis | 8 (0.7) | Acute pyelonephritis | 22 (1.9) |
| Hollow viscus perforation | 17 (1.4) | Intra-abdominal malignancy | 147 (12.4) |
| Renal ischemia | 10 (0.8) | - | - |
| Total | 240 | - | 475 |

NOMI, non-occlusive mesenteric ischemia; CT, computed tomography; COVID-19, coronavirus disease-2019.

73). The mean AA-CAS was calculated as 10.6 ± 12.1 (ranging from 0 to 48).

No significant difference in sex distribution was detected in relation to the presence of abdominal CT findings and AA-CAS.

Overall abdominal CT findings was not significantly different between smokers and non-smokers ($P = 0.49$). The most common underlying comorbidity related to positive abdominal CT findings was HT (40.89%), and a significant association was found be-

tween the presenting symptoms of diarrhea, anorexia, nausea, vomiting, epigastric pain, and upper GI bleeding and the presence of abdominal CT findings. The associations between each abdominal symptom and the presence of abdominal CT findings are summarized in Table 2. A significant association was identified between all the presenting symptoms and the presence of abdominal CT findings. The investigation into the relationship between abdominal symptoms and ischemic CT findings revealed that patients with diarrhea ($P = 0.001$) and nausea ($P = 0.027$) had significantly greater bowel wall thickening than patients without these symptoms. Mesenteric vein thrombosis ($P = 0.031$) (Figure 6), perivascular infiltration ($P = 0.008$), bowel wall thickening ($P < 0.001$), pneumatosis intestinalis ($P = 0.002$), and portal venous gas ($P < 0.001$) were found to be significantly more frequent in patients with anorexia, and patients with vomiting were significantly more prone to present with the ischemic findings of bowel wall thickening ($P = 0.010$), portal venous gas ($P = 0.025$), and renal ischemia ($P = 0.008$)



Figure 3. Axial unenhanced computed tomography image demonstrating a diffusely swollen pancreas and peripancreatic fat inflammation (arrows) consistent with edematous pancreatitis in a 65-year-old male patient with coronavirus disease-2019 who presented with abdominal pain.

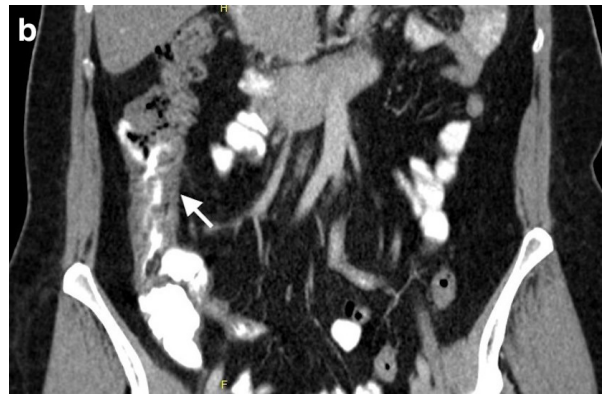


Figure 4. A 39-year-old woman with coronavirus disease-2019 presented with abdominal pain. Axial (a) and coronal (b) computed tomography images demonstrating the thickening of the ascending colon wall (arrows).

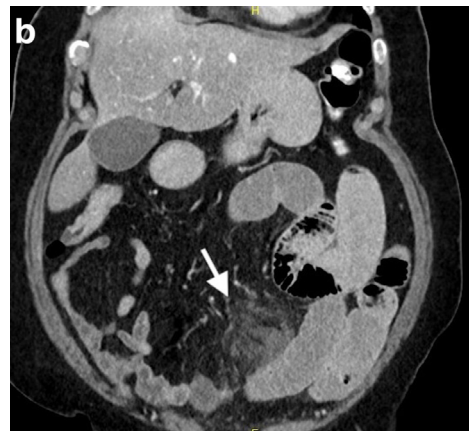
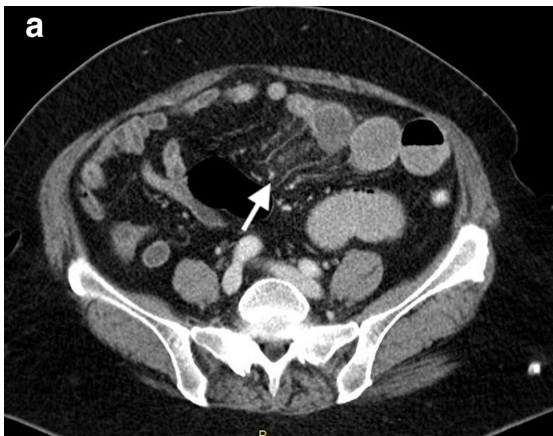


Figure 5. Axial (a) and coronal (b) contrast-enhanced computed tomography images of a 70-year-old female patient with coronavirus disease-2019 revealing perivascular infiltration, mesenteric stranding (arrows), and bowel dilatation, which indicates bowel ischemia. The patient underwent segmental bowel resection surgery because of the progressive deterioration in her clinical status.

Table 2. Association between abdominal symptoms and abdominal computed tomography findings of patients

| Symptoms | Presence of abdominal CT finding n (%) | P |
|---------------------------------|--|--------|
| Diarrhea (+) (-) | 54/131 (41.2) 306/1.050 (29.1) | 0.005 |
| Anorexia (+) (-) | 96/192 (50) 264/989 (26.7) | <0.001 |
| Nausea (+) (-) | 145/368 (39.4) 215/813 (26.4) | <0.001 |
| Vomiting (+) (-) | 120/281 (42.7) 240/900 (26.7) | <0.001 |
| Epigastric pain (+) (-) | 174/393 (44.3) 186/788 (23.6) | <0.001 |
| Upper GI bleeding (+) (-) | 17/31 (54.8) 343/1.150 (29.8) | 0.003 |

CT, computed tomography; GI, gastrointestinal.

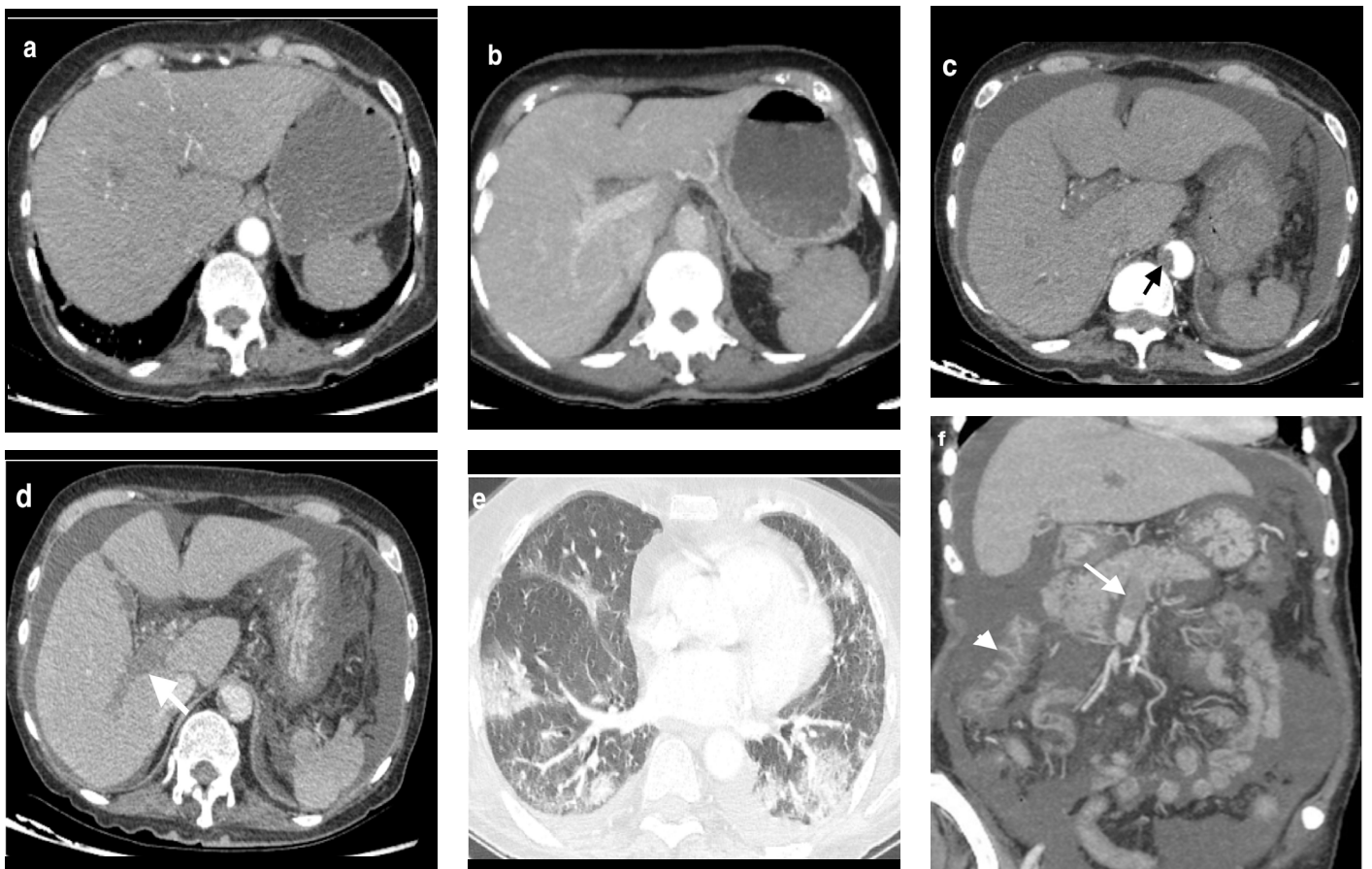


Figure 6. Acute superior mesenteric vein thrombosis. A 74-year-old woman with acute myeloid leukemia who presented with shortness of breath, abdominal pain, and diarrhea was diagnosed with coronavirus disease-2019. Axial contrast-enhanced abdominal computed tomography (CT) images (**a**, **b**) obtained 1 month before hospital admission reveal patent abdominal aorta and right portal vein. Axial arterial phase contrast-enhanced CT image obtained on hospital admission (**c**) demonstrating an acute thrombus in the abdominal aorta (arrow). Axial portal venous phase contrast-enhanced CT image (**d**) reveals an acute thrombus in the right portal vein (arrow). Axial chest CT image (**e**) demonstrating bilateral ground-glass opacities in both lungs. Coronal-reformatted abdominal CT image (**f**) showing an acute thrombus in the superior mesenteric vein (arrow). Note the bowel wall thickening of the ascending colon (arrowhead) and ascites.

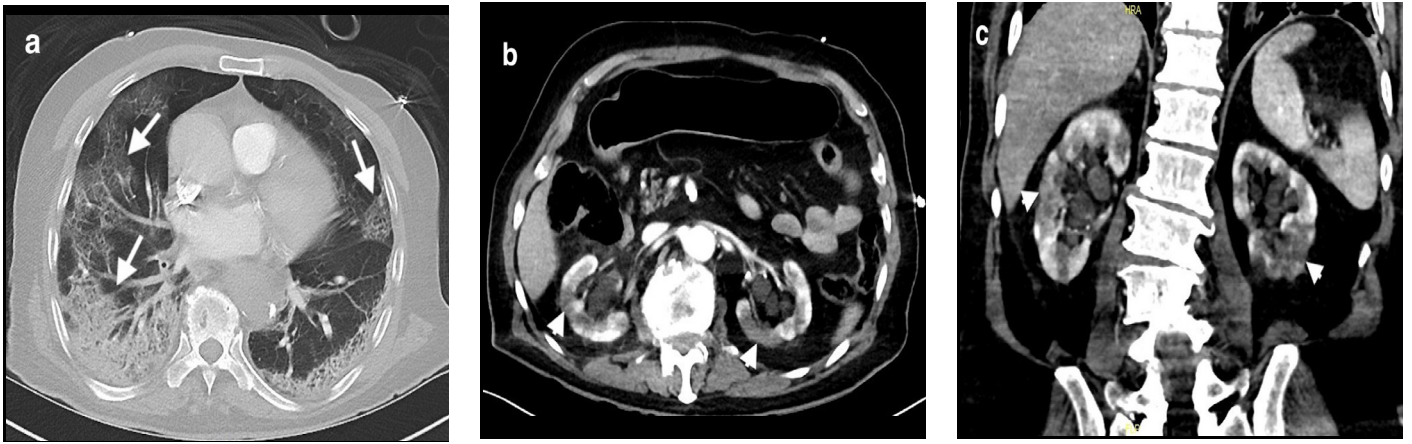


Figure 7. Renal infarct. (a) Axial chest computed tomography (CT) image showing bilateral ground-glass density and consolidations (arrows) in the peripheral portions of the lungs. Axial (b) and coronal (c) CT images reveal focal unenhanced areas (arrowheads) in the renal parenchyma, representing renal infarcts.

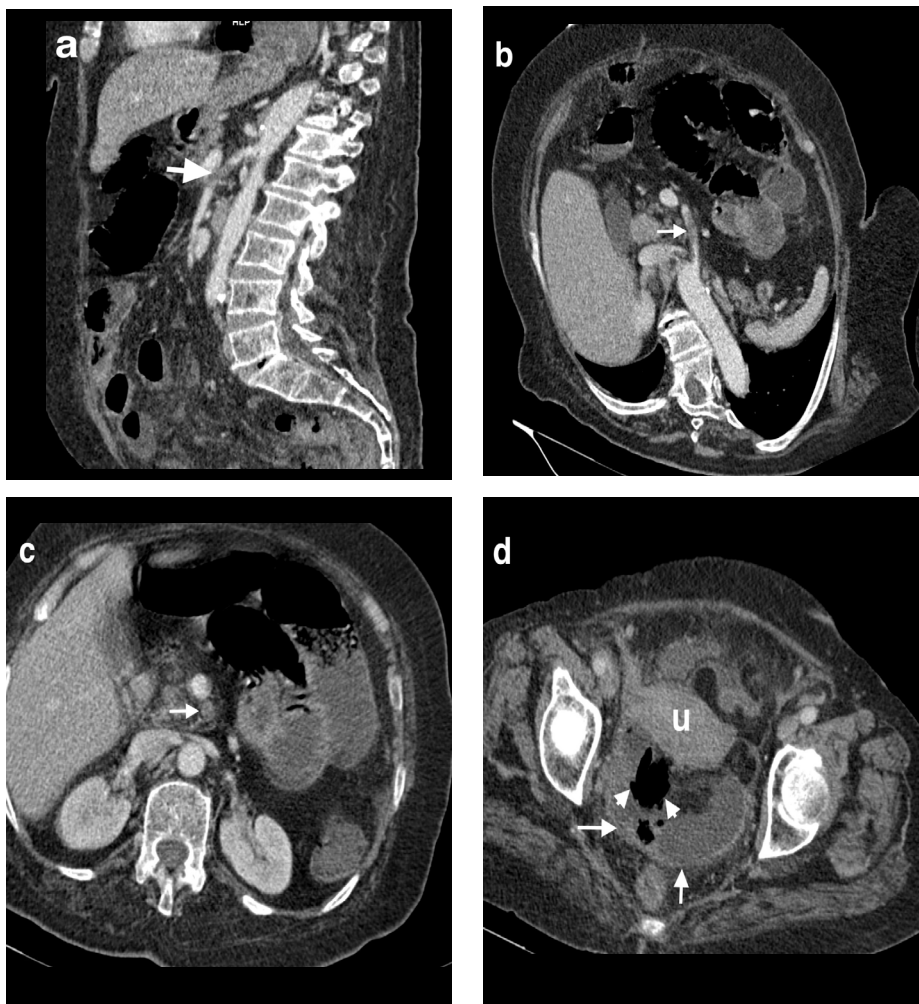


Figure 8. Acute superior mesenteric artery embolism. Sagittal (a), oblique reformatted (b), and axial (c) computed tomography (CT) images of a 61-year-old woman with sudden onset abdominal pain 6 days after the diagnosis of coronavirus disease-2019, revealing a hypodense filling defect (arrows) in the superior mesenteric artery lumen. Axial CT image (d) of the same patient at the pelvic level revealing hypo-enhancing segments of the ileum wall (arrows) and free intra-abdominal gas (arrowheads) behind the uterus (u), suggesting bowel wall ischemia and resultant perforation.

(Figure 7). Epigastric pain was significantly related to perivascular infiltration ($P = 0.001$), bowel wall thickening ($P < 0.001$), pneumatosis intestinalis ($P = 0.012$), portal venous gas ($P < 0.001$), hollow viscus perforation ($P = 0.024$), and renal ischemia ($P = 0.005$). Upper GI bleeding was found to be significantly related to perivascular infiltration ($P = 0.003$).

The association between the laboratory test results and abdominal CT findings is summarized in Supplementary Table 1. Liver function tests and D-dimer values were increased synchronously only in patients with acute mesenteric artery embolism (Figure 8), and D-dimer values were significantly increased in patients with the ischemic CT findings of perivascular infiltration, pneumatosis intestinalis, and bowel wall necrosis and non-ischemic CT findings of acute pancreatitis, diverticulitis, and appendicitis. No specific laboratory test parameters changed significantly with the ischemic CT findings.

The median and 95% CI of the median AA-CAS values in all patients was 5,^{4,6} and AA-CAS were not significantly different between sexes ($P = 0.399$). However, not surprisingly, smokers had a significantly higher AA-CAS than non-smokers [11 (1-22) vs. 4 (0-15), $P < 0.001$]. The AA-CAS was significantly higher in patients with ischemic abdominal CT findings ($n = 143$) than in those with non-ischemic abdominal CT findings ($n = 218$) [6 (0-26) vs. 4 (0-16), $P = 0.011$]. The association between the AA-CAS and ischemic abdominal CT findings is summarized in Table 3. The AA-CAS were significantly higher in patients with pneumatosis intestinalis, bowel wall necrosis, portal venous gas, acute cholecystitis, and acute appendicitis. However, the reliability of the statistical tests investigating the association between the AA-CAS and these subgroups was not high because of the low

number of patients in the subgroups, with the exception of intra-abdominal malignancy.

An association was detected between the presence of abdominal CT findings and COVID-19 outcomes. The duration of hospital stay was higher in patients with abdominal CT findings than in those without any positive findings (13.8 ± 13 vs. 10.4 ± 12.8 days, $P < 0.001$). The frequency of abdominal CT findings was significantly higher in patients who could not survive the infection than in patients discharged after recovery (41.7% vs. 27.4%, $P < 0.001$). Patients with NOMI, perivascular infiltration, bowel wall thickening, pneumatosis intestinalis, bowel wall necrosis, portal venous gas, renal ischemia, small bowel inflammation, colitis, acute appendicitis, and intra-abdominal malignancy had a significantly higher death rate than those without these findings (Table 4).

Discussion

This multicenter study revealed that a wide range of abdominal CT findings, including ischemic and non-ischemic abnormalities, may be encountered in patients with COVID-19. The most common underlying comorbidity related to positive abdominal CT findings was HT. Patients with COVID-19 with diarrhea, anorexia, nausea, vomiting, epigastric pain, and upper GI bleeding had high positive abdominal CT finding rates. The presence of abdominal CT findings was related to poor patient outcomes with an increased duration of hospital stay and higher mortality rate. Patients with a high AA-CAS had significantly greater ischemic abdominal CT findings than patients with a low AA-CAS.

The involvement of abdominal viscera in COVID-19 has been reported previously. The presence of abdominal symptoms in COVID-19 is not unexpected because SARS-CoV-2 ribonucleic acid has been isolated in the duodenal wall and feces of patients as well as in wastewater.¹³ The fecal positivity rate in COVID-19 infection is reported to be between 40% and 48%, whereas meta-analyses have demonstrated a prevalence of GI symptoms of 4%–12%.^{14,15} In addition to intestines, abdominal viscera also seem to be affected by COVID-19 because of the high surface expression of the ACE-2 receptor in vasculature. Besides GI findings, biliary tract, abdominal vasculature, and pancreas involvement with related radiological abnormalities have been reported.^{8,16–18}

In our study, we evaluated the abdominal CT findings as ischemic and non-ischemic CT findings. The high frequency of ischemic abdominal findings (20.3%) in this study was attributed to the abdominal vascular involvement of COVID-19. Perivascular infiltration on CT represents the previously reported perivascular inflammation and perivascular infiltration of T-cells that contribute to endothelial damage.^{9,19} In our study, the most common ischemic abdominal CT findings in patients with COVID-19 were bowel wall thickening (10.2%) and perivascular infiltration (3.4%), representing well-known non-specific CT findings in ischemic bowel disease. Bowel wall thickening has been highlighted as the most common CT finding in patients with COVID-19 with acute abdominal pain.²⁰ Perivascular infiltration, the second most commonly detected abdominal CT finding in our study, may represent endothelial damage in COVID-19 resulting from direct viral effects as well as perivascular inflammation.²¹ Due to its common presence in patients with COVID-19 and abdominal symptoms in our study, perivascular infiltration should alert radiologists to ischemic bowel disease when reviewing abdominal CT scans in these patients. In the non-ischemic group, large bowel inflammation (7.7%) and small bowel inflammation (6.2%) constituted the most frequent imaging finding except intra-abdominal malignancy. These results are consistent with previous reports that noted bowel wall thickening as the most common CT feature in patients with COVID-19 presenting with abdominal pain.^{1,2} Kidneys are the second most commonly targeted abdominal organ regarding ischemic events in COVID-19. Endothelial damage and the resulting occlusion in the microvasculature of the renal parenchyma have been demonstrated in the postmortem renal histopathologic analysis of patients who died from COVID-19.²² Renal parenchymal perfusion defects have also been identified in dual-energy CT scans.²³ For all these reasons, we paid special attention to kidneys when evaluating ischemic abdominal abnormalities. In addition to other examinations, we investigated the association between comorbidities and abdominal CT findings. Although it was impossible to verify a direct association between comorbidity subgroups and the overall CT findings, we noticed that HT was the comorbidity most commonly associated with abdominal CT findings. This finding may be related to HT being the most frequently observed comorbid disease since the beginning of the pandemic.

The most frequent respiratory symptoms in patients with COVID-19 are sore throat, shortness of breath, and cough. However, medical practitioners must also be vigilant to check for symptoms related to other organs. The presence of these symptoms in patients with COVID-19 should alert clinicians to the potential involvement of abdominal organs. Each abdominal symptom included in our study was found to be significantly associated with the presence of abdominal CT findings, which emphasizes the importance of increased vigilance toward the abdominal symptoms of COVID-19.

In our study, we also investigated the association between each abdominal symptom and the CT findings. The results revealed that abdominal symptoms may be associated with a wide range of CT findings, limiting the prediction of specific abdominal abnormalities to abdominal symptoms only. Although an association between abdominal symptoms and the presence of abdominal CT findings was found in our study, previous reports noted that fluid-filled colon and bowel wall thickening might be detected on CT in two-thirds of patients with COVID-19 who reported no abdominal symptoms.⁷ Other reports have highlighted the absence of any CT findings in patients with COVID-19 with acute abdominal pain.²⁴ The discrepancy between our results and those of some other reports may be due to a lack of standardization in the severity of symptoms.

When reviewing the CT images of patients, laboratory test results should be considered. Therefore, in our study, we investigated the laboratory test results of patients and their potential association with the abdominal CT findings. Elevated liver function tests are a common finding in the course of COVID-19.^{8,25,26} In this study, no specific laboratory test was found to predict ischemic abdominal CT findings. Acute mesenteric artery embolism was the only clinical entity in patients with COVID-19 that was synchronously elevated by liver enzymes. The D-dimer value, which was identified in previous reports as a helpful indicator for ischemic and thromboembolic changes in patients with COVID-19, was not detected as a specific laboratory test for ischemic abdominal changes in our study because a significant increase in D-dimer values was detected in both ischemic (perivascular infiltration, pneumatosis intestinalis, and bowel wall necrosis) and non-ischemic CT findings, including acute pancreatitis, diverticulitis, and appendicitis.⁷

Table 3. Association between abdominal aorta calcification score and abdominal computed tomography finding subgroups

| Abdominal CT findings | Median AA-CAS (95% CI for median) | <i>P</i> |
|---|--------------------------------------|----------|
| Acute mesenteric artery embolism (+) (-) | 22 (0–41.7) 5 (4–6) | 0.153 |
| Acute mesenteric vein thrombosis (+) (-) | 0 (0–29.4) 5 (4–6) | 0.109 |
| Non-occlusive mesenteric ischemia (+) (-) | 6.5 (3–11.5) 4 (4–6) | 0.505 |
| Perivascular infiltration (+) (-) | 4.5 (2.3–10) 5 (4–6) | 0.858 |
| Bowel wall thickening (+) (-) | 5 (3–10) 5 (4–6) | 0.506 |
| Pneumatosis intestinalis (+) (-) | 32 (9.3–44.4) 5 (4–6) | <0.001 |
| Bowel wall necrosis (+) (-) | 20 (4–45.5) 5 (4–6) | 0.013 |
| Portal venous gas (+) (-) | 31 (13.3–45.8) 5 (4–6) | <0.001 |
| Perforation (+) (-) | 3 (0–19.8) 5 (4–7) | 0.629 |
| Renal ischemia (+) (-) | 14.5 (0.95–45.1) 4 (4–6) | 0.099 |
| Small bowel inflammation (+) (-) | 4 (2–8.3) 5 (5–6.1) | 0.568 |
| Colitis (+) (-) | 6 (3–10) 5 (4–6) | 0.726 |
| Acute pyelonephritis (+) (-) | 16.5 (0–32.1) 5 (4–6) | 0.160 |
| Acute cholecystitis (+) (-) | 13 (8.6–19.3) 5 (3–6) | 0.013 |
| Acute pancreatitis (+) (-) | 8.5 (1–14) 5 (4–6) | 0.869 |
| Acute diverticulitis (+) (-) | 9 (0–23.9) 5 (4–6) | 0.941 |
| Acute appendicitis (+) (-) | 0 (0–1) 5 (5–7) | <0.001 |
| Bowel obstruction (+) (-) | 5 (3–10) 5 (4–6) | 0.756 |
| Intra-abdominal malignancy (+) (-) | 4 (2.1–6) 5 (4–7) | 0.079 |

AA-CAS, abdominal aorta calcification score; CT, computed tomography; CI, confidence interval.

Table 4. Association between abdominal computed tomography findings and outcomes of patients with COVID-19

| Abdominal CT finding | Incidence of death n (%) | P |
|---|----------------------------------|---------|
| Acute mesenteric artery embolism (+) (-) | 4/10 (40) 221/985 (22.4) | 0.305** |
| Acute mesenteric vein thrombosis (+) (-) | 1/6 (16.7) 223/1.014 (22) | 1** |
| Non-occlusive mesenteric ischemia (+) (-) | 16/38 (42.1) 233/1.063 (21.9) | 0.030* |
| Perivascular infiltration (+) (-) | 19/40 (47.5) 242/1.087 (22.3) | 0.007* |
| Bowel wall thickening (+) (-) | 48/120 (40) 219/1.059 (20.7) | <0.001* |
| Pneumatosis intestinalis (+) (-) | 11/12 (91.7) 255/1.165 (21.9) | <0.001* |
| Intestinal necrosis (+) (-) | 8/8 (100) 256/1.159 (22.1) | <0.001* |
| Portal venous gas (+) (-) | 7/9 (77.8) 260/1.171 (22.2) | 0.008* |
| Perforation (+) (-) | 6/17 (35.3) 262/1.164 (22.5) | 0.345* |
| Renal ischemia (+) (-) | 6/10 (60) 236/1.087 (21.7) | 0.042* |
| Small bowel inflammation (+) (-) | 26/73 (35.6) 242/1.108 (21.8) | 0.039* |
| Colitis (+) (-) | 39/91 (42.9) 229/1.089 (21) | <0.001* |
| Pyelonephritis (+) (-) | 6/22 (27.3) 257/1.146 (22.4) | 0.674* |
| Acute cholecystitis (+) (-) | 11/36 (30.6) 257/1.145 (22.4) | 0.378* |
| Acute pancreatitis (+) (-) | 13/38 (34.2) 255/1.142 (22.3) | 0.191* |
| Acute diverticulitis (+) (-) | 1/8 (12.5) 267/1.173 (22.8) | 1** |
| Acute appendicitis (+) (-) | 51/147 (34.7) 217/1.034 (21) | 0.005* |
| Intestinal obstruction (+) (-) | 13/42 (31) 255/1.139 (22.4) | 0.316* |
| Intra-abdominal malignancy (+) (-) | 51/147 (34.7) 217/1.034 (21) | 0.005* |
| Overall CT finding (+) (-) | 112/360 (31.1) 156/821 (19) | <0.001* |

Pearson's chi-square test* or Fisher's exact test** were used. CT, computed tomography; COVID-19, coronavirus disease-2019.

In our study, we categorized CT findings into ischemic and non-ischemic subgroups because it has been established that thrombophilia is induced in COVID-19, with resulting micro and macrovascular complications.²⁷ The presence of abdominal CT findings in patients with COVID-19 was found to be associated with poorer disease outcomes. We found that NOMI, perivascular infiltration, bowel wall thickening, pneumatosis intestinalis, bowel wall necrosis, portal venous gas, renal ischemia, small and large bowel inflammation, acute appendicitis, and intra-abdominal malignancy were significantly associated with mortality in patients with COVID-19. Our results indicate that ischemic CT findings in patients with COVID-19 are related to unfavorable clinical outcomes. Intestinal pneumatosis suggests severe intestinal ischemia, which may be because COVID-19 is associated with coagulopathy.⁷ Pneumatosis intestinalis has also been reported in patients with viral enteritis.²⁸

Since the beginning of the pandemic, vascular involvement and subsequent vascular abnormalities have been attributed to the tropism of SARS-CoV-2 to the vascular system.⁹ In this study, we also investigated whether patients with chronic vascular disease might be more vulnerable to vessel involvement during COVID-19. To test this hypothesis, we used the AA-CAS, which represents calcific atherosclerotic changes in the abdominal aorta, as a parameter. We assumed that the AA-CAS may also reflect the atherosclerotic disease burden in the abdominal visceral vessels. The AA-CAS measurement in this multicenter study was performed using a previously defined method, and the positive correlation between AA-CAS, age, and smoking suggested that the AA-CAS measurement in different centers in this multicenter study was conducted using the same approach, yielding similar results in patients with the same atherosclerotic changes in the abdominal aorta. A significantly higher AA-CAS in the ischemic abdominal CT finding group than in the non-ischemic group in our study suggests that patients with COVID-19 with a high AA-CAS are more likely to have a greater number of ischemic complications related to the disease.

The presence of abdominal CT findings in patients with COVID-19 was found to be related to poor outcomes and a significantly increased duration of hospital stay and mortality rate. The ischemic and non-ischemic abdominal CT findings revealed in this study represent serious clinical entities such as bowel ischemia, hollow viscus perforation,

inflammation, and renal ischemia, which can potentially extend a patient's hospital stay and increase the risk of death. The absence of a significant association with severe abdominal CT findings such as mesenteric artery embolism (n = 4) and mesenteric vein thrombosis (n = 1) in our study was attributed to the low number of patients in these groups, which limited the predictability of statistical tests. Investigations into the effect of abdominal involvement on COVID-19 outcomes indicated that patients with COVID-19 with GI symptoms tended to have a relatively long course between symptom onset and viral clearance. They also required longer medical care and hospital stay than patients with respiratory symptoms only.^{29,30}

Our study has several limitations. First, it is a retrospective multicenter study, and extracted medical records of patients from different centers, including clinical information, which may vary in terms of institutional treatment approaches. Despite this limitation, our study's multicenter design may be more representative of the general patient population than that of single-center studies. Second, the majority of CT findings were not verified using traditional gold standards such as surgical or pathological correlation. The relationship between abdominal CT findings and COVID-19 should be assessed with caution because GI involvement in the virus, in particular, depends on a theory suggesting that the virus enters the GI walls through the ACE-2 receptors. An assessment of abdominal CT images in 26 different medical centers increases heterogeneity in the evaluation of CT findings because of radiologists' different opinions on the same findings. To overcome this limitation, the CT assessment criteria in the abdominal CT findings, such as intestinal wall thickening and perivascular infiltration, were well defined and were relayed to the contributors at the initial phase of the study. Third, most studies have investigated the presence of ground-glass opacities at the base of the lungs as an ancillary finding in patients with COVID-19.⁷ In our study, we did not assess this finding. Finally, although fecal COVID-19 testing to confirm GI involvement is not a standard clinical approach, the absence of fecal COVID-19 testing in our cohort may be another limitation that is worth mentioning.

In conclusion, ischemic and non-ischemic abdominal CT findings may be encountered in patients with COVID-19. The presence of abdominal CT findings is related to a long hospital stay and unfavorable clinical outcomes. Moreover, infected patients with a

high AA-CAS are more likely to have ischemic abdominal findings.

Conflict of interest disclosure

The authors declared no conflicts of interest.

References

1. Kapoor MC. Respiratory and cardiovascular effects of COVID-19 infection and their management. *J Anaesthesiol Clin Pharmacol*. 2020;36(Suppl 1):S21-S28. [\[CrossRef\]](#)
2. Leng L, Cao R, Ma J, et al. Pathological features of COVID-19-associated lung injury: a preliminary proteomics report based on clinical samples. *Signal Transduct Target Ther*. 2020;5(1):240. [\[CrossRef\]](#)
3. Kanne JP, Bai H, Bernheim A, et al. COVID-19 imaging: what we know now and what remains unknown. *Radiology*. 2021;299(3):E262-E279. [\[CrossRef\]](#)
4. Poyiadji N, Shahin G, Noujaim D, Stone M, Patel S, Griffith B. COVID-19-associated acute hemorrhagic necrotizing encephalopathy: imaging features. *Radiology*. 2020;296(2):E119-E120. [\[CrossRef\]](#)
5. Catapano F, Marchitelli L, Cundari G, et al. Role of advanced imaging in COVID-19 cardiovascular complications. *Insights Imaging*. 2021;12(1):28. [\[CrossRef\]](#)
6. Ramani SL, Samet J, Franz CK, et al. Musculoskeletal involvement of COVID-19: review of imaging. *Skeletal Radiol*. 2021;50(9):1763-1773. [\[CrossRef\]](#)
7. Tirumani SH, Rahnamai-Azar AA, Pierce JD, et al. Are asymptomatic gastrointestinal findings on imaging more common in COVID-19 infection? Study to determine frequency of abdominal findings of COVID-19 infection in patients with and without abdominal symptoms and in patients with chest-only CT scans. *Abdom Radiol (NY)*. 2021;46(6):2407-2414. [\[CrossRef\]](#)
8. Bhayana R, Som A, Li MD, et al. Abdominal imaging findings in COVID-19: preliminary observations. *Radiology*. 2020;297(1):E207-E215. [\[CrossRef\]](#)
9. Boraschi P, Giugliano L, Mercogliano G, Donati F, Romano S, Neri E. Abdominal and gastrointestinal manifestations in COVID-19 patients: is imaging useful? *World J Gastroenterol*. 2021;27(26):4143-4159. [\[CrossRef\]](#)
10. Lui K, Wilson MP, Low G. Abdominal imaging findings in patients with SARS-CoV-2 infection: a scoping review. *Abdom Radiol (NY)*. 2021;46(3):1249-1255. [\[CrossRef\]](#)
11. Barkmeier DT, Stein EB, Bojicic K, et al. Abdominal CT in COVID-19 patients: incidence, indications, and findings. *Abdom Radiol (NY)*. 2021;46(3):1256-1262. [\[CrossRef\]](#)

12. Ozturk C, Gungor O, Kaplanoglu V, Kasikci M, Ramadan SU. Relationship between abdominal aortic calcification, abdominal adiposity, and liver density. *J Coll Physicians Surg Pak*. 2020;30(12):1245-1250. [\[CrossRef\]](#)
13. Safari S, Keyvani H, Malekpour Alamdari N, et al. Abdominal surgery in patients with COVID-19: detection of SARS-CoV-2 in abdominal and adipose tissues. *Ann Surg*. 2020;272(3):e253-e256. [\[CrossRef\]](#)
14. Cheung KS, Hung IFN, Chan PPY, et al. Gastrointestinal Manifestations of SARS-CoV-2 infection and virus load in fecal samples from a Hong Kong cohort: systematic review and meta-analysis. *Gastroenterology*. 2020;159(1):81-95. [\[CrossRef\]](#)
15. Parasa S, Desai M, Thoguluva Chandrasekar V, et al. Prevalence of gastrointestinal symptoms and fecal viral shedding in patients with coronavirus disease 2019: a systematic review and meta-analysis. *JAMA Netw Open*. 2020;3(6):e2011335. [\[CrossRef\]](#)
16. Shiralkar K, Chinapuvvula N, Ocazionez D. Cross-sectional abdominal imaging findings in patients with COVID-19. *Cureus*. 2020;12(8):e9538. [\[CrossRef\]](#)
17. Dane B, Smereka P, Wain R, Kim D, S Katz D. Hypercoagulability in patients with coronavirus disease (COVID-19): identification of arterial and venous thromboembolism in the abdomen, pelvis, and lower extremities. *AJR Am J Roentgenol*. 2021;216(1):104-105. [\[CrossRef\]](#)
18. Mazrouei SSA, Saeed GA, Al Helali AA. COVID-19-associated acute pancreatitis: a rare cause of acute abdomen. *Radiol Case Rep*. 2020;15(9):1601-1603. [\[CrossRef\]](#)
19. Ackermann M, Verleden SE, Kuehnel M, et al. Pulmonary vascular endothelialitis, thrombosis, and angiogenesis in Covid-19. *N Engl J Med*. 2020;383(2):120-128. [\[CrossRef\]](#)
20. Goldberg-Stein S, Fink A, Paroder V, Kobi M, Yee J, Chernyak V. Abdominopelvic CT findings in patients with novel coronavirus disease 2019 (COVID-19). *Abdom Radiol (NY)*. 2020;45(9):2613-2623. [\[CrossRef\]](#)
21. Varga Z, Flammer AJ, Steiger P, et al. Endothelial cell infection and endotheliitis in COVID-19. *Lancet*. 2020;395(10234):1417-1418. [\[CrossRef\]](#)
22. Su H, Yang M, Wan C, et al. Renal histopathological analysis of 26 postmortem findings of patients with COVID-19 in China. *Kidney Int*. 2020;98(1):219-227. [\[CrossRef\]](#)
23. Idilman IS, Telli Dizman G, Ardali Duzgun S, et al. Lung and kidney perfusion deficits diagnosed by dual-energy computed tomography in patients with COVID-19-related systemic microangiopathy. *Eur Radiol*. 2021;31(2):1090-1099. [\[CrossRef\]](#)
24. Gahide G, Frandon J, Vendrell JF. COVID-19 patients presenting with afebrile acute abdominal pain. *Clin Med (Lond)*. 2020;20(3):e4-e6. [\[CrossRef\]](#)
25. Taya M, Paroder V, Redelman-Sidi G, et al. Abdominal imaging findings on computed tomography in patients acutely infected with SARS-CoV-2: what are the findings? *Emerg Radiol*. 2021;28(6):1087-1096. [\[CrossRef\]](#)
26. Xiao F, Tang M, Zheng X, Liu Y, Li X, Shan H. Evidence for gastrointestinal infection of SARS-CoV-2. *Gastroenterology*. 2020;158(6):1831-1833.e3. [\[CrossRef\]](#)
27. Keshavarz P, Rafiee F, Kavandi H, Goudarzi S, Heidari F, Gholamrezanezhad A. Ischemic gastrointestinal complications of COVID-19: a systematic review on imaging presentation. *Clin Imaging*. 2021;73:86-95. [\[CrossRef\]](#)
28. Ho LM, Paulson EK, Thompson WM. Pneumatosis intestinalis in the adult: benign to life-threatening causes. *AJR Am J Roentgenol*. 2007;188(6):1604-1613. [\[CrossRef\]](#)
29. Han C, Duan C, Zhang S, et al. Digestive symptoms in COVID-19 patients with mild disease severity: clinical presentation, stool viral RNA testing, and outcomes. *Am J Gastroenterol*. 2020;115(6):916-923. [\[CrossRef\]](#)
30. Pan L, Mu M, Yang P, et al. Clinical characteristics of COVID-19 patients with digestive symptoms in Hubei, China: a descriptive, cross-sectional, multicenter study. *Am J Gastroenterol*. 2020;115(5):766-773. [\[CrossRef\]](#)

| Supplementary Table 1. Table showing differences in age and laboratory tests according to specific CT findings in study cohort | | | | | | |
|--|---------------|--------------------------------|--------------------------------|---------------------------------|----------------------------------|-----------------------------|
| | Age ± SD | Median AST (95% CI for median) | Median ALT (95% CI for median) | D. bilirubin 95% CI for median) | I. bilirubin (95% CI for median) | D-dimer (95% CI for median) |
| Acute mesenteric artery embolism | | | | | | |
| Present (n = 10) | 61.60 ± 24.09 | 67.5 (21.9–183.6) | 94 (25.5–163.9) | 1.67 (0.3–8.67) | 1.55 (0.46–3.59) | 33.5 (6.9–3491.9) |
| Absent (n = 1009) | 61.20 ± 17.46 | 30 (29–32) | 24 (22–25.1) | 0.21 (0.20–0.23) | 0.39 (0.36–0.40) | 159.5 (99.3–254.3) |
| <i>P</i> | 0.739 | 0.045* | 0.004* | 0.001* | 0.002* | 0.505 |
| Acute mesenteric vein thrombus | | | | | | |
| Present (n = 6) | 57.83 ± 15.51 | 93 (15.4–247.1) | 39.5 (18.3–240.6) | 1 (1–1) | 0.24 (0.16–0.30) | 444.0 (7–1231.9) |
| Absent (n = 1014) | 61.21 ± 17.55 | 30 (29–32) | 24 (23–26) | 0.21 (0.20–0.23) | 0.39 (0.36–0.40) | 156.5 (89.3–250.3) |
| <i>P</i> | 0.563 | 0.079 | 0.091 | 0.007* | <0.001* | 0.557 |
| Non-occlusive mesenteric ischemia | | | | | | |
| Present (n = 8) | 70.50 ± 15.82 | 32 (27–48.7) | 30 (20.3–36.8) | 0.30 (0.22–0.60) | 0.60 (0.42–0.85) | 420 (19.9–1253.1) |
| Absent (n = 1093) | 61.39 ± 17.54 | 30 (29–31) | 24 (22–25) | 0.20 (0.20–0.23) | 0.38 (0.35–0.40) | 170.5 (115.3–290.4) |
| <i>P</i> | 0.114 | 0.222 | 0.455 | 0.035* | <0.001* | 0.148 |
| Perivascular infiltration | | | | | | |
| Present (n = 40) | 59.52 ± 18.25 | 34 (28.3–52.7) | 27 (17.9–35.7) | 0.30 (0.22–0.57) | 0.62 (0.40–1) | 793 (94.5–1429.1) |
| Absent (n = 1087) | 61.59 ± 17.55 | 30 (29–31) | 24 (22.4–25) | 0.21 (0.20–0.23) | 0.38 (0.36–0.40) | 168.3 (112.3–277.7) |
| <i>P</i> | 0.451 | 0.102 | 0.976 | 0.057 | <0.001* | 0.023* |
| Bowel wall thickening | | | | | | |
| Present (n = 120) | 60.53 ± 18.76 | 31 (28.3–37.6) | 24 (19–30) | 0.25 (0.19–0.37) | 0.48 (0.42–0.54) | 243.5 (22.7–604.5) |
| Absent (n = 1059) | 61.68 ± 17.29 | 30 (28–31) | 24 (22–25) | 0.21 (0.20–0.23) | 0.36 (0.34–0.39) | 254 (167–379) |
| <i>P</i> | 0.649 | 0.370 | 0.518 | 0.032* | <0.001* | 0.378 |
| Pneumatosis intestinalis | | | | | | |
| Present (n = 12) | 71.83 ± 11.77 | 105 (50.3–205.7) | 52.5 (27.2–227.6) | 0.66 (0.30–1.49) | 0.70 (0.28–1.84) | 1469 (24.1–5002.3) |
| Absent (n = 1165) | 61.52 ± 17.43 | 30 (28–31) | 24 (22–25) | 0.21 (0.20–0.23) | 0.38 (0.35–0.40) | 254 (166.3–370.7) |
| <i>P</i> | 0.043* | <0.001* | 0.021* | 0.001* | 0.056 | 0.043* |
| Bowel wall necrosis | | | | | | |
| Present (n = 8) | 69.37 ± 11.62 | 165.5 (44.9–450.5) | 54.5 (23.3–403.4) | 0.43 (0.19–13.5) | 0.65 (0.22–6.47) | 1577.5 (165.2–7677.8) |
| Absent (n = 1159) | 61.57 ± 1.49 | 30 (28–31) | 24 (22–25) | 0.21 (0.20–0.23) | 0.37 (0.35–0.39) | 245.5 (157.8–350) |
| <i>P</i> | 0.234 | 0.002* | 0.034* | 0.034* | 0.267 | 0.025* |
| Air in the portal venous system | | | | | | |
| Present (n = 9) | 76.77 ± 12.86 | 99 (34.4–206) | 45 (27.3–231.7) | 0.66 (0.20–8.75) | 0.77 (0.28–10.1) | 200 (16.5–6688.1) |
| Absent (n = 1171) | 61.46 ± 17.43 | 30 (28–31) | 24 (22–25) | 0.21 (0.20–0.23) | 0.38 (0.36–0.40) | 254 (167–370) |
| <i>P</i> | 0.007* | 0.003* | 0.033* | 0.022* | 0.051 | 0.253 |
| Perforation | | | | | | |
| Present (n = 17) | 60.17 ± 17.62 | 40 (29–63.7) | 34 (21.5–49.6) | 0.19 (0.11–0.57) | 0.35 (0.17–0.63) | 7 (2.5–1397.4) |
| Absent (n = 1164) | 61.61 ± 17.44 | 30 (28–31) | 24 (22–25) | 0.21 (0.20–0.23) | 0.38 (0.36–0.40) | 254 (167–300) |
| <i>P</i> | 0.576 | 0.211 | 0.224 | 0.924 | 0.921 | 0.892 |
| Renal ischemia | | | | | | |
| Present (n = 10) | 69.9 ± 15.3 | 55 (23.5–786.8) | 74 (21.6–447.8) | 0.30 (0.13–1.57) | 0.54 (0.32–2.21) | 502.5 (8.4–3186.5) |
| Absent (n = 1087) | 61.4 ± 17.5 | 30 (28–31) | 24 (22–25) | 0.22 (0.20–0.23) | 0.38 (0.36–0.40) | 240 (150.3–350.4) |
| <i>P</i> | 0.156 | 0.085 | 0.006* | 0.312 | 0.102 | 0.233 |
| Small bowel inflammation | | | | | | |
| Present (n = 73) | 56.94 ± 18.86 | 31 (24–37) | 21 (15.4–30.6) | 0.30 (0.20–0.51) | 0.44 (0.37–0.56) | 24 (9–452.9) |
| Absent (n = 1108) | 61.90 ± 17.31 | 30 (28–31) | 24 (22.2–25) | 0.21 (0.20–0.23) | 0.37 (0.35–0.40) | 282.5 (175.3–389.9) |
| <i>P</i> | 0.018* | 0.964 | 0.284 | 0.010* | 0.008* | 0.857 |
| Colitis | | | | | | |
| Present (n = 91) | 59.59 ± 17.33 | 30 (25.3–35.7) | 24.8 (19.3–31) | 0.24 (0.17–0.37) | 0.47 (0.38–0.55) | 55.3 (13.6–467.3) |
| Absent (n = 1089) | 61.76 ± 17.45 | 30 (28–31) | 24 (22–25) | 0.21 (0.20–0.23) | 0.37 (0.35–0.40) | 269.5 (170.2–387.9) |
| <i>P</i> | 0.229 | 0.577 | 0.966 | 0.133 | 0.002* | 0.695 |
| Acute pyelonephritis | | | | | | |
| Present (n = 22) | 62.36 ± 20.50 | 28 (16.8–38.8) | 22 (16.7–44.6) | 0.19 (0.11–0.45) | 0.36 (0.19–0.46) | 494.5 (5.8–1331.1) |
| Absent (n = 1146) | 61.48 ± 17.42 | 30 (28–31) | 24 (22–25) | 0.21 (0.20–0.23) | 0.38 (0.35–0.40) | 257.5 (170.3–386.8) |
| <i>P</i> | 0.622 | 0.487 | 0.516 | 0.547 | 0.369 | 0.568 |
| Acute cholecystitis | | | | | | |
| Present (n = 36) | 70.27 ± 15.39 | 39 (32.4–65.7) | 29.5 (14–58.3) | 0.37 (0.25–0.57) | 0.51 (0.37–0.79) | 560.2 (8.6–1320.4) |
| Absent (n = 1145) | 61.32 ± 17.44 | 30 (28–31) | 24 (22–25) | 0.21 (0.20–0.22) | 0.37 (0.35–0.40) | 250 (165.2–350) |
| <i>P</i> | 0.001* | 0.045* | 0.578 | 0.001* | 0.003* | 0.576 |

Supplementary Table 1. continued

| | Age ± SD | Median AST (95% CI for median) | Median ALT (95% CI for median) | D. bilirubin 95% CI for median) | I. bilirubin (95% CI for median) | D-dimer (95% CI for median) |
|----------------------------------|---------------|--------------------------------------|-----------------------------------|------------------------------------|--|--------------------------------|
| Acute pancreatitis | | | | | | |
| Present (n = 38) | 62.94 ± 16.80 | 48 (33.7–74.3) | 46.5 (27.7–84.7) | 0.34 (0.26–0.51) | 0.41 (0.29–0.67) | 1231.3 (376.5–2541.1) |
| Absent (n = 1142) | 61.56 ± 17.47 | 29 (28–31) | 24 (22–25) | 0.21 (0.20–0.22) | 0.38 (0.35–0.40) | 235 (155.1–346.8) |
| <i>P</i> | 0.667 | 0.001* | 0.001* | 0.017* | 0.183 | 0.006* |
| Acute diverticulitis | | | | | | |
| Present (n = 8) | 65.87 ± 23.04 | 30 (15–419.5) | 21.5 (13.5–281.3) | 0.13 (0.10–0.25) | 0.34 (0.16–1.01) | 2092.8 (212.2– 11243.5) |
| Absent (n = 1173) | 61.56 ± 17.40 | 30 (28–31) | 24 (22–25) | 0.21 (0.20–0.23) | 0.38 (0.35–0.40) | 250 (165.3–350) |
| <i>P</i> | 0.370 | 0.781 | 0.889 | 0.153 | 0.762 | 0.032* |
| Acute appendicitis | | | | | | |
| Present (n = 18) | 40.94 ± 19.98 | 22 (19–35.6) | 21 (17.3–24.7) | 0.19 (0.11–0.45) | 0.44 (0.26–0.54) | 1.5 (0.6–82.1) |
| Absent (n = 1160) | 61.90 ± 17.23 | 30 (29–31) | 24 (22–25) | 0.21 (0.20–0.23) | 0.38 (0.35–0.40) | 284 (173.3–390) |
| <i>P</i> | <0.001* | 0.129 | 0.380 | 0.546 | 0.951 | 0.011* |
| Bowel obstruction | | | | | | |
| Present (n = 42) | 59.19 ± 15.34 | 32 (27.4–46.8) | 25 (19.5–33.5) | 0.28 (0.15–0.43) | 0.49 (0.40–0.77) | 370 (28.7–376.5) |
| Absent (n = 1139) | 61.68 ± 17.51 | 30 (28–31) | 24 (22–25) | 0.21 (0.20–0.23) | 0.37 (0.35–0.40) | 250 (161.6–351.4) |
| <i>P</i> | 0.257 | 0.107 | 0.905 | 0.212 | <0.001* | 0.124 |
| Intraabdominal malignancy | | | | | | |
| Present (n = 147) | 59.99 ± 14.61 | 32 (28–39) | 25 (20–32) | 0.30 (0.22–0.41) | 0.45 (0.40–0.51) | 134 (10.5–501.6) |
| Absent (n = 1034) | 61.82 ± 17.80 | 29 (28–31) | 24 (22–25) | 0.20 (0.19–0.22) | 0.36 (0.35–0.39) | 266 (170–390) |
| <i>P</i> | 0.257 | 0.362 | 0.884 | <0.001* | <0.001* | 0.600 |

*Represents statistical significance. Data were summarized as mean ± SD for normal distributed variables and, median (95% CI for median) for non-normal distributed variables. ALT, alanine aminotransferase; AST, aspartate aminotransferase; SD, standard deviation; CI, confidence interval.



Quantitative liver magnetic resonance imaging: correlation between conventional magnetic resonance imaging, laboratory values, and prognostic indices in Budd–Chiari syndrome

Ayşe Erden 
Diğdem Kuru Öz 
Mehmet Adıgüzel 
Funda Seher Özalp Ateş 

PURPOSE

In Budd–Chiari syndrome (BCS), unevenly distributed parenchymal changes and perfusion abnormalities occur due to hepatic venous outflow obstruction. This study aimed to evaluate the changes in the liver parenchyma in BCS using the quantitative magnetic resonance (MR) techniques of MR elastography, T1 and T2 mapping, and diffusion imaging and correlate the quantitative MR parameters through biochemical results and prognostic indices.

METHODS

Fourteen patients with BCS (seven men and seven women) were examined retrospectively. Liver stiffness (kPa), T1 relaxation times (ms) were achieved using the modified Look–Locker inversion recovery (MOLLI) 3(2)3(2)5 sequence and B1-corrected variable flip angle methods, T2 relaxation times (ms), and apparent diffusion coefficient (ADC) values (mm²/s) were measured using regions of interest placed in the same region in all quantitative methods. Measurements were repeated at the precontrast and postcontrast hepatobiliary phases. The reduction rate (RR; %) and adjusted postcontrast T1 (%) were calculated. The values obtained from different liver parenchyma areas (whole liver, caudate lobe, pathological T2 hyperintense tissue, and relatively preserved normal-appearing tissue) were compared using the Wilcoxon signed-rank test. Spearman's correlation coefficient was used to investigate the correlation between quantitative MR parameters and biochemical parameters/prognostic scores (Child–Pugh score, Clichy score, and Rotterdam index).

RESULTS

The parenchymal stiffness and precontrast T1 values of the caudate lobe were significantly lower than those of the remainder of the parenchyma, whereas the adjusted postcontrast T1 percentages (MOLLI) were significantly higher ($P \leq 0.027$). The parenchymal stiffness value, T1 and T2 values, percentages of RR (MOLLI), and adjusted postcontrast T1 values for the pathological tissue and relatively normal tissue were significantly different ($P < 0.028$). No significant difference was found in terms of ADC values between any of the distinct regions of the liver.

A strong correlation was detected between the Child–Pugh score, Clichy score, and precontrast T1 values obtained through the MOLLI sequence ($r = 0.867, P = 0.012, r = 0.821, P = 0.023$, respectively). No correlation was found between the whole liver stiffness values and the laboratory parameters, fibrosis markers, prognostic indices, or MR parameters. A significant correlation was identified between creatinine levels and several T1 parameters and the T2 relaxation time ($r \geq 0.661, P \leq 0.052$).

CONCLUSION

Tissue stiffness and T1 relaxation values are high in the areas identified as fibrosis compared with those in the relatively preserved parenchyma. The T1 relaxation time can offer quantitative information for assessing segmental functional changes and prognosis in BCS.

KEYWORDS

Budd–Chiari syndrome, diffusion weighted imaging, MR elastography, T1 mapping, T2 mapping

From the Department of Radiology (A.E., D.K.Ö. ✉ digdem_k@hotmail.com, M.A.), Ankara University Faculty of Medicine, Ankara, Turkey; Department of Biostatistics and Medical Informatics (F.S.Ö.A.), Manisa Celal Bayar University, Faculty of Medicine, Manisa, Turkey.

Received 21 February 2021; revision requested 27 March 2021; last revision received 27 August 2022; accepted 29 September 2022



Epub: 23.12.2022

Publication date: 30.05.2023

DOI: 10.4274/dir.2022.221462

You may cite this article as: Erden A, Kuru Öz D, Adıgüzel M, Özalp Ateş FS. Quantitative liver magnetic resonance imaging: correlation between conventional magnetic resonance imaging, laboratory values, and prognostic indices in Budd–Chiari syndrome. *Diagn Interv Radiol.* 2023;29(3):428–436.

Budd–Chiari syndrome (BCS) is a rare vascular disorder that develops as a result of the obstruction of hepatic venous drainage at any level between the hepatic venules and the right atrium. Liver damage in BCS is uneven, and the distribution and severity of parenchymal involvement vary according to the site and length of the venous segment involved as well as the chronicity of the disease process.^{1,2}

The histological changes (congestion, loss of hepatocytes without inflammatory infiltrates, coagulative necrosis, and/or fibrosis) in BCS are not pathognomonic. Given the diagnostic effectiveness of radiologic studies such as magnetic resonance imaging (MRI), liver biopsy is not usually necessary for the diagnosis. A biopsy is only essential for confirming BCS in the case of small intrahepatic vein obstruction in the presence of preserved large veins during imaging.³

As a non-invasive method, conventional MRI is relatively accurate (with a sensitivity and specificity >90%) for detecting the parenchymal changes and perfusional abnormalities observed in BCS.⁴ Quantitative MRI techniques such as MR elastography (MRE), T1 and T2 mapping, and apparent diffusion coefficient (ADC) measurements are known to be useful in evaluating congestive, necrotic, and fibrotic changes in the hepatic tissue.^{5–7} Because the venous obstruction affects the liver in a heterogeneous way, damage to the liver parenchyma also becomes unevenly distributed.⁸ To our knowledge, this uneven parenchymal involvement and the deterioration of regional and global hepatic function in BCS have not been extensively studied using MR quantification techniques.

This study aims to utilize the quantitative MR techniques of MRE, T1 and T2 mapping, and diffusion-weighted imaging (DWI) in

BCS to evaluate changes in the liver parenchyma caused by hepatic venous outflow obstruction and correlate quantitative MR parameters using laboratory parameters and prognostic indices.

Methods

Study participants

This study was approved by the Human Research Ethics Committee of the Faculty of Medicine, Ankara University (06/25/2021; 15-366-21), and written informed consent was waived because of the study's retrospective design. The BCS diagnosis was based on imaging findings. The data eligible for this study were obtained from patients with BCS who underwent MRE, T1 and T2 mapping, and DWI in addition to a standard unenhanced and dynamic gadoteric-acid-enhanced liver examination.

Twenty-two MR examinations, including through quantitative techniques, performed between November 2017 and November 2021, of 14 patients with BCS (seven men, seven women; median age, 35 years; age range, 20–60 years) were reanalyzed. Of the patients who received multiple scans, only the measurements on the parametric maps of recent examinations were used for statistical evaluation. The demographic variables (known duration of disease, etiologic/predisposing factors, which veins are occluded, endovascular treatment performed, and prognostic indices) are presented in Table 1. The results of laboratory tests [including alanine transaminase and aspartate transaminase (AST), serum bilirubin, prothrombin time (PT), international normalized ratio (INR), serum albumin, platelet count, serum creatinine, and serum sodium] from the visit closest to the MRI examination were recorded. The prognostic indices for BCS (Child–Pugh score, Clichy index, and Rotterdam BCS index) were calculated. For the Child–Pugh score, five variables (serum bilirubin, albumin, INR, ascites, and hepatic encephalopathy) were scored 1–3, with 3 indicating the most severe abnormality. Based on these variables, the patients were classified into categories A to C. The Clichy index was calculated as follows: (ascites score \times 0.75) + (age \times 0.037) + (Child–Pugh score \times 0.28) + (age \times 0.037) + (creatinine \times 0.0036), where ascites was scored as absent, controlled with sodium restriction or diuretics, or resistant to medical treatment (scored as 1, 2, or 3, respectively). The Rotterdam BCS index was calculated as follows: (1.27 \times encephalopathy) + (1.04 \times ascites) + (0.72 \times PT) + (0.004 \times bilirubin), where ascites

and hepatic encephalopathy were scored as present (1) or absent (0) and PT as higher (1) or equal/lower (0) than an INR of 2.3.⁹

In addition, the fibrosis score of the AST to platelet ratio index was determined. As reported previously, acute disease was defined as a clinical duration of less than one month, subacute disease from one to six months, and chronic disease as longer than six months.¹⁰ In this study, all cases were considered to be chronic BCS because the disease duration after diagnosis was longer than six months. The presence of intrahepatic collaterals, which are known to occur several months after thrombosis, in all patients also suggested the chronicity of the disease. A transjugular intrahepatic portosystemic shunt (TIPS) was performed in three of the patients. However, because we aimed to determine how the chronic parenchymal changes would be reflected when using quantitative methods, we did not exclude these patients.

Magnetic resonance image acquisition

All images were acquired using a 1.5-T MR scanner (Aera, Siemens Healthcare, Erlangen, Germany) after a 6-h fast. Standard body and spine matrix coils were used. A routine MR protocol consisting of a coronal T2-weighted half-fourier acquisition single-shot turbo spin echo, transverse T2-weighted fat-suppressed BLADE, transverse T2-weighted BLADE, and DWI were used in all patients. Gadoteric acid (Primovist, Bayer Healthcare, Leverkusen, Germany) was administered intravenously using an automatic injector at a rate of 4 mL/s for a total dose of 0.025 mmol/kg body weight, followed by a 25-mL saline flush. After the unenhanced phase, the arterial phase (25 s), portal venous phase (60 s), delayed phase (100–120 s), transient phase (about the tenth minute), and hepatobiliary (HB) phase (about the twentieth minute) were acquired using a fat-suppressed T1 volumetric interpolated breath-hold examination sequence.

Magnetic resonance elastography

MRE was performed using a phase-contrast two-dimensional gradient recalled echo sequence. Four 10-mm-thick transverse slices through the largest cross-section of the liver were obtained with breath holds at end-expiration. The parameters used for MRE were as follows: repetition time/echo time (TR/TE): 50/27.5 ms; flip angle: 25°; field of view (FOV): 400 \times 300 mm; matrix: 48 \times 128, slice thickness: 10 mm; averages: 1; wave frequency: 60 Hz; motion encoding gradient frequency:

Main points

- T1 mapping provides absolute and comparable data that can be used to estimate the heterogeneous distribution of liver function in patients with Budd–Chiari syndrome (BCS).
- The Child–Pugh score and serum creatinine level, which are important determinants of prognosis in BCS, were correlated with the liver T1 relaxation time.
- The combined use of T1 mapping and magnetic resonance (MR) elastography is beneficial because tissues with high stiffness values on MR elastograms may be compatible with congestion if they appear relatively preserved on T1 maps.

Table 1. Clinical and magnetic resonance image data of the 14 patients with Budd–Chiari syndrome

| Case | Sex | Age (y) | Known duration (y) | Etiology/predisposing factor | Obstructed veins | Vascular intervention | CP class | Rotterdam score | Clichy score | CP score | APRI score |
|------|-----|---------|--------------------|---|----------------------|-----------------------|----------|-----------------|--------------|----------|------------|
| 1 | F | 28 | 5 | Factor V Leiden mutation (heterozygote) Protein C and S deficiency Oral contraceptive Obesity Smoking | RHV, MHV | TIPS | A | 0.65 | 3.234 | 5 | 0.20 |
| 2 | F | 30 | 1 | -* | MHV, LHV | | A | 0.37 | 3.28 | 5 | 0.28 |
| 3 | M | 59 | 1 | Essential thrombocytosis | RHV, LHV, MPV | | A | 0.31 | 4.361 | 5 | 0.23 |
| 4 | M | 31 | 7 | - | MHV, LHV | TIPS | B | 1.91 | 5.19 | 9 | 1.13 |
| 5 | F | 32 | 9 | Resistance to activated protein C Oral contraceptive | RHV | | B | 1.12 | 3.916 | 7 | 0.88 |
| 6 | M | 20 | 1 | FMF Antiphospholipid syndrome | RHV, MHV | | B | 1.2 | 3.473 | 7 | 0.36 |
| 7 | F | 60 | 2? | Factor V Leiden mutation (heterozygote) | RHV, MHV LHV, RPV | | A | 0.22 | 4.39 | 5 | 0.40 |
| 8 | M | 40 | 10 | - | RHV, MHV | TIPS | A | 1.01 | 3.644 | 5 | 0.42 |
| 9 | F | 37 | 18 | Factor V Leiden mutation (homozygote) | RHV, MHV LHV | | C | 0.51 | 5.693 | 10 | 0.74 |
| 10 | M | 33 | 3 | - Smoking | RHV | | A | 3.07 | 3.396 | 5 | 0.12 |
| 11 | M | 45 | 15 | - Smoking | RHV, MHV LHV | | B | 0.45 | 4.404 | 7 | 0.27 |
| 12 | F | 45 | 13 | Protein C and S deficiency Factor V Leiden mutation Oral contraceptive | MHV, LHV | | A | 1.09 | 4.18 | 6 | 0.77 |
| 13 | M | 24 | 4 | Factor V Leiden mutation | RHV, MHV, IVC | | B | 0.3 | 4.648 | 8 | 0.54 |
| 14 | F | 43 | 10 | - | RHV | | A | 2.21 | 3.762 | 5 | 0.30 |

*, etiology is not determined; y, years; CP, Child–Pugh; APRI, aspartate transaminase to platelet ratio index; RHV, right hepatic vein; MHV, middle hepatic vein; LHV, left hepatic vein; MPV, main portal vein; RPV, right portal vein; IVC, inferior vena cava; FMF, familial mediterranean fever; TIPS, transjugular intrahepatic portosystemic shunt; F, female; M, male.

60 Hz; bandwidth: 250 Hz/pixel; and generalized autocalibrating partially parallel acquisitions (GRAPPA) reduction factor: 2; the scanning time of each slice was 17 s, and the total examination time was approximately 2 min, including four breath-hold and resting periods. Stiffness maps (elastograms), confidence maps, and wave images were then reconstructed using postprocessing software.

T1 mapping

A modified Look–Locker inversion recovery (MOLLI) technique was used for the precontrast (native) and contrast-enhanced T1 mapping. An electrocardiography-gated 3(2)3(2)5 sampling scheme was acquired with a balanced steady-state-free precession sequence. For T1 mapping, a single 10-mm-thick slice was taken from the same axial plane and selected for stiffness measurements in the elastogram confidence map.

The MOLLI 3(2)3(2)5 scheme was obtained with the following parameters: TR/

TE: 419/1.69 ms; inversion time: 260 ms; flip angle: 50°; FOV: 390 × 313 mm; matrix: 180 × 224; slice thickness: 10 mm; fat saturation: spectral adiabatic inversion recovery (SPAIR); averages: 1; bandwidth: 603 Hz/pixel; and GRAPPA reduction factor: 2. The acquisition time was 10–20 s. Inline T1 maps were constructed at the scanner using vendor-supplied software.

A B1 inhomogeneity-corrected volumetric T1 map using a variable flip angle (VFA) method was also performed for each participant. Cardiac gating was not used for the VFA method. Multisection data (72 slices) were obtained with a breath hold of 19 s. The sequence parameters were as follows: TR/TE 4.3/2.08 ms; flip angle: 3° and 15°; FOV: 380 × 309 mm; matrix: 156 × 256; slice thickness: 3.5 mm; distance factor: 20%; averages: 3; bandwidth: 350 Hz/pixel; and controlled aliasing in volumetric parallel imaging reduction factor: 2; the acquisition time was approximately 20 s. Although multiple slices were taken during the B1-corrected volumetric T1 mapping,

only one slice plane, from which the tissue stiffness was measured, was used for quantitative analysis.

T2 mapping

The T2 mapping was performed using a fast low-angle shot inversion-recovery gradient echo (FLASH) sequence with a slice thickness of 10 mm. Cardiac gating was used to time the image acquisition. Each slice had the same transverse anatomic level as in the T1 mapping. The sequence-specific parameters of the FLASH T2 mapping were as follows: TR/TE: 207/1.06 ms; flip angle: 12°; FOV: 360 × 289 mm; matrix: 116 × 192; slice thickness: 10 mm; averages: 1; bandwidth: 1184 Hz/pixel; and GRAPPA reduction factor: 2; the acquisition time was 7–12 s.

Diffusion-weighted imaging

The DWI technique was performed based on free breathing using fat-suppressed echo-planar imaging (EPI). Diffusion gradients at b values of 50, 400, and 800 s/mm²

were used. Images were obtained with the following parameters: TR/TE: 6.700/56 ms; EPI factor: 120; bandwidth: 2.332 Hz/pixel; FOV: 380 × 90 mm; matrix size: 134 × 100; averages: 2; slice thickness: 6 mm; distance factor, 20% (1.2 mm); and GRAPPA reduction factor: 2; in addition, SPAIR fat suppression was used. The acquisition time was approximately 2.40 min.

Image analysis

The quantitative analysis of the hepatic parenchyma and T1 measurements of the spleen was performed by an experienced radiologist (D.K.Ö.) on parametric maps at a workstation (Syngo Via, Siemens Medical Systems, Erlangen, Germany).

To determine liver stiffness (kPa), T1 and T2 relaxation times (ms), and ADC values (mm²/s), regions of interest (ROI) were placed at identical locations in each sequence, excluding large vessels and imaging artifacts. The T1 relaxation times of the liver and spleen before and 20 min after gadoteric acid administration were measured at the same slice level of the T1 maps acquired using the MOLLI 3(2)3(2)5 sequence and B1-corrected VFA technique. Measurements were taken from the whole liver, the caudate lobe, and the rest of the liver parenchyma (excluding the caudate lobe) using the free-hand geographic ROI method. Simultaneously, the pathologic [hyperintense areas on T2-weighted images (T2WIs)] and relatively preserved (normal-appearing) areas were quantitatively assessed by drawing circular ROIs (approximately 200 mm²). The measurements were repeated three times, and the averaged values were used for statistical analysis.

Gadoxetic acid-enhanced MRI-based liver function indices using the T1 relaxation time were calculated in the following manner, as described previously:¹¹

Reduction rate (RR) of T1 relaxation time = $[(T1 \text{ liver precontrast} - T1 \text{ liver HB}) / T1 \text{ liver precontrast}] \times 100$

The adjusted postcontrast T1 was calculated as described by Yoon et al.¹² using the following formula:

Adjusted postcontrast T1 = $(T1 \text{ liver HB} - T1 \text{ spleen} / T1 \text{ spleen HB}) \times 100$

To estimate the interobserver agreement, another radiologist (M.A.) also performed measurements from the same sequences.

Statistical analysis

All statistical analyses were performed using SPSS software for Windows, version 11.5. Descriptive statistics using the median (with minimum and maximum) were performed to present the clinical characteristics of the study participants and for the quantitative MR liver name abbreviation added function parameters. The Wilcoxon signed-rank test was used to compare the results of the quantitative parameters obtained from different regions of the liver. Spearman's correlation coefficient was used to measure the strength of correlation between the quantitative MR parameters and biochemical parameters and prognostic scores, where the value $r = 1$ represented a strong positive correlation and the value $r = -1$ was a strong negative correlation. The interobserver agreement was examined using the intraclass correlation coefficient (ICC). A P of <0.050 was considered statistically significant.

Results

The venous obstruction sites of the 14 patients with BCS involved in the study are presented in Table 1.

Comparison of quantitative parameters in the caudate lobe and the rest of the liver parenchyma

The median (minimum–maximum) stiffness, T1 (MOLLI sequence and B1-corrected VFA technique), T2, and ADC values in the caudate lobe and the remainder of the liver parenchyma are shown in Table 2. The MOLLI, T1 mapping, and T2 mapping measurements were performed on 10 patients.

The caudate lobe median stiffness value was significantly lower than that of the other parts of the parenchyma (3.29 vs. 5.07 kPa, $P = 0.001$).

A significant difference in the precontrast MOLLI T1 relaxation time ($P = 0.012$), precontrast B1-corrected VFA ($P = 0.006$), and adjusted postcontrast T1 ($P = 0.027$) was identified. The T1 values obtained using both mapping techniques were significantly lower in the caudate lobe than in the other parts of the parenchyma (Table 2). The T1 RR on both the MOLLI and B1-corrected VFA images revealed no significant difference (60% vs. 59%, $P = 0.172$; 67% vs. 66%, $P = 0.399$, respectively).

In addition, no significant difference was found in terms of median T2 value ($P = 0.141$) or ADC value ($P = 0.346$) (Table 2).

Comparison of quantitative parameters in areas seen as hyperintense on T2-weighted images and the relatively preserved parenchyma

The median (minimum–maximum) stiffness, T1, T2, and ADC values in areas seen as hyperintense on the T2WIs and relatively preserved normal-appearing liver parenchyma are presented in Table 2.

The T2 hyperintense region median tissue stiffness was significantly higher than that of the relatively normal-appearing liver parenchyma (6.14 vs. 2.96 kPa, $P = 0.001$) (Figure 1a, b).

Moreover, the median T2 relaxation time corresponding to the T2 hyperintense regions on the T2 map was significantly higher (55.5 ms) than that of the relatively normal-appearing liver parenchyma (50 ms) ($P = 0.030$) (Figure 1c).

The median T1 relaxation time corresponding to the T2 hyperintense regions in both mapping techniques was significantly higher than that of the relatively normal-appearing liver parenchyma (Table 2) (Figure 1d-g). The RR of the T1 relaxation time in the region corresponding to the hyperintense areas on the T2WIs (50%) was significantly lower than that of the relatively preserved parenchyma (61%) on the MOLLI sequence images ($P = 0.028$). However, no significant difference was found in the RR (%) of the T1 relaxation time (67% vs. 68%) ($P = 0.475$) on the T1 map achieved using the B1-corrected VFA technique.

The adjusted postcontrast T1 values (MOLLI and B1-corrected VFA) corresponding to the T2 hyperintense regions were significantly lower (93.5 and 136 ms) than those of the relatively normal-appearing liver parenchyma (128 and 147 ms) ($P = 0.028$ and 0.024 , respectively).

The median ADC value obtained from the areas corresponding to the hyperintense areas on the T2WIs was not statistically different from that obtained in the areas evaluated as relatively preserved ($1.167 \cdot 10^{-3}$ vs. $0.969 \cdot 10^{-3}$ mm²/s, $P = 0.173$).

Correlation between the quantitative magnetic resonance data and laboratory parameters, clinical scores, and prognostic indices

The median (minimum–maximum) values of the quantitative MR parameters measured from the entire cross-sectional surface of the liver are presented in Table 3.

Table 2. Comparison of the quantitative parameters of magnetic resonance elastography, T1 and T2 mapping, and the apparent diffusion coefficient in the caudate lobe vs. rest of the parenchyma and in areas seen as hyperintense on T2-weighted images vs. relatively preserved parenchyma

| Parameters | Caudate lobe median (min–max) | Rest of parenchyma median (min–max) | P | T2 hyperintense areas median (min–max) | Relatively preserved parenchyma median (min–max) | P |
|---|-------------------------------|-------------------------------------|---------|--|--|-------|
| Stiffness value (kPa) | 3.29 (1.69–5.54) | 5.07 (2.78–8.30) | 0.001 | 6.14 (3.44–12.13) | 2.96 (1.53–4.88) | 0.001 |
| Precontrast T1 value MOLLI 3(2)3(2)5* | 778 (617–933) | 867.5 (645–1.049) | 0.012 | 1.105.5 (729–1.471) | 699.5 (579–944) | 0.012 |
| Postcontrast T1 value MOLLI 3(2)3(2)5* | 329 (198–419) | 386 (225–452) | 0.018 | 493 (298–798) | 309 (163–416) | 0.018 |
| RR (%) MOLLI 3(2)3(2)5* | 60 (40–71) | 59 (38–65) | 0.172 | 50 (34–62) | 61 (36–77) | 0.028 |
| Adj. postcontrast T1 MOLLI 3(2)3(2)5* | 120.5 (75–133) | 112 (71–129) | 0.027 | 93.5 (65–119) | 128 (94–137) | 0.028 |
| Precontrast T1 value B1-corrected VFA | 928 (525–1.111) | 1,048 (655–1.347) | 0.006 | 1,014 (643–1.791) | 833 (598–1.008) | 0.004 |
| Postcontrast T1 value B1-corrected VFA | 317 (157–481) | 336 (151–567) | 0.086 | 354 (151–820) | 269 (136–429) | 0.021 |
| RR (%) B1-corrected VFA | 67 (36–78) | 66 (53–77) | 0.399 | 67 (35–81) | 68 (28–79) | 0.475 |
| Adj. postcontrast T1 B1-corrected VFA | 140 (87–191) | 136 (77–185) | 0.058** | 136 (82–177) | 147 (91–201) | 0.024 |
| T2 value in FLASH* | 54.5 (38–453) | 54.5 (41–629) | 0.141 | 55.5 (48–76) | 50 (39–59) | 0.030 |
| ADC value (10 ⁻³ mm ² /s) | 1.012 (0.891–2.041) | 1.049 (0.910–1.294) | 0.346 | 1.167 (0.853–1.847) | 0.969 (0.851–1.505) | 0.173 |

*, evaluated in 10 patients; **, marginally significant, T1 and T2 values are in ms; MOLLI, modified Look–Locker inversion recovery; RR, reduction rate; Adj, adjusted; VFA, variable flip angle; FLASH, fast low-angle shot; ADC, apparent diffusion coefficient.

No correlation was found between the whole liver stiffness values measured from the MR elastograms and the laboratory parameters/clinical scores and prognostic indices.

The platelet count was negatively correlated with the T1 relaxation time of the liver in the precontrast MOLLI sequence ($r = -0.893$, $P = 0.007$). A strong positive correlation was found between the Child–Pugh score and T1 relaxation times of the liver in both the precontrast MOLLI ($r = 0.867$, $P = 0.012$) and precontrast B1-corrected VFA ($r = 0.621$, $P = 0.055$) sequences. A strong positive correlation was identified between the direct bilirubin and T1 relaxation time in the precontrast B1-corrected VFA sequence ($r = 0.703$, $P = 0.035$).

The adjusted postcontrast T1 values showed a marginally significant, strong positive correlation with the AST level ($r = 0.872$, $P = 0.054$).

The Clichy score was positively correlated with the T1 relaxation time of the liver in the precontrast MOLLI sequence ($r = 0.821$, $P = 0.023$).

Table 3. Quantitative magnetic resonance parameters measured from the entire cross-sectional surface of the liver

| Quantitative MR parameters | Median (min–max) |
|---|-------------------|
| Stiffness value (kPa) | 5.07 (2.78–8.30) |
| Precontrast T1 value* MOLLI 3(2)3(2)5 | 867.5 (645–1.049) |
| Postcontrast T1 value* MOLLI 3(2)3(2)5 | 386 (225–452) |
| Reduction rate (%)* MOLLI 3(2)3(2)5 | 59 (38–65) |
| Adjusted postcontrast T1 MOLLI 3(2)3(2)5* | 112 (71–129) |
| Precontrast T1 value B1-corrected VFA | 1.048 (655–1.347) |
| Postcontrast T1 value B1-corrected VFA | 336 (151–567) |
| Reduction rate (%) B1-corrected VFA | 66 (53–77) |
| Adjusted postcontrast T1 B1-corrected VFA | 136 (77–185) |
| T2 value* | 52.9 (41–62.9) |

*, evaluated in 10 patients; MOLLI, modified Look–Locker inversion recovery; VFA, variable flip angle T1 and T2 values are in ms.

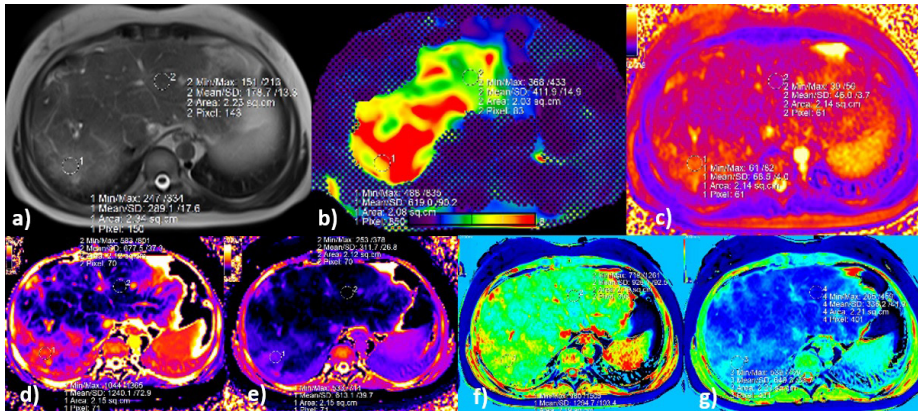


Figure 1. Magnetic resonance images acquired from a 32-year-old woman with occluded right and middle hepatic veins and a patent large left hepatic vein. (a) Axial T2-weighted image (T2WI), (b) color elastogram (confidence map), (c) T2 map, (d) pre-gadoxetic acid, and (e) post-gadoxetic acid T1 map acquired using the modified Look–Locker inversion (MOLLI) 3(2)3(2)5 sampling scheme, (f) pre-gadoxetic acid, and (g) post-gadoxetic acid B1-corrected variable flip angle (VFA) T1 map. All images were obtained at the same slice level. Regions of interest are drawn on the T2WIs (a) and copied and pasted onto the corresponding parametric maps (b–g).

Axial T2WI (a) showing peripheral hyperintense tissue in segment VII, which corresponds to a region of confluent fibrosis. The numeric values are seen on the parametric maps. Compared with the relatively preserved left lobe parenchyma, fibrotic tissue has higher stiffness (4.1 vs. 6.1 kPa) (b); longer T2 relaxation time (46 vs. 68 ms) (c); and longer T1 relaxation times (d); using the pre-gadoxetic acid T1 MOLLI technique (1.240 vs. 677 ms) (e); and in the pre-gadoxetic acid B1-corrected VFA T1 map (1.294 vs. 926 ms) (f).

T1 relaxation times obtained from the fibrotic region and normal-appearing parenchyma using the post-gadoxetic acid T1 MOLLI technique (e) are 613 and 311 ms, respectively, and in the post-gadoxetic acid B1-corrected VFA T1 map (f) 649 and 336 ms, respectively. The reduction rate (%) of the T1 relaxation time in the area considered as fibrosis is significantly lower than that in the normal-appearing parenchyma at the hepatobiliary phase approximately 20 min after gadoxetic acid administration (fibrosis/relatively preserved parenchyma %; MOLLI technique 50%/54%, B1-corrected VFA T1 map 49%/63%).

No significant correlation was found between the MR parameters and Rotterdam index.

Serum creatinine levels exhibited a strong positive correlation with the T1 relaxation time of the liver in the postcontrast MOLLI sequence ($r = 0.829$, $P = 0.042$) and the pre-contrast ($r = 0.661$, $P = 0.053$) and postcontrast ($r = 0.750$, $P = 0.052$) B1-corrected VFA sequences. The RR was negatively correlated with the creatinine level ($r = -0.943$, $P = 0.005$), and the serum creatinine level had a strong positive correlation with the T2 relaxation time in the FLASH sequence ($r = 0.857$, $P = 0.014$). A strong negative relationship was identified between the serum sodium level and T1 relaxation time of the liver in the postcontrast MOLLI sequence ($r = -0.928$, $P = 0.008$).

Interobserver agreement

The ICC for all the measured parameters was excellent [ICC ≥ 0.911 , (95% confidence interval, 0.651–0.981), $P < 0.001$].

Important qualitative findings observed on parametric magnetic resonance maps

In five patients, focal tissues that appeared normal on the T2WIs and T1 and T2 parametric maps were coded in yellow and/or red (indicating high stiffness) on the MREs (Figure 2). All of these patients (except one on which a contrast-enhanced examination could not be performed because of a previous history of a contrast media-related severe reaction) exhibited mottled parenchymal contrast enhancement, which is accepted as a manifestation of passive congestion of the liver.

In one patient, a segmental region, which seemed completely normal on the T2WI, exhibited abnormal findings when using mapping techniques and MRE.

Hepatocellular carcinoma was detected in two patients, and three patients, two of whom had undergone TIPS, had benign regenerative nodules in the liver.

Discussion

In the present study, quantitative MRI techniques enabled us to extract numeric data from parametric maps to assess of the parenchymal changes relative to normal-appearing (relatively preserved) tissues in BCS. Although the RR of the T1 relaxation time was not different, tissue stiffness and T1 relaxation values were lower in the caudate lobe than in the rest of the parenchyma, as expected. The ADC values, however, did not differ between normal-appearing and abnormal-appearing areas, including in the caudate lobe.

Edema and congestion, the important parenchymal alterations of acute BCS, are not prominent features in chronic BCS, as later stages are characterized by changes in fibrosis.¹⁰ As BCS becomes chronic, T2 hyperintense areas become more prominent in the subcapsular regions of the liver. Since the BCS history of the study participants was longer than six months, we considered that such T2 hyperintense areas may reflect fibrosis caused by chronic BCS. Our results revealed that the T1 and T2 relaxation times were longer and stiffness values high in T2 hyperintense tissues compared with those of relatively preserved parenchyma (Table 2). The RR of the T1 relaxation time in the region corresponding to the hyperintense areas on the T2WIs (50%) was significantly lower than that in the other parts of the parenchyma (61%) on the MOLLI sequence images. High signal intensity characteristics on the T2WIs can be explained in part by the large water content of advanced fibrosis, which leads to prolonged T1 and T2 relaxation times.¹³

In addition to the staging of liver fibrosis, the potential role of elastography methods in assessing liver tissue stiffness has also been investigated in BCS.¹⁴ Studies using ultrasound (US) elastography in BCS generally aim to evaluate parenchymal stiffness before and after vascular interventions. In these studies, a significant reduction in liver stiffness was found after treatment with balloon angioplasty.^{15,16}

MRE is generally accepted as superior to US elastography because the latter has significant limitations, such as operator dependence and measurement difficulties, in cases of ascites and severe obesity.¹⁷ Currently, there is a paucity of data in this context, and only two studies by the same author have reported MRE results in BCS.^{18,19} The

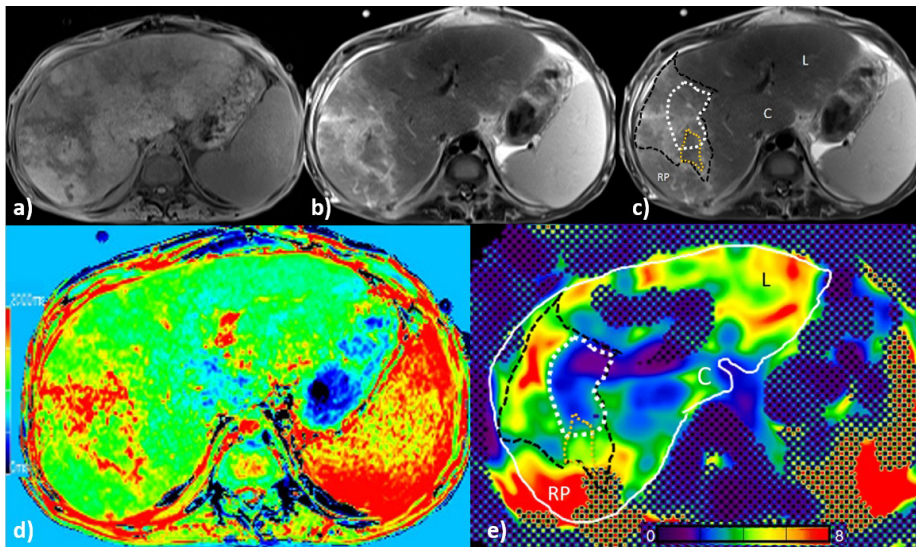


Figure 2. Magnetic resonance (MR) images acquired from a 24-year-old man with occluded right and middle hepatic veins and inferior vena cava. (a) Axial T1-weighted image (T1WI), (b, c) axial T2-weighted images (T2WIs), (d) native B1-corrected variable flip angle (VFA) T1 map, and (e) color elastogram (confidence map). All images are obtained at the same slice level.

T1WI (a) and T2WI (b) show peripheral mass-like tissue change, mainly located in the lateral aspect of the right lobe, with relatively sharp but irregular borders. This area, thought to be confluent fibrosis, is shown in (c) with its borders drawn in black. On the color B1-corrected VFA T1 map (d), the tissue in question is encoded with red and the T1 relaxation time is long. On T2WI (c), the medial part of the hyperintense area, which looks like a continuation of fibrosis (white outline), is encoded with blue in the MR elastogram (e); its stiffness values are not high enough to suggest fibrosis. By contrast, the area that appears normal compared with its surroundings (yellow outline) on the T2WI (c), the posterior subcapsular region in the right lobe, and the majority of the left hepatic lobe (L), are encoded with yellow and red in the MR elastogram, indicating high stiffness values. In the areas described, the possibility of congestion, which increases tissue stiffness, should be considered. Note also the relatively normal appearance of the caudate lobe (c), with normal signal intensity on conventional sequences (a, b) and blue encoding (normal) on the MR elastogram and B1-corrected VFA T1 map.

authors concluded that segmental stiffness measured through an MRE was a promising reproducible quantitative biomarker for monitoring the treatment response to endovascular intervention in patients with BCS.¹⁸ In the second study, the authors suggested that using an MRE for liver stiffness measurements was effective for evaluating liver function in BCS.¹⁹ However, none of the laboratory parameters and indices appeared to correlate with the liver stiffness values in our study. This may be due to the small sample size.

Although fibrosis could not be definitively excluded in the studies mentioned above performed using US and MRE, studies suggest that the increase in tissue stiffness seen in BCS is the result of congestion rather than fibrosis.¹⁸⁻²⁰ Hepatic congestion, which can spuriously increase liver stiffness measurements, may be differentiated from fibrosis through conventional imaging, clinical information, and liver function test results.⁷ With the onset of clinical findings, the hepatic mottled enhancement in the portal venous

phase of dynamic contrast-enhanced imaging reflects portal stasis and, indirectly, hepatic congestion.²¹ Sluggish flow, which can cause increased blood volume (congestion) in the portal vessels and sinusoids, is expected to develop in the early stages, but it can also be seen in the “acute on chronic” form of the disease with clinical exacerbation. The thrombotic extension could play a role in this scenario.²²

Estimating the hepatic functional reserve is important for the prognosis and management of patients with BCS. An essential but unanswered issue in BCS is how to take the degree of liver dysfunction into account when choosing the type of therapy.¹ In routine clinical practice, liver function in BCS is often determined using clinical signs and biochemical blood parameters.²³ However, the measurement of biochemical parameters provides only indirect information about hepatocyte injury. As individual segments are drained by unique hepatic vein branches, the development of hepatocyte damage is expected to be limited mainly to the region drained by the occluded vessel. Liver func-

tion tests may fail to detect this topographic segmental dysfunction. Although regional non-enhancement on dynamic imaging may indicate hepatocyte damage,²⁴ having a direct measurement of hepatocyte function is desirable. In this context, T1 mapping techniques are increasingly used in the medical arena to provide an objective observation of the damaged areas in the liver.²⁵

In our case series, we used gadoxetic acid-enhanced MRI to objectively evaluate global and regional liver function. The hepatic elimination of gadoxetic acid is dependent on the integrity of the hepatocyte mass. The uptake of the contrast medium by the hepatocytes allows a quantitative estimation of segmental liver function on parametric maps. T1 mapping of the liver can enable an evaluation of liver function by using pre-contrast and postcontrast HB phase images and the RR of T1 relaxation times (normally above 60%).^{26,27} Approximately 20 min after intravenous gadoxetic acid administration, we found that the RR of the T1 relaxation time was significantly lower than that of normal-appearing (relatively preserved) parenchyma because of the reduced hepatocyte uptake in the areas considered as fibrosis (50% vs. 61% in the MOLLI technique).

Several prognostic indices have been described to predict outcomes in BCS, including the Child–Pugh score, Clichy index, and Rotterdam index.^{9,28} We investigated the possible correlation between these three indices and quantitative MR parameters, revealing that the Child–Pugh score and serum creatinine level, which are important determinants of prognosis, were correlated with the T1 relaxation time of the liver. Patients with reduced liver function had longer precontrast T1 relaxation times when classified by the Child–Pugh score, which correlated positively with the progression of liver damage. The Clichy score was also positively correlated with the T1 relaxation time of the liver in the precontrast MOLLI sequence.

Renal failure secondary to liver parenchyma disease is usually functional and occurs in the absence of significant changes in renal histology.²⁹ In our case series, interestingly, we found that serum creatinine values exhibited a positive correlation with the T1 values obtained from precontrast and postcontrast T1 and T2 maps. Creatinine levels were also negatively correlated with the RR of the T1 relaxation time. In the study by Zeitoun et al.,³⁰ serum creatinine was identified as one of the four significant prognostic factors in a multivariate analysis of BCS patients. How-

ever, the creatinine levels of the patients in this study were within the normal range (0.40–1.34 mg/dL), indicating that although the correlation was statistically significant, it was not clinically significant in these cases, or at least not at this stage.

This study has several limitations. First, the sample size is small, which negatively affects the generalization of our findings; the low incidence of the disease in the general population is responsible for this limitation. However, because the condition is rare, the findings of this study offer new potentially useful information for this patient population. A larger number of patients, some in the acute stage, would have allowed us to make a more detailed evaluation. Second, this study has some inherent limitations because of its retrospective design, resulting in incomplete data (relaxation times obtained from electrocardiogram-gated T1 MOLLI and T2 maps) in four patients. Third, three of our patients had undergone TIPS, which may have led to a decrease in the MRE stiffness values. However, because these patients were in the chronic stage and we focused on relatively long-term parenchymal changes, we did not exclude these patients. We considered that except for minor tissue changes, any damage that appeared resulted in some degree of fibrosis. Fourth, we hypothesized that subcapsular hyperintensities in T2WIs were fibrosis (as detailed in the literature, i.e., in¹³), and in the present study, we identified a prolongation of both T1 and T2 relaxation times and increased stiffness values. An important limitation of our study is that the presence of fibrosis was not confirmed histopathologically. In five patients, we observed that focal tissues that appeared normal on the T2WIs and T1 and T2 parametric maps were coded in yellow and/or red (indicating high stiffness) on MR the elastograms. Mottled contrast enhancement was observed in these cases. Hepatic congestion (increased upload) was not distributed homogeneously, as can be inferred from multiparametric techniques and different parametric maps. We hypothesize that fibrotic tissues, in addition to their high stiffness in the MREs, display pathological appearance, both visually and quantitatively, relative to the rest of the parenchyma on the T1 maps. In this context, we believe that tissues that are stiff in the MRE but appear normal on the T2WIs and T1 maps might be congested. The combined use of T2WIs, T1 mapping, and MREs (i.e., a multiparametric MR approach) can be expedient to further understand the pathophysiology.

In conclusion, the relative shortening of the T1 relaxation time in the HB phase after hepatocyte-specific contrast administration allows for the quantitative evaluation of global and segmental liver function in BCS. By providing absolute and comparable data, T1 relaxation times can be used to estimate the heterogeneous distribution of liver function in patients with BCS. However, T2 mapping and ADC values do not significantly contribute to the quantitative assessment of tissue changes. In this syndrome, in addition to fibrosis, hepatic congestion and sinusoidal dilatation appear to be responsible for elevated tissue stiffness. In the follow-up of these patients, quantitative parameters obtained from MRE and T1 mapping techniques, along with laboratory and clinical parameters, may allow an objective temporal evaluation of segmental and global changes. An alteration in quantitative parameters over time with the progression of the chronic process may be used to predict the course of the disease. The T1 relaxation time has the potential to be an objective prognostic marker because it reveals a correlation with important prognostic determinants such as the Child–Pugh score and serum creatinine level. To establish the role of quantitative MR methods in BCS, further prospective studies with large sample sizes are required. We hope our study promotes further methodologic work to determine clinically important differences in BCS.

Conflict of interest disclosure

The authors declared no conflicts of interest.

References

- Janssen HL, Garcia-Pagan JC, et al. Budd-Chiari syndrome: a review by an expert panel. *J Hepatol*. 2003;38(3):364–371. [\[CrossRef\]](#)
- Valla DC. The diagnosis and management of the Budd-Chiari syndrome: consensus and controversies. *Hepatology*. 2003;38(4):793–803. [\[CrossRef\]](#)
- Plompen EPC, Darwish Murad S, Hansen BE, et al. Prothrombotic genetic risk factors are associated with an increased risk of liver fibrosis in the general population: the Rotterdam study. *J Hepatol*. 2015;63(6):1459–1465. [\[CrossRef\]](#)
- Xu P, Lyu L, Sami MU, et al. Diagnostic accuracy of magnetic resonance angiography for Budd-Chiari syndrome: a meta-analysis. *Exp Ther Med*. 2018;16(6):4873–4878. [\[CrossRef\]](#)
- Li Q, Chen T, Shi N, Ye W, Yuan M, Shi Y. Quantitative evaluation of hepatic fibrosis by fibro Scan and Gd-EOB-DTPA-enhanced T1 mapping magnetic resonance imaging

- in chronic hepatitis B. *Abdom Radiol (NY)*. 2022;47(2):684–692. [\[CrossRef\]](#)
- Simonetto DA, Yang HY, Yin M, et al. Chronic passive venous congestion drives hepatic fibrogenesis via sinusoidal thrombosis and mechanical forces. *Hepatology*. 2015;61(2):648–659. [\[CrossRef\]](#)
- Idilman IS, Li J, Yin M, Venkatesh SK. MR elastography of liver: current status and future perspectives. *Abdom Radiol (NY)*. 2020;45(11):3444–3462. [\[CrossRef\]](#)
- Cazals-Hatem D, Vilgrain V, Genin P, et al. Arterial and portal circulation and parenchymal changes in Budd-Chiari syndrome: a study in 17 explanted livers. *Hepatology*. 2003;37(3):510–519. [\[CrossRef\]](#)
- Sakr M, Abdelhakam SM, Elsayed SA, et al. Validation of prognostic indices in Egyptian Budd-Chiari syndrome patients: a single-center study. *World J Gastroenterol*. 2017;23(4):629–637. [\[CrossRef\]](#)
- Noone TC, Semelka RC, Siegelman ES, et al. Budd-Chiari syndrome: spectrum of appearances of acute, subacute, and chronic disease with magnetic resonance imaging. *J Magn Reson Imaging*. 2000;11(1):44–50. [\[CrossRef\]](#)
- Katsube T, Okada M, Kumano S, et al. Estimation of liver function using T1 mapping on Gd-EOB-DTPA-enhanced magnetic resonance imaging. *Invest Radiol*. 2011;46(4):277–283. Erratum in: *Invest Radiol*. 2013;48(2):112. [\[CrossRef\]](#)
- Yoon JH, Lee JM, Paek M, Han JK, Choi BI. Quantitative assessment of hepatic function: modified look-locker inversion recovery (MOLLI) sequence for T1 mapping on Gd-EOB-DTPA-enhanced liver MR imaging. *Eur Radiol*. 2016;26(6):1775–1782. [\[CrossRef\]](#)
- Faria SC, Ganesan K, Mwangi I, et al. MR imaging of liver fibrosis: current state of the art. *Radiographics*. 2009;29(6):1615–1635. [\[CrossRef\]](#)
- Ferraioli G, Barr R. Ultrasound liver elastography beyond liver fibrosis assessment. *World J Gastroenterol*. 2020;26(24):3413–3420. [\[CrossRef\]](#)
- Mukund A, Pargewar SS, Desai SN, Rajesh S, Sarin SK. Changes in liver congestion in patients with Budd-Chiari syndrome following endovascular interventions: assessment with transient elastography. *J Vasc Interv Radiol*. 2017;28(5):683–687. [\[CrossRef\]](#)
- Wang HW, Shi HN, Cheng J, Xie F, Luo YK, Tang J. Real-time shear wave elastography (SWE) assessment of short- and long-term treatment outcome in Budd-Chiari syndrome: a pilot study. *PLoS One*. 2018;13(5):e0197550. [\[CrossRef\]](#)
- Srinivasa Babu A, Wells ML, Teytelboym OM, et al. Elastography in chronic liver disease: modalities, techniques, limitations, and future directions. *Radiographics*. 2016;36(7):1987–2006. [\[CrossRef\]](#)

18. Xu P, Lyu L, Ge H, et al. Segmental liver stiffness evaluated with magnetic resonance elastography is responsive to endovascular intervention in patients with Budd-Chiari syndrome. *Korean J Radiol.* 2019;20(5):773-780. [\[CrossRef\]](#)
19. Xu P, Lyu L, Lu X, Hu C, Xu K. Evaluating the short-term clinical efficacy of magnetic resonance elastography in patients with Budd-Chiari syndrome. *Acad Radiol.* 2021;28(Suppl 1):S179-S183. [\[CrossRef\]](#)
20. Mukund A, Sarin SK. Budd-Chiari syndrome: a focussed and collaborative approach. *Hepatol Int.* 2018;12(6):483-486. [\[CrossRef\]](#)
21. Erden A, Erden I, Yurdaydin C, Karayalçin S. Hepatic outflow obstruction: enhancement patterns of the liver on MR angiography. *Eur J Radiol.* 2003;48(2):203-208. [\[CrossRef\]](#)
22. Mancuso A. An update on management of Budd-Chiari syndrome: the issues of timing and choice of treatment. *Eur J Gastroenterol Hepatol.* 2015;27(3):200-203. [\[CrossRef\]](#)
23. Coilly A, Potier P, Broué P, et al. Budd-Chiari syndrome. *Clin Res Hepatol Gastroenterol.* 2020;44(4):420-425. [\[CrossRef\]](#)
24. Erden A, Erden I, Karayalçin S, Yurdaydin C. Budd-Chiari syndrome: evaluation with multiphase contrast-enhanced three-dimensional MR angiography. *AJR Am J Roentgenol.* 2002;179(5):1287-1292. [\[CrossRef\]](#)
25. Nilsson H, Blomqvist L, Douglas L, et al. Dynamic gadoxetate-enhanced MRI for the assessment of total and segmental liver function and volume in primary sclerosing cholangitis. *J Magn Reson Imaging.* 2014;39(4):879-886. [\[CrossRef\]](#)
26. Kamimura K, Fukukura Y, Yoneyama T, et al. Quantitative evaluation of liver function with T1 relaxation time index on gadoxetic acid-enhanced MRI: comparison with signal intensity-based indices. *J Magn Reson Imaging.* 2014;40(4):884-889. [\[CrossRef\]](#)
27. Haimerl M, Verloh N, Zeman F, et al. Assessment of clinical signs of liver cirrhosis using T1 mapping on gadoxetic acid-enhanced 3T MRI. *PLoS One.* 2013;8(12):e85658. [\[CrossRef\]](#)
28. Qi X, Ren W, Wang Y, Guo X, Fan D. Survival and prognostic indicators in Budd-Chiari syndrome: a systematic review of 79 studies. *Expert Rev Gastroenterol Hepatol.* 2015;9(6):856-875. [\[CrossRef\]](#)
29. Fortune B, Cardenas A. Ascites, refractory ascites and hyponatremia in cirrhosis. *Gastroenterol Rep (Oxf).* 2017;5(2):104-112. [\[CrossRef\]](#)
30. Zeitoun G, Escolano S, Hadengue A, et al. Outcome of Budd Chiari syndrome: a multivariate analysis of factors related to survival including surgical portosystemic shunting. *Hepatology.* 1999;30(1):84-89. [\[CrossRef\]](#)



Copyright © Author(s) - Available online at dirjournal.org.
Content of this journal is licensed under a Creative Commons
Attribution-NonCommercial 4.0 International License.

LAVA HyperSense and deep-learning reconstruction for near-isotropic (3D) enhanced magnetic resonance enterography in patients with Crohn's disease: utility in noise reduction and image quality improvement

Jung Hee Son 
Yedaun Lee 
Ho-Joon Lee 
Joonsung Lee 
Hyunwoong Kim 
Marc R. Lebel 

From the Department of Radiology (J.H.S., Y.L. ✉), chosai81@gmail.com, H-J.L.), Inje University College of Medicine, Haeundae Paik Hospital, Busan, Republic of Korea; GE Healthcare Korea, Seoul, Republic of Korea (J.L.); Clinical Trial Center (H.K.), Inje University College of Medicine, Haeundae Paik Hospital, Busan, Republic of Korea; GE Healthcare Canada (M.R.L.), Calgary, Canada.

Received 18 January 2023; revision requested 18 January 2023; last revision received 30 March 2023; accepted 02 April 2023.



Epub: 25.04.2023

Publication date: 30.05.2023

DOI: 10.4274/dir.2023.232113

PURPOSE

This study aimed to compare near-isotropic contrast-enhanced T1-weighted (CE-T1W) magnetic resonance enterography (MRE) images reconstructed with vendor-supplied deep-learning reconstruction (DLR) with those reconstructed conventionally in terms of image quality.

METHODS

A total of 35 patients who underwent MRE for Crohn's disease between August 2021 and February 2022 were included in this retrospective study. The enteric phase CE-T1W MRE images of each patient were reconstructed with conventional reconstruction and no image filter (original), with conventional reconstruction and image filter (filtered), and with a prototype version of AIR™ Recon DL 3D (DLR), which were then reformatted into the axial plane to generate six image sets per patient. Two radiologists independently assessed the images for overall image quality, contrast, sharpness, presence of motion artifacts, blurring, and synthetic appearance for qualitative analysis, and the signal-to-noise ratio (SNR) was measured for quantitative analysis.

RESULTS

The mean scores of the DLR image set with respect to overall image quality, contrast, sharpness, motion artifacts, and blurring in the coronal and axial images were significantly superior to those of both the filtered and original images ($P < 0.001$). However, the DLR images showed a significantly more synthetic appearance than the other two images ($P < 0.05$). There was no statistically significant difference in all scores between the original and filtered images ($P > 0.05$). In the quantitative analysis, the SNR was significantly increased in the order of original, filtered, and DLR images ($P < 0.001$).

CONCLUSION

Using DLR for near-isotropic CE-T1W MRE improved the image quality and increased the SNR.

KEYWORDS

Crohn's disease, MR enterography, image quality, deep learning, noise reduction

Crohn's disease (CD) is a chronic bowel inflammatory disease characterized by transmural discontinuous asymmetric inflammation that affects the bowel wall and is frequently accompanied by extramural complications.^{1,2} Cross-sectional imaging plays an important role in CD diagnosis and monitoring. As CD often presents in young populations who require repeat imaging during their lifetimes,^{3,4} magnetic resonance enterography (MRE) is preferred because of its high-contrast resolution, multiple imaging parameters, and lack of ionizing radiation.⁵⁻⁷

You may cite this article as: Son JH, Lee Y, Lee H-J, Lee J, Kim H, Lebel MR. LAVA HyperSense and deep-learning reconstruction for near-isotropic (3D) enhanced magnetic resonance enterography in patients with Crohn's disease: utility in noise reduction and image quality improvement. *Diagn Interv Radiol.* 2023;29(3):437-449.

Contrast-enhanced T1-weighted (CE-T1W) coronal imaging is a key component of MRE for evaluating the extent and severity of bowel inflammation.⁸⁻¹⁰ CE-T1WCE-T1W coronal dynamic images are acquired using ultra-fast spoiled gradient-echo (GRE) sequences with fat suppression. Currently, three-dimensional (3D) volumetric imaging techniques allow us to obtain near-isotropic dynamic images that provide high-spatial-resolution images with a relatively short total acquisition time. As the pixels are nearly isotropic, 3D datasets can easily be reformatted in any plane without loss of image resolution and demonstrate fine anatomic detail with thin sections.¹¹ However, owing to bowel peristalsis or respiration and limited breath-holding duration, it is challenging to obtain high-resolution isotropic images without compromising image quality.

Compressed sensing (CS) enables near-isotropic CE-T1W coronal images to be obtained within a short scan time with a single-breath hold.^{12,13} It can also be useful for reducing noise. However, blurring can be introduced when the images are not sufficiently compressible or when excessive acceleration is used. Additionally, when the scan time is fixed for acquiring high-resolution images, the signal-to-noise ratio (SNR) can be decreased as a tradeoff between the SNR and resolution.¹⁴ Recent advances in MR imaging (MRI) technology have introduced deep learning to the image reconstruction process, which, in this study, was expected to improve the SNR and image sharpness compared with CS alone.¹⁵

However, the utility of deep learning to reduce noise and improve sharpness for MRE has not yet been investigated. Therefore, the purpose of this study was to compare near-isotropic CE-T1W images of MRE reconstructed using deep-learning reconstruction

(DLR), conventional reconstruction, and image filter (filtered) techniques as well as conventional reconstruction and no image filter (original) in terms of image quality.

Methods

This retrospective single-center study was approved by the Inje University Haeundae Paik Hospital Institutional Review Board Ethics Committee (protocol number: HPIRB 2022-04-028-001) on April 28, 2022, and the requirement for informed consent was waived.

Study population

We retrospectively registered consecutive patients with known or suspected CD who underwent MRE at our institution between August 2021 and February 2022. In total, 36 patients were identified; one was excluded because of severe degradation of image quality, and 35 patients were included in the final analysis. Patient demographics and CD-related patient characteristics at the time of MRE were collected from electronic medical records.

MRE protocol

After the oral administration of 1,000 mL of polyethylene glycol solution (Coolprep, Taejoon Pharmaceutical Co.), MRE was performed. Scans were acquired using a 3 T MRI scanner (SIGNA™ Architect, GE Healthcare) with two 30-channel surface coils (AIR™ anterior array coils). To avoid bowel peristalsis, 7.5 mg of cimetropium bromide (Alpit, Hana Pharmaceutical Co.) was administered at three different intervals during the examination; the first dose was administered just before the start of the scan, the second

dose was administered just before the diffusion-weighted image was obtained, and the third dose was administered just before the coronal T1-weighted images were obtained. The coronal T1-weighted spoiled GRE sequence [liver acquisition with acceleration volume acquisition (LAVA)] with fat suppression was acquired during breath-holding, before contrast injection, and at enteric and portal phases that were obtained after the intravenous administration (0.2 mL/kg at a rate of 2 mL/s) of gadoterate meglumine (Dotarem, Guerbet) followed by a saline bolus injection. A coronal enteric phase was obtained using bolus tracking when the contrast material arrived at the abdominal aorta. The coronal portal phase image was subsequently obtained after providing breath-holding instructions between the two phases. The typical imaging parameters of the fat-suppressed LAVA in this study are summarized in Table 1. The scan time was set to approximately 17 seconds, with slight variations made to accommodate the patient's size.

Three image sets of enteric phases were generated: one with conventional reconstruction and no image filter (original), one with conventional reconstruction and vendor-provided image filter (B, high sharpening, some smoothing) (filtered), and one with a vendor-supplied prototype of AIR™ Recon DL 3D (DLR).^{16,17} The DLRs were performed offline using an Intel (Santa Clara, CA) Core i7-10850H CPU (2.70 GHz and six cores), which took approximately one hour to complete each series. These image sets were then reformatted into an axial plane with a slice thickness of 1.4 mm.

In our institution, the filtered image is a standard-of-care (SOC) 3D reconstructed im-

Main points

- Deep learning in reconstruction (DLR) can improve image quality and increase the signal-to-noise ratio in contrast-enhanced T1-weighted (CE-T1W) magnetic resonance enterography (MRE).
- The DLR technique enables high-resolution near-isotropic CE-T1W MRE with diagnostic image quality.
- Near-isotropic CE-T1W MRE allows high-quality axial reformatted images to be obtained from the same dynamic phase, which is useful for the multiplanar evaluation of anatomical details of bowel segments or extramural complications of Crohn's disease.

Table 1. Scan parameters for coronal T1-weighted spoiled gradient-echo sequence (liver acquisition with acceleration volume acquisition) with fat suppression for the magnetic resonance enterography protocol in this study

| Parameter | Value |
|--|-----------------|
| Orientation | Coronal |
| TR/TE (ms/ms) | 3.6/1.6 |
| FOV (mm) | 380 x 304 |
| No. of slices | 120 |
| Bandwidth (kHz/pixel) | 83.33 |
| Matrix | 300 x 260 |
| Voxel size (mm ³) | 1.3 x 1.5 x 1.6 |
| Flip angle (degrees) | 10 |
| Fat saturation | SPECIAL |
| Acceleration factor | 2 x 1.8 |
| HyperSense factor | 1.2 |
| SPECIAL, spectral inversion at lipid; TR, repetition time; TE, echo time; FOV, field of view | |

age that uses a postprocessing filter after the image is reconstructed. The filter is applied as a postprocessing step after image reconstruction and works by trading-off noise reduction and image sharpening in the image domain. Specifically, the filter employs smoothing to reduce noise, which can cause the image to appear blurred, and image sharpening to enhance the clarity of the image, which can increase the noise level.

AIR™ Recon DL is a deep-learning-based reconstruction method for improving image sharpness by removing truncation artifacts while jointly denoising the image to improve its quality.¹⁶⁻¹⁸ It applies a convolutional neural network (CNN) in an image-reconstruc-

tion pipeline using raw k-space data to generate high-fidelity images. The CNN is trained in a supervised manner to generate high-resolution data with minimal ringing artifacts and very low noise levels.¹⁶ The AIR™ Recon DL, which was originally designed for 2D imaging, was extended to 3D to reduce noise and ringing in all three directions, thus improving both SNR and spatial resolution.^{17,18} The vendor-provided AIR™ Recon DL 3D prototype was applied offline to the raw k-space data following image acquisition. The prototype DLR allowed for tunable noise-reduction levels (25%, 50%, and 75%, with higher levels corresponding to greater denoising). After conducting phantom experiments and reaching a consensus during preliminary

reading sessions, the denoising level was selected at 75% based on agreement among the readers (Supplementary Figures 1, 2).

Image analysis

Two abdominal radiologists (J.H.S. and Y.L., with 8 and 15 years of experience in interpreting MRE, respectively) independently assessed each coronal and reformatted axial image of three image sets (original, filtered, and DLR) for subjective image quality using a 5-point Likert scale (with 5 being the highest quality). For unbiased evaluation, the readers were blinded to the patients' personal details and clinical and laboratory information as well as the reconstruction method that had

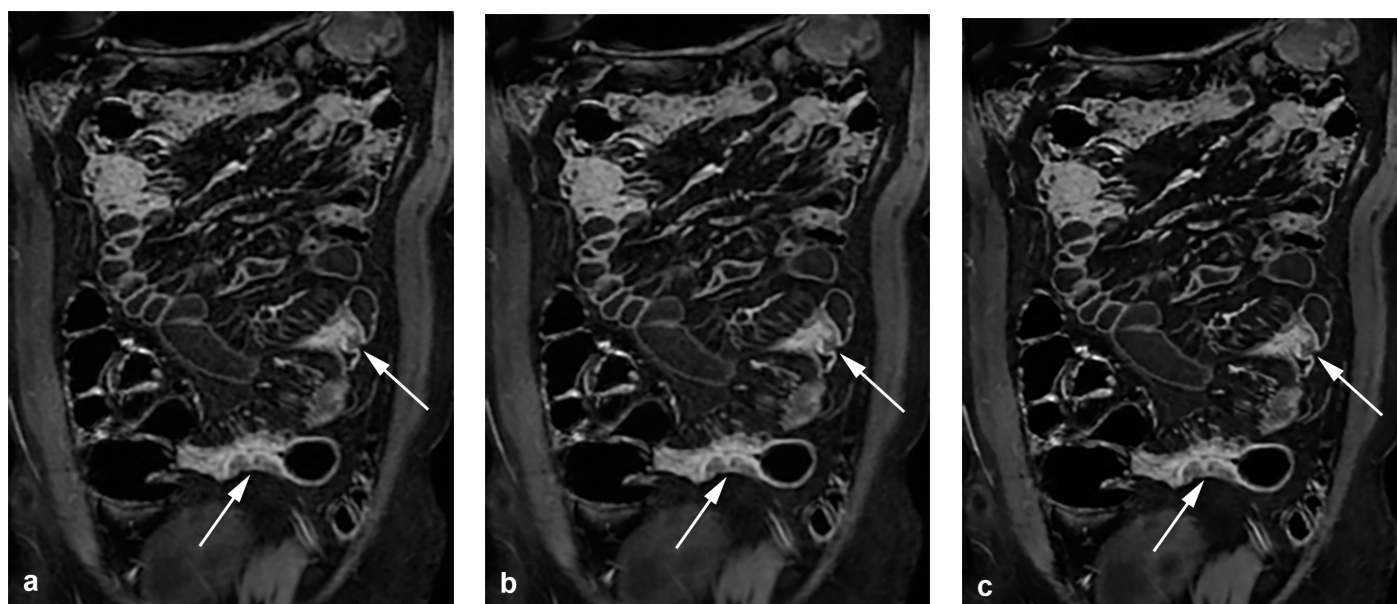


Figure 1. Dynamic enteric phase contrast-enhanced T1-weighted images of a 30-year-old man with active Crohn's disease. Three sets of coronal images were obtained, each with (a) conventional reconstruction and no image filter (original); (b) with conventional reconstruction and image filter (filtered); and (c) with deep-learning reconstruction (DLR) at the noise-reduction level of 75% (DLR). The DLR image (c) shows increased sharpness of bowel walls and mesenteric vessels, enabling better visualization of active inflammation of bowel segments and adjacent comb signs (arrows). A reduction of noise with a slight synthetic appearance is also noted in the DLR image (c) compared with the other two images (a, b).

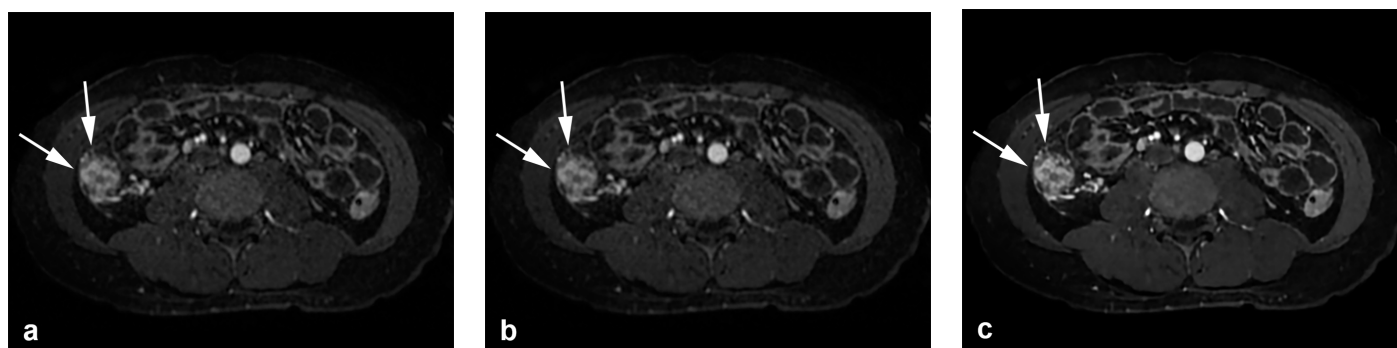


Figure 2. Dynamic enteric phase contrast-enhanced T1-weighted images of an 18-year-old man with active Crohn's disease. Three sets of images were obtained and reformatted in the axial plane with a 1.4-mm slice thickness: (a) with conventional reconstruction and no image filter (original); (b) with conventional reconstruction and image filter (filtered); and (c) with deep-learning reconstruction (DLR) at the noise-reduction level of 75% (DLR). The DLR image (c) better visualizes active inflammation in the ascending colon (arrows) with lower noise, a sharper margin of the bowel wall and vascularity, and better contrast of bowel wall stratification compared with the other two images (a, b). In the qualitative analysis, the DLR image was given a higher score (4 or 5) by two readers regarding overall image quality, contrast, sharpness, motion artifacts, and blurring than the other two images. The consecutive images of the same patient are also presented in Supplementary Video 1, available in the online supplement.

been applied. The analysis involved two separate image sessions without intervals: one for coronal images and the other for axial images. Blinding the image sets based on whether they were axial or coronal was not possible, and including an interval between the image sessions was deemed unnecessary, as no significant bias was likely to be generated as a result. In this qualitative analysis session, overall image quality, contrast, sharpness, presence of motion artifacts, blurring, and synthetic appearance were evaluated based on a previous study.¹² The overall image quality affecting diagnostic confidence was graded as follows: 1 = very poor image quality displaying non-diagnostic images; 2 = poor image quality with significantly impaired diagnostic confidence; 3 = fair image quality with slightly impaired diagnostic confidence; 4 = good image quality; and 5 = perfect image quality. The contrast and sharpness of the bowel walls, mesenteric vessels, and perienteric structures were evaluated analogously to the scales of overall image quality as follows: 1 = very poor contrast or sharpness with no detectable structures; 2 = poor contrast or sharpness rendering difficulty in distinguishing structures; 3 = fair contrast or sharpness with partially indistinguishable structures; 4 = good contrast or sharpness; and 5 = excellent contrast or sharpness. Motion artifacts, blurring of fine details, and synthetic appearance that could degrade image quality were rated as follows: 1 = severe artifacts or diagnostically unusable; 2 = substantial artifacts with major diagnostic impairment; 3 = moderate artifacts with minor diagnostic impairment; 4 = minimal artifacts; and 5 = no artifacts. Both blurring and synthetic appearance are artifacts that may occur with the CS technique and, potentially, with DLR.¹⁹⁻²¹ Synthetic appearance refers to a "plastic" or "cartoon-like" appearance that is attributed to various iterative reconstructions.^{20,21}

The radiologists were additionally asked to record the presence of any extramural complications in the small or large bowels (e.g., abscess, sinus tract, fistula, or inflammatory mass) and whether reviewing the reformatted axial images in addition to the coronal images was more helpful in detecting and evaluating penetrating disease than reviewing the coronal images alone.

For the quantitative image analysis, three representative locations were chosen in the coronal and axial planes (Supplementary Figure 3). For the coronal plane, images showing both the external iliac and femoral arteries at the level where multiple small bowel loops

are visible, aortic bifurcation, and kidneys at the level where the ascending and descending colons are visible were chosen to calculate the SNR in the anterior, middle, and posterior portions of the abdominal cavity, respectively. For the axial plane, images at the level of the superior mesenteric artery, aortic bifurcation, and pelvic cavity showing superior gluteal veins were chosen to calculate the SNR in the upper, middle, and lower portions of the abdominal cavity, respectively. The SNR was calculated by dividing the mean signal of the slice by the estimated noise levels given in the standard deviations.²² The noise levels were estimated using a hybrid discrete wavelet transform and edge information removal-based algorithm, which assumes that the energy of noise is equally distributed in sub-bands of wavelet coefficients but the energy of an image is mostly confined in low-low, low-high, and high-low sub-bands (Supplementary Figure 4).²³ We implemented the method using NumPy, pydicom, cv2, and pywt packages in Python (version 3.7.9).

Statistical analysis

In the qualitative analysis, mean scores for overall image quality, contrast, sharpness and presence of motion artifacts, blurring, and synthetic appearance in the three image sets measured by the two readers were compared using Friedman's test in the axial and coronal planes, respectively. If there was any significant difference between the three image groups, Bonferroni corrections were applied for multiple comparisons. The interobserver agreement of each score between the two readers was evaluated using quadratic weighted kappa coefficients. The kappa estimate was considered poor for $\kappa < 0.21$, fair for $\kappa = 0.21-0.40$, moderate for $\kappa = 0.41-0.60$, good for $\kappa = 0.61-0.80$, and excellent for $\kappa = 0.81-1.00$.²⁴ As the MRI images analyzed in this study were primarily used in real clinical practice, it was relatively unlikely that they were non-diagnostic images with very low-quality scores, of which the data distribution might be highly consistent and deviated. Therefore, when the weighted kappa values were not estimable because the data distribution of scores was too skewed, the overall proportion of agreement was calculated.^{25,26} In the quantitative analysis, a repeated-measures analysis of variance with a Greenhouse-Geisser correction was used to compare SNRs between the three image sets. For data with a non-normal distribution, the Friedman test was performed, and the Shapiro-Wilk test was used to check if a

variable followed a normal distribution. Bonferroni's method was applied in the post-hoc test. All statistical analyses were performed using SPSS version 25.0 (IBM Corp.) and MedCalc version 18 (MedCalc Software) software. Statistical significance was set at a value of $P < 0.05$.

Results

Patient characteristics

The characteristics of the study population are summarized in Supplementary Table 1. Four patients had a history of bowel surgery due to CD complications. The mean scan time was 15.86 ± 1.14 seconds (range: 14-18 seconds).

Qualitative image analysis

The results of the qualitative image analysis, which were expressed as the mean and standard deviation of the two readers' scores, are summarized in Table 2. The results of multiple comparisons among the three image sets are presented in Supplementary Table 2. The mean scores of the DLR image set with respect to overall image quality, contrast, sharpness, motion artifacts, and blurring in both the coronal and axial images were significantly superior to those of both the filtered and original images ($P < 0.001$). However, the mean scores for synthetic appearance in DLR were significantly lower than those of the filtered and original images ($P < 0.05$). The filtered images tended to score slightly higher than the original images for overall image quality, contrast, sharpness, motion artifacts, and blurring, although they were slightly lower for synthetic appearance; however, there was no statistically significant difference between their mean scores ($P > 0.05$) (Figures 1-3, and Supplementary Figure 5 and Supplementary Video 1, available in the online supplement).

The interobserver agreement for the overall image quality, contrast, sharpness, motion artifacts, and blurring in both the coronal and axial images was moderate to excellent (κ , 0.426-1.000); however, the blurring of the axial images showed fair agreement ($\kappa = 0.398$) (Table 3). The interobserver agreement for a synthetic appearance on the coronal and axial DLR images was also good to excellent (κ , 0.660-0.828). Since the interobserver agreement for synthetic appearance in both the original and filtered images was not estimable, the overall proportion of agreement was calculated: there was no discrepancy in the coronal and axial original images and

the axial filtered images (100% agreement), and there were four discrepancies out of 35 patients (88.6% agreement) in the coronal filtered images.

Presence of extramural complications

Both readers detected extramural complications in 10 patients. There was no discordant interpretation of the presence of extramural complication between the two readers. These findings were demonstrated

in the images of both the coronal and axial planes (Figure 3 and Supplementary Figure 6). Among the cases of extramural complications, the readers found that reviewing axial images in addition to coronal images was more helpful than reviewing coronal images alone in all cases (Supplementary Figure 6 and Supplementary Video 2, available in the online supplement).

Quantitative image analysis

The SNRs of the three different locations in both the coronal and axial planes were significantly increased in the order of original, filtered, and DLR images ($P < 0.001$) (Table 4). The mean SNRs of all three different locations were also compared between the three image sets in each coronal and axial plane. As a result, the mean SNR of the DLR measured was the highest, and the mean SNR of the original images was the lowest ($P < 0.001$) (Table 4).

Discussion

Our results demonstrated that the vendor-supplied prototype DLR significantly increased the SNR; improved the image quality, contrast, and sharpness; and decreased perceived motion artifacts in the enhanced T1W MRE images. Furthermore, using DLR enables high-resolution near-isotropic CE-T1W MRE with sufficient image quality. It allows high-quality axial reformatted images to be obtained from the same dynamic phase, which helps depict the anatomic details of bowel segments or extramural complications, such as fistulas or abscesses.

The CE-T1W sequence is important for evaluating active inflammation in CD.⁸⁻¹⁰ With the advantage of rapid acquisitions, the 3D-GRE sequence is the SOC technique for CE-T1W MRE. However, this sequence is susceptible to motion artifacts, as obtaining high-resolution CE-T1W MRE within one breath hold could be challenging due to bowel peristalsis, respiration, and limited breath holding. To overcome this challenge, several approaches have been used to accelerate MRI, such as parallel imaging and CS.¹³ However, excessive acceleration can cause a loss of SNR, which leads to reduced image quality.^{14,27}

Recent advances in DLR offer an additional way to improve image quality and shorten the scan time. To date, the current published reports on DLR for 3D-GRE are limited in diversity. One introduced algorithm combines super resolution (Siemens) with partial Fourier reconstruction.^{28,29} The algorithm is trained to perform both up-sampling in the phase-encoding direction and partial Fourier reconstruction. This technique showed a significant noise reduction and improvement of image sharpness and lesion conspicuity in abdominal MRI. In our study, we used the AIR™ Recon DL (GE Healthcare) technique on 3D LAVA with CS sequences to reduce noise and ringing in all three directions.

Table 2. Qualitative analysis of the contrast-enhanced T1-weighted images of magnetic resonance enterography with three different reconstruction methods

| | Original | Filtered | DLR | P value* |
|-----------------------|-------------|-------------|-------------|---------------------|
| Coronal | | | | |
| Overall image quality | 3.56 ± 0.54 | 3.77 ± 0.56 | 4.67 ± 0.51 | <0.001 [†] |
| Contrast | 3.96 ± 0.39 | 4.11 ± 0.46 | 4.69 ± 0.49 | <0.001 [†] |
| Sharpness | 3.57 ± 0.50 | 3.81 ± 0.49 | 4.69 ± 0.50 | <0.001 [†] |
| Motion artifacts | 3.67 ± 0.70 | 3.74 ± 0.79 | 4.33 ± 0.72 | <0.001 [†] |
| Blurring | 3.56 ± 0.53 | 3.70 ± 0.49 | 4.24 ± 0.43 | <0.001 [†] |
| Synthetic appearance | 5.00 ± 0.00 | 4.94 ± 0.16 | 4.44 ± 0.48 | <0.001 [†] |
| Axial | | | | |
| Overall image quality | 3.29 ± 0.47 | 3.59 ± 0.54 | 4.67 ± 0.53 | <0.001 [†] |
| Contrast | 3.90 ± 0.34 | 3.90 ± 0.27 | 4.71 ± 0.41 | <0.001 [†] |
| Sharpness | 3.17 ± 0.38 | 3.51 ± 0.49 | 4.64 ± 0.46 | <0.001 [†] |
| Motion artifacts | 3.64 ± 0.59 | 3.66 ± 0.60 | 4.34 ± 0.68 | <0.001 [†] |
| Blurring | 3.14 ± 0.38 | 3.46 ± 0.48 | 4.16 ± 0.34 | <0.001 [†] |
| Synthetic appearance | 5.00 ± 0.00 | 5.00 ± 0.00 | 4.43 ± 0.46 | <0.001 [†] |

Data are presented as mean ± standard deviation. *P values were obtained by comparing three different reconstruction methods using the Friedman test. [†]Post-hoc Bonferroni's test for multiple comparisons revealed significant differences between original and DLR images and between filtered and DLR images ($P < 0.05$) but not between the original and filtered images (Supplementary Table 2). Original, conventional reconstruction with no image filter; filtered, conventional reconstruction with image filter; DLR, deep-learning reconstruction.

Table 3. Interobserver agreement between the two readers for qualitative analysis

| | Original | Filtered | DLR |
|-----------------------|---------------------|---------------------|---------------------|
| | Kappa (95% CI) | Kappa (95% CI) | Kappa (95% CI) |
| Coronal | | | |
| Overall image quality | 0.859 (0.694–1.000) | 0.759 (0.573–0.944) | 0.846 (0.660–1.000) |
| Contrast | 0.615 (0.304–0.927) | 0.650 (0.380–0.920) | 0.687 (0.504–0.870) |
| Sharpness | 0.792 (0.619–0.965) | 0.731 (0.532–0.930) | 0.791 (0.645–0.937) |
| Motion artifacts | 0.760 (0.623–0.898) | 0.791 (0.678–0.905) | 0.867 (0.747–0.986) |
| Blurring | 0.766 (0.553–0.980) | 0.579 (0.386–0.773) | 0.672 (0.433–0.910) |
| Synthetic appearance | N/E | N/E | 0.828 (0.644–1.000) |
| Axial | | | |
| Overall image quality | 0.673 (0.412–0.934) | 0.857 (0.689–1.000) | 0.949 (0.846–1.000) |
| Contrast | 0.531 (0.165–0.896) | 0.481 (0.090–0.873) | 0.595 (0.325–0.865) |
| Sharpness | 0.426 (0.050–0.802) | 0.692 (0.483–0.901) | 0.815 (0.618–1.000) |
| Motion artifacts | 0.811 (0.668–0.953) | 0.784 (0.635–0.933) | 0.882 (0.765–0.999) |
| Blurring | 0.525 (0.164–0.886) | 0.598 (0.376–0.819) | 0.398 (0.072–0.724) |
| Synthetic appearance | N/E | N/E | 0.660 (0.427–0.893) |

Original, conventional reconstruction with no image filter; filtered, conventional reconstruction with image filter; DLR, deep-learning reconstruction; N/E, not estimable; CI, confidence interval.

Table 4. Comparison of signal-to-noise ratio between the contrast-enhanced T1-weighted images of magnetic resonance enterography with three different reconstruction methods

| | Original | Filtered | DLR | P value |
|----------------|---------------|---------------|----------------|---------------------|
| Coronal | | | | |
| Total* | 52.50 ± 8.85 | 64.85 ± 10.95 | 86.15 ± 12.96 | <0.001 [†] |
| Anterior | 55.10 ± 10.38 | 68.02 ± 12.85 | 87.87 ± 18.55 | <0.001 [†] |
| Middle | 57.25 ± 10.96 | 70.78 ± 13.58 | 94.68 ± 15.45 | <0.001 [†] |
| Posterior | 45.16 ± 6.87 | 55.76 ± 8.52 | 75.88 ± 9.43 | <0.001 [†] |
| Axial | | | | |
| Total* | 49.59 ± 6.79 | 59.23 ± 8.12 | 85.19 ± 12.32 | <0.001 [†] |
| Upper | 67.64 ± 13.98 | 80.04 ± 16.74 | 116.95 ± 26.25 | <0.001 [†] |
| Middle | 32.74 ± 3.83 | 39.96 ± 4.77 | 62.04 ± 9.65 | <0.001 [†] |
| Lower | 48.40 ± 7.02 | 57.69 ± 8.51 | 76.58 ± 9.60 | <0.001 [†] |

[†]P value was obtained by comparing three different reconstruction methods using repeated-measures analysis of variance with a Greenhouse–Geisser correction. Post-hoc Bonferroni's tests for multiple comparisons revealed a significant difference between the original and DLR, between the filtered and DLR, and between the original and filtered images ($P < 0.05$). [‡]P value was obtained by comparing three different reconstruction methods using the Friedman test. Post-hoc Bonferroni's tests for multiple comparisons revealed a significant difference between the original and DLR, between the filtered and DLR, and between the original and filtered images ($P < 0.05$). *Mean values of three different locations in each image set. Data are presented as mean ± standard deviation. Original, conventional reconstruction with no image filter; filtered, conventional reconstruction with image filter; DLR, deep-learning reconstruction.

The technique applies a CNN in the image reconstruction pipeline using raw k-space data. The AIR™ Recon DL technique enables the acquisition time to be reduced without affecting the image quality and high-resolution images to be obtained without reducing the SNR. We obtained high-resolution near-isotropic CE-T1W MRE images within a single breath hold and achieved sufficient image quality with the aid of CS and DLR. To our knowledge, this is the first study to evaluate the utility of DLR for 3D LAVA with CS for MRE in clinical practice.

In addition, these benefits are not restricted to the acquired imaging plane but are effective in the reformatted planes. With DLR, the SNR and image quality were improved not only in the plane but also through the plane. This can be particularly useful for improving the quality of reformatted images in clinical situations when multiple review planes can be helpful but simultaneous acquisition is required because of the time-dependent image contrast.

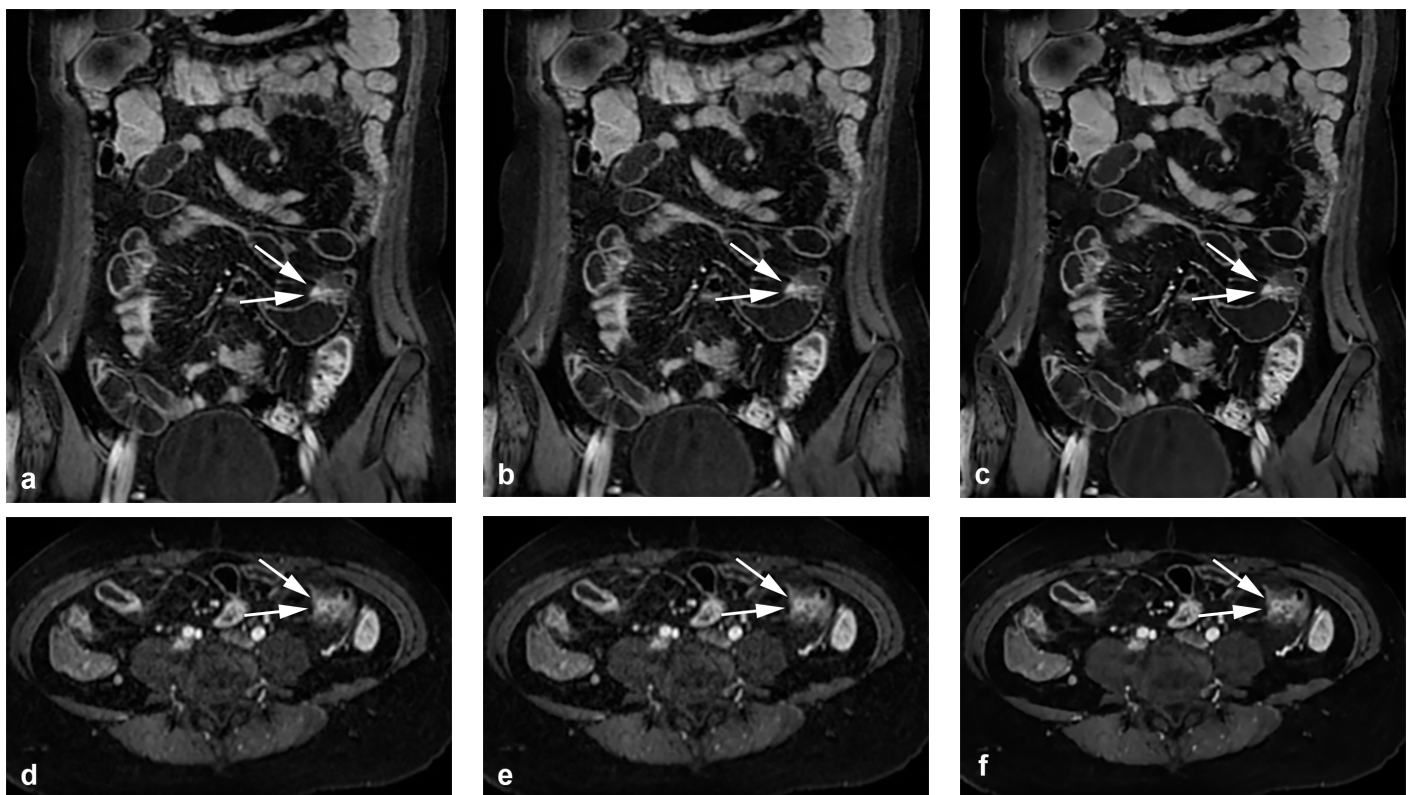


Figure 3. Dynamic enteric phase contrast-enhanced T1-weighted images of a 28-year-old woman with active Crohn's disease. Three sets of images were obtained, each with (a) conventional reconstruction and no image filter (original); (b) with conventional reconstruction and image filter (filtered); and (c) with deep-learning reconstruction (DLR) at the noise-reduction level of 75% (DLR). Axial images with a 1.4-mm slice thickness were reformatted from coronal images, respectively (d-f). The DLR images in both the coronal and axial planes (c,f) show lower noise, a sharper margin of the bowel wall and vasculature, and better contrast of bowel wall stratification than the other two images (a, b, d, e). In the coronal image sets, a small sinus tract is detected in the proximal ileum (arrows), which is better visualized in the DLR image (c). The corresponding penetrating lesion in the proximal ileum is also well visualized in the sets of axial images (arrows) and is most clearly visible in DLR (f), which helps increase diagnostic confidence.

Previously, we obtained CE-T1W images in the delayed phase after acquiring dynamic coronal T1W images. Delayed-phase axial images may help differentiate fibrosis from active inflammation.³⁰ However, as the bowel wall enhancement pattern and mesenteric vascularity indicative of active inflammation are most well depicted in earlier phases of the dynamic study,³¹ axial images in the delayed phase could limit the provision of detailed anatomic structures and hinder lesion detection and diagnosis due to its different and non-simultaneous acquisition timing compared with that of coronal dynamic images. Our axial-reformatted CE-T1W images of the simultaneous dynamic phase of the coronal images are superior to axial CE-T1W images of the delayed phase for evaluating active inflammation. Also, axial images help detect penetrating complications, such as fistulas and abscesses, by multiplanar correlation.³⁰ In our study, both readers stated that an additional review of the axial images was helpful in the detection and evaluation of penetrating disease in all cases. In addition, because we can obtain axial images without additional image acquisition, we can reduce the total scan time of MRE. Although the acquisition time of additional axial images is quite short, a shorter scan time is better for patient compliance because the oral administration of polyethylene glycol can cause the urge to evacuate during MR acquisition.

Our study has several limitations. First, the images were retrospectively reviewed. Second, the sample size was relatively small. Third, although we conducted a blinded analysis for each image set, the significant reduction in noise and the differences in image texture made perfect blinding impossible. Fourth, in our study, the generation of images with DLR took a relatively significant length of time, approximately one hour for each series, due to the computational intensity of the DLR technique. While this process could be accelerated significantly using graphics processing units, the long reconstruction time could be a drawback for using DLR in real practice. Nonetheless, this technique is currently available commercially and has been integrated into the hardware of MR machines; the reconstruction is generated immediately after image acquisition and is displayed almost simultaneously with the original image. Fifth, we acknowledge that our study's inclusion of only patients with CD, who tend to be young with a low body mass index, may limit the generalizability of our study results to the broader population. Further, we did not statistically analyze the

detection of penetrating disease in the axial reformatted images. The number of cases of penetrating disease was small, and penetrating disease could already be detected with coronal images. However, both readers mentioned that additional axial images could help increase their diagnostic confidence in all cases. Finally, we did not evaluate the diagnostic accuracy for active inflammation. Our study aimed to assess the image quality of near-isotropic CE-T1W MRE using DLR. Previous studies^{8,10,12,30,31} used endoscopic findings or findings from full-protocol MRE as the reference standard for active inflammation in CD. In our study, we compared the image quality between image sets obtained from the same image scan with different reconstructions. MRE has demonstrated high diagnostic performance for the diagnosis of active inflammation in CD.^{32,33} We believe that comparing diagnostic performance between image sets from the same scan image, which is already used in real clinical practice, is not essential. Furthermore, CE-T1W images play the most important role in evaluating active inflammation among the multiple sequences of MRE. Therefore, we considered that reference from full-protocol MRE was inappropriate in our study because the CE-T1W used as a reference standard was the same image as the image sets to be compared.

In conclusion, this is the first study to investigate DLR for CE-T1W MRE in clinical practice. The use of DLR for near-isotropic CE-T1W MRE provides improved image quality and an increased SNR. It allows high-quality axial reformatted images to be obtained from the same dynamic phase, which is useful for the multiplanar evaluation of anatomical details of bowel segments or extramural complications.

Conflict of interest disclosure

The authors declared no conflicts of interest.

Funding

This work is supported by the 2019 Inje University research grant.

References

1. Lichtenstein GR, Loftus EV, Isaacs KL, Regueiro MD, Gerson LB, Sands BE. ACG clinical guideline: management of Crohn's disease in adults. *Am J Gastroenterol.* 2018;113(4):481-517. Erratum in: *Am J Gastroenterol.* 2018;113(7):1101. [CrossRef]
2. Reinisch S, Schweiger K, Pablik E, et al. An index with improved diagnostic accuracy for the diagnosis of Crohn's disease derived from

the Lennard-Jones criteria. *Aliment Pharmacol Ther.* 2016;44(6):601-611. [CrossRef]

3. Kim SC, Ferry GD. Inflammatory bowel diseases in pediatric and adolescent patients: clinical, therapeutic, and psychosocial considerations. *Gastroenterology.* 2004;126(6):1550-1560. [CrossRef]
4. Park SH, Kim YJ, Rhee KH, et al. A 30-year trend analysis in the epidemiology of inflammatory bowel disease in the Songpa-Kangdong District of Seoul, Korea in 1986-2015. *J Crohns Colitis.* 2019;13(11):1410-1417. [CrossRef]
5. Horsthuis K, Bipat S, Stokkers PC, Stoker J. Magnetic resonance imaging for evaluation of disease activity in Crohn's disease: a systematic review. *Eur Radiol.* 2009;19(6):1450-1460. [CrossRef]
6. Messaris E, Chandolias N, Grand D, Pricolo V. Role of Magnetic resonance enterography in the management of Crohn disease. *Arch Surg.* 2010;145(5):471-475. [CrossRef]
7. Tolan DJ, Greenhalgh R, Zealley IA, Halligan S, Taylor SA. MR enterographic manifestations of small bowel Crohn disease. *RadioGraphics.* 2010;30(2):367-384. [CrossRef]
8. Low RN, Sebrests CP, Politoske DA, et al. Crohn disease with endoscopic correlation: single-shot fast spin-echo and gadolinium-enhanced fat-suppressed spoiled gradient-echo MR imaging. *Radiology.* 2002;222(3):652-660. [CrossRef]
9. Pupillo VA, Di Cesare E, Frieri G, Limbucci N, Tanga M, Masciocchi C. Assessment of inflammatory activity in Crohn's disease by means of dynamic contrast-enhanced MRI. *Radiol Med.* 2007;112(6):798-809. [CrossRef]
10. Spieler B, Hindman N, Levy J, et al. Contrast-enhanced MR enterography as a stand-alone tool to evaluate Crohn's disease in a paediatric population. *Clin Radiol.* 2013;68(10):1024-1030. [CrossRef]
11. Tongdee R, Narra VR, Oliveira EP, Chapman W, Elsayes KM, Brown JJ. Utility of 3D magnetic resonance imaging in preoperative evaluation of hepatobiliary diseases. *HPB (Oxford).* 2006;8(4):311-317. [CrossRef]
12. Kim J, Seo N, Bae H, et al. Comparison of Sensitivity Encoding (SENSE) and compressed sensing-SENSE for contrast-enhanced T1-weighted imaging in patients with Crohn disease undergoing MR enterography. *AJR Am J Roentgenol.* 2022;218(4):678-686. [CrossRef]
13. Yoon JH, Nickel MD, Peeters JM, Lee JM. Rapid imaging: recent advances in abdominal MRI for reducing acquisition time and its clinical applications. *Korean J Radiol.* 2019;20(12):1597-1615. [CrossRef]
14. Kale SC, Chen XJ, Henkelman RM. Trading off SNR and resolution in MR images. *NMR Biomed.* 2009;22(5):488-494. [CrossRef]
15. Ueda T, Ohno Y, Yamamoto K, et al. Compressed sensing and deep learning reconstruction for women's pelvic MRI denoising: utility for

- improving image quality and examination time in routine clinical practice. *Eur J Radiol.* 2021;134:109430. [\[CrossRef\]](#)
16. Lebel RM. Performance characterization of a novel deep learning-based MR image reconstruction pipeline. arXiv. 2020. [\[CrossRef\]](#)
 17. Sun S, Tan ET, Mintz DN, et al. Evaluation of deep learning reconstructed high-resolution 3D lumbar spine MRI. *Eur Radiol.* 2022;32(9):6167-6177. [\[CrossRef\]](#)
 18. Chazen JL, Tan ET, Fiore J, Nguyen JT, Sun S, Sneag DB. Rapid lumbar MRI protocol using 3D imaging and deep learning reconstruction. *Skeletal Radiol.* 2023. [\[CrossRef\]](#)
 19. Jaspan ON, Fleysher R, Lipton ML. Compressed sensing MRI: a review of the clinical literature. *Br J Radiol.* 2015;88(1056):20150487. [\[CrossRef\]](#)
 20. Shaikh J, Stoddard PB, Levine EG, et al. View-sharing artifact reduction with retrospective compressed sensing reconstruction in the context of contrast-enhanced liver MRI for hepatocellular carcinoma (HCC) screening. *J Magn Reson Imaging.* 2019;49(4):984-993. [\[CrossRef\]](#)
 21. Zhang T, Chowdhury S, Lustig M, et al. Clinical performance of contrast enhanced abdominal pediatric MRI with fast combined parallel imaging compressed sensing reconstruction. *J Magn Reson Imaging.* 2014;40(1):13-25. [\[CrossRef\]](#)
 22. Dietrich O, Raya JG, Reeder SB, Reiser MF, Schoenberg SO. Measurement of signal-to-noise ratios in MR images: influence of multichannel coils, parallel imaging, and reconstruction filters. *J Magn Reson Imaging.* 2007;26(2):375-385. [\[CrossRef\]](#)
 23. Pimpalkhute VA, Page R, Kothari A, Bhurchandi KM, Kamble VM. Digital image noise estimation using DWT coefficients. *IEEE Trans Image Process.* 2021;30:1962-1972. [\[CrossRef\]](#)
 24. Landis JR, Koch GG. The measurement of observer agreement for categorical data. *Biometrics.* 1977;33(1):159-174. [\[CrossRef\]](#)
 25. Kundel HL, Polansky M. Measurement of observer agreement. *Radiology.* 2003;228(2):303-308. [\[CrossRef\]](#)
 26. Llewellyn A, Whittington C, Stewart G, Higgins JP, Meader N. The use of Bayesian Networks to assess the quality of evidence from research synthesis: 2. inter-rater reliability and comparison with standard GRADE assessment. *PLoS One.* 2015;10(12):e0123511. [\[CrossRef\]](#)
 27. Yang RK, Roth CG, Ward RJ, deJesus JO, Mitchell DG. Optimizing abdominal MR imaging: approaches to common problems. *Radiographics.* 2010;30(1):185-199. [\[CrossRef\]](#)
 28. Almansour H, Herrmann J, Gassenmaier S, et al. Combined deep learning-based super-resolution and partial fourier reconstruction for gradient echo sequences in abdominal MRI at 3 Tesla: shortening breath-hold time and improving image sharpness and lesion conspicuity. *Acad Radiol.* 2022:S1076-6332(22)00327-0. [\[CrossRef\]](#)
 29. Wessling D, Herrmann J, Afat S, et al. Application of a deep learning algorithm for combined super-resolution and partial fourier reconstruction including time reduction in T1-weighted precontrast and postcontrast gradient echo imaging of abdominopelvic MR imaging. *Diagnostics (Basel).* 2022;12(10):2370. [\[CrossRef\]](#)
 30. Gee MS, Nimkin K, Hsu M, et al. Prospective evaluation of MR enterography as the primary imaging modality for pediatric Crohn disease assessment. *AJR Am J Roentgenol.* 2011;197(1):224-231. [\[CrossRef\]](#)
 31. Del Vecovo R, Sansoni I, Caviglia R, et al. Dynamic contrast enhanced magnetic resonance imaging of the terminal ileum: differentiation of activity of Crohn's disease. *Abdom Imaging.* 2008;33(4):417-424. [\[CrossRef\]](#)
 32. Church PC, Turner D, Feldman BM, et al. Systematic review with meta-analysis: magnetic resonance enterography signs for the detection of inflammation and intestinal damage in Crohn's disease. *Aliment Pharmacol Ther.* 2015;41(2):153-166. [\[CrossRef\]](#)
 33. Qiu Y, Mao R, Chen BL, et al. Systematic review with meta-analysis: magnetic resonance enterography vs. computed tomography enterography for evaluating disease activity in small bowel Crohn's disease. *Aliment Pharmacol Ther.* 2014;40(2):134-146. [\[CrossRef\]](#)

Supplementary Table 1. Demographics and Crohn's disease-related characteristics of the study population

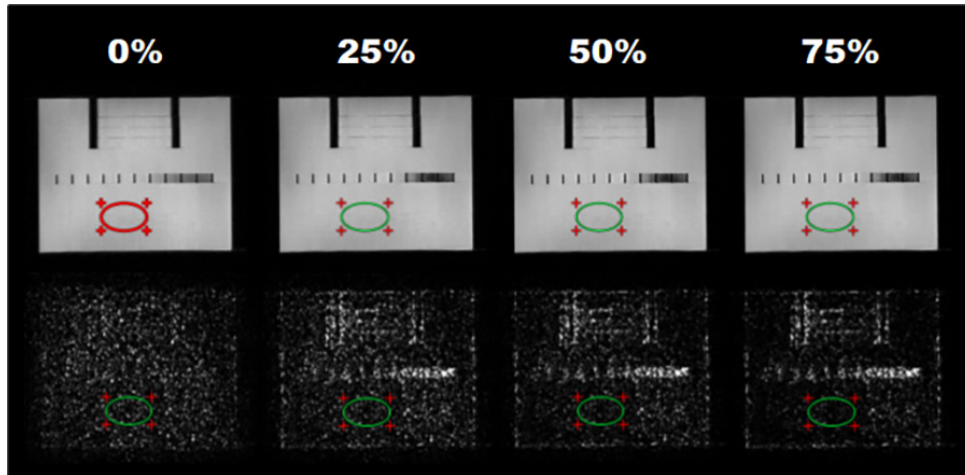
| Characteristics | Value |
|--------------------------------------|---------------------|
| Age (years)* | 31.8 ± 10.2 (16–51) |
| Sex | |
| Male | 19 (54.3) |
| Female | 16 (45.7) |
| Anthropometric data [†] | |
| Height (cm) | 167.0 (159.7–175.8) |
| Weight (kg) | 59.0 (51.7–69.0) |
| BMI (kg/m ²) | 21.5 (19.1–23.3) |
| Laboratory data [‡] | |
| Fecal calprotectin (mg/kg) | 300.0 (82.0–858.0) |
| CRP (mg/dL) | 0.13 (0.05–0.37) |
| Patients with previous bowel surgery | 4 (11.4) |

*Data are expressed as mean ± standard deviation, with ranges in parentheses. [†]Data are expressed as median, with interquartile range in parentheses. Unless otherwise specified, the data are numbers of patients, with percentages in parentheses. BMI, body mass index; CRP, C-reactive protein.

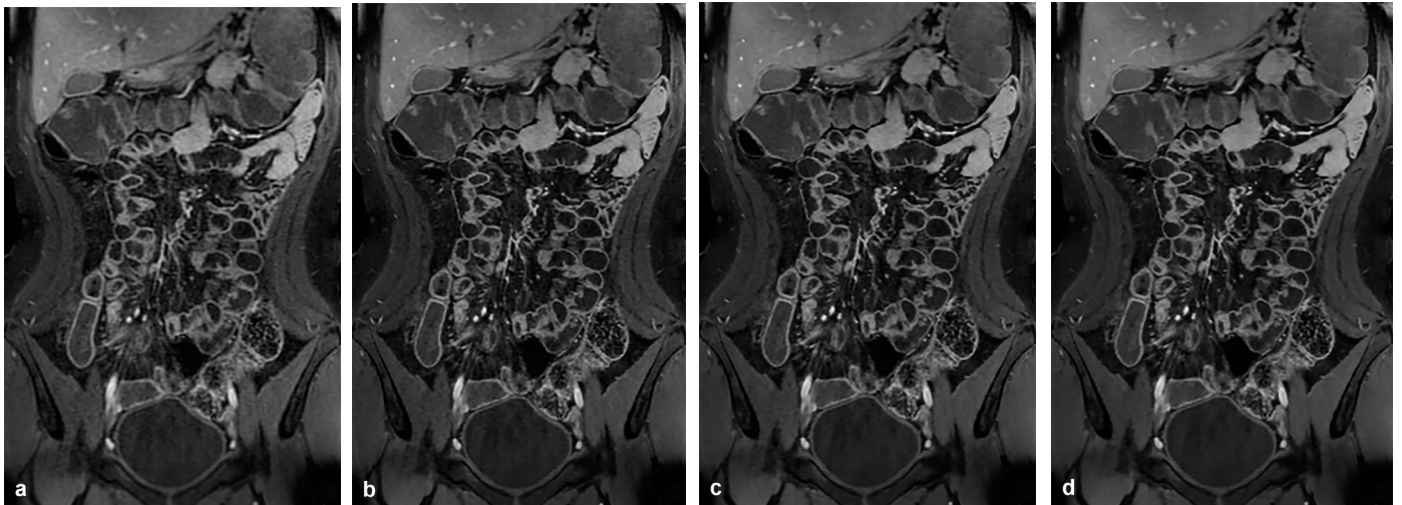
Supplementary Table 2. Results of the post-hoc Bonferroni's test for multiple comparisons among three different reconstruction methods in the qualitative analysis of the contrast-enhanced T1-weighted images of magnetic resonance enterography

| | Original vs. DLR | Filtered vs. DLR | Original vs. filtered |
|-----------------------|------------------|------------------|-----------------------|
| Coronal | | | |
| Overall image quality | <0.001 | <0.001 | 0.51 |
| Contrast | <0.001 | <0.001 | 0.77 |
| Sharpness | <0.001 | <0.001 | 0.36 |
| Motion artifacts | <0.001 | <0.001 | 1.00 |
| Blurring | <0.001 | <0.001 | 0.85 |
| Synthetic appearance | <0.001 | 0.003 | 1.00 |
| Axial | | | |
| Overall image quality | <0.001 | <0.001 | 0.28 |
| Contrast | <0.001 | <0.001 | 1.00 |
| Sharpness | <0.001 | <0.001 | 0.08 |
| Motion artifacts | <0.001 | <0.001 | 1.00 |
| Blurring | <0.001 | <0.001 | 0.06 |
| Synthetic appearance | <0.001 | <0.001 | 1.00 |

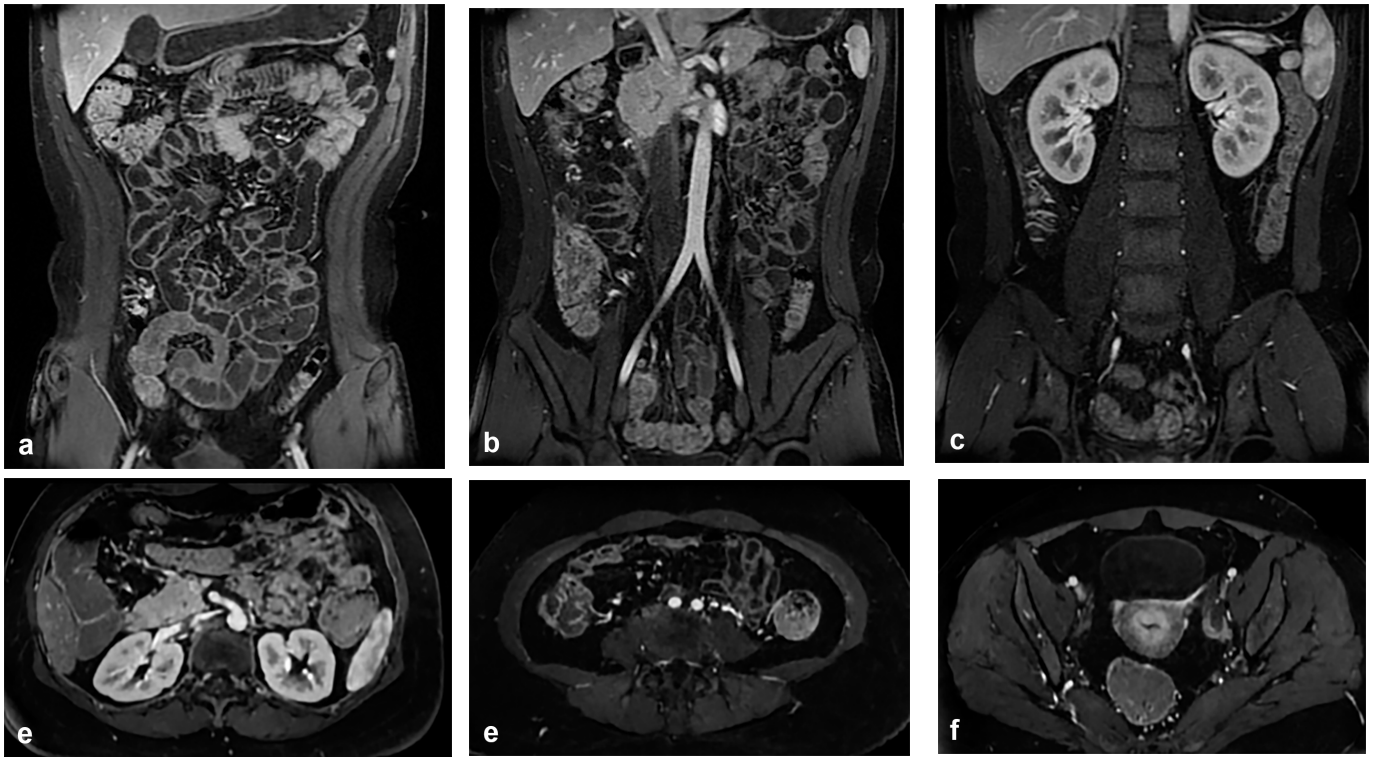
Data are presented as *P* values. Original, conventional reconstruction with no image filter; filtered, conventional reconstruction with image filter; DLR, deep-learning reconstruction.



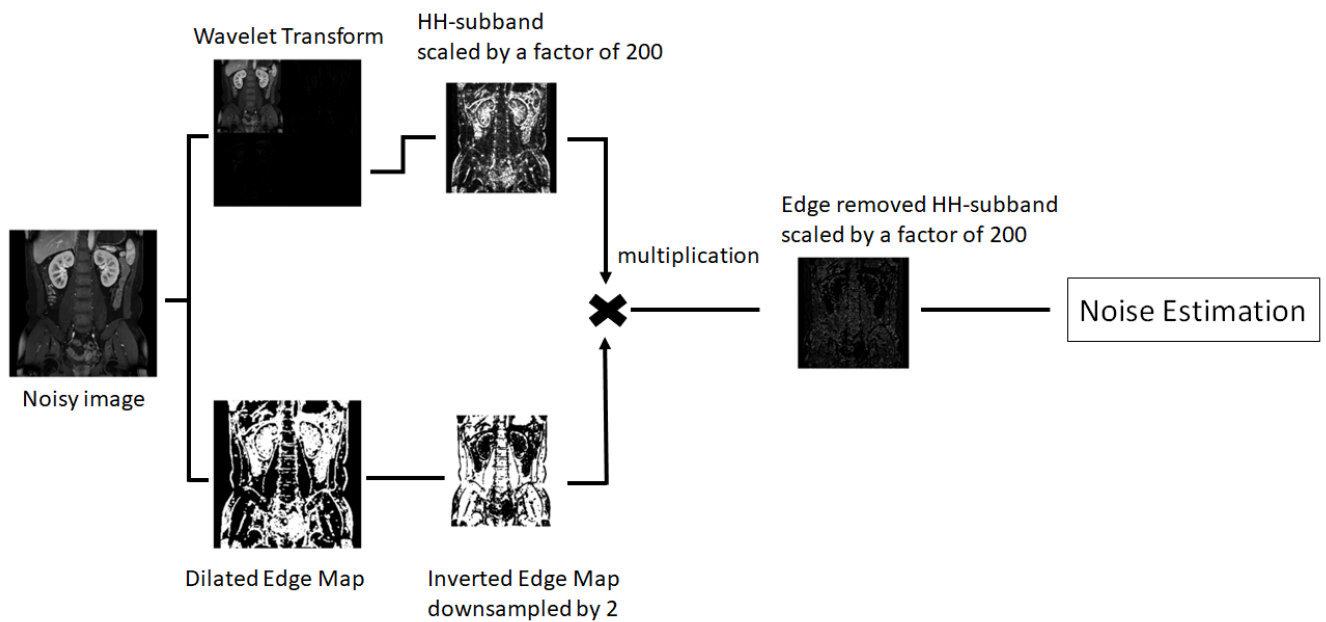
Supplementary Figure 1. The phantom experiments to evaluate the effects of different levels of noise reduction on deep-learning reconstruction (DLR). Phantom magnetic resonance images were processed using the prototype DLR with tunable noise-reduction factors of 0%, 25%, 50%, and 75%. As the noise-reduction levels increased, the signal-to-noise ratio calculated by placing a region of interest in each phantom image improved by 61.9, 66.6, 77.5, and 91.8.



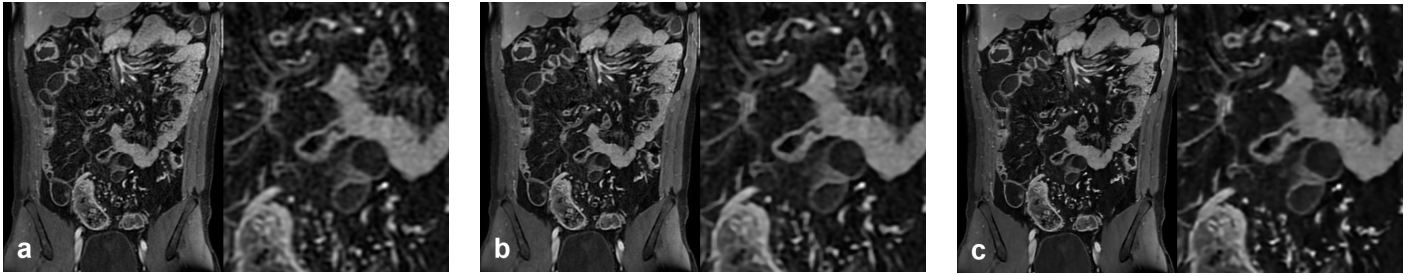
Supplementary Figure 2. The coronal images of dynamic enteric phase contrast-enhanced T1-weighted magnetic resonance enterography processed using deep-learning reconstruction (DLR) with different noise-reduction factors of (a) 0%, (b) 25%, (c) 50%, and (d) 75%. During preliminary reading sessions, the optimal denoising level was determined based on the consensus of the expert readers. The denoising level of 75% was chosen as it was found to yield the highest signal-to-noise ratio and the best image sharpness among the evaluated noise-reduction factors. Despite some synthetic appearance, it was concluded that the overall synthetic appearance produced by DLR was acceptable.



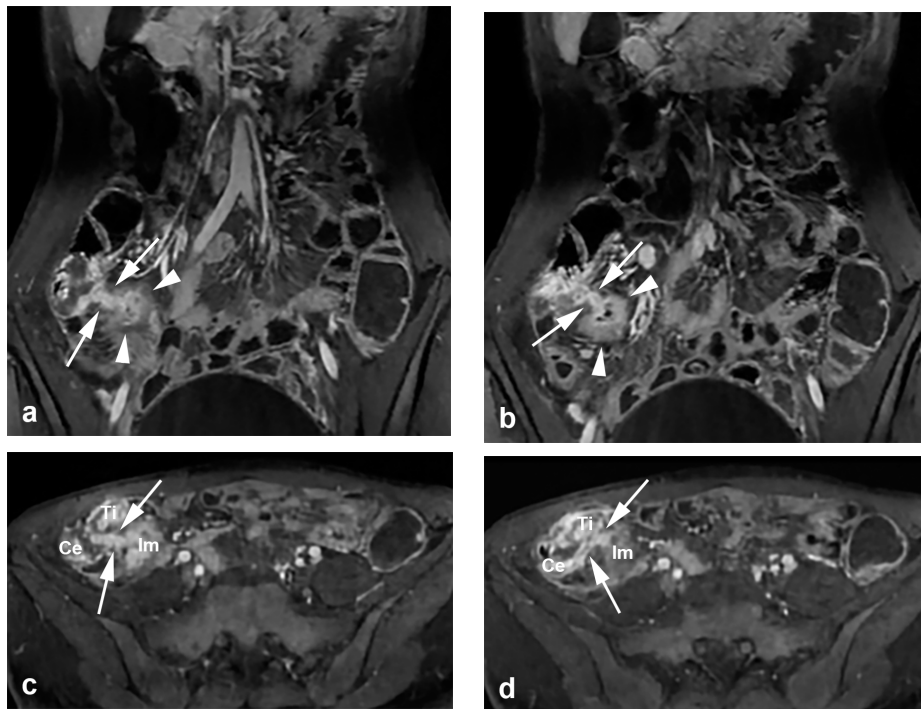
Supplementary Figure 3. Example of three representative locations selected to measure the signal-to-noise ratio (SNR) in each coronal (a-c) and axial (d-f) plane. For the coronal plane, images showing both external iliac and femoral arteries at the level where multiple small bowel loops are visible (a), aortic bifurcation (b), and kidneys at the level where the ascending and descending colon are visible (c) were chosen to calculate the SNR in the anterior, middle, and posterior portions of the abdominal cavity, respectively. For the axial plane, images at the level of (d) the superior mesenteric artery, (e) aortic bifurcation, and (f) the pelvic cavity showing superior gluteal veins were chosen to calculate the SNR in the upper, middle, and lower portions of the abdominal cavity, respectively.



Supplementary Figure 4. Flow chart of noise estimation in a coronal image at the level of the kidneys. For the noise estimation, the modified (HH) sub-band that contains coefficients corresponding only to noise was obtained by removing the HH sub-band coefficients corresponding to edges using discrete wavelet transform and edge map.



Supplementary Figure 5. Dynamic enteric phase contrast-enhanced T1-weighted images of a 41-year-old man with active Crohn's disease. Three sets of coronal images were obtained with a 1.4-mm slice thickness: (a) with conventional reconstruction and no image filter (original); (b) with conventional reconstruction and image filter (filtered); and (c) with deep-learning reconstruction (DLR) at the noise-reduction level of 75% (DLR). The portion of the small bowel mesentery and bowel loops is magnified to better illustrate the structures in each image. The DLR image (c) demonstrates reduced noise, whereas the other two images (a, b) still have noise that is well visualized in the background mesenteric fat. Note that better contrast and sharpness are seen for mesenteric vessels in DLR (c). However, DLR (c) typically demonstrates a synthetic appearance, which refers to a “plastic” or “cartoon-like” appearance.



Supplementary Figure 6. Dynamic enteric phase contrast-enhanced T1-weighted images of a 27-year-old woman with active Crohn's disease. The coronal images (a, b) were obtained using deep-learning reconstruction at the noise-reduction level of 75% and then reformatted to axial images (c, d). In the coronal images, an inflammatory mass in the ileocecal area (arrowheads) is noted with two fistulous tracts connected to the bowel loops (arrows). In the axial images, one of the fistulous tracts (arrows in a, c) reveals a connection between the inflammatory mass (Im) and the cecum (Ce), whereas the other tract (arrows in b and d) is a bidirectional fistula communicating between the cecum (Ce), terminal ileum (Ti), and inflammatory mass (Im). Two fistulas are demonstrated as more caudal to the ileocecal valve (not shown). Note that the relationship of the bidirectional fistulous tract between the bowel loops is clearly visible in the axial images, which help clarify anatomic detail when reviewed along with coronal images. The consecutive images of the same patient are also presented in Supplementary Video 2, available in the online supplement.

Supplementary Video 1 link: (a) https://www.youtube.com/watch?v=r2_jXqEte6Q
(b) <https://www.youtube.com/watch?v=7CKdrLCjhAg>
(c) <https://www.youtube.com/watch?v=t4xtnUj0-6A>

Supplementary Video 1. Videos of consecutive images from an 18-year-old man with active Crohn's disease who underwent dynamic enteric phase contrast-enhanced T1-weighted magnetic resonance enterography. Three sets of images were obtained and reformatted in the axial plane with a 1.4-mm slice thickness: (a) with conventional reconstruction and no image filter (original); (b) with conventional reconstruction and image filter (filtered); and (c) with deep-learning reconstruction (DLR) at the noise-reduction level of 75% (DLR). The videos were taken from all image sets at a fixed window level (2.666 HU) and width (5.320 HU). The DLR images (c) better visualize active inflammation in the ascending colon with lower noise, a sharper margin of the bowel wall and vascularity, and better contrast of bowel wall stratification compared with the other two images (a, b). In the qualitative analysis, the DLR image was given a higher score (5) by the two readers regarding overall image quality, contrast, sharpness, and motion artifacts than the other two images (both 4). The key images of the same patient are presented in Figure 2.

Supplementary Video 2 link: (a) <https://www.youtube.com/watch?v=reRKonWDGBM>
(b) <https://www.youtube.com/watch?v=Qo75KqG9Ql4>

Supplementary Video 2. Video of consecutive images from a 27-year-old woman with active Crohn's disease who underwent dynamic enteric phase contrast-enhanced T1-weighted magnetic resonance enterography. The coronal images (a) were obtained using deep-learning reconstruction at the noise-reduction level of 75% and then reformatted to axial images (b). In the coronal images, an inflammatory mass in the ileocecal area (Im) is noted with two fistulous tracts connected to bowel loops (red/white arrows in a). In the axial images, one of the fistulous tracts (red arrows in b) reveals a connection between the inflammatory mass and the cecum, whereas the other tract (white arrows in b) is a bidirectional fistula communicating between the cecum, the terminal ileum, and the inflammatory mass. Two fistulas are demonstrated more caudal to the ileocecal valve. Note that the relationship of the bidirectional fistulous tract between the bowel loops is clearly visible in the axial images, which help clarify anatomic detail when reviewed along with coronal images. The key images of the same patient are presented in Supplementary Figure 6.



Copyright © Author(s) - Available online at dirjournal.org.
Content of this journal is licensed under a Creative Commons
Attribution-NonCommercial 4.0 International License.

Comparison of quantitative volumetric analysis and linear measurement for predicting the survival of Barcelona Clinic Liver Cancer 0- and A stage hepatocellular carcinoma after radiofrequency ablation

Siwei Yang 
Zhiyuan Zhang 
Tianhao Su 
Qiyang Chen 
Haochen Wang 
Long Jin 

From the Department of Interventional Radiology (S.Y., Z.Z., T.S., H.W., L.J. ✉jinlong@ccmu.edu.cn), Beijing Friendship Hospital, Capital Medical University, Beijing, China; Department of Ultrasound (Q.C.), Beijing Tongren Hospital, Capital Medical University, Beijing, China.

Received 12 December 2022; revision requested 21 January 2023; last revision received 10 April 2023; accepted 13 April 2023.



Epub: 08.05.2023

Publication date: 30.05.2023

DOI: 10.4274/dir.2023.222055

PURPOSE

The prognostic role of the tumor volume in patients with hepatocellular carcinoma (HCC) at the Barcelona Clinic Liver Cancer (BCLC) 0 and A stages remains unclear. This study aims to compare the volumetric measurement with linear measurement in early HCC burden profile and clarify the optimal cut-off value of the tumor volume.

METHODS

The consecutive patients diagnosed with HCC who underwent initial and curative-intent radiofrequency ablation (RFA) were included retrospectively. The segmentation was performed semi-automatically, and enhanced tumor volume (ETV) as well as total tumor volume (TTV) were obtained. The patients were categorized into high- and low-tumor burden groups according to various cut-off values derived from commonly used diameter values, X-tile software, and decision-tree analysis. The inter- and intra-reviewer agreements were measured using the intra-class correlation coefficient. Univariate and multivariate time-to-event Cox regression analyses were performed to identify the prognostic factors of overall survival.

RESULTS

A total of 73 patients with 81 lesions were analyzed in the whole cohort with a median follow-up of 31.0 (interquartile range: 16.0–36.3). In tumor segmentation, excellent consistency was observed in intra- and inter-reviewer assessments. There was a strong correlation between diameter-derived spherical volume and ETV as well as ETV and TTV. As opposed to all linear candidates and 4,188 mm³ (sphere equivalent to 2 cm in diameter), ETV >14,137 mm³ (sphere equivalent to 3 cm in diameter) or 23,000 mm³ (sphere equivalent to 3.5 cm in diameter) was identified as an independent risk factor of survival. Considering the value of hazard ratio and convenience to use, when ETV was at 23,000 mm³, it was regarded as the optimal volumetric cut-off value in differentiating survival risk.

CONCLUSION

The volumetric measurement outperforms linear measurement on tumor burden evaluation for survival stratification in patients at BCLC 0 and A stages HCC after RFA.

KEYWORDS

Hepatocellular carcinoma, tumor burden, quantitative volumetric analysis, radiofrequency ablation, prognosis

Hepatocellular carcinoma (HCC) is the sixth most common malignancy worldwide and ranks third in terms of mortality.¹ Barcelona Clinic Liver Cancer staging system (BCLC) is widely used to guide clinical decision-making and survival risk stratification for patients with HCC. In practice, patient allocation for curative-intent therapies is a multifactorial deci-

You may cite this article as: Yang S, Zhang Z, Su T, Chen Q, Wang H, Jin L. Comparison of quantitative volumetric analysis and linear measurement for predicting the survival of Barcelona Clinic Liver Cancer 0- and A stage hepatocellular carcinoma after radiofrequency ablation. *Diagn Interv Radiol.* 2023;29(3):450-459.

sion. For patients with early-stage HCC, BCLC 0 and A stages, the tumor burden evaluation is considered the uppermost aspect; it combines the tumor number and the maximum diameter to stratify individual survival risk optimally.² However, the maximum diameter and diameter-based sphere alongside ellipsoid volume are difficult to represent the actual tumor burden due to the irregular 3D geometry of the tumor, which is largely derived from heterogeneity and non-rotational symmetry of tumor growth.^{3,4}

In the past decade, owing to the progress of semi-automatic tumor segmentation tools, published studies have validated the feasibility of volumetric segmentation and shown potential perspectives for radiological tumor response assessment.^{5,6} Compared with the established anatomic response criteria, such as Response Evaluation Criteria in Solid Tumors (RECIST), modified RECIST, or Milan criteria, the quantitative volumetric assessment has appeared to have better performance for prognostic stratification in intermediate-stage or advanced HCC patients.⁷⁻¹³ This is possibly because the changes in tumor diameter tend to lag behind changes in tumor volume and functional parameters as well as enhancement under locoregional therapies.¹⁴ As the minimal user interaction and quantitative steps in the semi-automatic segmentation, volumetric analysis of tumor burden has considerable superiority in accuracy, reproducibility, and interobserver or radiologic-pathologic agreement.^{15,16} Therefore, this technique should be applied in broader clinic settings.

Evidence on semi-automatic volumetry concerning the tumor burden of BCLC 0 or A stage HCC remains scarce. Such patients, especially with a maximum diameter of less than 3 cm, have relatively low tumor burden. Considering that necrosis is seldom presented, most relevant studies assessing the prog-

nostic role of tumor volume mainly adopt the mathematical, simulating formulae and manual contouring,¹⁷⁻²⁴ which is not accurate. Recently, the prognostic role of magnetic resonance imaging (MRI)-based tumor volume using semi-automatic segmentation was assessed,²⁵ but the predictive value is limited due to the absence of multifocal patients. Hence, this study hypothesized that tumor volume may amplify the subtle difference in diameter to reflect the actual tumor burden. The aim of this pilot study is to evaluate the potential capacity of volume analysis for survival stratification compared with linear measurement in the early HCC burden profile after radiofrequency ablation (RFA) and explore the optimal volumetric cut-off value.

Methods

Study cohort

The patients diagnosed with HCC who underwent initial and curative-intent RFA were analyzed retrospectively during 2016–2021. The inclusion criteria were as follows: 1) 18–75 years old; 2) the preoperative multi-phasic MRI was screened within two weeks; 3) BCLC 0 or A stage; 4) all targeted HCC lesions were ablated completely. The exclusion criteria were as follows: 1) previous HCC treatment history; 2) failure of radiological data retrieval; 3) loss of follow-up; 4) presence of secondary carcinoma. The flowchart of patient selection is illustrated in Figure 1. Finally, a total of 73 patients with HCC were analyzed. In twelve patients, HCC was biop-

sy-proven, and diagnoses in the remaining patients were established in concordance with Liver Imaging Reporting and Data System criteria.²⁶ Complete ablation evaluation of all targeted tumors was confirmed by contrast-enhanced MRI one month after RFA²⁷ combined with the eradication of serum level of alpha-fetoprotein (AFP). Demographic, clinical, and laboratory data of the cohort were reviewed and recorded from the electronic medical system. The study procedures conformed to the ethical guidelines of the Declaration of Helsinki, and the Bioethics Committee of Beijing Friendship Hospital, Capital Medical University approved this retrospective study (registration number: 2022-P2-290-01). The requirement for written informed consent for recruitment was waived.

Radiofrequency ablation

All RFA procedures, guided by computed tomography scan with a percutaneous approach, were performed under local anesthesia combined with procedural sedation and analgesia in all patients. Vital signs were monitored throughout the procedure. Two RFA systems, Rita Starburst Flex/talon electrode (RITA Medical Systems, Mountain View, Calif., USA) and CELON ProSurge (Olympus Winter & Ibe GmbH, Hamburg, Germany), with a 2–5 cm deployment, were determined by the type of generator model. They were equipped with internal liquid circulation (saline solution) to maintain surface temperature. The generator model selection and electrode shaft distribution depended on the size, location, and adjacent structure of the tumor. Multiplanar reformation ensured

Main points

- Tumor volume outperforms diameter for predicting survival in early patients with hepatocellular carcinoma (HCC).
- Volumetric tumor burden improves performance for high tumor burden case-finding in early HCC.
- A seed-growing algorithm in open-source software provides a feasible tumor segmentation.
- An optimal cut-point of tumor volume, namely 23,000 mm³, was given in Barcelona Clinic Liver Cancer 0 and A stages HCC patients.

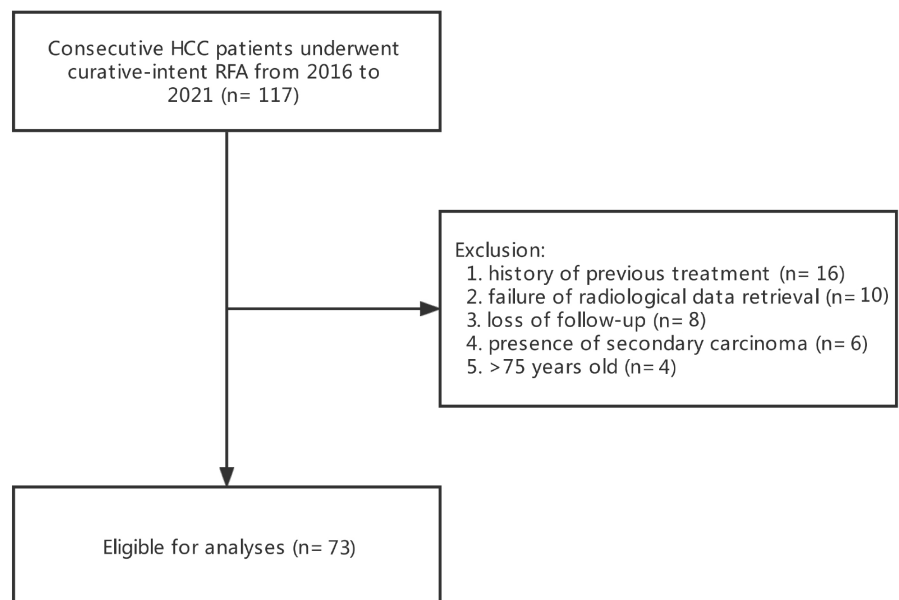


Figure 1. The flowchart of patient selection. HCC, hepatocellular carcinoma; RFA, radiofrequency ablation.

that the tip of the electrode shaft was inside or at the center of the tumor and covered in expandable needles with at least a 5–10 mm safety margin. Ablation-related parameters were set as per the manufacturer's instructions regarding tumor-related characteristics.

Magnetic resonance imaging image acquisition

A standardized MRI protocol with 3.0T MRI scanners (GE, GE Healthcare, Boston, USA) was performed for the routine liver imaging in the institution. Multiphase contrast-enhanced T1-weighted imaging (T1WI) was obtained in the arterial phase (25–35 sec after injection), portal venous phase (60–70 sec after injection), and delayed phase (3–5 min after injection). The contrast agent, an extracellular contrast agent, gadobenate dimeglumine (Magnevist, Bayer Schering Pharma, Berlin, Germany), was intravenously injected with a dose of 0.1 mmol/kg (maximum dose, 20 mL) at a rate of 2 mL/s followed by a 50 mL saline flush (2 mL/s).

Tumor measurement and segmentation

All images were exported in digital imaging and communication in medicine files from the workstation and segmented in cubic millimeters (mm³) using the open-source software ITK-SNAP (www.itksnap.org/pmwiki/pmwiki.php). The axial linear and volumetric measurements of all HCC lesions at the late arterial phase (20 sec) of baseline MRI were reviewed repeatedly with an interval of two weeks by two radiologists (SW.Y. and QY.C.) who were blinded to the patient's survival outcomes and who had five years of experience in abdominal imaging. Enhanced tumor volume (ETV) and total tumor volume (TTV) values were recorded in tumor volumetric analyses. The axial linear measurement and seed-setting evaluation were re-checked by another board-certified radiologist (TH.S) who had more than ten years of experience in radiology. The individual measurements were determined by the average of the two reviewers. Inconsistency between the two reviewers was resolved by consensus.

The segmentation was performed based on the volumetric mask on the MRI images at the late arterial phase (20 sec) with a seed-growing algorithm, namely a region-growth algorithm, as depicted in previous literature.^{25,28,29} Four quadrature regions of interest (ROIs) were prescribed in the liver parenchyma of the ipsilateral lobe, being ad-

acent to tumor boundaries and away from blood vessels, liver boundaries, and other structures.³⁰ The mean intensity value (MIV) was derived from the average value of four ROIs. When placing bubbles within the tumor, the necrotic areas, cysts, and vessels close to the index lesion at the certain slice were also avoided, as identified on T2WI or arterial early-phase images. Furthermore, the pre-enhanced T1W images were scrutinized to distinguish high signal intensity, like hemorrhage, to avoid overestimating ETV value. The exterior delineated bubbles were placed inside the edge of the enhanced part of the lesion, tangent to the inner margin in principle, and the interior delineated bubbles were placed randomly. Cross-referencing with coronal and sagittal reconstructed MRI images was used to supplement the bubble.

Any voxel inside or peripheral of the seed was clustered if the intensity was located in the interval threshold between the MIV+2 standard deviations (SD) and abdominal aorta signal intensity. In this step, the corresponding voxels were combined and considered as the viable tumor part, then ETV was obtained. The low or delayed enhancement part as well as the non-enhanced part within the tumor would then be supplemented to get TTV value. The detailed descriptions are shown in Supplementary Material 1. The color map reflecting tumor enhancement heterogeneity is presented in Figure 2.

Definitions

The study endpoint was overall survival (OS), which was calculated by subtracting the RFA date from the date of death or the last follow-up visit date (May 31, 2022). Volumetric and linear cut-off values were used to distinguish the high and low tumor burden groups. The ETV and TTV refer to the volume of all targeted lesions in the presence of multiple tumors. Index tumor was the dominant HCC lesion, and it refers to the one with the largest diameter in multifocal patients. The cut-off value of elevated AFP levels was defined as 400 ng/mL in reference to the initial assessment in the HCC guideline.³¹

Cut-off values selection

According to the cut-off value in defining BCLC 0 and A stages as well as another cut-off value of small HCC, a maximum diameter of 2 and 3 cm were chosen as the linear cut-off values, respectively. The corresponding maximum diameter-derived respective spherical volumes, 4,188 mm³ and 14,137 mm³ (equation), were used as volumetric cut-off values as suggested by the previous publications.^{8,10} In addition, another volumetric value, obtained from binary classification in the endpoint-related decision-tree model, was used as the third cut-off value. The software X-tile was used to determine the fourth volumetric cut-off value based on the maximum log-rank statistic.³²

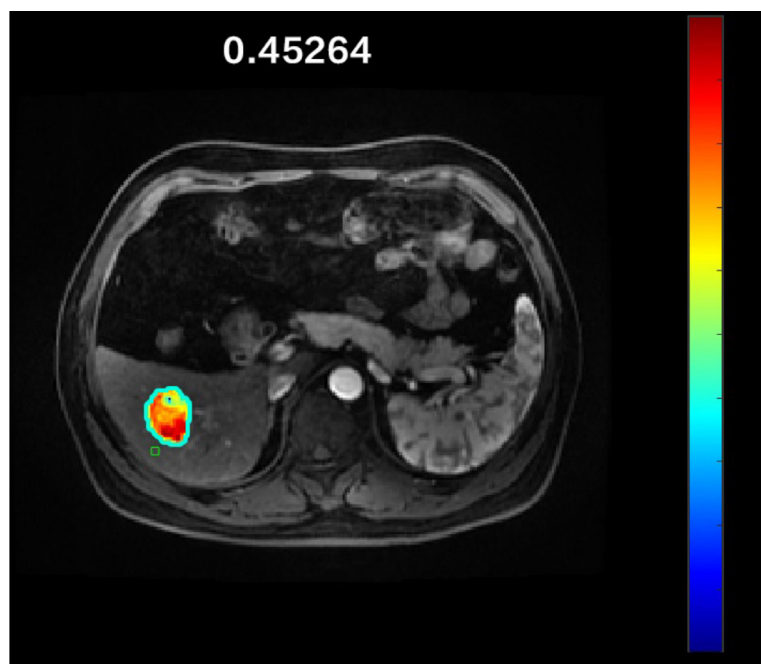


Figure 2. The color map. The number value on the image is the average signal intensity within the normalized regions of interest. The color on the spectrum column represents the signal intensity. Compared with the liver parenchyma signal intensity, the closer the color is to red, the higher the signal intensity, and the closer the color is to blue, the lower the signal intensity. Visual display of signal intensity inside the tumor is provided.

Statistical analysis

Continuous variables expressed as the mean \pm SD or median (interquartile range) depending on the data distribution type were compared using two-sample t-tests or Mann–Whitney U tests, and categorical variables expressed as number (percentage) were compared using the χ^2 test or Fisher's exact tests. The comparison between diameter-derived sphere volume and tumor volume was performed using the Paired-Samples test. The intraclass correlation coefficient (ICC) was calculated for inter-reviewer agreement. Generally, ICC ≥ 0.90 indicates excellent consistency, and ≥ 0.75 indicates good consistency between both reviewers.³³ The Pearson correlation and Bland–Altman analysis were used to evaluate the correlation and consistency between the linear measurement and volume of the tumor. Risk factors for live status were identified in univariate and multivariate binary logistic regression, and the cut-off values for continuous risk factors were determined in decision-tree analysis using the statistical package R version (version 4.2.1, www.r-project.org).

The Kaplan–Meier method using the log-rank test was applied to compare the survival curves of patients with different tumor burdens. After testing the proportional hazards assumption using Schoenfeld resid-

uals, univariate time-to-event Cox regression was performed to identify the prognostic factors of OS. The variables with $P < 0.1$ were selected in the adjusted multivariate analysis (forward step-wise). Regarding the tumor burden value, either linear or volumetric measurement as dichotomization according to the corresponding cut-off value was incorporated into the model. The two-tailed $P < 0.05$ was indicative of a significant difference. All statistical analyses were performed in the SPSS (Version 26.0; IBM Corp., Armonk, NY) and R software.

Results

Baseline characteristics of the cohort

The demographics and clinical characteristics of the cohort are summarized in Table 1. The mean age of the participants was 59.3 ± 10.5 years, and 65.8% of them were men. Out of 73 participants, 58 (79.5%) had HBV-related liver disease.

Solitary tumor was the predominant subtype (90.4%), and the mean tumor maximum diameter was $2.2 \text{ cm} \pm 1.1 \text{ cm}$, with 37 (50.7%) being more than 2 cm and 16 (21.9%) being more than 3 cm in diameter. A total of 81 lesions were analyzed in the cohort. ETV and TTV were $4,748.00 \text{ mm}^3$ (2,076.68, 10,845.50) mm^3 and $47,48.00$ (2,076.68, 11,981.00) mm^3 ,

respectively. In addition, Child–Pugh class A (79.5%) was mostly observed in the liver function reserve evaluation.

Additional volumetric cut-off values

After univariate and multivariate binary logistic regressions, BCLC A stage and ETV were identified as risk factors associated with survival; therefore, two variables were selected in the decision-tree analysis. The cut-off value of ETV ($>23,000 \text{ mm}^3$) in the decision-tree model is shown in Figure 3.

Additionally, X-tile software showed that a plateau of ETV values ranging from $12,424.00 \text{ mm}^3$ (sphere equivalent to 2.87 cm in diameter) to $13,560.32 \text{ mm}^3$ (sphere equivalent to 2.94 cm in diameter) enables significant stratifications in survival analysis. As the above-mentioned values were close to $14,137 \text{ mm}^3$, a total of three volumetric cut-off values were analyzed in Cox regression models, including $4,188 \text{ mm}^3$ (sphere equivalent to 2 cm in diameter), $14,137 \text{ mm}^3$ (sphere equivalent to 3 cm in diameter), and $23,000 \text{ mm}^3$ (sphere equivalent to 3.5 cm in diameter). The analytical process in X-tile is exhibited in Supplementary Material 1.

Intra- and inter-reviewer agreement assessment and correlation between linear and volumetric measurement

Table 2 illustrates that there was excellent consistency in intra- and inter-reviewer assessments. Considering the presence of multiple tumors, the correlation between linear and volumetric measurement were analyzed for index tumor. Figure 4 shows that the maximum tumor diameter was robustly positively correlated with ETV ($R = 0.846$, $P < 0.001$), and good consistency was observed between diameter-derived spherical volume and ETV, especially for individuals with a volume $<30,000 \text{ mm}^3$ (Figure 5). It is noted that diameter-derived spherical volume was overestimated in comparison with ETV ($P = 0.003$). Similarly, there was a strong correlation between ETV and TTV ($R = 0.966$, $P < 0.001$).

Tumor burden measurements associated with survival

After a median follow-up of 31.0 (16.0, 36.3) months, 14 patients died. The cumulative OS at 1, 3, and 5 years was 97.0%, 82.1%, and 72.2%, respectively. As for survival stratification regarding the tumor burden, patients could be divided into two groups according to 3 cm in diameter or all volumetric cut-off values, with significant differences in

Table 1. Demographics and clinical characteristics of the cohort

| Variable | Cohort (n = 73) |
|--|--------------------------------|
| Sex (male, %) | 50 (65.8) |
| Age (year) | 59.32 ± 10.5 |
| Etiology (HBV/HCV/alcoholic/others, %) | 58 (79.5)/1(1.4)/7(9.6)/7(9.6) |
| BCLC stage (0/A, %) | 34 (46.6)/39 (53.4) |
| Tumor number (single/multiple, %) | 66 (90.4)/7 (9.6) |
| Child–Pugh class (A/B, %) | 58 (79.5)/15 (20.5) |
| MELD–Na score | 8.55 ± 2.7 |
| ALB (g/L) | 36.06 ± 5.6 |
| TBIL | 16.23 (12.03,22.03) |
| ALT | 25.07 ± 10.3 |
| PLT | 111 (75.5, 175.5) |
| GGT | 42 (27.5,68.0) |
| AFP | 5.66 (3.17, 22.91) |
| Tumor maximum diameter (cm) | 2.2 ± 1.1 |
| $\leq 2 \text{ cm}/>2 \text{ cm}$, % | 36 (49.3)/37 (50.7) |
| $\leq 3 \text{ cm}/>3 \text{ cm}$, % | 57 (78.1)/16 (21.9) |
| ETV (mm^3) | 4748.00 (2076.68, 10845.50) |
| TTV (mm^3) | 4748.00 (2076.68, 11981.00) |

Continuous variables with non-normal distribution were expressed as median (interquartile range), otherwise expressed as mean \pm standard deviation. BCLC, Barcelona Clinic Liver Cancer staging system; MELD–Na, model for end-stage liver disease incorporating sodium; ALB, albumin; TBIL, total bilirubin; ALT, alanine aminotransferase; PLT, platelet; GGT, glutamyl transferase; AFP, alpha-fetoprotein; ETV, enhancing tumor volume; TTV, total tumor volume.

survival analysis between high and low tumor burden groups and a markedly worse prognostic status in the high tumor burden group (all $P < 0.05$). The corresponding survival curves are displayed in Figure 6.

Comparison among different multivariate Cox models incorporating tumor burden measurements

After the univariate Cox regression (Table 3), each eligible tumor burden cut-off value was analyzed in the multivariate Cox model as a covariate. A total of four models were constructed, as shown in Table 4.

At multivariate analysis, ETV cut-off values, 14,137 mm³ [hazard ratio, 3.896; 95% confidence interval (CI): 1.012–14.993] or 23,000 mm³ (hazard ratio: 4.343; 95% CI: 1.176–16.034), were associated with impaired long-term survival. Considering hazard odd and ease of use, 23,000 mm³ was regarded as the optimal tumor burden cut-off value. Except for tumor volume, BCLC stage and elevated serum AFP level were also associated with a reduced survival rate in other models.

Discussion

In this study, the comparison of prognostic performance between linear and volumetric measurements in differentiating survival was presented. ETV was a better parameter than the diameter for assessing tumor burden in patients with HCC at BCLC 0 and A stages after RFA. For those patients, a volumetric value of 23,000 mm³ was the optimal cut-off value in terms of maximum statistical power and convenience of use.

An important finding from this study is the recognition that HCC patients at BCLC 0 and A stages who achieved longer survival had lower ETV, which aligns with prior results.^{8,34} The linear measurement is still the mainstay

of tumor burden marker. Regarding tumor volumetry at BCLC 0 and A stages, most prior studies adopted diameter-derived formulas to assess tumor volume. However, compared with semi-automatic segmentation, the formula estimation appears to be idealistic and ignores the discrepancies in tumor growth among different planes.³⁵

In clinical practice, HCC lesions at early stages are characterized by small size and little avascular necrosis, thus rendering diameter-based assessment feasible. However, tumor diameter could not thoroughly reflect the actual tumor burden compared with tumor volume.⁶ In this study, tumor volume appeared to be more sensitive and accurate than the diameter in predicting survival. It is surmised that tumor volume could amplify the subtle difference in diameter.

In addition, it is noted that HCC lesions at BCLC A stage were comparable to each other in most cases, possibly because of multiple-center carcinogenesis. Even though some studies indicated that there was no additional predicting value when comparing

single index lesion with all targeted ones,^{34,36} their conclusions were drawn from intermediate-stage or advanced patients with HCC cohort. Therefore, for multifocal HCCs, the total volumetric tumor burden, consisting of all radiologic measurable lesions, was calculated and included in survival analysis rather than the maximum diameter or volume of the index lesion.

This study also aimed to optimize the volumetric cut-point for patients with HCC at BCLC 0 and A stages. With respect to intermediate-stage HCC, mounting studies have adopted cut-off values derived from sphere volume equivalent to 3 or 5 cm in diameter and proved that volumetric cut-points derived from the Milan or RECIST criteria were effective to identify a survival benefit or a more positive tumor response compared with current linear criteria.^{6,8,10,12,13} As such, the cut-off values, 4,188 mm³ and 14,137 mm³ (sphere volume equivalent to 2 or 3 cm in diameter), in reference to BCLC 0 or A stage, were selected. Moreover, with the purpose of maximizing the statistical power and avoiding redundancy from other endpoint-related variables,

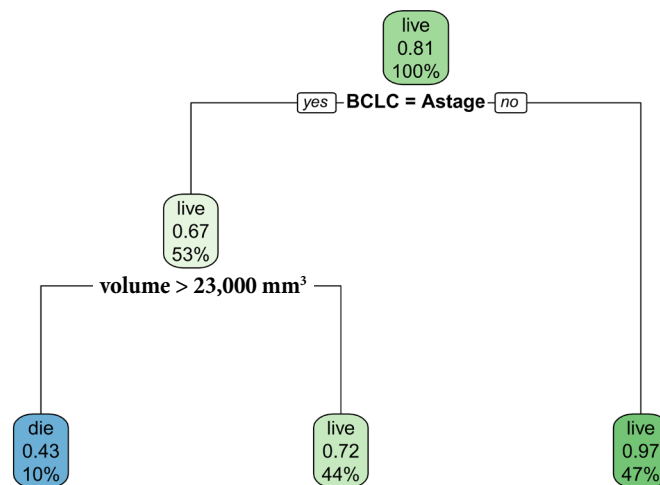


Figure 3. The decision-tree analysis for selecting a cut-off value. The cut-off value of tumor volume, 23,000 mm³, and Barcelona Clinic Liver Cancer stage were selected in the decision-tree model. BCLC, Barcelona Clinic Liver Cancer staging system.

Table 2. The evaluations of intra- and inter-reviewer agreements in various tumor burden parameters and correlations between diameter and volume as well as ETV and TTV

| Parameters | Intra-reviewer agreement | | Inter-reviewer agreement | |
|------------------------|--------------------------|---------|--------------------------|---------|
| | HR (95% CI) | P value | HR (95% CI) | P value |
| Maximum tumor diameter | 0.986 (0.968–0.992) | <0.001 | 0.964 (0.944–0.978) | <0.001 |
| Index tumor volume | 0.930 (0.878, 0.955) | <0.001 | 0.942 (0.880, 0.956) | <0.001 |
| ETV | 0.912 (0.863, 0.950) | <0.001 | 0.846 (0.790, 0.880) | <0.001 |
| TTV | 0.914 (0.866, 0.958) | <0.001 | 0.840 (0.774, 0.868) | <0.001 |
| | Correlation (r) | | P value | |
| Diameter vs. ETV | 0.846 | | <0.001 | |
| ETV vs. TTV | 0.966 | | <0.001 | |

HR, hazard ratio; CI, confidence interval; ETV, enhancing tumor volume; TTV, total tumor volume.

X-tile and decision-tree analysis were used to select additional volumetric cut-off values. In the decision-tree analysis, as one of two bifurcate variables, larger tumor volume was associated with higher mortality, being a prerequisite of the BCLC A stage. Furthermore, tumor volume is expected to grow in importance as a powerful marker in the context of HCC at BCLC A stage, possibly because the difference in individual tumor volume widens substantially with the increase in tumor diameter and number.

In the selection of tumor burden parameter, ETV as a volumetric candidate was used in prognostic evaluation rather than TTV, thereby minimizing the user interaction in the segmentation process. There was a strong agreement between ETV and TTV, likely owing to the fact that early HCC lesions were seldom prone to tumor necrosis and signal heterogeneity, especially for those less than 3 cm in diameter. This study's results showed that the diameter-derived sphere volume was larger than the tumor volume on the basis of the assumption of rotational symmetry, which was consistent with prior findings in experimental and clinical animal studies.³⁷⁻³⁹ Consequently, the spherical cut-points may facilitate the re-identification in patient subgroups that possibly benefit from locoregional or salvage therapies.^{34,38}

This study's analyses showed a high intra- or inter-reviewer consistency in the results of semi-automated tumor segmentation of ETV and TTV. The algorithm adopted a combination of quantitative steps (signal in-

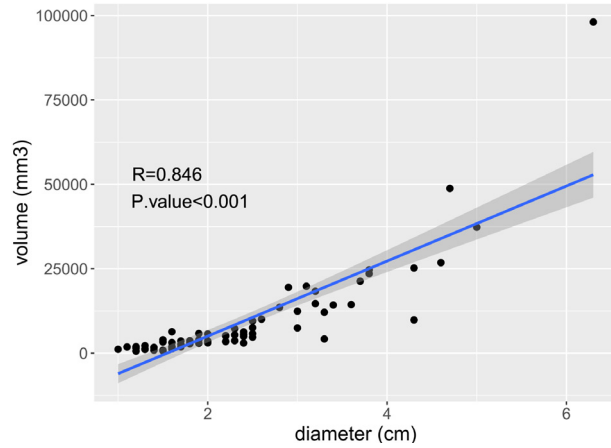


Figure 4. The maximum tumor diameter was robustly positively correlated with tumor volume.

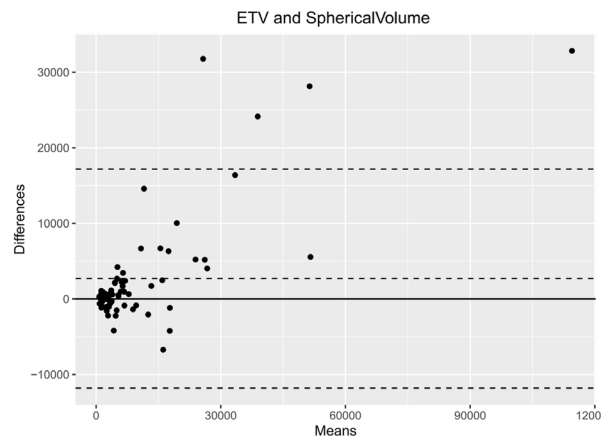


Figure 5. The Bland–Altman analysis. A good consistency was observed between diameter-derived spherical volume and the enhanced tumor volume, especially for individuals with volume <30,000 mm³. ETV, enhancing tumor volume.

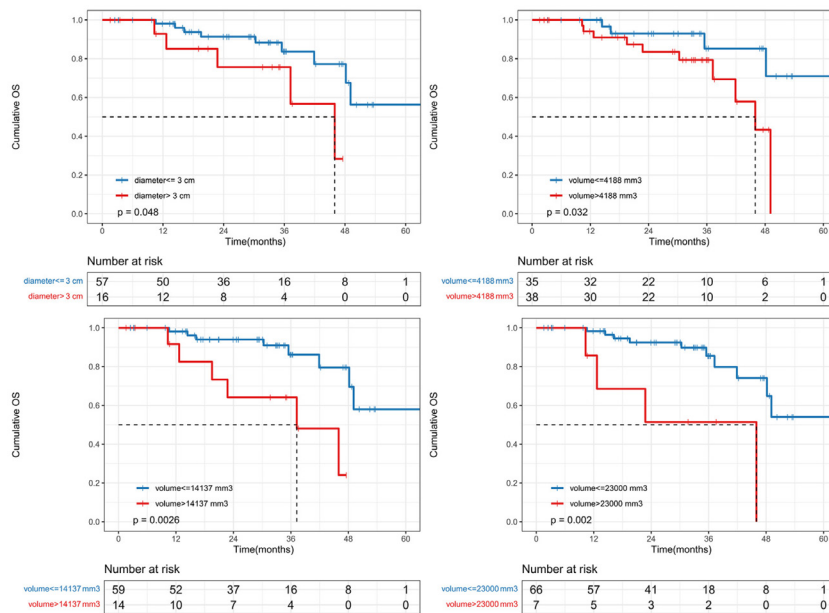


Figure 6. Four survival curves stratified by different tumor burden cut-off values. The 3 cm diameter and 3 volumetric cut-off values achieved good separation of the survival curves.

Table 3. Univariate Cox regression analyses of risk factors associated with overall survival

| Variable | Univariate | |
|--------------------------------|------------------------|---------|
| | HR (95% CI) | P value |
| Sex (male) | 3.919 (0.866, 17.727) | 0.176 |
| Age (>60 years) | 0.860 (0.300, 2.463) | 0.779 |
| Etiology (HBV) | 0.244 (0.083, 0.715) | 0.150 |
| BCLC (A) | 12.595 (1.638, 96.849) | <0.001 |
| Tumor number (multiple) | 3.314 (0.886, 12.394) | 0.112 |
| Child–Pugh (B) | 1.932 (0.658, 5.668) | 0.231 |
| MELD–Na score | 1.089 (0.950, 1.247) | 0.221 |
| ALB (<35 g/L) | 1.548 (0.510, 4.703) | 0.440 |
| GGT (>40 U/L) | 2.522 (0.873, 7.281) | 0.077 |
| PLT | 1.804 (0.588, 5.537) | 0.302 |
| AFP (>400 ng/mL) | 4.369 (1.151, 16.590) | 0.024 |
| Diameter (>2 cm) | 2.071 (0.689, 6.225) | 0.195 |
| Diameter (>3 cm) | 3.032 (0.956, 9.568) | 0.048 |
| ETV (>4,188 mm ³) | 3.462 (1.046, 11.458) | 0.032 |
| ETV (>14,137 mm ³) | 4.832 (1.553, 15.035) | 0.003 |
| ETV (>23,000 mm ³) | 5.439 (1.631, 18.139) | 0.002 |

HR, hazard ratio; CI, confidence interval; BCLC, Barcelona Clinic Liver Cancer staging system; MELD–Na, model for end-stage liver disease incorporating sodium; ALB, albumin; TBIL, total bilirubin; ALT, alanine aminotransferase; PLT, platelet; GGT, glutamyl transferase; AFP, alpha-fetoprotein; ETV, enhancing tumor volume; TTV, total tumor volume.

Table 4. Multivariate Cox regression models incorporating different tumor burden parameters

| Variable | Model 1 | Model 2 | Model 3 | Model 4 |
|--------------------------------|------------------------------|------------------------------|-----------------------------|------------------------------|
| HR (95% CI) P value | | | | |
| BCLC (A) | 12.032 (1.560, 92.794) 0.017 | 12.032 (1.560, 92.794) 0.017 | | |
| AFP (>400 ng/mL) | | | 6.886 (1.459, 32.511) 0.015 | 9.257 (1.801, 47, 591) 0.008 |
| GGT (>40 U/L) | | | | |
| Diameter (>3 cm) | | | | |
| ETV (>4,188 mm ³) | | | | |
| ETV (>14,137 mm ³) | | | 3.896 (1.012, 14.993) 0.048 | |
| ETV (>23,000 mm ³) | | | | 4.343 (1.176, 16.034) 0.028 |

Tumor burden measurements incorporated in model 1: diameter >3 cm; model 2: ETV >4,188 mm³; model 3: ETV >14,137 mm³; model 4: ETV >23,000 mm³. HR, hazard ratio; CI, confidence interval; BCLC, Barcelona Clinic Liver Cancer staging system; GGT, glutamyl transferase; AFP, alpha-fetoprotein; ETV, enhancing tumor volume; TTV, total tumor volume.

tensity determination, region-growing) and visual identification (seed-point), exhibiting a strong correlation on radiologic-pathologic assessment.^{40,41} Compared with full-automated segmentation, the accuracy and agreement as well as necessary subjective adjustment were balanced in semi-automated segmentation.^{40,42,43}

Collectively, this study presented a potential algorithm for case-finding of higher tumor burden in patients at BCLC 0 and A stages to improve predicting performance. However, several limitations persisted. First, the limited number of multifocal patients

necessitates further validation for volumetric cut-off value. Second, the tumor volume assessment required sophisticated processing using patent commercial software in prior publications. An algorithm of tumor segmentation in the open-source software was provided in this study, yet the individual segmentation process would still take about 3–5 minutes, which inevitably poses a time-consuming challenge for practitioners. Third, the single-center and retrospective nature of this study as well as a limited sample size could lead to a cautious interpretation of the results.

In conclusion, the volumetric measurement outperforms the linear measurement on tumor burden evaluation for survival stratification in patients at BCLC 0 and A stages HCC, and ETV >23,000 mm³ suggests patients with poorer survival.

Conflict of interest disclosure

The authors declared no conflicts of interest.

References

- Sung H, Ferlay J, Siegel RL, et al. Global Cancer Statistics 2020: GLOBOCAN Estimates of Incidence and Mortality Worldwide for 36 Cancers in 185 Countries. *CA Cancer J Clin.* 2021;71(3):209-249. [CrossRef]
- Reig M, Forner A, Rimola J, et al. BCLC strategy for prognosis prediction and treatment recommendation: The 2022 update. *J Hepatol.* 2022;76(3):681-693. [CrossRef]
- Gonzalez-Guindalini FD, Botelho MP, Harmath CB, et al. Assessment of liver tumor response to therapy: role of quantitative imaging. *Radiographics.* 2013;33(6):1781-1800. [CrossRef]
- Mantatzis M, Kakolyris S, Amarantidis K, Karayiannakis A, Prassopoulos P. Treatment response classification of liver metastatic disease evaluated on imaging. Are RECIST unidimensional measurements accurate? *Eur Radiol.* 2009;19(7):1809-1816. [CrossRef]
- Lin M, Pellerin O, Bhagat N, et al. Quantitative and volumetric European Association for the Study of the Liver and Response Evaluation Criteria in Solid Tumors measurements: feasibility of a semiautomated software method to assess tumor response after transcatheter arterial chemoembolization. *J Vasc Interv Radiol.* 2012;23(12):1629-1637. [CrossRef]
- Tacher V, Lin M, Duran R, et al. Comparison of existing response criteria in patients with hepatocellular carcinoma treated with transarterial chemoembolization using a 3D quantitative approach. *Radiology.* 2016;278(1):275-284. [CrossRef]
- Bonekamp S, Li Z, Geschwind JF, et al. Unresectable hepatocellular carcinoma: MR imaging after intraarterial therapy. Part I. Identification and validation of volumetric functional response criteria. *Radiology.* 2013;268(2):420-430. [CrossRef]
- Chapiro J, Duran R, Lin M, et al. Identifying staging markers for hepatocellular carcinoma before transarterial chemoembolization: comparison of three-dimensional quantitative versus non-three-dimensional imaging markers. *Radiology.* 2015;275(2):438-447. [CrossRef]
- King MJ, Tong A, Dane B, Huang C, Zhan C, Shanbhogue K. Response assessment of hepatocellular carcinoma treated with yttrium-90 radioembolization: inter-reader variability,

- comparison with 3D quantitative approach, and role in the prediction of clinical outcomes. *Eur J Radiol.* 2020;133:109351. [\[CrossRef\]](#)
10. Borde T, Nezami N, Laage Gaupp F, et al. Optimization of the BCLC Staging system for locoregional therapy for hepatocellular carcinoma by using quantitative tumor burden imaging biomarkers at MRI. *Radiology.* 2022;304(1):228-237. [\[CrossRef\]](#)
 11. Khalaf AM, Fuentes D, Morshid A, et al. Hepatocellular carcinoma response to transcatheter arterial chemoembolisation using automatically generated pre-therapeutic tumour volumes by a random forest-based segmentation protocol. *Clin Radiol.* 2019;74(12):974.e13-974.e20. [\[CrossRef\]](#)
 12. Doemel LA, Chapiro J, Laage Gaupp F, et al. Reliable prediction of survival in advanced-stage hepatocellular carcinoma treated with sorafenib: comparing 1D and 3D quantitative tumor response criteria on MRI. *Eur Radiol.* 2021;31(5):2737-2746. [\[CrossRef\]](#)
 13. Lüdemann W, Kahn J, Pustelnik D, et al. Yttrium-90 radioembolization for unresectable hepatocellular carcinoma: predictive modeling strategies to anticipate tumor response and improve patient selection. *Eur Radiol.* 2022;32(7):4687-4698. [\[CrossRef\]](#)
 14. Therasse P, Arbusck SG, Eisenhauer EA, et al. New guidelines to evaluate the response to treatment in solid tumors. European Organization for Research and Treatment of Cancer, National Cancer Institute of the United States, National Cancer Institute of Canada. *J Natl Cancer Inst.* 2000;92(3):205-216. [\[CrossRef\]](#)
 15. Chapiro J, Lin M, Duran R, Scherthaner RE, Geschwind JF. Assessing tumor response after loco-regional liver cancer therapies: the role of 3D MRI. *Expert Rev Anticancer Ther.* 2015;15(2):199-205. [\[CrossRef\]](#)
 16. Chapiro J, Wood LD, Lin M, et al. Radiologic-pathologic analysis of contrast-enhanced and diffusion-weighted MR imaging in patients with HCC after TACE: diagnostic accuracy of 3D quantitative image analysis. *Radiology.* 2014;273(3):746-758. [\[CrossRef\]](#)
 17. Sharma Y, Weaver MJ, Ludwig DR, et al. Serum alpha-fetoprotein level per total tumor volume as a predictor of recurrence of hepatocellular carcinoma after resection. *Surgery.* 2018;163(5):1002-1007. [\[CrossRef\]](#)
 18. Kim DK, Kwon JH, Won JY, et al. Ablation volume measurement after percutaneous cryoablation using a two-cryo-probe technique for small hepatocellular carcinomas. *Cardiovasc Intervent Radiol.* 2019;42(2):220-229. [\[CrossRef\]](#)
 19. Zhuang BW, Li W, Qiao B, et al. Preoperative prognostic value of alfa-fetoprotein density in patients with hepatocellular carcinoma undergoing radiofrequency ablation. *Int J Hyperthermia.* 2022;39(1):1143-1151. [\[CrossRef\]](#)
 20. Dong SY, Wang WT, Chen XS, et al. Microvascular invasion of small hepatocellular carcinoma can be preoperatively predicted by the 3D quantification of MRI. *Eur Radiol.* 2022;32(6):4198-4209. [\[CrossRef\]](#)
 21. Jiang T, Zhang XS, Pan F, et al. The ratio of preoperative alpha-fetoprotein level to total tumor volume as a prognostic factor of hepatocellular carcinoma after liver transplantation. *Medicine (Baltimore).* 2021;100(26):e26487. [\[CrossRef\]](#)
 22. Lai Y, Lee JC, Hung HC, et al. Models to predict disease-free survival for hepatocellular carcinoma patients with surgical resections. *J Surg Oncol.* 2020;122(7):1444-1452. [\[CrossRef\]](#)
 23. Hwang S, Joh JW, Wang HJ, et al. Prognostic prediction models for resection of large hepatocellular carcinoma: a Korean multicenter study. *World J Surg.* 2018;42(8):2579-2591. [\[CrossRef\]](#)
 24. Ho SY, Hsu CY, Liu PH, et al. Albumin-bilirubin (ALBI) grade-based nomogram to predict tumor recurrence in patients with hepatocellular carcinoma. *Eur J Surg Oncol.* 2019;45(5):776-781. [\[CrossRef\]](#)
 25. Jeon SK, Lee DH, Park J, et al. Tumor volume measured using MR volumetry as a predictor of prognosis after surgical resection of single hepatocellular carcinoma. *Eur J Radiol.* 2021;144:109962. [\[CrossRef\]](#)
 26. Granata V, Fusco R, Avallone A, et al. Major and ancillary magnetic resonance features of LI-RADS to assess HCC: an overview and update. *Infect Agent Cancer.* 2017;12:23.
 27. Ahmed M, Solbiati L, Brace CL, et al. Image-guided tumor ablation: standardization of terminology and reporting criteria--a 10-year update. *Radiology.* 2014;273(1):241-260.
 28. Rothe JH, Grieser C, Lehmkuhl L, et al. Size determination and response assessment of liver metastases with computed tomography-comparison of RECIST and volumetric algorithms. *Eur J Radiol.* 2013;82(11):1831-1839. [\[CrossRef\]](#)
 29. Frich L, Hagen G, Brabrand K, et al. Local tumor progression after radiofrequency ablation of colorectal liver metastases: evaluation of ablative margin and three-dimensional volumetric analysis. *J Vasc Interv Radiol.* 2007;18(9):1134-1140. [\[CrossRef\]](#)
 30. Chockalingam A, Duran R, Sohn JH, et al. Radiologic-pathologic analysis of quantitative 3D tumour enhancement on contrast-enhanced MR imaging: a study of ROI placement. *Eur Radiol.* 2016;26(1):103-113. [\[CrossRef\]](#)
 31. Department of Medical Administration, National Health and Health Commission of the People's Republic of China. [Guidelines for diagnosis and treatment of primary liver cancer in China (2019 edition)]. *Zhonghua Gan Zang Bing Za Zhi.* 2020;28(2):112-128. [\[CrossRef\]](#)
 32. Camp RL, Dolled-Filhart M, Rimm DL. X-tile: a new bio-informatics tool for biomarker assessment and outcome-based cut-point optimization. *Clin Cancer Res.* 2004;10(21):7252-7259. [\[CrossRef\]](#)
 33. Koo TK, Li MY. A guideline of selecting and reporting intraclass correlation coefficients for reliability research. *J Chiropr Med.* 2016;15(2):155-163. [\[CrossRef\]](#)
 34. Fleckenstein FN, Scherthaner RE, Duran R, et al. 3D Quantitative tumour burden analysis in patients with hepatocellular carcinoma before TACE: comparing single-lesion vs. multi-lesion imaging biomarkers as predictors of patient survival. *Eur Radiol.* 2016;26(9):3243-3252. [\[CrossRef\]](#)
 35. Galizia MS, Töre HG, Chalian H, Yaghmai V. Evaluation of hepatocellular carcinoma size using two-dimensional and volumetric analysis: effect on liver transplantation eligibility. *Acad Radiol.* 2011;18(12):1555-1560. [\[CrossRef\]](#)
 36. Kim BK, Kim SU, Kim MJ, et al. Number of target lesions for EASL and modified RECIST to predict survivals in hepatocellular carcinoma treated with chemoembolization. *Clin Cancer Res.* 2013;19(6):1503-1511. [\[CrossRef\]](#)
 37. Bangard C, Rösgen S, Wahba R, et al. Large-volume multi-tined expandable RF ablation in pig livers: comparison of 2D and volumetric measurements of the ablation zone. *Eur Radiol.* 2010;20(5):1073-1078. [\[CrossRef\]](#)
 38. Kashkoush S, El Moghazy W, Kawahara T, Gala-Lopez B, Toso C, Kneteman NM. Three-dimensional tumor volume and serum alpha-fetoprotein are predictors of hepatocellular carcinoma recurrence after liver transplantation: refined selection criteria. *Clin Transplant.* 2014;28(6):728-736. [\[CrossRef\]](#)
 39. Galizia MS, Töre HG, Chalian H, McCarthy R, Salem R, Yaghmai V. MDCT necrosis quantification in the assessment of hepatocellular carcinoma response to yttrium 90 radioembolization therapy: comparison of two-dimensional and volumetric techniques. *Acad Radiol.* 2012;19(1):48-54. [\[CrossRef\]](#)
 40. Pellerin O, Lin M, Bhagat N, Ardon R, Mory B, Geschwind JF. Comparison of semi-automatic volumetric VX2 hepatic tumor segmentation from cone beam CT and multi-detector CT with histology in rabbit models. *Acad Radiol.* 2013;20(1):115-121. [\[CrossRef\]](#)
 41. Beer AJ, Wieder HA, Lordick F, et al. Adenocarcinomas of esophagogastric junction: multi-detector row CT to evaluate early response to neoadjuvant chemotherapy. *Radiology.* 2006;239(2):472-480. [\[CrossRef\]](#)
 42. Budjan J, Sauter EA, Morelli JN, et al. Semi-automatic Volumetric Measurement of Treatment Response in Hepatocellular Carcinoma After Trans-arterial Chemoembolization. *Anticancer Res.* 2016;36(8):4353-4358. [\[CrossRef\]](#)
 43. Bonekamp D, Bonekamp S, Halappa VG, et al. Interobserver agreement of semi-automated and manual measurements of functional MRI metrics of treatment response in hepatocellular carcinoma. *Eur J Radiol.* 2014;83(3):487-496. [\[CrossRef\]](#)

Supplementary Material 1.

1. Tumor segmentation

In most cases, tumor burden analysis is limited to sophisticated processing and patent commercial software, leading to the utilization of linear tumor measurement, like diameter or cross-product on a single axial slice, as a proxy for actual volume. Here, we use an open-source software ITK-SNAP (www.itksnap.org/pmwiki/pmwiki.php) with a region-growth computed algorithm to calculate tumor volume and enhanced volume, with the aim of a cost-effective, standardized, and repeatable measurement in routine clinical settings.

The segmentation processes were based on a seed-growing algorithm, namely region-growth algorithm. This algorithm was based on voxel thresholding, thereby quantifying the signal in a voxel-by-voxel fashion.

1) Four quadrate regions of interest (ROIs), within the ipsilateral lobe of the lesion if possible, were prescribed on the magnetic resonance imaging (MRI) at the late arterial phase (20 sec) in areas adjacent to tumor boundaries, away from blood vessels, liver boundaries, and other structures. And at least 2 ROIs were placed in which the largest tumor area

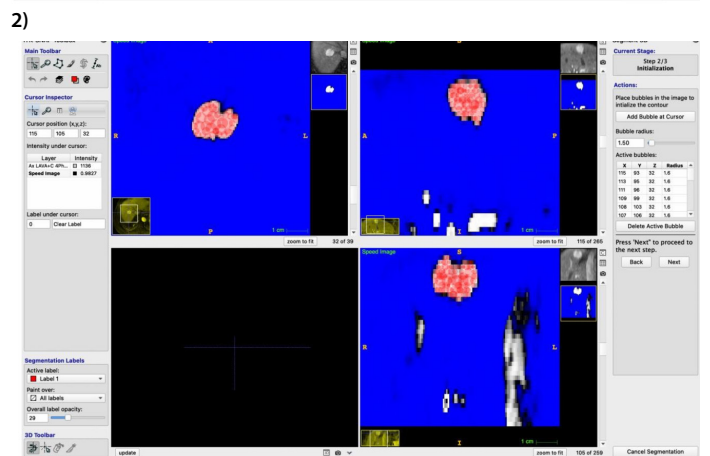
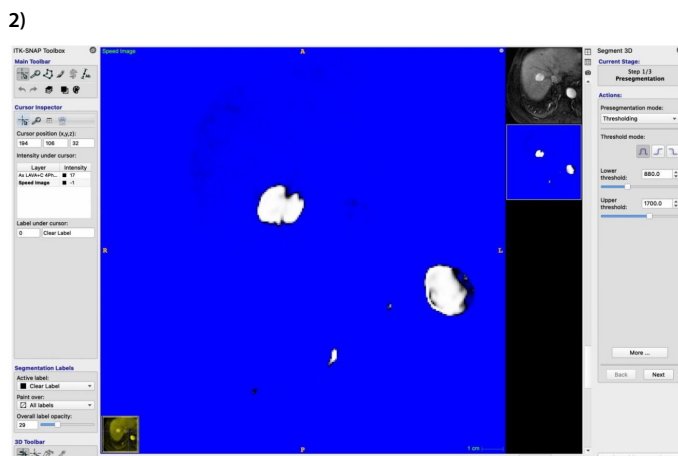
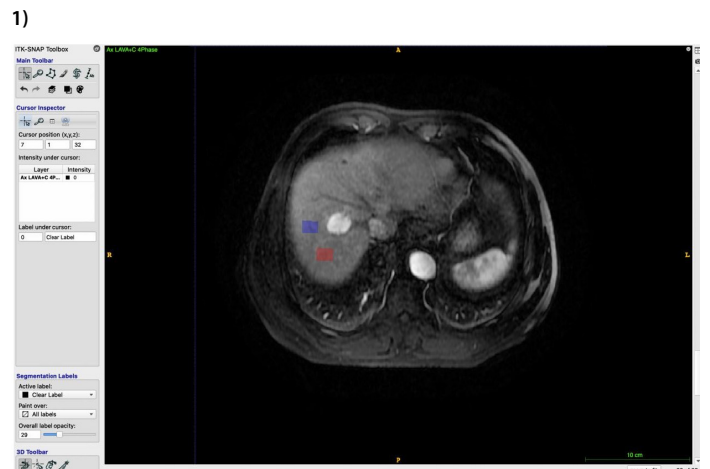
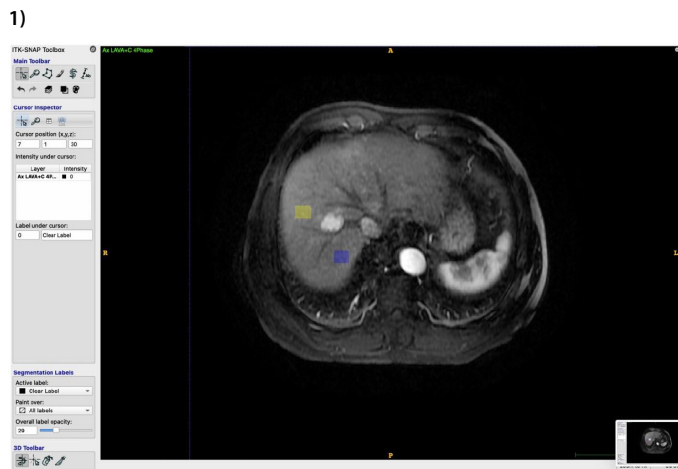
was emerging. The signal intensity of each ROI region is the average value of the signal intensity of the voxels in the corresponding region. The final threshold, namely the mean intensity value (MIV), is the average value of the four ROI regions.

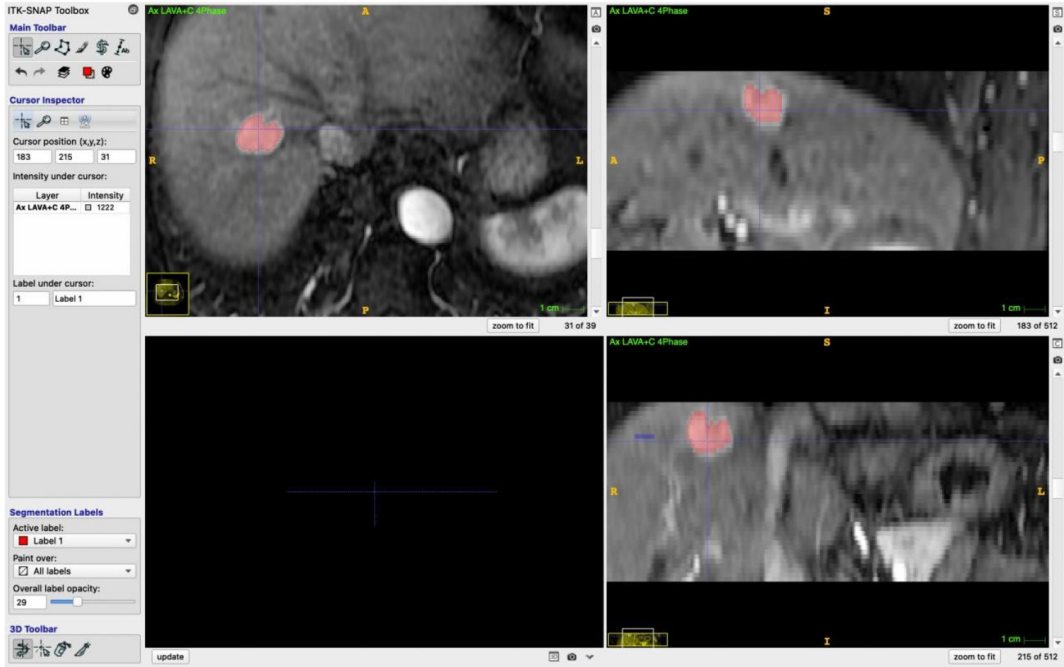
2) When the segment tool was set up, a region including the index tumor was chosen manually using a square frame.

3) The seed points were set in the hyper-enhancement part of the tumor visually based on the hepatocellular carcinoma (HCC) enhanced characteristic. The necrotic areas, cysts, and vessels related to each lesion at the certain slice were also avoided, as identified on T2-weighted imaging (T2WI) or arterial early phase images. Meanwhile, the pre-enhanced T1WI image was scrutinized to distinguish high signal intensity, like hemorrhage, so as to avoid overestimate enhanced tumor volume value. Using the “color map editor” function to adjust the signal intensity contrast between the tumor and liver background with aim of easier bubble placement. The exterior delineated bubbles were placed inside the edge of the enhanced part of lesion with being tangent to the inner margin in principle, and the interior delineated bubbles were placed randomly.

The bubble radius was adjustable to accommodate tumors of different sizes. In addition, the cross-referencing with coronal and sagittal reconstructed MRI images were used for an accurate supplement of bubble.

4) After placing the bubbles, the number of iterations of the bubble evolution needs to be set, which is determined the tumor size, region competition force and smoothing force. The latter two parameters can be adjusted, with reference to the animation presentation. In this study, the region competition force was set as 0.8, and smoothing force value was set as default value. In regard to the small HCC diameter in this study, the numbers of iterations of the bubble evolution were set as 8-12. The voxel inside or peripheral of the seed was clustered if the signal intensity was distributed within the threshold interval, ranging from the $MIV+2$ standard deviations to abdominal aorta signal intensity. In this step, tumor enhanced volume was obtained. Considering the presence of low or delayed enhancement components, such as fibrotic scarring within the tumor, the brush tool was used to cover the unmasked components in the tumor. Then, the total tumor volume was calculated.





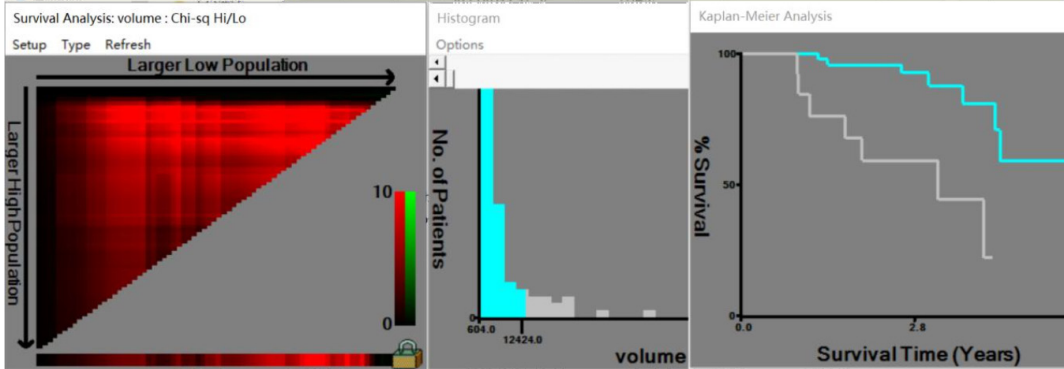
X-tile

File Show X-tile Setup

Version 3.6.1

Copyright Yale University

| Pt No | % Total | Events | Rate | Rank | Range | Miller-Seigmund P | Chi-sq Hi/Lo | Relative Risk 1 vs 2 |
|-------|---------|--------|-------|----------|------------------------|-------------------|--------------|----------------------|
| 58 | 79.45 | 7 | 12.07 | 0 to 57 | 604.00 thru 12424.00 | 0.0078 | 13.4231 | 1.00 / 3.87 |
| 15 | 20.55 | 7 | 46.67 | 58 to 72 | 13560.32 thru 98090.00 | | | |
| 73 | 100.00 | 14 | 19.18 | 0 to 72 | 604.00 thru 98090.00 | | | |





Prediction of carcinogenic human papillomavirus types in cervical cancer from multiparametric magnetic resonance images with machine learning-based radiomics models

Okan İnce

Emre Uysal

Görkem Durak

Suzan Önel

Binnur Dönmez Yılmaz

Şükrü Mehmet Ertürk

Hakan Önder

PURPOSE

This study aimed to evaluate the potential of machine learning-based models for predicting carcinogenic human papillomavirus (HPV) oncogene types using radiomics features from magnetic resonance imaging (MRI).

METHODS

Pre-treatment MRI images of patients with cervical cancer were collected retrospectively. An HPV DNA oncogene analysis was performed based on cervical biopsy specimens. Radiomics features were extracted from contrast-enhanced T1-weighted images (CE-T1) and T2-weighted images (T2WI). A third feature subset was created as a combined group by concatenating the CE-T1 and T2WI subsets. Feature selection was performed using Pearson's correlation coefficient and wrapper-based sequential-feature selection. Two models were built with each feature subset, using support vector machine (SVM) and logistic regression (LR) classifiers. The models were validated using a five-fold cross-validation technique and compared using Wilcoxon's signed rank and Friedman's tests.

RESULTS

Forty-one patients were enrolled in the study (26 were positive for carcinogenic HPV oncogenes, and 15 were negative). A total of 851 features were extracted from each imaging sequence. After feature selection, 5, 17, and 20 features remained in the CE-T1, T2WI, and combined groups, respectively. The SVM models showed 83%, 95%, and 95% accuracy scores, and the LR models revealed 83%, 81%, and 92.5% accuracy scores in the CE-T1, T2WI, and combined groups, respectively. The SVM algorithm performed better than the LR algorithm in the T2WI feature subset ($P = 0.005$), and the feature sets in the T2WI and the combined group performed better than CE-T1 in the SVM model ($P = 0.033$ and 0.006 , respectively). The combined group feature subset performed better than T2WI in the LR model ($P = 0.023$).

CONCLUSION

Machine learning-based radiomics models based on pre-treatment MRI can detect carcinogenic HPV status with discriminative accuracy.

KEYWORDS

Artificial intelligence, human papillomavirus DNA tests, machine learning, radiology, uterine cervical neoplasms

From the Clinic of Radiology (O.İ. ✉ okan_ince@yahoo.com, S.Ö. H.Ö.), University of Health Sciences Turkey, Prof. Dr. Cemil Taşçıoğlu City Hospital, İstanbul, Turkey; Clinic of Radiation Oncology (E.U., B.D.Y.), University of Health Sciences Turkey, Prof. Dr. Cemil Taşçıoğlu City Hospital, İstanbul, Turkey; Department of Radiology (G.D., Ş.M.E.), İstanbul University, İstanbul Faculty of Medicine, İstanbul, Turkey.

Received 11 Jan 2022; revision requested 21 Feb 2022; last revision received 11 Oct 2022; accepted 16 Nov 2022.



Epub: 21.12.2022

Publication date: 30.05.2023

DOI: 10.4274/dir.2022.221335

Cervical cancer is the fourth most common female cancer and the second most common in women aged 15–44.¹ The etiological factor in more than 95% of cervical cancer cases is human papillomavirus (HPV).²⁻⁴ Fifteen of more than 200 oncogene types are identified as high risk, and type-16 and -18 HPV infections are the most common in women with cervical cancer.⁵ In addition, several studies in the literature report that HPV DNA sta-

You may cite this article as: Ince O, Uysal E, Durak G, et al. Prediction of carcinogenic human papillomavirus types in cervical cancer from multiparametric magnetic resonance images with machine learning-based radiomics models. *Diagn Interv Radiol.* 2023;29(3):460-468.

tus is associated with treatment response, disease-free survival, and overall survival in patients with cervical carcinoma.⁶⁻¹⁰

Radiomics is a method for extracting quantitative features from medical imaging. In medical imaging, hundreds of radiomic features can be extracted from pixels invisible to the human eye.¹¹ Various studies have been published using radiomics features to predict tumor histopathology, stage, grade, and clinical outcomes in cervical cancer.¹¹⁻¹⁵ Additionally, different high-accuracy performance machine learning-based models have been created to predict HPV status in oropharyngeal cancer using radiomics features.^{16,17} However, no studies have been reported that investigate the prediction of HPV status in cervical cancer using radiomics features obtained from magnetic resonance imaging (MRI).

This study aimed to evaluate the potential value of machine learning-based models for predicting carcinogenic HPV oncogene types in cervical cancer by extracting radiomics features from MRI.

Methods

Ethics

This was a retrospective study conducted with the approval of our institutional ethics review board (approval number: 514.10/35). Informed consent was waived due to retrospective nature of the study.

Patient eligibility

Patients admitted to our radiation oncology department between 2015 and 2018 with squamous cell carcinoma of the uterine cervix were enrolled in this study. Their clinical data (age, smoking history in years, and tumor stage) were reviewed. The tumor stage was determined by assessing lymph node involvement by positron emission tomography-computed tomography images and

the presence of distant metastasis. Pre-treatment pelvic MRI images were evaluated. Patients without pre-treatment MRI images in our Picture Archiving and Communication Systems and those in whom the images had prominent artifacts were excluded. Figure 1 summarizes the radiomics work pipeline.

The authors acknowledge that some of the patients' data were used in another study investigating the correlation between radiotherapy response and HPV infection status.¹⁸

Gold standard

The gold standard for the study was HPV-DNA oncogene analysis performed with reverse-transcriptase polymerase chain reaction (rt-PCR) from cervical biopsy materials. A dedicated research laboratory performed the HPV-DNA oncogene analysis.

MRI technique

The two primary pelvic MRI sequences selected for the radiomics input were the sagittal T2 weighted images (T2WI) and the contrast-enhanced three-dimensional fast spoiled gradient echo sequence (CE-T1) (T1W high-resolution isotropic volume examination/liver acquisition with volume acquisition). MRI examinations were performed using two 1.5-T unit MRI scanners [Achieva 1.5-T (Philips Healthcare, Netherlands) and Signa Dx (GE Medical Systems, USA)] using phased-array body coils. The imaging protocol for sagittal T2WI was repetition time/echo time (TR/TE): 5,300/100 ms, field of view (FOV): 24 cm, matrix: 320 × 256, and slice thickness/slice gap: 5/2 mm. The parameters selected for CE-T1 were TR/TE: 4.1/1.1 ms, FOV: 32 cm, matrix: 288 × 192, and slice thickness/slice gap: 3/0.3 mm. The

time delay was set at 40 sec to achieve the late arterial phase.

Image preprocessing and feature extraction

The images were preprocessed with an N4ITK magnetic bias-field correction algorithm to avoid the intensity differences and substantial noise caused by different scanners.¹⁹ After preprocessing, pixels were rescaled to 1 × 1 mm² with a cubic B-spline interpolation, and gray levels were discretized to a fixed gray-level bin width of 3.²⁰

Segmentations were performed from sagittal T2WI and sagittal reconstructed CE-T1 images semi-automatically by two radiologists, one with experience of more than 20 years in abdominal radiology and a fourth-year resident, with consensus. For better orientation to the tumor, axial images of CE-T1 were used when needed. The largest cross-sectional area of cervical tumors was segmented with the freely available 3D Slicer software (v.4.10.2) (Figure 2). A 2-mm shrinkage was applied to every segmented label to extract the exact tumor texture. Six subgroups of radiomics features were extracted from the original and wavelet-filtered images by the PyRadiomics extension package included in the 3D Slicer software.²¹

Feature selection and data handling

For the stability of the machine learning models, data preprocessing steps that majorly impact classification solvers²² were followed as standardization and discretization to 10 bins, with a uniform bin width.

Feature selection is a requisite to avoid overfitting the model with high-dimensional data, as it reduces dimension. A two-step process was followed for feature selection.

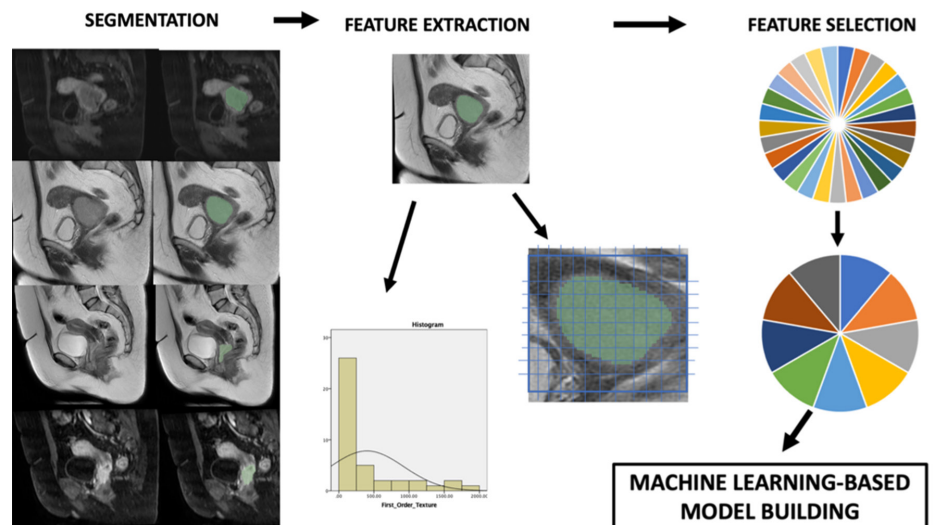


Figure 1. Summary of radiomics pipeline.

Main points

- Prediction of carcinogenic human papillomavirus (HPV) oncogenes enables the identification of high-risk patients and can be used as a prognostic marker.
- Machine learning-based radiomics models can predict carcinogenic HPV DNA status in cervical cancer.
- Similar accuracy rates from different algorithms show the feasibility of machine learning-based models.

First, Pearson's correlation coefficient was used to select and drop redundant features. Feature pairs with higher collinearity than the 0.7 thresholds were detected, and those with high collinearity to the other features were dropped.²³ Second, non-redundant features were used to input a wrapper-based sequential-feature selection algorithm with a support vector machine (SVM) algorithm as a learning estimator. The wrapper-based sequential-feature selection was performed with backward propagation with five-fold cross validation. In this wrapper method, multiple learning models with various feature subsets were trained with training folds and tested with the remaining test fold using a five-fold cross-validation technique. The data were divided into five equal parts. In a five-fold turn, one data part was selected as test data, with the remaining four as training data. A different part of the data was selected as test data in each fold. Thus, the phenomenon of "double-dipping" was avoided.²⁴ As with the backward propagated wrapper method, the models were initiated with all the features included. The selection process was performed by eliminating the least important ones until the stopping conditions were satisfied.

Model building

The selected features from T2WI, CE-T1, and the combined datasets were included as inputs to the machine learning models. To evaluate the feasibility of the machine learning algorithms, two different models with different contexts were built by coding in Python (v.3). The algorithm of the first model was SVM, with hyperparameters of C:1.0 and kernel: "linear." The second algorithm was selected as logistic regression (LR), with hyperparameters of C:1, solver: "liblinear," and regularization penalty: "L2." A five-fold cross-validation method evaluated the performance of the models.

Statistical analysis

Descriptive statistics of the data are presented as numbers and percentages (n, %), non-normalized variables are shown as medians (interquartile range), and normalized variables (for parametric tests) as mean \pm standard deviation. An independent-samples *t*-test and a Mann-Whitney U test were performed on the numeric variables after a normality analysis using the Kolmogorov-Smirnov test. Fisher's exact test and the Fisher-Freeman-Halton exact test were performed when appropriate. Receiver operating characteristics (ROC) curves were plotted in the Python coding environment using the

"sci-kit learn" library. The area under the ROC curve (AUC) was calculated with *P* values.

Comparisons between the models with LR and SVM algorithms were performed using Wilcoxon's signed rank test. Comparisons of the models with different feature subsets were performed using Friedman's test. The Dunn-Bonferroni post-hoc test was conducted if statistical significance was found. Statistical analysis was performed using SPSS software v.23,²⁵ and the statistical significance level selected was *P* < 0.05.

Results

Patients

There were 98 patients enrolled in the study. Fifty patients were excluded due to a lack of imaging, and seven were excluded because of prominent artifacts in their images. Twenty-six (63%) patients were positive for HPV-DNA oncogenes (types 16, 31, 45, or 52) according to the rt-PCR test. Fifteen (37%) patients were negative for HPV-DNA oncogenes. Table 1 summarizes the characteristics of the patients.

Feature extraction and selection

A total of 851 features from each of the CE-T1 and T2WI images were extracted. Features were grouped as follows: 14 (1.64%) shape, 18 (2.11%) first order, 14 (1.64%) gray-level dependence matrix, 24 (2.82%) gray-level co-occurrence matrix, 16 (1.88%) gray-level run-length matrix, 16 (1.88%) gray-level size-zone matrix, 5 (0.06%) neighboring gray-tone difference matrix, and 744 (87.97%) wavelet-derived texture features. A combined dataset was created by concatenating features from T2WI and CE-T1.

Pearson's correlation coefficient determined 32, 49, and 75 features as non-redundant in CE-T1, T2WI, and the combined group, respectively. After the wrapper-based sequential feature selection step, the final feature subsets consisted of five features in CE-T1, 17 in T2WI, and 20 in the combined group. Table 2 and Figure 3 provide details of the selected features.

Classification performance

The SVM models had 83.10%, 95.20%, and 95.30% accuracy scores in the CE-T1, T2WI, and combined groups, respectively. The AUC values and 95% confidence intervals (CI) were 0.85 95% CI: 0.99, 0.71; 0.96, 95% CI: 1, 0.93; and 0.98, 95% CI: 1, 0.95, *P* = 0.001 for the CE-T1, T2WI, and combined groups, respectively.

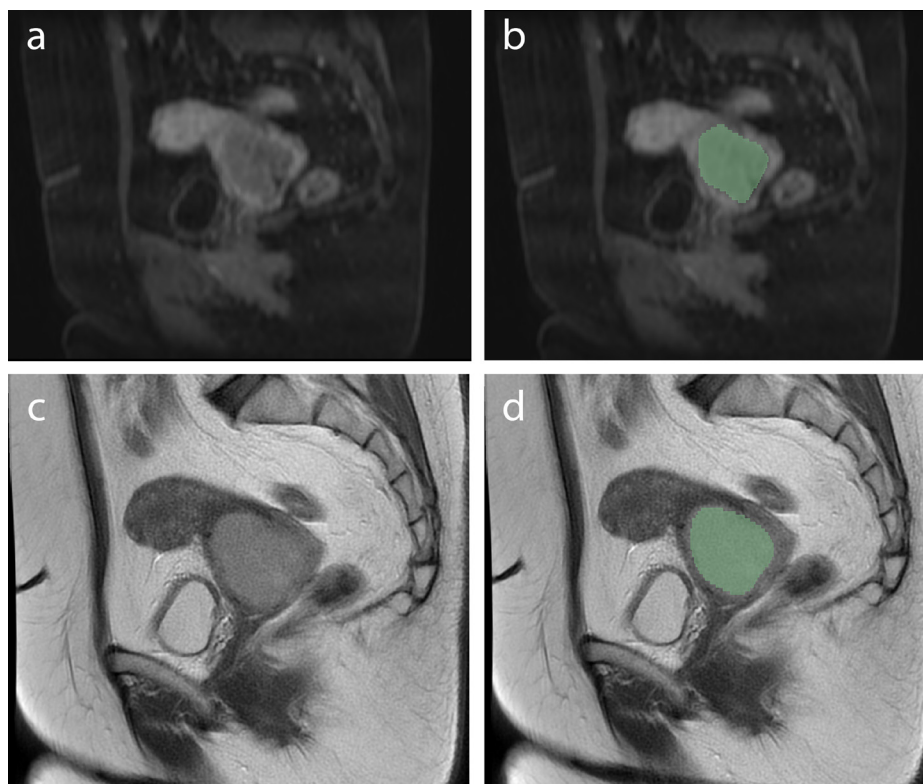


Figure 2. The segmentation process from contrast-enhanced T1-weighted images (a-b) and T2-weighted images (c-d).

Table 1. Characteristics of patients

| | HPV-DNA oncogene (-) | HPV-DNA oncogene (+) | P value |
|---|--------------------------|---------------------------|---------|
| Age (mean ± SD) (95% CI) | 55 ± 12 (51.4, 58.6) | 53 ± 12 (49.3 – 56.7) | 0.980 |
| History of smoking n (%) | | | |
| Present | 3 (27.27%) | 8 (73.73%) | 0.716 |
| Absent | 12 (40%) | 18 (60%) | |
| Years of smoking (median) (IQR) | 30 (15-45) | 20 (17.5-25) | 0.497 |
| Mean tumor diameter (mm) (mean ± SD) (95% CI) | 40.8 ± 15.7 (35.9, 45.6) | 45.3 ± 15.18 (40.7, 49.9) | 0.500 |
| Tumor stage n (%) | | | |
| 2 B (n = 25) | 9 (36%) | 16 (64%) | 1.000 |
| C1 (n = 10) | 4 (40%) | 6 (60%) | |
| 3 C2 (n = 6) | 2 (28.50%) | 4 (71.50%) | |

HPV, human papillomavirus; SD, standard deviation; CI, confidence intervals; IQR, interquartile range.

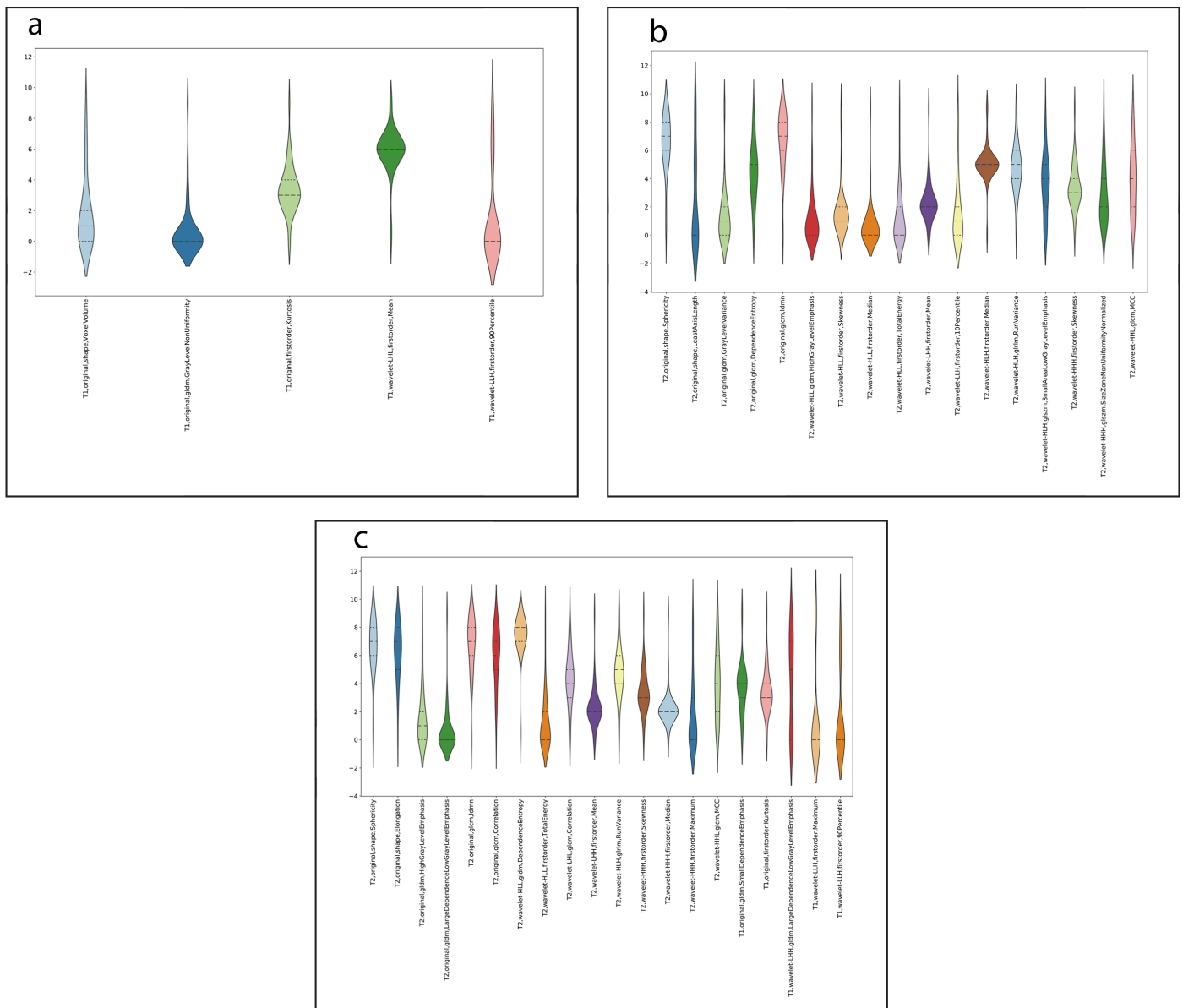


Figure 3. The distribution of the selected features from contrast-enhanced T1-weighted images (a), T2-weighted images (b), and the combined group (c) after the data preprocessing steps.

dictability of carcinogenic HPV status from pre-treatment MRI. Therefore, we were not able to compare our results with those of other studies.

Practical implications

The results of our study could be helpful in clinical practice. HPV plays a significant role in the development of cervical cancer. Additionally, many studies have investigated

the impact of pre-treatment HPV status on prognosis. A recently published meta-analysis indicated that positive HPV DNA status favors good prognosis in cervical cancer.²⁶ The tests that detect HPV DNA are divided into nucleic acid hybridization assays, signal amplification assays, and nucleic acid amplification assays. HPV DNA is detected by rt-PCR and Hybrid Capture II tests. However, the HPV DNA test is not routinely performed

in patients with cervical cancer, especially in middle- and low-income countries.²⁷ Considering that cervical cancer is mostly fatal in countries with a low socioeconomic status,²⁸ the prediction of carcinogenic HPV DNA from MRI can be an alternative to molecular HPV DNA tests.

Although the prognostic role of HPV in cervical cancer has been reported in a comprehensive meta-analysis,²⁷ several studies

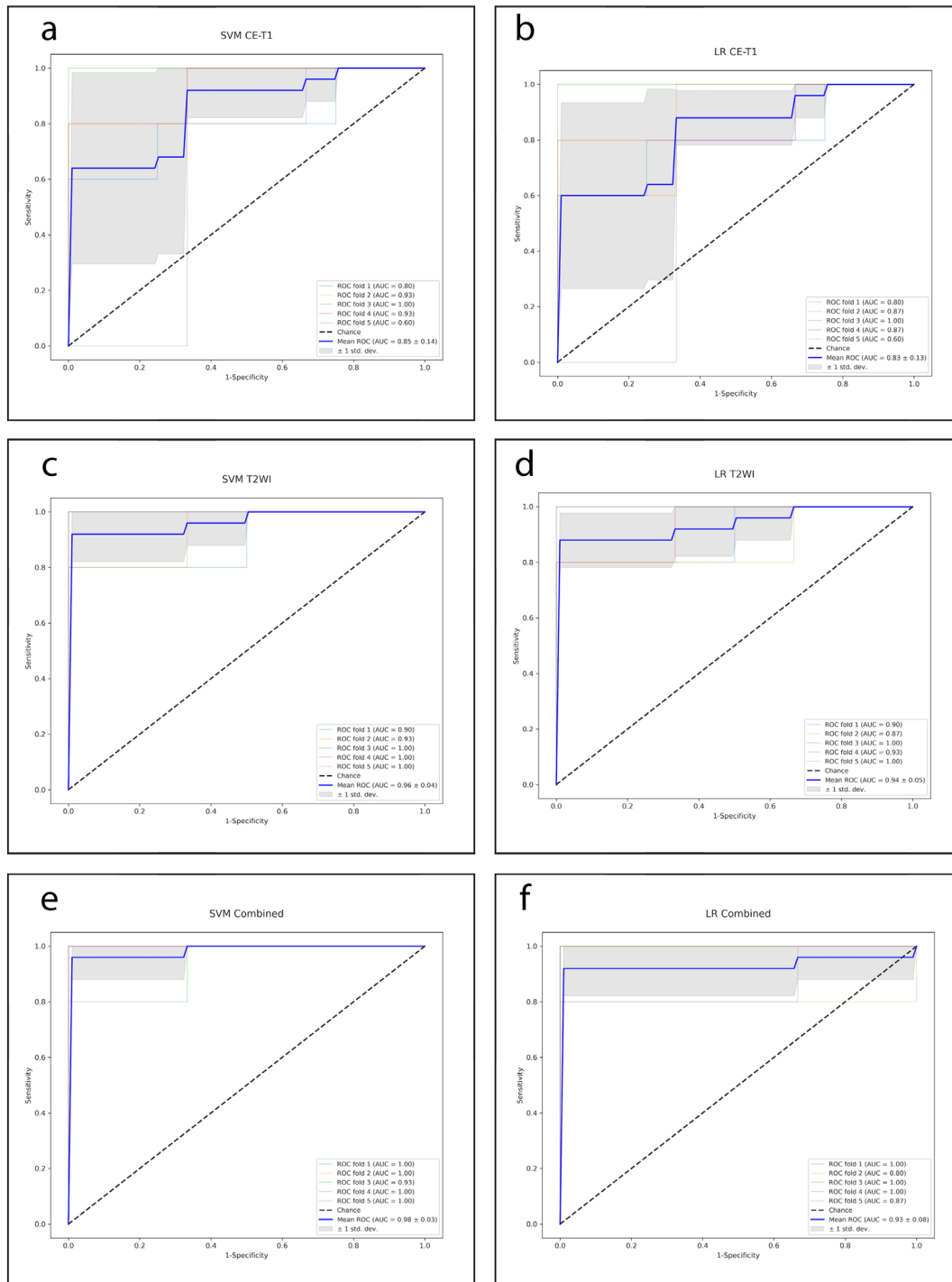


Figure 4. (a-f) The ROC curves achieved in all the models for each test fold. SVM, support vector machine; LR, logistic regression; CE-T1, contrast-enhanced T1 images; T2WI, T2-weighted images; ROC, receiver operating characteristic; AUC, area under the receiver operating characteristics curve.

have shown that HPV status does not have any prognostic significance.²⁹⁻³² In addition to the studies showing that HPV negativity before treatment is a poor prognostic factor for disease-free survival and overall survival,^{8,9,31,33,34} one study has shown that the carcinogenic HPV subtype has prognostic significance.³¹ Based on these findings, it is clinically beneficial to detect HPV DNA status before treatment.

The present study investigated the prediction of HPV status using pre-treatment MRI images. However, the changes in HPV status after treatment have also been shown to impact prognosis. Persistent HPV positivity in patients after radiotherapy is a poor prognostic factor.^{6,7,10}

Limitations and generalizability

Our study has several limitations. First, this was a retrospective study; since all the data were obtained from previous recordings, this could have led to a selection bias. Second, the images were obtained from two scanners, which, although it may be challenging for machine learning models, simulates clinical practice. With the image preprocessing steps, we aimed to standardize the variation from different scanners and protocols to be able to generalize machine learning-based models. Third, the segmentations were performed semi-automatically by two radiologists in consensus to increase the segmentation accuracy. Therefore, a reproducibility analysis could not be per-

formed. Fourth, the authors segmented the most significant slice of the tumor in two-dimensional planes. According to tumor heterogeneity, volumetric segmentation may be a more precise method; however, it is impractical and needs excessive time. Moreover, most studies on texture analysis in cervical cancers are designed based on this technique. Fifth, features from quantitative MRI maps, such as the apparent diffusion coefficient, could not be extracted due to a lack of diffusion-weighted imaging sequences in the imaging protocols.³⁵ Finally, we did not split our data into training and test sets. However, we used a five-fold cross-validation technique. Since our patient population was small, we could not af-

Table 3. Detailed performance metrics of the models

| Models | Accuracy | Sensitivity | Specificity | Precision | Recall | F1 | AUC (95% CI) | P AUC | AUC SE |
|--------------|----------|-------------|-------------|-----------|--------|------|-------------------|-------|--------|
| SVM-CE-T1 | 83.10% | 0.84 | 0.82 | 0.88 | 0.84 | 0.86 | 0.85 (0.99, 0.71) | 0.001 | 0.071 |
| LR-CE-T1 | 83.13% | 0.88 | 0.75 | 0.86 | 0.88 | 0.87 | 0.83 (0.96, 0.70) | 0.001 | 0.051 |
| SVM-T2WI | 95.20% | 0.92 | 0.99 | 0.99 | 0.92 | 0.96 | 0.96 (1, 0.93) | 0.001 | 0.017 |
| LR-T2WI | 81.20% | 0.84 | 0.76 | 0.85 | 0.84 | 0.84 | 0.94 (0.99, 0.89) | 0.001 | 0.025 |
| SVM-combined | 95.30% | 0.99 | 0.86 | 0.94 | 0.99 | 0.97 | 0.98 (1, 0.95) | 0.001 | 0.012 |
| LR-combined | 92.50% | 0.91 | 0.93 | 0.96 | 0.92 | 0.94 | 0.93 (1, 0.85) | 0.001 | 0.038 |

SVM, support vector machine; CE-T1, contrast-enhanced T1-weighted images; LR, logistic regression; T2WI, T2-weighted images; AUC, area under the receiver operating characteristics curve; F1 measure, a harmonic of precision and recall; SE, standard error; P AUC, P values of the AUC.

Table 4. Comparisons between performances of support vector machine and logistic regression algorithms according to the Wilcoxon signed rank test

| Algorithm comparison (SVM vs. LR) | | |
|-----------------------------------|------------------|--------------|
| Imaging sequence | Median (IQR) | P |
| CE-T1 SVM | 0.85 (0.82-0.88) | 1.000 |
| CE-T1 LR | 0.84 (0.75-0.88) | |
| T2WI SVM | 0.96 (0.92-0.99) | 0.005 |
| T2WI LR | 0.84 (0.76-0.94) | |
| Combined SVM | 0.95 (0.86-0.99) | 1.000 |
| Combined LR | 0.93 (0.91-0.96) | |

SVM, support vector machine; LR, logistic regression; CE-T1, contrast-enhanced T1-weighted images; T2WI, T2-weighted images; IQR, interquartile range.

Table 5. Comparisons between the same algorithm-based models with features from different imaging sequences according to Friedman's test

| Algorithms | Imaging sequence | Median (IQR) | Mean rank | P value of pairwise comparisons |
|---------------------------|------------------|------------------|-----------|---|
| SVM (P = 0.004) | CE-T1 | 0.85 (0.82-0.86) | 1.0 | 0.033 (vs. T2WI) 0.006 (vs. combined) |
| | T2WI | 0.96 (0.92-0.99) | 2.36 | 0.033 (vs. CE-T1) 1.000 (vs. combined) |
| | Combined | 0.95 (0.86-0.99) | 2.64 | 0.006 (vs. CE-T1) 1.000 (vs. T2WI) |
| LR (P = 0.018) | CE-T1 | 0.84 (0.77-0.87) | 1.71 | 1.000 (vs. T2WI) 0.090 (vs. combined) |
| | T2WI | 0.84 (0.76-0.94) | 1.43 | 1.000 (vs. CE-T1) 0.023 (vs. combined) |
| | Combined | 0.93 (0.91-0.96) | 2.86 | 0.090 (vs. CE-T1) 0.023 (vs. T2WI) |

SVM, support vector machine; LR, logistic regression; CE-T1, contrast-enhanced T1-weighted images; T2WI, T2-weighted images; IQR, interquartile range.

ford losing any information that could have been beneficial for training.

In conclusion, machine learning-based radiomics models based on pre-treatment MRI can detect carcinogenic HPV status with discriminative accuracy. The fact that HPV status, an essential prognostic factor in survival, can be predicted by MRI raises the issue of whether we can predict survival using MRI.

Acknowledgments

HPV-DNA oncogene analysis was performed with the financial support of the Turkish Society for Radiation Oncology (AP-DP-TROD-2019-2).

Conflict of interest disclosure

The authors declared no conflicts of interest.

References

1. Bailey HH, Chuang LT, duPont NC, et al. American Society of Clinical Oncology Statement: Human Papillomavirus Vaccination for Cancer Prevention. *J Clin Oncol*. 2016;34(15):1803-1812. [CrossRef]
2. Cancer Genome Atlas Research Network; Albert Einstein College of Medicine; Analytical Biological Services, et al. Integrated genomic and molecular characterization of cervical cancer. *Nature*. 2017;543(7645):378-384. [CrossRef]
3. No authors listed. National Institutes of Health Consensus Development Conference statement on cervical cancer. April 1-3, 1996. *Gynecol Oncol*. 1997;66(3):351-361. [CrossRef]
4. Muñoz N, Bosch FX, de Sanjosé S, Shah KV. The role of HPV in the etiology of cervical cancer. *Mutat Res*. 1994;305(2):293-301. [CrossRef]
5. Shukla S, Bharti AC, Mahata S, et al. Infection of human papillomaviruses in cancers of different human organ sites. *Indian J Med Res*. 2009;130(3):222-233. [CrossRef]
6. Nagai Y, Toma T, Moromizato H, et al. Persistence of human papillomavirus infection as a predictor for recurrence in carcinoma of the cervix after radiotherapy. *Am J Obstet Gynecol*. 2004;191(6):1907-1913. [CrossRef]
7. Badaracco G, Savarese A, Micheli A, et al. Persistence of HPV after radio-chemotherapy in locally advanced cervical cancer. *Oncol Rep*. 2010;23(4):1093-1099. [CrossRef]
8. Okuma K, Yamashita H, Yokoyama T, Nakagawa K, Kawana K. Undetected human papillomavirus DNA and uterine cervical carcinoma: association with cancer recurrence. *Strahlenther Onkol*. 2016;192(1):55-62. [CrossRef]
9. Lindel K, Burri P, Studer HU, Altermatt HJ, Greiner RH, Gruber G. Human papillomavirus status in advanced cervical cancer: predictive and prognostic significance for curative radiation treatment. *Int J Gynecol Cancer*. 2005;15(2):278-284. [CrossRef]
10. Song YJ, Kim JY, Lee SK, et al. Persistent human papillomavirus DNA is associated with local recurrence after radiotherapy of uterine cervical cancer. *Int J Cancer*. 2011;129(4):896-902. [CrossRef]
11. Lambin P, Rios-Velazquez E, Leijenaar R, et al. Radiomics: extracting more information from medical images using advanced feature analysis. *Eur J Cancer*. 2012;48(4):441-446. [CrossRef]
12. Wu Q, Shi D, Dou S, et al. Radiomics analysis of multiparametric MRI evaluates the pathological features of cervical squamous cell carcinoma. *J Magn Reson Imaging*. 2019;49(4):1141-1148. [CrossRef]
13. Fang M, Kan Y, Dong D, et al. Multi-habitat based radiomics for the prediction of treatment response to concurrent chemotherapy and radiation therapy in locally advanced cervical cancer. *Front Oncol*. 2020;10:563. [CrossRef]
14. Lucia F, Visvikis D, Desseroit MC, et al. Prediction of outcome using pretreatment (18)F-FDG PET/CT and MRI radiomics in locally advanced cervical cancer treated with chemoradiotherapy. *Eur J Nucl Med Mol Imaging*. 2018;45(5):768-786. [CrossRef]
15. Deng X, Liu M, Sun J, et al. Feasibility of MRI-based radiomics features for predicting lymph node metastases and VEGF expression in cervical cancer. *Eur J Radiol*. 2021;134:109429. [CrossRef]
16. Sohn B, Choi YS, Ahn SS, et al. Machine Learning Based Radiomic HPV phenotyping of oropharyngeal SCC: a feasibility study using MRI. *Laryngoscope*. 2021;131:851-856. [CrossRef]
17. Suh CH, Lee KH, Choi YJ, et al. Oropharyngeal squamous cell carcinoma: radiomic machine-learning classifiers from multiparametric MR images for determination of HPV infection status. *Sci Rep*. 2020;10(1):17525. [CrossRef]
18. Yılmaz BD, Uysal E, Gurdal N, Ozkan A. Is there any correlation between HPV and early radioresponse before brachytherapy in cervix uteri carcinoma? *Radiol Med*. 2020;125(10):981-989. [CrossRef]
19. Tustison NJ, Avants BB, Cook PA, et al. N4ITK: improved N3 bias correction. *IEEE Trans Med Imaging*. 2010;29(6):1310-1320. [CrossRef]
20. Shafiq-Ul-Hassan M, Latifi K, Zhang G, Ullah G, Gillies R, Moros E. Voxel size and gray level normalization of CT radiomic features in lung cancer. *Sci Rep*. 2018;8(1):10545. [CrossRef]
21. van Griethuysen JJM, Fedorov A, Parmar C, et al. Computational radiomics system to decode the radiographic phenotype. *Cancer Res*. 2017;77(21):104-107. [CrossRef]
22. Koçak B, Durmaz EŞ, Ateş E, Kılıçkesmez Ö. Radiomics with artificial intelligence: a practical guide for beginners. *Diagn Interv Radiol*. 2019;25(6):485-495. [CrossRef]
23. Dormann CF, Elith J, Bacher S. Collinearity: a review of methods to deal with it and a simulation study evaluating their performance. *Ecography*. 2013;36(1):27-46. [CrossRef]
24. Ball TM, Squeglia LM, Tapert SF, Paulus MP. Double dipping in machine learning: problems and solutions. *Biol Psychiatry Cogn Neurosci Neuroimaging*. 2020;5(3):261-263. [CrossRef]
25. IBM Corp. Released 2015. IBM SPSS Statistics for Windows, Version 23.0. Armonk NIC. No Title. <https://scirp.org/reference/ReferencesPapers.aspx?ReferencelD=2611745>
26. Li P, Tan Y, Zhu LX, et al. Prognostic value of HPV DNA status in cervical cancer before treatment: a systematic review and meta-analysis. *Oncotarget*. 2017;8(39):66352-66359. [CrossRef]
27. Pimple SA, Mishra GA. Optimizing high risk HPV-based primary screening for cervical cancer in low- and middle-income countries: opportunities and challenges. *Minerva Ginecol*. 2019;71(5):365-371. [CrossRef]
28. Bray F, Ferlay J, Soerjomataram I, Siegel RL, Torre LA, Jemal A. Global cancer statistics 2018: GLOBOCAN estimates of incidence and mortality worldwide for 36 cancers in 185 countries. *CA Cancer J Clin*. 2018;68(6):394-424. [CrossRef]
29. Tong SY, Lee YS, Park JS, Namkoong SE. Human papillomavirus genotype as a prognostic factor in carcinoma of the uterine cervix. *Int J Gynecol Cancer*. 2007;17(6):1307-1313. [CrossRef]
30. Dabić MM, Nola M, Tomićić I, Dotlić S, Petrovečki M, Jukić S. Adenocarcinoma of the uterine cervix: prognostic significance of clinicopathologic parameters, flow cytometry analysis and HPV infection. *Acta Obstet Gynecol Scand*. 2008;87(3):366-372. [CrossRef]
31. de Cremoux P, de la Rochefordière A, Savignoni A, et al. Different outcome of invasive cervical cancer associated with high-risk versus intermediate-risk HPV genotype. *Int J Cancer*. 2009;124(4):778-782. [CrossRef]
32. Feng D, Xu H, Li X, et al. An association analysis between mitochondrial DNA content, G10398A polymorphism, HPV infection, and the prognosis of cervical cancer in the Chinese Han population. *Tumor Biol*. 2016;37(4):5599-5607. [CrossRef]

33. Rodríguez-Carunchio L, Soveral I, Steenbergen RD, et al. HPV-negative carcinoma of the uterine cervix: a distinct type of cervical cancer with poor prognosis. *BJOG*. 2015;122(1):119-127. [\[CrossRef\]](#)
34. Harima Y, Sawada S, Nagata K, Sougawa M, Ohnishi T. Human papilloma virus (HPV) DNA associated with prognosis of cervical cancer after radiotherapy. *Int J Radiat Oncol Biol Phys*. 2002;52(5):1345-1351. [\[CrossRef\]](#)
35. Thomas JV, Abou Elkassem AM, Ganeshan B, Smith AD. MR Imaging Texture Analysis in the Abdomen and Pelvis. *Magn Reson Imaging Clin N Am*. 2020;28(3):447-456. [\[CrossRef\]](#)



Combining primary tumor features derived from conventional and contrast-enhanced ultrasound facilitates the prediction of positive axillary lymph nodes in Breast Imaging Reporting and Data System category 4 malignant breast lesions

Yu Du

Chun-Bei Yi

Li-Wen Du

Hai-Yan Gong

Li-Jun Ling

Xin-Hua Ye

Min Zong

Cui-Ying Li

Yu Du and Chun-Bei Yi have contributed equally to this study and should be considered as co-first authors.

From the Department of Ultrasound (Y.D., C-B.Y., L-W.D., H-Y.G., X-H.Y., C-Y.L. ✉lcy_njmu@163.com), The First Affiliated Hospital of Nanjing Medical University, Nanjing, China; Department of Breast Surgery (L-J.L.), The First Affiliated Hospital of Nanjing Medical University, Nanjing, China; Department of Radiology (M.Z. ✉mzong@njmu.edu.cn), The First Affiliated Hospital of Nanjing Medical University, Nanjing, China.

Received 23 May 2021; revision requested 06 August 2021; last revision received 20 June 2022; accepted 30 July 2022.



Epub: 25.01.2023

Publication date: 30.05.2023

DOI: 10.4274/dir.2022.22534

PURPOSE

To determine whether the primary tumor features derived from conventional ultrasound (US) and contrast-enhanced US (CEUS) facilitate the prediction of positive axillary lymph nodes (ALNs) in breast cancer diagnosed as Breast Imaging Reporting and Data System (BI-RADS) category 4.

METHODS

A total of 240 women with breast cancer who underwent preoperative conventional US, strain elastography, and CEUS between September 2016 and December 2019 were included. The multiple parameters of the primary tumor were obtained, and univariate and multivariate analyses were performed to predict positive ALNs. Then three prediction models (conventional US features, CEUS features, and the combined features) were developed, and the diagnostic performance was evaluated with receiver operating characteristic curves.

RESULTS

On conventional US, the traits of large size and the non-circumscribed margin of the primary tumor were marked as two independent predictors. On CEUS, the features of vessel perforation or distortion and the enhanced range of the primary tumor were marked as two independent predictors for positive ALNs. Three prediction models were then developed: model A (conventional US features), model B (CEUS features), and model C (model A plus B). Model C yielded the highest area under the curve (AUC) of 0.82 [95% confidence interval (CI), 0.75–0.88] compared with model A (AUC 0.74; 95% CI, 0.68–0.81; $P = 0.008$) and model B (AUC 0.72; 95% CI, 0.65–0.80; $P < 0.001$) as per the DeLong test.

CONCLUSION

CEUS, as a non-invasive examination technique, can be used to predict ALN metastasis. Combining conventional US and CEUS may produce favorable predictive accuracy for positive ALNs in BI-RADS category 4 breast cancer.

KEYWORDS

Conventional ultrasound, contrast enhanced ultrasound, BI-RADS category, breast cancer, axillary lymph node metastasis

Advancements in ultrasound (US) equipment have significantly increased the value of US in breast imaging. Especially in routine breast screening among women aged <50 years old, the application of US in the detection of mammographically occult masses has considerably increased.¹⁻³ The Breast Imaging Reporting and Data System (BI-RADS) by the American College of Radiology (ACR) is a comprehensive and normative quality control tool that was designed to standardize reporting and reduce confusion over breast imaging interpretations and management recommendations and enhance the US monitoring outcome. In 2013, the fifth edition of the BI-RADS US lexicon was published with a seven-category BI-

You may cite this article as: Du Y, Yi CB, Du LW, et al. Combining primary tumor features derived from conventional and contrast-enhanced ultrasound facilitates the prediction of positive axillary lymph nodes in Breast Imaging Reporting and Data System category 4 malignant breast lesions. *Diagn Interv Radiol.* 2023;29(3):469-477.

RADS classification system from 0 to 6, which has reinforced the standardization of breast lesion characterization with US.⁴ Despite the advances in equipment and US physician experience, BI-RADS category 4 remains an issue of concern.⁵ Category 4 has a wide range of malignant probabilities, from 2% to 95%,^{4,6} and covers sufficiently suspicious lesions without typical malignant features, for which a biopsy is recommended. In addition, the presence or absence of regional positive lymph nodes (LN) is critical to the staging, treatment, and prognosis of breast cancer. It is considered significant to the preoperative identification of positive axillary lymph nodes (ALNs) in BI-RADS category 4 malignant lesions so as to facilitate clinical decision making on patient management.

In the past decade, the clinical use of contrast-enhanced US (CEUS) has expanded research on its application.^{7,8} CEUS can provide more information about microvasculature and hemodynamics than US.⁹⁻¹¹ Distinguishing malignant and benign breast lesions by CEUS alone or incorporating the BI-RADS with CEUS has been extensively approved.¹² These studies demonstrate that CEUS or US+CEUS has better diagnostic performance than US alone in differentiating breast lesions, and particularly, US+CEUS has a low negative likelihood ratio.¹²⁻¹⁵ Several studies have shown that the US characteristics of primary breast cancer are closely related to ALN metastasis and may more accurately predict the status of preoperative clinical LNs.¹⁶⁻¹⁸ However, relevant literature rarely exists to report whether CEUS is useful for detecting positive ALNs in suspicious breast cancer lesions of BI-RADS category 4.

Hence, in this study, we aimed to investigate whether CEUS tumor features may help predict positive ALNs in breast cancer diagnosed as BI-RADS category 4 and probe the role of CEUS in increasing diagnostic performance.

Methods

The protocol of this study was approved by the Ethics Committee of The First Affili-

ated Hospital of Nanjing Medical University, and written informed consent was waived due to the retrospective nature of the study. From the breast US database, a total of 1036 breast US examinations were performed between September 2016 and December 2019 in our institution.

Subjects and lesions

We searched our breast imaging US report database for findings classified as BI-RADS category 4, regardless of clinical data or additional imaging studies. These detections were performed by L.C.Y. owing to more than 20 years of experience in breast US. Patients were included if one or more suspicious lesions were considered as BI-RADS category 4. Patients were excluded if (1) their lesions manifested as non-mass-like types, which mainly refers to the ductal hypoechoic area, non-ductal hypoechoic area, a vague area of altered echotexture with associated architectural distortion and indistinct hypoechoic area with associated posterior acoustic shadowing; (2) their pathologic results were benign; (3) their lesions underwent radiotherapy and chemotherapy before US examination; (4) they did not undergo any pathologic evaluation or adequate location correspondence between their US findings and the pathologic description in our online database; (5) they had not performed any US and CEUS examination; and (6) they had been multifocal on the US.

The reviewers found 944 suspicious lesions in 840 patients. Among them, 36 lesions did not have available pathologic results, 85 were confirmed to be benign, 20 could not accord certain location with the final pathology, 95 showed non-mass-like lesions, 26 underwent radiotherapy and chemotherapy, 430 lacked CEUS results, and 12 showed more than one lesion. These lesions detailed above were excluded from the study. Finally, our study group comprised of 240 lesions, which were subjected to conventional US and CEUS. The diagram of the selection of the study population is shown in Figure 1.

Conventional ultrasound and CEUS on primary tumors

US equipment (MyLab, Twice, ESAOTE S.p.A. Italy) with a linear 4–13 MHz probe (LA523) was introduced for routine US examination, and the images of each lesion were recorded in at least two coordinate planes. Deviations in the description and evaluation of the US images were prevented by employing a single professional doctor (C.Y.L.)

who had more than 20 years of experience in breast US. The doctor was blinded to other imaging examinations, such as mammography and magnetic resonance imaging. A junior doctor recorded the reports. The US features of grayscale were described according to the ACR US-BI-RADS standard descriptors.¹⁹ The classifications of color Doppler^{20,21} and strain elastography²²⁻²⁴ are presented in the form of figures (Figures 2, 3). Masses with characteristics such as growth not parallel to the skin or posterior echo attenuation were considered minor suspicion. Intermediate suspicion was defined as having a rich blood supply accompanied by a peak systolic velocity (PSV) of ≥ 20 cm/s or resistance index (RI) of ≥ 0.7 or having high elasticity scores (scores 4 and 5) or strain ratio characteristics. Masses with irregular morphology, non-circumscribed margins, or inner microcalcification characteristics were defined as significant suspicion. Lesions with minor findings associated with one intermediate descriptor were classified as BI-RADS category 4A. Lesions with one significant and one minor or intermediate characteristic or two intermediate characteristics were considered BI-RADS 4B. Lesions with one significant and at least two intermediate suspicious findings or two significant suspicious findings were considered BI-RADS 4C.

After a grayscale US examination, CEUS was performed in a timely manner by using an US system (MyLab Twice, ESAOTE S.p.A., Italy) at 3–9 MHz linear probe (LA522) frequencies. CEUS examination was also performed by C.Y.L. Low mechanical index values were applied (< 0.2) to reduce the destruction of the contrast agent. The microbubbles (SonoVue™ BRACCO Imaging, S.p.A, Milan, Italy) that were used as a contrast agent were reconstituted with 5 mL of saline (NaCl 0.9%). The contrast agent with 2.4 mL of SonoVue was injected intravenously into an elbow vein according to the manufacturer's instructions at the start of the built-in timer of the US instrument. The US contrast process was continuously recorded in the original data format into the hard disk of the instrument instantly. The enhanced morphological features were then analyzed, and the quantitative parameters of the lesions and normal tissues were assessed with quantification software (QontraXt, AMID and Bracco, Milan, Italy) on the basis of a region of interest over the maximum signal intensity zones. The contrast enhancement pattern of the lesion and the migration and distribution of microbubbles was observed dynamically. The enhancement degree of the lesion was com-

Main points

- Larger size and a non-circumscribed margin are positive axillary lymph node (ALN) predictors on conventional ultrasound (US).
- Distortion of vessels and enhancement range are important predictive factors for ALNs on contrast-enhanced US (CEUS).
- Combining conventional US and CEUS can help predict positive ALNs.

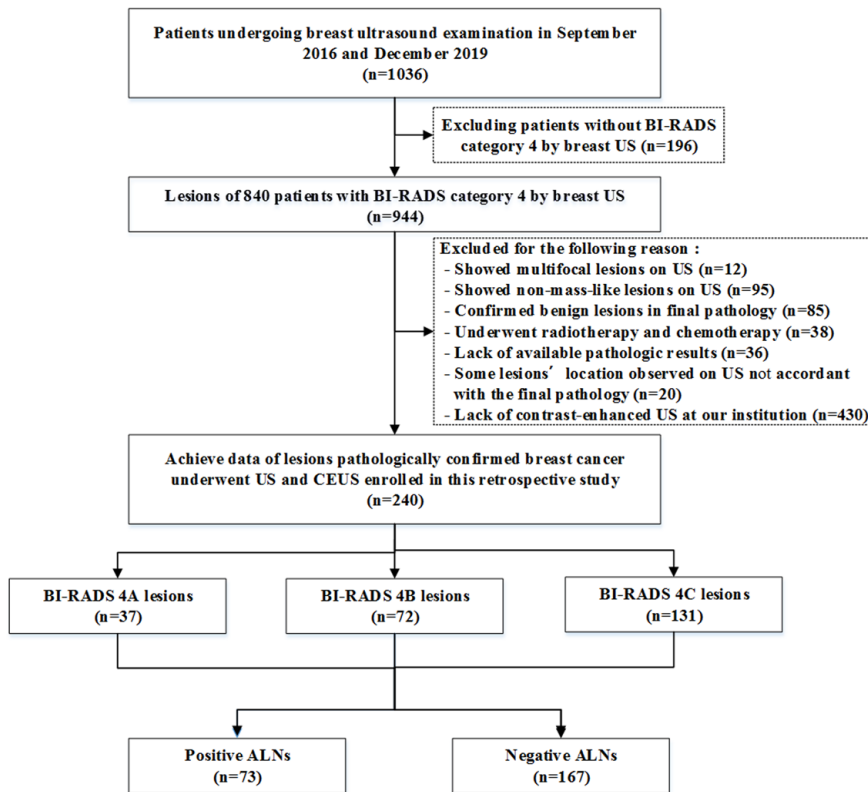


Figure 1. Flowchart illustrating the selection of the study population. US, ultrasound; CEUS, contrast-enhanced US; ALN, axillary lymph node; BI-RADS, Breast Imaging Reporting and Data System.

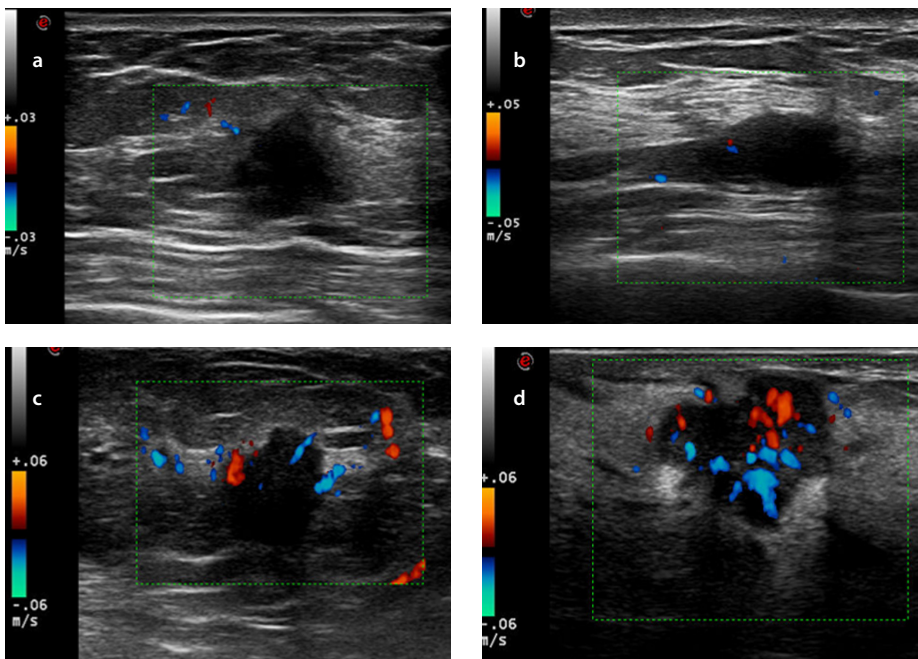


Figure 2. Images of Adler blood flow classification: (a) grade 0 mapped no color flow signals in the solid breast mass; (b) grade I revealed minimal blood flow signals and mapped punctate color flow; (c) grade II revealed moderate blood flow signals and mapped more punctate color flow than grade I or visualized one thick vessel (the diameter of the largest vessel was between 2 and 3 mm) penetrating through the solid breast mass; (d) grade III revealed marked blood flow signals and mapped more punctate color flow than grade II or visualized equal or more than two thick vessels interwoven with each other in the solid breast mass.

pared with that of the surrounding breast tissue, including no or iso-enhancement, hypo-enhancement, medium or moderate enhancement, and hyperenhancement.^{25,26} Enhancement patterns were characterized as entire or segmental, punctate, linear, or rim enhancements after the administration of the contrast medium.²⁷ Lesion boundaries were characterized as clear or blurred if most of its circumference (>50%) was clearly or poorly visible after contrast agent administration, respectively. Enhancement morphology was defined as regular or irregular. The presence or absence of perfusion defects and radial penetrating vessels depended on the surrounding tissue toward the lesion. The enhancement order of the lesion was as follows: centripetal enhancement was defined as enhancement from the lesion's periphery towards its center; centrifugal enhancement was defined as beginning from the lesion's center towards its periphery; and diffusion enhancement was manifested as enhancement simultaneously deriving between the lesion's periphery and center.²⁸ The time-intensity curve (TIC) was defined as slow-in and slow-out, slow-in and fast-out, fast-in and slow-out, and fast-in and fast-out according to the tracing pattern. The quantitative parameters derived from the TIC included: (a) peak intensity (%) calculated by the fraction [(postcontrast intensity–precontrast intensity)/precontrast intensity] × 100%; (b) time to peak (s) defined as the time that elapses between the moment when the contrast medium first reaches the lesion and the time of maximum signal intensity after contrast medium administration; (c) enhancement range was defined as a lesion extent enlarged compared with the conventional US; (d) enhancement area as ≥50% or <50%; and (e) area under the curve (AUC) the TIC.

Model development and classification

The multivariable regression analysis with forward elimination was performed with variables that had *P* values of less than 0.050 on univariate analysis, and three scenario models were developed: (1) model A (conventional US features); (2) model B (CEUS features); and (3) model C (model A plus model B). Receiver operating characteristic (ROC) curves were used to evaluate the discriminatory efficiency of the models. The comparison of the models was assessed using the DeLong test.

Statistical analysis

The data analyzed included the age of the subjects, lesion size, stratification derived from US imaging characteristics (BI-RADS category 4A, 4B, or 4C), CEUS characteristics, and categorized pathologic results. Statistical analysis was conducted using the software packages SPSS v25.0 and MedCalc v12.7. Continuous data were compared with the independent t-test as appropriate, and variables with abnormal or non-normal distribution were analyzed by the Mann-Whitney U test. Categorical variables were compared using Fisher's exact test or the Pearson chi-square test. Then, multivariate logistic regression analyses were introduced to determine the most valuable variables for identifying positive LNs through conventional US and CEUS. Multiple ROC curves were drawn to illustrate and compare the value of identified risk variables in the prediction of a positive LN. ALN prediction capacity was assessed by the AUC, sensitivity, and specificity, and the comparison of the models was evaluated using the DeLong test. A *P* value of <0.05 was considered to illustrate a statistically significant difference.

Results

A detailed list of lesion descriptors stratified in accordance with the estimated malignancy risk in BI-RADS category 4 is shown in Table 1. The most common breast cancer in this study was infiltrative ductal carcinoma, which was found in 183 of 240 malignant patients (76.1%), followed by ductal carcinoma in situ in 34 of 240 patients (14.2%). Increased histological grades of 2 or 3 and positive ALN rates were found in BI-RADS 4C, then 4B, and lastly, 4A. Table 2 shows the age, pathological types, histological grades, and positive LN results in groups 4A, 4B, and 4C.

Univariate analyses are presented in Table 3 regarding the US and CEUS descriptors for predicting positive LNs. In the conventional US features, the univariate analyses showed that lesion size, margin, blood flow, PSV, RI, posterior echo, and BI-RADS category were associated with positive ALNs (*P* < 0.05). In the CEUS features, vessel perforation or distortion, enhancement range, and TIC curves were significantly different between positive and negative groups (*P* < 0.05). Among the multivariate analyses (Table 4), lesion size [odds ratio (OR), 1.11; 95% confidence interval (CI), 1.06–1.64], margin (OR, 3.39; 95% CI, 1.75–6.57), perforation or distortion vessels (OR, 3.94; 95% CI, 2.04–7.63), and enhancement range (OR, 0.28; 95% CI,

0.15–0.55) were the most important factors to distinguish positive ALNs (*P* < 0.001). These imaging features of the tumor are shown in Figures 4 and 5. The ROC curves (Figure 6) showed that model C yielded the better AUC of 0.82 (95% CI, 0.75–0.88) than model A (AUC, 0.74; 95% CI, 0.68–0.81) and model B (AUC, 0.72; 95% CI, 0.65–0.80). Model C yielded optimal diagnostic performance in predicting positive ALN compared with the other two models (both *P* < 0.05, as per the DeLong test). The sensitivity of model A, B, and C were 67.1%, 41.1%, and 80.8%, respectively, while the specificity was 73.1%, 92.2%, and 72.9%, respectively.

Discussion

The present study identified that the traits of larger size and non-circumscribed margin are marked as two independent predictors for positive ALNs on conventional US. We also found that vessel perforation or distortion and a conspicuous TIC curve are the other two important predictive factors for positive ALNs on CEUS. ROC curve comparison showed that the performance of the combined conventional US and CEUS is better than the performance of each alone. On conventional US, an excellent relationship was established between the primary tumor size and the prevalence of positive ALNs in this study. Sopik and Narod²⁹ demonstrated there was a clear linear correlation between tumor size and metastasis for breast cancers about 7 and 60 mm in size. Akissue de Camargo Teixeira et al.³⁰ agreed that tumor size could be taken as a traditional predictor of ALN status. The average pre-surgical tumor size was 3.3 ± 2.1 cm in patients with LN metastasis and 2.5 ± 1.4 cm in patients without metastasis.³⁰ These findings are consistent with our results. Cancer cells inside the tumor spread, survive, and then pervade to regional LNs and further to other distant sites.³¹ Therefore, more cancer cells are available in a larger-sized tumor to metastasize. Tseng et al.³² proved that tumor size was closely relevant to lymphovascular invasion, which was confirmed to be the standard of LN metastasis pathology and consequently closely connected with positive ALNs. In this study, invasive ductal carcinoma also dominated, which indicated the remarkable significance of the maximum diameter of the tumor in predicting positive ALNs.

In addition, the non-circumscribed margin was identically correlated with positive ALNs. Costantini et al.³³ pointed out that sonographic signs, such as margin burrs and angular and microlobulated margins, are

important factors for biological behaviors associated with metastatic pervasion. The unevenness of the tumor margin indicates a high possibility of invasive growth with a malignant tendency. In breast cancer with high aggressiveness and tumor burden, carcinoma cells can infiltrate the surrounding tissues, lymphatic vessels, and blood vessels at different growth speeds, resulting in a non-smooth tumor margin.¹⁷

Through CEUS examination, we found that vessel perforation or distortion is important to the prediction of positive ALNs. A malignant tumor has vascular contortions because its blood vessels cannot maintain their regular shapes during the rapid growth of the lesions.¹² Santamaría et al.³⁴ demonstrated that tumor arteries detected by color Doppler and sonographic tumor size were an independent predictor of ALN status. Yu et al.³⁵ demonstrated that perforating vessels are also a risk factor of LN metastasis in patients suffering from small breast cancer. These findings almost matched our results showing that vessel perforation or distortion is strongly linked with positive ALNs in patients with small breast cancer (maximum diameter ≤2.0 cm) and also bounded with breast carcinoma in the T2 stage (2.0 cm < maximum diameter ≤5.0 cm) dominating in this study. This finding could explain why large tumors with abundant blood supply are usually accompanied by thick vessels.

Furthermore, this study also discovered the perfusion pattern of the fast-in and fast-out pattern as the only quantitative parameter for identifying positive ALNs with a significant difference. This finding was consistent with the report of Wang et al.³⁶, which revealed that the perfusion performance of the peripheral region of breast cancer is characterized by hyperechoic enhancement and fast-in and fast-out patterns. The shape of the dynamic enhancement curve is related to the microscopic characteristics of the main components of poorly differentiated tumors, which are scattered malignant vascular endothelial cells.^{37,38} The lack of capillary networks and incomplete cavities resulted in the rapid flushing of the contrast agent. Such features thereby influence the ALN status through the hemodynamic principle.³⁹

Regarding the correlation between qualitative and quantitative CEUS characteristics and pathological prognostic factors in patients with breast cancer, Vraha et al.²⁷ suggested that the qualitative assessment of the enhancement pattern is better than quantitative assessment for differentiating malign-

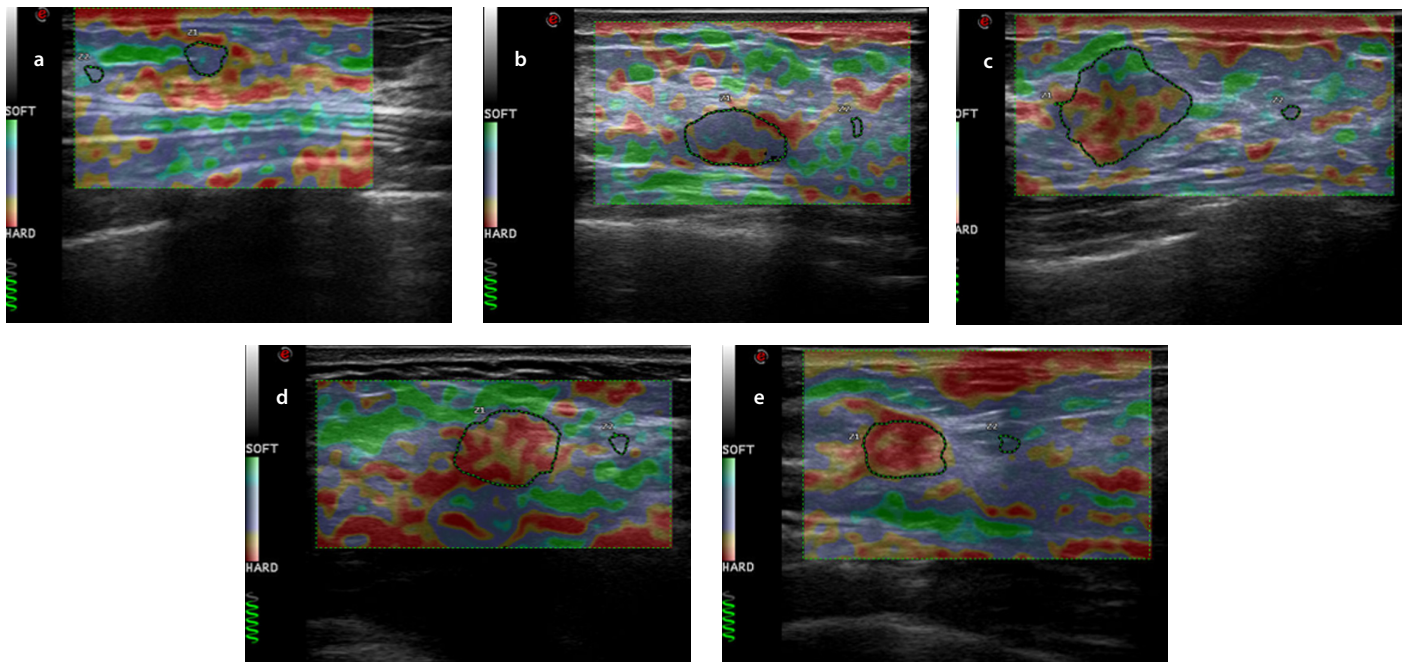


Figure 3. Images of elasticity classification: (a) score 1: the entire lesion or nearly the entire lesion was green, and the elastic strain ratio was <2.5 ; (b) score 2: the focus was red in the center and homogeneous elasticity in the periphery, and the elastic strain ratio was <2.5 ; (c) score 3: the proportions of green and red in the range of lesion were the same, and the elastic strain ratio was <2.5 ; (d) score 4: the entire lesion was red or little green was found inside the lesion, and the elastic strain ratio was ≥ 2.5 ; (e) score 5: the lesion and surrounding tissues were all shown in red, with or without green in the inner part, and the elastic strain ratio was far beyond 2.5.

Table 1. Lesion descriptors stratified in accordance with the estimated malignancy risk

| Minor | Intermediate | Major |
|----------------------------|----------------------------------|--------------------------|
| Non-parallel to skin | Adler blood flow grade: 2 or 3 | Larger tumor size |
| Posterior echo attenuation | PSV ≥ 20 cm/s | Irregular shape |
| | RI ≥ 0.7 | Non-circumscribed margin |
| | Elastic score: 4 or 5 | Microcalcification |
| | Elastic strain ratio: ≥ 2.5 | |

PSV, peak systolic velocity; RI, resistance index.

Table 2. Source of clinical and pathological materials

| BI-RADS | 4A | 4B | 4C |
|---------------------------------|-------------------|-------------------|-------------------|
| Age | 49.55 \pm 11.89 | 49.38 \pm 11.53 | 51.73 \pm 11.67 |
| Pathology types | | | |
| Invasive ductal carcinoma | 17 (7.2%) | 50 (20.9%) | 115 (48.0%) |
| Ductal carcinoma <i>in situ</i> | 12 (5.0%) | 13 (5.4%) | 9 (3.8%) |
| Mucinous carcinoma | 5 (2.1%) | 4 (1.7%) | 3 (1.3%) |
| Papillary carcinoma | 3 (1.1%) | 4 (1.5%) | 1 (0.4%) |
| Others | 1 (0.4%) | 2 (0.8%) | 1 (0.4%) |
| Histological grades | | | |
| 1 | 3 (1.4%) | 2 (0.9%) | 3 (1.2%) |
| 2 | 14 (5.8%) | 34 (14.1%) | 60 (24.9%) |
| 3 | 16 (6.8%) | 36 (14.8%) | 53 (22.1%) |
| Unknown | 19 (8.0%) | | |
| ALNs | | | |
| Negative | 33 (13.8%) | 53 (22.0%) | 81 (33.8%) |
| Positive | 4 (1.7%) | 19 (7.9%) | 50 (20.8%) |

ALN, axillary lymph node; BI-RADS, Breast Imaging Reporting and Data System.

Table 3. Univariate analysis of conventional ultrasound, elastography, and CEUS for the prediction of positive ALNs in BI-RADS category 4 lesions

| Descriptors | | Negative ALNs (n = 167), n (%) | Positive ALNs (n = 73), n (%) | P value |
|--|------------------------|-----------------------------------|----------------------------------|---------|
| Conventional US plus elastography | | | | |
| Size (mm) | | 21.21 ± 7.19 | 25.78 ± 5.83 | <0.001* |
| Shape | Regular | 49 (29.3) | 19 (26.0) | 0.600 |
| | Irregular | 118 (70.7) | 54 (74.0) | |
| Margin | Circumscribed | 80 (47.9) | 18 (24.7) | 0.001* |
| | Non-circumscribed | 87 (52.1) | 55 (75.3) | |
| Orientation | Parallel | 88 (52.7) | 35 (47.9) | 0.498 |
| | Non-parallel | 79 (47.3) | 38 (52.1) | |
| Posterior echo | Unaltered or enhanced | 157 (94.0) | 63 (86.3) | 0.047* |
| | Attenuation | 10 (6.0) | 10 (13.7) | |
| Micro-calcification | Without | 124 (74.3) | 59 (80.8) | 0.271 |
| | With | 43 (25.7) | 14 (19.2) | |
| RI | <0.7 | 94 (56.3) | 30 (41.1) | 0.030* |
| | ≥0.7 | 73 (43.7) | 43 (58.9) | |
| Elastic | Score 1–2 | 18 (10.8) | 7 (9.6) | 0.920 |
| | Score 3–4 | 133 (79.6) | 58 (79.5) | |
| | Score 5 | 16 (9.6) | 8 (10.9) | |
| Adler blood flow | Grade 0–I | 47 (28.1) | 15 (20.5) | 0.216 |
| | Grade II–III | 120 (71.9) | 58 (79.5) | |
| BI-RADS category | 4A | 33 (19.8) | 4 (5.5) | 0.004* |
| | 4B | 53 (31.7) | 19 (26.0) | |
| | 4C | 81 (48.5) | 50 (68.5) | |
| PSV (cm/s) | | 11.86 ± 3.46 | 12.94 ± 4.08 | 0.036* |
| Elastic strain ratio | | 2.15 ± 0.38 | 2.10 ± 0.34 | 0.362 |
| Contrast-enhanced US | | | | |
| Enhancement boundary | Distinct | 86 (51.5) | 40 (54.8) | 0.638 |
| | Indistinct | 81 (48.5) | 33 (45.2) | |
| Enhancement morphology | Regular | 41 (24.6) | 18 (24.7) | 0.986 |
| | Irregular | 126 (81.4) | 55 (75.3) | |
| Enhancement degree | Iso- or no enhancement | 8 (4.8) | 2 (2.7) | 0.622 |
| | Hypo-enhancement | 19 (11.4) | 10 (13.7) | |
| | Moderate enhancement | 10 (6.0) | 7 (9.6) | |
| | Hyper-enhancement | 130 (77.8) | 54 (74.0) | |
| Enhancement pattern | Entire | 100 (59.9) | 47 (63.4) | 0.348 |
| | Segmental | 39 (23.3) | 19 (26.0) | |
| | Others | 28 (16.8) | 7 (9.6) | |
| Enhancement order | Centripetal | 129 (77.2) | 55 (75.3) | 0.955 |
| | Centrifugal | 34 (20.4) | 16 (21.9) | |
| | Diffuse | 4 (2.4) | 2 (2.7) | |
| Perfusion defects | Without | 97 (58.1) | 35 (47.9) | 0.146 |
| | With | 70 (41.9) | 38 (52.1) | |
| Perforation or distortion vessels | Without | 116 (69.5) | 27 (37.0) | <0.001* |
| | With | 51 (30.5) | 46 (63.0) | |

Table 3. Continues

| Descriptors | | Negative ALNs (n = 167), n (%) | Positive ALNs (n = 73), n (%) | P value |
|-------------------|----------------------|-----------------------------------|----------------------------------|---------|
| Enhancement area | <50% | 24 (14.4) | 12 (16.4) | 0.680 |
| | ≥50% | 143 (85.6) | 61 (83.6) | |
| Enhancement range | None | 111 (66.5) | 28 (38.4) | <0.001* |
| | Enlarged | 56 (33.5) | 45 (61.6) | |
| Peak intensity | - | 50.35 ± 3.49 | 50.96 ± 3.77 | 0.229 |
| TTP | - | 56.27 ± 6.43 | 57.06 ± 6.71 | 0.396 |
| AUC | - | 5.14 ± 3.05 | 5.24 ± 2.40 | 0.793 |
| TIC curve | Slow-in and slow-out | 71 (42.5) | 19 (26.0) | <0.001* |
| | Slow-in and fast-out | 29 (17.4) | 5 (6.9) | |
| | Fast-in and slow-out | 46 (27.5) | 12 (16.4) | |
| | Fast-in and fast-out | 21 (12.6) | 37 (50.7) | |

P value is derived from the univariate association analyses between each of the variables and ALN status. *P value of <0.05. ALN, axillary lymph node; PSV, peak systolic velocity; RI, resistance index; TTP, time to peak; AUC, area under the curve; TIC, time-intensity curve; BI-RADS, Breast Imaging Reporting and Data System; CEUS, contrast-enhanced ultrasound.

Table 4. Multivariate analysis of the comparison between conventional ultrasound and CEUS for predicting positive ALNs in BI-RADS category 4 lesions

| Characteristics | Odds ratio | 95% confidence Interval | P value |
|-----------------------------------|------------|-------------------------|---------|
| Size | 1.110 | 1.061–1.161 | <0.001 |
| Margin | | | |
| Circumscribed | Reference | | |
| Non-circumscribed | 3.393 | 1.752–6.570 | <0.001 |
| Perforation or distortion vessels | | | |
| Without | Reference | | |
| With | 3.941 | 2.037–7.625 | <0.001 |
| Enhancement range | | | |
| None | Reference | | |
| Enlarged | 0.283 | 0.146–0.550 | <0.001 |
| TIC curve | | | |
| Slow-in and slow-out | Reference | | |
| Slow-in and fast-out | 0.741 | 0.239–2.301 | 0.604 |
| Fast-in and slow-out | 1.222 | 0.507–2.942 | 0.655 |
| Fast-in and fast-out | 7.092 | 3.142–16.010 | <0.001 |

TIC, time-intensity curve; CEUS, contrast-enhanced ultrasound; ALN, axillary lymph node; BI-RADS, Breast Imaging Reporting and Data System.

nant lesions. Wang et al.⁴⁰ also demonstrated that qualitative parameters significantly improve the performance of CEUS in the distinction of benign and malignant breast lesions, which is clinically promising. Our study showed similar results and demonstrated the positive role of CEUS, especially its qualitative parameters, for the differentiation of positive ALNs in BI-RADS category 4 malignant breast lesions. The superiority of qualitative CEUS parameters lies in the fact that the reviewer's experience could rectify probable technological errors, which could not be achieved in quantitative parameters. In addition, some uncontrolled factors, such as patient respiration movements and a preselected inter-

est area by the CEUS performer, can impact the quantitative parameters' evaluation of the received images during video recording. Meanwhile, quantitative parameters were created by an offline workstation, which is another technological restriction. Thus, further studies regarding more advanced equipment and optimized software need to be performed in this field to improve the accuracy of CEUS.

Three predictive models based on conventional US features (model A), CEUS features (model B), and the combined model A + B (model C) were then constructed and compared. Model C illustrated significant

improvement in diagnostic accuracy and model fit in predicting positive ALNs. The multivariate-based combination model can be extracted to reveal tumor microvascular imaging and to evaluate the comprehensive characterization of underlying malignant tumor signs. This model plays a potential role in avoiding subject diagnosis. Tumors with nodal metastasis have completely different grayscale ultrasonic, color Doppler, and internal construction enhancement characteristics. The four best-performing combination features were tumor size, margin, vessel perforation or distortion, and TIC curve. Discriminating positive ALNs by using a single sonography factor is difficult. The incorpora-

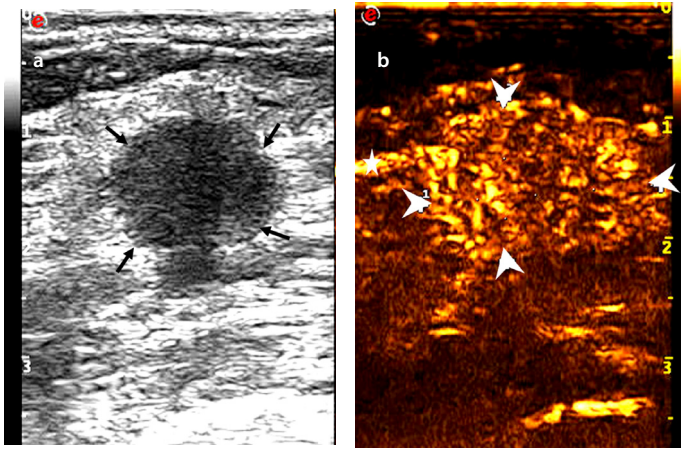


Figure 4. Images of a 53-year-old female diagnosed with invasive ductal carcinoma in the right breast: (a) tumor with a maximum diameter of 1.7 cm showed a circumscribed margin on the conventional ultrasound (thin arrow), and no suspicious axillary lymph node was observed; (b) tumor with an extended range of 2.1 cm showed an unclear boundary (thick arrow) and vessel perforation entering from surrounding tissue into the mass (fine arrow). One-node macrometastasis was found in the final pathological results.

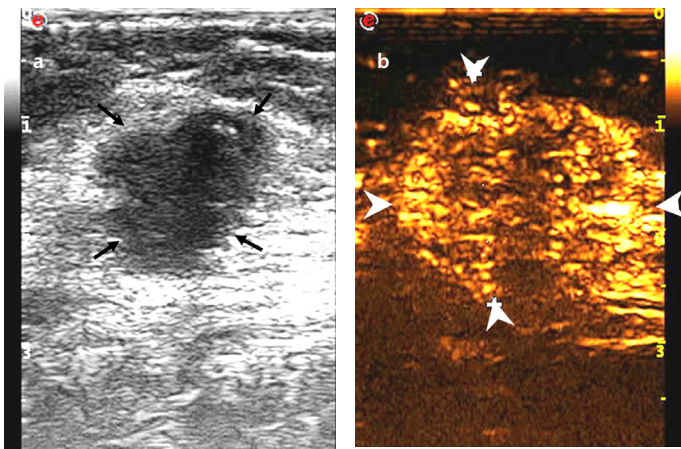


Figure 5. Images of a 55-year-old female diagnosed with invasive ductal carcinoma in the right breast: (a) tumor with a maximum diameter of 2.0 cm showed a non-circumscribed margin on the conventional ultrasound (thin arrow), and no suspicious axillary lymph node was present; (b) tumor with an extended range of 2.6 cm showed a clear boundary, and vessel perforation (thick arrow) in surrounding tissue or mass was absent. Non-node metastasis was found in the final pathological results.

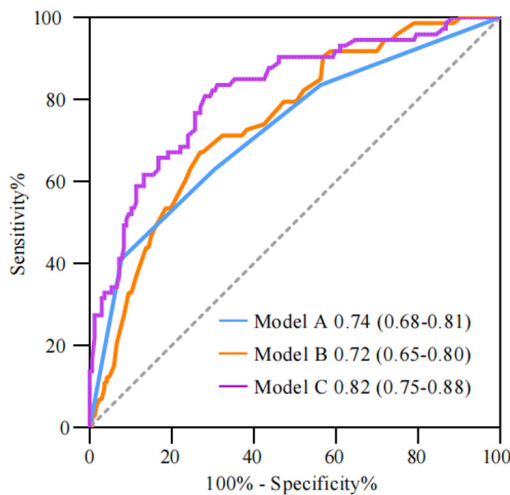


Figure 6. Receiver operating characteristic curves using the three different diagnostic models of differentiating non-metastatic and metastatic groups: model A, conventional ultrasound (US) model; model B, contrast-enhanced US (CEUS) model; model C, conventional US plus CEUS model.

tion of multiple factors can provide a comprehensive and robust approach. The multivariate-based combination model, which can discriminate positive ALNs from negative ones, showed significant improvement compared with models A or B alone.

We acknowledge several limitations of our study. First, patient selection bias may exist because of its retrospective nature. Second, the data applied in our study are from a single institution. Thus, our findings lack a general and robust assessment. Therefore, a rigorous analysis should be planned with data from a larger number of patients collected from more institutions in different areas. Third, the external validation of different races or populations was absent because of the relatively small single sample size of CEUS. Fourth, intra- and inter-observer reliability was not evaluated in this study.

In conclusion, the combination of conventional US and CEUS could facilitate increasing diagnostic performance during the prediction of positive ALNs in BI-RADS category 4 breast cancer lesions. Therefore, our predictive model may also facilitate clinical decision making and potentially improve the diagnostic performance of the selected patients.

Conflict of interest disclosure

The authors declared no conflicts of interest.

References

1. Elverici E, Barça AN, Aktaş H, et al. Nonpalpable BI-RADS 4 breast lesions: sonographic findings and pathology correlation. *Diagn Interv Radiol.* 2015;21(3):189-194. [\[CrossRef\]](#)
2. Hong AS, Rosen EL, Soo MS, Baker JA. BI-RADS for sonography: positive and negative predictive values of sonographic features. *AJR Am J Roentgenol.* 2005;184(4):1260-1265. [\[CrossRef\]](#)
3. Heinig J, Witteler R, Schmitz R, Kiesel L, Steinhard J. Accuracy of classification of breast ultrasound findings based on criteria used for BI-RADS. *Ultrasound Obstet Gynecol.* 2008;32(4):573-578. [\[CrossRef\]](#)
4. Magny SJ, Shikhman R, Keppke AL. Breast Imaging Reporting and Data System. StatPearls. Treasure Island (FL): StatPearls Publishing Copyright© 2021, StatPearls Publishing LLC., 2021. [\[CrossRef\]](#)
5. Spinelli Varella MA, Teixeira da Cruz J, Rauber A, Varella IS, Fleck JF, Moreira LF. Role of BI-RADS Ultrasound Subcategories 4A to 4C in Predicting Breast Cancer. *Clin Breast Cancer.* 2018;18(4):507-511. [\[CrossRef\]](#)

6. Sedgwick EL, Ebuoma L, Hamame A, et al. BI-RADS update for breast cancer caregivers. *Breast Cancer Res Treat.* 2015;150(2):243-254. [\[CrossRef\]](#)
7. Ouyang Q, Chen L, Zhao H, Xu R, Lin Q. Detecting metastasis of lymph nodes and predicting aggressiveness in patients with breast carcinomas. *J Ultrasound Med.* 2010;29(3):343-352. [\[CrossRef\]](#)
8. Rubaltelli L, Beltrame V, Scagliori E, et al. Potential use of contrast-enhanced ultrasound (CEUS) in the detection of metastatic superficial lymph nodes in melanoma patients. *Ultraschall Med.* 2014;35(1):67-71. [\[CrossRef\]](#)
9. Saracco A, Szabó BK, Aspelin P, et al. Differentiation between benign and malignant breast tumors using kinetic features of real-time harmonic contrast-enhanced ultrasound. *Acta Radiol.* 2012;53(4):382-388. [\[CrossRef\]](#)
10. Liu H, Jiang YX, Liu JB, Zhu QL, Sun Q, Chang XY. Contrast-enhanced breast ultrasonography: Imaging features with histopathologic correlation. *J Ultrasound Med.* 2009;28(7):911-920. [\[CrossRef\]](#)
11. Balleyguier C, Opolon P, Mathieu MC, et al. New potential and applications of contrast-enhanced ultrasound of the breast: own investigations and review of the literature. *Eur J Radiol.* 2009;69(1):14-23. [\[CrossRef\]](#)
12. Wan CF, Du J, Fang H, Li FH, Zhu JS, Liu Q. Enhancement patterns and parameters of breast cancers at contrast-enhanced US: correlation with prognostic factors. *Radiology.* 2012;262(2):450-459. [\[CrossRef\]](#)
13. Zhang JX, Cai LS, Chen L, Dai JL, Song GH. CEUS helps to re-rate small breast tumors of BI-RADS category 3 and category 4. *Biomed Res Int.* 2014;2014:572532. [\[CrossRef\]](#)
14. Li Q, Hu M, Chen Z, et al. Meta-analysis: contrast-enhanced ultrasound versus conventional ultrasound for differentiation of benign and malignant breast lesions. *Ultrasound Med Biol.* 2018;44(5):919-929. [\[CrossRef\]](#)
15. Xiao X, Dong L, Jiang Q, Guan X, Wu H, Luo B. Incorporating contrast-enhanced ultrasound into the bi-rads scoring system improves accuracy in breast tumor diagnosis: a preliminary study in China. *Ultrasound Med Biol.* 2016;42(11):2630-2638. [\[CrossRef\]](#)
16. Ansari B, Morton MJ, Adamczyk DL, et al. Distance of breast cancer from the skin and nipple impacts axillary nodal metastases. *Ann Surg Oncol.* 2011;18(11):3174-3180. [\[CrossRef\]](#)
17. Bae MS, Shin SU, Song SE, Ryu HS, Han W, Moon WK. Association between US features of primary tumor and axillary lymph node metastasis in patients with clinical T1-T2N0 breast cancer. *Acta Radiol.* 2018;59(4):402-408. [\[CrossRef\]](#)
18. Zhou LQ, Wu XL, Huang SY, et al. Lymph node metastasis prediction from primary breast cancer US images using deep learning. *Radiology.* 2020;294(1):19-28. [\[CrossRef\]](#)
19. Berg WA, Cosgrove DO, Doré CJ, et al. Shear-wave elastography improves the specificity of breast US: the BE1 multinational study of 939 masses. *Radiology.* 2012;262(2):435-449. [\[CrossRef\]](#)
20. Adler DD, Carson PL, Rubin JM, Quinn-Reid D. Doppler ultrasound color flow imaging in the study of breast cancer: preliminary findings. *Ultrasound Med Biol.* 1990;16(6):553-559. [\[CrossRef\]](#)
21. Ecanow JS, Abe H, Newstead GM, Ecanow DB, Jeske JM. Axillary staging of breast cancer: what the radiologist should know. *Radiographics.* 2013;33(6):1589-1612. [\[CrossRef\]](#)
22. Youk JH, Son EJ, Kim JA, Gweon HM. Pre-operative evaluation of axillary lymph node status in patients with suspected breast cancer using shear wave elastography. *Ultrasound Med Biol.* 2017;43(8):1581-1586. [\[CrossRef\]](#)
23. Itoh A, Ueno E, Tohno E, et al. Breast disease: clinical application of US elastography for diagnosis. *Radiology.* 2006;239(2):341-350. [\[CrossRef\]](#)
24. Kanagaraju V, Dhivya B, Devanand B, Maheswaran V. Utility of ultrasound strain elastography to differentiate benign from malignant lesions of the breast. *J Med Ultrasound.* 2021;29(2):89-93. [\[CrossRef\]](#)
25. Wan C, Du J, Fang H, Li F, Wang L. Evaluation of breast lesions by contrast enhanced ultrasound: qualitative and quantitative analysis. *Eur J Radiol.* 2012;81(4):444-450. [\[CrossRef\]](#)
26. Du LW, Liu HL, Gong HY, et al. Adding contrast-enhanced ultrasound markers to conventional axillary ultrasound improves specificity for predicting axillary lymph node metastasis in patients with breast cancer. *Br J Radiol.* 2021;94(1118):20200874. [\[CrossRef\]](#)
27. Vraika I, Panourgias E, Sifakis E, et al. Correlation between contrast-enhanced ultrasound characteristics (qualitative and quantitative) and pathological prognostic factors in breast cancer. *In Vivo.* 2018;32(4):945-954. [\[CrossRef\]](#)
28. Leng X, Huang G, Ma F, Yao L. Regional contrast-enhanced ultrasonography (CEUS) characteristics of breast cancer and correlation with microvessel density (MVD). *Med Sci Monit.* 2017;23:3428-3436. [\[CrossRef\]](#)
29. Sopik V, Narod SA. The relationship between tumour size, nodal status and distant metastases: on the origins of breast cancer. *Breast Cancer Res Treat.* 2018;170:647-656. [\[CrossRef\]](#)
30. Akissue de Camargo Teixeira P, Chala LF, Shimizu C, et al. Axillary lymph node sonographic features and breast tumor characteristics as predictors of malignancy: a nomogram to predict risk. *Ultrasound Med Biol.* 2017;43:1837-1845. [\[CrossRef\]](#)
31. Boughey JC, Ballman KV, Hunt KK, et al. Axillary ultrasound after neoadjuvant chemotherapy and its impact on sentinel lymph node surgery: results from the American College of Surgeons Oncology Group Z1071 Trial (Alliance). *J Clin Oncol.* 2015;33(30):3386-3393. [\[CrossRef\]](#)
32. Tseng HS, Chen LS, Kuo SJ, Chen ST, Wang YF, Chen DR. Tumor characteristics of breast cancer in predicting axillary lymph node metastasis. *Med Sci Monit.* 2014;20:1155-1161. [\[CrossRef\]](#)
33. Costantini M, Belli P, Ierardi C, Franceschini G, La Torre G, Bonomo L. Solid breast mass characterisation: use of the sonographic BI-RADS classification. *Radiol Med.* 2007;112(6):877-894. [\[CrossRef\]](#)
34. Santamaría G, Velasco M, Farré X, Vanrell JA, Cardesa A, Fernández PL. Power Doppler sonography of invasive breast carcinoma: does tumor vascularization contribute to prediction of axillary status? *Radiology.* 2005;234(2):374-380. [\[CrossRef\]](#)
35. Yu X, Hao X, Wan J, Wang Y, Yu L, Liu B. Correlation between ultrasound appearance of small breast cancer and axillary lymph node metastasis. *Ultrasound Med Biol.* 2018;44(2):342-349. [\[CrossRef\]](#)
36. Wang X, Xu P, Wang Y, Grant EG. Contrast-enhanced ultrasonographic findings of different histopathologic types of breast cancer. *Acta Radiol.* 2011;52:248-255. [\[CrossRef\]](#)
37. Metz S, Daldrup-Unk HE, Richter T, et al. Detection and quantification of breast tumor necrosis with MR imaging: value of the necrosis-avid contrast agent gadophrin-3. *Acad Radiol.* 2003;10(5):484-490. [\[CrossRef\]](#)
38. Colpaert C, Vermeulen P, van Beest P, et al. Intratumoral hypoxia resulting in the presence of a fibrotic focus is an independent predictor of early distant relapse in lymph node-negative breast cancer patients. *Histopathology.* 2001;39(4):416-425. [\[CrossRef\]](#)
39. Teifke A, Behr O, Schmidt M, et al. Dynamic MR imaging of breast lesions: correlation with microvessel distribution pattern and histologic characteristics of prognosis. *Radiology.* 2006;239(2):351-360. [\[CrossRef\]](#)
40. Wang Y, Fan W, Zhao S, et al. Qualitative, quantitative and combination score systems in differential diagnosis of breast lesions by contrast-enhanced ultrasound. *Eur J Radiol.* 2016;85(1):48-54. [\[CrossRef\]](#)



Risk factors for air embolism following computed tomography-guided percutaneous transthoracic needle biopsy: a systematic review and meta-analysis

Hanfei Zhang 
Shan Wang 
Feiyang Zhong 
Meiyan Liao 

ABSTRACT

To quantitatively analyze the risk factors for air embolism following computed tomography (CT)-guided percutaneous transthoracic needle biopsy (PTNB) and qualitatively review their characteristics.

The databases of PubMed, Embase, Web of Science, Wanfang Data, VIP information, and China National Knowledge Infrastructure were searched on January 4, 2021, for studies reporting the occurrence of air embolisms following CT-guided PTNB. After study selection, data extraction, and quality assessment, the characteristics of the included cases were qualitatively and quantitatively analyzed.

A total of 154 cases of air embolism following CT-guided PTNB were reported. The reported incidence was 0.06% to 4.80%, and 35 (22.73%) patients were asymptomatic. An unconscious or unresponsive state was the most common symptom (29.87%). Air was most commonly found in the left ventricle (44.81%), and 104 (67.53%) patients recovered without sequelae. Air location ($P < 0.001$), emphysema ($P = 0.061$), and cough ($P = 0.076$) were associated with clinical symptoms. Air location ($P = 0.015$) and symptoms ($P < 0.001$) were significantly associated with prognosis. Lesion location [odds ratio (OR): 1.85, $P = 0.017$], lesion subtype (OR: 3.78, $P = 0.01$), pneumothorax (OR: 2.16, $P = 0.003$), hemorrhage (OR: 3.20, $P < 0.001$), and lesions located above the left atrium (OR: 4.35, $P = 0.042$) were significant risk factors for air embolism.

Based on the current evidence, a subsolid lesion, being located in the lower lobe, the presence of pneumothorax or hemorrhage, and lesions located above the left atrium were significant risk factors for air embolism.

KEYWORDS

Air embolism, CT-guided PTNB, meta-analysis, risk factor

From the Department of Radiology (H.Z., S.W., F.Z., M.L.)
✉ liaomy@whu.edu.cn, Zhongnan Hospital of Wuhan
University, Wuhan, China.

Received 17 November 2021; revision requested 12
December 2021; last revision received 25 February 2022;
accepted 07 March 2022.



Epub: 20.03.2023

Publication date: 30.05.2023

DOI: 10.4274/dir.2022.221187

Lung cancer is the leading cause of cancer incidence and mortality worldwide; with 2.1 million new cases and 1.8 million deaths in 2018, it represents approximately 18.4% of all cancer deaths.¹ As 70% of lung cancers are discovered in advanced stages and are unresectable, needle biopsy techniques are the primary diagnostic methods.² These techniques include computed tomography- (CT) or ultrasound-guided percutaneous transthoracic needle biopsy (PTNB) and endobronchial ultrasound-guided biopsy.³ Endobronchial ultrasound-guided biopsy is best suited to central lesions. The use of ultrasound-guided PTNB is limited by its low resolution and is suitable only for lesions of the peripheral lung, chest wall, and mediastinum.⁴ CT-guided PTNB is the most widely used technique due to its high-resolution display of lung lesions, its wide availability to both central and peripheral lung lesions, and its minimal invasiveness and high accuracy.^{5,6}

The most common complications of CT-guided PTNB are pneumothorax and hemorrhage.^{7,8} Air embolisms are rare but potentially fatal complications.^{7,9} The direct injection of

You may cite this article as: Zhang H, Wang S, Zhong F, Liao M. Risk factors for air embolism following computed tomography-guided percutaneous transthoracic needle biopsy: a systematic review and meta-analysis. *Diagn Interv Radiol.* 2023;29(3):478-491.

2 mL of air into the cerebral circulation is enough to be fatal, and just 0.5–1.0 mL of air injected into a coronary artery can cause cardiac arrest.¹⁰ The clinical features of air embolism vary from confusion to stroke, arrhythmia, cardiac ischemic features, loss of consciousness, and death.

As the incidence of air embolism is rare, few studies have systematically reported the characteristics and risk factors for air embolism following CT-guided PTNB. Thus, we conducted this systematic review and meta-analysis to qualitatively summarize the characteristics of air embolism following CT-guided PTNB and quantitatively analyze its risk factors.

Methods

This manuscript was reported according to the Preferred Reporting Items for Systematic Reviews and Meta-Analyses (PRISMA) statement.¹¹ Ethical approval was not required.

Search strategy

A literature search was performed on January 4, 2021, on the PubMed, Embase, and Web of Science databases and on three Chinese databases (Wanfang Data, VIP information, and China National Knowledge Infrastructure) using combinations of the following search terms and their synonyms and variations without time and language restrictions: “lung,” “chest,” “biopsy,” “air embolism,” and “systematic air embolism.” Medical subject headings were applied if available.

Main points

- Air embolism is a rare but potentially fatal complication of computed tomography-guided percutaneous transthoracic needle biopsy.
- The most common symptoms of air embolism were an unconscious or unresponsive state, hemiplegia, hypotension, and cardiopulmonary arrest; the air was most commonly located in the left ventricle, aorta, and cerebral artery.
- Patients with emphysema, cough, and air located in the left heart, aorta, cerebral artery, and coronary artery were more likely to develop clinical symptoms than patients without these conditions; air location and symptoms were significantly related to patient prognosis.
- Lesion location (lower lung lobe), lesion subtype (subsolid), pneumothorax, hemorrhage, and lesions located above the left atrium were significant risk factors for air embolism.

The reference lists of the retrieved articles, including reviews, were searched manually for other relevant studies. Two authors performed the search independently and reviewed all the identified publications for inclusion using predetermined criteria.

Inclusion criteria

The inclusion criteria were (a) air embolism defined as air density in the cardiovascular system found on CT images and (b) if air embolism was found during, immediately after, or at least in a clear temporal coincidence with CT-guided PTNB. The exclusion criteria were (a) air embolism caused by trauma, transbronchial lung biopsy, CT-guided marking of lung lesions, or CT-guided radiofrequency ablation other than CT-guided biopsy; (b) comments and review articles in which the exact data of patients with air embolism could not be extracted; and (c) studies reported neither in Chinese nor in English.

Data extraction and quality assessment

A standardized extraction form was used to collect the characteristics of the study: (a) study characteristics, including the first author, publication year, and country; (b) patient characteristics, including age and sex; (c) lesion characteristics, including location (upper, middle, or lower lobe), diameter (maximum axial diameter of the lesion), and cavity contained in the lesion; (d) CT-guided biopsy characteristics, including the number of biopsies, the diameter of the biopsy needle, patient's position when biopsied, and the use of the coaxial biopsy technique; (e) complications, including pneumothorax, pulmonary hemorrhage or hemoptysis, and cough, and (f) the location of air in the cardiovascular system (the air location in each patient was analyzed individually), clinical symptoms, treatments, and prognoses.

The methodological quality of the studies included in the meta-analysis was assessed using the Newcastle–Ottawa Scale.¹² Data extraction and quality assessment were performed independently by two reviewers, and any disagreement was resolved by consensus.

Statistical analysis

Information about the number of air embolism cases, patient characteristics, lesions, biopsy processes, treatments, and prognoses was extracted from the individual cases in the included studies. These clinical characteristics were reported as mean \pm standard values or proportions according to whether they were continuous or categorical vari-

ables. Differences in these variables in different symptomatic groups and prognostic groups were compared, and a two-sided value of $P < 0.05$ was considered statistically significant. A chi-squared test or Fisher's exact test was used for nominal variables, while a Mann–Whitney test was used for continuous variables with an abnormal distribution. The above statistical analyses were performed using SPSS 21.0 software (IBM).

Odds ratios (ORs) and corresponding 95% confidence intervals (CIs) were used to assess the strength of the association between the different factors and the occurrence of air embolism. Heterogeneity between different studies was evaluated by an I^2 test, with values of 25%, 50%, and 75% indicating low, moderate, and high heterogeneity, respectively. A random-effects model (the DerSimonian–Laird model) was used if $I^2 > 50\%$ or $P \leq 0.01$. Otherwise, a fixed-effects model (the Mantel–Haenszel model) was used. Publication bias was evaluated using a Begg's funnel plot. Differences were considered statistically significant if $P > 0.05$. Statistical analyses were performed using STATA 12.0 (StataCorp).

Results

Study selection and characteristics

Figure 1 presents this study's PRISMA flow diagram, which summarizes the screening process and the reasons for exclusion. A total of 104 studies^{13–116} that reported the characteristics of air embolism after CT-guided PTNB were included in the systematic review (Supplementary Table 1). Five studies^{99–101,117,118} that reported the risk factors for air embolism were included in the quantitative meta-analysis (Supplementary Table 2).

Qualitative analysis

A total of 154 patients from 104 studies were included. The reported incidence of air embolism after CT-guided PTNB ranged from 0.06% to 4.80%. The most common symptoms were an unconscious or unresponsive state (29.87%), hemiplegia (16.23%), hypotension (14.29%), and cardiopulmonary arrest (14.29%) (Supplementary Table 3). Thirty-five patients (22.73%) were asymptomatic. Air was most commonly found in the left ventricle (44.81%), aorta (40.91%), cerebral artery (29.87%), coronary artery (22.73%), and left atrium (14.94%) (Supplementary Table 4). Air is not always present in one site alone, but in multiple locations at the same time.

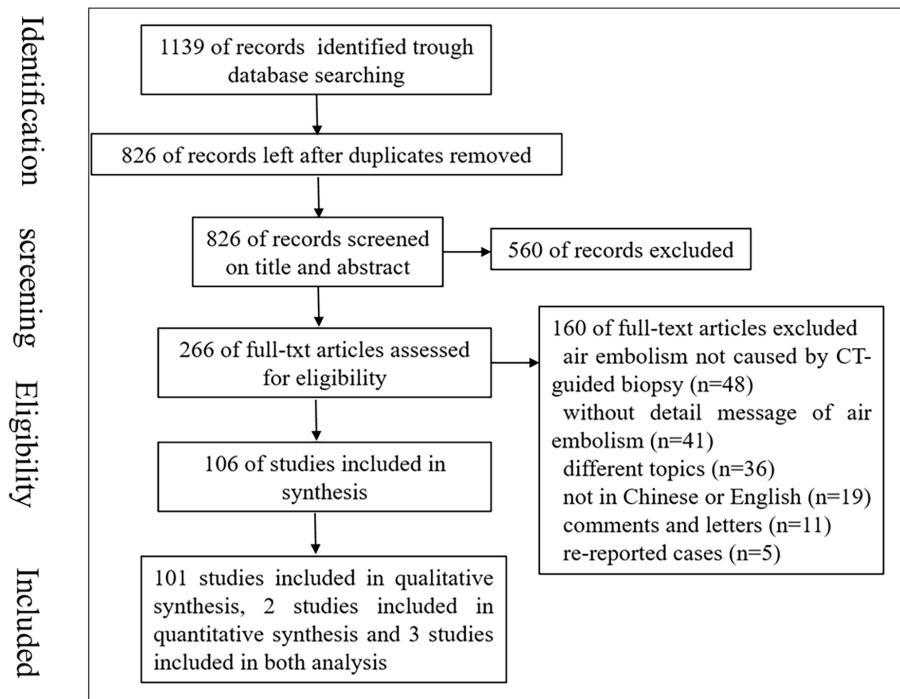


Figure 1. Preferred reporting items for systematic reviews and meta-analyses flow diagram of the study selection process. CT, computed tomography.

Air location was significantly associated with the occurrence of clinical symptoms ($P < 0.001$) (Table 1), with air located in the cerebral artery, coronary artery, aorta, and left heart the most likely to result in clinical symptoms. Similarly, patients with emphysema and cough were the most likely to develop clinical symptoms ($P = 0.061$ and 0.076 , respectively). Air location ($P = 0.015$) and symptoms ($P < 0.001$) were also significantly associated with prognosis (Table 2), with air located in the pulmonary vein/artery (100%), left heart (86.42%), aorta (78.94%), and right heart (75%) most likely to have the best outcomes. Of the 154 patients, 144 reported clinical outcomes, 104 (67.53%) recovered without sequelae, 21 (13.63%) patients recovered with sequelae, and 19 (12.34%) patients died. All asymptomatic patients recovered without sequelae.

Quantitative analysis

As shown in Table 3, the risk factors for air embolism following CT-guided PTNB were quantitatively analyzed. Data from 7,811 patients were extracted^{99-101,117,118} to analyze the relationship between air embolism and lesion location. The pooled OR was 1.85 (95% CI: 1.12–3.05, $P = 0.017$) (Figure 2). Data from 5,798 patients^{99-101,117,118} were extracted to analyze the relationship between air embolism and lesion subtype. The pooled OR was 3.78 (95% CI: 1.37–10.45, $P = 0.01$) (Figure 3). Data from 7,633 patients^{99-101,117,118} were extracted

to analyze the relationship between pneumothorax and air embolism. The pooled OR was 2.16 (95% CI: 1.31–3.57, $P = 0.003$) (Figure 4). Data from 7,397 patients^{99-101,117,118} were extracted to analyze the relationship between air embolism and hemorrhage. The pooled OR was 3.20 (95% CI: 1.95–5.26, $P < 0.001$) (Figure 5). Data from 4,464 patients were extracted^{99,117,118} to analyze the relationship between air embolism and lesion location above the level of the left atrium. The pooled OR was 4.35 (95% CI: 1.06–17.86, $P = 0.042$) (Figure 6). The funnel plots did not reveal any publication bias.

Data from five studies^{99-101,117,118} were used to analyze the relationship between air embolism and patient gender; the pooled OR was 0.99 (95% CI: 0.64–1.54, $P = 0.979$). The relationship between emphysema and air embolism was analyzed in data from four studies;^{99-101,117,118} the pooled OR was 0.96 (95% CI: 0.58–1.61, $P = 0.884$). Data from five studies^{99-101,117,118} were used to analyze the relationship between air embolism and biopsy position; the pooled OR was 1.10 (95% CI: 0.24–5.16, $P = 0.901$). Data from three studies⁹⁹⁻¹⁰¹ were used to analyze the relationship between air embolism and the use of the coaxial method; the pooled OR was 1.93 (95% CI: 0.66–5.64, $P = 0.228$). Data from two studies (100,118) were used to analyze the relationship between air embolism and needle-tip location; the pooled OR was 0.46 (95% CI: 0.11–1.94, $P = 0.293$).

Discussion

This study qualitatively summarized the characteristics of air embolism after CT-guided PTNB and quantitatively analyzed the risk factors for air embolism. The most common symptoms of air embolism were an unconscious or unresponsive state, hemiplegia, hypotension, and cardiopulmonary arrest. Air was most commonly found in the left ventricle, aorta, cerebral artery, and coronary artery. Patients with emphysema, cough, and air located in the left heart, aorta, cerebral artery, and coronary artery were more likely to develop clinical symptoms than patients without these conditions, and air location and symptoms were also significantly related to patient prognosis. Lesion location (lower lung lobe), lesion subtype (subsolid), pneumothorax, hemorrhage, and lesions located above the left atrium were significant risk factors for air embolism.

The reported incidence of air embolism after CT-guided PTNB was 0.06% to 4.80%. This varied because the controlled CT scan after CT-guided PTNB was limited to the target area, and some asymptomatic air embolism cases were not found. A study led by Monnin-Bares showed that by limiting the volume of the post-procedure CT scan to the target area, the rate of air embolism detection was just 1% instead of 4.8%.¹¹⁸ However, the good news is that, usually, these asymptomatic air embolisms will not have serious consequences. Therefore, doctors should weigh up the risk of increased radiation exposure from an enlarged scanning area against the expected benefits of an early diagnosis.

The CT-guided PTNB of lesions in the lower lobe is more likely to result in air embolism than a biopsy performed in other lobes. This difference may be due to gravity, resulting in larger vessels in the lower lobes and a more obvious respiratory motion. Thus, procedures performed in the lower lobe may pose a higher risk of injuring the veins and causing air embolism.¹⁰¹ Additionally, the respiratory motion of the lung may complicate the procedure and necessitate a high number of needle redirections to reach the lesion, leading to increased injury of the pulmonary vein and airway.¹⁰¹ Usually, a prone or lateral position with lesions on the upper side is selected to perform a CT-guided PTNB of lesions in the lower lobe. In areas higher than the left atrium, the pressure in both the pulmonary artery and alveoli is greater than that in the pulmonary vein.¹¹⁹ If a bronchopulmonary venous fistula or an alveolopulmonary vein fistula forms, the air is more likely to enter the

Table 1. Characteristics of asymptomatic and symptomatic air embolism following computed tomography-guided percutaneous transthoracic needle biopsy

| Characteristics | Asymptomatic | Symptomatic | <i>P</i> |
|---------------------------------|---------------|---------------|----------|
| Gender | | | |
| Male | 11 | 79 | 0.325 |
| Female | 8 | 35 | |
| NA | 16 | 5 | |
| Age (years) | 61.28 (27–75) | 64.21 (25–85) | 0.397 |
| Lesion location | | | |
| Up and middle | 9 | 38 | 0.430 |
| Lower | 9 | 57 | |
| NA | 17 | 24 | |
| Lesion density | | | |
| Solid | 13 | 47 | 0.213 |
| Subsolid | 3 | 4 | |
| NA | 18 | 69 | |
| Cavity | | | |
| Yes | 0 | 4 | 0.565 |
| No | 16 | 47 | |
| NA | 18 | 69 | |
| Emphysema | | | |
| Yes | 0 | 4 | 0.061 |
| No | 5 | 2 | |
| NA | 29 | 114 | |
| Puncture needle diameter | | | |
| >18 gauge | 8 | 43 | 0.668 |
| ≤18 gauge | 10 | 43 | |
| NA | 18 | 32 | |
| Position | | | |
| Supine | 4 | 23 | 0.318 |
| Lateral | 2 | 20 | |
| Prone | 12 | 39 | |
| NA | 17 | 37 | |
| Cough | | | |
| Yes | 7 | 33 | 0.076 |
| No | 8 | 13 | |
| NA | 19 | 74 | |
| Pneumothorax | | | |
| Yes | 6 | 27 | 0.413 |
| No | 3 | 7 | |
| NA | 25 | 86 | |
| Hemorrhage | | | |
| Yes | 12 | 34 | 0.655 |
| No | 2 | 4 | |
| NA | 21 | 81 | |
| Coaxial | | | |
| Yes | 16 | 60 | 0.448 |
| No | 1 | 12 | |
| NA | 18 | 47 | |
| Air location | | | |
| Left heart | 33 | 55 | <0.001 |
| Right heart | 1 | 4 | |
| Aorta | 11 | 62 | |
| Cerebral artery | 2 | 54 | |
| Coronary artery | 3 | 41 | |
| Pulmonary vein/artery | 3 | 11 | |
| Other arteries | 2 | 6 | |

NA, not applicable.

Table 2. Risk factors for prognosis of air embolism following computed tomography-guided percutaneous transthoracic lung needle biopsy

| Characteristics | Without sequelae | With sequelae | Death | <i>P</i> |
|----------------------------------|------------------|---------------|---------------|----------|
| Gender | | | | |
| Male | 54 | 16 | 14 | 0.342 |
| Female | 30 | 4 | 5 | |
| NA | 20 | 1 | 0 | |
| Age (years) | 65.63 (27–82) | 62.4 (32–85) | 59.42 (35–75) | 0.192 |
| Lesion location | | | | |
| Up and middle | 30 | 11 | 4 | 0.197 |
| Lower | 46 | 7 | 8 | |
| NA | 28 | 3 | 7 | |
| Lesion density | | | | |
| Solid | 42 | 9 | 7 | 0.314 |
| Subsolid | 5 | 0 | 2 | |
| NA | 57 | 12 | 10 | |
| Cavity | | | | |
| Yes | 6 | 2 | 1 | 0.729 |
| No | 41 | 7 | 8 | |
| NA | 57 | 12 | 10 | |
| Emphysema | | | | |
| Yes | 4 | 0 | 0 | 0.428 |
| No | 6 | 1 | 0 | |
| NA | 94 | 20 | 19 | |
| Puncture needle diameter | | | | |
| ≥18 gauge | 36 | 10 | 4 | 0.597 |
| <18 gauge | 36 | 8 | 7 | |
| NA | 32 | 3 | 8 | |
| Position | | | | |
| Supine | 19 | 3 | 3 | 0.715 |
| Lateral | 13 | 5 | 2 | |
| Prone | 38 | 6 | 5 | |
| NA | 34 | 7 | 9 | |
| Cough | | | | |
| Yes | 27 | 7 | 5 | 0.608 |
| No | 14 | 2 | 4 | |
| NA | 63 | 12 | 10 | |
| Pneumothorax | | | | |
| Yes | 24 | 4 | 5 | 0.730 |
| No | 6 | 2 | 2 | |
| NA | 74 | 15 | 12 | |
| Hemorrhage | | | | |
| Yes | 33 | 9 | 5 | 0.299 |
| No | 3 | 1 | 2 | |
| NA | 68 | 11 | 12 | |
| Coaxial | | | | |
| Yes | 56 | 11 | 6 | 0.708 |
| No | 9 | 2 | 2 | |
| NA | 39 | 8 | 11 | |
| Air location | | | | |
| Left heart | 70 | 7 | 4 | 0.015 |
| Right heart | 3 | 0 | 1 | |
| Aorta | 45 | 6 | 6 | |
| Cerebral artery | 23 | 10 | 8 | |
| Coronary artery | 21 | 3 | 8 | |
| Pulmonary vein/artery | 10 | 0 | 0 | |
| Other arteries | 6 | 1 | 2 | |
| Hyperbaric oxygen therapy | | | | |
| Yes | 27 | 8 | 4 | 0.305 |
| No | 63 | 9 | 5 | |
| NA | 14 | 4 | 10 | |
| Trendelenburg position | | | | |
| Yes | 7 | 2 | 1 | 0.801 |
| No | 3 | 1 | 0 | |
| NA | 94 | 8 | 28 | |
| Symptomatic | | | | |
| Yes | 69 | 21 | 19 | <0.001 |
| No | 35 | 0 | 0 | |

NA, not applicable.

Table 3. Pooled analysis of risk factors for air embolism following computed tomography-guided percutaneous transthoracic needle biopsy

| Risk factors | Air embolism | Non-air embolism | OR (95% CI) | Model chosen for meta-analysis (fixed/random) | Publication bias (P value) |
|--|--------------|------------------|-------------------|---|----------------------------|
| Lesion location | | | | | |
| Lower lung lobe | 33 | 2.439 | 1.85 (1.12–3.05) | Fixed (I ² : 0, P = 0.408) | 0.308 |
| Upper and middle lung lobe | 32 | 5.307 | | | |
| Lesion subtype | | | | | |
| Subsolid | 23 | 823 | 3.78 (1.37–10.45) | Random (I ² : 61.7%, P = 0.050) | 0.734 |
| Solid | 42 | 4.910 | | | |
| Pneumothorax | | | | | |
| Yes | 29 | 2.144 | 2.16 (1.31–3.57) | Fixed (I ² : 0, P = 0.965) | 0.462 |
| No | 58 | 5.402 | | | |
| Hemorrhage | | | | | |
| Yes | 65 | 3.841 | 3.20 (1.95–5.26) | Fixed (I ² : 0, P = 0.438) | >0.990 |
| No | 22 | 3.469 | | | |
| Lesion located above the level of left atrium | | | | | |
| Yes | 61 | 2.260 | 4.35 (1.06–17.86) | Random (I ² : 75.5%, P = 0.025) | >0.990 |
| No | 10 | 2.131 | | | |
| Gender | | | | | |
| Male | 53 | 4.617 | 0.99 (0.64–1.54) | Fixed (I ² : 0, P = 0.543) | 0.609 |
| Female | 34 | 2.986 | | | |
| Emphysema | | | | | |
| Yes | 41 | 3.790 | 0.96 (0.58–1.61) | Fixed (I ² : 0, P = 0.804) | 0.017 |
| No | 24 | 1.943 | | | |
| Biopsy position | | | | | |
| Prone and lateral | 54 | 4.555 | 1.10 (0.24–5.16) | Random (I ² : 89.6%, P = 0) | 0.580 |
| Supine | 36 | 3.043 | | | |
| Coaxial method | | | | | |
| Yes | 27 | 3.557 | 1.93 (0.66–5.64) | Fixed (I ² : 0, P = 0.721) | 0.599 |
| No | 11 | 1.595 | | | |
| Location of needle tip | | | | | |
| Inside lesion | 22 | 1.159 | 0.46 (0.11–1.94) | Random (I ² : 70.8%, P = 0.064) | 0.620 |
| Outside lesion | 14 | 360 | | | |

OR, odds ratio; CI, confidence interval.

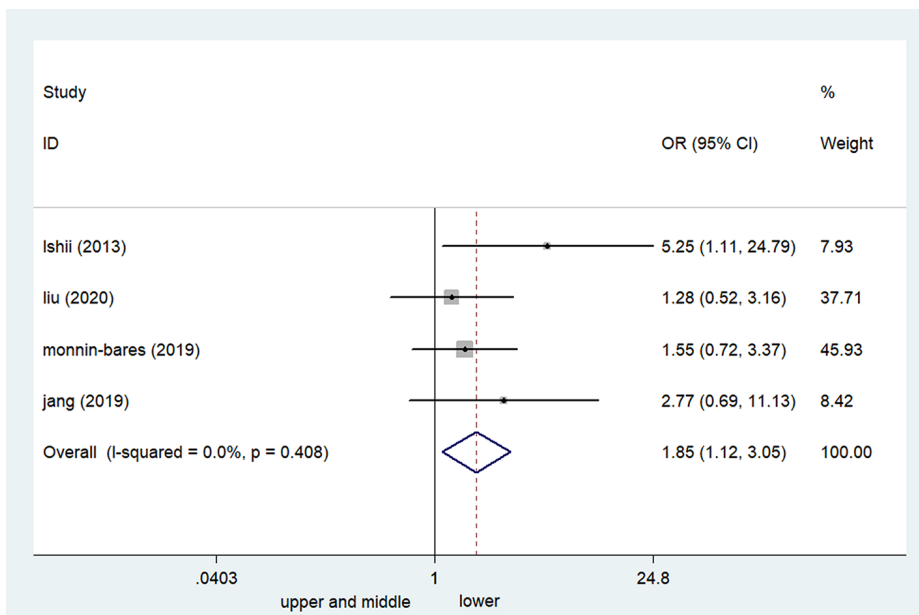


Figure 2. Forest plots of the relationship between lesion location (upper and middle lobe vs. lower lobe) and air embolism following computed tomography-guided percutaneous transthoracic lung needle biopsy. CI, confidence interval; OR, odds ratio.

pulmonary vein, resulting in air embolism. In fact, our study found that lesions located

above the level of the left atrium are a risk factor for air embolism.

Some studies recommend transthoracic biopsy with the patient in an ipsilateral-dependent position to prevent air embolism.¹¹⁷ Even though this approach has been shown to decrease the rate of pneumothorax, it is related to increased alveolar hemorrhage.¹¹⁷ Additionally, this position may complicate the biopsy process, as the biopsy must pass through more lung area. The choice of the transthoracic biopsy position is still debatable, and we must consider the accuracy and safety of the procedure comprehensively.

Pneumothorax and hemorrhage are also risk factors. There may be two explanations for this: the first is that the presence of pneumothorax and hemorrhage means that alveolar, bronchial, or pulmonary vessels are injured. This injury can lead to a broncho-venous fistula, increasing the risk of air embolism.¹¹¹ Therefore, when a lung biopsy is performed, patients should try to avoid cough-

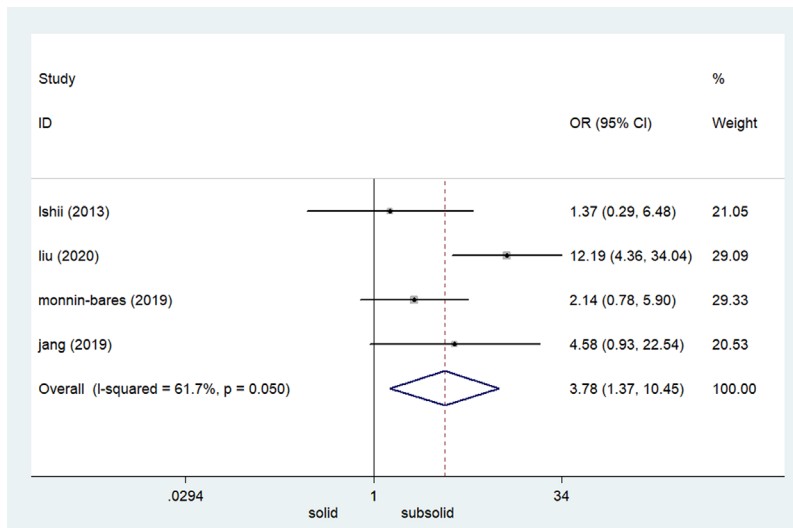


Figure 3. Forest plots of the relationship between lesion subtype (solid vs. subsolid) and air embolism following computed tomography-guided percutaneous transthoracic lung needle biopsy. CI, confidence interval; OR, odds ratio.

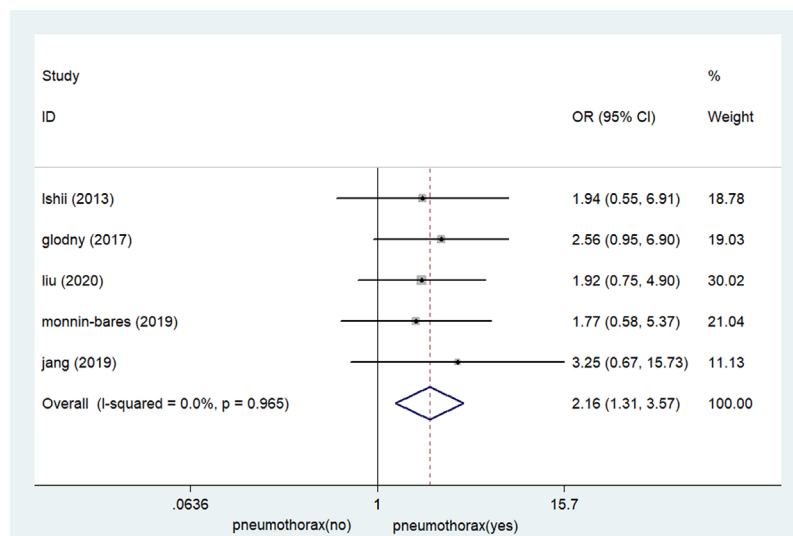


Figure 4. Forest plots of the relationship between pneumothorax and air embolism following computed tomography-guided percutaneous transthoracic lung needle biopsy. CI, confidence interval; OR, odds ratio.

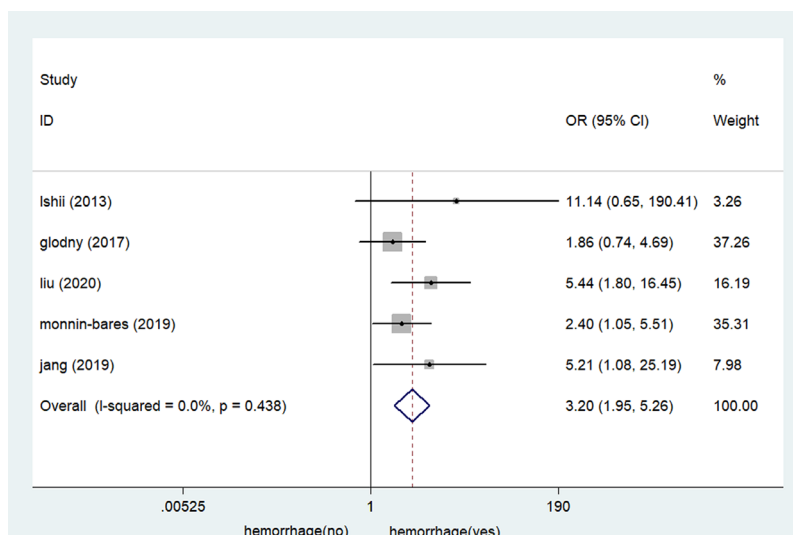


Figure 5. Forest plots of the relationship between hemorrhage and air embolism following computed tomography-guided percutaneous transthoracic lung needle biopsy. CI, confidence interval; OR, odds ratio.

ing or cough as little as possible during and after the procedure. For patients who cough frequently, medicine can be used to control their coughing before biopsy.

The lesion subtype is another risk factor. Subsolid nodules contain ground-glass opacities, which do not cover the normal parenchymal structures, including the airways and vessels, and can be visualized on chest CT images.¹²⁰ These normal parenchymal structures in the nodules increase the opportunity for air embolism during the biopsy.

Only three studies analyzed if the coaxial method was a risk for air embolism, with the results showing that it was unrelated to air embolism. In addition, only two studies analyzed if the needle-tip location was a risk factor for air embolism. Our analysis showed that it was not a risk factor; however, future studies should investigate this further.

The optimal positioning of patients following air embolism is controversial.¹⁰⁰ Some patients were placed in the right lateral decubitus or Trendelenburg position when air embolism occurred, while some studies recommend not changing the biopsy position. However, turning a patient from a prone position to a supine position should be avoided, as it can facilitate the antegrade passage of air.¹²¹ In addition to position, 100% oxygen should be administered promptly to assist nitrogen-oxygen exchange within the air bubbles and accelerate their resorption.¹²² The most effective treatment for air embolism is hyperbaric oxygen therapy, which can improve the oxygenation of the affected tissue and dissolve emboli by increasing nitrogen reabsorption.⁸¹ In our analysis, the Trendelenburg position and hyperbaric oxygen therapy were not related to patient outcome; however, further studies are required on this topic.

Our study has some limitations. First, because of limited access to all the databases and the language barrier to understanding literature not published in English or Chinese, we searched only the databases suggested by the Cochrane Reviewer's Handbook and evaluated literature published only in English and Chinese. Second, the number of studies suitable for quantitative analysis was limited, and they differed in terms of factors related to air embolism; therefore, some factors were not quantitatively analyzed. Some factors, for example, the proximity of the targeted lesion to the segmental or subsegmental airways or vascular structures (especially the pulmonary veins), may relate to air embolism but

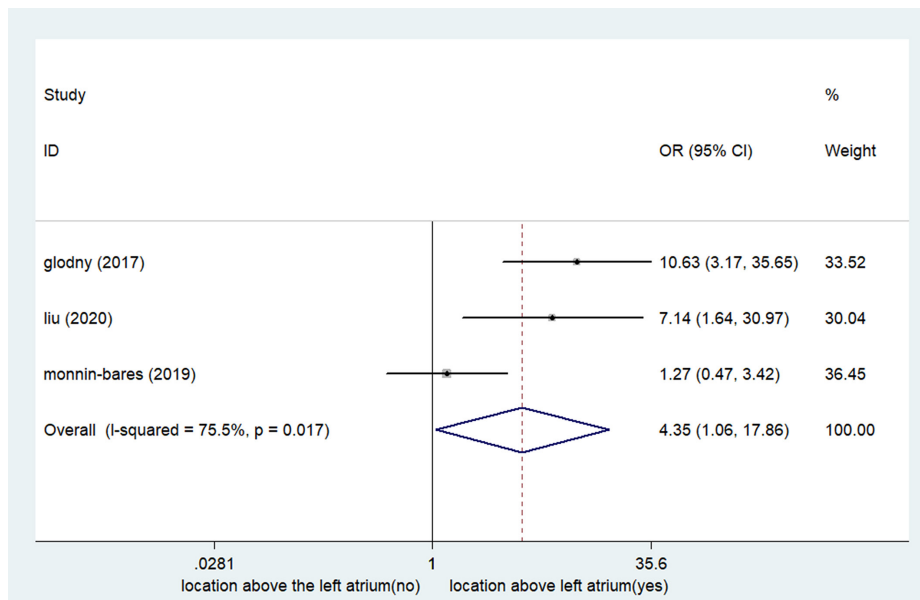


Figure 6. Forest plots of lesion location above the level of the left atrium. CI, confidence interval; OR, odds ratio.

were not evaluated in the original studies. Third, most studies included were case reports; hence, data from these studies were incomplete. Fourth, in most institutions, the extent of the post-procedure CT scan was limited to the target nodule area, so some asymptomatic air embolisms may not have been found. This may have introduced bias when analyzing the risks related to asymptomatic and symptomatic air embolism following CT-guided PTNB. Finally, we analyzed only air embolism following CT-guided PTNB without considering other techniques (e.g., ultrasound-guided PTNB); as the techniques are used for different types of lung lesions, the complication rates may also differ. Additional studies can be undertaken to analyze the characteristics and risk factors for air embolism with other techniques.

Conclusion

Based on current evidence, lesion location (lower lobe) and subtype (subsolid), pneumothorax, hemorrhage, and lesions located above the left atrium were significant risk factors for air embolism following CT-guided PTNB. The most common symptoms of air embolism were an unconscious or unresponsive state, hemiplegia, hypotension, and cardiopulmonary arrest. The air was most commonly located in the left ventricle, aorta, cerebral artery, and coronary artery. Emphysema, cough, and air location were related to patient symptoms, and air location and symptoms were significantly associated with patient outcomes.

Conflict of interest disclosure

The authors declared no conflicts of interest.

Reference

1. Bray F, Ferlay J, Soerjomataram I, Siegel RL, Torre LA, Jemal A. Global cancer statistics 2018: GLOBOCAN estimates of incidence and mortality worldwide for 36 cancers in 185 countries. *CA Cancer J Clin.* 2018;68(6):394-424. Erratum in: *CA Cancer J Clin.* 2020;70(4):313. [\[CrossRef\]](#)
2. Travis WD, Brambilla E, Noguchi M, et al. Diagnosis of lung cancer in small biopsies and cytology: implications of the 2011 International Association for the Study of Lung Cancer/American Thoracic Society/European Respiratory Society classification. *Arch Pathol Lab Med.* 2013;137(5):668-684. [\[CrossRef\]](#)
3. Yasufuku K, Fujisawa T. Staging and diagnosis of non-small cell lung cancer: invasive modalities. *Respirology.* 2007;12(2):173-183. [\[CrossRef\]](#)
4. Huang W, Chen L, Xu N, et al. Diagnostic value and safety of color doppler ultrasound-guided transthoracic core needle biopsy of thoracic disease. *Biosci Rep.* 2019;39(6):BSR20190104. [\[CrossRef\]](#)
5. Cham MD, Lane ME, Henschke CI, Yankelevitz DF. Lung biopsy: special techniques. *Semin Respir Crit Care Med.* 2008;29(4):335-349. [\[CrossRef\]](#)
6. Lee SM, Park CM, Lee KH, Bahn YE, Kim JI, Goo JM. C-arm cone-beam CT-guided percutaneous transthoracic needle biopsy of lung nodules: clinical experience in 1108 patients. *Radiology.* 2014;271(1):291-300. [\[CrossRef\]](#)

7. Heerink WJ, de Bock GH, de Jonge GJ, Groen HJ, Vliegenthart R, Oudkerk M. Complication rates of CT-guided transthoracic lung biopsy: meta-analysis. *Eur Radiol.* 2017;27(1):138-148. [\[CrossRef\]](#)
8. Yoon SH, Park CM, Lee KH, et al. Analysis of complications of percutaneous transthoracic needle biopsy using CT-guidance modalities in a multicenter cohort of 10568 biopsies. *Korean J Radiol.* 2019;20(2):323-331. Erratum in: *Korean J Radiol.* 2019;20(3):531. [\[CrossRef\]](#)
9. Wiener RS, Wiener DC, Gould MK. Risks of transthoracic needle biopsy: how high? *Clin Pulm Med.* 2013;20(1):29-35. [\[CrossRef\]](#)
10. Ho AM, Ling E. Systemic air embolism after lung trauma. *Anesthesiology.* 1999;90(2):564-575. [\[CrossRef\]](#)
11. Moher D, Liberati A, Tetzlaff J, Altman DG; PRISMA Group. Preferred reporting items for systematic reviews and meta-analyses: the PRISMA statement. *BMJ.* 2009;339:b2535. [\[CrossRef\]](#)
12. Wells GA, Shea B, O'Connell D, Peterson J, Welch V, PT LM. The Newcastle-Ottawa scale (NOS) for assessing the quality of nonrandomised studies in meta-analyses. *Ottawa Hospital Research Institute.* 2014. [\[CrossRef\]](#)
13. Wu YF, Huang TW, Kao CC, Lee SC. Air embolism complicating computed tomography-guided core needle biopsy of the lung. *Interact Cardiovasc Thorac Surg.* 2012;14(6):771-772. [\[CrossRef\]](#)
14. Kawaji T, Shiomi H, Togashi Y, et al. Coronary air embolism and cardiogenic shock during computed tomography-guided needle biopsy of the lung. *Circulation.* 2012;126(13):e195-e197. [\[CrossRef\]](#)
15. Dalal P, Varma D. Left ventricular air embolism following computerized tomography-guided lung biopsy successfully treated with hyperbaric oxygen therapy. *Chest.* 2012;142(4):94A. [\[CrossRef\]](#)
16. Al-Ali WM, Browne T, Jones R. A case of cranial air embolism after transthoracic lung biopsy. *Am J Respir Crit Care Med.* 2012;186(11):1193-1195. [\[CrossRef\]](#)
17. Thomas R, Thangakunam B, Cherian RA, Gupta R, Christopher DJ. Cerebral air embolism complicating CT-guided trans-thoracic needle biopsy of the lung. *Clin Respir J.* 2011;5(2):e1-e3. [\[CrossRef\]](#)
18. Singh A, Ramanakumar A, Hannan J. Simultaneous left ventricular and cerebral artery air embolism after computed tomographic-guided transthoracic needle biopsy of the lung. *Tex Heart Inst J.* 2011;38(4):424-426. [\[CrossRef\]](#)
19. Shroff GR, Sarraf M, Sprenkle MD, Karim RM. Air embolism involving the coronary and pulmonary circulation: an unusual cause of sudden cardiac death. *Circulation.* 2011;124(25):2949-2950. [\[CrossRef\]](#)

20. Mokart D, Sarra A, Barthélémy A, et al. Systemic air embolism during lung biopsy. *Br J Anaesth*. 2011;107(2):277-278. [\[CrossRef\]](#)
21. Kuo HL, Cheng L, Chung TJ. Systemic air embolism detected during percutaneous transthoracic needle biopsy: report of two cases and a proposal for a routine postprocedure computed tomography scan of the aorto-cardiac region. *Clin Imaging*. 2010;34(1):53-56. [\[CrossRef\]](#)
22. Cheng HM, Chiang KH, Chang PY, et al. Coronary artery air embolism: a potentially fatal complication of CT-guided percutaneous lung biopsy. *Br J Radiol*. 2010;83(988):e83-e85. [\[CrossRef\]](#)
23. Bou-Assaly W, Pernicano P, Hoeffner E. Systemic air embolism after transthoracic lung biopsy: A case report and review of literature. *World J Radiol*. 2010;2(5):193-196. [\[CrossRef\]](#)
24. Um SJ, Lee SK, Yang DK, et al. Four cases of a cerebral air embolism complicating a percutaneous transthoracic needle biopsy. *Korean J Radiol*. 2009;10(1):81-84. [\[CrossRef\]](#)
25. Ishikawa Y, Matsuguma H, Nakahara R, Ui A, Suzuki H, Yokoi K. Arterial air embolism: a rare but life-threatening complication of percutaneous needle biopsy of the lung. *Ann Thorac Surg*. 2009;87(5):1622. [\[CrossRef\]](#)
26. Hsi DH, Thompson TN, Fruchter A, Collins MS, Lieberg OU, Boepple H. Simultaneous coronary and cerebral air embolism after CT-guided core needle biopsy of the lung. *Tex Heart Inst J*. 2008;35(4):472-474. Erratum in: *Tex Heart Inst J*. 2009;36(1):80. [\[CrossRef\]](#)
27. Ibukuro K, Tanaka R, Takeguchi T, Fukuda H, Abe S, Tobe K. Air embolism and needle track implantation complicating CT-guided percutaneous thoracic biopsy: single-institution experience. *AJR Am J Roentgenol*. 2009;193(5):W430-W436. [\[CrossRef\]](#)
28. Bhatia S. Systemic air embolism following CT-guided lung biopsy. *J Vasc Interv Radiol*. 2009;20(6):709-711. [\[CrossRef\]](#)
29. Tomabechi M, Kato K, Sone M, et al. Cerebral air embolism treated with hyperbaric oxygen therapy following percutaneous transthoracic computed tomography-guided needle biopsy of the lung. *Radiat Med*. 2008;26(6):379-383. [\[CrossRef\]](#)
30. Kau T, Rabitsch E, Celedin S, Habernig SM, Weber JR, Hausegger KA. When coughing can cause stroke—a case-based update on cerebral air embolism complicating biopsy of the lung. *Cardiovasc Intervent Radiol*. 2008;31(5):848-853. [\[CrossRef\]](#)
31. Hiraki T, Fujiwara H, Sakurai J, et al. Nonfatal systemic air embolism complicating percutaneous CT-guided transthoracic needle biopsy: four cases from a single institution. *Chest*. 2007;132(2):684-690. [\[CrossRef\]](#)
32. Ghafoori M, Varedi P. Systemic air embolism after percutaneous transthoracic needle biopsy of the lung. *Emerg Radiol*. 2008;15(5):353-356. [\[CrossRef\]](#)
33. Lattin G Jr, O'Brien W Sr, McCrary B, Kearney P, Gover D. Massive systemic air embolism treated with hyperbaric oxygen therapy following CT-guided transthoracic needle biopsy of a pulmonary nodule. *J Vasc Interv Radiol*. 2006;17(8):1355-1358. [\[CrossRef\]](#)
34. Mansour A, AbdelRaouf S, Qandeel M, Swaidan M. Acute coronary artery air embolism following CT-guided lung biopsy. *Cardiovasc Intervent Radiol*. 2005;28(1):131-134. [\[CrossRef\]](#)
35. Chakravarti R, Singh V, Isaac R, John MJ. Fatal paradoxical pulmonary air embolism complicating percutaneous computed tomography-guided needle biopsy of the lung. *Australas Radiol*. 2004;48(2):204-206. [\[CrossRef\]](#)
36. Ashizawa K, Watanabe H, Morooka H, Hayashi K. Hyperbaric oxygen therapy for air embolism complicating CT-guided needle biopsy of the lung. *AJR Am J Roentgenol*. 2004;182(6):1606-1607. [\[CrossRef\]](#)
37. Mokhlesi B, Ansaarie I, Bader M, Tareen M, Boatman J. Coronary artery air embolism complicating a CT-guided transthoracic needle biopsy of the lung. *Chest*. 2002;121(3):993-996. [\[CrossRef\]](#)
38. Arnold BW, Zwiebel WJ. Percutaneous transthoracic needle biopsy complicated by air embolism. *AJR Am J Roentgenol*. 2002;178(6):1400-1402. [\[CrossRef\]](#)
39. Ohashi S, Endoh H, Honda T, Komura N, Satoh K. Cerebral air embolism complicating percutaneous thin-needle biopsy of the lung: complete neurological recovery after hyperbaric oxygen therapy. *J Anesth*. 2001;15(4):233-236. [\[CrossRef\]](#)
40. King P, Ferraro D, Burguete S, Anzueto A. A rare cause of air embolism. *Chest*. 2013;144(4):903A. [\[CrossRef\]](#)
41. Kok HK, Leong S, Salati U, Torreggiani WC, Govender P. Left atrial and systemic air embolism after lung biopsy: importance of treatment positioning. *J Vasc Interv Radiol*. 2013;24(10):1587-1588. [\[CrossRef\]](#)
42. Shi L, Zhang R, Wang Z, Zhou P. Delayed cerebral air embolism complicating percutaneous needle biopsy of the lung. *Am J Med Sci*. 2013;345(6):501-503. [\[CrossRef\]](#)
43. Chang HC, Yang MC. Systemic air embolism after percutaneous computed tomography-guided lung biopsy due to a kink in the coaxial biopsy system: a case report. *BMC Med Imaging*. 2018;18(1):1. [\[CrossRef\]](#)
44. Smit DR, Kleijn SA, de Voogt WG. Coronary and cerebral air embolism: a rare complication of computed tomography-guided transthoracic lung biopsy. *Neth Heart J*. 2013;21(10):464-466. [\[CrossRef\]](#)
45. Suzuki K, Ueda M, Muraga K, et al. An unusual cerebral air embolism developing within the posterior circulation territory after a needle lung biopsy. *Intern Med*. 2013;52(1):115-117. [\[CrossRef\]](#)
46. Franke M, Reinhardt HC, von Bergwelt-Baildon M, Bangard C. Massive air embolism after lung biopsy. *Circulation*. 2014;129(9):1046-1047. [\[CrossRef\]](#)
47. Ramaswamy R, Narsinh KH, Tuan A, Kinney TB. Systemic air embolism following percutaneous lung biopsy. *Semin Intervent Radiol*. 2014;31(4):375-377. [\[CrossRef\]](#)
48. Shin KM, Lim JK, Kim CH. Delayed presentation of cerebellar and spinal cord infarction as a complication of computed tomography-guided transthoracic lung biopsy: a case report. *J Med Case Rep*. 2014;8:272. [\[CrossRef\]](#)
49. Hung WH, Chang CC, Ho SY, Liao CY, Wang BY. Systemic air embolism causing acute stroke and myocardial infarction after percutaneous transthoracic lung biopsy—a case report. *J Cardiothorac Surg*. 2015;10:121. [\[CrossRef\]](#)
50. Olgun DC, Samanci C, Ergin AS, Akman C. Life-threatening complication of percutaneous transthoracic fine-needle aspiration biopsy: systemic arterial air embolism. *Eurasian J Med*. 2015;47(1):72-74. [\[CrossRef\]](#)
51. Pando Sandoval A, Ariza Prota MA, García Clemente M, Prieto A, Fole Vázquez D, Casán P. Air embolism: a complication of computed tomography-guided transthoracic needle biopsy. *Respirol Case Rep*. 2015;3(2):48-50. [\[CrossRef\]](#)
52. Rocha RD, Azevedo AA, Falsarella PM, Rahal A, Garcia RG. Cerebral air embolism during CT-guided lung biopsy. *Thorax*. 2015;70(11):1099-1100. [\[CrossRef\]](#)
53. Kazimirko DN, Beam WB, Saleh K, Patel AM. Beware of positive pressure: coronary artery air embolism following percutaneous lung biopsy. *Radiol Case Rep*. 2016;11(4):344-347. [\[CrossRef\]](#)
54. Sun C, Bian J, Lai S, Li X. Systemic air embolism as a complication of CT-guided percutaneous core needle lung biopsy: a case report and review of the literature. *Exp Ther Med*. 2015;10(3):1157-1160. [\[CrossRef\]](#)
55. Rahman ZU, Murtaza G, Pourmorteza M, et al. Cardiac arrest as a consequence of air embolism: a case report and literature review. *Case Rep Med*. 2016;2016:8236845. [\[CrossRef\]](#)
56. Yamamoto A, Suzuki K, Iwashita Y, et al. Controlled normothermia for a cerebral air embolism complicating computed tomography-guided transthoracic needle biopsy of the lung. *Acute Med Surg*. 2016;3(4):411-414. [\[CrossRef\]](#)
57. Fintelmann FJ, Sharma A, Shepard JO. Prevention of air embolism during transthoracic biopsy of the lung. *AJR Am J Roentgenol*. 2017;209(6):W404. [\[CrossRef\]](#)
58. Fiore L, Frenk NE, Martins GLP, Viana PCC, de Menezes MR. Systemic air embolism after percutaneous lung biopsy: a manageable

- complication. *J Radiol Case Rep.* 2017;11(6):6-14. [\[CrossRef\]](#)
59. Galvis JM, Nunley DR, Zheyi T, Dinglasan LAV. Left ventricle and systemic air embolism after percutaneous lung biopsy. *Respir Med Case Rep.* 2017;22:206-208. [\[CrossRef\]](#)
 60. Ialongo P, Ciarpaglini L, Tinti MD, Suadoni MN, Cardillo G. Systemic air embolism as a complication of percutaneous computed tomography-guided transthoracic lung biopsy. *Ann R Coll Surg Engl.* 2017;99(6):e174-e176. [\[CrossRef\]](#)
 61. April D, Sandow T, Scheibal J, DeVun D, Kay D. Clinical images: left atrial air embolism following computed tomography-guided lung biopsy. *Ochsner J.* 2017;17(2):141-143. [\[CrossRef\]](#)
 62. Kukuljan M, Kolić Z, Vukas D, Bonifačić D, Vrbanc K. Nonfatal systemic air embolism: a grave complication of computed tomography-guided percutaneous transthoracic needle biopsy. *Eurasian J Med.* 2018;50(1):44-46. [\[CrossRef\]](#)
 63. Lang D, Reinelt V, Horner A, et al. Complications of CT-guided transthoracic lung biopsy: a short report on current literature and a case of systemic air embolism. *Wien Klin Wochenschr.* 2018;130(7-8):288-292. [\[CrossRef\]](#)
 64. Ren M, Zavodni A. Aortic and cardiac air emboli in an older woman. *CMAJ.* 2018;190(5):E137-E138. [\[CrossRef\]](#)
 65. Ornelas E, Fernandez-Vilches S, Gallardo X, Mesquida J. Massive coronary air embolism after CT-guided lung needle biopsy. *Intensive Care Med.* 2018;44(10):1748-1749. [\[CrossRef\]](#)
 66. Matsuura H, Takaishi A, Oonishi N, et al. Air embolism and CT-guided lung biopsy. *QJM.* 2017;110(7):465-466. [\[CrossRef\]](#)
 67. Sakatani T, Amano Y, Sato J, Nagase T. Air embolism after CT-guided percutaneous lung biopsy. *Jpn J Clin Oncol.* 2018;48(7):699-700. [\[CrossRef\]](#)
 68. Tavare AN, Patel A, Saini A, Creer DD, Hare SS. Systemic air embolism as a complication of percutaneous lung biopsy. *Br J Hosp Med (Lond).* 2018;79(2):106-107. [\[CrossRef\]](#)
 69. Viqas Z, Yar A, Yaseen M, Khalid M. Cardiac arrest due to air embolism: complicating image-guided lung biopsy. *Cureus.* 2018;10(9):e3295. [\[CrossRef\]](#)
 70. Abid H, Kumar A, Siddiqui N, Kramer B. Systemic air embolism following computed tomography-guided lung biopsy. *Cureus.* 2019;11(8):e5408. [\[CrossRef\]](#)
 71. Beliaev AM, Milne D, Sames C, O'Brien B, Ramanathan T. Massive arteriovenous air embolism after computed tomography-guided lung tumour biopsy. *ANZ J Surg.* 2019;89(4):434-436. [\[CrossRef\]](#)
 72. Edwards K, Amarna M, Biosca R, Adada H. Air embolus: a fatal complication of solitary lung nodule management. *Chest.* 2017;152(4):A271. [\[CrossRef\]](#)
 73. Li J, He Z, Ouyang X, Chen C. Massive air in the heart complicating percutaneous lung biopsy. *Intensive Care Med.* 2019;45(10):1476-1477. [\[CrossRef\]](#)
 74. Lonni S, Ceruti P. Systemic air embolism after percutaneous CT-guided lung biopsy. *Chest.* 2019;156(4):A238. [\[CrossRef\]](#)
 75. Marchak K, Hong MJ, Schramm KM. Systemic air embolism following CT-guided percutaneous core needle biopsy of the lung: case report and review of the literature. *Semin Intervent Radiol.* 2019;36(2):68-71. [\[CrossRef\]](#)
 76. De Oliveira DS, Pinto BD, Vale TC, Pires LA. Stroke after lung biopsy. *Pract Neurol.* 2019;19(6):543-544. [\[CrossRef\]](#)
 77. Deshmukh A, Kadavani N, Kakkar R, Desai S, Bhat GM. Coronary artery air embolism complicating a CT-guided percutaneous lung biopsy. *Indian J Radiol Imaging.* 2019;29(1):81-84. [\[CrossRef\]](#)
 78. El Homsy M, Haydar A, Dughayli J, Al-Kutoubi A. Trans-catheter aspiration of systemic air embolism causing cardiac compromise during CT-guided lung biopsy, a potentially lifesaving maneuver. *Cardiovasc Intervent Radiol.* 2019;42(1):150-153. [\[CrossRef\]](#)
 79. Hellinger L, Keppler AM, Schoepenthaus H, Perras J, Bender R. Hyperbaric oxygen therapy for iatrogenic arterial gas embolism after CT-guided lung biopsy: a case report. *Anaesthetist.* 2019;68(7):456-460. [\[CrossRef\]](#)
 80. Hare SS, Gupta A, Goncalves AT, Souza CA, Matzinger F, Seely JM. Systemic arterial air embolism after percutaneous lung biopsy. *Clin Radiol.* 2011;66(7):589-596. [\[CrossRef\]](#)
 81. Warren S, Somers A, Chambers B, Gardner K. A case study: percutaneous lung biopsy and symptomatic arterial air embolus. *Journal of Radiology Nursing.* 2019;38(3):174-176. [\[CrossRef\]](#)
 82. Rott G, Boecker F. Influenceable and avoidable risk factors for systemic air embolism due to percutaneous CT-guided lung biopsy: patient positioning and coaxial biopsy technique-case report, systematic literature review, and a technical note. *Radiol Res Pract.* 2014;2014:349062. [\[CrossRef\]](#)
 83. Lederer W, Schlimp CJ, Glodny B, Wiedermann FJ. Air embolism during CT-guided transthoracic needle biopsy. *BMJ Case Rep.* 2011;2011:bcr04201114113. [\[CrossRef\]](#)
 84. Khalid F, Rehman S, AbdulRahman R, Gupta S. Fatal air embolism following local anaesthetisation: does needle size matter? *BMJ Case Rep.* 2018;2018:bcr2017222254. [\[CrossRef\]](#)
 85. Tomiyama N, Yasuhara Y, Nakajima Y, et al. CT-guided needle biopsy of lung lesions: a survey of severe complication based on 9783 biopsies in Japan. *Eur J Radiol.* 2006;59(1):60-64. [\[CrossRef\]](#)
 86. Piccoli F, Lanza E, Lutman RF. Cerebral Air Embolism After CT-guided lung biopsy: a case of early diagnosis and successful treatment. *Arch Bronconeumol (Engl Ed).* 2019;55(11):599-600. [\[CrossRef\]](#)
 87. Oh HJ, Jeong WG, Lim Y, et al. Potentially fatal complications of systemic air embolism after computed tomography-guided transthoracic needle biopsy in lung cancer harboring epithelial growth factor receptor mutation: a case report. *Thorac Cancer.* 2020;11(11):3401-3406. [\[CrossRef\]](#)
 88. Ko MA, Lee JH, Jeon SB. Ischemic penumbra and blood-brain barrier disruption in cerebral air embolism. *Am J Respir Crit Care Med.* 2020;201(3):369-370. [\[CrossRef\]](#)
 89. Grandjean F, Galderoux J, Cousin F. Acute Coronary Artery air-embolism after percutaneous lung biopsy. *J Belg Soc Radiol.* 2020;104(1):68. [\[CrossRef\]](#)
 90. Regge D, Gallo T, Galli J, Bertinetti A, Gallino C, Scappaticci E. Systemic arterial air embolism and tension pneumothorax: two complications of transthoracic percutaneous thin-needle biopsy in the same patient. *Eur Radiol.* 1997;7(2):173-175. [\[CrossRef\]](#)
 91. Khatri S. Cerebral artery gas embolism (CAGE) following fine needle aspiration biopsy of the lung. *Aust N Z J Med.* 1997;27(3):338. [\[CrossRef\]](#)
 92. Wong RS, Ketai L, Temes RT, Follis FM, Ashby R. Air embolus complicating transthoracic percutaneous needle biopsy. *Ann Thorac Surg.* 1995;59(4):1010-1011. [\[CrossRef\]](#)
 93. Tolly TL, Feldmeier JE, Czarnecki D. Air embolism complicating percutaneous lung biopsy. *AJR Am J Roentgenol.* 1988;150(3):555-556. [\[CrossRef\]](#)
 94. Baker BK, Awwad EE. Computed tomography of fatal cerebral air embolism following percutaneous aspiration biopsy of the lung. *J Comput Assist Tomogr.* 1988;12(6):1082-1083. [\[CrossRef\]](#)
 95. Cianci P, Posin JP, Shimshak RR, Singzon J. Air embolism complicating percutaneous thin needle biopsy of lung. *Chest.* 1987;92(4):749-751. [\[CrossRef\]](#)
 96. Aberle DR, Gamsu G, Golden JA. Fatal systemic arterial air embolism following lung needle aspiration. *Radiology.* 1987;165(2):351-353. [\[CrossRef\]](#)
 97. Matz S, Segal A, Nemes L, Spitzer S, Atsmon A. Diagnosis of air embolism to the brain by computerized axial tomography. *Comput Tomogr.* 1980;4(2):107-110. [\[CrossRef\]](#)
 98. Omenaas E, Moerkve O, Thomassen L, et al. Cerebral air embolism after transthoracic aspiration with a 0.6 mm (23 gauge) needle. *Eur Respir J.* 1989;2(9):908-910. [\[CrossRef\]](#)
 99. Liu SH, Fu Q, Yu HL, et al. A retrospective analysis of the risk factors associated with systemic air embolism following percutaneous lung biopsy. *Exp Ther Med.* 2020;19(1):347-352. [\[CrossRef\]](#)

100. Jang H, Rho JY, Suh YJ, Jeong YJ. Asymptomatic systemic air embolism after CT-guided percutaneous transthoracic needle biopsy. *Clin Imaging*. 2019;53:49-57. [\[CrossRef\]](#)
101. Ishii H, Hiraki T, Gobara H, et al. Risk factors for systemic air embolism as a complication of percutaneous CT-guided lung biopsy: multicenter case-control study. *Cardiovasc Intervent Radiol*. 2014;37(5):1312-1320. [\[CrossRef\]](#)
102. Kogut M, Linville R, Bastawrous S, Padia S, Maki J, Bhargava P. Systemic air embolization during percutaneous transthoracic needle biopsy: imaging findings, management strategies, and review of the literature. *Clin Pulm Med*. 2012;19(4):188-190. [\[CrossRef\]](#)
103. Thapa J, Varma D, Dalal P, Sitaula S. Hyperbaric oxygen therapy for cerebral artery air embolism- a rare complication of lung biopsy. *Crit Care Med*. 2013;41(12):A337. [\[CrossRef\]](#)
104. Khalid F, Alluri K, Rehman S, Fernainy K, Gupta S. Fatal air embolism following lung biopsy: does needle size really matter? *American Journal of Respiratory and Critical Care Medicine*. 2016;193:A3263. [\[CrossRef\]](#)
105. Martins J, Casimiro C, Tomás J, Mendonc NDM. Cerebral ischemia: potential complication of gas embolism after pulmonar biopsy? *Neuroradiology*. 2012;54(1):91-92. [\[CrossRef\]](#)
106. Wang L, Gao H. A case of percutaneous lung puncture complicating with acute cerebral infarction. *Journal of Intervention Radiology*. 2007;16(11):792. [\[CrossRef\]](#)
107. Luo L, Yu X. A case of secondary air embolism after ct-guided percutaneous pulmonary puncture biopsy and literature review. *Practical Clinical Medicine*. 2015;16(10):22-23. [\[CrossRef\]](#)
108. Song X, Xu X, Lin D, Zhang S. Rescue of secondary air embolism after ct-guided percutaneous pulmonary puncture biopsy: a case report. *Today Nurse*. 2016(09):130-131. [\[CrossRef\]](#)
109. Wu H, Tan K, Liu H. Analysis of 3 cases of serious complications in CT-guided lung puncture biopsy. *Zhejiang Practical Medicine*. 2016;21(3):223-225. [\[CrossRef\]](#)
110. Li C, Liu J, Zhao K. Air embolism secondary to CT-guided puncture biopsy in one patient. *Journal of Interventional Radiology(china)*. 2017;26(7):645-646. [\[CrossRef\]](#)
111. Liu S, Yu H, Fu Q, Tang X, Zhang L, Zhang C. Risk factors of complicated systemic circulation air embolism in CT-guided percutaneous lung biopsy. *Chinese Journal of Interventional Imaging and Therapy*. 2018;15(10):592-596. [\[CrossRef\]](#)
112. Niu D, Li J, Zhao H. CT-guided pulmonary puncture biopsy complicated with circulating air embolism was successfully resuscitated: a case report. *Chinese medical Journal*. 2018;98(8):631-632. [\[CrossRef\]](#)
113. Milano-Johnson D, Weir D, Ashter Y. Cerebral air emboli after percutaneous computed tomography-guided transthoracic needle biopsy of the lung. *Am J Respir Crit Care Med*. 2017;195. [\[CrossRef\]](#)
114. Njuguna N. Coronary air embolism during percutaneous thoracic procedures: recognizing and managing a potentially fatal complication. *Cardiovasc Intervent Radiol*. 2019;42(3):S269. [\[CrossRef\]](#)
115. Shamsid-Deen N, Abidali M, Ardiles T. Performing under pressure: successful recovery after massive left ventricular air embolism using hyperbaric oxygen therapy. *Am J Respir Crit Care Med*. 2017;195:A1982. [\[CrossRef\]](#)
116. Espinal A, Bendor-Grynbaum C, Shankar S, et al. Arterial air embolism causing hemiplegia in a patient who underwent ir-guided lung biopsy. *Crit Care Med*. 2019;47(1):517. [\[CrossRef\]](#)
117. Glodny B, Schönherr E, Freund MC, et al. Measures to prevent air embolism in transthoracic biopsy of the lung. *AJR Am J Roentgenol*. 2017;208(5):W184-W191. [\[CrossRef\]](#)
118. Monnin-Bares V, Chassagnon G, Vernhet-Kovacsik H, et al. Systemic air embolism depicted on systematic whole thoracic CT acquisition after percutaneous lung biopsy: incidence and risk factors. *Eur J Radiol*. 2019;117:26-32. [\[CrossRef\]](#)
119. West JB, Dollery CT, Naimark A. Distribution of blood flow in isolated lung: relation to vascular and alveolar pressures. *J Appl Physiol*. 1964;19:713-724. [\[CrossRef\]](#)
120. Naidich DP, Bankier AA, MacMahon H, et al. Recommendations for the management of subsolid pulmonary nodules detected at CT: a statement from the Fleischner Society. *Radiology*. 2013;266(1):304-317. [\[CrossRef\]](#)
121. Bhatia S. Systemic air embolism following CT-guided lung biopsy. *J Vasc Interv Radiol*. 2009;20(6):709-711. [\[CrossRef\]](#)
122. Wu CC, Maher MM, Shepard JA. Complications of CT-guided percutaneous needle biopsy of the chest: prevention and management. *AJR Am J Roentgenol*. 2011;196(6):W678-W682. [\[CrossRef\]](#)

Supplementary Table 1. Characteristics of studies included in the systematic review

| No | Studies | Country | Study design | No of patients with air embolism | Age (years) | Gender | Symptomatic | Outcomes |
|----|--|-------------|--------------|----------------------------------|-------------|----------|-------------|----------------------------|
| 1 | Wu et al. ¹³ 2012 | China | Case report | 1 | NA | F | No | Without sequelae |
| 2 | Kawaji et al. ¹⁴ 2012 | Japan | Case report | 1 | 77 | M | Yes | Without sequelae |
| 3 | Dalal and Varma ¹⁵ 2012 | U.S.A. | Case report | 1 | 46 | M | No | Without sequelae |
| 4 | Al-Ali et al. ¹⁶ 2012 | New Zealand | Case report | 1 | 54 | F | Yes | With sequelae |
| 5 | Thomas et al. ¹⁷ 2011 | India | Case report | 1 | 25 | F | Yes | Died |
| 6 | Singh et al. ¹⁸ 2011 | U.S.A. | Case report | 1 | 75 | M | Yes | Without sequelae |
| 7 | Shroff et al. ¹⁹ 2011 | U.S.A. | Case report | 1 | 58 | M | Yes | Died |
| 8 | Mokart et al. ²⁰ 2011 | NA | Case report | 1 | 57 | M | Yes | Without sequelae |
| 9 | Kuo et al. ²¹ 2010 | China | Case series | 2 | 44, 74 | M | 1 yes, 1 no | Without sequelae |
| 10 | Cheng et al. ²² 2010 | China | Case report | 1 | 35 | M | 1 | Died |
| 11 | Bou-Assaly et al. ²³ 2010 | U.S.A. | Case report | 1 | 76 | M | Yes | Died |
| 12 | Um et al. ²⁴ 2009 | Korea | Case series | 4 | 40–75 | 3 M, 1 F | Yes | 2 without sequelae, 2 died |
| 13 | Ishikawa et al. ²⁵ 2009 | Japan | Case report | 1 | 51 | M | Yes | Without sequelae |
| 14 | Hsi et al. ²⁶ 2009 | U.S.A. | Case report | 1 | 67 | M | Yes | Without sequelae |
| 15 | Ibukuro et al. ²⁷ 2009 | Japan | Case report | 3 | 59–72 | 1 M, 2 F | Yes | Without sequelae |
| 16 | Bhatia ²⁸ 2009 | U.S.A. | Case report | 1 | NA | F | Yes | Without sequelae |
| 17 | Tomabechei et al. ²⁹ 2008 | Japan | Case report | 1 | 71 | M | Yes | Without sequelae |
| 18 | Kau et al. ³⁰ 2008 | Austria | Case report | 1 | 50 | M | Yes | With sequelae |
| 19 | Hiraki et al. ³¹ 2007 | Japan | Case report | 1 | 69 | F | Yes | With sequelae |
| 20 | Ghafoori and Varedi ³² 2008 | Iran | Case report | 1 | 50 | F | Yes | Died |
| 21 | Lattin et al. ³³ 2006 | U.S.A. | Case report | 1 | 47 | M | No | Without sequelae |
| 22 | Mansour et al. ³⁴ 2005 | Jordan | Case report | 1 | 52 | M | Yes | NA |
| 23 | Chakravarti et al. ³⁵ 2004 | India | Case report | 1 | 63 | M | Yes | NA |
| 24 | Ashizawa et al. ³⁶ 2004 | Japan | Case report | 1 | 65 | M | Yes | Without sequelae |
| 25 | Mokhlesi et al. ³⁷ 2002 | U.S.A. | Case report | 1 | 77 | M | Yes | Without sequelae |
| 26 | Arnold and Zwiebel ³⁸ 2002 | U.S.A. | Case report | 1 | 60 | M | Yes | Died |
| 27 | Ohashi et al. ³⁹ 2001 | Japan | Case report | 1 | 75 | M | Yes | Without sequelae |
| 28 | King et al. ⁴⁰ 2013 | U.S.A. | Case report | 1 | 60 | M | Yes | With sequelae |
| 29 | Kok et al. ⁴¹ 2013 | Ireland | Case report | 1 | 83 | F | Yes | Without sequelae |
| 30 | Shi et al. ⁴² 2013 | China | Case report | 1 | 85 | M | Yes | With sequelae |
| 31 | Chang and Yang ⁴³ 2018 | China | Case report | 1 | 73 | M | No | Without sequelae |
| 32 | Smit et al. ⁴⁴ 2013 | Netherlands | Case report | 1 | 71 | M | Yes | Without sequelae |
| 33 | Suzuki et al. ⁴⁵ 2013 | Japan | Case report | 1 | 75 | F | Yes | Without sequelae |
| 34 | Franke et al. ⁴⁶ 2014 | Germany | Case report | 1 | 69 | M | Yes | Died |
| 35 | Ramaswamy et al. ⁴⁷ 2014 | U.S.A. | Case report | 1 | 75 | F | Yes | Without sequelae |
| 36 | Shin et al. ⁴⁸ 2014 | Korea | Case report | 1 | 70 | F | Yes | Without sequelae |
| 37 | Hung et al. ⁴⁹ 2015 | China | Case report | 1 | 63 | M | Yes | Without sequelae |
| 38 | Olgun et al. ⁵⁰ 2015 | Turkey | Case report | 1 | 69 | M | Yes | Without sequelae |
| 39 | Pando Sandoval et al. ⁵¹ 2015 | Spain | Case series | 2 | 67, 69 | M | Yes | With sequelae |
| 40 | Rocha et al. ⁵² 2015 | Brazil | Case report | 1 | NA | NA | Yes | With sequelae |
| 41 | Kazimirko et al. ⁵³ 2016 | America | Case report | 1 | 65 | M | Yes | Without sequelae |
| 42 | Sun et al. ⁵⁴ 2015 | China | Case report | 1 | 53 | F | Yes | Died |
| 43 | Rahman et al. ⁵⁵ 2016 | U.S.A. | Case report | 1 | 82 | F | Yes | Without sequelae |
| 44 | Yamamoto et al. ⁵⁶ 2016 | Japan | Case report | 1 | 74 | F | Yes | Without sequelae |
| 45 | Fintelmann et al. ⁵⁷ 2017 | England | Case report | 1 | 75 | M | Yes | Died |
| 46 | Fiore et al. ⁵⁸ 2017 | Brazil | Case report | 1 | 57 | F | Yes | Without sequelae |

Supplementary Table 1. Continued

| | | | | | | | | |
|----|---------------------------------------|-------------|---------------|----|-------|-------------|----------------|---|
| 47 | Galvis et al. ⁵⁹ 2017 | U.S.A. | Case report | 1 | 60 | M | Yes | Without sequelae |
| 48 | Ialongo et al. ⁶⁰ 2017 | Italy | Case report | 1 | 57 | M | Yes | Died |
| 49 | April et al. ⁶¹ 2017 | U.S.A. | Case report | 1 | 65 | M | No | Without sequelae |
| 50 | Kukuljan et al. ⁶² 2018 | Croatia | Case report | 1 | 60 | NA | Yes | Without sequelae |
| 51 | Lang et al. ⁶³ 2018 | Austria | Case report | 1 | 69 | M | Yes | Without sequelae |
| 52 | Ren and Zavodni ⁶⁴ 2018 | Canada | Case report | 1 | 68 | F | Yes | Without sequelae |
| 53 | Ornelas et al. ⁶⁵ 2018 | Spain | Case report | 1 | 70 | F | Yes | NA |
| 54 | Matsuura et al. ⁶⁶ 2017 | Japan | Case report | 1 | 74 | M | Yes | Without sequelae |
| 55 | Sakatani et al. ⁶⁷ 2018 | Japan | Case report | 1 | 72 | M | Yes | Without sequelae |
| 56 | Tavare et al. ⁶⁸ 2018 | England | Case report | 1 | 58 | M | Yes | Without sequelae |
| 57 | Viqas et al. ⁶⁹ 2018 | Pakistan | Case report | 1 | 67 | M | Yes | With sequelae |
| 58 | Abid et al. ⁷⁰ 2018 | U.S.A. | Case report | 1 | 61 | M | Yes | Without sequelae |
| 59 | Beliaev et al. ⁷¹ 2019 | New Zealand | Case report | 1 | 69 | M | Yes | With sequelae |
| 60 | Edwards et al. ⁷² 2017 | England | Case report | 1 | 75 | M | Yes | Died |
| 61 | Li et al. ⁷³ 2019 | China | Case report | 1 | 50 | F | Yes | Died |
| 62 | Lonni and Ceruti ⁷⁴ 2019 | NA | Case report | 1 | 70 | M | Yes | Without sequelae |
| 63 | Marchak et al. ⁷⁵ 2019 | U.S.A. | Case report | 1 | 78 | F | Yes | Without sequelae |
| 64 | De Oliveira et al. ⁷⁶ 2019 | Brazil | Case report | 1 | 69 | M | Yes | Died |
| 65 | Deshmukh et al. ⁷⁷ 2019 | India | Case report | 1 | 52 | M | Yes | Without sequelae |
| 66 | El Homsy et al. ⁷⁸ 2019 | Lebanon | Case report | 1 | 57 | M | Yes | Without sequelae |
| 67 | Hellinger et al. ⁷⁹ 2019 | Germany | Case report | 1 | 74 | M | Yes | NA |
| 68 | Hare et al. ⁸⁰ 2011 | France | Case series | 4 | 63–73 | 2 W, 2 F | 2 yes, 2 no | Without sequelae |
| 69 | Warren et al. ⁸¹ 2019 | U.S.A. | Case report | 1 | 60 | M | Yes | Without sequelae |
| 70 | Rott and Boecker ⁸² 2014 | Germany | Case report | 1 | 57 | M | Yes | With sequelae |
| 71 | Lederer et al. ⁸³ 2011 | Austria | Case report | 1 | 27 | M | No | Without sequelae |
| 72 | Khalid et al. ⁸⁴ 2018 | U.S.A. | Case report | 1 | 61 | M | Yes | Without sequelae |
| 73 | Tomiya et al. ⁸⁵ 2006 | Japan | Case series | 6 | 57–75 | 4 M, 2 F | Yes | 1 died, 1 with sequelae, 4 without sequelae |
| 74 | Piccoli et al. ⁸⁶ 2019 | Italy | Case report | 1 | 36 | M | Yes | Without sequelae |
| 75 | Oh et al. ⁸⁷ 2020 | Korea | Case report | 1 | 81 | M | Yes | With sequelae |
| 76 | Ko et al. ⁸⁸ 2019 | Korea | Case report | 1 | 78 | M | Yes | NA |
| 77 | Grandjean et al. ⁸⁹ 2020 | France | Case report | 1 | 62 | M | Yes | Without sequelae |
| 78 | Regge et al. ⁹⁰ 1997 | Italy | Case report | 1 | 40 | F | Yes | Without sequelae |
| 79 | Khatri ⁹¹ 1997 | Italy | Case report | 1 | 54 | M | Yes | Without sequelae |
| 80 | Wong et al. ⁹² 1995 | U.S.A. | Case report | 1 | 62 | M | Yes | With sequelae |
| 81 | Tolly et al. ⁹³ 1988 | U.S.A. | Case report | 1 | 32 | M | Yes | With sequelae |
| 82 | Baker and Awwad ⁹⁴ 1988 | U.S.A. | Case report | 1 | 39 | M | Yes | NA |
| 83 | Cianci et al. ⁹⁵ 1987 | U.S.A. | Case report | 1 | 63 | F | Yes | With sequelae |
| 84 | Aberle et al. ⁹⁶ 1987 | U.S.A. | Case report | 1 | 60 | M | Yes | Died |
| 85 | Matz et al. ⁹⁷ 1980 | Israel | Case report | 1 | 70 | M | Yes | Died |
| 86 | Omenaas et al. ⁹⁸ 1989 | Norway | Case report | 1 | 54 | M | Yes | Without sequelae |
| 87 | Liu et al. ⁹⁹ 2020 | China | Retrospective | 19 | NA | NA | 3 yes, 16 no | Without sequelae |
| 88 | Jang et al. ¹⁰⁰ 2019 | Korea | Retrospective | 9 | 55–74 | 6 M, 3 F | 2 yes, 7 no | 1 without and 8 with sequelae |
| 89 | Ishii et al. ¹⁰¹ 2014 | Japan | Case control | 10 | 53–80 | 5 M and 5 F | 5 yes and 5 no | 1 without and 9 with sequelae |
| 90 | Kogut et al. ¹⁰² 2012 | U.S.A. | Case report | 1 | 76 | M | Yes | Without sequelae |
| 91 | Thapa et al. ¹⁰³ 2013 | U.S.A. | Case report | 1 | 66 | M | Yes | NA |
| 92 | Khalid et al. ¹⁰⁴ 2016 | U.S.A. | Case report | 1 | 76 | M | Yes | NA |
| 93 | Martins et al. ¹⁰⁵ 2012 | Portugal | Case report | 1 | 64 | M | Yes | Without sequelae |
| 94 | Wang and Gao ¹⁰⁶ 2007 | China | Case report | 1 | 29 | M | Yes | With sequelae |

Supplementary Table 1. Continued

| | | | | | | | | |
|-----|---|--------|-------------|---|----|---|-----|------------------|
| 95 | Luo and Yu ¹⁰⁷ 2015 | China | Case report | 1 | 58 | M | Yes | Without sequelae |
| 96 | Song et al. ¹⁰⁸ 2016 | China | Case report | 1 | 58 | M | Yes | Without sequelae |
| 97 | Wu et al. ¹⁰⁹ 2016 | China | Case report | 1 | 57 | M | Yes | With sequelae |
| 98 | Li ¹¹⁰ 2017 | China | Case report | 1 | 60 | M | Yes | Without sequelae |
| 99 | Liu et al. ¹¹¹ 2018 | China | Case report | 1 | 67 | F | Yes | Without sequelae |
| 100 | Niu et al. ¹¹² 2018 | China | Case report | 1 | 58 | M | Yes | With sequelae |
| 101 | Milano-Johnson et al. ¹¹³ 2017 | U.S.A. | Case report | 1 | 65 | M | Yes | NA |
| 102 | Njuguna ¹¹⁴ 2019 | U.S.A. | Case report | 1 | 60 | M | Yes | Died |
| 103 | Shamsid-Deen et al. ¹¹⁵ 2017 | U.S.A. | Case report | 1 | 80 | M | Yes | Without sequelae |
| 104 | Espinal et al. ¹¹⁶ 2019 | U.S.A. | Case report | 1 | 70 | F | Yes | NA |

NA, not applicable; male; F, female.

Supplementary Table 2. Characteristics of the studies included for quantitative meta-analysis

| Studies | Country | Study design | Patients with air embolism | Patients without air embolism | Overall quality |
|---|---------|---------------|----------------------------|-------------------------------|-----------------|
| Liu et al. ⁹⁹ 2020 | China | Retrospective | 19 | 2.007 | 7 |
| Jang et al. ¹⁰⁰ 2019 | Korea | Retrospective | 9 | 1.005 | 7 |
| Ishii et al. ¹⁰¹ 2014 | Japan | Case control | 10 | 2.206 | 7 |
| Monnin-Bares et al. ¹¹⁸ 2019 | France | Retrospective | 24 | 532 | 7 |
| Glodny et al. ¹¹⁷ 2017 | Austria | Retrospective | 25 | 1.853 | 7 |

Supplementary Table 3. Clinical symptoms and signs of patients with air embolism following computed tomography-guided percutaneous transthoracic lung needle biopsy

| Clinical symptoms and signs | Number of patients (%) |
|--|------------------------|
| Asymptomatic | 35 (22.73) |
| Unconscious or unresponsive state | 46 (29.87) |
| Hemiplegia | 25 (16.23) |
| Cardiopulmonary arrest | 22 (14.29) |
| Hypotension | 22 (14.29) |
| Chest pain | 17 (11.04) |
| Arrhythmia | 14 (9.09) |
| Hemianopsia or conjugate eye deviation | 11 (7.14) |
| ST segment elevation | 10 (6.49) |
| Seizure | 9 (5.84) |
| Aphasia or facioplegia | 8 (5.819) |
| Bradycardia | 9 (5.84) |
| Dyspnea | 6 (3.90) |
| Dizziness | 5 (3.25) |
| Hypertension | 4 (2.60) |
| Tachycardia | 2 (1.30) |
| Urine incontinence | 3 (1.95) |
| Tachypnea | 2 (1.30) |
| Abdominal pain | 2 (1.30) |
| Pulselessness | 2 (1.30) |
| Altered mental status | 1 (0.65) |

Supplementary Table 4. Air location in patients with air embolism following computed tomography-guided percutaneous transthoracic lung needle biopsy

| Location | Number of patients (%) |
|---------------------------|------------------------|
| Left ventricle | 69 (44.81) |
| Aorta | 63 (40.91) |
| Cerebral artery | 46 (29.87) |
| Coronary artery | 35 (22.73) |
| Left atrium | 23 (14.94) |
| Pulmonary vein | 11 (7.14) |
| Right atrium | 4 (2.60) |
| Right ventricle | 3 (1.95) |
| Pulmonary artery | 3 (1.95) |
| Renal artery | 1 (0.65) |
| Intercostal artery | 1 (0.65) |
| Spinal cord artery | 1 (0.65) |
| Superior vena vein | 1 (0.65) |
| Subclavian vein | 1 (0.65) |
| Vertebral artery | 1 (0.65) |
| Subclavian artery | 1 (0.65) |
| Vertebral artery | 1 (0.65) |
| Left subclavian artery | 1 (0.65) |
| Truncus brachiocephalicus | 1 (0.65) |
| Internal carotid artery | 1 (0.65) |
| Unclear | 7 (4.55) |



Technical success and associated economic implications of conventional re-entry devices in subintimal recanalization of femoro-popliteal chronic total occlusions

Katharina Rippel

Hannes Ruhnke

Bertram Jehs

Thomas Kroencke

Christian Scheurig-Muenkler

PURPOSE

Re-entry devices contribute to the high success rate of subintimal recanalization of chronic total occlusions (CTO). However, to date, there are no studies comparing the available conventional re-entry devices concerning the impact of their technical success on economic aspects, as these devices differ greatly in their acquisition costs. This prospective observational study intends to contribute to this question.

METHODS

Prior to the start of the prospective study, all previous applications of the Outback® in femoro-popliteal CTO since its introduction to our hospital were analyzed retrospectively (n = 31). From June 2018 until January 2020, all patients with femoro-popliteal CTO treated with clear subintimal recanalization were included (n = 109). In the case of failed spontaneous re-entry, either the OffRoad® (study arm I, n = 20) or the Enteer® catheter (study arm II, n = 20) was used. If assisted re-entry failed, the Outback® device was used as a bailout. Baseline demographic and clinical data, morphologic characteristics, and technical success were documented. Additional per-patient costs due to the use of re-entry devices were analyzed.

RESULTS

A retrospective evaluation of all Outback® applications revealed a technical success rate of 97% (30/31). In the prospective study, 63% (68/109) were successfully treated without using re-entry devices. The overall procedural success was 95% (103/109). In study arm I, the OffRoad® achieved a success rate of 45% (9/20), with a subsequent successful application of the Outback® in 80% (8/10) of the failed cases. In study arm II, the Enteer® was successfully employed in 60% (12/20) of cases, and the Outback® was then used successfully in a further 62% (5/8) of cases. Too large a distance between the device and the target lumen was a knockout criterion for all tested devices, leading to a subgroup analysis with the exclusion of three cases, resulting in a success rate of 47% for the OffRoad® and 67% for the Enteer® device. Furthermore, in severe calcification, only the Outback® reliably enabled revascularization. Significant savings of almost €600 were only achieved in study arm II according to German prices.

CONCLUSION

With proper patient selection, a gradual approach with the Enteer® as the primarily used device, with the Outback® used additionally in case of failure, leads to significant savings and can be recommended. In severe calcification, the Outback® should be used as the primary device.

KEYWORDS

Outback®, Enteer®, OffRoad®, re-entry device, economic evaluation, subintimal angioplasty, femoro-popliteal, chronic total occlusion

From the Clinic of Diagnostic and Interventional Radiology (K.R. ✉ katharina.rippel@uk-augsburg.de, H.R., B.J., T.K., C.S.-M.), University Hospital Augsburg, Augsburg, Germany.

Received 08 November 2021; revision requested 20 December 2021; last revision received 23 February 2022; accepted 07 March 2022.



Epub: 13.02.2023

Publication date: 30.05.2023

DOI: 10.4274/dir.2022.221107

You may cite this article as: Rippel K, Ruhnke H, Jehs B, Kroencke T, Scheurig-Muenkler C. Technical success and associated economic implications of conventional re-entry devices in subintimal recanalization of femoro-popliteal chronic total occlusions. *Diagn Interv Radiol.* 2023;29(3):492-499.

The number of patients requiring interventional treatment for symptomatic peripheral artery disease (PAD) has been rising continuously over recent years.¹ Therefore, a large number of angioplasties for the treatment of chronic total occlusions (CTO) end up being subintimal revascularizations. In about 20% of all subintimal recanalizations of femoro-popliteal arteries, spontaneous re-entry into the true lumen distally to the CTO may fail and thus jeopardizes a successful revascularization.² As well as retrograde access, re-entry catheters have shown to be helpful in this regard.^{3,4} The high acquisition costs, however, deter many potential users. But ultimately, an unsuccessful, aborted recanalization with a subsequent second attempt or bypass surgery is more expensive for the healthcare system than the use of a re-entry device in selected cases. In this regard, the Outback® catheter (Cordis – a Cardinal Health company, Santa Clara, CA, USA) has been the first available system on the market since 2003, and there are several studies on femoro-popliteal subintimal revascularization confirming a technical success rate clearly exceeding 90%.^{4,5} In 2012, the Enteer® catheter (Medtronic, Minneapolis, MN, USA) was released with a published success rate of 86%.⁶ Finally, in 2013, the OffRoad® catheter (Boston Scientific, Marlborough, MA, USA) followed with a technical success rate of 84.8%.⁷ These three conventional re-entry devices differ much greater in their acquisition costs than in their stated effectiveness, implying a great potential for savings. So far, there are no studies comparing the potential economic savings of the catheters, as well as their technical efficiency and limitations in this regard.

Methods

The institutional review board approved the conduction of this study and the subsequent analysis of anonymized patient data (BKF-A-2018-11) and waived the need for informed consent. The study was performed concordantly with the ethical standards of

Main points

- When primarily using the Enteer® catheter for device-assisted re-entry in femoro-popliteal occlusions, a relevant and significant cost reduction can be achieved per patient.
- When treating heavily calcified re-entry sites, the Outback® device has a clear advantage over the other tested re-entry devices.
- For a large distance to the true lumen due to a wide dissection, all tested re-entry devices show distinct weaknesses and should be omitted.

the 1946 Declaration of Helsinki and its later amendments.

Introduction of the devices

The OffRoad® system consists of a 6F catheter with a pear-shaped 5.4 mm positioning balloon at the tip for alignment within the dissection and direction of the tip towards the true lumen. A separately supplied microcatheter lancet with a narrow lumen sufficient for a 0.014" wire is inserted coaxially. The balloon catheter can be guided to the target position via a 0.035" wire. However, the exceptionally poor crossing profile at the catheter tip regularly necessitates pre-dilation of the passed occlusion. After positioning the catheter tip in the desired position and inflation of the balloon, the puncture is made with the lancet, and finally, the further course of the vessel is probed with the 0.014" wire. The needle can be bent slightly at the tip for better targeting.

In contrast to this, the Enteer® device is advanced over 0.014" or 0.018" wires. The crossing profile is comparable to standard 0.018" balloons and thus optimal for the passage of even long, complex occlusions regularly without pre-dilation. The distal end of the catheter is positioned within the dissection parallel to the target lumen. After the inflation of the flat-shaped balloon at the tip of the catheter for its self-orientation, re-entry ensues using the 0.018" Enteer® guidewire. Its short, angled tip allows the selection of the appropriate side hole on the side of the balloon facing the true lumen. The guidewire is available in three degrees of stiffness (flexible, standard, and stiff). During this study, we regularly used the stiff guidewire for penetrating the dissection membrane.

The Outback® catheter is advanced to the desired re-entry site using a 0.014" wire. Due to the adequately shaped profile and the stiff catheter shaft, the catheter can usually be advanced without pre-dilation. Positioned parallel to the true lumen, the catheter tip is correctly aligned under fluoroscopy at two projection angles, once with the catheter in overlay with the target vessel and once with the catheter and target vessel exactly parallel to each other. A needle is then deployed laterally, and the target lumen is punctured. This system offers the best direct control of the direction of puncture. However, the Outback® catheter shows a clear disadvantage for crossover maneuvers in steep aortic bifurcations due to its rigid catheter, which either tends to break in extreme cases just below the stiff deployment site of the needle (Outback® Elite) or is just not able to cross the bi-

furcation (Outback® LTD). This restriction has already been detailed by Raskin et al.⁸

All procedures were performed by one of three experienced interventionalists with at least six successful applications of the Outback® catheter in femoro-popliteal CTO. Prior to the first use of the OffRoad® and the Enteer® device in the context of this study, all interventionalists were instructed by a product specialist, and the first three applications for each device were performed in the presence of at least two of the interventionalists. No initial application was carried out by a sole individual.

Economic considerations

The potential economic savings for the initial application of either the OffRoad® or the Enteer® device in contrast to the solitary utilization of the Outback® catheter were calculated. Since the economic break-even point depends on the prices, the formula »*price of competitor * 100/price of Outback®*« can be used to calculate the needed success rate for the economically sensible use of different devices. When using the offered prices in Germany (Outback®, €1,700; OffRoad®, €795; Enteer®, €540; all before tax), the break-even point for the Enteer® device equates to a success rate of 32%, while the OffRoad® needs a success rate of 47%. With published technical success rates beyond 80%, relevant savings should be achievable with both systems.

Retrospective evaluation

The prospective observational study was preceded by a retrospective evaluation of the experience with the Outback®. All consecutive patients who had ever been treated with the Outback® re-entry device in the setting of percutaneous subintimal recanalization of femoro-popliteal CTO since its introduction to this tertiary hospital in December 2015 were included. For every patient, the demographic baseline data, lesion characteristics, and technical success rate of the device were noted.

Prospective analysis

The prospective observational part of the study started in June 2018 and lasted until January 2020. In those 20 months, all consecutive patients presenting with a femoro-popliteal CTO, who were treated with a percutaneous subintimal recanalization, were included, whether or not a re-entry catheter was used. No hybrid procedures were included. The exclusion criteria were luminal pas-

sage of the occlusion, previous interventions with the necessity of femoro-popliteal placement of stents or stent grafts, or any previous angioplasty of the target lesion within the three months before the index procedure. Acute or subacute occlusion with a sudden onset of symptoms consistent with arterial thrombosis or thromboembolism were also excluded. Except for these exclusions, all consecutive interventions were included and documented in detail. In the case of unsuccessful primary re-entry with the standard wire techniques, a re-entry device was used in the distal femoral or popliteal artery. For the first 20 patients (study arm I), the OffRoad® catheter was used, while the following 20 patients (study arm II) were treated with the Enteer® catheter. In the case of failure of assisted re-entry, the Outback® catheter was employed as a bailout. The patient collection started with the first OffRoad® device being used and was completed after the inclusion of the twentieth patient being treated with the Enteer® re-entry device. Figure 1 illustrates the course of the study as a flowchart.

Baseline and procedural characteristics

For all patients, demographic baseline data, relevant comorbidities, and clinical stage of PAD according to the Rutherford classification were documented. In addition, lesion characteristics such as location; length; the degree of calcification documented as none, mild (<25% circumference), moderate (25%–50%), or severe (>50%); the level of re-entry to the true lumen; and the time until spontaneous re-entry were noted.⁹ The technical success of the re-entry maneuver itself, either with or without a re-entry de-

vice, as well as the overall procedural success defined as successful target vessel recanalization, were documented. Furthermore, in the case of an assisted re-entry, the time until successful re-entry was noted (time from insertion of the device until successful access to the true lumen with the 0.014" wire in minutes). Subgroup analyses were performed after excluding patients in whom a re-entry catheter was foreseen to fail before use and in all patients with severe re-entry site calcification. Device-related complications were documented and classified according to the Society of Interventional Radiology Classification System for Complications by Outcome.

Procedure

All procedures were performed in a standard angiography suite using a Philips Allura Xper FD20 angiography system (Philips Healthcare, Best, The Netherlands). All procedures were conducted percutaneously. Whenever possible, an antegrade approach via the ipsilateral common femoral artery was chosen with the placement of a 6 or 7 French sheath. If an antegrade approach was not possible due to obesity or a proximal start of the occlusion, a retrograde approach via the contralateral common femoral artery and subsequent crossover maneuver was chosen. A 45 cm long, 6 French Destination® (Terumo Corporation, Tokyo, Japan) or Fortress® (Biotronik, Berlin, Germany) sheath was introduced and used as access to the target lesion.

Under roadmap guidance, subintimal probing of the occluded vessel segment was performed using either a diagnostic catheter with a short angled tip (Cordis® Tempo® Vertebral Catheter, Cordis, a Cardinal Health Company, Santa Clara, CA, USA) in combination with a 0.035" hydrophilic guidewire (Radiofocus® Guidewire M Standard Type, Terumo Corporation, Tokyo, Japan) or a low-profile support catheter (0.018" Trail-Blazer™, Medtronic, Minneapolis, MN, USA) combined with a 0.018" CTO wire (Hi-Torque Command ES guidewire, Abbott, Chicago, IL, USA). The time after passage of the CTO, either until successful spontaneous re-entry or until the decision to introduce a re-entry device, was noted. In the first 20 patients, the OffRoad® catheter was used, and in the following 20 patients, the Enteer® catheter was used. In a case of failed assisted re-entry with either of these systems, the Outback® catheter was used as a bailout tool.

After successful re-entry balloon angioplasty and in the case of residual stenosis due to dissection, recoil, or heavy calcification, self-expandable nitinol stents or stent grafts (Innova®, Boston Scientific, Marlborough, MA, USA; GORE® VIABAHN® and TIGRIS®, W. L. Gore & Associates, Inc., Newark, DE, USA; Supera®, Abbott Vascular, Santa Clara, CA, USA; Astron Pulsar®, Biotronik, Berlin, Germany) were deployed to secure the result. The number of stents and stent grafts used to treat the lesion was documented.

Statistical analysis

Demographic and clinical baseline data are presented as means with corresponding standard deviations (SD) for metric variables and with absolute counts and percentages for nominal variables. Baseline variables were compared between the retrospective and the prospective cohort as well as between the two study arms using the t-test for unpaired samples for all metric variables and the chi-square test for nominal variables. For the latter, categories of lesion and re-entry site calcification were simplified to none, mild, and moderate vs. severe. The performance of the two OffRoad® and Enteer® re-entry devices was compared with the overall performance of the study arm determined by the combined success rate of the Outback® or the Enteer® device and the occasionally necessary subsequent use of the Outback® catheter. The chi-square test was used for this purpose. The cost-benefit of the primary use of either of the two systems studied was then investigated. The actual additional per-patient costs caused by using one or two re-entry devices were compared with the fictitious costs that would have been incurred by the primary and sole use of the more expensive

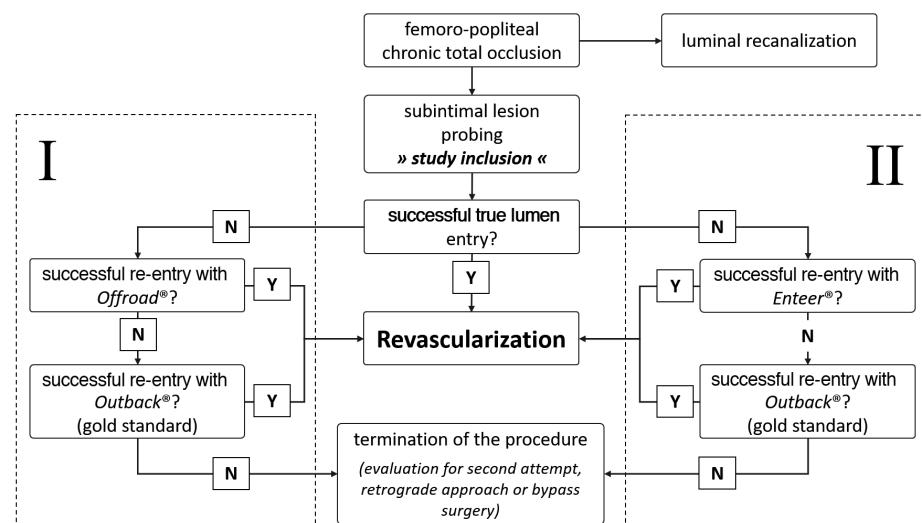


Figure 1. Illustration of the course of the prospective block-randomized study with the OffRoad® catheter used in study arm I and the Enteer® catheter used in study arm II. Each study arm includes 20 lesions that required the use of a corresponding re-entry device. Y, yes; N, no.

Outback® device. The comparison was made using the Mann–Whitney U test.

Results

Retrospective analysis

Since its introduction in our clinic in December 2015 and before the start of the prospective study in June 2018, 31 lesions in 31 patients were treated with the Outback® device during subintimal revascularization of femoro-popliteal CTO. Table 1 shows the demographic baseline data and lesion characteristics for the included patients. The deployment of the Outback® re-entry device was successful in 30 patients, resulting in a technical success rate of 97%. This justified its definition as a gold standard in the context of this study.

Prospective analysis

Table 1 offers basic demographic data for all enrolled patients as well as for each study arm separately. There were no statistically significant differences between the retro-

spective and prospective cohort in general in terms of patient age, lesion length, and lesion, as well as re-entry site calcification. However, in the prospective cohort, target lesion and re-entry site calcifications were significantly more often severe in the study arms, necessitating the use of re-entry catheters compared to those patients with spontaneous re-entry ($P < 0.010$).

An unassisted re-entry could be achieved in 68 of 109 treatments, which amounts to a primary procedural success rate of 63%. The average time until spontaneous re-entry was 1.7 min (SD: 5.1). In one case, the passage of the chronic artery occlusion was not possible due to massive calcification and was counted as primary procedural failure (0.9%). We deemed spontaneous re-entry a failure after an average of 6.7 min (SD: 5.6) of probing and proceeded with the use of a re-entry device.

Figure 2 offers an overview of the results regarding the technical and procedural success. The OffRoad® was successfully deployed in 9/20 (45%) cases with an average time until successful re-entry of 12.5 min (SD:

6.4). In the case of failure of the OffRoad®, the Outback® catheter ensured success in another 8/10 (80%) procedures after a mean total time from the use of the first device until re-entry of 15.2 min (SD: 12.9). During one procedure, re-entry was achieved spontaneously further distal from the originally chosen re-entry site after an unsuccessful attempt with the OffRoad® device and before using the Outback® catheter according to the study protocol. The Enteer® re-entry device was successfully used in 12/20 (60%) patients. Another 5/8 (63%) re-entries could be achieved by the usage of the Outback® catheter. The average time until successful re-entry was 6.65 min (SD: 6.4) for the Enteer® catheter and 8.25 min (SD: 12.9) when the additional use of the Outback® catheter was necessary. The technical success rate for the OffRoad® catheter was significantly worse than the overall performance after additional use of the Outback® catheter in study arm I ($P = 0.003$). The success rate of the Enteer® catheter only narrowly missed that significance level in study arm II ($P = 0.077$).

Table 1. Demographic baseline data

| | | Retrospective cohort | | Prospective cohort | | P values* | |
|---------------------------------------|----------|----------------------|-----------------|----------------------|------------------------|-------------|------------------------|
| | | Outback® | Complete cohort | Spontaneous re-entry | Study arm I (OffRoad®) | | Study arm II (Enteer®) |
| Number of patients | | 31 | 99 | 60 | 19 | 20 | - |
| Number of lesions | | 31 | 109 | 69 | 20 | 20 | - |
| Age in years given as mean (SD) | | 75 (9.1) | 74.2 (9.7) | 73.1 (9.7) | 74.6 (10.1) | 74.2 (9.3) | 0.674/0.207 |
| Sex (M:F) | | 15:16 | 67:32 | 49:20 | 13:7 | 11:9 | 0.052/0.519 |
| Rutherford stage | | - | - | - | - | - | 0.522/0.381 |
| | 1 | 0 (0) | 1 (1) | 1 (1.5) | 0 (0) | 0 (0) | - |
| | 2 | 2 (7) | 2 (2) | 1 (1.5) | 0 (0) | 1 (5) | - |
| | 3 | 13 (42) | 36 (33) | 25 (36) | 8 (40) | 3 (15) | - |
| | 4 | 3 (11) | 15 (14) | 9 (13) | 3 (15) | 3 (15) | - |
| | 5 | 10 (33) | 40 (36) | 24 (35) | 7 (35) | 9 (55) | - |
| | 6 | 2 (7) | 15 (14) | 9 (13) | 2 (10) | 4 (20) | - |
| Lesion length (cm) given as mean (SD) | | 17.5 (9.5) | 18.1 (10.7) | 17.4 (10.6) | 16.9 (9.2) | 19.9 (12.1) | 0.815/0.361 |
| Target lesion calcification | | - | - | - | - | - | 0.120/0.197 |
| None | | 5 (16) | 25 (23) | 18 (26) | 3 (15) | 4 (20) | - |
| | Mild | 13 (42) | 28 (26) | 27 (39) | 1 (5) | 0 (0) | - |
| | Moderate | 7 (23) | 19 (17) | 10 (15) | 6 (30) | 2 (10) | - |
| | Severe | 6 (19) | 37 (34) | 14 (20) | 10 (50) | 14 (70) | - |
| Calcification of re-entry site | | - | - | - | - | - | 0.883/1 |
| None | | 6 (19) | 27 (25) | 20 (29) | 3 (15) | 4 (20) | - |
| | Mild | 14 (45) | 31 (28) | 27 (39) | 2 (10) | 2 (10) | - |
| | Moderate | 4 (13) | 25 (23) | 13 (19) | 6 (30) | 5 (25) | - |
| | Severe | 7 (23) | 26 (24) | 9 (13) | 9 (45) | 9 (45) | - |

*P values for the statistical significance testing for "retrospective collective vs. complete prospective collective" / "study arm I vs. study arm II". SD, standard deviation; M, male; F, female.

When analyzing possible causes of device failure, three cases were clearly due to a wide dissection, resulting in a great distance between the true lumen and the re-entry device. Retrospectively, these cases were highly unlikely to be successful from the outset, and the primary omission of a re-entry device would have been legitimate. However, according to the study protocol, the devices were used regardless of the probable failure to avoid selection bias. A subgroup analysis with exclusion of these three cases revealed the results presented in Figure 3. With this clinically justifiable modification, not only was the technical success rate of the OffRoad® catheter significantly worse than the overall re-entry device performance in study arm I ($P = 0.001$) but it was also now worse than the rate of the Enteer® catheter in study arm II ($P = 0.035$).

The success rate of the Outback® device as a backup tool in the prospective study arms was 13/18 (72%) for the entire study popula-

tion and 13/15 (87%) in the reduced cohort, according to Figure 3. In conjunction with the success rate in the retrospective part of the study, this results in an overall technical success rate of 43/49 (88%) and 43/46 (93%), respectively.

Another subgroup analysis was introduced to examine possible differences in spontaneous and device-assisted re-entry in severely calcified vessels. Table 2 shows the cases of severely calcified re-entry sites with the exclusion of the above-mentioned predictable failures and their success rates.

After the successful passage of the target lesion, subsequent angioplasty in all and additional stent/stent-graft placement in 94/109 (86%) lesions were conducted. On average, 1.7 (SD: 0.8) stents or stent grafts were used for treating the target lesion. Considering all prospectively enrolled patients, the overall procedural success rate equates to 95% (103/109).

Economic evaluation

The additional costs resulting from the use of one or two re-entry catheters were calculated separately for each study arm. The additional costs in study arm I could amount to €795 for the sole use of the OffRoad® device or €2.495 (795 + 1.700) in the case of the additional necessary use of the Outback® catheter. Similarly, additional costs in study arm II amounted to €540 or €2.240 (540 + 1.700). This also explains the wide range of SDs. The statistically insignificant mean reduction of per-patient costs for each study arm was €55 (SD: 850) (3%) for the OffRoad® and €480 (SD: 833) (28%) for the Enteer® device. When excluding the three cases with predictable technical failure, the per-patient cost reduction rose to €100 (SD: 849) (6%) for the OffRoad® and €593 (SD: 801) (35%) for the Enteer® device, the latter now reaching significance ($P = 0.036$) despite the fact that the success rate of the Enteer® device was significantly inferior to the overall re-entry device performance with the help of the Outback® catheter.

Discussion

The major perspective of this study was the comparison of re-entry devices to evaluate possible economic savings. However, the actual calculated savings were much lower than anticipated. When looking at the literature, the performance of both prospectively compared re-entry devices should have been better, resulting in a considerably larger effect size when looking at the potentially saved costs. With a success rate of 93%–96% for the Outback® catheter, 84.5% for the OffRoad® catheter,⁷ and 86% for the Enteer® catheter¹⁰ and vastly different acquisition prices, the number of patients needed to demonstrate significant economic savings in the chosen study design were expected to be low. This partly explains the small number of patients planned for the analysis. However, despite the surprisingly low success rate of the two compared devices, a significant

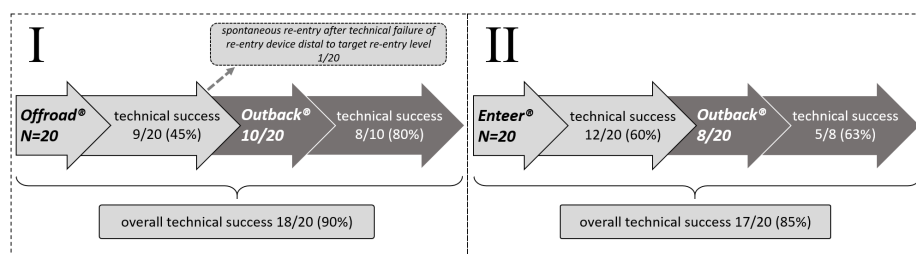


Figure 2. Overview of the technical success rates of the used devices in the two sequentially arranged study arms.

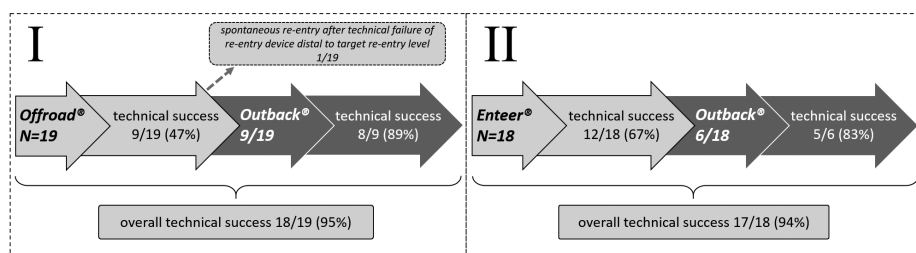


Figure 3. Overview of the technical success rates of the used devices in the two sequentially arranged study arms in a subgroup analysis with the exclusion of three cases with predictable device failure due to a wide distance between the true lumen and the re-entry device.

| Table 2. Subgroup “severely calcified re-entry sites” | | | | |
|---|--------------------|--------------|--------------------------------|-----------------------------------|
| Subgroup “severely calcified re-entry sites” | Number of patients | Success rate | Additional use of the Outback® | Success of the secondary Outback® |
| Retrospective cohort (Outback®) (%) | 7 | 7/7 (100) | - | - |
| Prospective cohort (%) | | | | |
| Complete collective | 24 | 14/24 (58) | 10 | 9/10 (90) |
| Spontaneous re-entry | 9 | 9/24 (38) | - | - |
| Study arm I (OffRoad®) | 8 | 3/8 (38) | 5 | 5/5 (100) |
| Study arm II (Enteer®) | 7 | 2/7 (29) | 5 | 4/5 (80) |

reduction in costs could only be achieved by primarily using the Enteer® device and the Outback® catheter as a bailout device after excluding three cases with anticipated failure due to a large distance between the device and the target vessel lumen.

In addition, the chosen low number of patients per study arm seemed appropriate, as we did not expect a long initial training period since fast and intuitive handling for those rarely used devices is essential. Therefore, it is important that every interventionalist can successfully employ them after a short training interval in the femoro-popliteal segment. Other locations, such as the tibio-peroneal arteries, certainly require more experience.^{11,12} Furthermore, the initial training period for the gold standard, the Outback® catheter, was also included in this study to facilitate the comparison between the re-entry devices. To minimize the effect of three separate learning curves in three interventionalists, all were instructed beforehand by a product specialist and were able to test the systems *in vitro*. The first applications were then always conducted in a team until everyone was aware of the individual advantages and disadvantages of the systems and could work quickly with the same level of experience.

With a success rate of only 45%, this study showed a considerably lower success rate for the OffRoad® catheter than that by Schmidt et al.⁷ However, Schmidt et al.⁷ did exclude almost all patients with severe calcification of the target lesion from the study, resulting in a rate of severe calcifications of only 5.4%. For those few included cases with severe calcification, a success rate of only 60% was documented, while cases with mild calcifications showed a success rate of 93%. Moreover, the OffRoad® catheter was used primarily without previously trying to achieve a spontaneous re-entry, which is a rather unusual study design for such a device. With an average time until re-entry of 11.1 min (SD: 10.5), this time is comparable to that in our study (12.5 min; SD: 6.4). Finally, it should be mentioned that the study was not conducted independently of the manufacturer, which may explain the deficiencies in the study design and the interpretation of the results. The first study of this device in humans, with the inclusion of just six patients, indicated a success rate of 83% when using the OffRoad® catheter after failed primary revascularization, even in cases of severe calcification.¹³ We were not able to reproduce this success rate.

One big advantage of the Enteer® catheter, in contrast to the OffRoad® device, is its sleek crossing profile. A passage to the desired re-entry site can be achieved without issue. The comparably much shorter time until re-entry of only 6.65 min vs. 12.5 min with the OffRoad® device reflects this. However, the maximum 67% success rate of the Enteer® device shown in this study was much lower than in the peripheral facilitated antegrade steering technique-CTO trial, where a success rate of 86% for the Enteer® catheter after failed primary recanalization was documented.¹⁰ There, the re-entry device was used in 21 out of 66 cases. The exact lesion characteristics were not described, but only in 45% of the 66 patients were the vessels described as moderately or severely calcified. In our study, 16 out of 20 target lesions (80%) were at least moderately calcified. This may explain the lower success rate and also emphasize the necessity of careful consideration of the chosen re-entry device. Ultimately, the Enteer® catheter failed to achieve the expected technical success rate in the present study. However, when excluding patients with expected failure of the device due to a large distance between the device and the true lumen, the calculated economic savings per patient of almost €600 were significant and relevant.

When comparing the group with spontaneous re-entry to those with the need for re-entry devices, the impact of re-entry site calcification becomes obvious. Only 13% (9/69) of re-entry sites were severely calcified in the group with spontaneous re-entry. On the other hand, 45% (18/40) of re-entry sites in study arms I and II were severely calcified. Hence, the grade of calcification can be used as a predictor for the necessity of a re-entry device. The Enteer® catheter also revealed its greatest weakness in the presence of severe calcification, with an associated technical success rate of only 29%. Contrary to the results of Shin et al.¹⁴, the Outback® device showed excellent results even in the severely calcified re-entry sites with a success rate of 90% (25/27). Thus, the extent of calcification of the re-entry site can certainly be used as an additional selection criterion, with the Outback® favored over the Enteer® catheter in such cases. Hence, it should be possible to achieve an even greater cost advantage. In our study, the Outback® device proved its great performance despite being used only in difficult cases when the other re-entry devices had failed. With a retrospective success rate of 97% (30/31) and a success rate of up to 87% (13/15) in the prospective study

as a bail out, the overall success rate of the Outback® catheter was 93% (43/46). This concurs with other studies.^{5,15,16} Hence, the definition as a gold standard was justified. As already described in previous studies, possible predictors of failed assisted re-entries were heavy calcification with consecutive difficulty tracking the device over the wire or an acute angle of the aortic bifurcation in crossover recanalization.^{8,14} However, in the majority of cases, it impresses with its very easy and swift application, which was proven by the documented re-entry times when used as a bail out. When using the OffRoad® device, a re-entry time of 12.5 min (SD: 6.4) was documented. However, if it failed, the combined time until re-entry with the additionally used Outback® device took, on average, no more than three minutes longer (15.2 min; SD: 12.9). The same was shown for the Enteer® device. By itself, a time of 6.65 min (SD: 6.4) until re-entry was documented, and in the case of failure, the entire re-entry time with the additionally used Outback® catheter was only two minutes greater (8.25 min; SD: 12.9).

The primary procedural success rate without a re-entry device in this study was 63%. Other studies have shown a higher primary success rate between 80% and 92%.² In this meta-analysis, lesion characteristics and the exact procedural events were not mentioned and, therefore, cannot be compared to our study. Since we started including patients with the use of the first re-entry device and closed the acquisition with the use of the fortieth re-entry device, we artificially distorted the actual primary success rate. Furthermore, we placed a great deal of importance on a targeted re-entry, which prevented us from using aggressive wire maneuvers to ensure re-entry. Moreover, we refrained from using any additional auxiliaries, such as the subintimal application of balloons to achieve re-entry, to keep the subintimal space as narrow as possible and, thus, the starting conditions for the devices as comparable as possible. In the context of this study, we also refrained from using a retrograde access to the lesion, which is, of course, a viable and cheap, but no less complex, alternative.¹⁷ The learning curve for the distal retrograde access (either pedal, tibio-peroneal, or popliteal) and for the corresponding access site management is longer than for the application of the Outback® catheter, and the possible complications of the additional access site could be much more serious, especially when considering the popliteal artery. We, therefore, never use this approach in claudicants and think that re-entry devices

are an ideal tool to deal with these situations via a single access route. For the purpose of the study, we have generally avoided this technique. Another very exciting application is the retrograde insertion of the Outback® catheter in lesions that cannot be treated in any other way.¹⁸ With growing experience and confidence in the use of retrograde access and the Outback® catheter, this option can be a game changer in selected cases.

The selection of devices used in our study was based on the great difference in their acquisition costs in comparison to the Outback® device and, thus, the potential for economic savings. The Pioneer Plus® re-entry device would have been a possible alternative as a gold standard. However, a lack of experience with this device prevented its use in our study. Furthermore, despite comparable acquisition costs for the Pioneer Plus® and the Outback® catheter, the additional need for an intravascular ultrasound system for the Pioneer Plus® may imply an additional hurdle for most users. Moreover, its use is usually reserved for more complex applications.¹⁹ For this study, selected off-the-shelf devices can all be applied without additional equipment, with the exception of the guidewires, and can thus be implemented in the daily routine without problems.

A recently introduced device is the GoBack® catheter (UPSTREAM Peripheral Technologies Ltd., Israel). However, the cost of this re-entry device is comparable to the Outback® catheter. Its use suggests no possibility of economic savings, so we excluded it from this study. A prospective head-to-head comparison with the Outback® catheter would be a useful study. However, the GoBack® catheter is being promoted with the additional characteristic of a crossing device, which differs greatly from the included devices in this study. To compare such vastly different devices in the setting of this study would have been problematic. Nevertheless, in this study, there was only one case in which the passage of the target lesions was not possible using the standard guidewire technique. So, the number of cases in which the promoted characteristic of a crossing device of the GoBack® catheter being an advantage seems to be limited.

The main limitations of the present work are the comparatively small number of patients per study arm, which has already been discussed, but also the lack of clinical follow-up of the patients. However, this seemed irrelevant to the study objective. Clinical success and value of femoro-popliteal recanal-

izations in symptomatic PAD, as well as the value of subintimal recanalization, have been sufficiently investigated in larger cohorts.²⁰ Our study would not have contributed any decisive added value, and this information would have merely overloaded the manuscript.

In conclusion, due to its low success rate, the OffRoad® re-entry device offers no options for cost savings. The Enteer® catheter, in contrast, seems to offer the possibility of significant savings in a gradual approach with the Enteer® catheter as the primarily used device and the Outback® catheter only utilized in the case of failure of the Enteer®. Predictable failures for any device result from too great a distance between the device and the target lumen in a wide dissection. In these cases, the additional use of a re-entry device and the associated costs can be omitted. In cases of severely calcified re-entry sites, the primary use of the Enteer® device cannot be recommended. In these cases, the primary use of the Outback® catheter offers higher chances of success. Thus, the significant average savings per patient documented in this study may even be exceeded.

Conflict of interest disclosure

The authors declared no conflicts of interest.

References


1. Decker JA, Varga-Szemes A, Schoepf UJ, et al. In-patient care trends in peripheral artery disease in the German healthcare system over the past decade. *Eur Radiol.* 2022;32(3):1697-1708. [Crossref]
2. Met R, Van Lienden KP, Koelmay MJ, Bipat S, Legemate DA, Reekers JA. Subintimal angioplasty for peripheral arterial occlusive disease: a systematic review. *Cardiovasc Intervent Radiol.* 2008;31(4):687-697. [Crossref]
3. Bazan HA, Le L, Donovan M, Sidhom T, Smith TA, Sternbergh WC 3rd. Retrograde pedal access for patients with critical limb ischemia. *J Vasc Surg.* 2014;60(2):375-381. [Crossref]
4. Aslam MS, Allaqband S, Haddadian B, Mori N, Bajwa T, Mewissen M. Subintimal angioplasty with a true reentry device for treatment of chronic total occlusion of the arteries of the lower extremity. *Catheter Cardiovasc Interv.* 2013;82(5):701-706. [Crossref]
5. Gandini R, Fabiano S, Spano S, et al. Randomized control study of the outback LTD reentry catheter versus manual reentry for the treatment of chronic total occlusions in the superficial femoral artery. *Catheter Cardiovasc Interv.* 2013;82(3):485-492. [Crossref]

6. Wosik J, Shorrock D, Christopoulos G, et al. Systematic review of the bridgepoint system for crossing coronary and peripheral chronic total occlusions. *J Invasive Cardiol.* 2015;27(6):269-276. [Crossref]
7. Schmidt A, Keirse K, Blessing E, Langhoff R, Diaz-Cartelle J; European Study Group. Offroad re-entry catheter system for subintimal recanalization of chronic total occlusions in femoropopliteal arteries: primary safety and effectiveness results of the re-route trial. *J Cardiovasc Surg (Torino).* 2014;55(4):551-558. [Crossref]
8. Raskin D, Khaitovich B, Balan S, Silverberg D, Halak M, Rimon U. The aortic bifurcation angle as a factor in application of the outback for femoropopliteal lesions in ipsilateral versus contralateral approaches. *Cardiovasc Intervent Radiol.* 2018;41(1):37-42. [Crossref]
9. Stoner MC, Calligaro KD, Chaer RA, et al. Reporting standards of the society for vascular surgery for endovascular treatment of chronic lower extremity peripheral artery disease. *J Vasc Surg.* 2016;64(1):E1-E21. [Crossref]
10. Gray W. Peripheral facilitated antegrade steering technique in chronic total occlusions (pFAST-CTO). Paper presented at: Vascular Interventional Advances (VIVA) Conference; 2012; Las Vegas, Nevada. [Crossref]
11. Diamantopoulos A, Santonocito S, Thulasidasan N, et al. Initial experience with the outback catheter for targeted reentry during subintimal angioplasty of the infragenicular arteries. *J Endovasc Ther.* 2018;25(2):178-182. [Crossref]
12. Rippel K, Ruhnke H, Jehs B, Decker J, Kroencke T, Scheurig-Muenkler C. Targeted tibio-peroneal re-entry during subintimal revascularization using the Outback® catheter. *CVIR Endovasc.* 2021;4(1):18. [Crossref]
13. Airoidi F, Faglia E, Losa S, et al. A novel device for true lumen re-entry after subintimal recanalization of superficial femoral arteries: first-in-man experience and technical description. *Cardiovasc Intervent Radiol.* 2011;34(1):166-169. [Crossref]
14. Shin SH, Baril D, Chaer R, Rhee R, Makaroun M, Marone L. Limitations of the outback LTD re-entry device in femoropopliteal chronic total occlusions. *J Vasc Surg.* 2011;53(5):1260-1264. [Crossref]
15. Husmann M, Federer J, Keo HH, et al. Bailout revascularization of chronic femoral artery occlusions with the new outback catheter following failed conventional endovascular intervention. *J Endovasc Ther.* 2009;16(2):206-212. [Crossref]
16. Kitrou P, Parthipun A, Diamantopoulos A, Paraskevopoulos I, Karunanithy N, Katsanos K. Targeted true lumen re-entry with the outback catheter: accuracy, success, and complications in 100 peripheral chronic total occlusions and systematic review of the literature. *J Endovasc Ther.* 2015;22(4):538-545. [Crossref]

17. Martin G, Covani M, Saab F, Mustapha J, Malina M, Patrone L. A systematic review of the ipsilateral retrograde approach to the treatment of femoropopliteal arterial lesions. *J Vasc Surg.* 2021;74(4):1394-1405. [\[Crossref\]](#)
18. Patrone L, Dharmarajah B, Korosoglou G, et al. Retrograde use of the outback re-entry catheter in complex infrainguinal arterial recanalizations. *J Vasc Surg.* 2022;75(1):177-185. [\[Crossref\]](#)
19. Krishnamurthy VN, Eliason JL, Henke PK, Rectenwald JE. Intravascular ultrasound-guided true lumen reentry device for recanalization of unilateral chronic total occlusion of iliac arteries: technique and follow-up. *Ann Vasc Surg.* 2010;24(4):487-497. [\[Crossref\]](#)
20. Kokkinidis DG, Katsaros I, Jonnalagadda AK, et al. Use, safety and effectiveness of subintimal angioplasty and re-entry devices for the treatment of femoropopliteal chronic total occlusions: a systematic review of 87 studies and 4,665 patients. *Cardiovasc Revasc Med.* 2020;21(1):34-45. [\[Crossref\]](#)



Inferior vena cava filter retrievals using advanced techniques: a systematic review

Nikhil Kethidi 
Kyrillos Barsoum 
Pratik A. Shukla 
Abhishek Kumar 

ABSTRACT

This study aimed to assess the safety of complex inferior vena cava (IVC) filter retrieval techniques through a systematic review of published literature.

Using PubMed, a systematic review was conducted in line with the 2020 Preferred Reporting Items for Systematic Review and Meta-Analysis guidelines to identify articles published through April 2020 that reported on complex IVC filter retrieval techniques in >5 patients. Case reports, review papers, and studies that did not report on primary outcomes or variables of interest were excluded. Risk of bias was assessed using a modified Newcastle–Ottawa Quality Assessment scale. Pooled success and complication rates were calculated for the overall number of complex retrieval attempts as well as for each filter type and each complex retrieval method.

Sixteen fair-quality and three good-quality studies met the inclusion criteria, with 758 patients (428 female) who had undergone 770 advanced retrieval attempts. The mean age of the patients was 46.5 ± 7.1 years (range: 14.1–90), and the mean dwell time was 602.5 ± 388.6 days (range: 5–7336). Regarding filters, 92.6% (702/758) were retrievable and 7.4% (56/758) were permanent. Indications for complex retrieval included the failure of standard retrieval (89.2%; 676/758) and tilting or embedding in the caval wall (53.8%; 408/758); 92.6% (713/770) of the advanced retrieval attempts were successful. The pooled success rate was 92.0% (602/654) for retrievable filters and 96.4% (53/55) for permanent filters ($P = 0.422$). Only 2.8% (21/758) of patients experienced major complications, and the major complication rate was not significantly associated with filter type ($P = 0.183$).

Advanced techniques for IVC filter retrieval appear safe for the retrieval of retrievable filters and certain permanent filters, with a low short-term major complication rate. Further studies on complex retrieval techniques used to remove permanent filters should be conducted to clarify their safety with respect to filter type.

KEYWORDS

Advanced filter retrieval, complex filter retrieval, pulmonary embolism, thromboembolism, venous thromboembolism

From the Department of Radiology, Division of Vascular and Interventional Radiology (N.K., K.B., P.A.S., A.K. [✉kumarab@njms.rutgers.edu](mailto:kumarab@njms.rutgers.edu)), Rutgers New Jersey Medical School, Newark, NJ, USA.

Received 26 August 2021; revision requested 11 October 2021; last revision received 02 March 2022; accepted 07 March 2022.



Epub: 27.02.2023

Publication date: 30.05.2023

DOI: 10.4274/dir.2022.22908

Following a 1998 clinical trial that demonstrated the short-term efficacy of inferior vena cava (IVC) filters in preventing pulmonary embolism (PE), the implantation rate of IVC filters increased for years before peaking in 2010.^{1,2} These filters are not always intended for permanent use, and in 2010, the US Food and Drug Administration recommended the removal of retrievable IVC filters that were no longer required, reinforcing this recommendation in 2014.³ Although Brown et al.⁴ reported an increase in the 1-year retrieval rates of IVC filters from 14% to 24%, the majority of implanted filters are not retrieved.⁵ Many factors may contribute to low retrieval rates, including the difficulty of removing filters. Ray et al.⁶ reported that approximately 15% of filter retrievals were not successful using standard techniques in a population of closely followed patients. Reported causes for standard retrieval failures include tilted, damaged, or thrombosed filters.^{6,7}

Furthermore, not all patients are closely followed up after filter placement, leading to longer dwell times before an attempted retrieval and increased technical complexity during retrieval. In a study of patients with a mean dwell time of 685 days, 60% were referred for

You may cite this article as: Kethidi N, Barsoum K, Shukla PA, Kumar A. Inferior vena cava filter retrievals using advanced techniques: a systematic review. *Diagn Interv Radiol.* 2023;29(3):500-508.

complex retrievals, which require the use of techniques and equipment beyond standard snares or dedicated retrieval devices.⁸ Complex IVC filter retrieval techniques using modified loop snares, forceps, and lasers have been described in the literature. However, further analysis is needed to understand the current usage and safety of these techniques. Herein, we conduct a systematic review of existing literature to assess the safety of complex IVC filter retrievals.

Methods

A systematic review was conducted in line with the 2020 Preferred Reporting Items for Systematic Review and Meta-Analysis guidelines of peer-reviewed literature on complex or advanced retrieval techniques attempted on patients with implanted IVC filters. This study qualifies as “non-human subject research” as per the protocol set by the institutional review board (IRB) at our institution and was thus excluded from a formal IRB review.

Search strategy and study selection

A structured PubMed search was performed for literature published up to and including April 2020. The search performed was as follows: “[(IVC filter retrieval) OR (IVC filter retrieval)] AND [(advanced) OR (advanced technique) OR (complex) OR (complex retrieval) OR (forceps) OR (loop) OR (laser)].” Two authors (NK and KB) used Rayyan QCRI software (Doha, Qatar) to systematically screen article titles and abstracts independently.⁹ Decisions on studies eligible for a full-text review were made mutually after discussion.

Data extraction

After the preliminary screening of titles and abstracts, the full texts were reviewed for definitive inclusion. The primary out-

comes of interest were the number of successful attempts, failed attempts, and major complications. Other variables of interest included demographic data, filter dwell times, filter types, retrieval indications, and retrieval methods. In this review, days are the units used to report dwell time. If studies reported dwell time in months or years, we converted these data to days (365.25 days: 1 year: 12 months). Authors NK and KB independently collected primary outcomes and other variables of interest using Microsoft Excel (Microsoft, Redmond, WA, USA) to determine which study results to include in the data synthesis and to tabulate results. During the full-text screening, bibliography reviews were conducted to find additional relevant publications. Once identified, their full texts were subsequently reviewed. Full texts were also screened for overlapping patient cohorts if study authors were listed in multiple publications. When overlapping cohorts were identified, only the most recent publication was included. The publications in this systematic review provided measures of central tendencies instead of individual patient data; thus, weighted averages were used based on sample size.

Eligibility criteria

This review includes studies reporting the retrieval of IVC filters involving a complex retrieval technique in >5 patients. A complex or advanced technique was defined as any technique other than one involving routine venous access with a snare for the filter hook (apex) or one involving a dedicated retrieval device. Advanced techniques used alone, in combination with other advanced techniques, or subsequent to failure with standard techniques were all included in this review. Case reports were excluded from this review due to the increased risk of selection bias, and review papers were excluded because of the lack of unique retrieval data. Both retrospective and prospective studies were included. Studies that did not provide specific patient demographics, filter dwell times, filter type, retrieval method, success rate, or major complication rate were excluded. Studies were grouped by filter type and retrieval method.

Definition of outcome measures

Incidence of successful retrievals and incidence of major complications were the primary outcomes of interest. If study authors reported multiple advanced retrieval failures followed by a retrieval success, all

attempts were considered. Three studies reported failed advanced retrieval attempts prior to successful advanced retrieval but did not quantify previous advanced attempts or detail which methods were used.¹⁰⁻¹² As a result, only the final retrieval attempt was considered from these three studies in this review. Study authors also reported complications only for final retrieval attempts; thus, complications following previous failed retrieval attempts were not reported in the complication rate. Successful retrieval was defined as the removal of at least the body of the filter. If another filter part was not removed, such as a tip, hook, barb, or strut, the retrieval attempt was deemed successful but also included as a major complication. Major complications were defined according to the Society of Interventional Radiology (SIR) Clinical Practice guidelines and were assessed using postretrieval IVC imaging in all patients.¹³ These complications included death, permanent adverse sequelae, prolonged hospitalization, additional therapy, and an unplanned increase in the level of care. Fractured unretrieved parts of IVC filters pose the risk of filter-related morbidity in patients and therefore qualified as potential severe adverse sequelae.^{14,15} Complications that required only nominal therapy, such as overnight observation, were not deemed major under these guidelines. The number of successful retrievals was summed across all studies. A pooled success rate was calculated using the total number of complex retrieval attempts, including past failed attempts. Similarly, the number of major complications were summed across all studies. However, the major complication rate was computed without the inclusion of past failed attempts because most study authors did not report data on complications following previous attempts. Additional success and complication rates were calculated for permanent and retrievable filters as well as for each complex retrieval method. Patient-level data were not available in the majority of studies, precluding the computation of adjusted effect measures.

Statistical analysis

Descriptive statistics for age and dwell time are presented as mean \pm standard deviation. For categorical variables, statistics are presented as percentage (%) and frequency. Success and complication rates for permanent and retrievable filters were compared using two-sided Fisher’s exact tests. Separate rates for permanent and retrievable filters were identified in all but one study, which

Main points

- Advanced retrieval techniques demonstrated promising pooled success rates of 92.0% and 96.4% for retrievable and permanent filters, respectively.
- Advanced retrieval techniques demonstrated a low pooled short-term major complication rate of 2.8%, and no patient mortality resulting from procedure-related complications was reported.
- Further studies on complex retrieval techniques used to remove permanent filters should be conducted to clarify their safety with respect to filter type.

was included in the overall success and complication rates but excluded from the filter type statistical analysis.¹⁶ Success rate was also compared between the three most common retrieval methods (forceps, laser, and loop-snare) using a two-sided Fisher's exact test. Two studies did not report the retrieval method used in their retrieval failures and were thus not included in the filter technique statistical analysis.^{10,17} Results were considered significant with $P < 0.05$. The analysis was performed using SPSS software, version 25 (IBM, Armonk, NY, USA).

Risk-of-bias assessment

Authors NK and KB independently assessed all included studies for risk of bias using a modified Newcastle–Ottawa Quality Assessment scale (NOS) for cohort studies. Modifications included use of a 48-h follow-up time cut-off in line with the SIR Clinical Practice guideline definition of prolonged postprocedural hospitalization of >48 h.¹³ Further modification included requiring studies to report on consecutive eligible patients to receive a star for the representativeness of their exposed cohort, thus identifying studies with an increased risk of reporting bias. Studies were deemed good quality if they received at least seven of nine possible stars, fair quality with between four and six stars, and low quality with three or fewer stars.

Results

Studies meeting inclusion criteria

In total, 152 unique studies were identified, 147 through PubMed and 5 through a bibliography review (Figure 1). Of these studies, 58 were deemed eligible for a full-text review, including all five studies identified through the bibliography review. After the full-text review, 19 studies were included in this analysis. Seventeen studies were retrospective reviews, and two were prospective. A summary of these studies is provided in Table 1. All included studies contained advanced retrieval-specific data on patient age, sex, filter dwell time, success rate, and complication rate. Filter types were provided in all but one study. Six additional studies met the inclusion and exclusion criteria of this review but included overlapping patient cohorts with the 19 included studies.^{15,18–22} These studies were therefore excluded.

Demographics and filter data

Among the 19 studies in this analysis, data were provided on 758 patients (428 women; mean age: 46.5 ± 7.1 years; range: 14.1–90 years) with implanted IVC filters that required advanced techniques for removal. The mean dwell time of the IVC filters was 602.5 ± 388.6 days (range: 5–7366 days). The

majority (92.6%; 702/758) of filters in our analysis were designed as retrievable filters (Table 2). The most common retrievable filters were Günther Tulip (26.5%; 186/702), Celect (21.9%; 154/702), and Option (16.7%; 117/702). The most common permanent filter was TrapEase (41.1%; 23/56). In 35 patients, the exact filter brand was not provided,^{17,23} although they were identified as retrievable.

Indications for retrieval

Indications for IVC filter retrieval were provided in 67.9% (515/758) of patients. Initial indications for retrieval were categorized as either asymptomatic (81.4%; 419/515) or symptomatic (18.6%; 96/515). Asymptomatic patients underwent retrieval because the IVC filtration was no longer needed. Symptomatic patients experienced filter-related morbidities, such as pain resulting from IVC occlusion or stenosis.

The advanced retrieval methods were commonly indicated after failed attempts using standard retrieval. Of all the filters, 89.2% (676/758) were found to be refractory to standard retrieval methods. Of the remaining 82 filters, an advanced retrieval was the first technique attempted in 40 patients, and standard retrieval attempts were not specified in 42 patients. Radiographic findings were explicitly discussed for 53.8% (408/758) of patients. These 408 patients were all found to have tilted filters or filters embedded in the caval wall. These findings were commonly considered the reason for the failed standard retrieval.

Retrieval success and methods

Of the 758 filters, 770 advanced retrieval attempts were reported. The additional 12 attempts failed previous retrieval attempts with an advanced technique prior to a successful retrieval.^{16,23–26} In four cases, a failed loop-snare method led to the use of forceps.²⁵ In another three cases, forceps retrieval failure led to the use of loop-snare-type methods.^{24,26} In three more cases, snare retrieval with aggressive traction failed, and patient discomfort required a re-attempt under general anesthesia in the two remaining previous advanced retrieval attempts.^{16,23,26} A total of 92.6% (713/770) of attempts were successful using an advanced technique or combination of advanced techniques. In four patients, filter bodies were successfully removed from the IVC. However, filter fractures resulted in adherent or migrated struts, for which complex retrieval methods were not attempted, or retrieval was not possible.^{17,25–27} These four retrieval attempts were

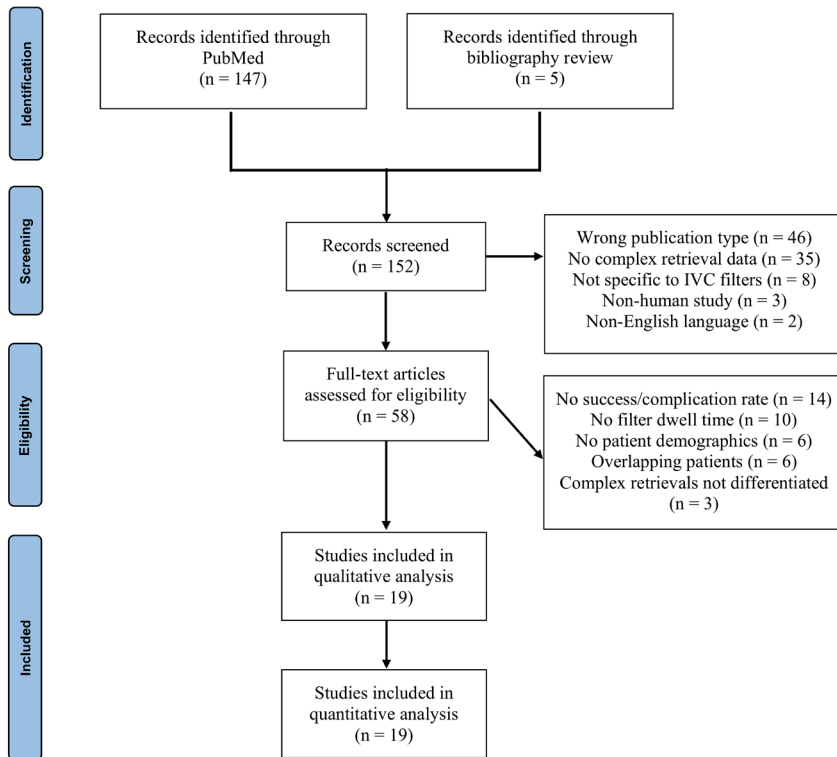


Figure 1. Preferred reporting items for systematic review and meta-analysis flowchart documenting the selection process for articles included in this systematic review. IVC, inferior vena cava.

deemed successful but counted as major complications because of the risk of severe adverse sequelae. In one study of 60 patients (59 retrievable filters and one permanent filter) and 61 advanced retrieval attempts, the filter type was not identified for the retrieval failures and complications. This study was included in the overall success and complication rate but excluded from the filter type success or complication statistical analysis.¹⁶ The success rate was 92.0% (602/654) for retrievable filters and 96.4% (53/55) for permanent filters ($P = 0.422$; Table 3).

Although various advanced retrieval methods were used, three methods were the most common: forceps (37.9%; 292/770), laser (32.7%; 252/770), and modified loop-snare (19.9%; 153/770). Two studies did not report the technique used in their retrieval failures;^{10,17} these were included in the overall success rate but excluded from individual retrieval method success rate analysis. The success rate of retrieval attempts was 95.5% (273/286) for the forceps method, 98.8% (249/252) for the laser method, and 86.0% (123/143) for the modified loop-snare method. The success rate was significantly different between the three retrieval methods ($P < 0.001$; Table 3).

Major complications

Major complications occurred in 2.8% (21/758) of patients during or after retrieval

attempts, with no patient mortality reported as a result of a procedure-related complication. This included a 2.5% (16/643) complication rate for retrievable filters and 5.5% (3/55) complication rate for permanent filters. Filter type was not provided for two complications. Complication rate was not significantly associated with filter type ($P = 0.183$; Table 3). No procedure-related mortality was reported.

Eleven patients had major complications localized to the IVC. Six patients experienced IVC thrombosis, which was treated using catheter-directed thrombolysis followed by angioplasty if needed.^{26,28} One additional patient had a pseudo-aneurysm of the IVC that was treated with balloon tamponade.¹² Another patient experienced an extravasation in the IVC wall, and another experienced an IVC dissection that was treated with anticoagulation.^{16,17} A patient also experienced non-occlusive IVC stenosis, managed through angioplasty, and one patient had a filter strut within the IVC that could not be captured.^{27,29} Ten major complications were non-localized. Three patients had a significant retroperitoneal hemorrhage, requiring stent graft placement in two of these patients and a 5-day hospitalization in the other patient.^{16,28} At the femoral vein access sites, one patient experienced a right common femoral vein laceration attributed to the incomplete sheathing of a filter.¹¹ This filter could not be removed, and surgical cutdown and venous

closure were required. Another patient also required urgent cutdown and repair of the access-site vein.¹⁷ One other patient experienced access-site thrombosis.¹¹ Patients with femoral vein complications did not require prolonged hospitalization. Finally, four patients experienced migratory events after retrieval attempts. Filter struts were found to have migrated in three of these patients to the right heart ventricle, pulmonary artery, or retroperitoneum;^{17,25,26} attempts to retrieve these struts were unsuccessful or not attempted. In another case, a patient experienced a subsegmental PE that was attributed to filter manipulation, although a filter part was not explicitly identified as the cause.³⁰

Risk of bias

Based on the modified NOS, all included studies were of fair or good quality. All studies received a star for reporting on consecutive patient cohorts. None of the studies statistically controlled for the patient or filter factors and therefore did not receive stars for comparability. The risk-of-bias assessments are summarized in Table 4.

Discussion

As yearly retrieval rates of IVC filters remain low and standard retrieval techniques continue to have limitations, further evaluation of complex IVC filter retrievals is warrant-

Table 1a. Summary of included studies

| Study | Type | Year | Patient # | Mean age (years) | Filter dwell time (days) |
|-----------------------------------|---------------|------|-----------|------------------|--------------------------|
| Al-Hakim et al. ²⁴ | Retrospective | 2015 | 11 | 47.5 | 194.5 |
| Avery et al. ²⁵ | Retrospective | 2015 | 13 | 51 | 421.5 |
| Brahmandam et al. ¹⁷ | Retrospective | 2019 | 34 | 51.2 | 161.4 |
| Cho et al. ³⁴ | Retrospective | 2015 | 16 | 60.6 | 315.7 |
| Doody et al. ³⁰ | Retrospective | 2009 | 33 | 36.9 | 168.9 |
| Dowell et al. ¹⁰ | Retrospective | 2016 | 20 | 54.5 | 104.5 |
| Du et al. ³⁶ | Retrospective | 2017 | 15 | 44.1 | 46.6 |
| Kuo et al. ⁸ | Retrospective | 2012 | 10 | 46.7 | 684.9 |
| Kuo et al. ²⁶ | Retrospective | 2009 | 13 | 40 | 511.6 |
| Kuo et al. ²⁸ | Prospective | 2017 | 251 | 46 | 979 |
| Kuo et al. ⁴¹ | Prospective | 2013 | 50 | 42 | 815 |
| Lian et al. ⁴² | Retrospective | 2019 | 27 | 57.9 | 327 |
| Lynch ²⁷ | Retrospective | 2009 | 10 | 35.4 | 258.7 |
| Moriarty et al. ²³ | Retrospective | 2020 | 23 | 47.7 | 228 |
| Posham et al. ¹¹ | Retrospective | 2017 | 25 | 55.1 | 134 |
| Stavropoulos et al. ¹² | Retrospective | 2015 | 114 | 43 | 465 |
| Su et al. ³² | Retrospective | 2019 | 21 | 41.5 | 42.8 |
| Tamrazi et al. ²⁹ | Retrospective | 2016 | 12 | 54.9 | 1862.8 |
| Tavri et al. ¹⁶ | Retrospective | 2019 | 60 | 49.3 | 565 |

#Refers to the number of patients included in the study.

ed.^{4,6} This is particularly true when patients present for the retrieval of filters that have tilted substantially or have been implanted for long periods of time. In our analysis, the average filter dwell time was 602.5 days, and filters were tilted or embedded explicitly in a majority of patients, requiring advanced retrieval techniques. We found that 92.6% (713/770) of advanced retrievals were successful. In comparison, standard retrievals in studies with average dwell times under one year were approximately 85% successful, although this number varied greatly between studies.^{6,31} Studies reported a higher overall success rate when including standard and

advanced retrievals in their retrieval protocols. For example, Su et al.³² reported an increase in retrieval rate from 92.1% to 98.4% after the inclusion of advanced retrieval methods.

Our literature review found three commonly used advanced techniques for complex filter retrieval, categorized as forceps, modified loop-snare, and laser sheath. In the forceps category, forceps are used to dissect embedded filter tips. Although a jugular approach is most commonly used, a femoral approach with filter eversion is also possible.¹¹ The forceps method has also been

used to remove localized filter fragments.¹⁵ For instance, a Celect filter leg was found embedded in a vertebral body adjacent to the IVC, producing a complaint of back pain. The filter leg was removed from the bone using considerable force applied with forceps. The loop-snare methods in our analysis required adjunct techniques, including a snare-over-guide wire loop (SOGL) method, a hangman method, and a double-loop method.^{24,29,33} Kuo et al.³³ describe a SOGL method in which a wire loop is created through the interstices of the filter body, and an internal jugular vein approach is used. A femoral vein approach can also be employed.³⁴ In another variation,

Table 1b. Summary of included studies

| Study | Filter type (#) | Initial retrieval indication (#) | Retrieval method (#) | Success rate (%) | Major complication rate (%) |
|-----------------------------------|--|--------------------------------------|---|------------------|-----------------------------|
| Al-Hakim et al. ²⁴ | Option (6), Celect (3), Günther Tulip (2) | Not specified (11) | Loop-snare (11), Forceps (1) | 9/12 (75) | 0/11 |
| Avery et al. ²⁵ | Celect (7), G2X (6) | Not specified (13) | Forceps (13), Loop-snare (4) | 11/17 (64.7) | 1/13 (7.7) |
| Brahmandam et al. ¹⁷ | Not specified (34) | Asymptomatic (33), symptomatic (1) | Combination (34) | 25/34 (73.5) | 3/34 (8.8) |
| Cho et al. ³⁴ | Celect (12), OptEase (3), Günther Tulip (1) | Asymptomatic (14), symptomatic (2) | Loop-snare (16) | 14/16 (87.5) | 0/16 |
| Doody et al. ³⁰ | Celect (20), Günther Tulip (13) | Not specified (33) | Loop-snare (33) | 23/33 (69.7) | 1/33 (3) |
| Dowell et al. ¹⁰ | Celect (9), Option (7), Denali (2), ALN (1), Günther Tulip (1) | Not specified (20) | Loop-snare (10), Forceps (6), Not specified (4) | 13/20 (65) | 0/20 |
| Du et al. ³⁶ | OptEase (11), Aegisy (4) | Asymptomatic (15), symptomatic (0) | Loop-snare (15) | 15/15 (100) | 0/15 |
| Kuo et al. ⁸ | Günther Tulip (5), G2 (1), OptEase (1), Celect (1), Simon Nitinol (1), VenaTech (1) | Not specified (10) | Forceps (3), Loop-snare (3), Laser (3), Other (1) | 10/10 (100) | 0/10 |
| Kuo et al. ²⁶ | Günther Tulip (8), OptEase (2), Recovery (2), G2 (1) | Asymptomatic (7), symptomatic (6) | Loop-snare (8), Other (8), Forceps (2) | 13/18 (72.2) | 5/13 (38.5) |
| Kuo et al. ²⁸ | Günther Tulip (101), Option (40), OptEase (37), Celect (27), TrapEase (13), Titanium Greenfield (11), Stainless Steel Greenfield (10), Simon Nitinol (6), Denali (4), Meridian (2) | Asymptomatic (194), symptomatic (57) | Laser (236), Combination (15) | 249/251 (99.2) | 4/251 (1.6) |
| Kuo et al. ⁴¹ | G2X (23), G2 (9), Celect (7), Recovery (4), Eclipse (3), OptEase (2), ALN (1), Simon Nitinol (1) | Asymptomatic (28), symptomatic (22) | Forceps (40), Laser (5), Loop-snare (5) | 50/50 (100) | 0/50 |
| Lian et al. ⁴² | Günther Tulip (12), Celect (9), Aegisy (4), OptEase (2) | Not specified (27) | Forceps (27) | 27/27 (100) | 0/27 |
| Lynch ²⁷ | G2 (7), Recovery (3) | Asymptomatic (5), symptomatic (5) | Other (10) | 8/10 (80) | 1/10 (10) |
| Moriarty et al. ²³ | Celect (20), ALN (2), Not specified (1) | Not specified (23) | Loop-snare (24) | 23/24 (95.8) | 0/23 |
| Posham et al. ¹¹ | Option (25) | Not specified (25) | Forceps (25) | 25/25 (100) | 2/25 (8) |
| Stavropoulos et al. ¹² | G2 (33), Celect (31), Günther Tulip (13), Eclipse (11), Recovery (10), G2X (8), Option (6), ALN (1), OptEase (1) | Asymptomatic (114), symptomatic (0) | Forceps (114) | 109/114 (95.6) | 1/114 (0.9) |
| Su et al. ³² | Günther Tulip (21) | Not specified (21) | Loop-snare (21) | 20/21 (95.2) | 0/21 |
| Tamrazi et al. ²⁹ | TrapEase (10), Simon Nitinol (2) | Asymptomatic (9), symptomatic (3) | Laser (8), Loop-snare (3), Combination (1) | 11/12 (91.7) | 1/12 (8.3) |
| Tavri et al. ¹⁶ | Option (33), Günther Tulip (9), Celect (8), G2 (4), Eclipse (3), OptEase (2), Simon Nitinol (1) | Not specified (60) | Forceps (61) | 58/61 (95.1) | 2/60 (3.3) |

#Indicates the number of patients with the stated filter type, retrieval indication, or retrieval method.

Table 2. Retrieval outcomes and characteristics

| | |
|--|--------------------|
| Women n (%) | 428/758 (56.5) |
| Men n (%) | 330/758 (43.5) |
| Mean age (mean ± SD) | 46.5 ± 7.1 years |
| Mean dwell time (mean ± SD) | 602.5 ± 388.6 days |
| Successful retrieval n (%) | 713/770 (92.6) |
| Complications n (%) | 21/758 (2.8) |
| Complex retrieval indications | |
| Refractory to standard retrieval n (%) | 676/758 (89.2) |
| Tilted/embedded filters n (%) | 408/758 (53.8) |
| Filter types | |
| Retrievable n (%) | 702/758 (92.6) |
| Permanent n (%) | 56/758 (7.4) |
| Retrieval methods | |
| Forceps n (%) | 292/770 (37.9) |
| Laser n (%) | 252/770 (32.7) |
| Loop-snare n (%) | 153/770 (19.9) |
| Combination/other/not specified n (%) | 73/770 (9.5) |

SD, standard deviation.

Table 3. Statistical analysis by filter type and retrieval technique

| | Retrievable filters | Permanent filters | P value | |
|----------------------------|---------------------|-------------------|----------------|------------------|
| Successful retrieval n (%) | 602/654 (92.0) | 53/55 (96.4) | 0.422 | |
| Complication n (%) | 16/643 (2.5) | 3/55 (5.5) | 0.183 | |
| | Forceps | Laser | Loop-snare | P value |
| Successful retrieval n (%) | 273/286 (95.5) | 249/252 (98.8) | 123/143 (86.0) | <0.001 |

Table 4. Modified Newcastle–Ottawa scale for assessing the quality of non-randomized studies

| Study | Selection | Comparability | Outcome | Total score/quality |
|-----------------------------------|-----------|---------------|---------|---------------------|
| Al-Hakim et al. ²⁴ | **** | - | *** | 7/good |
| Avery et al. ²⁵ | *** | - | *** | 6/fair |
| Brahmandam et al. ¹⁷ | **** | - | *** | 7/good |
| Cho et al. ³⁴ | *** | - | *** | 6/fair |
| Doody et al. ³⁰ | *** | - | *** | 6/fair |
| Dowell et al. ¹⁰ | **** | - | *** | 7/good |
| Du et al. ³⁶ | *** | - | *** | 6/fair |
| Kuo et al. ⁸ | *** | - | *** | 6/fair |
| Kuo et al. ²⁶ | *** | - | *** | 6/fair |
| Kuo et al. ²⁸ | *** | - | *** | 6/fair |
| Kuo et al. ⁴¹ | *** | - | *** | 6/fair |
| Lian et al. ⁴² | *** | - | *** | 6/fair |
| Lynch ²⁷ | *** | - | *** | 6/fair |
| Moriarty et al. ²³ | *** | - | *** | 6/fair |
| Posham et al. ¹¹ | *** | - | *** | 6/fair |
| Stavropoulos et al. ¹² | *** | - | *** | 6/fair |
| Su et al. ³² | *** | - | *** | 6/fair |
| Tamrazi et al. ²⁹ | *** | - | *** | 6/fair |
| Tavri et al. ¹⁶ | *** | - | *** | 6/fair |

***Indicates the number of points assigned as per the rating metric in the Modified NOS.

the hangman technique creates a wire loop around the neck of the IVC filter instead of through the interstices of the filter body.^{23,24} This technique is helpful when the apex of the filter is embedded in the IVC wall. Su et al.³² describe a technique in which the wire loop is created through the filter struts similar to the SOGL method or around the neck of the filter similar to the hangman method. Tamrazi et al.²⁹ describe a method in which two wire loops are formed around the superior and inferior aspects of a TrapEase filter. As a result, internal jugular vein and common femoral vein approaches are both used.²⁹ Blunt dissection with a vascular sheath is then used on both sides of the filter to capture it. In the laser method, photothermal ablation is used to remove the tissue responsible for the embedding of the filter.³⁵ Specifically, this technique can be used to excise adherent struts in cases where the filter tip is not embedded or is unembedded using another technique.^{28,29} Additionally, combinations of advanced retrieval methods were used substantially in 16 cases, particularly forceps used with laser sheaths to capture intraluminal fragments.^{28,29}

Not all filter retrievals required forceps, laser, or loop-snare methods. Alternative advanced retrievals were attempted in 19 patients. A dual access bi-snare method was attempted in two cases in which snares approaching from the right internal jugular and common femoral veins provided opposite tractions on embedded filters.^{8,26} Although Du et al.³⁶ also describe a similar bi-snare technique, the SOGL technique was also used. As a result, these cases were categorized as using a modified loop-snare method. Balloon angioplasty was used to free embedded filters in 10 cases,²⁷ and filters were then extracted using a standard recovery cone. Finally, seven cases required aggressive traction using a standard retrieval snare.²⁶ This method was categorized as advanced because of the level of traction. The retrieval methods were unspecified in four patients and were an unspecified combination of methods in 34 patients.^{10,17} Ultimately, based on our review, several different advanced techniques and combinations thereof may be employed for filter retrieval with promising success rates.

The major complication rate was 2.8% (21/758) in this systematic review. All complications were dealt with during hospitalization, and no mortalities were reported. However, other studies have noted that complications arise considerably more frequently when using advanced techniques than for

standard retrievals, and a few patients in this review experienced significant short-term sequelae such as hemorrhage. Ahmed et al.³¹ reported a major complication rate of 2.1% for advanced retrievals compared with 0% for standard retrievals, and Brahmandam et al.¹⁷ reported an overall complication rate in advanced retrievals four times that of standard retrievals. However, the complications noted in our analysis were not always attributed directly to the retrieval methods. Filter tilts and IVC wall embedding inherently pose a risk of complications or retrieval failure regardless of retrieval method. For example, the pseudo-aneurysm reported in our review was located at the site of filter leg penetrations into the IVC wall rather than the site of the forceps dissection of embedding tissue.¹²

As with all systematic reviews, our review has limitations. The data in this review is limited by the study authors' reporting, making definitions of successful retrieval and complications difficult to standardize. Individual patient-level data were also not available in the included studies. As a result, we could not compare the retrieval attempt outcomes of different subgroups, such as asymptomatic versus symptomatic retrieval indications. The majority of studies were also retrospective, increasing the possibility of positive reporting bias. Although we excluded small sample case reports through our exclusion criteria, the studies varied greatly in sample size, with smaller studies potentially not representing a full breadth of cases. Finally, the NOS used to assess the risk of bias in this review has limitations because it has not been externally validated, and studies have reported vagueness in its decision rules as well as poor-to-fair inter-rater reliability between reviewers using NOS.^{37,38} Detailed guidance on how to objectively apply and interpret the scale would have benefited our bias assessment.

Importantly, the majority of the filter retrievals in this review came from institutions that had refined their techniques over a number of years. The success and complication rates are likely subject to the protocol modifications that study authors have implemented in response to early retrieval challenges and increasing technique familiarity. The two largest groups in this review reported outcome improvements after initial retrieval failures and complications. Kuo et al.²⁶ reported implementing an anticoagulation protocol and modifying their retrieval technique to minimize caval wall collapse after four cases of postprocedural caval thrombosis, and Stavropoulos et al.¹² noted that three of four

retrieval failures occurred in the first 15 attempted cases of a 114-patient study. As a result, studies from these groups reported high success and low complication rates despite most likely encountering difficult cases given their large sample sizes. These results appear unique to high-volume centers specializing in advanced filter retrieval, a sentiment supported by a 2018 survey of vascular specialists that found that the majority of responders were not comfortable using forceps or laser sheath methods.³⁹ Our review reveals that complex retrievals often involve tilted or embedded filters, and when complications do occur, they can be significant and require urgent therapy. To improve retrieval rates and prioritize patient safety, these advanced techniques should be performed in a center with experienced operators and where detailed informed consent is obtained from the patient. Further research on these retrievals should include reporting on protocol modifications and should document the positive changes in quantifiable outcomes that result from iterative protocol refinement. Finally, as demonstrated by Minocha et al.⁴⁰, implementing a dedicated retrieval clinic may increase retrieval attempts.

Although our review did not identify any significant difference in complication rates between permanent and retrievable filters, it is important to note that only 56 permanent filters were reported in the 19 studies in this review, suggesting that a further evaluation of complex retrieval techniques on permanent filters is needed before conclusions can be drawn. Similarly, 17 filter brands are represented in this review with three comprising the majority of the filters (Günther Tulip, Celect, and Option). Further studies on other filter brands would be helpful in drawing more substantiated conclusions about the retrieval of those filters. Additionally, long-term advanced retrieval-specific follow-up data were not uniformly reported in studies, limiting conclusions to short-term postprocedural complications and warranting further study into long-term complications.

Conclusion

In conclusion, our systematic review suggests that advanced techniques for IVC filter retrieval may be safe for the retrieval of retrievable filters and certain permanent filters with a low short-term major complication rate. These techniques may be successful for IVC filter retrieval when standard techniques fail, particularly when performed by experienced operators who have honed their protocols over a lengthy period of time. Future prospective studies would be beneficial for

evaluating individual retrieval techniques and their relation to filter types.

Conflict of interest disclosure

The authors declared no conflicts of interest.

References

- Decousus H, Leizorovicz A, Parent F, et al. A clinical trial of vena caval filters in the prevention of pulmonary embolism in patients with proximal deep-vein thrombosis. Prévention du Risque d'Embolie Pulmonaire par Interruption Cave Study Group. *N Engl J Med*. 1998;338(7):409-416. [\[CrossRef\]](#)
- Reddy S, Lakhter V, Zack CJ, Zhao H, Chatterjee S, Bashir R. Association between contemporary trends in inferior vena cava filter placement and the 2010 US Food and Drug Administration Advisory. *JAMA Int Med*. 2017;177(9):1373-1374. [\[CrossRef\]](#)
- Endovascular Today. (2014, May 7). FDA Updates Safety Communication on IVC Filter Retrieval. [\[CrossRef\]](#)
- Brown JD, Raissi D, Han Q, Adams VR, Talbert JC. Vena cava filter retrieval rates and factors associated with retrieval in a large US cohort. *J Am Heart Assoc*. 2017;6(9):e006708. [\[CrossRef\]](#)
- Ahmed O, Wadhwa V, Patel K, Patel MV, Turba UC, Arslan B. Rising retrieval rates of inferior vena cava filters in the United States: insights from the 2012 to 2016 Summary Medicare Claims Data. *J Am Coll Rad*. 2018;15(11):1553-1557. [\[CrossRef\]](#)
- Ray CE Jr, Mitchell E, Zipser S, Kao EY, Brown CF, Moneta GL. Outcomes with retrievable inferior vena cava filters: a multicenter study. *J Vasc Interv Radiol*. 2006;17(10):1595-1604. [\[CrossRef\]](#)
- Rosenthal D, Wellons ED, Levitt AB, Shuler FW, O'Conner RE, Henderson VJ. Role of Prophylactic Temporary Inferior Vena Cava Filters Placed at the ICU bedside under intravascular ultrasound guidance in patients with multiple trauma. *J Vasc Surg*. 2004;40(5):958-964. [\[CrossRef\]](#)
- Kuo WT, Cupp JS, Louie JD, et al. Complex Retrieval of Embedded IVC filters: alternative techniques and histologic tissue analysis. *Cardiovasc Interv Radiol*. 2012;35(3):588-597. [\[CrossRef\]](#)
- Ouzzani M, Hammady H, Fedorowicz Z, Elmagarmid A. Rayyan - a Web and Mobile app for systematic reviews. *Syst Rev*. 2016;5(1):210. [\[CrossRef\]](#)
- Dowell JD, Wagner D, Elliott E, Yildiz VO, Pan X. Factors associated with advanced inferior vena cava filter removals: a single-center retrospective study of 203 patients over 7 years. *Cardiovasc Intervent Radiol*. 2016;39(2):218-226. [\[CrossRef\]](#)
- Posham R, Fischman AM, Nowakowski FS, et al. Transfemoral filter eversion technique following unsuccessful retrieval of option inferior vena cava filters: a single center experience. *J Vasc Interv Radiol*. 2017;28(6):889-894. [\[CrossRef\]](#)
- Stavropoulos SW, Ge BH, Mondschein JI, et al. Retrieval of tip-embedded inferior vena cava filters by using the endobronchial forceps technique: experience at a single institution. *Radiology*. 2015;275(3):900-907. [\[CrossRef\]](#)
- Sacks D, McClenny TE, Cardella JF, Lewis CA. Society of Interventional Radiology Clinical Practice guidelines. *J Vasc Interv Radiol*. 2003;14(9 Pt 2):199-202. [\[CrossRef\]](#)
- Tam MD, Spain J, Lieber M, Geisinger M, Sands MJ, Wang W. Fracture and distant migration of the bard recovery filter: a retrospective review of 363 implantations for potentially life-threatening complications. *J Vasc Interv Radiol*. 2012;23(2):199-205. [\[CrossRef\]](#)
- Trerotola SO, Stavropoulos SW. Management of fractured inferior vena cava filters: outcomes by fragment location. *Radiology*. 2017;284(3):887-896. [\[CrossRef\]](#)
- Tavri S, Patel IJ, Kavali P, Irani Z, Ganguli S, Walker TG. Endobronchial forceps-assisted complex retrieval of inferior vena cava filters. *J Vasc Surg Venous Lymphat Disord*. 2019;7(3):413-419. [\[CrossRef\]](#)
- Brahmandam A, Skrip L, Mojibian H, et al. Costs and complications of endovascular inferior vena cava filter retrieval. *J Vasc Surg Venous Lymphat Disord*. 2019;7(5):653-659. [\[CrossRef\]](#)
- Chick JF, Stavropoulos SW, Shin BJ, et al. A 16-F sheath with endobronchial forceps improves reported retrieval success of long-dwelling "closed cell" inferior vena cava filter designs. *J Vasc Interv Radiol*. 2016;27(7):1027-1033. [\[CrossRef\]](#)
- Kuo WT, Odegaard JI, Louie JD, et al. Photothermal ablation with the excimer laser sheath technique for embedded inferior vena cava filter removal: initial results from a prospective study. *J Vasc Interv Radiol*. 2011;22(6):813-823. [\[CrossRef\]](#)
- Kuo WT, Odegaard JI, Rosenberg JK, Hofmann LV. Excimer laser-assisted removal of embedded inferior vena cava filters: a single-center prospective study. *Circ Cardiovasc Interv*. 2013;6(5):560-566. [\[CrossRef\]](#)
- Mintz JD, Stavropoulos SW, Trerotola SO. Is a venacavogram necessary after inferior vena cava filter retrieval? *J Vasc Interv Radiol*. 2016;27(12):1857-1864. [\[CrossRef\]](#)
- Stavropoulos SW, Dixon RG, Burke CT, et al. Embedded inferior vena cava filter removal: use of endobronchial forceps. *J Vasc Interv Radiol*. 2008;19(9):1297-1301. [\[CrossRef\]](#)
- Moriarty HK, Marshall E, Clements W. A 7-year retrospective review of the technical success of the "low-profile" hangman technique for complicated inferior vena cava (IVC) filter retrievals. *Diagn Interv Radiol*. 2020;26(2):118-123. [\[CrossRef\]](#)
- Al-Hakim R, McWilliams JP, Derry W, Kee ST. The hangman technique: a modified loop snare technique for the retrieval of inferior vena cava filters with embedded hooks. *J Vasc Interv Radiol*. 2015;26(1):107-110. [\[CrossRef\]](#)
- Avery A, Stephens M, Redmond K, Harper J. Initial experience using the rigid forceps technique to remove wall-embedded IVC filters. *J Med Imaging Radiat Oncol*. 2015;59(3):306-311. [\[CrossRef\]](#)
- Kuo WT, Tong RT, Hwang GL, et al. High-risk retrieval of adherent and chronically implanted IVC filters: techniques for removal and management of thrombotic complications. *J Vasc Interv Radiol*. 2009;20(12):1548-1556. [\[CrossRef\]](#)
- Lynch FC. Balloon-assisted removal of tilted inferior vena cava filters with embedded tips. *J Vasc Interv Radiol*. 2009;20(9):1210-1214. [\[CrossRef\]](#)
- Kuo WT, Odegaard JI, Rosenberg JK, Hofmann LV. Laser-assisted removal of embedded vena cava filters: a 5-year first-in-human study. *Chest*. 2017;151(2):417-424. [\[CrossRef\]](#)
- Tamrazi A, Wadhwa V, Holly B, et al. Percutaneous retrieval of permanent inferior vena cava filters. *Cardiovasc Intervent Radiol*. 2016;39(4):538-546. [\[CrossRef\]](#)
- Doody O, Noë G, Given MF, Foley PT, Lyon SM. Assessment of snared-loop technique when standard retrieval of inferior vena cava filters fails. *Cardiovasc Intervent Radiol*. 2009;32(1):145-149. [\[CrossRef\]](#)
- Ahmed O, Kim YJ, Patel MV, et al. A Single-institutional comparative analysis of advanced versus standard snare removal of inferior vena cava filters. *J Vasc Interv Radiol*. 2020;31(1):53-60. [\[CrossRef\]](#)
- Su Q, Ding X, Dong Z, Liu Y, Li G, Jiang J. A modified loop snare technique for difficult retrievals of inferior vena cava filter and migrated coil. *Int Heart J*. 2019;60(1):93-99. [\[CrossRef\]](#)
- Kuo WT, Bostaph AS, Loh CT, Frisoli JK, Kee ST. Retrieval of trapped Günther Tulip inferior vena cava filters: snare-over-guide wire loop technique. *J Vasc Interv Radiol*. 2006;17(11 Pt 1):1845-1849. [\[CrossRef\]](#)
- Cho E, Lim KJ, Jo JH, Jung GS, Park BH. Failed inferior vena cava filter retrieval by conventional method: analysis of its causes and retrieval of it by modified double-loop technique. *Phlebology*. 2015;30(8):549-556. [\[CrossRef\]](#)
- Kuo WT, Cupp JS. The excimer laser sheath technique for embedded inferior vena cava filter removal. *J Vasc Interv Radiol*. 2010;21(12):1896-1899. [\[CrossRef\]](#)

36. Du X, Li C, Qian A, et al. Bidirectional pull-back technique for retrieval of strut-embedded cylinder-shaped filters in inferior vena cava. *Med Sci Monit.* 2017;23:2796-2804. [\[CrossRef\]](#)
37. Stang A. Critical evaluation of the Newcastle-Ottawa scale for the assessment of the quality of nonrandomized studies in meta-analyses. *Eur J Epidemiol.* 2010;25(9):603-605. [\[CrossRef\]](#)
38. Hartling L, Milne A, Hamm MP, et al. Testing the Newcastle Ottawa scale showed low reliability between individual reviewers. *J Clin Epidemiol.* 2013;66(9):982-993. [\[CrossRef\]](#)
39. Brahmandam A, Skrip L, Sumpio B, et al. A survey of vascular specialists' practice patterns of inferior vena cava filter placement and retrieval. *Vascular.* 2019;27(3):291-298. [\[CrossRef\]](#)
40. Minocha J, Idakoji I, Riaz A, et al. Improving inferior vena cava filter retrieval rates: impact of a dedicated inferior vena cava filter clinic. *J Vasc Interv Radiol.* 2010;21(12):1847-1851. [\[CrossRef\]](#)
41. Kuo WT, Robertson SW, Odegaard JI, Hofmann LV. Complex retrieval of fractured, embedded, and penetrating inferior vena cava filters: a prospective study with histologic and electron microscopic analysis. *J Vasc Interv Radiol.* 2013;24(5):622-630. [\[CrossRef\]](#)
42. Lian W, Tian F, Li S, Gu X, Jia Z. Forceps-assisted removal of difficult-to-retrieve filters: preliminary results. *Ann Vasc Surg.* 2019;61:371-376. [\[CrossRef\]](#)



Outcomes of two types of iodine-125 seed delivery with metal stents in treating malignant biliary obstruction: a systematic review and meta-analysis

Xiaobo Fu

Han Qi

Zhenkang Qiu

Weiwei Jiang

Zixiong Chen

Fei Gao

PURPOSE

To conduct a meta-analysis comparing the efficacy and safety of two types of iodine-125 (I-125) seed delivery with metal stents (the study group) versus conventional metal stents (the control group) in patients with malignant biliary obstruction (MBO).

METHODS

Our team systematically searched the PubMed, Embase, and Cochrane Library databases for relevant studies published from January 2012 up to July 2021. Survival time and stent dysfunction were the primary measured outcomes. Subgroup analyses were conducted according to the type of I-125 seed delivery.

RESULTS

Eleven studies, including 1057 patients in total, were pooled for stent dysfunction. The study group showed a lower risk of stent dysfunction than the control group [odds ratio (OR): 0.61, 95% confidence interval (CI) 0.46–0.81, $P = 0.001$]. The pooled results of six studies reporting overall survival (OS) showed that the study group had a better survival outcome than the control group [hazard ratio (HR): 0.34, 95% CI: 0.28–0.42, $P < 0.001$]. In the subgroup analyses, the I-125 seed stent group had significantly less stent dysfunction than the control group (OR: 0.49, 95% CI: 0.31–0.76, $P = 0.002$). Meanwhile, the metal stents + I-125 radioactive seed strand group showed significantly more improvement in OS than the control group (HR: 0.33, 95% CI: 0.26–0.42, $P < 0.001$). Moreover, our analysis suggests that using I-125 seeds did not result in increasing related adverse events compared with using metal stents alone (all $P > 0.05$). The study group was significantly superior to the control group, with better survival and decreased stent dysfunction. Meanwhile, the delivery of I-125 seeds did not increase adverse events.

CONCLUSION

The delivery of I-125 with metal stents may be considered a preferable technique for MBO.

KEYWORDS

Malignant biliary obstruction, iodine-125 seed, biliary stent, meta-analysis

From the Department of Minimally Invasive & Interventional Radiology (X.F., H.Q., Z.Q., W.J., Z.C., F.G. ✉ gaof@sysucc.org.cn), Sun Yat-sen University Cancer Center and Sun Yat-sen University State Key Laboratory of Oncology in South China, and Collaborative Innovation Center for Cancer Medicine, Guangzhou, Guangdong, China.

Received 25 December 2021; revision requested 29 January 2022; last revision received 02 March 2022; 14 March 2022.



Epub: 21.02.2023

Publication date: 30.05.2023

DOI: 10.5152/dir.2022.211277

Malignant biliary obstruction (MBO) is the stenosis or obstruction of the hepatic duct and bile duct system.¹ Frequently, clinicians need to treat this condition when managing malignant tumors,²⁻⁷ such as cholangiocarcinoma, gallbladder cancer, pancreatic carcinoma, and metastatic lymph nodes.⁸

Because there are no early clinical indications of these malignant tumors, symptoms only gradually appear until invasion occurs in the hepatic–biliary system. Consequently, MBO is detected at an advanced stage, which leads to obstructive jaundice and low quality of life.^{2,4,5,7,9} As 80% of patients diagnosed are no longer surgical candidates,^{1,2} MBO can become a com-

mon refractory complication of these malignant cancers. Only approximately 10%–20% of patients are medically ready for surgical resection of the obstructive lump.^{9–11} Sadly, the three- and five-year survival rates after surgical excision remain unsatisfactory at 18%–52% and 5%–31%, respectively.¹²

Metal stent insertion is widely accepted as the preferred palliative treatment to relieve symptoms caused by MBO for inoperable patients.^{3–7,9,13–17} Metal stents have no therapeutic action on tumors, and post-stent procedures have high rates of stent dysfunction, which limits the long-term efficacy of palliative treatment.³ Conventional metal stent insertions are not sufficient for MBO patients, and the current methods of delivering iodine-125 (I-125) seeds have shown a promising future, including radioactive I-125 seed-loaded stent [consisting of a self-expandable metal stent (SEMS) and several I-125 seeds] and metal stents insertion + I-125 radioactive seed strand (IRSS) (IRSS is a thin catheter containing several I-125 seeds). Previously, two meta-analyses compared I-125 seed delivery + stents with stents alone.^{18,19} However, the trials did not distinguish between the two different delivery types, namely radioactive stent and IRSS, making their results insufficient. Recently, several randomized controlled trials (RCTs) and retrospective studies on the use of metal stents + IRSS or I-125 seed stents were conducted. As such, we conducted a meta-analysis to compare the efficacy and safety of these two methods of I-125 seed delivery, namely metal stents + IRSS and radioactive I-125 seed stents. We then compared this with conventional metal stents in patients with MBO and reported the outcomes in terms of stent dysfunction, survival, clinical success, and complications.

Methods

Our meta-analysis was guided by the publication “Preferred Reporting Items for

Main points

- Iodine-125 (I-125) played a significant role in inhibiting tumor growth through its unique radioactive function.
- Metal stents + I-125 radioactive seed strand or I-125 seed-loaded stents demonstrated superior survival and decreased stent occlusion compared with conventional metal stents in the treatment of inoperable malignant biliary obstruction.
- The two types of I-125 delivery with metal stents did not increase the risk of procedure-related complications when compared with conventional metal stents.

Systematic reviews and Meta-Analysis” (PRISMA).²⁰

Inclusion and exclusion criteria

A study had to satisfy particular conditions. The inclusion criteria were as follows: (a) patients who had a confirmed diagnosis of MBO; (b) patients who refused surgical resection or inoperable cases; (c) studies that compared metal stents + IRSS or I-125 seed stents (the study group) versus conventional metal stents alone (the control group) in patients with MBO; and (d) studies published in English.

Exclusion criteria were: (a) case reports; (b) narrative reviews; (c) non-English studies; (d) studies on plastic biliary stents; and (e) animal studies.

Literature search and study selection

The PubMed, Embase, and Cochrane Library databases were systemically searched to find correlating studies from January 2012 to July 2021 using the following search string: (SEMS OR stent) AND (I125 OR 125I OR I-125 OR irradiation OR radioactive OR seed) AND (jaundice OR biliary). We also reviewed the references of identified articles. All studies chosen were in the English language.

Types of studies

We initially included only RCTs, but this produced a small sample size. As this could have reduced the statistical significance of the meta-analysis and led to bias, we decided to include matched retrospective cohort studies also.

Data extraction and quality assessment

Data were extracted from 18 full-text-identified articles by two independent investigators. Discrepancy problems were solved by a third investigator. A data extraction sheet was produced that included baseline study data (authors, publication year, period of enrollment, region of the conducted studies, trial types, interventions); patient baseline data (mean age, sex, sample size, cancer types, type of MBO); and treatment-related data (clinical success, stent dysfunction, complications, survival). The potential bias of RCTs was gauged by applying the Cochrane risk-of-bias tool, where possible bias relating to selection, detection, performance, reporting, attribution, and other issues was assessed. Disagreements were resolved by consensus.

Retrospective studies were scored by the Newcastle–Ottawa scale ([http://www.ohri.](http://www.ohri.ca/programs/clinical_epidemiology/oxford.asp)

[ca/programs/clinical_epidemiology/oxford.asp](http://www.ohri.ca/programs/clinical_epidemiology/oxford.asp)), and selection methods and comparability were assessed. Studies could be awarded a maximum score of 9 points, with lower scores assigned as follows: <4 = high bias risk; 4–6 = moderate bias risk; and ≥7 = low bias risk.

Publication biases were assessed by visual estimation of funnel plots, while quantitative assessment was carried out by performing Egger's test.²¹ We considered a *P* value of less than 0.05 to represent the possibility of small-study effects.

Endpoints and definitions

The original primary study endpoints for the current analysis included stent dysfunction and overall survival (OS), while the secondary study endpoints included procedure-related complications and clinical success. The relief of jaundice was defined as a clinical success if bilirubin levels were a minimum of 30% lower in two weeks or 70% lower in four weeks. Stent dysfunction was defined as the relapsing of jaundice with elevated bilirubin levels or signs related to MBO with evidence of bile duct dilation through imaging techniques. The time between stent insertion and death was defined as the patient survival period. Procedure-related complications mainly included cholangitis, cholecystitis, pancreatitis, and hemobilia. Cholangitis and cholecystitis were defined as having symptoms of abdominal pain and fever (temperature above 38°C) that required antibiotic administration within 24 hours after the procedure, with no indications of any other system being infected. Pancreatitis was diagnosed when serum amylase levels rose to more than three times the normal limit (60–180 U/L), with persistent abdominal pain after the procedure. Hemobilia was defined as the requirement for a blood transfusion or hemostatic surgery.

Statistical analysis

Dichotomous variables and event frequencies were extracted from the identified studies. We calculated the odds ratios (ORs) with 95% confidence intervals (CIs). Hazard ratios (HRs) and 95% CIs were used to assess the OS. The heterogeneity was assessed via χ^2 and *I*² tests. The OR was pooled by using either a fixed-effect or random-effect model. If heterogeneity was not high (*I*² <50%), data were pooled using a fixed-effect model. In contrast, if heterogeneity was present (*I*² >50%), data were appropriately analyzed with a random-effect model. In addition, subgroup analysis was performed to as-

sess the potential causes of heterogeneity, depending on the type of I-125 delivery via metal stents (I-125 seed stents or metal stents + IRSS). The results of this subgroup analysis were reported. Sensitivity analysis was performed by omitting each study from the analysis individually and measuring the impact this had on the results. The potential for publication bias was tested by applying funnel plots. Egger's test was also used to assess each publication's bias for pooled values with 95% CIs ($P < 0.05$ was considered significant bias). The statistical analysis was conducted using RevMan Cochrane Collaboration software, Review Manager (RevMan) version 5.4, and STATA v15.1 (Stata Corp, College Station, Texas, USA).

Results

Study selection and baseline characteristics

We initially gathered 301 potentially relevant articles based on the inclusion and exclusion criteria (Figure 1). Eighteen studies with full texts were selected to conduct the meta-analysis (Table 1). In these studies, seven were RCTs,²²⁻²⁸ and the remaining 11 were retrospective studies.²⁹⁻³⁹ Three RCTs (with 383 total participants) and two retrospective studies (with 114 total participants) compared I-125 seed-loaded stents with conven-

tional metal stents.^{23,26,27,31,39} Four RCTs (with 217 total participants) and nine retrospective studies (with 852 total participants) compared metal stents + IRSS with metal stents alone.^{22,24,25,28-30,32-38} Details of the baseline features included in these studies are shown in Table 1. Most of the baseline characteristics were comparable, with all studies being conducted in China. The target population was patients with MBO for all studies. The causes of MBO included cholangiocarcinoma, gallbladder carcinoma, pancreatic carcinoma, hepatocellular carcinoma, and cancer metastases, among others. The interventional modality in the study group was the delivery of I-125 seeds via metal stents, while the control group was implanted with conventional metal stents.

In addition, all metal stents in the control groups were SEMS. Stent implantation occurred via endoscopic retrograde cholangiopancreatography or percutaneous transhepatic cholangiography. Five studies used I-125 seed stents, and the remaining 13 used metal stents + IRSS. Two types of I-125 seed delivery were analyzed as subgroups.

Stent dysfunction

In the analysis of stent dysfunction, 11 studies^{22,23,25,26,29,30,33,34,37-39} reported data on dysfunction rates, including five RCTs and six

retrospective studies. The heterogeneity was low among these 11 studies ($I^2 = 41.7\%$; $P_h = 0.071$). The pooled OR was significant (OR: 0.61, 95% CI: 0.46–0.81, $P = 0.001$), which was demonstrated by using a fixed-effect model (Figure 2a). These results suggest that the study group had a significantly reduced incidence of stent dysfunction.

Overall survival

Six retrospective studies reported the HR of OS.^{32,34,35,37-39} These studies included 276 total patients in the study group and 290 total patients in the control group. The study group (patients who underwent surgery to implant metal stents + IRSS or I-125 seed stents) was compared with the control group (patients who underwent implantation of conventional metal stents). We pooled the HRs and revealed a significant extension of OS in the study group (HR: 0.34, 95% CI: 0.28–0.42, $P < 0.001$) ($I^2 = 0.0\%$; $P_h = 0.771$) (Figure 2b).

Clinical success

Eight studies^{25,26,30,34-36,38,39} reported data on clinical success (Table 1). There was no significant difference in success rates between the study group and the control group (OR: 1.27, 95% CI: 0.71–2.27, $P = 0.424$) ($I^2 = 0.0\%$; $P_h = 0.469$) (Figure 3).

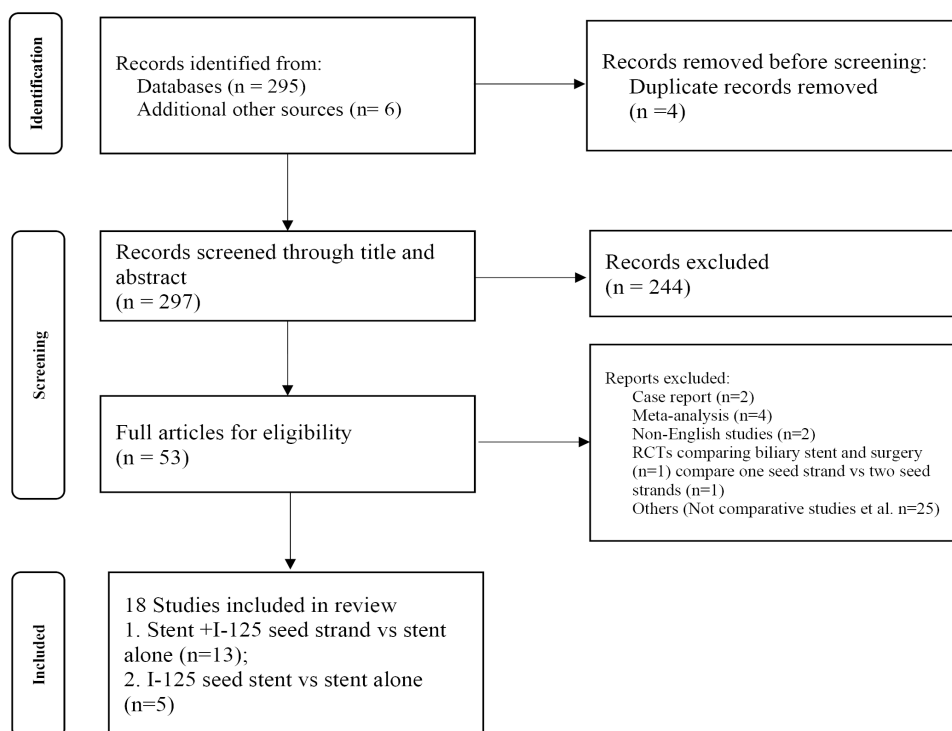


Figure 1. The process of article identification, inclusion, and exclusion according to the preferred reporting items for systematic reviews, meta-analyses guidelines and above criteria.

Table 1. Characteristics of the studies included

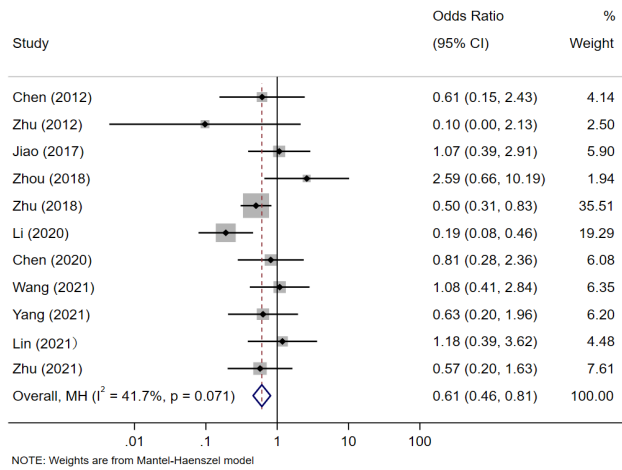
| Studies | Intervention | Sample size (M/F) | Country | Study type | Cause of MBO | MBO site | Age (mean/median, years) | Follow-up (mean/median, months) | Mean seed number | Clinical success | Stent dysfunction (%) | OS (median, days) | NOS |
|----------------------------------|---------------------------|-------------------|---------|---------------|--|------------------|--------------------------|---------------------------------|------------------|------------------|-----------------------|-------------------|-----|
| Chen et al. ²² 2012 | Stent + I-125 seed strand | 17 (12/5) | China | RCT | Cholangiocarcinoma, hepatocellular carcinoma, pancreatic carcinoma, metastases | Hilar and distal | 61 | 10.2 | 10.9 | NG | 6/17 (35.3%) | NG | - |
| | Stent | 17 (10/7) | | | | | 64 | 7.2 | | | 8/17 (47.1%) | | |
| Zhu et al. ²³ 2012 | I-125 seed stent | 12 (7/5) | China | RCT | Primary adenocarcinoma, metastatic adenocarcinoma | Hilar and distal | 63 | 4.5 for all | NG | NG | 0/12 (0) | 222 | - |
| | Stent | 11 (9/2) | | | | | 71 | | | | 3/11 (27.3%) | 75 | |
| Hasimu et al. ²⁴ 2017 | Stent + I-125 seed strand | 28 (11/17) | China | RCT | Cholangiocarcinoma, gallbladder carcinoma | Hilar and distal | 71 | 7.4 | 15.5 | NG | NG | 241 | - |
| | Stent | 27 (14/13) | | | | | 70 | 4.6 | | | | 142 | |
| Jiao et al. ²⁵ 2017 | Stent + I-125 seed strand | 29 (12/17) | China | RCT | Primary adenocarcinoma, metastatic adenocarcinoma | Hilar and distal | 63 | 9.1 for all | 10.5 | 31/31 (100%) | 16/31 (51.6%) | 355 | - |
| | Stent | 30 (16/14) | | | | | 64 | | | 28/30 (93.3%) | 15/30 (50%) | 271 | |
| Zhu et al. ²⁶ 2018 | I-125 seed stent | 164 (103/61) | China | RCT | Biliary tract cancer, pancreatic carcinoma, lymph node metastases | Hilar and distal | 65 | 5.6 for all | NG | 152/164 (93%) | 34/164 (20.7%) | 202 | - |
| | Stent | 164 (109/55) | | | | | 64 | | | 155/164 (95%) | 56/164 (34.1%) | 140 | |
| Chen et al. ²⁷ 2018 | I-125 seed stent | 13 (8/5) | China | RCT | Cholangiocarcinoma, gallbladder carcinoma, pancreatic carcinoma, ampullary carcinoma | Distal | 66 | 9.9 | NG | NG | NG | 298 | - |
| | Stent | 19 (12/7) | | | | | 68 | 4.6 | | | | 139 | |
| Wang et al. ²⁸ 2021 | Stent + I-125 seed strand | 32 (16/16) | China | RCT | pancreatic carcinoma, gallbladder carcinoma, cholangiocarcinoma, lymph node metastasis from digestive malignant tumors | Hilar and distal | 63 | NG | NG | NG | 18/32 (56.3%) | 330 | - |
| | Stent | 35 (15/20) | | | | | 63 | | | | 19/35 (54.2%) | 210 | |
| Wang et al. ²⁹ 2017 | Stent + I-125 seed strand | 24 | China | Retrospective | Cholangiocarcinoma, hilar lymph node metastases, pancreatic carcinoma, ampullary carcinoma | Hilar and distal | 57 for all | NG | 18.8 | NG | NG | 306 | 6 |
| | Stent | 26 | | | | | | | | | | 262 | |
| Zhou et al. ³⁰ 2018 | Stent + I-125 seed strand | 45 (31/14) | China | Retrospective | Cholangiocarcinoma, gallbladder carcinoma, pancreatic carcinoma, hepatocellular carcinoma, gastric cancer, ampullary carcinoma, metastases | Hilar and distal | 61 | 7.5 | | 42/45 (93.3%) | 5/45 (11.1%) | 196 | 8 |
| | Stent | 87 (59/28) | | | | | 64 | 4.5 | 14 | 83/87 (95.4%) | 4/87 (4.6%) | 96 | |

Table 1. continued

| Studies | Intervention | Sample size (M/F) | Country | Study type | Cause of MBO | MBO site | Age (mean/median, years) | Follow-up (mean/median, months) | Mean seed number | Clinical success | Stent dysfunction (%) | OS (median, days) | NOS |
|--------------------------------|---------------------------|-------------------|---------|---------------|--|------------------|--------------------------|---------------------------------|------------------|------------------|-----------------------|-------------------|-----|
| Wang et al. ³¹ 2019 | I-125 seed stent | 17 (7/10) | China | Retrospective | Pancreatic carcinoma | Distal | 59 | NG | 16 | NG | NG | 312 | 6 |
| | Stent | 15 (6/9) | | | | | 60 | | | | | 291 | |
| Pang et al. ³² 2019 | Stent + I-125 seed strand | 113 (75/38) | China | Retrospective | Cholangiocarcinoma | Hilar and distal | 68 | NG | NG | NG | NG | 390 | 6 |
| | Stent | 71 (43/28) | | | | | 68 | | | | | 240 | |
| Li et al. ³³ 2020 | Stent + I-125 seed strand | 48 (33/15) | China | Retrospective | Pancreatic carcinoma | Distal | 66 | NG | NG | NG | 9/48 (18.8%) | 209 | 8 |
| | Stent | 62 (37/25) | | | | | 65 | | | | 34/62 (54.8%) | 202 | |
| Chen et al. ³⁴ 2020 | Stent + I-125 seed strand | 35 (20/15) | China | Retrospective | Cholangiocarcinoma, gallbladder carcinoma | Hilar | 66 | NG | NG | 35/35 (100%) | 7/36 (19.4%) | 250 | 8 |
| | Stent | 45 (26/19) | | | | | 65 | | | 42/45 (93.3) | 11/48 (22.9) | 188 | |
| Pan et al. ³⁵ 2020 | Stent + I-125 seed strand | 30 (23/7) | China | Retrospective | NG | Hilar and distal | 59 for all | NG | NG | 27/30 (90%) | NG | 311 | 6 |
| | Stent | 54 (35/19) | | | | | | | | 48/54 (88.9) | | 173 | |
| Zhou et al. ³⁶ 2020 | Stent + I-125 seed strand | 40 (21/19) | China | Retrospective | Cholangiocarcinoma, pancreatic carcinoma, gallbladder carcinoma, duodenal carcinoma, metastatic carcinoma. | Hilar | 70 | NG | 15.2 | 38/40 (95%) | NG | 177 | 8 |
| | Stent | 36 (21/15) | | | | | 68 | | | 35/36 (97.2) | | 123 | |
| Yang et al. ³⁷ 2021 | Stent + I-125 seed strand | 31 (18/13) | China | Retrospective | Cholangiocarcinoma | Distal | 65 | NG | 9.9 | NG | 6/31 (19.4%) | 242 | 8 |
| | Stent | 40 (24/16) | | | | | 67 | | | | 11/40 (27.5%) | 182 | |
| Lin et al. ³⁸ 2021 | Stent + I-125 seed strand | 30 (18/12) | China | Retrospective | Cholangiocarcinoma | Hilar | 67 | NG | 11 | 30/30 (100%) | 7/30 (23.3%) | 256 | 8 |
| | Stent | 35 (21/14) | | | | | 66 | | | 33/35 (86.8) | 9/35 (25.7%) | 198 | |
| Zhu et al. ³⁹ 2021 | I-125 seed stent | 37 (20/17) | China | Retrospective | Cholangiocarcinoma, secondary biliary adenocarcinoma | Distal | 68 | NG | NG | 37/37 (100%) | 7/37 (18.9%) | 250 | 8 |
| | Stent | 45 (27/18) | | | | | 66 | | | 41/45 (91.1) | 13/45 (28.9%) | 176 | |

RCT, randomized controlled trial; MBO, malignant biliary obstruction; M, male; F, female; OS, overall survival; NOS, Newcastle–Ottawa scale; NG, not given.

a



b

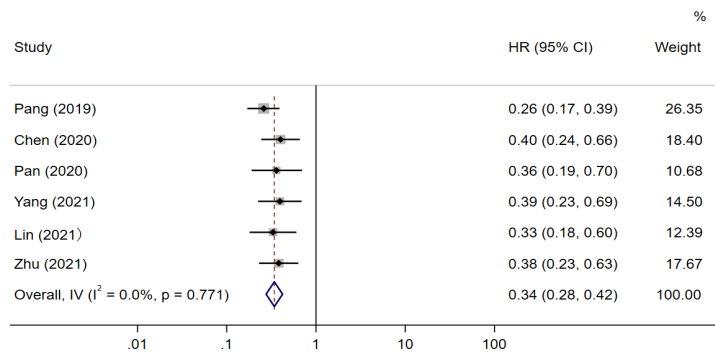


Figure 2. (a) Group analysis results of stent dysfunction rate; (b) group analysis of overall survival.

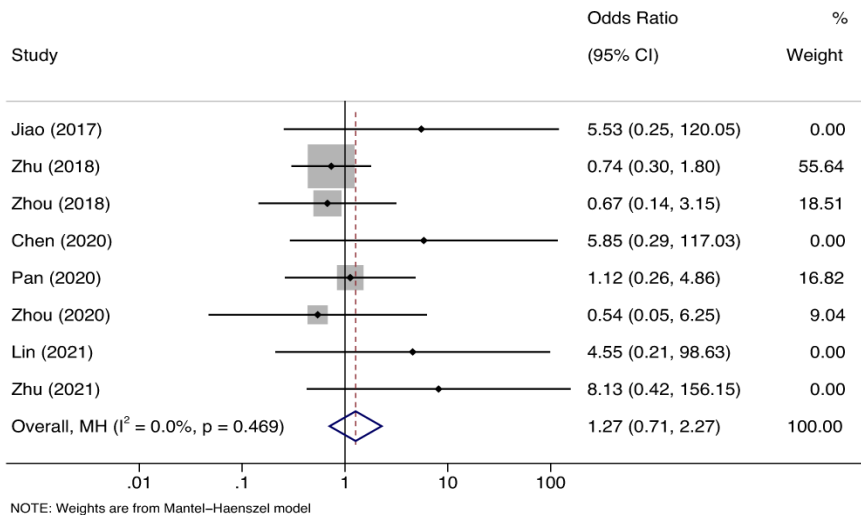


Figure 3. Group analysis results of clinical success rate.

Complications

All adverse events from studies, including cholangitis, pancreatitis, hemophilia, and cholecystitis, were reported. However, the differences between the study and the control group were not statistically significant. Heterogeneity among the studies was not significant when compared with the control group (all $P = 0.0\%$, all $P_h > 0.05$), including for cholangitis (OR: 1.00, 95% CI: 0.66–1.53, $P = 0.992$) (Figure 4a), cholecystitis (OR: 1.82, 95% CI: 0.55–6.0, $P = 0.326$) (Figure 4b), pancreatitis (OR: 1.79, 95% CI: 0.48–6.70, $P = 0.390$) (Figure 4c), and hemobilia (OR: 1.11, 95% CI: 0.47–2.65, $P = 0.813$) (Figure 4d).

Subgroup analysis

Subgroup analyses were conducted to analyze the dysfunction rates for the two different methods of I-125 seed deployment. The I-125 seed stents significantly decreased stent occlusion rates compared with metal stents alone ($I^2 = 0$; $P_h = 0.560$) (OR: 0.49, 95% CI: 0.31–0.76, $P = 0.002$) (Figure 5a). However, only three studies^{23,26,39} reported this data. The heterogeneity was high for the metal stents + IRSS groups versus the metal stents group ($I^2 = 51.2\%$; $P_h = 0.045$). Using a random-effect model to pool ORs, the analysis demonstrated no obvious reduction in stent dysfunction between the two groups (OR: 0.78, 95% CI: 0.45–1.36, $P = 0.378$) (Figure 5b). In the subgroup analysis of survival, five studies were included.^{32,34,35,37,38} Survival was obviously improved in patients who received the metal stents + IRSS compared with patients who received conventional metal stents (HR: 0.33, 95% CI: 0.26–0.42, $P < 0.001$) ($I^2 = 0.0\%$; $P_h = 0.680$) (Figure 5c).

Sensitivity analysis

In our sensitivity analysis, 11 studies reported that stent dysfunction ranged from a low of 0.58 (95% CI: 0.44–0.78, $I^2 = 30.2\%$; $P_h = 0.177$), after omitting the 2018 report by Zhou et al.³⁰, to a high of 0.73 (95% CI: 0.54–0.99; $I^2 = 0.0\%$; $P_h = 0.464$), after omitting the 2020 report by Li et al.³³, and results were generally similar. Six studies reported specific HRs for OS, from a low of 0.38 (95% CI: 0.26–0.42, $I^2 = 47.2\%$; $P_h = 0.048$), after omitting the 2020 report by Chen et al.³⁴, to a high of 0.38 (95% CI: 0.29–0.42; $I^2 = 0.0\%$; $P_h = 0.996$), after omitting the 2019 report by Pang et al.³² Again, results were similar without great fluctuation. Our sensitivity analysis indicates that there were no significant variations in the combined effect sizes after

excluding any one of the studies, which confirms the stability of the overall results.

Study quality assessment

In total, 18 studies were conducted in China. Although these authors described the use of proper randomization methods, some studies did not provide details of patient allocation; as such, the validity of seven RCTs was assessed in detail (Figure 6). The scores of 11 retrospective studies were 6–8 (Table 1).

Publication bias

No publication bias was found in this meta-analysis. A funnel plot analysis showed no asymmetry. Additionally, Egger's test was used to assess the stent dysfunction results ($P = 0.227$ for OS; $P = 0.167$ for stent dysfunction) (Supplementary Figures 1, 2). The included studies indicated no evident publication bias.

Discussion

Principle findings

The main palliative treatment for MBO is stent insertion, with relief of stenosis being

its main purpose. However, stent dysfunction remains a severe challenge for clinical practitioners and directly leads to patient mortality. Therefore, we conducted this meta-analysis to provide evidence of the advantages of metal stents + IRSS or I-125 seed stents. I-125 seed deployment resulted in lower stent dysfunction rates than conventional metal stent implantation. Moreover, the OS of patients who suffered MBO and received the I-125 seed stents had obvious improvement. Aligning with our results, Xiang et al.¹⁹ also found that I-125 seeds did not increase procedure-related complications, which demonstrates that the treatment is generally safe.

Tumors can easily grow into the lumen via the stent mesh. This can lead to the recurrent occlusion of the stent and to symptoms such as jaundice.^{18,40} In addition, the formation of granulation tissue and epithelial hyperplasia may also contribute to stent failure.^{11,41} Radioactive stents may help to avoid this stent dysfunction. First, I-125 seeds serve as the sustained radiation source. I-125 plays an important role in damaging the DNA of malignant cells, which triggers apoptosis.⁴² Second, the I-125 insertion may trigger the activation of CD3+ and CD4+ cells and cause an anticancer immune response.⁴³ Conventional

metal stents lack this unique radioactive function, which limits their longer-term benefits. These characteristics may explain why metal stents + IRSS and I-125 seed stents demonstrate a lower rate of restenosis and longer OS than conventional metal stents.

Comparison with other studies

A previous meta-analysis by Huang et al.⁴⁴ compared IRSS+ stents with stents alone in MBO treatment. However, the inclusion of only three RCTs did not provide sufficient evidence. In addition, Huang et al.⁴⁴ did not include patients who used I-125 seed stents. In our meta-analysis, we included I-125 seed stents and conducted subgroup analyses on survival and stent dysfunction for the two different deployments of I-125 seeds.

Another similar meta-analysis conducted by Xiang et al.¹⁹ compared two different methods of deploying I-125 seeds and found no significant difference in survival between the brachytherapy group and the control group. The brachytherapy group had decreased stent occlusion rates regardless of the method of I-125 deployment. This evidence is consistent with our results.

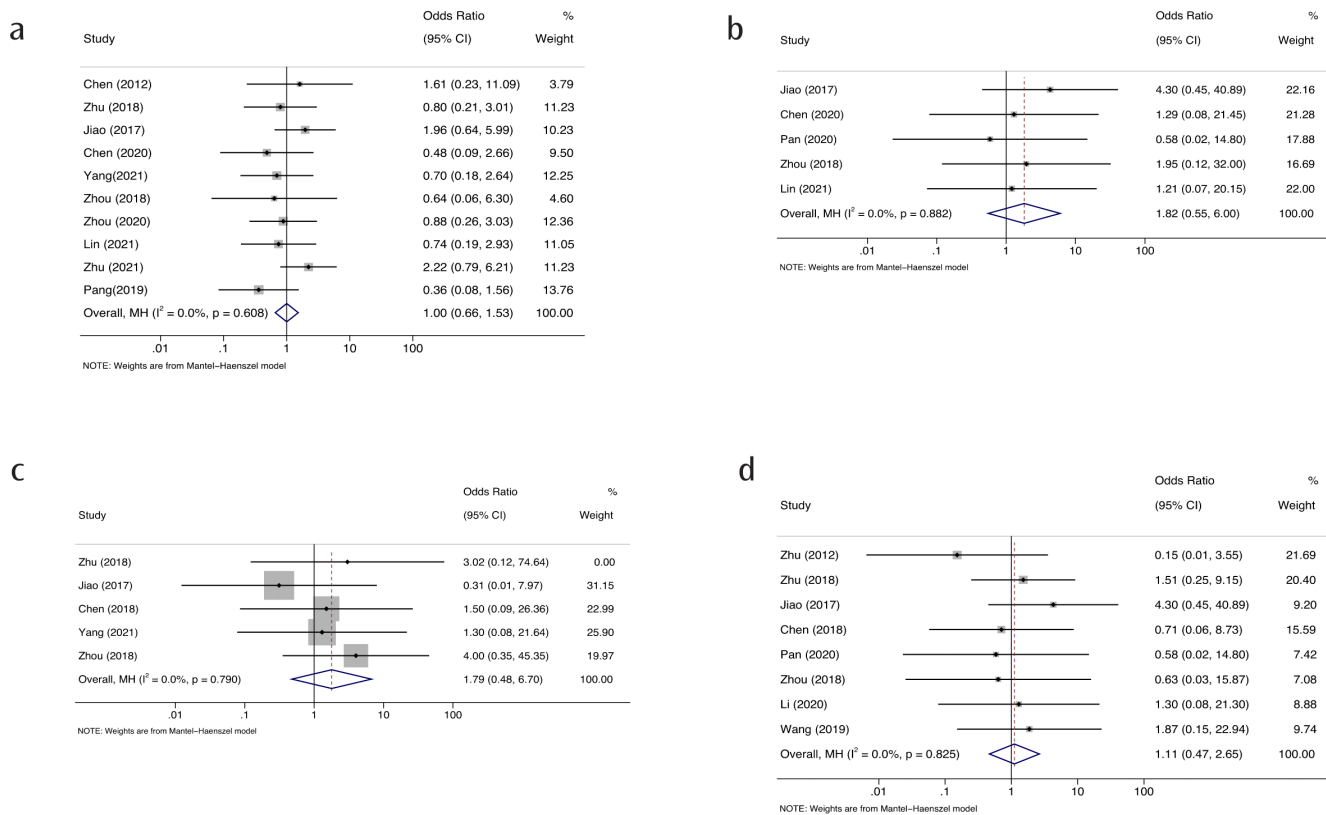


Figure 4. (a) Group analysis result of cholangitis; (b) group analysis result of cholecystitis; (c) group analysis result of pancreatitis; (d) group analysis result of hemobilia.

Two studies associated with high-dose-rate 192 iridium (Ir) intraluminal brachytherapy for MBO patients demonstrated a survival time of 9.2–9.4 months.^{45,46} In our included studies, the median survival period was longer than that of the control group (Table 1). Nevertheless, there are several shortcomings of HDR-192 Ir. First, it cannot provide the sustained radiation associated with I-125

seeds.²⁴ Second, it increases biliary infection through the procedure.²⁵ Third, for a few patients who suffer from MBO, the tissue of the biliary tract is relatively thin, which makes it difficult to complete the procedure.²⁵ Environmental requirements are also demanding, necessitating an isolated, well-shielded room.⁴⁷

Frequently, I-125 seeds are deployed via either IRSS or the use of I-125 seed stents. To fully cover the stent surface, the manufacturing process of I-125 seed stents is rigorous. The existing meta-analysis tends to emphasize the IRSS approach. However, theoretically, the latter method may be more suitable for luminal diseases such as MBO. Hopefully, more studies will be designed to compare the efficacy rates of these different deployment methods in MBO patients.

Strengths and limitations

In our meta-analysis, we included seven RCTs and 11 retrospective studies. Compared with previous meta-analyses,^{19,44} we provided relatively useful evidence. In addition, we conducted subgroup analysis between two different types of I-125 delivery with metal stents, which may provide more individualized treatment options for patients experiencing MBO. Moreover, our publication bias and sensitivity analyses indicate the reliability and stability of the results.

However, some RCTs lacked blinding procedures, which could possibly result in selection bias, with only Zhu et al.²⁶ employing a multi-center randomized research approach. Eleven studies were not RCTs in design; as such, these studies may be prone to bias,

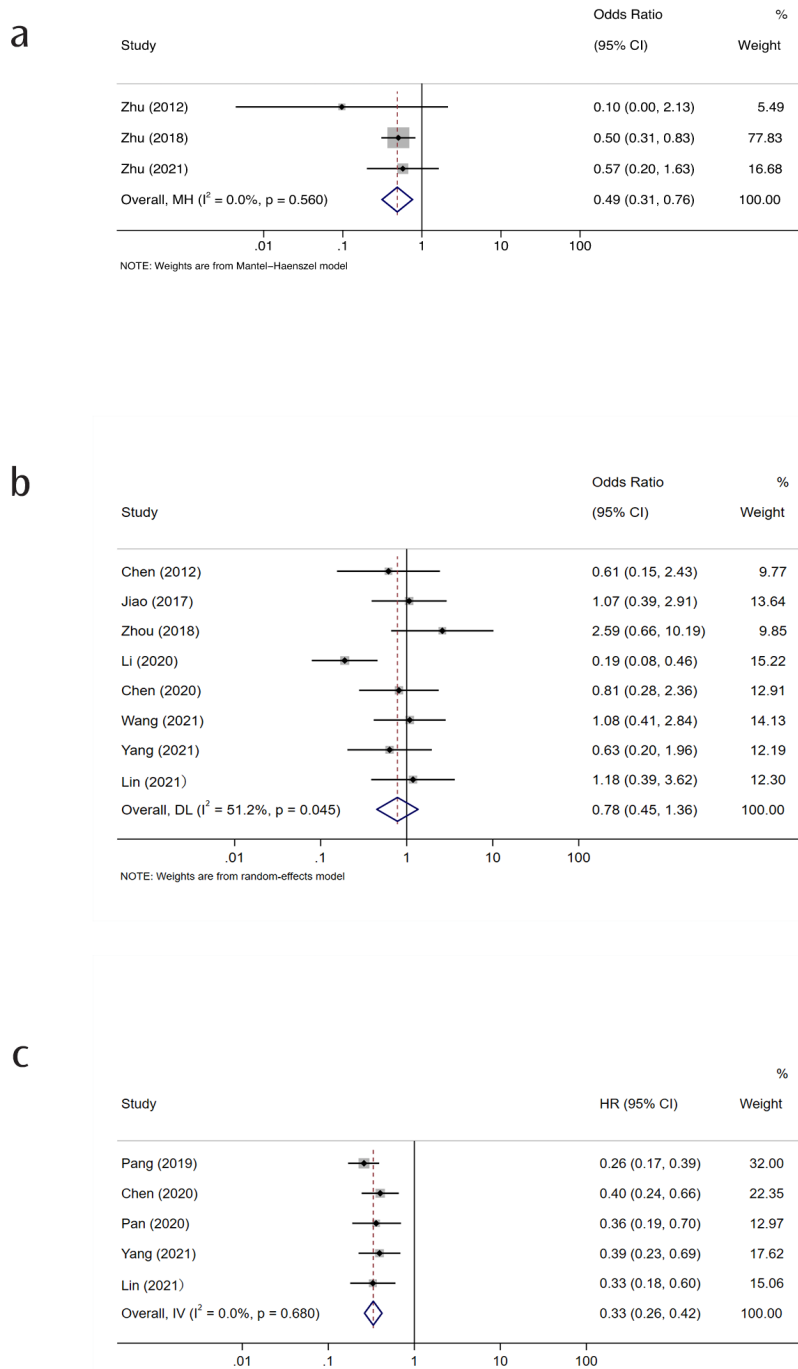


Figure 5. (a) Subgroup analysis results of the dysfunction rate (I-125 seed stents group versus control group); (b) subgroup analysis results of the dysfunction rate (metal stents + IRSS group versus control group); (c) subgroup analysis results of overall survival (metal stents + IRSS group versus control group).

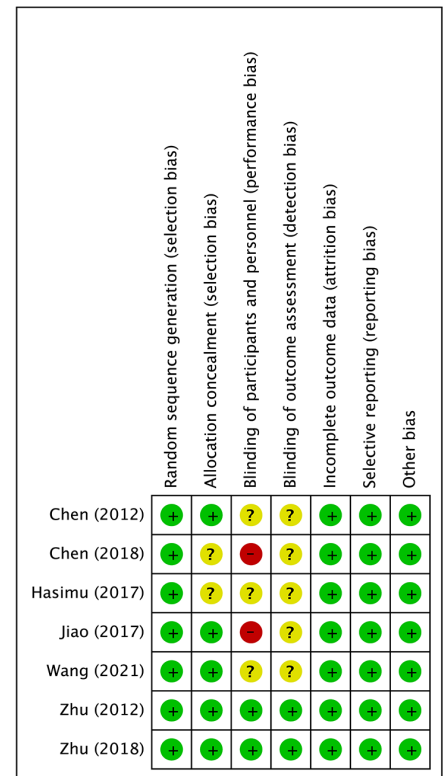


Figure 6. Quality assessment of randomized controlled trials.

which could affect the reliability of the data. All studies but four^{32,33,37,38} included participants with MBO who suffered from different malignant tumors. In addition, the obstruction sites were not well distinguished. Subgroup analysis based on the anatomic levels and cancer types could not be conducted. Future studies are necessary to evaluate related study endpoints in single-type cancers. Additionally, different sites of obstruction of MBO should be further explored for treatment.

In theory, radioactive stenting is more effective, as it loads the I-125 seeds around the implanted stent. Unsatisfactorily, five studies mention only one type of radioactive stent made from a SEMS with radioactive I-125 seeds.^{23,26,27,31,39} Moreover, studies on different radioactive stents (I-125 seed stents or other sources of radioactive material) are very rare, and more studies are urgently required.

Moreover, all included studies were conducted in China because the I-125 seed strand was developed by Chinese researchers.²⁶ A series of studies could be performed in the future when the application of I-125 seed stents becomes more accepted in other countries.

Implications

MBO is caused by various cancers, and only approximately 10%–20% of patients who suffer from MBO are eligible for surgical resection.^{9–11,14,48} Even after successful surgery, the three- and five-year survival rates remain at 18%–52% and 5%–31%, respectively.^{12,49,50} Metal stent insertion is widely used in MBO patients to relieve stenosis. I-125 seeds have a radioactive half-life of approximately 59.6 days and can persistently suppress tumorous cells.²⁷ Moreover, I-125 seeds can reliably inhibit the growth of neoplasm into the mesh of the stent, which greatly avoids stent dysfunction. This meta-analysis proves this method's advantages. Using I-125 seed strand or radioactive stents can provide a better prognosis than conventional metal stents without increasing complications, which provides clinical practitioners with an optimal choice for handling this difficult medical condition. When the symptoms were relieved, the quality of life of patients greatly improved. Indeed, according to our results, the study group had a longer survival rate than the conventional metal stent group. Large RCTs are required to verify these results.

In conclusion, the study group (using metal stents + IRSS or I-125 seed stents) was

significantly superior to the conventional metal stent group, with a superior survival rate and decreased stent occlusion. In addition, the two types of I-125 seed delivery did not increase the risk of procedure-related complications when compared with conventional metal stents. More strictly designed, multiple-center RCTs are required to confirm these findings.

Conflict of interest disclosure

The authors declared no conflicts of interest.

References

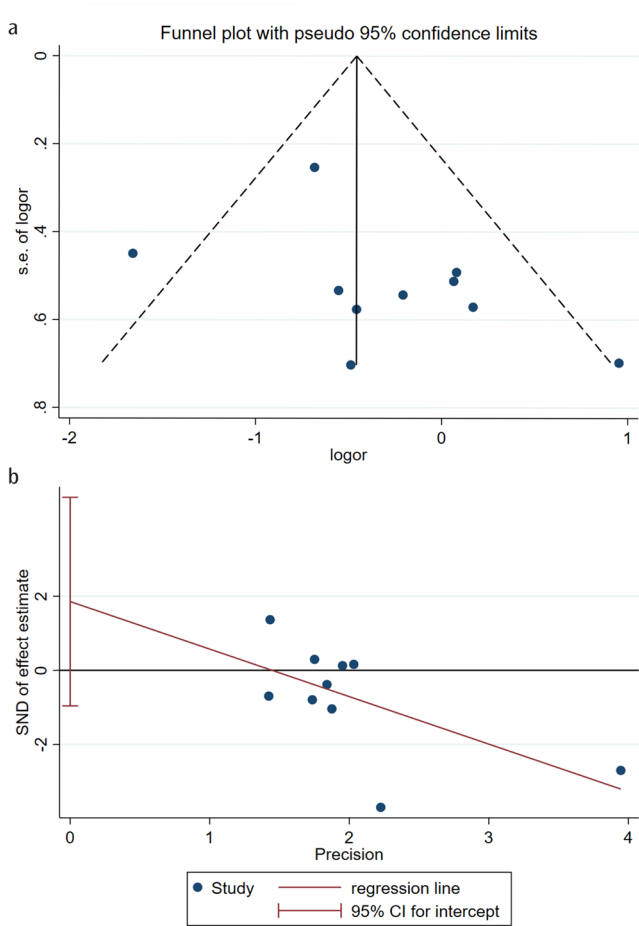
1. Fu YF, Xu YS, Shi YB, Zong RL, Cao C. Percutaneous metal stenting for malignant hilar biliary obstruction: a systematic review and meta-analysis of unilateral versus bilateral stenting. *Abdom Radiol (NY)*. 2021;46(2):749–756. [\[CrossRef\]](#)
2. Yin X, Li DM, Yang F, Liu TG, Xia FF, Fu YF. Self-expanded metallic stent insertion for hilar cholangiocarcinoma: comparison of unilateral and bilateral stenting. *J Laparoendosc Adv Surg Tech A*. 2019;29(12):1501–1506. [\[CrossRef\]](#)
3. Li M, Bai M, Qi X, et al. Percutaneous transhepatic biliary metal stent for malignant hilar obstruction: results and predictive factors for efficacy in 159 patients from a single center. *Cardiovasc Intervent Radiol*. 2015;38(3):709–721. [\[CrossRef\]](#)
4. Zhao XQ, Dong JH, Jiang K, Huang XQ, Zhang WZ. Comparison of percutaneous transhepatic biliary drainage and endoscopic biliary drainage in the management of malignant biliary tract obstruction: a meta-analysis. *Dig Endosc*. 2015;27(1):137–145. [\[CrossRef\]](#)
5. Fu YF, Zhou WJ, Shi YB, Cao W, Cao C. Percutaneous stenting for malignant hilar biliary obstruction: a randomized controlled trial of unilateral versus bilateral stenting. *Abdom Radiol (NY)*. 2019;44(8):2900–2908. [\[CrossRef\]](#)
6. Chen ZK, Zhang W, Xu YS, Li Y. Unilateral versus side-by-side metal stenting for malignant hilar biliary obstruction: a meta-analysis. *J Laparoendosc Adv Surg Tech A*. 2021;31(2):203–209. [\[CrossRef\]](#)
7. Chang G, Xia FF, Li HF, et al. Unilateral versus bilateral stent insertion for malignant hilar biliary obstruction. *Abdom Radiol (NY)*. 2017;42(11):2745–2751. [\[CrossRef\]](#)
8. Krokidis M, Hatzidakis A. Percutaneous minimally invasive treatment of malignant biliary strictures: current status. *Cardiovasc Intervent Radiol*. 2014;37(2):316–323. [\[CrossRef\]](#)
9. Gupta P, Maralakunte M, Rathee S, et al. Percutaneous transhepatic biliary drainage in patients at higher risk for adverse events:

experience from a tertiary care referral center. *Abdom Radiol (NY)*. 2020;45(8):2547–2553.

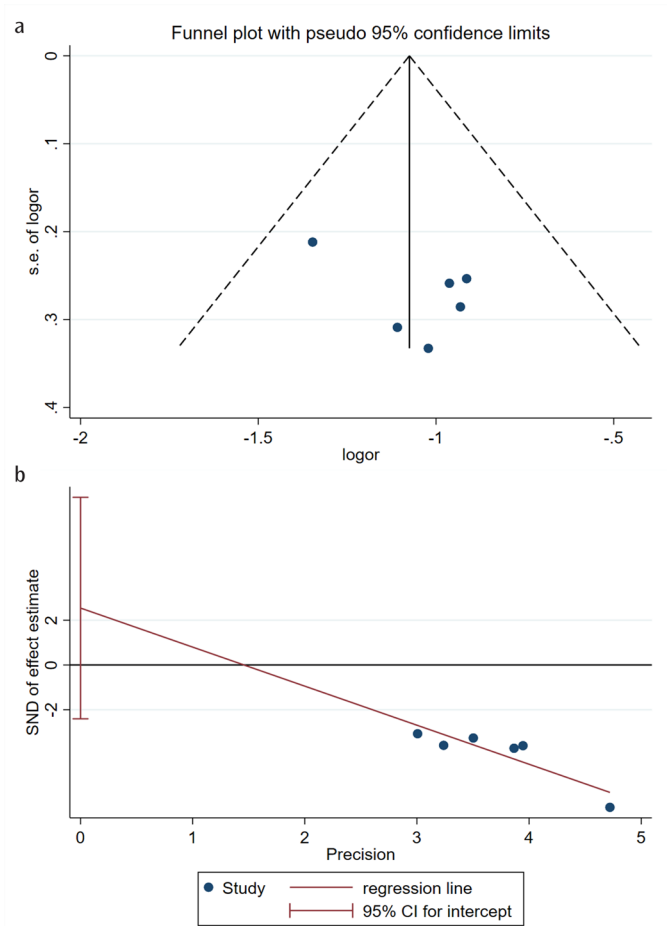
[\[CrossRef\]](#)

10. Stain SC, Baer HU, Dennison AR, Blumgart LH. Current management of hilar cholangiocarcinoma. *Surg Gynecol Obstet*. 1992;175(6):579–588. [\[CrossRef\]](#)
11. Almadi MA, Barkun A, Martel M. Plastic vs. Self-expandable metal stents for palliation in malignant biliary obstruction: a series of meta-analyses. *Am J Gastroenterol*. 2017;112(2):260–273. [\[CrossRef\]](#)
12. Petrowsky H, Hong JC. Current surgical management of hilar and intrahepatic cholangiocarcinoma: the role of resection and orthotopic liver transplantation. *Transplant Proc*. 2009;41(10):4023–4035. [\[CrossRef\]](#)
13. Yasumoto T, Yokoyama S, Nagaike K. Percutaneous transcholecystic metallic stent placement for malignant obstruction of the common bile duct: preliminary clinical evaluation. *J Vasc Interv Radiol*. 2010;21(2):252–258. [\[CrossRef\]](#)
14. Pu LZ, Singh R, Loong CK, de Moura E. Malignant biliary obstruction: evidence for best practice. *Gastroenterol Res Pract*. 2016;2016:3296801. [\[CrossRef\]](#)
15. Li M, Li K, Qi X, et al. Percutaneous transhepatic biliary stent implantation for obstructive jaundice of perihilar cholangiocarcinoma: a prospective study on predictors of stent patency and survival in 92 patients. *J Vasc Interv Radiol*. 2016;27(7):1047–1055. [\[CrossRef\]](#)
16. Han YH, Kim MY, Kim SY, et al. Percutaneous insertion of silver stent in malignant biliary obstruction. *Abdom Imaging*. 2006;31(4):433–438. [\[CrossRef\]](#)
17. Dumonceau JM, Tringali A, Blero D, et al. Biliary stenting: indications, choice of stents and results: European Society of Gastrointestinal Endoscopy (ESGE) clinical guideline. *Endoscopy*. 2012;44(3):277–298. [\[CrossRef\]](#)
18. Xu X, Li J, Wu J, Zhu R, Ji W. A systematic review and meta-analysis of Intraluminal brachytherapy versus stent alone in the treatment of malignant obstructive jaundice. *Cardiovasc Intervent Radiol*. 2018;41(2):206–217. [\[CrossRef\]](#)
19. Xiang Y, Lu S, Li Y, Liu Z, Wang W. Iodine-125 seeds combined with biliary stent placement versus stent placement alone for unresectable malignant biliary obstruction: a meta-analysis of randomized controlled trials. *J Cancer*. 2021;12(5):1334–1342. [\[CrossRef\]](#)
20. Moher D, Liberati A, Tetzlaff J, Altman DG; PRISMA Group. Preferred reporting items for systematic reviews and meta-analyses: the PRISMA statement. *PLoS Med*. 2009;6(7):e1000097. [\[CrossRef\]](#)
21. Egger M, Davey Smith G, Schneider M, Minder C. Bias in meta-analysis detected by a simple, graphical test. *BMJ*. 1997;315(7109):629–634. [\[CrossRef\]](#)

22. Chen Y, Wang XL, Yan ZP, et al. The use of ¹²⁵I seed strands for intraluminal brachytherapy of malignant obstructive jaundice. *Cancer Biother Radiopharm.* 2012;27(5) 317-323. [\[CrossRef\]](#)
23. Zhu HD, Guo JH, Zhu GY, et al. A novel biliary stent loaded with (125)I seeds in patients with malignant biliary obstruction: preliminary results versus a conventional biliary stent. *J Hepatol.* 2012;56(5):1104-1111. [\[CrossRef\]](#)
24. Hasimu A, Gu JP, Ji WZ, Zhang HX, Zhu DW, Ren WX. Comparative study of percutaneous transhepatic biliary stent placement with or without iodine-125 seeds for treating patients with malignant biliary obstruction. *J Vasc Interv Radiol.* 2017;28(4):583-593. [\[CrossRef\]](#)
25. Jiao D, Wu G, Ren J, Han X. Study of self-expandable metallic stent placement intraluminal (125)I seed strands brachytherapy of malignant biliary obstruction. *Surg Endosc.* 2017;31(12):4996-5005. [\[CrossRef\]](#)
26. Zhu HD, Guo JH, Huang M, et al. Irradiation stents vs. conventional metal stents for unresectable malignant biliary obstruction: a multicenter trial. *J Hepatol.* 2018;68(5):970-977. [\[CrossRef\]](#)
27. Chen W, Fang XM, Wang X, Sudarshan SKP, Hu XY, Chen HW. Preliminary clinical application of integrated 125I seeds stents in the therapy of malignant lower biliary tract obstruction. *J Xray Sci Technol.* 2018;26(5):865-875. [\[CrossRef\]](#)
28. Wang HW, Li XJ, Li SJ, Lu JR, He DF. Biliary stent combined with iodine-125 seed strand implantation in malignant obstructive jaundice. *World J Clin Cases.* 2021;9(4):801-811. [\[CrossRef\]](#)
29. Wang T, Liu S, Zheng YB, et al. Clinical Study on using (125)I seeds articles combined with biliary stent implantation in the treatment of malignant obstructive jaundice. *Anticancer Res.* 2017;37(8):4649-4653. [\[CrossRef\]](#)
30. Zhou WZ, Fu YM, Yang ZQ, et al. Study of percutaneous stent placement with iodine-125 seed strand for malignant biliary obstruction. *Cardiovasc Intervent Radiol.* 2019;42(2):268-275. [\[CrossRef\]](#)
31. Wang W, Li P, Wang Y, Liu B, Li Y. Percutaneous stenting and chemotherapy for unresectable pancreatic cancer: comparison of irradiation stents vs conventional metal stents. *Pancreatol.* 2019;19(7):957-962. [\[CrossRef\]](#)
32. Pang Q, Zhou L, Hu XS. Biliary stenting alone versus biliary stenting combined with (125)I particles intracavitary irradiation for the treatment of advanced cholangiocarcinoma. *Sci Rep.* 2019;9(1):11348. [\[CrossRef\]](#)
33. Li J, Yu T, Zhang L, et al. An iodine-125 seed strand combined with a metal stent versus a metal stent alone for obstructive jaundice caused by pancreatic ductal adenocarcinoma. *Brachytherapy.* 2021;20(2):446-453. [\[CrossRef\]](#)
34. Chen G, Zhang M, Sheng YG, et al. Stent with radioactive seeds strand insertion for malignant hilar biliary obstruction. *Minim Invasive Ther Allied Technol.* 2020;30(6):356-362. [\[CrossRef\]](#)
35. Pan T, Li MA, Mu LW, Zhu D, Qian JS, Li ZR. Stent placement with iodine-125 seeds strand effectively extends the duration of stent patency and survival in patients with unresectable malignant obstructive jaundice. *Scand J Gastroenterol.* 2020;55(1):123-128. [\[CrossRef\]](#)
36. Zhou C, Li H, Huang Q, Wang J, Gao K. Biliary self-expandable metallic stent combined with Iodine-125 seeds strand in the treatment of hilar malignant biliary obstruction. *J Int Med Res.* 2020;48(4):300060519887843. [\[CrossRef\]](#)
37. Yang S, Liu Y, Teng F, et al. Radioactive stent insertion for inoperable malignant common biliary obstruction. *Surg Laparosc Endosc Percutan Tech.* 2020;31(1):61-65. [\[CrossRef\]](#)
38. Lin J, Wu AL, Teng F, et al. Stent insertion for inoperable hilar cholangiocarcinoma: comparison of radioactive and normal stenting. *Medicine (Baltimore).* 2021;100(21):e26192. [\[CrossRef\]](#)
39. Zhu BY, Chen DK, Yin HH, et al. Irradiation stent insertion for distal biliary obstruction secondary to primary common biliary cancer. *Minim Invasive Ther Allied Technol.* 2022;31(5):747-752. [\[CrossRef\]](#)
40. Kim HS, Lee DK, Kim HG, et al. Features of malignant biliary obstruction affecting the patency of metallic stents: a multicenter study. *Gastrointest Endosc.* 2002;55(3):359-365. [\[CrossRef\]](#)
41. Loew BJ, Howell DA, Sanders MK, et al. Comparative performance of uncoated, self-expanding metal biliary stents of different designs in 2 diameters: final results of an international multicenter, randomized, controlled trial. *Gastrointest Endosc.* 2009;70(3):445-453. [\[CrossRef\]](#)
42. Monk BJ, Tewari KS, Puthawala AA, Syed AM, Haugen JA, Burger RA. Treatment of recurrent gynecologic malignancies with iodine-125 permanent interstitial irradiation. *Int J Radiat Oncol Biol Phys.* 2002;52(3):806-815. [\[CrossRef\]](#)
43. Xiang GA, Chen KY, Wang HN, Xiao JF. Immunological influence of iodine-125 implantation in patients with hepatocellular carcinoma resection. *Nan Fang Yi Ke Da Xue Xue Bao.* 2010;30(2):292-294. [\[CrossRef\]](#)
44. Huang YY, Xu XJ, Huang XZ, Cheng H. A stent with radioactive seed strand insertion for inoperable malignant biliary obstruction: a meta-analysis. *Brachytherapy.* 2021;20(3):638-644. [\[CrossRef\]](#)
45. Dvorák J, Jandík P, Melichar B, et al. Intraluminal high dose rate brachytherapy in the treatment of bile duct and gallbladder carcinomas. *Hepatogastroenterology.* 2002;49(46):916-917. [\[CrossRef\]](#)
46. Chen Y, Wang XL, Yan ZP, et al. HDR-192Ir intraluminal brachytherapy in treatment of malignant obstructive jaundice. *World J Gastroenterol.* 2004;10(23):3506-3510. [\[CrossRef\]](#)
47. Aggarwal R, Patel FD, Kapoor R, Kang M, Kumar P, Chander Sharma S. Evaluation of high-dose-rate intraluminal brachytherapy by percutaneous transhepatic biliary drainage in the palliative management of malignant biliary obstruction—a pilot study. *Brachytherapy.* 2013;12(2):162-170. [\[CrossRef\]](#)
48. Bismuth H, Castaing D, Traynor O. Resection or palliation: priority of surgery in the treatment of hilar cancer. *World J Surg.* 1988;12(1):39-47. [\[CrossRef\]](#)
49. Khan SA, Thomas HC, Davidson BR, Taylor-Robinson SD. Cholangiocarcinoma. *Lancet.* 2005;366(9493):1303-1314. [\[CrossRef\]](#)
50. Jemal A, Siegel R, Ward E, Hao Y, Xu J, Thun MJ. Cancer statistics, 2009. *CA Cancer J Clin.* 2009;59(4):225-249. [\[CrossRef\]](#)





Supplementary Figure 1. (a, b) Funnel plot and Egger's test on stent dysfunction. CI, confidence interval.



Supplementary Figure 2. (a, b) Funnel plot and Egger's test on overall survival. CI, confidence interval.



Inversed albumin-to-globulin ratio and underlying liver disease severity as a prognostic factor for survival in hepatocellular carcinoma patients undergoing transarterial chemoembolization

Jinlong Li* 
Zhi Li* 
Shirui Hao* 
Jitao Wang* 
Wei Chen 
Shoufang Dai 
Zhenguo Hou 
Borun Chen 
Yewei Zhang 
Dengxiang Liu 

*Jinlong Li, Zhi Li, Shirui Hao, and Jitao Wang contributed equally to this work.

From the Xingtai Institute of Cancer Control (J.L., S.H., J.W., W.C., S.D., Z.H., B.C., D.L. ✉ rmyy666@163.com), Xingtai People's Hospital, Hebei, China; Department of Infection Management (Z.L., Y.Z., ✉ zhangyewei@njmu.edu.cn), Xingtai General Hospital of North China Healthcare Group, Hebei, China; School of Medicine (J.W.), Southeast University Faculty of Medicine, Nanjing, China; Department of Hepatobiliary and Pancreatic Surgery (Y.Z.), The Second Affiliated Hospital of Nanjing Medical University, Nanjing, China.

Received 12 November 2021; revision requested 12 January 2022; accepted 14 March 2022.



Epub: 23.01.2023

Publication date: 30.05.2023

DOI: 10.5152/dir.2022.211166

PURPOSE

Previous studies have shown that an inversed albumin-to-globulin ratio (IAGR) is a predictor of the prognosis of many cancers. However, the prognostic value of an IAGR for patients with hepatocellular carcinoma (HCC) who undergo transarterial chemoembolization (TACE) is still unclear. This study aims to evaluate the predictive value of an IAGR for the prognosis of those patients.

METHODS

This study retrospectively analyzed 396 patients with HCC who received TACE. Using a cut-off value of 1.0 for the albumin-to-globulin ratio, patients were divided into a normal albumin-to-globulin ratio (NAGR) (≥ 1) and an IAGR (< 1) group. Univariate and multivariate analyses and time-dependent receiver operating characteristic analyses were performed to identify risk factors of overall survival (OS) and cancer-specific survival (CSS). Survival nomograms were constructed based on the multivariable analysis results and further evaluated using the consistency index (C-index) and calibration curve.

RESULTS

A total of 396 patients were included in the final analysis and were divided into the NAGR group ($n = 298$, 75.3%) and the IAGR ($n = 98$, 24.7%) group. The median OS and CSS were significantly worse in the IAGR group than in the NAGR group (OS: 8 vs. 26 months, CSS: 10 vs. 41 months, both $P < 0.001$). Multivariate analyses demonstrated that an IAGR was an independent risk factor for predicting worse OS [hazard ratio (HR), 2.024; 95% confidence interval (CI): 1.460–2.806] and CSS (HR: 2.439; 95% CI: 1.651–3.601). The nomogram-based model-related C-indexes for OS and CSS prediction were 0.715 (95% CI: 0.697–0.733) and 0.750 (95% CI: 0.729–0.771), and the calibration of the nomogram showed good consistency.

CONCLUSION

The IAGR along with underlying liver disease severity were the useful prognostic predictors of OS and CSS among patients with HCC undergoing TACE and might be useful to identify high-risk patients.

KEYWORDS

Hepatocellular carcinoma, transarterial chemoembolization, albumin-to-globulin ratio, overall survival, cancer-specific survival

Hepatocellular carcinoma (HCC) is the fourth most common cause of cancer-related death and ranks sixth in terms of incident cases worldwide.¹ However, most patients, when diagnosed with HCC, are ineligible for curative surgery.² Transarterial chemoembolization (TACE) is considered a first-line treatment for HCC patients with Barcelona Clinic Liver Cancer (BCLC) stage B^{1,3} and has survival benefits comparable with other palliative treatments.^{4,5} For HCC patients with BCLC stage C, TACE is also used as one of the critical treatment

options and may provide survival benefits.⁶⁻⁹ Successful initial treatment is critical for HCC patients; therefore, a simple and effective prognostic scoring system is needed for HCC patients undergoing TACE.

In numerous clinical studies on HCC that focused on patient prognosis, liver function was found to affect overall survival (OS).¹⁰ Commonly used clinical liver function assessments include assessment of the levels of serum albumin, globulin, bilirubin, transaminases, and coagulation testing.¹¹ A low serum albumin level can indicate poor nutritional status or poor albumin synthesis in the liver; a high globulin level indicates excessive immune activation, which is common in patients with HCC.¹² The albumin-to-globulin ratio (AGR) is calculated as serum albumin/(total protein–albumin) and is often greater than 1.0 in healthy people. Severe inflammatory liver disease or cirrhosis frequently results in an inversed albumin-to-globulin ratio (IAGR) (<1.0).¹³ The IAGR has been demonstrated to correlate with the prognosis of HCC patients.¹⁴⁻¹⁶ Since the cohorts of previous studies¹⁴⁻¹⁶ only included patients with early-stage HCC, no published study has focused on the prognostic value of the AGR in patients with intermediate and advanced HCC scheduled to undergo therapeutic TACE.

The present study aims to develop a nomogram model based on the AGR to predict the prognosis in patients undergoing TACE treatment for BCLC stage B/C HCC.

Methods

Patient enrollment

Patients who had HCC and underwent the first session of conventional TACE treatment between January 2016 and October 2020 at Xingtai People's Hospital were identified, and their clinical data were retrospectively analyzed. The inclusion criteria were as fol-

lows: [1] 18–75 years old, [2] a diagnosis of HCC confirmed by pathological examination or clinical feature criteria according to the European Association for the Study of the Liver guidelines,² [3] conventional TACE used for the first-line treatment of liver cancer, and [4] presence of BCLC stage B/C. The exclusion criteria included the following: [1] the presence of another cancer; [2] the presence of serious concomitant diseases, such as acute myocardial infarction, pulmonary embolism, or cerebral hemorrhage; or [3] missing data on important prognostic variables. This study was approved by the ethical committee of our institution [no. 2020(089)]. Written informed consent was obtained from each patient. Complete follow-up information was obtained through telephone interviews.

Data collection

Clinical characteristics, including the demographic data and pathological results, were obtained from the medical record system. Laboratory features were measured within two days before TACE and included levels of albumin, globulin (total protein–albumin), total bilirubin, alanine aminotransferase (ALT), aspartate transaminase (AST), hemoglobin, platelets, international normalized ratio (INR), serum creatinine, and alpha-fetoprotein (AFP), as well as hepatitis B surface antigen (HBsAg) status. Data on tumor-related variables were obtained using computed tomography (CT) or magnetic resonance imaging (MRI) and included maximum tumor size, tumor numbers, vascular invasion, and distant metastasis. Vascular invasion was defined as the tumor involving the hepatic artery, portal vein, hepatic vein, or inferior vena cava as assessed by preoperative CT or MRI images.¹⁷ The Child–Pugh grade¹⁸ and albumin–bilirubin (ALBI) grade¹⁰ were determined based on liver function and tumor-related variables. The AGR was calculated as serum albumin/(total protein–albumin). Patients with an AGR >1.0 and <1.0 were allocated to the normal AGR (NAGR) and IAGR groups, respectively.

TACE procedure

Conventional TACE was performed by three doctors with 15, 12, and 10 years of tumor interventional treatment experience, respectively, as described previously.^{19,20} It was conducted by selective hepatic artery cannulation and superselection to the artery supplying the tumor, followed by an injection of a mixed emulsion of 5 mL of iodized oil (Lipiodol; Guerbet, Bloomington, IN, US) and 50 mg doxorubicin hydrochloride or cis-

platin (2 mg/kg body weight). Finally, a gelatin sponge strip (Upjohn, Kalamazoo, MI, US) was used to embolize the tumor-supplying artery.

Follow-up

Periodic follow-ups were done on each patient until death or until the study was completed on October 15, 2021. OS was computed from the time of TACE treatment to the date of death. Cancer-specific survival (CSS) was defined as patients who died of liver cancer. All patients underwent laboratory testing and contrast-enhanced CT or MRI and were followed up with every three months for the first year. If the patient had an uneventful first year, the follow-up interval was thereafter changed to once every six months. Two independent clinicians completed the follow-up and review to reduce potential biases.

Statistical analysis

The variables were calculated as the mean \pm standard deviation or median (interquartile range) for continuous data. Categorical data were expressed as numbers and percentages. The unpaired Student's t-test was used to compare continuous parametric variables, and the Mann–Whitney U test was used for continuous non-parametric variables. Pearson's chi-squared test and Fisher's exact test were used for categorical variables. To balance the baseline data, which consisted of maximum tumor size, hemoglobin, platelets, INR, ALT, AST, bilirubin, creatinine, and AFP, the two groups were compared by propensity-score matching (PSM) analysis at a 1:1 ratio to remove selection bias with a 1.0 caliper value. Kaplan–Meier curves were drafted to evaluate OS and CSS, and comparisons were performed using the log-rank test between the two groups. To identify the prognostic variables independently related to OS and CSS, a multivariable Cox regression analysis was performed using variables with a *P* value of <0.100 in the univariate analysis. Results of the regression analysis are shown as hazard ratios (HRs) and 95% confidence intervals (CIs). To compare the predictive ability among the clinical models (including the Child–Pugh and ALBI grades), the area under the time-dependent receiver operating characteristic (ROC) curves (AUC) (*t* = 1, 2, and 3 years) was calculated for OS and CSS.²¹ Survival nomogram models were constructed based on the results of the multivariable analysis. The bootstrap resampling method was used for internal validation of the predictive models by selecting 1,000 repetitions

Main points

- An inversed albumin-to-globulin ratio (IAGR) before transarterial chemoembolization (TACE) treatment is an independent prognostic factor for worse overall survival and cancer-specific survival in hepatocellular carcinoma (HCC) patients.
- An IAGR and underlying liver disease severity can be used to identify high-risk HCC patients.
- The albumin-to-globulin-based nomograms showed good performance in predicting the prognosis of HCC patients who had undergone TACE.

from the regression models for OS and CSS.²² Statistical analyses were performed using R software version 4.0.5 (The R Foundation for Statistical Computing, Vienna, Austria; www.r-project.org), with the “MatchIt,” “survival,” “timeROC,” and “rms” packages. A *P* value of <0.05 was considered statistically significant.

Results

Patient characteristics

Using the predetermined inclusion and exclusion criteria, 396 patients (302 males, 94 females) were enrolled (Figure 1). The mean patient age was 61.1 ± 9.1 years. Using a cut-off value of 1.0 for the AGR (16), the patients were stratified into either the NAGR group (*n* = 298, 75.3%) or the IAGR group (*n* = 98, 24.7%) (mean AGR: 1.34 vs. 0.84, respectively). Patients in the IAGR group had a higher percentage of diabetes (18.4% vs. 9.4%), larger tumor size (mean: 6.9 vs. 6.0 cm), worse Child–Pugh grading (grade B: 43.9% vs. 13.1%), and worse ALBI grading (grades 2 and 3: 84.7% vs. 50.0%) than the NAGR group (Table 1). Several laboratory parameters, including albumin, globulin, AST, hemoglobin, platelets, serum creatinine, and INR, were significantly different between the two groups. No significant distribution differences were identified in the two groups for age, sex, HBsAg status, tumor number, or AFP level. Af-

ter PSM, there was no significant difference except albumin and globulin in the baseline data between the two groups (Table 1).

The prognostic outcomes of the IAGR and NAGR groups are compared in Table 2. The median and maximum follow-up periods were 13 and 62 months, respectively. During the observation period, 227 patients died, and 159 of them died of liver cancer. The death rate and the percentage of deaths due to liver cancer were significantly higher in the IAGR group than in the NAGR group (73.4% vs. 52.0% and 62.2% vs. 32.9%, respectively; both *P* < 0.001). The median OS and CSS were significantly worse in the IAGR group than in the NAGR group (8 vs. 26 months, and 10 vs. 41 months, respectively; both *P* < 0.001). The three-year OS and CSS rates were 41.2% and 21.9%, respectively, in the IAGR group, which were significantly worse than those of the NAGR group (65.0% and 29.5%, respectively, both *P* < 0.001). After PSM, the prognosis of patients in the IAGR group was significantly worse compared with the NAGR group, and the results were similar to those before PSM (Table 2). The comparison of the OS and CSS curves of the two groups are shown in Figure 2. As Figure 3 shows, although there was a difference in Child–Pugh grading between the NAGR and IAGR groups, the comparison of the OS curves of the Child–Pugh A and B showed no statistically significant difference (*P* = 0.182).

Univariate and multivariate analysis for OS and CSS

The results of the univariate and multivariate Cox regression analyses used to determine independent variables with OS and CSS after TACE treatment for HCC are shown in Tables 3 and 4. Multivariate analyses indicated that prognostic factors for worse OS and CSS [HR (95% CI)] were an IAGR [OS: 2.024 (1.460–2.806), CSS: 2.439 (1.651–3.601)], vascular invasion [OS: 2.089 (1.481–2.947), CSS: 1.869 (1.234–2.832)], distant metastasis [OS: 2.087 (1.427–3.053), CSS: 2.062 (1.311–3.243)], and maximum tumor size [OS: 1.683 (1.180–2.401), CSS: 1.768 (1.131–2.764)]. The AST level was also an independent risk factor for OS [1.488 (1.062–2.084)]. Nomograms for predicting OS and CSS were built based on the multivariate Cox regression model (Figure 4). The consistency indexes (C-indexes) for OS and CSS prediction were up to 0.715 (95% CI: 0.697–0.733) and 0.750 (95% CI: 0.729–0.771), respectively. The calibration of the nomogram for the probability of OS and CSS at one, two, and three years are shown in Figure 5. The results of the time-dependent ROC analysis comparing the values of various clinical scores in predicting OS and CSS are shown in Table 5. The AUC values of the AGR at one, two, and three years for OS were 66.4, 65.4, and 60.9, respectively; and 71.2, 70.4, and 62.9, respectively, for CSS. These values were better than the Child–Pugh grade at each timepoint (*P* < 0.050 for all) but similar to the ALBI grade (*P* > 0.050 for all).

Discussion

This study demonstrates that an IAGR could serve as an independent prognostic factor predicting unfavorable prognosis for OS and CSS in HCC patients who received TACE therapy. In addition, the AGR had a similar predictive value as the ALBI grade but a better predictive value than the Child–Pugh grade.

Several studies have reported that inflammation and malnutrition are closely related to the occurrence and development of cancer.^{23,24} HCC often occurs at lesions caused by cirrhosis,²⁵ which induces local inflammatory responses and the release of inflammatory cytokines, thereby promoting an inflammatory microenvironment around the tumor.^{26,27} The inflammatory microenvironment has the potential to induce deoxyribonucleic acid (DNA) damage and genomic instability, increase mutation rates, and enhance the proliferation of mutated cells.^{28,29} Conversely, DNA damage could lead to inflammation

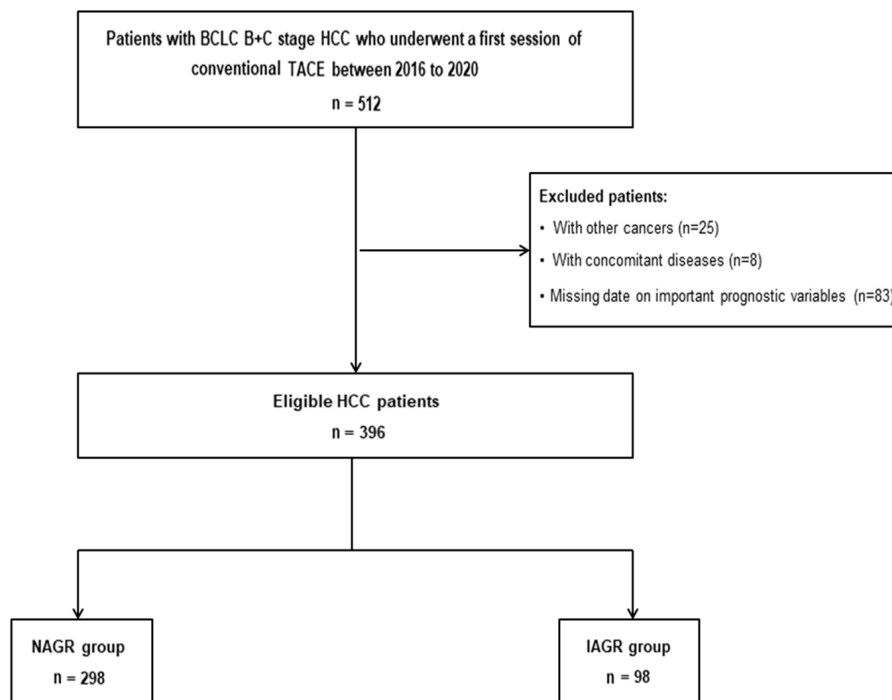


Figure 1. Flow chart of the study population. BCLC, Barcelona Clinic Liver Cancer; HCC, hepatocellular carcinoma; IAGR, inversed albumin-to-globulin ratio; NAGR, normal albumin-to-globulin ratio; TACE, transarterial chemoembolization.

Table 1. Comparisons of characteristics between the IAGR and NAGR groups before and after PSM

| Characteristics | Before PSM | | | | After PSM | | | |
|----------------------------|------------------------|-----------------------|------------------------|---------|-----------------------|----------------------|----------------------|---------|
| | Total (n = 396) | IAGR (n = 98) | NAGR (n = 298) | P value | Total (n = 154) | IAGR (n = 77) | NAGR (n = 77) | P value |
| Age, years† | 61.1 ± 9.1 | 61.4 ± 9.2 | 61.0 ± 9.0 | 0.704 | 60.6 ± 9.2 | 61.4 ± 8.9 | 59.8 ± 9.5 | 0.290 |
| Male sex | 302 (76.3) | 77 (78.6) | 225 (75.5) | 0.630 | 119 (77.3) | 64 (83.1) | 55 (71.4) | 0.123 |
| BMI‡ | 23.6 (21.4-25.9) | 22.9 (21.0-25.9) | 23.7 (21.5-25.9) | 0.132 | 23.4 (21.1-25.9) | 22.9 (20.9-25.6) | 23.8 (21.4-26) | 0.274 |
| HBsAg (+) | 282 (71.2) | 73 (74.5) | 209 (70.1) | 0.485 | 106 (68.8) | 58 (75.3) | 48 (62.3) | 0.117 |
| Vascular invasion | 56 (14.1) | 20 (20.4) | 36 (12.1) | 0.059 | 27 (17.5) | 17 (22.1) | 10 (13) | 0.203 |
| Distant metastasis | 56 (14.1) | 17 (17.4) | 39 (13.1) | 0.377 | 30 (19.5) | 13 (16.9) | 17 (22.1) | 0.542 |
| Multiple tumors, ≥2 | 210/186 (53.0/47.0) | 49/49 (50.0/50.0) | 161/137 (54.0/46.0) | 0.340 | 73/81 (48.1/52.9) | 38/39 (49.4/51.6) | 35/42 (45.5/54.5) | 0.657 |
| Maximum tumor size, cm† | 6.0 (3.7-7.5) | 6.0 (5.0-8.0) | 5.9 (3.6-7.2) | 0.003* | 6.0 (5.0-7.5) | 6.0 (3.9-7.5) | 6.0 (5.0-7.5) | 0.952 |
| Hemoglobin, g/L† | 128 (116-140) | 119 (105-131) | 131 (119-143) | <0.001* | 120 (105-134) | 120 (108-133) | 119 (97-135) | 0.932 |
| Platelets, 109/L† | 126 (87-179) | 147 (94-222) | 121 (83-167) | 0.003* | 141 (92-222) | 133 (92-211) | 155 (96-226) | 0.569 |
| INR† | 1.11 (1.04-1.19) | 1.15 (1.08-1.26) | 1.09 (1.03-1.17) | <0.001* | 1.13 (1.05-1.21) | 1.14 (1.06-1.23) | 1.11 (1.05-1.19) | 0.126 |
| ALT, U/L† | 29.0 (19.9-43.7) | 32.2 (22.2-46.8) | 28.6 (18.5-41.8) | 0.083 | 30.2 (21.5-47.8) | 33.0 (23.0-49.5) | 27.0 (19.9-44.5) | 0.152 |
| AST, U/L† | 35.0 (25.0-54.1) | 43.6 (29.0-74.1) | 32.7 (24.5-48.6) | <0.001* | 39.0 (27.1-67.0) | 43.0 (29.0-77.1) | 33.0 (25.0-56.0) | 0.054 |
| Albumin, g/L† | 37.9 ± 6.4 | 31.8 ± 4.8 | 39.9 ± 5.6 | <0.001* | 35.4 ± 6.9 | 31.5 ± 4.8 | 39.3 ± 6.4 | <0.001* |
| Globulin, g/L† | 31.2 (27.5-35.8) | 38.6 (35.5-41.9) | 29.9 (26.5-32.6) | <0.001* | 34.32 ± 6.59 | 38.29 ± 5.51 | 30.35 ± 5.02 | <0.001* |
| Bilirubin, μmol/L† | 19.2 (14.0-25.7) | 22.3 (15.5-29.8) | 18.7 (13.9-25.1) | 0.049* | 19.7 (14.1-26.7) | 22.6 (14.0-29.8) | 18.8 (14.7-24.8) | 0.376 |
| Creatinine, μmol/L† | 62.1 (54.0-73.1) | 59.1 (50.8-70.9) | 63.5 (55.3-73.6) | 0.027* | 61.2 (51.4-76.8) | 59.4 (50.8-71.5) | 64.9 (55.0-79.0) | 0.067 |
| AFP, IU/mL† | 4.92 (2.42-28.37) | 4.92 (1.77-41.09) | 4.92 (2.52-25.36) | 0.960 | 4.9 (2.1-23.7) | 4.9 (1.8-31.5) | 4.1 (2.2-14.9) | 0.447 |
| Child–Pugh grade, A/B | 314/82 (79.3/20.7) | 55/43 (56.1/43.9) | 259/39 (86.9/13.1) | <0.001* | 104/50 (67.5/32.5) | 42/35 (54.6/45.4) | 62/15 (80.5/19.5) | <0.001* |
| ALBI gradet | -2.41 (-2.77-1.98) | -1.85 (-2.18-1.53) | -2.59 (-2.88-2.26) | <0.001* | -2.1 ± 0.6 | -1.8 ± 0.4 | -2.5 ± 0.6 | <0.001* |
| Albumin-to-globulin ratio† | 1.25 (1.01-1.48) | 0.84 (0.77-0.91) | 1.34 (1.19-1.52) | <0.001* | 1.0 (0.9-1.3) | 0.8 (0.8-0.9) | 1.3 (1.1-1.5) | <0.001* |

†values are mean ± standard deviation or median (interquartile range); *P values <0.050. AFP, alpha-fetoprotein; ALBI, albumin–bilirubin; ALT, alanine aminotransferase; AST, aspartate transaminase; HBsAg, hepatitis B surface antigen; IAGR, inversed albumin-to-globulin ratio; INR, international normalized ratio; MELD, Model for End-Stage Liver Disease; NAGR, normal albumin-to-globulin ratio; PSM, propensity score matching.

Table 2. Comparisons of long-term oncologic outcomes between the IAGR and NAGR groups before and after PSM

| n (%) | Before PSM | | | | After PSM | | | |
|--|------------------|-----------------|------------------|---------|------------------|-----------------|------------------|---------|
| | Total (n = 396) | IAGR (n = 98) | NAGR (n = 298) | P value | Total (n = 154) | IAGR (n = 77) | NAGR (n = 77) | P value |
| Survival time, months† | 13.0 (6.0-30.0) | 6 (3.0-17.5) | 16 (8.0-33.8) | <0.001* | 11.0 (5.0-27.0) | 8.0 (3.0-18.0) | 12.0 (6.0-30.0) | 0.007* |
| Death during the follow-up | 227 (57.3) | 72 (73.5) | 155 (52.0) | <0.001* | 103 (66.9) | 55 (71.4) | 48 (62.3) | 0.304 |
| Death due to liver cancer during the follow-up | 159 (40.2) | 61 (62.2) | 98 (32.9) | <0.001* | 70 (45.5) | 44 (57.1) | 26 (33.8) | 0.006* |
| OS, months‡ | 19.0 (14.0-23.9) | 8.0 (4.9-11.1) | 26.0 (19.2-32.8) | <0.001* | 12.0 (9.0-15.0) | 10.0 (5.5-14.5) | 17 (5.8-28.4) | 0.040* |
| 1-year OS rate, % | 59.8 | 38.7 | 66.7 | | 48.2 | 39.9 | 56.2 | |
| 2-year OS rate, % | 45.8 | 27.8 | 51.2 | | 36.8 | 29.4 | 43.9 | |
| 3-year OS rate, % | 36.5 | 21.9 | 41.2 | | 28.9 | 22.6 | 35.4 | |
| CSS, months‡ | 37.0 (34.3-39.7) | 10.0 (4.5-15.5) | 41.0 (36.9-43.2) | <0.001* | 35.0 (19.1-51.0) | 12.0 (6.4-17.6) | 38.0 (32.8-43.2) | 0.002* |
| 1-year DFS rate, % | 70.3 | 43.9 | 78.8 | | 62.2 | 46.5 | 78.1 | |
| 2-year DFS rate, % | 61 | 37.5 | 68.7 | | 54.3 | 40.1 | 68.8 | |
| 3-year DFS rate, % | 50.3 | 29.5 | 57.1 | | 45.1 | 32.8 | 58.1 | |

†values are mean ± standard deviation; ‡values are median and 95% confidence interval; *P values <0.050. OS, overall survival; CSS, cancer-specific survival; PSM, propensity score matching; IAGR, inversed albumin-to-globulin ratio; NAGR, normal albumin-to-globulin ratio.

and subsequently promote tumorigenesis, similar to that in the diethylnitrosamine HCC model.^{29,30} In addition to the development of cancer cachexia, chronic systemic inflammation contributes to progressive nutritional decline.^{15,24} Malnutrition in patients with cancer cannot be reversed by simple nutritional supply alone, and it could eventually lead to a poor prognosis.²⁴

Serum albumin, which is produced by the liver, is commonly used as a marker of liver function and nutritional status. Serum albumin has been reported to suppress HCC proliferation by decreasing the phosphorylation of the Rb protein and increasing the expression of p21 and p57 following an increase in the G0/G1-phase cell population.³¹ Multiple studies have reported that hypoalbuminemia reflects liver dysfunction and malnu-

trition, which eventually impair immunity,¹² and that it affects the long-term OS and tumor recurrence.^{31,32} Serum albumin assessment is one of the common components in the clinical models, such as the Child-Pugh grade and the ALBI grade, which are widely used to stratify HCC patients into prognostically distinct groups.³³

Globulins consist of several pro-inflammatory proteins,¹⁴ including C-reactive protein, α 2-macroglobulin, fibrinogen, prothrombin, and serum amyloid A.³⁴ Since immunoglobulins in humans are mainly metabolized by the liver, the ability to clear immunoglobulins in patients with severe hepatic dysfunction may be reduced, resulting in hyperglobulinemia.^{35,36} Tumor-related inflammation stimulates the production of various cytokines, such as interleukin (IL)-1, IL-6, and tumor necrosis factor,³⁷ which can act on the liver and induce the synthesis of positive acute-phase reactants.³⁴ This might explain the increased serum globulin levels observed in this study. Moreover, several studies have reported that pro-inflammatory factors are associated with the prognosis of HCC patients.^{38,39}

The AGR reflects the relative levels of albumin and globulin, which indicate hepatic nutritional and inflammatory states as well as the degree of hepatic functional impairment.¹⁵ These may contribute to the observed correlation with HCC prognosis.¹⁴⁻¹⁶ In addition, Suh et al.⁴⁰ demonstrated that a low AGR was a risk indicator for both short- and long-term cancer development in the general population.

The study results show that patients with intermediate- and advanced-stage HCC who have a low AGR are predicted to have poor prognosis after TACE. Therefore, if there is a high risk of adverse effects from TACE therapy, or limited potential benefits, clinicians should be cautious when selecting the therapeutic method. In the present study, vascular invasion and distant metastasis were identified as the independent risk factors for worse OS and CSS; AST was an independent risk for only OS. Each of these risk factors has been reported previously.^{16,41} Based on the results of multivariate analysis, an AGR-based nomogram model for predicting OS and CSS was constructed, which can be used to predict the prognosis of HCC patients receiving TACE and to screen high-risk prognostic subgroups. This AGR-based nomogram model performs well in predicting the prognosis OS and CSS, and the C-indexes and calibration curves support survival prediction.

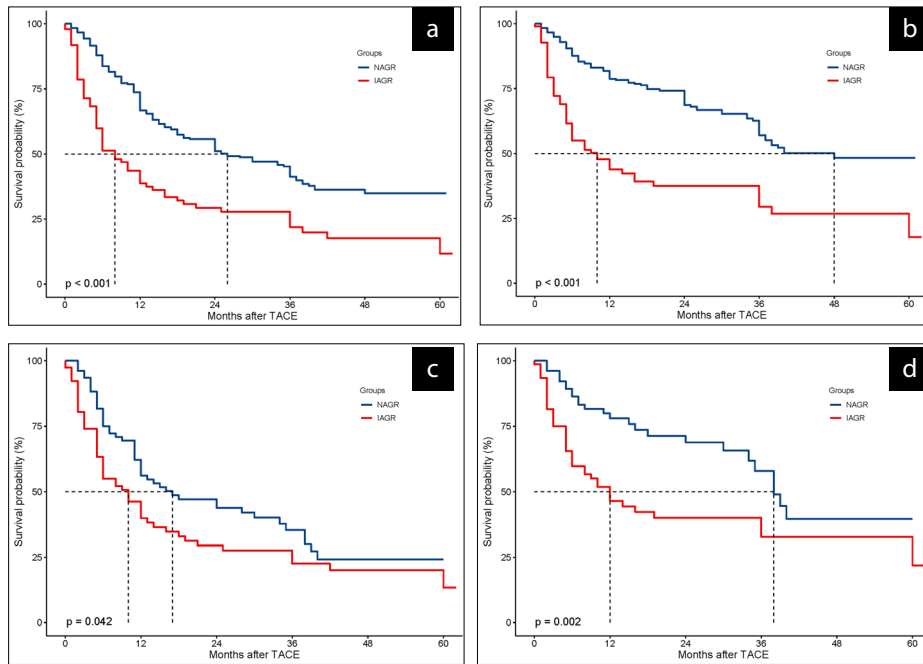


Figure 2. (a-d) Overall survival (OS) and cancer-specific survival (CSS) curves comparisons between the IAGR and NAGR groups before and after propensity score matching (PSM): (a), OS before PSM; (b), CSS before PSM; (c), OS after PSM; (d), CSS after PSM. IAGR, inverted albumin-to-globulin ratio; NAGR, normal albumin-to-globulin ratio; TACE, transarterial chemoembolization.

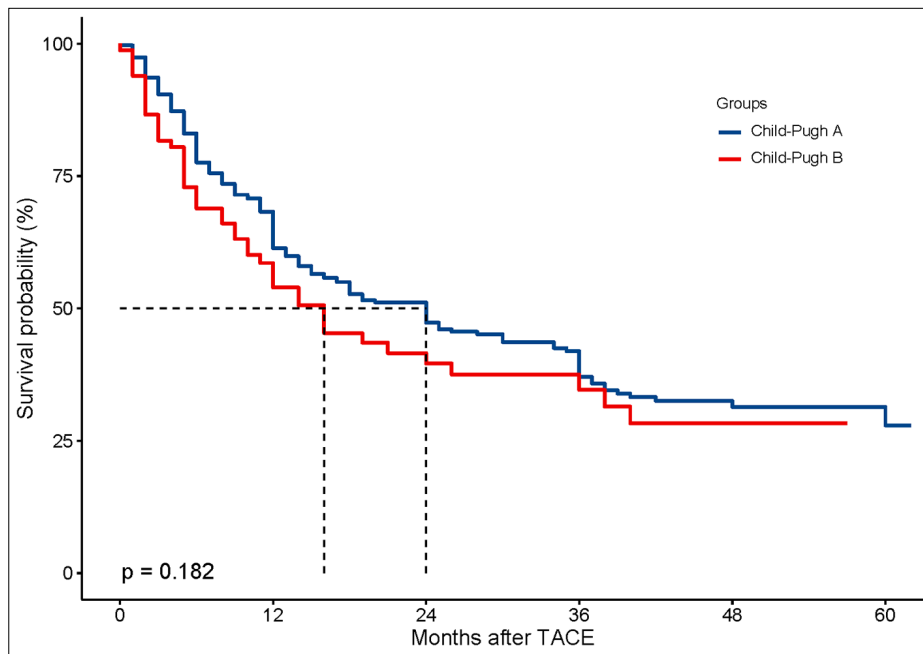


Figure 3. Overall survival curves comparisons between the Child-Pugh score A and B. TACE, transarterial chemoembolization.

Table 3. Univariable and multivariable Cox regression analyses in predicting overall survival

| Characteristics | UV HR (95% CI) | UV P value | MV HR (95% CI) ² | MV P value* |
|-----------------------------------|---------------------|------------|-----------------------------|-------------|
| Age, >60 years | 0.832 (0.640-1.082) | 0.170 | | |
| Male sex | 0.909 (0.676-1.223) | 0.529 | | |
| Hypertension | 1.273 (0.939-1.725) | 0.120 | | |
| HBsAg (+) | 0.906 (0.686-1.197) | 0.488 | | |
| Vascular invasion | 2.846 (2.064-3.924) | <0.001 | 2.089 (1.481-2.947) | <0.001 |
| Distant metastasis | 2.477 (1.786-3.435) | <0.001 | 2.087 (1.427-3.053) | <0.001 |
| Maximum tumor size, >5 cm | 2.655 (1.945-3.625) | <0.001 | 1.683 (1.180-2.401) | 0.004 |
| Multiple tumors | 1.804 (1.386-2.348) | <0.001 | NS | 0.387 |
| Child–Pugh grade B | 1.237 (0.897-1.706) | 0.194 | | |
| IAGR | 2.151 (1.625-2.847) | <0.001 | 2.024 (1.460-2.806) | <0.001 |
| ALBI grade 2 + 3 | 1.503 (1.144-1.974) | 0.003 | NS | 0.689 |
| ALT, >40 U/L | 1.345 (1.019-1.775) | 0.036 | NS | 0.731 |
| AST, >40 U/L | 2.099 (1.616-2.727) | <0.001 | 1.488 (1.062-2.084) | 0.021 |
| Bilirubin, >17.1 µmol/L | 0.967 (0.739-1.263) | 0.803 | | |
| Creatinine, >80 µmol/L | 1.109 (0.782-1.571) | 0.562 | | |
| Hemoglobin, <110 g/L | 1.512 (1.111-2.057) | 0.008 | NS | 0.403 |
| Platelet, <100 10 ⁹ /L | 0.717 (0.540-0.953) | 0.022 | NS | 0.538 |
| INR, >1.17 | 1.213 (0.911-1.615) | 0.187 | | |
| AFP, >200 IU/mL | 1.754 (1.236-2.488) | 0.002 | NS | 0.246 |

Those variables found significant at **P* < 0.100 in univariable analyses were entered into multivariable Cox regression analyses. AFP, alpha-fetoprotein; ALBI, albumin–bilirubin; ALT, alanine aminotransferase; AST, aspartate transaminase; CI, confidence interval; HBsAg, hepatitis B surface antigen; HR, hazard ratio; IAGR, inversed albumin-to-globulin ratio; INR, international normalized ratio; MV, multivariable; NS, not significant; UV, univariable.

Table 4. Univariable and multivariable Cox regression analyses in predicting cancer-specific survival

| Characteristics | UV HR (95% CI) | UV P value | MV HR (95% CI) ² | MV P value* |
|-----------------------------------|---------------------|------------|-----------------------------|-------------|
| Age, >60 years | 0.935 (0.682-1.283) | 0.679 | | |
| Male sex | 0.876 (0.615-1.247) | 0.462 | | |
| Hypertension | 0.879 (0.588-1.315) | 0.531 | | |
| HBsAg (+) | 1.127 (0.796-1.594) | 0.501 | | |
| Vascular invasion | 2.687 (1.820-3.966) | <0.001 | 1.869 (1.234-2.832) | 0.003 |
| Distant metastasis | 2.468 (1.675-3.638) | <0.001 | 2.062 (1.311-3.243) | 0.002 |
| Maximum tumor size, >5 cm | 2.977 (2.024-4.378) | <0.001 | 1.768 (1.131-2.764) | 0.012 |
| Multiple tumors | 1.963 (1.429-2.696) | <0.001 | NS | 0.168 |
| Child–Pugh grade B | 1.412 (0.977-2.041) | 0.066 | NS | 0.164 |
| IAGR | 2.769 (2.010-3.815) | <0.001 | 2.439 (1.651-3.601) | <0.001 |
| ALBI grade 2 + 3 | 1.910 (1.357-2.687) | <0.001 | NS | 0.496 |
| ALT, >40 U/L | 1.357 (0.976-1.887) | 0.069 | NS | 0.764 |
| AST, >40 U/L | 2.128 (1.556-2.910) | <0.001 | NS | 0.116 |
| Bilirubin, >17.1 µmol/L | 1.185 (0.853-1.645) | 0.312 | | |
| Creatinine, >80 µmol/L | 1.188 (0.789-1.787) | 0.409 | | |
| Hemoglobin, <110 g/L | 1.539 (1.068-2.216) | 0.021 | NS | 0.759 |
| Platelet, <100 10 ⁹ /L | 0.572 (0.400-0.819) | 0.002 | NS | 0.087 |
| INR, >1.17 | 1.328 (0.948-1.859) | 0.099 | NS | 0.161 |
| AFP, >200 IU/mL | 2.014 (1.351-3.002) | 0.001 | NS | 0.074 |

Those variables found significant at **P* < 0.100 in univariable analyses were entered into multivariable Cox regression analyses. AFP, alpha-fetoprotein; ALBI, albumin–bilirubin; ALT, alanine aminotransferase; AST, aspartate transaminase; CI, confidence interval; HBsAg, hepatitis B surface antigen; HR, hazard ratio; IAGR, inversed albumin-to-globulin ratio; INR, international normalized ratio; MV, multivariable; NS, not significant; UV, univariable.

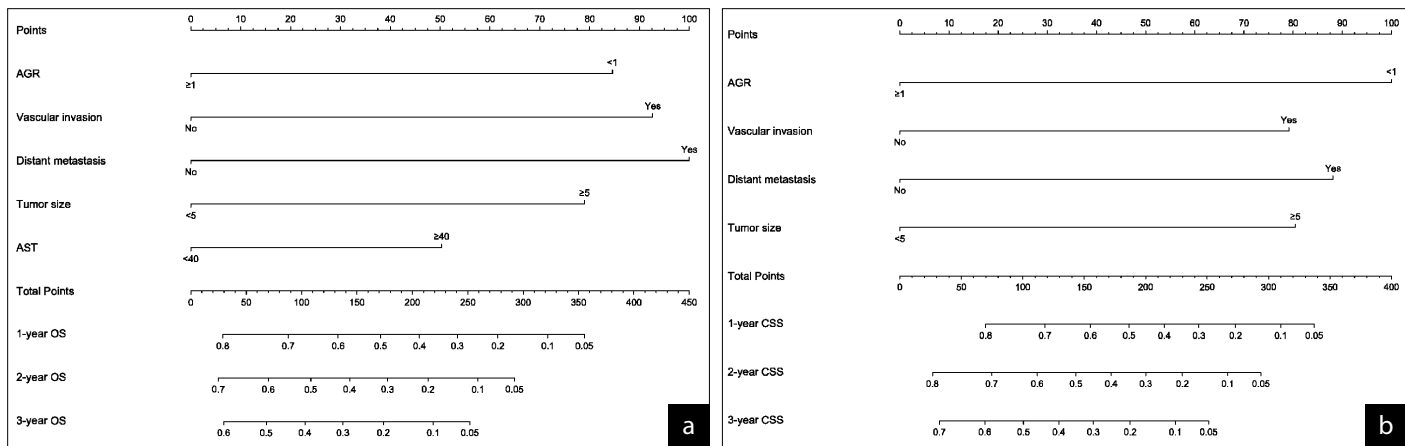


Figure 4. (a-b) Nomogram for predicting 1-, 2-, and 3-year overall survival (OS) and cancer-specific survival (CSS): (a), nomogram for OS; (b), nomogram for CSS. AGR, albumin-to-globulin ratio; AST, aspartate transaminase; CSS, cancer-specific survival; OS, overall survival.

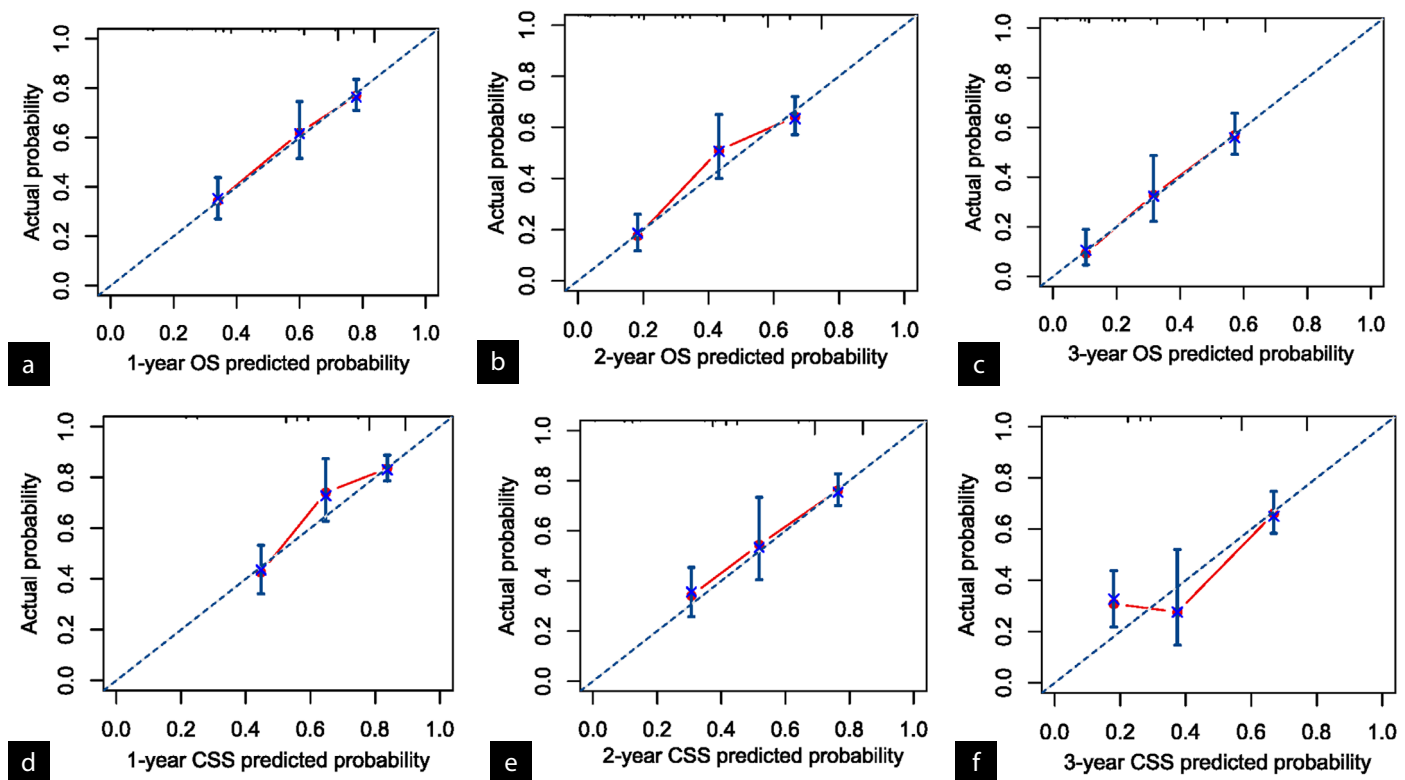


Figure 5. (a-f) Calibration curves for 1-, 2-, and 3-year overall survival (OS) and cancer-specific survival (CSS): (a), 1-year OS; (b), 2-year OS; (c), 3-year OS; (d), 1-year CSS; (e), 2-year CSS; (f), 3-year CSS.

Table 5. Comparisons of time-dependent ROC analysis for the prediction of overall survival and disease-specific survival

| Time-dependent AUC (95% CI) | 1-year | 2-year | 3-year |
|----------------------------------|-------------------|-------------------|-------------------|
| Overall survival | | | |
| AGR | 66.4 (60.3-72.6) | 65.4 (59.3-71.5) | 60.9 (53.7-68.2) |
| Child-Pugh grade | 57.0 (51.2-62.8)* | 57.2 (51.6-62.9)* | 57.6 (50.9-64.3)* |
| ALBI grade | 64.4 (58.3-70.6) | 64.1 (58.0-70.3) | 63.5 (56.3-70.6) |
| Disease-specific survival | | | |
| AGR | 71.2 (65.0-77.4) | 70.4 (63.8-77.0) | 62.9 (55.0-70.9) |
| Child-Pugh grade | 54.0 (49.0-59.0)* | 55.9 (50.9-60.9)* | 53.9 (48.4-59.4)* |
| ALBI grade | 67.5 (61.1-73.9) | 69.1 (62.5-75.7) | 65.9 (58.1-73.8) |

*P values <0.050 for statistical difference in the AUC values compared with AGR. AGR, albumin-to-globulin ratio; ALBI, albumin-bilirubin; AUC, area under the receiver operating characteristic curve; CI, confidence interval; ROC, receiver operating characteristic.

The present study has several limitations. First, it has the limitations inherent in a retrospective study. Some patients may have received other anti-tumor treatments during the follow-up period. Second, all patients were recruited from one hospital in China, and most of them had chronic hepatitis B virus infection; therefore, these results may not apply to other populations. Third, the cut-off AGR value used was 1.0, which is commonly used in clinical practice, but the cut-off threshold might need further optimization. In addition, further prospective studies are necessary to examine how the AGR could influence treatment options for HCC patients.

In conclusion, this study demonstrated that an IAGR before TACE treatment for HCC is an independent prognostic factor for worse OS and CSS. The AGR-based nomograms showed good performance in predicting patient prognoses and could be used to identify HCC patients with BCLC stage B/C who are at high risk when undergoing TACE treatment.

Conflict of interest disclosure

The authors declare no conflicts of interest.









References

- Villanueva A. Hepatocellular carcinoma. *N Engl J Med*. 2019;380(15):1450-1462. [\[CrossRef\]](#)
- European Association for the Study of the Liver. Electronic address: easloffice@easloffice.eu; European Association for the Study of the Liver. EASL Clinical Practice Guidelines: Management of hepatocellular carcinoma. *J Hepatol*. 2018;69(1):182-236. [\[CrossRef\]](#)
- Lencioni R, de Baere T, Soulen MC, Rilling WS, Geschwind JF. Lipiodol transarterial chemoembolization for hepatocellular carcinoma: a systematic review of efficacy and safety data. *Hepatology*. 2016;64(1):106-116. [\[CrossRef\]](#)
- Llovet JM, Bruix J. Systematic review of randomized trials for unresectable hepatocellular carcinoma: chemoembolization improves survival. *Hepatology*. 2003;37(2):429-442. [\[CrossRef\]](#)
- Bruix J, Sherman M; Practice Guidelines Committee, American Association for the Study of Liver Diseases. Management of hepatocellular carcinoma. *Hepatology*. 2005;42(5):1208-1236. [\[CrossRef\]](#)
- Han K, Kim JH. Transarterial chemoembolization in hepatocellular carcinoma treatment: Barcelona clinic liver cancer staging system. *World J Gastroenterol*. 2015;21(36):10327-10335. [\[CrossRef\]](#)
- Kong JY, Li SM, Fan HY, Zhang L, Zhao HJ, Li SM. Transarterial chemoembolization extends long-term survival in patients with unresectable hepatocellular carcinoma. *Medicine (Baltimore)*. 2018;97(33):e11872. [\[CrossRef\]](#)
- Zhao Y, Duran R, Chapiro J, et al. Transarterial chemoembolization for the treatment of advanced-stage hepatocellular carcinoma. *J Gastrointest Surg*. 2016;20(12):2002-2009. [\[CrossRef\]](#)
- Golfieri R, Bargellini I, Spreafico C, Trevisani F. Patients with Barcelona Clinic Liver Cancer stages B and C hepatocellular carcinoma: time for a subclassification. *Liver Cancer*. 2019;8(2):78-91. [\[CrossRef\]](#)
- Johnson PJ, Berhane S, Kagebayashi C, et al. Assessment of liver function in patients with hepatocellular carcinoma: a new evidence-based approach—the ALBI grade. *J Clin Oncol*. 2015;33(6):550-558. [\[CrossRef\]](#)
- Hoekstra LT, de Graaf W, Nibourg GA, et al. Physiological and biochemical basis of clinical liver function tests: a review. *Ann Surg*. 2013;257(1):27-36. [\[CrossRef\]](#)
- Arroyo V, García-Martínez R, Salvatella X. Human serum albumin, systemic inflammation, and cirrhosis. *J Hepatol*. 2014;61(2):396-407. [\[CrossRef\]](#)
- Tsochatzis EA, Bosch J, Burroughs AK. Liver cirrhosis. *Lancet*. 2014;383(9930):1749-1761. [\[CrossRef\]](#)
- Deng Y, Pang Q, Miao RC, et al. Prognostic significance of pretreatment albumin/globulin ratio in patients with hepatocellular carcinoma. *Oncotargets Ther*. 2016;9:5317-5328. [\[CrossRef\]](#)
- Zhang J, Liu X, Yang Z, Chen Y, Luo R. The pretreatment albumin to globulin ratio, a validated biomarker, predicts prognosis in hepatocellular carcinoma. *J Buon*. 2016;21(4):925-934. [\[CrossRef\]](#)
- Zhang CC, Zhang CW, Xing H, et al. Preoperative inverted albumin-to-globulin ratio predicts worse oncologic prognosis following curative hepatectomy for hepatocellular carcinoma. *Cancer Manag Res*. 2020;12:9929-9939. [\[CrossRef\]](#)
- Mokdad AA, Singal AG, Marrero JA, Zhu H, Yopp AC. Vascular invasion and metastasis is predictive of outcome in barcelona clinic liver cancer stage C hepatocellular carcinoma. *J Natl Compr Canc Netw*. 2017;15(2):197-204. [\[CrossRef\]](#)
- Child CG, Turcotte JG. Surgery and portal hypertension. *Major Probl Clin Surg*. 1964;1:1-85. [\[CrossRef\]](#)
- Gaba RC, Lewandowski RJ, Hickey R, et al. Transcatheter therapy for hepatic malignancy: standardization of terminology and reporting criteria. *J Vasc Interv Radiol*. 2016;27(4):457-473. [\[CrossRef\]](#)
- Gaba RC, Lokken RP, Hickey RM, et al. Quality improvement guidelines for transarterial chemoembolization and embolization of hepatic malignancy. *J Vasc Interv Radiol*. 2017;28(9):1210-1223. [\[CrossRef\]](#)
- Heagerty PJ, Lumley T, Pepe MS. Time-dependent ROC curves for censored survival data and a diagnostic marker. *Biometrics*. 2000;56(2):337-344. [\[CrossRef\]](#)
- Iasonos A, Schrag D, Raj GV, Panageas KS. How to build and interpret a nomogram for cancer prognosis. *J Clin Oncol*. 2008;26(8):1364-1370. [\[CrossRef\]](#)
- Gupta D, Lis CG. Pretreatment serum albumin as a predictor of cancer survival: a systematic review of the epidemiological literature. *Nutr J*. 2010;9:69. [\[CrossRef\]](#)
- Laviano A, Koverech A, Mari A. Cachexia: clinical features when inflammation drives malnutrition. *Proc Nutr Soc*. 2015;74(4):348-354. [\[CrossRef\]](#)
- Bard-Chapeau EA, Nguyen AT, Rust AG, et al. Transposon mutagenesis identifies genes driving hepatocellular carcinoma in a chronic hepatitis B mouse model. *Nat Genet*. 2014;46(1):24-32. [\[CrossRef\]](#)
- Mohs A, Kuttkat N, Reissing J, et al. Functional role of CCL5/RANTES for HCC progression during chronic liver disease. *J Hepatol*. 2017;66(4):743-753. [\[CrossRef\]](#)
- Endig J, Buitrago-Molina LE, Marhenke S, et al. Dual role of the adaptive immune system in liver injury and hepatocellular carcinoma development. *Cancer Cell*. 2016;30(2):308-323. [\[CrossRef\]](#)
- Coussens LM, Werb Z. Inflammation and cancer. *Nature*. 2002;420(6917):860-867. [\[CrossRef\]](#)
- Grivennikov SI, Greten FR, Karin M. Immunity, inflammation, and cancer. *Cell*. 2010;140(6):883-899. [\[CrossRef\]](#)
- Sakurai T, He G, Matsuzawa A, et al. Hepatocyte necrosis induced by oxidative stress and IL-1 α release mediate carcinogen-induced compensatory proliferation and liver tumorigenesis. *Cancer Cell*. 2008;14(2):156-165. [\[CrossRef\]](#)
- Nojiri S, Joh T. Albumin suppresses human hepatocellular carcinoma proliferation and the cell cycle. *Int J Mol Sci*. 2014;15(3):5163-5174. [\[CrossRef\]](#)
- Nojiri S, Kusakabe A, Shinkai N, et al. Factors influencing distant recurrence of hepatocellular carcinoma following combined radiofrequency ablation and transarterial chemoembolization therapy in patients with hepatitis C. *Cancer Manag Res*. 2011;3:267-272. [\[CrossRef\]](#)
- Wang YY, Zhao XH, Ma L, et al. Comparison of the ability of Child-Pugh score, MELD score, and ICG-R15 to assess preoperative hepatic functional reserve in patients with hepatocellular carcinoma. *J Surg Oncol*. 2018;118(3):440-445. [\[CrossRef\]](#)
- Xing Y, Guo ZN, Yan S, Jin H, Wang S, Yang Y. Increased globulin and its association with

- hemorrhagic transformation in patients receiving intra-arterial thrombolysis therapy. *Neurosci Bull.* 2014;30(3):469-476. [\[CrossRef\]](#)
35. Doi H, Hayashi E, Arai J, et al. Enhanced B-cell differentiation driven by advanced cirrhosis resulting in hyperglobulinemia. *J Gastroenterol Hepatol.* 2018. [\[CrossRef\]](#)
36. Tanaka S, Okamoto Y, Yamazaki M, Mitani N, Nakajima Y, Fukui H. Significance of hyperglobulinemia in severe chronic liver diseases—with special reference to the correlation between serum globulin/IgG level and ICG clearance. *Hepatogastroenterology.* 2007;54(80):2301-2305. [\[CrossRef\]](#)
37. Balkwill FR, Mantovani A. Cancer-related inflammation: common themes and therapeutic opportunities. *Semin Cancer Biol.* 2012;22(1):33-40. [\[CrossRef\]](#)
38. Akkiz H, Carr BI, Bag HG, et al. Serum levels of inflammatory markers CRP, ESR and albumin in relation to survival for patients with hepatocellular carcinoma. *Int J Clin Pract.* 2021;75(2):e13593. [\[CrossRef\]](#)
39. Rekić S, Guyot E, Bhais M, et al. The CRP level and STATE score predict survival in cirrhotic patients with hepatocellular carcinoma treated by transarterial embolization. *Dig Liver Dis.* 2016;48(9):1088-1092. [\[CrossRef\]](#)
40. Suh B, Park S, Shin DW, et al. Low albumin-to-globulin ratio associated with cancer incidence and mortality in generally healthy adults. *Ann Oncol.* 2014;25(11):2260-2266. [\[CrossRef\]](#)
41. Xu XF, Xing H, Han J, et al. Risk factors, patterns, and outcomes of late recurrence after liver resection for hepatocellular carcinoma: a multicenter study from China. *JAMA Surg.* 2019;154(3):209-217. [\[CrossRef\]](#)



The reproducibility of interventional radiology randomized controlled trials and external validation of a classification system

Assala Aslan 
 Christopher Stevens 
 Amro Saad Aldine 
 Ahmed Mamilly 
 Luis De Alba 
 Octavio Arevalo 
 Chaitanya Ahuja 
 Hugo H. Cuellar 

PURPOSE

The fragility index (FI) measures the robustness of randomized controlled trials (RCTs). It complements the *P* value by taking into account the number of outcome events. In this study, the authors measured the FI for major interventional radiology RCTs.

METHODS

Interventional radiology RCTs published between January 2010 and December 2022 relating to trans-jugular intrahepatic portosystemic shunt, trans-arterial chemoembolization, needle biopsy, angiography, angioplasty, thrombolysis, and nephrostomy tube insertion were analyzed to measure the FI and robustness of the studies.

RESULTS

A total of 34 RCTs were included. The median FI of those studies was 4.5 (range 1–68). Seven trials (20.6%) had a number of patients lost to follow-up that was higher than their FI, and 15 (44.1%) had a FI of 1–3.

CONCLUSION

The median FI, and hence the reproducibility of interventional radiology RCTs, is low compared to other medical fields, with some having a FI of 1, which should be interrupted cautiously.

KEYWORDS

Fragility index, interventional, radiology, RCT, reproducibility

The study was accepted and presented as a digital poster at the RSNA meeting.

From the Department of Radiology and Interventional Radiology (A.A. ✉ aslan.asala@hotmail.com, C.S., A.S.A., A.M., L.D.A., O.A., C.A., H.H.C.), Ochsner-Louisiana State University, Shreveport, United States.

Received 19 January 2023; revision requested 06 February 2023; accepted 24 February 2023.



Epub: 18.04.2023

Publication date: 30.05.2023

DOI: 10.4274/dir.2023.222052

Randomized controlled trials (RCTs) serve as the gold standard and represent the highest level of evidence for determining optimal and effective treatment strategies in evidence-based medicine.¹ Therefore, numerous RCTs related to the interventional radiology field have been performed within the last decade. These trials usually assess the efficacy of an intervention against medical management or another intervention, with a dichotomized primary endpoint and a *P* value used to compare the outcomes.² However, little attention has been paid to the critical importance of the number of outcome events in each study arm.³⁻⁵

The fragility index (FI) measures the robustness (or fragility) of the results from a clinical trial with dichotomous outcomes.⁶ It is defined as the minimum number of patients in one group (usually the study group) whose event status would be required to change from an event to a non-event to change a statistically significant result to a non-significant result. It is considered an important tool in interpreting the results from clinical trials and may provide value in addition to the commonly reported *P* value, risk reductions, and confidence interval. It also aids in determining when statistical significance in the trial may be lost because of a shift of a few additional events from the experimental group to the control one.¹ The larger the FI, the more robust and reproducible the trial is.⁶ While a low FI indicates that the study hinges on only a few events for statistical significance, Adeeb et al.² proposed a classification system for clinical trials based on the FI, number of patients lost to follow-up, and fragility quotient (FQ). The lat-

ter two factors are equally fundamental measures for the robustness of the studies, given that the patients lost to follow-up could potentially change the study's outcome had they remained in the trial, particularly when the FI is low. The FQ is calculated by dividing the FI by the sample size to provide an adjusted FI value. The proposed classification stratifies trials into three groups: statistically robust (class I), intermediate (class II), and fragile (class III).²

In this study, the authors aim to evaluate the FI for key Interventional Radiology RCTs over the last decade and externally validate Adeeb's classification.

Methods

A systematic search for published interventional radiology RCTs between January 2010 and December 2022 was performed by two researchers using PubMed. Six main areas were selected: trans-jugular intrahepatic portosystemic shunt (TIPS), trans-arterial chemoembolization (TACE), angioplasty, needle biopsy, nephrostomy, and thrombolysis. The following terms were used to identify the studies: "trans jugular intrahepatic portosystemic shunt", "trans arterial chemoembolization", "angioplasty", "needle biopsy", "nephrostomy", "thrombolysis", "randomized controlled trial", "interventional radiology", and "clinical trial".

Studies that showed no statistically different outcomes between study groups, studies where outcomes were not dichotomized, or studies that compared more than two groups were excluded (Figure 1). The data extracted included the publication year, methodology, primary endpoint, number of cases and events in each group, number of patients lost to follow-up, and the *P* value.

Given that the study did not involve human or animal subjects, institutional review board approval and patient consent were not required.

Fragility index

An online calculator, <http://clincalc.com/Stats/FragilityIndex.aspx>, was used to calculate the FI for the included trials.

Statistical analysis

The analysis was carried out using SPSS 26.0 (IBM Corp., Armonk, NY). Given the non-parametric data distribution, the Spearman test was used for correlation analysis between the FI, FQ, and trial characteristics. Numerical variables were presented as median (range), and a comparison was made between groups using the Mann-Whitney U and Kruskal-Wallis non-parametric tests. Statistical significance was defined as *P* < 0.050.

Results

A total of 34 clinical trials met the inclusion criteria and were included in this study (Supplementary Table 1).⁷⁻⁴⁰ The median FI was 4.5 (range 1–68). The median number of patients lost to follow-up was 0 (range 0–43). The number of patients lost to follow-up was higher than the FI in seven (20.6%) studies, and 15 (44.1%) trials had a FI of 1–3. The median FQ was 0.029 (range 0.01–0.34).

There was a negative correlation between the *P* value and FI ($r = -0.78, P < 0.001$), while there was a positive correlation between the FI and the sample size ($r = 0.46, P = 0.007$).

Studies related to angiography had the highest median FI (median 13, range 1–25) followed by TIPS (median 6, range 3–68), while TACE (median 4.5, range 2–14) and angioplasty (median 3, range 1–11) had the lowest FI. However, the difference was not statistically significant (*P* = 0.793).

Given that Adeeb's classification was based on the correlation between the number of patients lost to treatment minus the FI on one side and the FQ on another side, the authors externally studied that correlation to validate the classification system. Class I was associated with a significantly higher FQ (median 0.082), followed by class II (median 0.022), and then class III (median 0.015) (*P* = 0.009).

In this study, 12 (35.3%) RCTs were class I, 17 (50%) were class II, and five (14.7%) were class III, with no significant difference between the clinical study type (*P* = 0.773).

Discussion

In this study, the median FI for main interventional radiology RCTs was 4.5. In seven (20.6%) studies, the number of patients lost to follow-up was higher than the FI, and 15 (44.1%) had a FI of 1–3. Approximately one-third of the trials fell under class I in the classification system proposed by Adeeb et al.,² which the authors externally validated in this study, while 14.7% were considered statistically fragile (class III).

The FI has been reported for a number of medical and surgical RCTs, including cerebrovascular surgery,² critical care,^{4,41} nephrology,⁴² hand surgery,⁵ and cardiovascular trials.⁴³ To the authors' knowledge, this is the first study to evaluate the FI for interventional radiology trials. Given that most RCTs in this field have relatively small sample sizes with limited outcome events, the sole reporting of the *P* value limits the clinician's ability to determine the statistical fragility of the result and its clinical usefulness. Therefore, including FI analysis in these trials can help guide the interpretation and implementation of the results. Trials with a low FI indicate that their results are sensitive to even small changes in the data, suggesting that the findings may not be reliable. On the

Main points

- The fragility index measures the robustness (or fragility) of the results from a clinical trial that uses dichotomous outcomes, taking into account the number of events in each study arm.
- Several studies analyzed fragility indices for randomized controlled trials (RCTs) published in different medical fields, but this is the first study to perform that analysis for interventional radiology RCTs.
- The median fragility index of those studies was 4.5, with nearly half having a fragility index of 1–3, which is considerably low compared to other fields.

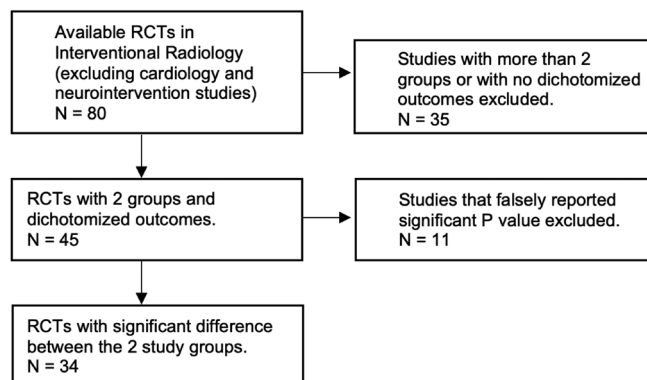


Figure 1. Flowchart illustrating the inclusion of randomized controlled trials in this study. RCT, randomized controlled trials.

contrary, the results will be robust and less sensitive to changes when the FI is higher. In previous studies, a positive correlation was found between the sample size and the FI, while there was a negative correlation with the *P* value.²⁻⁴ In the authors' study, there was a negative correlation between the FI and *P* value but no significant correlation with sample size. The FQ provides more understanding of the stability of the trial's results and the risk of false positives by standardizing the fragility of a trial to its sample size. A smaller FQ also indicates a less robust study outcome.⁴¹

Adeeb et al.² proposed a classification system that aimed to quantitatively assess the reproducibility of RCTs. RCTs are classified into three classes based on the relationship between the FI, sample size, and number of patients lost to follow-up. Class I studies (statistically robust) are likely to be reproducible and can reliably be incorporated into clinical guidelines. Class III studies (statistically fragile) are more likely to be subject to counterturn by future studies and, therefore, should be interpreted cautiously. Class II studies should be interpreted on an individual basis.² This classification provides a framework for evaluating the robustness and generalizability of trial results, highlighting the potential limitations of small or underpowered trials, and informing decisions about the use of these results in clinical practice and further research.

The median FI related to Interventional Radiology is low compared to other surgical fields, with some having a FI of 1, meaning that if only one patient did not reach the primary outcome in the study group, the results would not be statistically significant. Therefore, one should exercise caution when interpreting the results of those RCTs, especially when the sample size and event numbers are small and there is a high number of patients who were lost to follow-up.

Conflict of interest disclosure

The authors declared no conflicts of interest.

References

- Tignanelli CJ, Napolitano LM. The fragility index in randomized clinical trials as a means of optimizing patient care. *JAMA Surg.* 2019;154(1):74-79. [\[CrossRef\]](#)
- Adeeb N, Terrell DL, Whipple SG, et al. The reproducibility of cerebrovascular randomized controlled trials. *World Neurosurg.* 2020;140:e46-e52. [\[CrossRef\]](#)
- Evaniew N, Files C, Smith C, et al. The fragility of statistically significant findings from randomized trials in spine surgery: a systematic survey. *Spine J.* 2015;15(10):2188-2197. [\[CrossRef\]](#)
- Ridgeon EE, Young PJ, Bellomo R, Muchetti M, Lembo R, Landoni G. The fragility index in multicenter randomized controlled critical care trials. *Crit Care Med.* 2016;44(7):1278-1284. [\[CrossRef\]](#)
- Ruzbarsky JJ, Khormae S, Daluiski A. The fragility index in hand surgery randomized controlled trials. *J Hand Surg Am.* 2019;44(8):698.e1-698.e7. [\[CrossRef\]](#)
- Dettori JR, Norvell DC. How fragile are the results of a trial? The fragility index. *Global Spine J.* 2020;10(7):940-942. [\[CrossRef\]](#)
- Orloff MJ, Vaida F, Haynes KS, Hye RJ, Isenberg JI, Jinich-Brook H. Randomized controlled trial of emergency transjugular intrahepatic portosystemic shunt versus emergency portacaval shunt treatment of acute bleeding esophageal varices in cirrhosis. *J Gastrointest Surg.* 2012;16(11):2094-2111. [\[CrossRef\]](#)
- Orloff MJ, Hye RJ, Wheeler HO, et al. Randomized trials of endoscopic therapy and transjugular intrahepatic portosystemic shunt versus portacaval shunt for emergency and elective treatment of bleeding gastric varices in cirrhosis. *Surgery.* 2015;157(6):1028-1045. [\[CrossRef\]](#)
- Sauerbruch T, Mengel M, Dollinger M, et al. Prevention of rebleeding from esophageal varices in patients with cirrhosis receiving small-diameter stents versus hemodynamically controlled medical therapy. *Gastroenterology.* 2015;149(3):660-668. [\[CrossRef\]](#)
- Luo X, Wang Z, Tsauo J, Zhou B, Zhang H, Li X. Advanced cirrhosis combined with portal vein thrombosis: a randomized trial of TIPS versus endoscopic band ligation plus propranolol for the prevention of recurrent esophageal variceal bleeding. *Radiology.* 2015;276(1):286-293. [\[CrossRef\]](#)
- Wang L, Xiao Z, Yue Z, et al. Efficacy of covered and bare stent in TIPS for cirrhotic portal hypertension: a single-center randomized trial. *Sci Rep.* 2016;6:21011. [\[CrossRef\]](#)
- Lv Y, Qi X, He C, et al. Covered TIPS versus endoscopic band ligation plus propranolol for the prevention of variceal rebleeding in cirrhotic patients with portal vein thrombosis: a randomised controlled trial. *Gut.* 2018;67(12):2156-2168. [\[CrossRef\]](#)
- Holster IL, Tjwa ET, Moelker A, et al. Covered transjugular intrahepatic portosystemic shunt versus endoscopic therapy + β -blocker for prevention of variceal rebleeding. *Hepatology.* 2016;63(2):581-589. [\[CrossRef\]](#)
- Bureau C, Thabut D, Jezequel C, et al. The use of rifaximin in the prevention of overt hepatic encephalopathy after transjugular intrahepatic portosystemic shunt: a randomized controlled trial. *Ann Intern Med.* 2021;174(5):633-640. [\[CrossRef\]](#)
- Meng YL, Hu HT, Li HL, et al. The clinical therapeutic effects of arsenic trioxide combined with transcatheter arterial chemoembolization in treating primary liver cancer with pulmonary metastases. *Zhonghua Nei Ke Za Zhi.* 2012;51(12):971-974. [\[CrossRef\]](#)
- Goode SD, Cleveland TJ, Gaines PA; STAG trial collaborators. Randomized clinical trial of stents versus angioplasty for the treatment of iliac artery occlusions (STAG trial). *Br J Surg.* 2013;100(9):1148-1153. [\[CrossRef\]](#)
- Metussin A, Patanwala I, Cross TJ. Partial hepatectomy vs. transcatheter arterial chemoembolization for resectable multiple hepatocellular carcinoma beyond Milan criteria: a RCT. *J Hepatol.* 2015;62:747-748. [\[CrossRef\]](#)
- Lee TY, Lin CC, Chen CY, et al. Combination of transcatheter arterial chemoembolization and interrupted dosing sorafenib improves patient survival in early-intermediate stage hepatocellular carcinoma: a post hoc analysis of the START trial. *Medicine (Baltimore).* 2017;96(37):e7655. [\[CrossRef\]](#)
- Hu HT, Yao QJ, Meng YL, et al. Arsenic trioxide intravenous infusion combined with transcatheter arterial chemoembolization for the treatment of hepatocellular carcinoma with pulmonary metastasis: Long-term outcome analysis. *J Gastroenterol Hepatol.* 2017;32(2):295-300. [\[CrossRef\]](#)
- Chang G, Xie LL, Li WY, et al. Application of oxaliplatin in combination with epirubicin in transcatheter arterial chemoembolization in the treatment of primary liver carcinoma. *J Biol Regul Homeost Agents.* 2017;31(2):459-464. [\[CrossRef\]](#)
- Ogasawara S, Chiba T, Ooka Y, et al. A randomized placebo-controlled trial of prophylactic dexamethasone for transcatheter arterial chemoembolization. *Hepatology.* 2018;67(2):575-585. [\[CrossRef\]](#)
- Geng W, Tian X, Fu X, et al. Early routine angioplasty versus selective angioplasty after successful thrombolysis in acute ST-segment elevation myocardial infarction. *Coron Artery Dis.* 2013;24(3):238-243. [\[CrossRef\]](#)
- Spreen MI, Martens JM, Hansen BE, et al. Percutaneous transluminal angioplasty and drug-eluting stents for infrapopliteal lesions in critical limb ischemia (PADI) trial. *Circ Cardiovasc Interv.* 2016;9(2):e002376. [\[CrossRef\]](#)
- Wang Q, Li K, He C, et al. Angioplasty with versus without routine stent placement for Budd-Chiari syndrome: a randomised controlled trial. *Lancet Gastroenterol Hepatol.* 2019;4(9):686-697. [\[CrossRef\]](#)
- Zamboni P, Galeotti R, Salvi F, et al. Effects of venous angioplasty on cerebral lesions in multiple sclerosis: expanded analysis of the brave dreams double-blind, sham-

- controlled randomized trial. *J Endovasc Ther.* 2020;27(1):1526602819890110. Erratum in: *J Endovasc Ther.* 2020;27(1):NP1. [\[CrossRef\]](#)
26. Schroeder H, Werner M, Meyer DR, et al. Low-dose paclitaxel-coated versus uncoated percutaneous transluminal balloon angioplasty for femoropopliteal peripheral artery disease: one-year results of the ILLUMENATE European Randomized Clinical Trial (randomized trial of a novel paclitaxel-coated percutaneous angioplasty balloon). *Circulation.* 2017;135(23):2227-2236. [\[CrossRef\]](#)
 27. Haskal ZJ, Saad TF, Hoggard JG, et al. Prospective, randomized, concurrently-controlled study of a stent graft versus balloon angioplasty for treatment of arteriovenous access graft stenosis: 2-year results of the RENOVA study. *J Vasc Interv Radiol.* 2016;27(8):1105-1114. [\[CrossRef\]](#)
 28. Sharifi M, Bay C, Skrocki L, Rahimi F, Mehdipour M; "MOPETT" Investigators. Moderate pulmonary embolism treated with thrombolysis (from the "MOPETT" Trial). *Am J Cardiol.* 2013;111(2):273-277. [\[CrossRef\]](#)
 29. Xu B, Tu S, Song L, et al. Angiographic quantitative flow ratio-guided coronary intervention (FAVOR III China): a multicentre, randomised, sham-controlled trial. *Lancet.* 2021;398(10317):2149-2159. [\[CrossRef\]](#)
 30. Seeger J, Markovic S, Birkemeyer R, et al. Paclitaxel-coated balloon plus bare-metal stent for de-novo coronary artery disease: final 5-year results of a randomized prospective multicenter trial. *Coron Artery Dis.* 2016;27(2):84-88. [\[CrossRef\]](#)
 31. van Riet PA, Larghi A, Attili F, et al. A multicenter randomized trial comparing a 25-gauge EUS fine-needle aspiration device with a 20-gauge EUS fine-needle biopsy device. *Gastrointest Endosc.* 2019;89(2):329-339. [\[CrossRef\]](#)
 32. Metintas M, Yildirim H, Kaya T, et al. CT scan-guided Abrams' needle pleural biopsy versus ultrasound-assisted cutting needle pleural biopsy for diagnosis in patients with pleural effusion: a randomized, controlled trial. *Respiration.* 2016;91(2):156-163. [\[CrossRef\]](#)
 33. Cho E, Park CH, Kim TH, et al. A prospective, randomized, multicenter clinical trial comparing 25-gauge and 20-gauge biopsy needles for endoscopic ultrasound-guided sampling of solid pancreatic lesions. *Surg Endosc.* 2020;34(3):1310-1317. [\[CrossRef\]](#)
 34. Wang D, Fu HJ, Xu HX, et al. Comparison of fine needle aspiration and non-aspiration cytology for diagnosis of thyroid nodules: a prospective, randomized, and controlled trial. *Clin Hemorheol Microcirc.* 2017;66(1):67-81. [\[CrossRef\]](#)
 35. Oh D, Kong J, Ko SW, et al. A comparison between 25-gauge and 22-gauge Franseen needles for endoscopic ultrasound-guided sampling of pancreatic and peripancreatic masses: a randomized non-inferiority study. *Endoscopy.* 2021;53(11):1122-1129. [\[CrossRef\]](#)
 36. Laquière A, Lefort C, Maire F, et al. 19 G nitinol needle versus 22 G needle for transduodenal endoscopic ultrasound-guided sampling of pancreatic solid masses: a randomized study. *Endoscopy.* 2019;51(5):436-443. [\[CrossRef\]](#)
 37. Moosanejad N, Firouzian A, Hashemi SA, Bahari M, Fazli M. Comparison of totally tubeless percutaneous nephrolithotomy and standard percutaneous nephrolithotomy for kidney stones: a randomized, clinical trial. *Braz J Med Biol Res.* 2016;49(4):e4878. [\[CrossRef\]](#)
 38. Thomalla G, Simonsen CZ, Boutitie F, et al. MRI-guided thrombolysis for stroke with unknown time of onset. *N Engl J Med.* 2018;379(7):611-622. [\[CrossRef\]](#)
 39. Berglund A, Svensson L, Sjöstrand C, et al. Higher prehospital priority level of stroke improves thrombolysis frequency and time to stroke unit: the Hyper Acute STroke Alarm (HASTA) study. *Stroke.* 2012;43(10):2666-2670. [\[CrossRef\]](#)
 40. Barlinn K, Tsvigoulis G, Barreto AD, et al. Outcomes following sonothrombolysis in severe acute ischemic stroke: subgroup analysis of the CLOTBUST trial. *Int J Stroke.* 2014;9(8):1006-1010. [\[CrossRef\]](#)
 41. Vargas M, Marra A, Buonanno P, Coviello A, Iacovazzo C, Servillo G. Fragility index and fragility quotient in randomized controlled trials on corticosteroids in ARDS due to COVID-19 and non-COVID-19 etiology. *J Clin Med.* 2021;10(22):5287. [\[CrossRef\]](#)
 42. Shochet LN, Kerr PG, Polkinghorne KR. The fragility of significant results underscores the need of larger randomized controlled trials in nephrology. *Kidney International.* 2017;92(2):1469-1475. [\[CrossRef\]](#)
 43. Khan MS, Ochani RK, Shaikh A, et al. Fragility index in cardiovascular randomized controlled trials. *Circulation: Cardiovascular Quality and Outcomes.* 2019;12(12):e005755. [\[CrossRef\]](#)

Supplementary Table 1. Interventional radiology trials included in the study

| Trial | Field | Year | Sample size | Reported <i>P</i> value | Fragility index | Lost to follow-up | Adeeb classification | |
|-------|---|-------------|-------------|-------------------------|-----------------|-------------------|----------------------|---|
| 1 | Randomized controlled trial of emergency TIPS versus emergency portacaval shunt treatment of acute bleeding esophageal varices in cirrhosis | TIPS | 2012 | 154 | <0.001 | 52 | 0 | 1 |
| 2 | Randomized trials of endoscopic therapy and TIPS versus portacaval shunt for emergency and elective treatment of bleeding gastric varices in cirrhosis | TIPS | 2015 | 220 | <0.001 | 68 | 0 | 1 |
| 3 | Efficacy of covered and bare stent in TIPS for cirrhotic portal hypertension: a single-center randomized trial | TIPS | 2016 | 258 | 0.004 | 6 | 30 | 3 |
| 4 | Advanced cirrhosis combined with portal vein thrombosis: a randomized trial of TIPS versus endoscopic band ligation plus propranolol for the prevention of recurrent esophageal variceal bleeding | TIPS | 2015 | 73 | 0.002 | 6 | 0 | 1 |
| 5 | Prevention of rebleeding from esophageal varices in patients with cirrhosis receiving small-diameter stents versus hemodynamically controlled medical therapy | TIPS | 2015 | 185 | 0.002 | 7 | 0 | 1 |
| 6 | The use of rifaximin in the prevention of overt hepatic encephalopathy after TIPS: a randomized controlled trial | TIPS | 2021 | 197 | 0.012 | 3 | 17 | 3 |
| 7 | Covered TIPS versus endoscopic therapy + β -blocker for prevention of variceal rebleeding | TIPS | 2016 | 72 | 0.001 | 4 | 0 | 2 |
| 8 | Covered TIPS versus endoscopic band ligation plus propranolol for the prevention of variceal rebleeding in cirrhotic patients with portal vein thrombosis: a randomized controlled trial | TIPS | 2018 | 49 | 0.008 | 3 | 2 | 2 |
| 9 | The clinical therapeutic effects of arsenic trioxide combined with TACE in treating primary liver cancer with pulmonary metastases | TACE | 2012 | 60 | 0.008 | 2 | 0 | 2 |
| 10 | Partial hepatectomy vs. TACE for resectable multiple hepatocellular carcinomas beyond milan criteria: a randomized controlled trial | TACE | 2014 | 173 | <0.001 | 14 | 7 | 1 |
| 11 | A randomized placebo-controlled trial of prophylactic dexamethasone for TACE | TACE | 2018 | 119 | <0.001 | 9 | 7 | 2 |
| 12 | Combination of TACE and interrupted dosing sorafenib improves patient survival in early to intermediate stage hepatocellular carcinoma: a post hoc analysis of the START trial | TACE | 2017 | 72 | 0.012 | 2 | 0 | 2 |
| 13 | Arsenic trioxide intravenous infusion combined with TACE for the treatment of hepatocellular carcinoma with pulmonary metastasis: long-term outcome analysis | TACE | 2017 | 60 | 0.001 | 2 | 0 | 2 |
| 14 | Application of oxaliplatin in combination with epirubicin in TACE in the treatment of primary liver carcinoma | TACE | 2017 | 218 | <0.050 | 7 | 0 | 1 |
| 15 | Randomized clinical trial of stents versus angioplasty for the treatment of iliac artery occlusions (STAG trial) | Angioplasty | 2013 | 112 | 0.007 | 3 | 0 | 2 |
| 16 | Early routine angioplasty versus selective angioplasty after successful thrombolysis in acute ST-segment elevation myocardial infarction | Angioplasty | 2013 | 224 | 0.0219 | 2 | 0 | 2 |
| 17 | Percutaneous transluminal angioplasty and drug-eluting stents for infrapopliteal lesions in critical limb ischemia (PADI) trial | Angioplasty | 2016 | 158 | 0.037 | 1 | 0 | 2 |
| 18 | Angioplasty with versus without routine stent placement for Budd-Chiari syndrome: a randomized controlled trial | Angioplasty | 2019 | 88 | <0.0001 | 11 | 0 | 1 |
| 19 | Effects of venous angioplasty on cerebral lesions in multiple sclerosis: expanded analysis of the brave dreams double-blind, sham-controlled randomized trial | Angioplasty | 2020 | 130 | 0.032 | 1 | 5 | 2 |

Supplementary Table 1. Interventional radiology trials included in the study

| Trial | Field | Year | Sample size | Reported <i>P</i> value | Fragility index | Lost to follow-up | Adeeb classification | |
|-------|--|---------------|-------------|-------------------------|-----------------|-------------------|----------------------|---|
| 20 | Low-dose paclitaxel-coated versus uncoated percutaneous transluminal balloon angioplasty for femoropopliteal peripheral artery disease: one-year results of the ILLUMENATE European randomized clinical trial (randomized trial of a novel paclitaxel-coated percutaneous angioplasty balloon) | Angioplasty | 2017 | 333 | <0.001 | 10 | 43 | 3 |
| 21 | Prospective, randomized, concurrently-controlled study of a stent graft versus balloon angioplasty for treatment of arteriovenous access graft stenosis: 2-year results of the RENOVA study | Angioplasty | 2016 | 191 | <0.001 | 8 | 5 | 2 |
| 22 | Moderate pulmonary embolism treated with thrombolysis (from the "MOPETT" Trial) | Angiography | 2013 | 121 | <0.001 | 13 | 7 | 1 |
| 23 | Angiographic quantitative flow ratio-guided coronary intervention (FAVOR III China): a multicentre, randomized, sham-controlled trial | Angiography | 2021 | 3825 | 0.0004 | 25 | 0 | 1 |
| 24 | Paclitaxel-coated balloon plus bare-metal stent for de-novo coronary artery disease: final 5-year results of a randomized prospective multicenter trial | Angiography | 2016 | 120 | <0.050 | 1 | 0 | 2 |
| 25 | A multicenter randomized trial comparing a 25-gauge EUS fine-needle aspiration device with a 20-gauge EUS fine-needle biopsy device | Needle biopsy | 2019 | 608 | 0.002 | 10 | 0 | 1 |
| 26 | CT scan-guided Abrams needle pleural biopsy versus ultrasound-assisted cutting needle pleural biopsy for diagnosis in patients with pleural effusion: a randomized, controlled Trial | Needle biopsy | 2016 | 150 | 0.029 | 2 | 7 | 3 |
| 27 | A prospective, randomized, multicenter clinical trial comparing 25-gauge and 20-gauge biopsy needles for endoscopic ultrasound-guided sampling of solid pancreatic lesions | Needle biopsy | 2020 | 88 | 0.037 | 1 | 0 | 2 |
| 28 | A comparison between 25-gauge and 22-gauge Franseen needles for endoscopic ultrasound-guided sampling of pancreatic and peripancreatic masses: a randomized non-inferiority study | Needle biopsy | 2021 | 140 | <0.001 | 17 | 0 | 1 |
| 29 | 19 G nitinol needle versus 22 G needle for transduodenal endoscopic ultrasound-guided sampling of pancreatic solid masses: a randomized study | Needle biopsy | 2019 | 122 | 0.02 | 2 | 0 | 2 |
| 30 | Comparison of fine needle aspiration and non-aspiration cytology for diagnosis of thyroid nodules: a prospective, randomized, and controlled trial | Needle biopsy | 2017 | 629 | <0.050 | 4 | 0 | 2 |
| 31 | Comparison of totally tubeless percutaneous nephrolithotomy and standard percutaneous nephrolithotomy for kidney stones: a randomized, clinical trial | Nephrostomy | 2016 | 90 | 0.007 | 2 | 6 | 2 |
| 32 | MRI-guided thrombolysis for stroke with unknown time of onset | Thrombolysis | 2018 | 503 | 0.020 | 5 | 13 | 3 |
| 33 | Higher prehospital priority level of stroke improves thrombolysis frequency and time to stroke unit: the hyper acute stroke alarm study | Thrombolysis | 2012 | 490 | <0.001 | 16 | 0 | 1 |
| 34 | Outcomes following sonothrombolysis in severe acute ischemic stroke: subgroup analysis of the CLOTBUST trial | Thrombolysis | 2014 | 85 | 0.032 | 1 | 0 | 2 |

TIPS, trans-jugular intrahepatic portosystemic shunt; TACE, transcatheter arterial chemoembolization; MRI, magnetic resonance imaging.



Propensity score-matched analysis of six-month outcomes of paclitaxel-coated balloons combined with UltraScore balloons versus conventional scoring balloons for femoropopliteal lesions

Takuya Haraguchi 
Masanaga Tsujimoto 
Ryo Otake 
Yoshifumi Kashima 
Katsuhiko Sato 
Tsutomu Fujita 

PURPOSE

Combination angioplasty with paclitaxel-coated balloons (PCBs) and conventional scoring balloons for femoropopliteal lesions has demonstrated satisfactory results, even for complex lesions. The UltraScore balloon (Becton Dickinson, New Jersey, USA), which has a maximum length of 300 mm, has two longitudinal 0.010-inch stainless steel wires and is a new treatment option for complex femoropopliteal lesions. However, no studies have evaluated the effect of the UltraScore balloon on femoropopliteal lesions. This study aimed to compare the clinical efficacy of angioplasty over a six-month period using UltraScore balloons versus conventional scoring balloons for the treatment of atherosclerotic femoropopliteal lesions with PCBs.

METHODS

A retrospective single-center observational study enrolled 272 patients who underwent PCB angioplasty combined with an UltraScore balloon ($n = 58$) or conventional scoring balloon ($n = 214$) without bailout stenting. Propensity score matching was used to minimize intergroup differences in baseline characteristics, and six-month outcomes were compared between the two groups. The primary endpoint was a technical success (i.e., residual angiographic stenosis of $<30\%$ with non-severe dissection). The secondary endpoints were the incidences of periprocedural complications, restenosis, and target lesion revascularization (TLR).

RESULTS

After propensity score matching, 50 matched pairs of patients were selected for analysis. The UltraScore group had a significantly longer vessel length (192.8 ± 94.9 versus 36.6 ± 7.9 mm, $P < 0.001$), a lower frequency of non-compliant balloon (26.0% versus 56.0% , $P = 0.002$), and a smaller PCB diameter (5.32 ± 0.65 versus 5.66 ± 0.52 mm, $P = 0.002$) compared with the scoring group. The primary endpoint of technical success was significantly higher in the UltraScore group than in the scoring group (76.0% versus 56.0% , $P = 0.035$). There were no significant differences in periprocedural complications (4.0% versus 2.0% , $P = 0.562$), six-month restenosis (4.0% versus 8.0% , $P = 0.339$), and TLR (2.0% versus 4.0% , $P = 0.500$) between both groups. The multivariate logistic regression analysis showed that UltraScore use was independently associated with an increase in technical success (odds ratio: 2.58; 95% confidence interval: 1.05–6.36, $P = 0.040$).

CONCLUSION

The use of an UltraScore balloon during PCB angioplasty for femoropopliteal lesions significantly improved technical success compared with conventional scoring balloons. UltraScore use was an independent predictor of technical success, indicating its potential advantages in peripheral intervention procedures.

KEYWORDS

Balloon angioplasty, endovascular treatment, UltraScore balloon, conventional scoring balloon, cutting balloon, drug-coated balloon, femoropopliteal lesions, peripheral artery disease

From the Department of Cardiology (T.H. ✉t.haraguchi@scvc.jp, M.T., R.O., Y.K., K.S., T.F.), Asia Medical Group, Sapporo Heart Center, Sapporo Cardio Vascular Clinic, Sapporo, Japan.

Received 16 January 2023; revision requested 22 February 2023; accepted 16 March 2023.



Epub: 17.04.2023

Publication date: 30.05.2023

DOI: 10.4274/dir.2023.232114

You may cite this article as: Haraguchi T, Tsujimoto M, Otake R, Kashima Y, Sato K, Fujita T. Propensity score-matched analysis of six-month outcomes of paclitaxel-coated balloons combined with UltraScore balloons versus conventional scoring balloons for femoropopliteal lesions. *Diagn Interv Radiol.* 2023;29(3):535-541.

Endovascular therapy has been a standard treatment for femoropopliteal lesions due to its improved device performance over other treatments. Several studies have demonstrated satisfactory results after paclitaxel-coated balloon (PCB) angioplasty for femoropopliteal lesions.¹⁻³ However, severely calcified lesions, particularly concentric calcifications, present a challenge in achieving adequate lumen enlargement and paclitaxel absorption by PCB angioplasty, leading to increased restenosis risk.⁴ Therefore, proper vessel preparation is essential to ensure good PCB outcomes; additionally, a larger minimum lumen area is associated with a decreased risk of restenosis.⁵

Conventional scoring balloons have been used for severely calcified or poorly dilated lesions. Conventional scoring balloon angioplasty has been found to restore larger lumen gain and reduce the incidence of severe dissection compared with plain balloon angioplasty in short femoropopliteal lesions.^{6,7} However, the short length of conventional scoring balloons limits their use in long lesions. The UltraScore balloon (Becton Dickinson, New Jersey, USA), which has a maximum length of 300 mm, has two longitudinal 0.010-inch stainless steel wires and is a new treatment option for complex femoropopliteal lesions, including longer lesions. However, no studies have evaluated the effect of the UltraScore balloon on femoropopliteal lesions. This study aims to compare the clinical efficacy of angioplasty over a six-month period using UltraScore balloons versus conventional scoring balloons for the treatment of atherosclerotic femoropopliteal lesions with PCBs.

Methods

Study population

This study retrospectively and non-randomly analyzed symptomatic atherosclerotic femoropopliteal lesions in 731 patients (Rutherford classification 2 and 6) treated with a PCB without a bailout stent procedure

from July 2018 to June 2022 at Sapporo Heart Center. Of this total, the following 459 patients were excluded based on treatment type: standard balloons (n = 398), scaffolds (n = 19), in-stent lesions (n = 14), and restenosis after PCB angioplasty (n = 27). Finally, this study enrolled 272 patients (272 limbs; average age 76.9 ± 9.3 years; female 37.1%). The present study compared the periprocedural and clinical outcomes for up to six months between patients treated with conventional scoring balloons (n = 214) and those treated with UltraScore balloons (n = 58) for vessel preparation before PCB use. The Cutting balloon (n = 54; Boston Scientific, Marlborough, Massachusetts, USA) and the AngioSculpt (n = 160; Philips, San Diego, California, USA) were used in the scoring group. All participants were asked to visit our center 6 ± 1 months after PCB angioplasty to evaluate for restenosis occurrence. A propensity score-matched analysis was conducted as described in the statistical analysis section. The study protocol was designed in accordance with the Declaration of Helsinki and was approved by the Sapporo Heart Center Ethics Committee of our institution (approval no: 20230001). Informed consent was obtained from all participants or their family members before using the balloon for comparison in this study.

Endovascular procedures and medical therapy

The indication for endovascular treatment for symptomatic femoropopliteal lesions was a >70% diameter stenosis with Rutherford classification categories between 2 and 6. The femoropopliteal vasculature was treated in a single session. The approach site for each common femoral artery was determined based on the location of the lesion, and a 6-Fr sheath was inserted. A 5,000-IU dose of unfractionated heparin was subsequently injected from the sheath, targeting an activated coagulation time of >250 s. A 0.014- or 0.035-inch guidewire was used to cross the lesions. The selection of different types of balloons was based on the morphology and location of the lesions. The UltraScore and conventional scoring balloons were primarily used in complex lesions such as long lesions, chronic total occlusions (CTO), and severe calcifications that were difficult to dilate with conventional balloon angioplasty. Angiography or intravascular ultrasound (IVUS)-evaluated balloon diameters were used. Standard balloon and PCB angioplasties were performed to cover the lesion as completely as possible. The choice of balloon (UltraScore,

Cutting balloon, and AngioSculpt) and PCB (IN.PACT Admiral: Medtronic, Santa Clara, USA; Ranger: Boston Scientific, Marlborough, USA; and Lutonix: Becton Dickinson, New Jersey, USA) was determined at the operator's discretion, taking into consideration factors such as lesion length, degree of stenosis, and the presence of occlusions or calcifications. These factors were evaluated case by case to determine each patient's most appropriate treatment strategy. Post-dilation was performed if the residual stenosis after PCB angioplasty was >50% using a balloon that was appropriately sized and selected based on angiography or IVUS evaluation. Patients who underwent the bailout stent procedure were excluded. Atherectomy devices were not used because they were unavailable in Japan during the study period. Hemostasis was achieved using manual compression or device closure.

After the intervention, patients were prescribed daily doses of 100 mg aspirin and 75 mg clopidogrel for three months. Patients who received anticoagulation therapy were prescribed a regular dose of aspirin and clopidogrel for one month. The patients were then switched to long-term anticoagulation and aspirin therapy.

Study endpoints

The primary endpoint was technical success, defined as residual angiographic stenosis of less than 30% with non-severe dissection, classified as a dissection grade from none to type C according to the National Heart, Lung, and Blood Institute classification system for coronary arteries.⁸ Secondary endpoints included periprocedural complications, defined as intraoperative complications within seven days postoperatively; restenosis rate at six months, defined as a target lesion with significant stenosis (a peak systolic velocity ratio >2.4 on duplex ultrasound at intervals of one and six months or >50% stenosis on digital subtraction angiography or computed tomography angiography); and target lesion revascularization (TLR) at six months, defined as repeat endovascular or surgical bypass procedures for limbs with recurrent symptoms accompanied by recurrent stenosis >50% as measured by angiography.

Statistical analysis

The baseline characteristics of the study were summarized as mean ± standard deviation for continuous variables and frequency (percentage) for categorical variables unless otherwise specified. The unpaired t-test or

Main points

- The UltraScore balloon improved technical success in femoropopliteal lesions during paclitaxel-coated balloon angioplasty more than conventional scoring balloons.
- Comparable six-month outcomes were observed between the groups using UltraScore and conventional scoring balloons.
- UltraScore balloon use was an independent predictor of technical success.

chi-square test was used to compare continuous or categorical variables between the two groups. A *P* value of <0.050 was considered statistically significant. Propensity score matching was performed to minimize the intergroup differences in baseline characteristics. The propensity score was calculated using a binary logistic regression model that included sex, hypertension, diabetes mellitus, hemodialysis, chronic limb-threatening ischemia, lesion length >150 mm, coronary artery disease, CTO, and bilateral calcification as explanatory variables. Matching of the two groups was performed using the logit of the propensity score, within a caliper of 0.2 standard deviations of the logit of the propensity score (caliper 0.029), to ensure balance in the baseline characteristics between the two groups. We extracted as many matched samples as possible to maximize the statistical power for detecting intergroup prognostic differences. After matching, intergroup differences were analyzed with stratification by pairs, and weighted descriptive statistics were reported to provide a comprehensive overview of the data. The

balance in baseline characteristics between the groups was assessed with the standardized difference. Patient characteristics, treatment strategies, and clinical outcomes were compared between patients treated using the UltraScore and conventional scoring balloons (Cutting balloon or AngioSculpt). Descriptive statistics were used to summarize the baseline and outcome variables. Independent predictors of technical success were determined using multivariate logistic regression, including all univariate parameters with a *P* value of <0.100, and 95% confidence intervals were reported where appropriate. Statistical analyses were performed using IBM SPSS Statistics software version 29.0.

Results

This study included 272 patients, with 58 patients (21.3%) receiving treatment with UltraScore balloons. After propensity score matching, 50 matched pairs of patients were selected for analysis. Baseline patient and lesion characteristics were comparable between the two groups, as presented in Table

1. Procedural characteristics are summarized in Table 2. In vessel preparation, the UltraScore group had a significantly longer length (192.8 ± 94.9 versus 36.6 ± 7.9 mm, *P* < 0.001), a lower frequency non-compliant balloon (26.0% versus 56.0%, *P* = 0.002), and smaller PCB diameter (5.32 ± 0.65 versus 5.66 ± 0.52 mm, *P* = 0.002) compared with the scoring group.

Table 3 presents the postprocedural outcomes of the two groups. The primary endpoint of technical success was significantly higher in the UltraScore group than in the scoring group (76.0% versus 56.0%, *P* = 0.035). Residual stenosis <30% was achieved more frequently in the UltraScore group than in the scoring group (90.0% versus 68.0%, *P* = 0.007), whereas non-severe dissection was similar in both groups (86.0% versus 84.0%, *P* = 0.779). There were no significant differences in periprocedural complications (4.0% versus 2.0%, *P* = 0.562), six-month restenosis (4.0% versus 8.0%, *P* = 0.339), and TLR (2.0% versus 4.0%, *P* = 0.500) between the two groups. The arterial dissection patterns, summarized

Table 1. Patient and lesion characteristics

| Variable | Overall population (before matching) | | | Matched population | | |
|------------------------------------|--------------------------------------|--------------------|----------------|----------------------|-------------------|----------------|
| | UltraScore n = 58 | Scoring n = 214 | <i>P</i> value | UltraScore n = 50 | Scoring n = 50 | <i>P</i> value |
| Age, y | 76.9 ± 9.6 | 76.9 ± 9.3 | 0.997 | 76.7 ± 9.5 | 78.3 ± 9.9 | 0.399 |
| Female | 27 (46.6) | 74 (34.6) | 0.094 | 23 (46.0) | 22 (44.0) | 0.841 |
| Body mass index, kg/m ² | 22.9 ± 3.7 | 22.6 ± 3.8 | 0.556 | 23.0 ± 3.6 | 23.1 ± 3.8 | 0.882 |
| Ambulatory | 41 (70.7) | 161 (75.2) | 0.483 | 38 (76.0) | 36 (72.0) | 0.648 |
| Hypertension | 45 (78.9) | 185 (86.9) | 0.136 | 41 (82.0) | 41 (82.0) | - |
| Dyslipidemia | 35 (61.4) | 137 (64.6) | 0.653 | 31 (62.0) | 33 (66.0) | 0.677 |
| Diabetes mellitus | 36 (63.2) | 119 (56.1) | 0.341 | 32 (64.0) | 32 (64.0) | - |
| Current smoker | 10 (17.5) | 51 (23.8) | 0.312 | 10 (20.0) | 15 (30.0) | 0.248 |
| Chronic renal disease | 40 (70.2) | 125 (59.2) | 0.132 | 36 (72.0) | 31 (62.0) | 0.288 |
| Hemodialysis | 15 (26.3) | 47 (22.5) | 0.545 | 12 (24.0) | 9 (18.0) | 0.461 |
| Coronary artery disease | 20 (34.5) | 134 (62.6) | <0.001 | 20 (40.0) | 20 (40.0) | - |
| Cerebrovascular disease | 10 (17.5) | 31 (14.9) | 0.625 | 9 (18.0) | 10 (20.0) | 0.799 |
| Heart failure | 10 (17.5) | 29 (14.0) | 0.505 | 10 (20.0) | 6 (12.2) | 0.295 |
| Antiplatelet therapy | 50 (86.2) | 198 (92.5) | 0.122 | 42 (84.0) | 47 (94.0) | 0.112 |
| Anticoagulation | 9 (15.8) | 30 (14.0) | 0.735 | 8 (16.0) | 6 (12.0) | 0.564 |
| Statin | 33 (57.9) | 107 (50.0) | 0.289 | 29 (58.0) | 26 (52.0) | 0.546 |
| Preprocedural ankle-brachial index | 0.59 ± 0.30 | 0.69 ± 0.28 | 0.018 | 0.59 ± 0.30 | 0.64 ± 0.30 | 0.208 |
| Rutherford classification | 3.9 ± 1.2 | 3.5 ± 1.1 | 0.026 | 3.8 ± 1.3 | 3.6 ± 1.0 | 0.298 |
| Chronic limb-threatening ischemia | 28 (49.1) | 78 (36.6) | 0.086 | 23 (46.0) | 18 (36.0) | 0.309 |
| Preoperative stenosis (%) | 93.0 ± 8.5 | 90.7 ± 9.5 | 0.085 | 93.2 ± 8.1 | 93.6 ± 8.6 | 0.803 |
| Reference vessel diameter, mm | 4.3 ± 0.9 | 4.7 ± 1.0 | 0.019 | 4.4 ± 0.8 | 4.6 ± 1.0 | 0.183 |
| Lesion length, mm | 222.9 ± 106.9 | 133.0 ± 109.0 | <0.001 | 214.8 ± 107.5 | 216.8 ± 113.3 | 0.928 |
| Chronic total occlusion | 17 (29.3) | 40 (18.7) | 0.078 | 15 (30.0) | 15 (30.0) | - |

Table 1. Continued

| Variable | Overall population (before matching) | | | Matched population | | |
|--|--------------------------------------|--------------------|---------|----------------------|-------------------|---------|
| | UltraScore n = 58 | Scoring n = 214 | P value | UltraScore n = 50 | Scoring n = 50 | P value |
| TASC II classification | | | | | | |
| A | 5 (8.6) | 80 (37.4) | <0.001 | 5 (10.0) | 8 (16.0) | 0.372 |
| B | 9 (15.5) | 54 (25.2) | 0.120 | 8 (16.0) | 5 (10.0) | 0.372 |
| C | 37 (63.8) | 66 (30.8) | <0.001 | 30 (60.0) | 32 (64.0) | 0.680 |
| D | 7 (12.1) | 14 (6.5) | 0.162 | 7 (14.0) | 5 (10.0) | 0.538 |
| Calcification graded by PACSS grade | | | | | | |
| 0 | 9 (15.5) | 65 (30.4) | 0.024 | 8 (16.0) | 9 (18.0) | 0.790 |
| 1 | 8 (13.8) | 17 (7.9) | 0.171 | 6 (12.0) | 4 (8.0) | 0.505 |
| 2 | 2 (3.4) | 20 (9.3) | 0.144 | 2 (4.0) | 4 (8.0) | 0.339 |
| 3 | 11 (19.0) | 39 (18.2) | 0.897 | 11 (22.0) | 7 (14.0) | 0.298 |
| 4 | 28 (48.3) | 73 (34.1) | 0.048 | 23 (46.0) | 26 (52.0) | 0.548 |
| Below-the-knee artery poor runoff ≤ 1 | 25 (43.1) | 66 (30.8) | 0.079 | 20 (40.0) | 19 (38.0) | 0.838 |

Data are presented as number (percentage) or mean \pm standard deviation unless otherwise specified. PACSS, peripheral artery calcium scoring system; TASC, TransAtlantic Inter-Society Consensus.

Table 2. Procedure characteristics

| Variable | Overall population (before matching) | | | Matched population | | |
|------------------------------|--------------------------------------|--------------------|---------|----------------------|-------------------|---------|
| | UltraScore n = 58 | Scoring n = 214 | P value | UltraScore n = 50 | Scoring n = 50 | P value |
| Vessel preparation | | | | | | |
| Diameter, mm | 5.12 \pm 0.59 | 5.37 \pm 0.80 | 0.009 | 5.14 \pm 0.57 | 5.34 \pm 0.77 | 0.145 |
| Diameter-to-artery ratio | 1.22 \pm 0.28 | 1.20 \pm 0.36 | 0.654 | 1.19 \pm 0.25 | 1.21 \pm 0.33 | 0.804 |
| Specific balloon length, mm | 197.9 \pm 95.9 | 34.8 \pm 9.1 | <.001 | 192.8 \pm 94.9 | 36.6 \pm 7.9 | <0.001 |
| Inflation pressure, atm | 13.5 \pm 2.7 | 13.5 \pm 2.5 | 0.934 | 13.6 \pm 2.6 | 14.0 \pm 2.3 | 0.414 |
| Cutting balloon | - | 54 (25.2) | - | - | 8 (16.0) | - |
| AngioSculpt | - | 160 (74.8) | - | - | 42 (84.0) | - |
| Semicompliant balloon | 20 (34.5) | 28 (13.1) | <0.001 | 18 (36.0) | 14 (28.0) | 0.391 |
| Non-compliant balloon | 15 (25.9) | 79 (36.9) | 0.116 | 13 (26.0) | 28 (56.0) | 0.002 |
| Drug-coated balloon | | | | | | |
| Model | | | | | | |
| IN.PACT admiral | 2 (3.4) | 54 (25.2) | <0.001 | 12 (24.0) | 2 (4.0) | 0.004 |
| Lutonix | 14 (24.1) | 120 (56.1) | <0.001 | 14 (28.0) | 23 (46.0) | 0.062 |
| Ranger | 42 (72.4) | 40 (18.7) | <0.001 | 34 (68.0) | 15 (30.0) | <0.001 |
| Diameter, mm | 5.28 \pm 0.67 | 5.65 \pm 0.58 | <0.001 | 5.32 \pm 0.65 | 5.66 \pm 0.52 | 0.002 |
| Diameter-to-artery ratio | 1.25 \pm 0.26 | 1.26 \pm 0.34 | 0.816 | 1.23 \pm 0.23 | 1.29 \pm 0.34 | 0.310 |
| Total length, mm | 246.5 \pm 109.5 | 150.0 \pm 98.3 | <0.001 | 239.0 \pm 108.4 | 225.2 \pm 101.6 | 0.256 |
| Inflation pressure, atm | 13.3 \pm 2.9 | 13.2 \pm 2.3 | 0.889 | 13.4 \pm 2.7 | 14.0 \pm 2.2 | 0.261 |
| Inflation time, sec | 165.5 \pm 25.9 | 146.4 \pm 29.8 | <0.001 | 163.2 \pm 27.2 | 152.4 \pm 30.2 | 0.063 |
| Additional balloon | 4 (6.9) | 22 (10.3) | 0.439 | 4 (8.0) | 5 (10.0) | 0.500 |
| Intravascular ultrasound use | 14 (24.1) | 49 (22.9) | 0.843 | 13 (26.0) | 14 (28.0) | 0.822 |

Data are presented as number (percentage) or mean \pm standard deviation unless otherwise specified.

in Figure 1 and Table 3, did not differ significantly between the two groups. The interaction analysis for restenosis is presented in Table 4. The multivariate logistic regression analysis showed that UltraScore balloon use was independently associated with an increase in technical success (odds ratio, 2.58; 95% confidence interval: 1.05–6.36, $P = 0.040$). The Rutherford classification improved similarly in both groups, as is shown in Figure 2.

Discussion

This study demonstrated that the use of UltraScore balloons during PCB angioplasty for femoropopliteal lesions resulted in a significantly higher technical success rate than conventional scoring balloons. UltraScore balloon use was identified as an independent predictor of technical success.

Conventional scoring balloons have been commonly used to treat severe calcifications and non-dilatable lesions, where conventional standard balloon angioplasty may not be effective. A previous study showed that scoring balloons were more effective than plain balloon angioplasty in plaque modification for short femoropopliteal lesions.⁹ The success of balloon angioplasty was positively associated with scoring balloon use but inversely associated with CTO and longer lesion length. Another retrospective study comparing long and short balloons

for femoropopliteal occlusions found that longer balloons decreased the frequency of dilation over the length of the lesion compared to shorter balloons, reducing the risk of balloon edge dissection and technical failure.¹⁰ In this study, the UltraScore group had a significantly longer balloon length than the scoring group. The presence of two long wire elements on a long UltraScore balloon may have positively impacted vessel preparation and contributed to achieving a lower residual stenosis rate compared to conventional short-scoring balloons. Consequently, UltraScore balloon use was a significant positive factor for technical success. Furthermore, this study found that the severity of calcification, as graded by the Peripheral Artery Calcium

Scoring System, CTOs, and long lesions did not impact technical success, suggesting that the scoring element of the balloons used in this study was effective in treating complex lesions, consistent with the results of a previous study.⁹

Drug-coated balloons (DCBs) have consistently demonstrated improved efficacy compared with standard balloon angioplasty in treating femoropopliteal lesions.¹⁻³ As such, DCB angioplasty is recommended as the first-line treatment for femoropopliteal lesions instead of uncoated balloon angioplasty.^{11,12} Nevertheless, the rate of bailout stenting tended to be higher in longer lesions.¹³ In this study, bailout stenting procedures per-

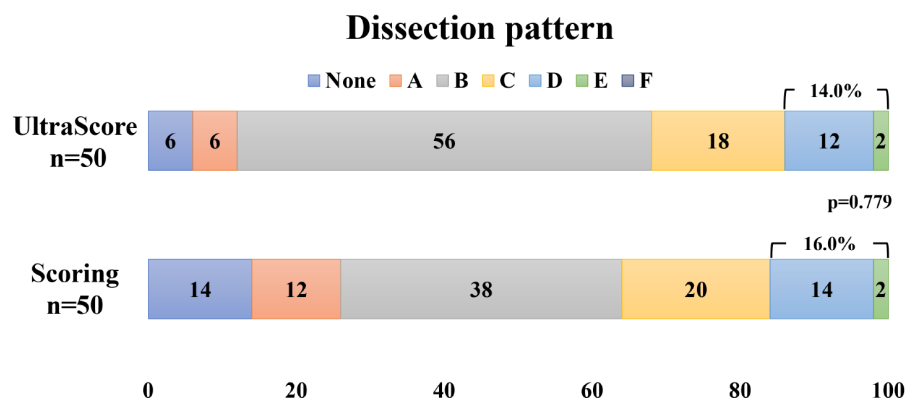


Figure 1. Comparison of dissection patterns between paclitaxel-coated balloon angioplasty with UltraScore and conventional scoring balloons (print color requested). The incidence of severe dissection, defined as type D or greater, was not significantly different between the two groups.

| Variable | Overall population (before matching) | | | Matched population | | |
|--|--------------------------------------|--------------------|----------------|----------------------|-------------------|----------------|
| | UltraScore n = 58 | Scoring n = 214 | <i>P</i> value | UltraScore n = 50 | Scoring n = 50 | <i>P</i> value |
| Technical success | 74.1% (43) | 65.4% (140) | 0.211 | 76.0% (38) | 56.0% (28) | 0.035 |
| Residual stenosis <30% | 89.6% (52) | 70.6% (151) | 0.003 | 90.0% (45) | 68.0% (34) | 0.007 |
| Non-severe dissection; none to type C | 84.5% (49) | 88.8% (190) | 0.375 | 86.0% (43) | 84.0% (42) | 0.779 |
| Periprocedural complications | 3.4% (2) | 1.9% (4) | 0.469 | 4.0% (2) | 2.0% (1) | 0.562 |
| Restenosis rate at six months | 3.4% (2) | 4.2% (9) | 0.796 | 4.0% (2) | 8.0% (4) | 0.339 |
| Target lesion revascularization rate at six months | 1.7% (1) | 2.3% (5) | 0.779 | 2.0% (1) | 4.0% (2) | 0.500 |
| Postoperative stenosis (%) | 14.6 ± 7.7 | 18.2 ± 13.4 | 0.103 | 2.5 ± 7.6 | 9.5 ± 15.1 | 0.004 |
| Postoperative ankle-brachial index | 0.89 ± 0.16 | 0.94 ± 0.18 | 0.062 | 0.92 ± 0.14 | 0.91 ± 0.15 | 0.746 |
| Dissection pattern | | | | | | |
| None | 5.2% (3) | 20.1% (43) | 0.007 | 6.0% (3) | 14.0% (7) | 0.182 |
| A | 5.2% (3) | 18.2% (39) | 0.015 | 6.0% (3) | 12.0% (6) | 0.243 |
| B | 53.4% (31) | 35.5% (76) | 0.013 | 56.0% (28) | 38.0% (19) | 0.071 |
| C | 20.7% (12) | 14.9% (32) | 0.294 | 18.0% (9) | 20.0% (10) | 0.799 |
| D | 12.1% (7) | 9.8% (21) | 0.618 | 12.0% (6) | 14.0% (7) | 0.766 |
| Flow-limited dissection | 3.4% (2) | 1.4% (3) | 0.305 | 2.0% (1) | 2.0% (1) | 0.753 |

Data are presented as number (percentage) or mean ± standard deviation unless otherwise specified.

Table 4. Predictors of technical success

| Variables | Univariate analysis | | Multivariate analysis | |
|--|-----------------------|---------|-----------------------|---------|
| | Hazard ratio (95% CI) | P value | Hazard ratio (95% CI) | P value |
| Female | 1.26 (0.55–2.92) | 0.582 | | |
| Ambulatory | 1.04 (0.40–2.66) | 0.939 | | |
| Diabetes mellitus | 0.95 (0.40–2.26) | 0.916 | | |
| Dyslipidemia | 0.78 (0.33–1.88) | 0.586 | | |
| Diabetes mellitus | 1.24 (0.74–2.08) | 0.409 | | |
| Hemodialysis | 0.80 (0.29–2.16) | 0.656 | | |
| Coronary artery disease | 0.93 (0.40–2.16) | 0.863 | | |
| Statin | 0.79 (0.34–1.82) | 0.582 | | |
| Distal reference vessel diameter <5.0 mm | 0.57 (0.22–1.47) | 0.249 | | |
| Lesion length <100 mm | 2.81 (0.87–9.11) | 0.085 | 1.90 (0.51–7.08) | 0.338 |
| Chronic total occlusion | 0.46 (0.19–1.11) | 0.083 | 0.42 (0.16–1.08) | 0.072 |
| PACSS grade 4 | 0.38 (0.16–0.89) | 0.026 | 0.44 (0.17–1.16) | 0.096 |
| UltraScore use | 2.49 (1.06–5.86) | 0.037 | 2.58 (1.05–6.36) | 0.040 |
| Cutting balloon use | 0.75 (0.16–3.41) | 0.710 | | |
| IVUS use | 0.54 (0.22–1.34) | 0.183 | | |

Data are presented as number (percentage) or mean ± standard deviation unless otherwise specified. PACSS, peripheral artery calcium scoring system; CI, confidence interval; IVUS, intravascular ultrasound.

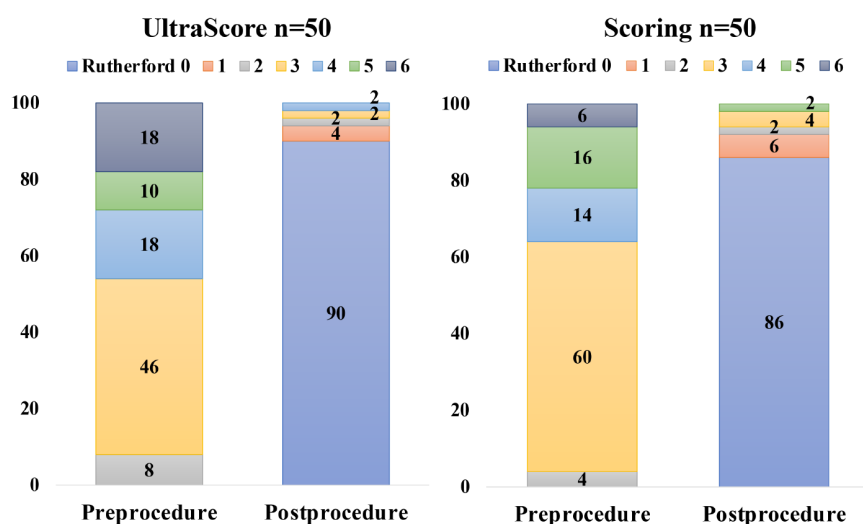


Figure 2. Change in Rutherford classification category before and after the procedure.

formed after PCB angioplasty were excluded, and acceptable rates of technical success, six-month restenosis, and TLR were observed in both groups, even though the study population had severe underlying lesions. Combining PCBs with scoring balloons, including UltraScore balloons, may improve paclitaxel's absorption and antiproliferative effects, resulting in better outcomes. The DCB-Trak registry, which used PCBs combined with the VascuTrak balloon (Becton Dickinson, New Jersey, USA), a scoring balloon with one longitudinal body wire, demonstrated good efficacy for short femoropopliteal lesions.¹⁴ A previous case series using combination therapy with UltraScore and sirolimus-coated balloons (Selution SLR; MedAlliance SA,

Nyon, Switzerland) also demonstrated satisfactory technical and procedural success.¹⁵ However, the clinical outcomes of combining UltraScore balloons with PCBs had not been researched until the present study, which revealed that UltraScore balloons had a positive effect on longer femoropopliteal lesions and had similar effects to conventional scoring balloons for short to medium-length lesions. The results of this study suggest that combining PCBs with scoring balloons, including the UltraScore balloon, was a clinically effective treatment strategy for femoropopliteal lesions, with comparable six-month restenosis and TLR rates in both groups.

The current study had several limitations. First, it was a retrospective, single-center

study with a small sample size, which may limit the generalizability of the findings. Second, the scoring group included only the Cutting balloon and AngioSculpt balloon; no other types of scoring balloons were included. The limited variety of balloons used may have affected the results. Third, no atherectomy devices were used. While previous studies have demonstrated the effectiveness and safety of using atherectomy devices followed by DCB angioplasty, these devices are expensive and mainly used as adjunctive treatments for focal lesions.^{16,17} No studies have compared DCB combined therapy using atherectomy devices and scoring balloons. Furthermore, given the limited financial resources of the health system,¹⁸ a cost-effectiveness analysis should be conducted in future randomized controlled trials evaluating the usefulness of these combination therapies. Finally, the follow-up period was only six months, and the long-term clinical outcomes of this combination therapy are unknown. Therefore, further studies with larger sample sizes and longer follow-up periods are necessary to confirm this study's results and evaluate the efficacy and safety of UltraScore and other scoring balloons in combination with PCB angioplasty.

In conclusion, this study demonstrated that using UltraScore balloons during PCB angioplasty for femoropopliteal lesions significantly improved technical success compared with conventional scoring balloons. UltraScore balloon use was an independent predictor of technical success. These results indicate the potential advantages of using

UltraScore balloons in peripheral intervention procedures.

Acknowledgements

The authors thank all the members of Sapporo Heart Center.

Conflict of interest disclosure

The authors declared no conflicts of interest.

References

1. Laird JA, Schneider PA, Jaff MR, et al. Long-term clinical effectiveness of a drug-coated balloon for the treatment of femoropopliteal lesions. *Circ Cardiovasc Interv.* 2019;12(6):e007702. [\[CrossRef\]](#)
2. Sachar R, Soga Y, Ansari MM, et al. 1-year results from the RANGER II SFA randomized trial of the ranger drug-coated balloon. *JACC Cardiovasc Interv.* 2021;14(10):1123-1133. [\[CrossRef\]](#)
3. Rosenfield K, Jaff MR, White CJ, et al. Trial of a paclitaxel-coated balloon for femoropopliteal artery disease. *N Engl J Med.* 2015;373(2):145-153. [\[CrossRef\]](#)
4. Fanelli F, Cannavale A, Gazzetti M, et al. Calcium burden assessment and impact on drug-eluting balloons in peripheral arterial disease. *Cardiovasc Intervent Radiol.* 2014;37(4):898-907. [\[CrossRef\]](#)
5. Horie K, Tanaka A, Taguri M, Inoue N. Impact of baseline and postprocedural intravascular ultrasound findings on 1-year primary patency after drug-coated balloon treatment of femoropopliteal lesions. *J Endovasc Ther.* 2022;29(1):66-75. [\[CrossRef\]](#)
6. Canaud L, Alric P, Berthet JP, Marty-Ané C, Mercier G, Branchereau P. Intrainguinal cutting balloon angioplasty in de novo arterial lesions. *J Vasc Surg.* 2008;48(5):1182-1188. [\[CrossRef\]](#)
7. Poncyłjusz W, Falkowski A, Safranow K, Rać M, Zawierucha D. Cutting-balloon angioplasty versus balloon angioplasty as treatment for short atherosclerotic lesions in the superficial femoral artery: randomized controlled trial. *Cardiovasc Intervent Radiol.* 2013;36(6):1500-1507. [\[CrossRef\]](#)
8. Rogers JH, Lasala JM. Coronary artery dissection and perforation complicating percutaneous coronary intervention. *J Invasive Cardiol.* 2004;16(9):493-499. [\[CrossRef\]](#)
9. Horie K, Tanaka A, Taguri M, Inoue N. Impact of scoring balloons on percutaneous transluminal angioplasty outcomes in femoropopliteal lesions. *J Endovasc Ther.* 2020;27(3):481-491. [\[CrossRef\]](#)
10. Tan M, Urasawa K, Koshida R, et al. Comparison of angiographic dissection patterns caused by long vs short balloons during balloon angioplasty of chronic femoropopliteal occlusions. *J Endovasc Ther.* 2018;25(2):192-200. [\[CrossRef\]](#)
11. Feldman DN, Armstrong EJ, Aronow HD, et al. SCAI consensus guidelines for device selection in femoral-popliteal arterial interventions. *Catheter Cardiovasc Interv.* 2018;92(1):124-140. [\[CrossRef\]](#)
12. Aboyans V, Ricco JB, Bartelink MEL, et al. 2017 ESC guidelines on the diagnosis and treatment of peripheral arterial diseases, in collaboration with the European Society for Vascular Surgery (ESVS): document covering atherosclerotic disease of extracranial carotid and vertebral, mesenteric, renal, upper and lower extremity arteries Endorsed by: the European Stroke Organization (ESO) The Task Force for the Diagnosis and Treatment of Peripheral Arterial Diseases of the European Society of Cardiology (ESC) and of the European Society for Vascular Surgery (ESVS). *Eur Heart J.* 2018;39(9):763-816. [\[CrossRef\]](#)
13. Steiner S, Schmidt A, Zeller T, et al. COMPARE: prospective, randomized, non-inferiority trial of high- vs. low-dose paclitaxel drug-coated balloons for femoropopliteal interventions. *Eur Heart J.* 2020;41(27):2541-2552. [\[CrossRef\]](#)
14. Baumhäkel M, Chkhetia S, Kindermann M. Treatment of femoro-popliteal lesions with scoring and drug-coated balloon angioplasty: 12-month results of the DCB-Trak registry. *Diagn Interv Radiol.* 2018;24(3):153-157. [\[CrossRef\]](#)
15. Bong TS, Yap CJ, Soon SX, Tang TY. Combination therapy using scoring and sirolimus drug-coated balloons during lower limb endovascular revascularization for chronic limb threatening ischaemia: A case series. *SAGE Open Med Case Rep.* 2022;10:2050313X221085859. [\[CrossRef\]](#)
16. Iida O, Urasawa K, Shibata Y, et al. Clinical safety and efficacy of rotational atherectomy in Japanese patients with peripheral arterial disease presenting femoropopliteal lesions: the J-SUPREME and J-SUPREME II trials. *J Endovasc Ther.* 2022;29(2):240-247. [\[CrossRef\]](#)
17. Zeller T, Langhoff R, Rocha-Singh KJ, et al. Directional atherectomy followed by a paclitaxel-coated balloon to inhibit restenosis and maintain vessel patency: twelve-month results of the DEFINITIVE AR study. *Circ Cardiovasc Interv.* 2017;10(9):e004848. [\[CrossRef\]](#)
18. Katsanos K, Geisler BP, Garner AM, Zayed H, Cleveland T, Pietzsch JB. Economic analysis of endovascular drug-eluting treatments for femoropopliteal artery disease in the UK. *BMJ Open.* 2016;6(5):e011245. [\[CrossRef\]](#)



A comparison of lymphatic embolization and sclerotherapy in the management of iatrogenic abdominopelvic lymphoceles following oncological surgery

Amgad M. Moussa

Ahmed K. Aly

Majid Maybody

Juan C. Camacho

Fourat Ridouani

Adrian J. Gonzalez-Aguirre

Ernesto Santos

From the Department of Radiology, Division of Interventional Radiology (A.M.M. ✉ amgadmousa89@gmail.com, A.K.A., M.M., F.R., A.J.G.-A., E.S.), Memorial Sloan Kettering Cancer Center, New York, United States; Department of Radiology, Division of Interventional Radiology (J.C.C.), Florida Atlantic University, Florida, United States.

Received 30 January 2023; revision requested 04 March 2023; last revision received 04 April 2023; accepted 10 April 2023.

The material was presented at the Society of Interventional Oncology (SIO) 2022 Annual Scientific Meeting.



Epub: 09.05.2023

Publication date: 30.05.2023

DOI: 10.4274/dir.2023.232135

PURPOSE

To compare the safety and efficacy of sclerotherapy and lymphatic embolization (LE) in the treatment of symptomatic iatrogenic lymphoceles following the placement of a percutaneous drainage catheter.

METHODS

This is a retrospective study of 46 patients who underwent sclerotherapy (17 patients) or LE (29 patients) for the management of symptomatic iatrogenic lymphoceles following percutaneous drain placement between January 2017 and December 2021. The demographic characteristics, time between surgery and lymphatic intervention, clinical presentation, number of procedures, drain output pre- and post-intervention, time from intervention to drain removal, and adverse events were collected and compared for both groups. The clinical success rate, defined as the successful removal of the drain after one procedure, was calculated. Adverse events were reported according to the Society of Interventional Radiology classification. A statistical analysis was conducted using SPSS, and the *P* value for statistical significance was set at 0.05. The Mann–Whitney U test was used to compare differences in the scale variables, and Fisher's exact test was used to compare the categorical and ordinal variables between both groups.

RESULTS

A total of 46 patients with 49 lymphoceles met the inclusion criteria of the study. Of these patients, 17 patients (19 lymphoceles) underwent sclerotherapy, and 29 patients (30 lymphoceles) underwent LE as their initial procedures. The clinical success after one procedure was significantly higher (83% vs. 47%, *P* = 0.011), and the median time between the first intervention and drain removal was significantly shorter in the LE group (median duration of 6 vs. 13 days, *P* = 0.018) compared with the sclerotherapy group. No statistically significant difference in adverse events was noted between both groups (0.26 vs. 0.10, *P* = 0.11).

CONCLUSION

This study found that LE had a higher clinical success rate after the first procedure and a shorter time to drain removal compared with sclerotherapy. There was no difference in the rate of adverse events between both groups. Although LE is a safe and promising technique, a prospective study is needed to further compare the efficacy of both treatment modalities.

KEYWORDS

Embolization, lymphangiography, lymphatic, lymphocele, sclerotherapy

Lymph node dissection is an integral part of oncological surgery. Lymphatic injury and lymphocele development is a known complication of lymph node dissection. The reported incidence of lymphocele varies in the literature, with incidences of symptomatic lymphoceles ranging between 2.5% and 34.5%.^{1,2} Symptoms are often due to infection within the lymphocele, or pressure on surrounding structures, with urinary frequency, constipation, hydronephrosis, pain and lower extremity edema all reported in the literature.³

You may cite this article as: Moussa AM, Aly AK, Maybody M, et al. A comparison of lymphatic embolization and sclerotherapy in the management of iatrogenic abdominopelvic lymphoceles following oncological surgery. *Diagn Interv Radiol.* 2023;29(3):542-547.

Percutaneous catheter drainage is the mainstay of treatment for symptomatic lymphoceles. However, further intervention is often required to decrease the drain output, and subsequently, the drain dwell time.^{4,5} Sclerotherapy induces local inflammation and fibrosis of the wall of the lymphocele with subsequent obliteration of the lymphatic leak, and safety and efficacy has been reported.⁶ Although this treatment is sometimes successful after one session, the literature reports the average number of required sclerotherapy procedures to be between one and four procedures, with patients sometimes requiring up to 14 procedures.⁷ Lymphangiography followed by lymphatic embolization (LE) is another approach to identify and occlude the source of lymphatic leak. The intranodal technique has made lymphangiography much less cumbersome and technically demanding than in the past. Once the leak has been identified, LE using an n-butyl cyanoacrylate (n-BCA) and lipiodol mixture is conducted under fluoroscopic guidance, and safety and efficacy has also been reported.⁸

Studies comparing these two treatment modalities are limited.^{3,9} The aim of this single center retrospective study is to compare the efficacy and safety of sclerotherapy and LE in the treatment of pelvic and abdominal iatrogenic lymphoceles following oncologic surgery.

Methods

Patient population

This retrospective study was approved by the Memorial Sloan Kettering Cancer Center Institutional Review Board under protocol

number 16-402, and the need for informed consent was waived. Medical records were reviewed to identify patients with abdominal or pelvic iatrogenic symptomatic lymphoceles following oncological surgery. Patients treated with percutaneous drainage followed by sclerotherapy or LE were included. Patients were excluded if no follow-up data was available to evaluate the clinical outcome or if the percutaneous drain was removed before clinical resolution was confirmed through decreased drain output.

A total of 55 patients with 59 lymphoceles were identified (Table 1). The decision to treat with sclerotherapy or LE was based on the operator's discretion. One patient had lymphangiography followed by sclerotherapy in the same session when no leak was identified and was subsequently excluded from further analysis. Eight patients had the drain removed on the same day as the sclerotherapy procedure, and there were no available data to evaluate the success of the treatment later. Therefore, they were excluded, as this clinical approach was later abandoned. The remaining 46 patients were divided into 17 patients (19 lymphoceles) who underwent sclerotherapy and 29 patients (30 lymphoceles) who underwent intranodal lymphangiography (INL) and LE as their initial procedures (Figure 1). Twenty of the 29 patients who underwent LE in this study were also involved in a prior study that was focused on proving the safety and efficacy of LE.⁸ They have been included in this study as part of the LE cohort, as this study focuses on comparing the outcomes of LE and sclerotherapy.

The most common cancer diagnosis was prostate cancer (63%). No statistically significant difference was noted in the baseline characteristics except in the presenting symptoms, as no patients in the sclerotherapy group presented with fever.

Sclerotherapy technique

The procedure was performed under moderate sedation. Under aseptic conditions, all patients had a percutaneous drain placed under imaging guidance [computed tomography (CT) or ultrasound]. The fluid collection was drained fully, and the drained volume was recorded. A similar volume of iodinated contrast was then injected into the lymphocele cavity under fluoroscopic imaging or CT to ensure the absence of communication with adjacent structures (Figure 2). The contrast was then aspirated, and the sclerosant material was injected through the drain and left to dwell in the collection for 30–120 minutes according to the operator's preference. Absolute ethanol and povidone iodine volumes were determined based on the amount of contrast that was required to fill the cavity without having pericatheter leakage or intravasation. In cases of sodium tetradecyl sulphate (STS) 3% (Sotradecol, AngioDynamics, Inc., Queensbury, NY, USA), it was mixed with air in a 1:3 ratio to form foam, which was then instilled through the drain. It was then aspirated, and the drain was left in place. The drain output was monitored over the following days. The drain was removed once the output dropped below 20 cc/24 hrs over 3 consecutive days. If the drain output remained consistently elevated for several

Table 1. Baseline characteristics of the study population

| | INL/LE | Sclerotherapy | P value |
|----------------------------|------------|---------------|---------|
| Age (mean) | 61 | 64 | 0.35 |
| Gender | | | |
| Male | 25 (86%) | 15 (88%) | 0.84 |
| Female | 4 (14%) | 2 (12%) | |
| Diagnosis | | | |
| Prostate cancer | 18 (62.1%) | 11 (64.7%) | 0.17 |
| Ovarian cancer | 2 (6.9%) | 1 (5.9%) | |
| Testicular cancer | 3 (10.3%) | 1 (5.9%) | |
| Urinary bladder cancer | 4 (3.8%) | 0 (0%) | |
| Other* | 2 (6.9%) | 4 (23.5%) | |
| Presenting symptoms | | | |
| Pain | 10 (35%) | 8 (47%) | 0.013 |
| Fever | 9 (30%) | 0 (0%) | |
| Pressure symptoms** | 10 (35%) | 6 (35%) | |
| Other*** | 0 (0%) | 3 (18%) | |
| Lymphocele location | | | |
| Pelvic | 24 (80%) | 18 (95%) | 0.22 |
| Retroperitoneal | 6 (20%) | 1 (5%) | |

*Other cancers included; **pressure symptoms included frequency, lower extremity edema, and hydronephrosis; ***others included incidental, high output in surgical drain. INL/LE, intranodal lymphangiography and lymphatic embolization.

Main points

- Symptomatic lymphoceles are a relatively common occurrence after lymph node dissection in oncological surgery.
- Percutaneous drainage is the treatment of choice, but it may require prolonged drain dwell times, which affect patients' quality of life.
- Sclerotherapy is the primary treatment to decrease the drain dwell time, but it often requires multiple procedures.
- Intranodal lymphangiography and lymphatic embolization (LE) are newer treatment options.
- This retrospective study showed that LE was associated with a significantly shorter drainage drain dwell time than sclerotherapy and required fewer procedures.

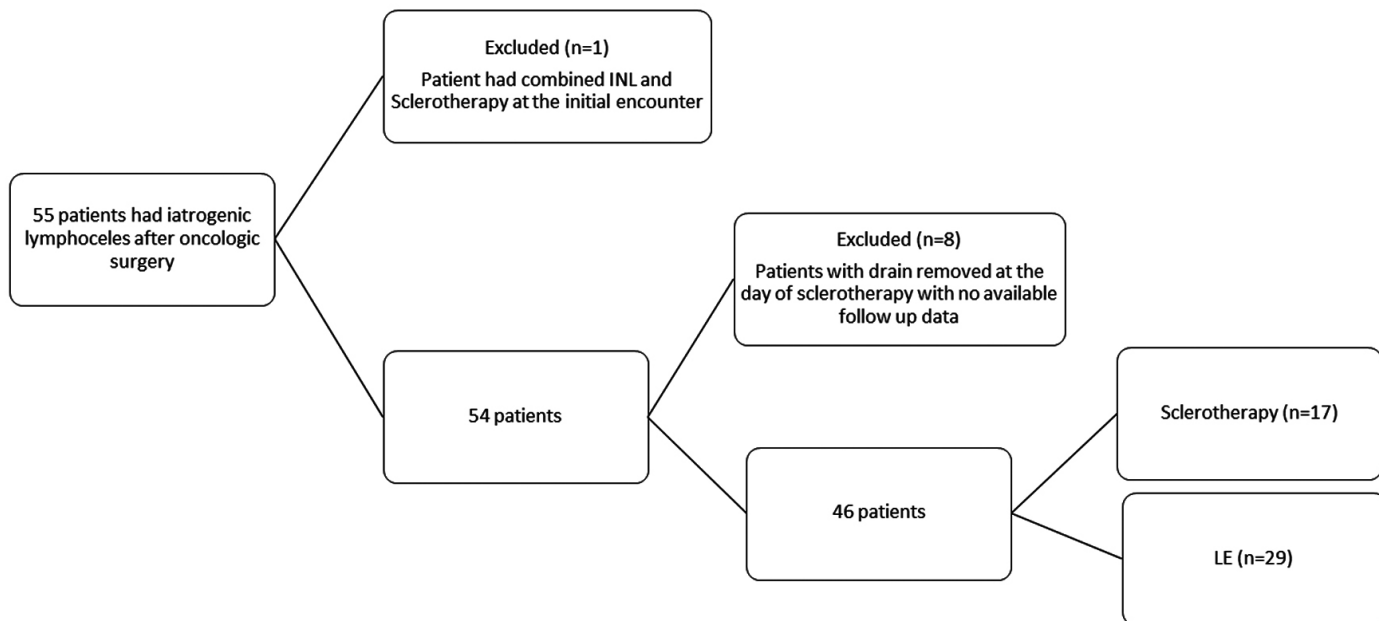


Figure 1. Flowchart for study inclusion. INL, intra-nodal lymphangiography; LE, lymphatic embolization.

days following the procedure, the sclerotherapy procedure was repeated based on the interventional radiologist's assessment. The sclerosant materials that were used included absolute ethanol, STS 3%, doxycycline, and/or povidone iodine (Betadine, Purdue-Fredrick, Norwalk, Conn). The choice of the sclerosant and dwell time was based on the operator's preference.

Lymphangiography and lymphatic embolization technique

The procedure was performed under moderate sedation by one of six interventional radiologists with 2–26 years of experience. Under ultrasound imaging guidance, a 25-gauge needle was placed into an inguinal lymph node at the side of the pelvic lymphocele with the tip located at the corticomedullary junction (Figure 3). Bilateral lymph node access was obtained in cases of bilateral pelvic lymphoceles or retroperitoneal lymphoceles. A total of 6 cc of lipiodol (Guerbet, Villepinte, France) was injected by hand under intermittent fluoroscopy. Once the contrast extravasation was noted into the lymphocele, the point of leak was identified. LE was then performed by advancing a 20- or 22-gauge needle into the leaking lymphatic vessel or the closest proximal lymph node under fluoroscopic guidance (Video 1). An injection of dextrose 5% through the 22-gauge needle with the clearing of the lipiodol in the lymphatic vessel confirmed access (Video 2). LE was then performed using a mixture of lipiodol and n-BCA (Trufill; Codman Neuro, Raynham, Massachusetts) (Video 3). The di-

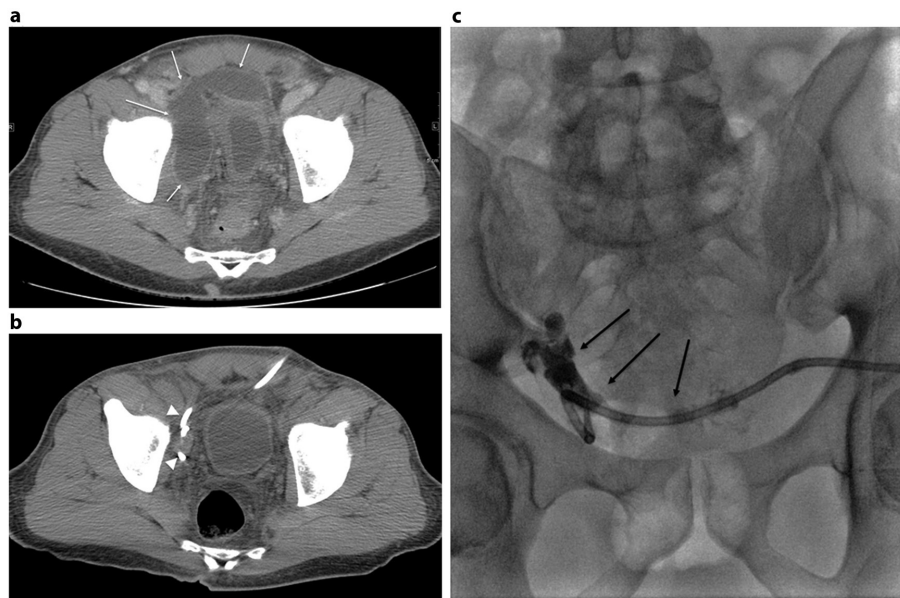


Figure 2. A 57-year-old male with a history of robotic prostatectomy and pelvic lymphadenectomy presenting with pelvic pain. (a) Computed tomography of the abdomen and pelvis showing right pelvic fluid collection (white arrows). (b) Collection completely drained with a 10.5 Fr drainage catheter (white arrow heads), but a consistently high output of 195 cc/day was noted for the following 2 weeks. (c) The residual cavity filled with 12 cc of contrast with no evidence of communication with the surrounding structures (black arrows). A total of 12 cc of 3% sodium tetradecyl sulphate (STS) mixture (2 mL STS, 8 mL iodinated water-soluble contrast, 2 mL air) was subsequently injected (not shown) and allowed to dwell for 2 hours. Output subsequently dropped to 5 cc/day, and the drain was removed after 7 days.

lution of the n-BCA was determined based on the distance between the site of injection and the point of leak according to the operator's preference, ranging between 1:2 and 1:10. If the drain output remained consistently elevated for several days following the procedure, the lymphangiogram procedure was repeated based on the interventional radiologist's assessment.

Outcomes

Technical success of sclerotherapy was defined as the ability to inject sclerosant and complete the procedure. Technical success of INL was defined as the ability to inject lipiodol and visualize the lymphatic vessels under fluoroscopy. Technical success of LE was defined as the ability to inject n-BCA into the leaking lymphatic vessel or closest proximal

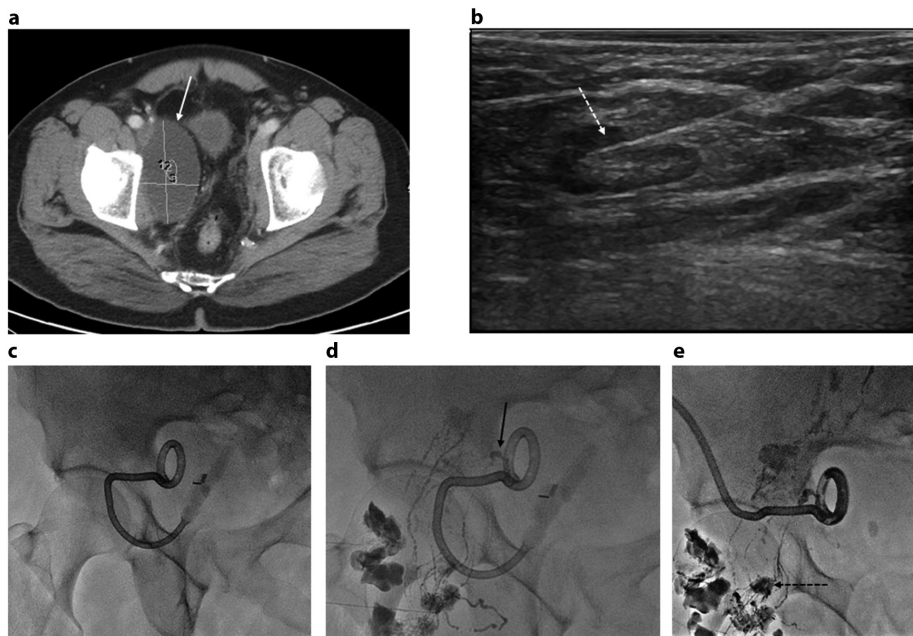


Figure 3. A 61-year-old male with a history of prostatectomy and pelvic lymphadenectomy presenting with pelvic pain and right lower extremity edema. (a) Computed tomography of the abdomen and pelvis showing right pelvic fluid collection (white arrow) compressing the external iliac vein. Consistently high output of the drain noted (200 cc/day). (b) Ultrasound-guided access in one of the right inguinal lymph nodes with the needle tip placed at the corticomedullary junction (dotted white arrow). (c, d) Fluoro spot images before and during intra-nodal lymphangiography showing the focal area of contrast extravasation within the expected location of the collection (black arrow). Leak confirmed by flushing and aspirating the drain (not shown). (e) Access obtained under fluoroscopy to the lymph node closest to the leak (dotted black arrow). Position confirmed by injecting 5% dextrose, and then embolization was performed with 0.33 cc of n-butyl cyanoacrylate/lipiodol mixture (1:4). The output dropped, and the drain was removed 7 days later.

LE group, lymphatic leak was identified and subsequently embolized in 31 out of 35 procedures. Clinical success occurred after the first sclerotherapy procedure in eight out of 17 patients (47%). Five patients needed one additional sclerotherapy procedure, and four patients needed two additional sclerotherapy procedures. Clinical success following the first INL/LE was achieved in 24/29 patients (83%), which was significantly higher than the sclerotherapy group (83% vs. 47%, $P = 0.011$). Four patients needed one additional procedure, and one patient needed two additional procedures (Figure 1).

The INL/LE group had the drain for a significantly shorter duration (median of 6 vs. 13 days, $P = 0.018$). In the 27 patients who had recorded an output prior to sclerotherapy or INL/LE, the pre-procedure output (378 vs. 101 mL, $P = 0.005$) and change in the output after the first procedure (315 vs. 69 mL, $P = 0.002$) were higher in the INL/LE group. In the sclerotherapy group, the sclerosants were used as per the operator's discretion and included absolute ethanol (18 times, median volume of 9 cc), sodium-tetradecyl sulfate 3% (four times, median volume 6.5 cc), povidone iodine (three times, median volume of 10 cc), doxycycline (one time, volume of 20 cc), and a combination of sclerosants was used four times (absolute ethanol three times, STS 3% one time, povidone iodine was used in the post-procedure drain flushes in the outpatient setting). No statistically significant difference was noted in the rate of adverse events between both groups (Table 3). Post-procedure pain and fever were noted in patients within both groups. The drain was clogged and had to be changed in three patients after INL/LE. Ipsilateral lower limb edema that resolved with conservative treatment was noted after INL/LE.

Discussion

The results show that INL/LE is associated with a higher clinical success rate after one procedure, fewer procedures for treatment, and a shorter drain dwell time. Those superior results were in spite of a higher initial daily drain output.

Percutaneous drainage and sclerotherapy have long been the standard treatment of symptomatic lymphoceles due to superior outcomes compared with drainage alone.^{3,5,10,11} To the authors' knowledge, no specific sclerosant has been proven to be superior to others.^{5,7} Multiple studies have shown the efficacy of INL/LE in the treatment of lymphoceles; INL alone was associated

Table 2. Clinical outcomes of the procedure

| | INL/LE | Sclerotherapy | P value |
|--|-----------|---------------|--------------|
| Clinical success after the first procedure (%) | 24 (83) | 8 (47) | 0.011 |
| Number of additional procedures (%) | | | |
| 1 | 4 (14) | 5 (29) | 0.026 |
| 2 | 1 (3) | 4 (24) | |
| Time from the first INL/LE or sclerotherapy procedure to drain removal in days (range) | 6 (1–41) | 13 (5–57) | 0.018 |
| Mean pre-procedure output in mL (standard deviation) | 378 (332) | 101 (77) | 0.005 |
| Mean change in output in mL (standard deviation) | 315 (257) | 69 (54) | 0.002 |

INL/LE, intranodal lymphangiography and lymphatic embolization.

lymph node when a leak was identified. Clinical success was defined as a reduction in the drain output to less than 20 cc/24 hrs for 3 consecutive days with subsequent drain removal. The need to repeat the procedure and the number of procedures needed to achieve clinical success were recorded. Changes in the drain output and the time to drain removal following the first procedure were calculated. Adverse events after the procedure were reported according to the Society of Interventional Radiology classification.

Statistical analysis

Baseline demographics of patients and clinical characteristics were compared using

Fisher's exact test and an independent sample t-test as appropriate. IBM SPSS Statistics for Windows, version 26 (IBM Corp., Armonk, N.Y., USA) was used for the statistical analysis. The differences in the treatment outcomes between the two procedures were tested using different statistical tests based on the outcome variable category. The Mann-Whitney U test was used to compare the differences in the scale variables, and Fisher's exact test was used to compare the categorical and ordinal variables between both groups.

Results

All sclerotherapy and INL procedures were technically successful (Table 2). In the INL/

| Table 3. Adverse events | | | |
|---|--|---|---------|
| | INL/LE | Sclerotherapy | P value |
| Adverse events (per total number of procedures) | 9/35 | 3/28 | 0.11 |
| Mild (SIR grade 2) | - Ipsilateral lower limb edema resolving with compression stockings after 1 and 2 months (two patients) - Post procedure pain resolving spontaneously | - Post-procedure pain resolving spontaneously | |
| Moderate (SIR grade 3) | - Drain clogged requiring exchange (three patients) - Fever requiring drain exchange (two patients) - Ipsilateral lower limb edema and consequent infection requiring admission and intravenous antibiotics. Edema resolved with compression stockings after 12 months | - Fever requiring drain exchange - Pain requiring emergency room visit | |

INL/LE, intranodal lymphangiography and lymphatic embolization; SIR, Society of Interventional Radiology.

with clinical success in around 70% of cases, which dropped to 35% in cases with high outputs (>500 mL/day).¹²⁻¹⁴ When combined with LE, clinical success climbs up to 100% with an average drain dwell time of 5–7 days.^{3,8,15-18} Concern for a lengthy procedure, similar to thoracic duct embolization procedures, is unfounded, as lipiodol has to travel a much shorter distance to the site of leakage in the pelvis or retroperitoneum, rather than all the way to the cisterna chyli.^{3,8}

There is a paucity of data comparing the two treatment approaches, which is the primary objective of this study. In their systematic review of literature, Ten Hove et al.³ did not identify any studies comparing both modalities for the treatment of lymphoceles. However, they did note a higher proportion of success and shorter duration of treatment in studies using INL/LE. Kim et al.⁹ compared INL/LE with ethanol sclerotherapy in their cohort of 33 patients, which included patients with chylous ascites in the INL/LE group. They found a higher success rate with INL/LE of 83.3% compared with 43.8% with sclerotherapy, which they attributed to their institutional limitations on the number of procedures and duration of treatment. This is in line with the reported rate of clinical success after one sclerotherapy procedure of 47% that was reported in this study, which increased to 77% after a second sclerotherapy procedure. In the INL/LE group, clinical success after one procedure was 83%, which was significantly higher.

This head-to-head comparison emphasizes the difference in clinical success and, equally important, the difference in drain dwell time between the two treatment modalities. Percutaneous drainage catheters significantly affect patients' quality of life,

as they limit clothing and activities. In their study, Kim et al.⁹ noted a mean shorter drain dwell time with an INL/LE of 7.1 days vs. 12.3 days in the sclerotherapy group. However, the difference was not statistically significant. This study found a statistically significant lower median drain dwell time of 6 days in the INL/LE group compared with 13 days in the sclerotherapy group, which can be attributed to the larger sample size.

There were no major adverse events in either group. The incidence of mild or moderate adverse events with sclerotherapy was 10.7%, which is comparable to the incidence reported in the literature (0%–24%). There was no report of sclerosant extravasation, which is the most serious complication reported in the literature.^{5,7,10,11,19-21} The complication rate with LE was higher than the sclerotherapy group (26.4%) but not statistically significant, and it was slightly higher than in other studies (8%–20%).^{9,14} Most adverse events noted with LE were related to the drain occlusion having to be exchanged, which is why the authors advocate for exchanging the drainage catheter after LE in the same session. Ipsilateral lower limb edema was also noted in three patients in the LE group and is likely related to the occlusion of the lymphatic vessels draining that limb during embolization. In all cases, the edema resolved with compression stockings and no additional procedures, though it took up to 1 year in one patient.

The main limitations of this study are its retrospective nature and small sample size. The choice of treatment modality was based on the operator's preference, which introduces a selection bias. INL/LE is a relatively novel procedure compared with sclerotherapy, which also contributes to the selection

bias; however, the authors controlled that factor by limiting the start date to 2017. The heterogeneity of the sclerotherapy technique is also a limitation of this study, but it reflects the real-world experience, where sclerotherapy techniques vary greatly between operators, even those within the same institution. The experience of the different operators with INL/LE is not homogeneous, even within this study, which can limit the generalization of the results to other settings with a smaller number of cases.

In conclusion, INL/LE is a safe and effective treatment for symptomatic lymphoceles that develop after oncological surgeries. It is associated with a higher clinical success rate after the first procedure and shorter drain dwell time than sclerotherapy. A randomized, prospective study comparing the two treatment modalities is needed to confirm these results.

Conflict of interest disclosure

The authors declared no conflicts of interest.

Funding

This research was funded in part through the NIH/NCI Cancer Center Support Grant P30 CA008748.

References

1. Tsaur I, Thomas C. Risk factors, complications and management of lymphocele formation after radical prostatectomy: A mini-review. *Int J Urol.* 2019;26(7):711-716. [CrossRef]
2. Song SY, Park M, Kang BH, et al. Distribution of lymphocele following lymphadenectomy in patients with gynecological malignancies. *Obstet Gynecol Sci.* 2020;63(6):700-708. [CrossRef]
3. Ten Hove AS, Tjong MY, Zijlstra IAJ. Treatment of symptomatic postoperative pelvic lymphoceles: a systematic review. *Eur J Radiol.* 2021;134:109459. [CrossRef]
4. Kim JK, Jeong YY, Kim YH, Kim YC, Kang HK, Choi HS. Postoperative pelvic lymphocele: treatment with simple percutaneous catheter drainage. *Radiology.* 1999;212(2):390-394. [CrossRef]
5. Alago W Jr, Deodhar A, Michell H, et al. Management of postoperative lymphoceles after lymphadenectomy: percutaneous catheter drainage with and without povidone-iodine sclerotherapy. *Cardiovasc Intervent Radiol.* 2013;36(2):466-471. [CrossRef]
6. Khorshidi F, Majdalany BS, Peters G, et al. Minimally invasive treatment of abdominal lymphocele: a review of contemporary options and how to approach them. *Lymphology.* 2021;54(2):56-67. [CrossRef]

7. Mahrer A, Ramchandani P, Trerotola SO, Shlansky-Goldberg RD, Itkin M. Sclerotherapy in the management of postoperative lymphocele. *J Vasc Interv Radiol*. 2010;21(7):1050-1053. [\[CrossRef\]](#)
8. Moussa AM, Camacho JC, Maybody M et al. Percutaneous lymphatic embolization as primary management of pelvic and retroperitoneal iatrogenic lymphoceles. *J Vasc Interv Radiol*. 2021;32(11):1529-1535. [\[CrossRef\]](#)
9. Kim SW, Hur S, Kim SY, et al. The efficacy of lymph node embolization using n-butyl cyanoacrylate compared to ethanol sclerotherapy in the management of symptomatic lymphorrhea after pelvic surgery. *J Vasc Interv Radiol*. 2019;30(2):195-202. [\[CrossRef\]](#)
10. Kim Y, Jeon GS, Choi SY, Kim MD, Lee SJ. Evaluation of sclerotherapy for the treatment of infected postoperative lymphocele. *Taiwan J Obstet Gynecol*. 2017;56(4):477-481. [\[CrossRef\]](#)
11. Klode J, Klötgen K, Körber A, Schadendorf D, Dissemmond J. Polidocanol foam sclerotherapy is a new and effective treatment for postoperative lymphorrhea and lymphocele. *J Eur Acad Dermatol Venereol*. 2010;24(8):904-909. [\[CrossRef\]](#)
12. Alexandre-Lafont E, Krompiec C, Rau WS, Krombach GA. Effectiveness of therapeutic lymphography on lymphatic leakage. *Acta Radiol*. 2011;52(3):305-311. [\[CrossRef\]](#)
13. Gruber-Rouh T, Naguib NNN, Lehnert T, et al. Direct lymphangiography as treatment option of lymphatic leakage: indications, outcomes and role in patient's management. *Eur J Radiol*. 2014;83(12):2167-2171. [\[CrossRef\]](#)
14. Hur S, Jun H, Jeong YS. Novel interventional radiological management for lymphatic leakages after gynecologic surgery: lymphangiography and embolization. *Gland Surg*. 2021;10(3):1260-1267. [\[CrossRef\]](#)
15. Smolock AR, Nadolski G, Itkin M. Intranodal glue embolization for the management of postsurgical groin lymphocele and lymphorrhea. *J Vasc Interv Radiol*. 2018;29(10):1462-1465. [\[CrossRef\]](#)
16. Baek Y, Won JH, Chang SJ, et al. Lymphatic embolization for the treatment of pelvic lymphoceles: preliminary experience in five patients. *J Vasc Interv Radiol*. 2016;27(8):1170-1176. [\[CrossRef\]](#)
17. Chu HH, Shin JH, Kim JW, Noh SY, Yang WJ, Park S. Lymphangiography and lymphatic embolization for the management of pelvic lymphocele after radical prostatectomy in prostatic cancer. *Cardiovasc Intervent Radiol*. 2019;42(6):873-879. [\[CrossRef\]](#)
18. Hur S, Shin JH, Lee IJ, et al. Early experience in the management of postoperative lymphatic leakage using lipiodol lymphangiography and adjunctive glue embolization. *J Vasc Interv Radiol*. 2016;27(8):1177-1186. [\[CrossRef\]](#)
19. Baboudjian M, Tadrast A, Gondran-Tellier B, et al. Povidone-iodine sclerotherapy of primary symptomatic lymphocele after kidney transplantation. *Int Urol Nephrol*. 2021;53(4):685-690. [\[CrossRef\]](#)
20. Kerlan RK Jr, LaBerge JM, Gordon RL, Ring EJ. Bleomycin sclerosis of pelvic lymphoceles. *J Vasc Interv Radiol*. 1997;8(5):885-887. [\[CrossRef\]](#)
21. Zuckerman DA, Yeager TD. Percutaneous ethanol sclerotherapy of postoperative lymphoceles. *AJR Am J Roentgenol*. 1997;169(2):433-437. [\[CrossRef\]](#)

.....

Video 1 link: <https://www.youtube.com/watch?v=uWXhbp79P2A>

Video 1. Fluoroscopy-guided lymph node access. The most proximal lymph node is targeted with the 20-gauge needle under fluoroscopic guidance.

Video 2 link: <https://www.youtube.com/watch?v=Kc2slfYC0RQ>

Video 2. Dextrose 5% intranodal flush. Dextrose 5% is injected after needle placement to confirm an adequate needle position. Notice the flow of the lipiodol in the lymphatic vessels toward the leak as it gets pushed by the D5% flush. Also note the lymph node getting less dense as the lipiodol is pushed out of it.

Video 3 link: https://www.youtube.com/watch?v=_PtgyYyeikE

Video 3. n-butyl cyanoacrylate (n-BCA) embolization. The N-BCA/lipiodol combination fills the access lymph node and the lymphatic vessels, causing a leak and the complete embolization of the leaking vessel. Injection stopped when extra-nodal extravasation was noted.



The role of (¹⁸F)-fluoro-D-glucose positron emission tomography/computed tomography in the surveillance of abnormal myocardial energy metabolism and cardiac dysfunction in a rat model of cardiopulmonary resuscitation

Liming Pan

Fan Zhang

Yingqi Ran

Lei Bi

Hongjun Jin

Lan Yao

PURPOSE

To investigate the feasibility and usefulness of 2-deoxy-2-(¹⁸F)-fluoro-D-glucose positron emission tomography/computed tomography [(¹⁸F)-FDG PET/CT] as a novel examination in the surveillance of abnormal myocardial energy metabolism and cardiac dysfunction after cardiopulmonary resuscitation (CPR).

METHODS

Thirteen male Sprague–Dawley rats were randomly divided into a sham group (n = 4), CPR group (n = 4), and trimetazidine (TMZ) + CPR group (n = 5). The expression levels of the myocardial injury marker cardiac troponin I (CTNI) in serum were tested at 6 hours after CPR or TMZ + CPR. The ejection fraction and fraction shortening were evaluated by echocardiography. (¹⁸F)-FDG PET/CT was used to measure the FDG uptake and the standardized uptake value (SUV) after CPR or TMZ + CPR for 6 hours. The intermediary carbohydrate metabolites of glycolysis including phosphoenolpyruvate, 3-phospho-D-glycerate, and the lactate/pyruvate ratio were detected through the multiple reaction monitoring approach. Simultaneously, the authors also tested the expression levels of the total adenosine triphosphate (ATP) and the key intermediate products of glucose oxidation as alpha ketoglutarate, citrate, and succinate in the myocardium.

RESULTS

The authors found that the aerobic oxidation of glucose was reduced, and the anaerobic glycolysis was significantly enhanced in the myocardium in the early stage of CPR. Meanwhile, the myocardial injury marker CTNI was upregulated considerably ($P = 0.014$, $P = 0.021$), and the left ventricular function of the animal heart also markedly deteriorated with the downregulation of ATP after CPR. In contrast, myocardial injury and cardiac function were greatly improved with the increase of ATP in the CPR + TMZ group. In addition, aerobic glucose oxidation metabolites were significantly increased ($P < 0.05$) and anaerobic glycolysis metabolites were significantly decreased ($P < 0.05$) after CPR in the myocardium. Surprisingly, (¹⁸F)-FDG PET/CT could track the above changes by detecting the FDG uptake value and the SUV.

CONCLUSION

Glucose metabolism is an essential factor for myocardial self-repair after CPR. (¹⁸F) FDG PET/CT, as a non-invasive technology, can monitor myocardial energy metabolism and cardiac function by tracking changes in glucose metabolism after CPR.

KEYWORDS

Cardiac function, cardiopulmonary resuscitation, glucose metabolism, myocardial energy metabolism, (¹⁸F)-FDG PET/CT

From the Department of Emergency (L.P., F.Z., Y.R., L.Y.),
✉yaolan2@mail.sysu.edu.cn), the Fifth Affiliated Hospital,
Sun Yat-Sen University, Zhuhai, China; Key Laboratory of
Biomedical Imaging (L.B., H.J.), Fifth Affiliated Hospital,
Sun Yat-Sen University, Zhuhai, China.

Received 02 October 2022; revision requested 31 January
2023; accepted 26 March 2023.



Epub: 08.05.2023

Publication date: 30.05.2023

DOI: 10.4274/dir.2023.221932

You may cite this article as: Pan L, Zhang F, Ran Y, Bi L, Jin H, Yao L. The role of (¹⁸F)-fluoro-D-glucose positron emission tomography/computed tomography in the surveillance of abnormal myocardial energy metabolism and cardiac dysfunction in a rat model of cardiopulmonary resuscitation. *Diagn Interv Radiol.* 2023;29(3):548-554.

Mycocardial dysfunction remains a leading problem in the early period following the return of spontaneous circulation (ROSC) after cardiac arrest. Post-resuscitation myocardial injury is evidently due to oxidative stress, calcium overload, neutrophil accumulation, microvascular damage, and abnormal energy metabolism, among other causes.¹⁻³ As one of the most common pathological mechanisms after the ROSC, energy metabolism disorder in the myocardium leads to a series of detrimental changes in the energy supply and substrate metabolism related to the regulation of mitochondrial function, oxidative stress, and inflammation.^{4,5}

Glucose and fatty acids are important energy substrates for myocardial metabolism.⁶ Sixty to seventy percent of the energy required for cardiac contraction under normal physiological conditions is mainly furnished by the oxidative metabolism of fatty acids, with the remainder predominantly from glucose.⁷ The metabolism of fatty acids and glucose undergoes adaptive changes in the myocardium due to ischemia-reperfusion injury after cardiopulmonary resuscitation (CPR). The rate of aerobic oxidation of free fatty acids and glucose in cardiomyocytes is decreased, yet the rate of anaerobic glycolysis is enhanced.^{8,9} Glucose anaerobic metabolism becomes progressively more mainstream in the heart after the ROSC. Some *in vitro* experiments demonstrated that early intervention in cardiac metabolism disorder attenuated myocardial damage and dysfunction. Therefore, it is crucial in the clinical setting to detect myocardial metabolism conditions in real-time to evaluate the latent cardiac injury and make optimum treatment plans during the ROSC. Nevertheless, there is no proven technique to track cardiac metabolism changes after CPR.

2-deoxy-2-(¹⁸F)-fluoro-D-glucose [¹⁸F]-FDG], as an analog of glucose, is transported into the cell by facilitated diffusion and is phosphorylated to (¹⁸F)-FDG-6-phosphate.¹⁰

Once inside the cardiac myocyte, (¹⁸F)-FDG-6-phosphate is not metabolized further and has the potential to track glucose uptake and glycolysis.¹¹⁻¹⁴ The glucose analog 2-(¹⁸F)-fluoro-2-deoxy-D-glucose was used to quantify glucose uptake and glycolytic activity in native and transplanted hearts. (¹⁸F)-FDG positron emission tomography/computed tomography (PET/CT) has been widely used to identify malignant neoplasms by evaluating aerobic glycolysis conditions in cancer cells. In the present study, the authors investigate whether metabolic disorders of cardiac cells can be traced and detected by (¹⁸F)-FDG PET/CT to estimate myocardial impairment and prognosis, given the vital role of abnormal glycolysis in the myocardium after CPR.

Methods

Ethics statement

This study was approved by the Laboratory Animal Management Committee prior to all animal experiments (no: 00053).

Animal model

All rats (males aged 18–20 weeks, body weight of 350 ± 25 g) were purchased from the Animal Care and Use Committee. All rats were randomly divided into the sham group (n = 4), CPR group (n = 4), and trimetazidine (TMZ) + CPR group (n = 5). The three groups of animals were fed normal feed for the first two weeks to adapt to the environment, and then the establishment of CPR model animals began. Animals were anesthetized with sodium pentobarbital (45 mg/kg) by intraperitoneal injection and then were subjected to ventilator-assisted breathing (rate of 50 breaths/minute, volume of 0.6 mL/100 g, fraction of inspired oxygen of 0.21). A polyethylene (PE)-50 catheter was inserted from the right carotid artery into the right ventricle. Another PE-50 catheter was inserted into the aorta from the left femoral artery for hemodynamic and arterial pressure monitoring.¹⁵ A 4F PE catheter was inserted into the right external jugular vein and into the right atrium for electrical induction of ventricular fibrillation (VF).

The cardiac rhythm of the rats was monitored by electrocardiogram (ECG) and recorded on ECG drawings. The rats' body temperature was maintained at 36.8 ± 0.2°C throughout the experiment. Hemodynamic data were recorded by a WinDaq data acquisition system (DataQ, Akron, Ohio). Then, the 60 Hz current was gradually increased to a maximum of 3 mAs to the right ventri-

cle endocardium through the guidewire inserted into the right ventricle to induce VF. Mechanical ventilation was stopped, and the induced current was maintained for 8 minutes after the onset of VF. After 8 minutes of untreated VF, CPR (chest compression of 250 beats/minute, with adjustment of chest compression depth by maintaining aortic pressure between 26 and 28 mmHg) and mechanical ventilation (100% oxygen, compression-to-ventilation ratio of 5:1) were started. After 2 minutes of CPR, 0.1 mL of epinephrine (0.1 mg/mL) was injected into the left femoral artery. After 4 minutes of CPR, a 3-J biphasic waveform shock was started at 60-second intervals until the heart rhythm returned to normal. CPR was declared a failure if the rat still had no ROSC after 10 minutes of CPR. After CPR, the rats in the experimental group were given an intraperitoneal injection of TMZ at 10 mg/kg, while the control group was given an intraperitoneal injection. After the ROSC, the oxygen concentration received by the animal through mechanical ventilation gradually decreased from 100% to 21% and was monitored for 3 hours.¹⁶ The ROSC was defined as an organized rhythm with an average aortic pressure of 60 mmHg lasting at least 10 minutes or longer.¹⁷

Serological testing

Whole blood (200 µL) was collected from rats via the retro-orbital plexuses into Eppendorf tubes containing ethylenediaminetetraacetic acid. The plasma was separated by centrifugation at 4,000 rpm for 15 minutes and stored at -80°C until assayed. The levels of cardiac troponin I (CTNI) were measured using the CTNI Assay Kit according to the manufacturer's instructions.

Echocardiography and hemodynamics

Transthoracic echocardiography (a Vevo 3100 Imaging System with an advanced ultra-high-frequency ultrasound) for small animal research was performed. Then, the left ventricular ejection fraction (EF) and fraction shortening (FS) of the left ventricle were measured. The mean values were obtained from at least three different cardiac cycles.

Targeted myocardial metabolomics analysis

Targeted metabolomics analysis based on the multiple reaction monitoring approach was performed to determine the number of myocardial metabolites. The analysis of targeted energy and glucose metabolism markers was performed by Shanghai Applied Protein Technology Co. Ltd. Briefly, 40 mg

Main points

- Impaired energy metabolism was closely related to myocardial damage after cardiopulmonary resuscitation (CPR).
- Abnormal glycolysis is an important manifestation of myocardial damage after CPR.
- (¹⁸F)-fluoro-D-glucose positron emission tomography/computed tomography can be used to evaluate myocardial damage after CPR by monitoring abnormal glucose metabolism.

of cardiac tissue was preconditioned with 2000 μL of cool ultrapure water for multi-pass homogenization. Then, 800 μL of pre-cooled methanol/acetonitrile (1:1, v/v) was added, and the mixture was sonicated in an ice bath for 30 minutes and incubated for 1 hour at -20°C to precipitate the proteins. The samples were subsequently centrifuged at 14,000 rcf for 20 minutes at 4°C , and the supernatants were collected. Finally, the analysis of supernatants was performed on an Agilent 1290 Infinity LC system coupled with an AB 5500 QTRAP mass spectrometer in the negative ion mode, followed by the identification and quantification of targeted metabolites, including adenosine triphosphate (ATP), lactate, phosphoenolpyruvate (PEP), 3-phospho-D-glycerate, pyruvate, succinate, citrate, and alpha-ketoglutarate (AKG).

PET imaging

A special micro-PET/CT scanner (United Image Inc., Shanghai, China) was used for this experiment. To further explore the role of myocardial energy metabolism in the heart after CPR, the authors performed dynamic (^{18}F)-FDG PET imaging in 40 rats. The animals had fasted for 12 hours before the experiment, but they could drink water freely, and each rat was fed separately to avoid eating each other's food. Fasting blood glucose was measured in all rats via the tail vein before imaging, and the fasting blood glucose was in the range of 140–160 mg/dL. All experimental animals were administered (^{18}F)-FDG (4.63 MBq) intravenously. PET imaging of anesthetized rats (sodium pentobarbital, 45 mg/kg) was performed using a micro-PET/CT hybrid scanner. All PET images were reconstructed using two iterations of the three-dimensional ordered subset expectation-maximization algorithm (12 subsets) and 18 iterations of the accelerated version of 3D-MAP (i.e., FASTMAP), with a matrix size of $128 \times 128 \times 159$. Attenuation correction was applied to datasets from CT images acquired just before each PET scan. No partial volume corrections were performed. Dynamic PET scans were acquired in list mode format over 90 minutes, starting just prior to the radiotracer injection. The resulting data were sorted into 0.5-mm sinogram bins and 19-time frames for image reconstruction (4×15 s, 4×60 s, 11×300 s). For subsequent studies, static PET scans (10 minutes) were acquired at ~ 70 minutes after injection of the radiotracer. PET images were analyzed by a PET radiologist and senior PET technologist with >5 years of experience in quantifying pulmonary (^{18}F)-FDG uptake.

Statistical analysis

IBM SPSS statistics 19.0 software (SPSS Inc., Chicago, IL, USA) was used to analyze the data. The Kolmogorov–Smirnov test was used to determine whether the data conformed to a normal distribution. Numerical variables with a normal distribution were represented as mean \pm standard deviation values and categorical variables as numbers (n). A One-Way ANOVA was performed to compare more than two groups. The unpaired two-sample t-test was used for a two-group comparison. Statistical significance was defined as a two-tailed value of $P < 0.05$.

Results

The myocardial injury markers, intermediary carbohydrate metabolites of glycolysis, key intermediate products of glucose oxidation, SUVs, and cardiac dysfunction parameters of the sham, CPR, and CPR + TMZ groups are presented in Table 1. To explore the effect of energy metabolism on the heart after CPR, the authors first successfully established a rat CPR model. The serological test results showed that compared with that in the sham group, the expression of CTNI in the serum of animals after CPR increased significantly ($P = 0.014$, Figure 1a). Echocardiography and hemodynamic measurements showed that CPR treatment induced lower EF% and FS% than sham treatment ($P = 0.000$, Figure

1c, d). Meanwhile, the level of the energy metabolism marker ATP was remarkably downregulated in the hearts of animals after CPR for 6 hours ($P = 0.01$, Figure 1b). The level of total ATP was remarkably upregulated in the hearts of TMZ + CPR rats compared with CPR rats ($P = 0.034$, Figure 1b). Interestingly, with the increase in total ATP expression level, the tail venous blood of all rats was collected for testing, and the results showed that the CTNI level was significantly attenuated in the hearts of TMZ + CPR rats ($P = 0.021$, Figure 1a). In addition, echocardiography and hemodynamic measurements revealed that after CPR with TMZ the animals treated had higher EF% ($P = 0.065$, Figure 1c) and FS% ($P = 0.165$, Figure 1d) than those of CPR rats for 6 hours. It could be observed from the figure (Figures 1c, d) that EF% and FS% in the CPR + TMZ group were higher than the CPR group for 6 hours, but the difference was not significant after statistical analysis. This unsatisfactory result might be due to the small sample size and the short observation time. Because echocardiography and hemodynamic measurements revealed that after CPR with TMZ the rats had remarkably higher EF% ($P = 0.026$, Figure 1c) and FS% ($P = 0.014$, Figure 1d) than the rats treated only with CPR for 24 hours. These data showed that energy metabolism was an essential factor in myocardial damage and cardiac function in the heart after CPR.

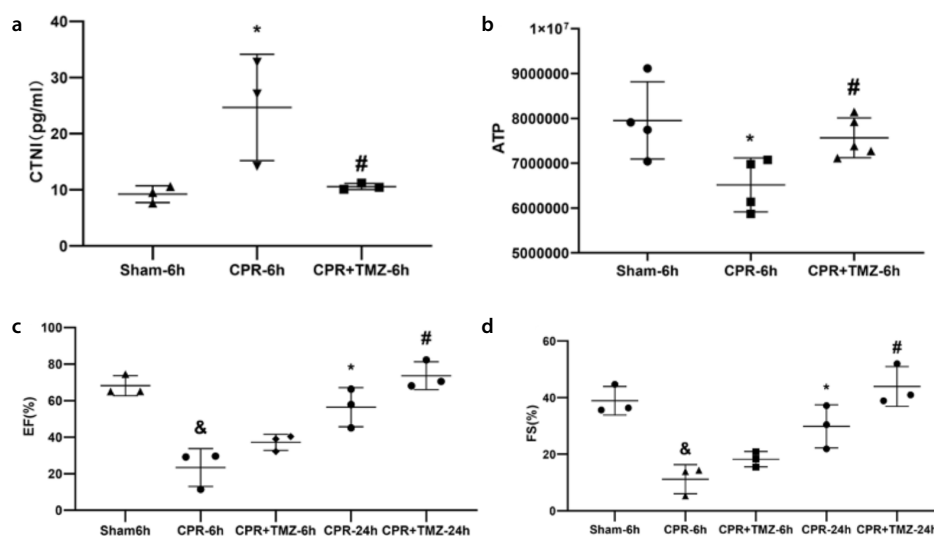


Figure 1. (a–d) Energy production and function are significantly impaired in the heart after cardiopulmonary resuscitation (CPR). (a) Expression levels of cardiac troponin I in the hearts of wild-type rats was detected with Assay Kit I after sham, CPR, and trimetazidine (TMZ) + CPR treatment for 6 hours ($n = 4$ –5 rats per experimental group, $\#P < 0.05$ vs. CPR 6 hours); (b) the results of the multiple reaction monitoring approach showed the levels of energy metabolism marker adenosine triphosphate in wild-type rats after TMZ + CPR, CPR, and sham treatment for 6 hours ($n = 4$ –5 rats per experimental group, $\#P < 0.05$ vs. CPR 6 hours); (c, d) Statistical results for the parameters of the echocardiographic results, including ejection fraction and fraction shortening in wild-type rats after sham surgery, CPR, and TMZ + CPR for 6 or 24 hours ($n = 3$ rats per experimental group, $\#P < 0.05$ vs. CPR 24 hours).

Abnormal glycolysis is an important manifestation of myocardial damage after CPR.

After CPR, targeted metabolomics analysis results showed that the expression of PEP ($P = 0.014$, Figure 2a) and 3-phospho-D-glycerate ($P = 0.000$, Figure 2b) were significantly upregulated in myocardial tissue after CPR for 6 hours. And the lactate/pyruvate ratio also increased ($P = 0.000$, Figure 2c). The expression of AKG was significantly downregulated ($P = 0.034$, Figure 2d). In addition, the expression of succinate ($P = 0.009$, Figure 2e) and citrate ($P = 0.003$, Figure 2f) were significantly upregulated in myocardial tissue after CPR for 6 hours. These data suggested that glucose metabolism was altered considerably, and the degree of aerobic glucose metabolism may be significantly reduced. Nevertheless, anaerobic glycolysis may be dramatically augmented in the myocardium after CPR. In addition, TMZ treatment significantly declined the levels of PEP ($P = 0.038$, Figure 2a) and 3-phospho-D-glycerate ($P = 0.005$, Figure 2b) in the hearts of rats after CPR for 6 hours. The expression of succinate ($P = 0.026$, Figure 2e) and citrate ($P = 0.002$, Figure 2f) were significantly decreased in TMZ-treated rats after CPR for 6 hours. And the expression of AKG was significantly upregulated ($P = 0.006$, Figure 2d). Moreover, the lactate/pyruvate ratio also decreased ($P = 0.026$, Figure 2c). Furthermore, the total ATP expression was significantly increased in the hearts of TMZ-treated rats compared with control rats ($P = 0.034$, Figure 1b). All results comprehensively prompted that aerobic glucose metabolism may be ameliorated, but anaerobic glycolysis may be diminished in the myocardium of TMZ-treated rats after CPR. With the improvement in glucose metabolism, energy production was significantly increased in the heart after CPR. Collectively, the glucose metabolism in the myocardium was very important to myocardial energy metabolism after CPR.

To further explore the effect of glucose metabolism on the heart after CPR, the authors measured the glucose uptake of the rat heart 6 hours after CPR by the (^{18}F) -FDG PET/CT non-invasive technique. (^{18}F) -FDG PET/CT imaging showed higher FDG uptake in the heart after CPR for 6 hours compared to that in sham hearts (Figure 3a). The results showed that the value of standardized uptake value (SUV) was dramatically higher in rats after CPR for 6 hours ($P = 0.000$, Figure 3b). On the contrary, (^{18}F) -FDG PET/CT data showed that TMZ-treated rats after CPR for 6 hours exhibited remarkably lower FDG uptake and SUV values ($P = 0.000$, Figure 3a and b).

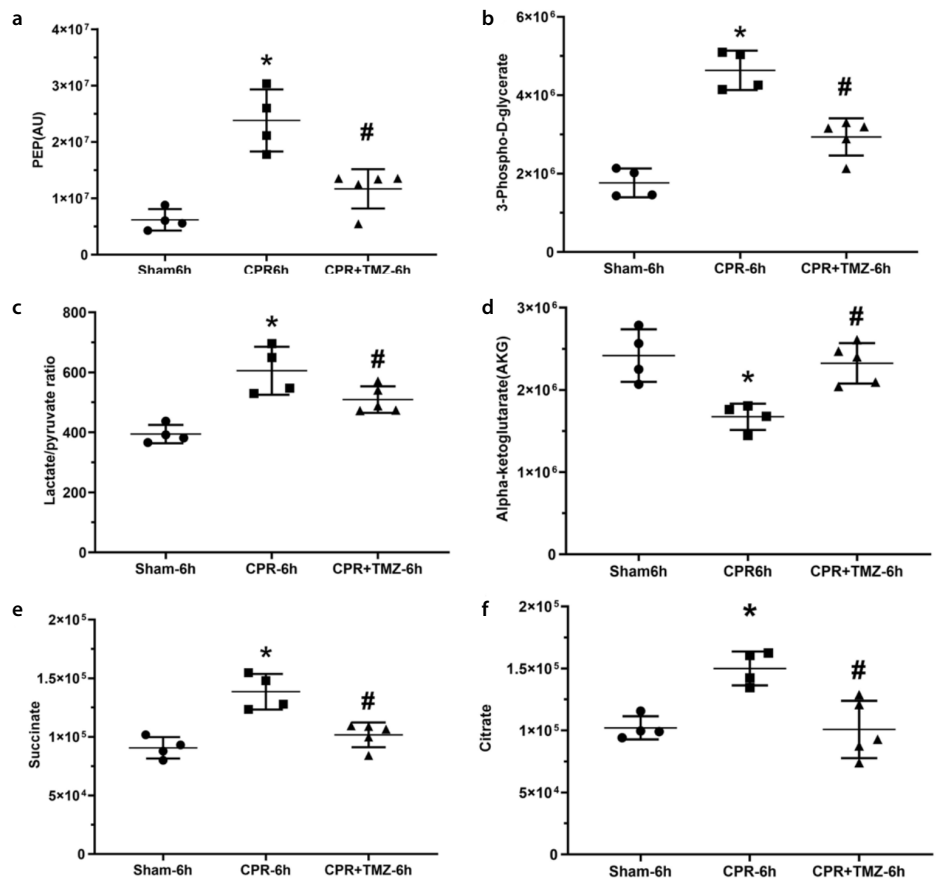


Figure 2. (a-f) Glucose uptake and abnormal glycolysis are significantly enhanced in the animal heart after cardiopulmonary resuscitation (CPR). (a, b) Expression levels of phosphoenolpyruvate and 3-phospho-D-glycerate were increased in the hearts of wild-type rats, detected with the multiple reaction monitoring (MRM) approach after sham, CPR, and trimetazidine (TMZ) + CPR surgery for 6 hours ($n = 4-5$ rats per experimental group, $\#P < 0.05$ vs. CPR 6 hours); (c) the lactate/pyruvate ratio was detected after sham, CPR, and TMZ + CPR surgery for 6 hours. ($n = 4-5$ rats per experimental group, $\#P < 0.05$ vs. CPR 6 hours); (d-f) The results of the MRM approach showed the expression of alpha-ketoglutarate, succinate, and citrate in Sprague-Dawley rats' hearts after sham, CPR, and TMZ + CPR treatment for 6 hours. ($n = 4-5$ rats per experimental group, $\#P < 0.05$ vs. CPR 6 hours).

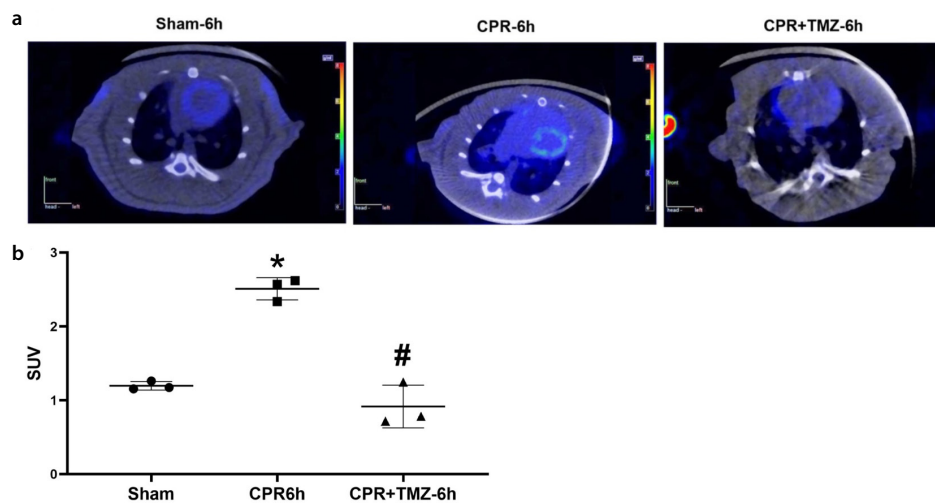


Figure 3. (a, b) (^{18}F) -fluoro-D-glucose (FDG) positron emission tomography/computed tomography [(^{18}F) -FDG PET/CT] can monitor the changes in cardiac function and myocardial energy metabolism after cardiopulmonary resuscitation (CPR) by tracking glucose metabolism. (a) (^{18}F) -FDG PET/CT imaging showed FDG uptake after sham, CPR, and trimetazidine (TMZ) + CPR treatment for 6 hours ($n = 3$ rats per experimental group, $\#P < 0.05$ vs. CPR 6 hours); (b) Statistical results for the value of standardized uptake value in the hearts of TMZ-treated wild-type rats after CPR or sham treatment for 6 hours ($n = 3$ rats per experimental group, $\#P < 0.05$ vs. CPR 6 hours).

Discussion

In this research, the authors' findings showed that the non-invasive (¹⁸F)-FDG PET/CT technology could predict early changes in myocardial damage and cardiac function by tracking glucose metabolism in the heart after CPR. In the initial stage of the experiment, the authors successfully established a rat CPR model and found that the total ATP decreased significantly in the heart after CPR. This finding suggested that myocardial energy metabolism was dysfunctional after CPR. Furthermore, myocardial damage was aggra-

vated, and heart function was significantly attenuated with decreased ATP expression levels. Subsequently, the authors tested the important intermediate products of aerobic oxidation and anaerobic glycolysis of glucose. As a result, it was found that the aerobic oxidation of glucose may be reduced, and anaerobic glycolysis may be significantly enhanced in the myocardium in the early stage of CPR. The authors used TMZ to increase the aerobic oxidation of glucose to further clarify the role of glucose metabolism in the myocardium after CPR. The results revealed that myocardial damage was also significantly re-

duced, and cardiac function was significantly improved with the significantly increased ATP levels. These data indicate that the functional status of the myocardium after CPR was closely related to glucose metabolism. Therefore, the authors successfully tracked the changes in glucose metabolism and cardiac function in the heart after CPR through the measurement of the myocardial glucose uptake rate and the SUV value by (¹⁸F)-FDG PET/CT.

In the past decades, many studies have shown that glucose and fatty acids are im-

Table 1. Comparison of the myocardial injury marker, intermediary carbohydrate metabolites of glycolysis, key intermediate products of glucose oxidation, SUVs, and cardiac dysfunction between the groups

| Variable | Groups | | | P | | |
|---|-----------------------------|--------------------------------|--------------------------------------|---|---------------------------------------|--|
| Myocardial injury marker | Sham (Mean ± SD) | CPR 6 h (Mean ± SD) | CPR + TMZ 6 h (Mean ± SD) | | | |
| CTNI | 9.25 ± 1.49 | 24.69 ± 9.49 | 10.59 ± 0.55 | Sham vs. CPR 6 h, 0.014 CPR 6 h vs. CPR + TMZ 6 h, 0.021 | | |
| The intermediary carbohydrate metabolites of glycolysis | | | | | | |
| PEP | 6180136.89 ± 1903793.06 | 23823999.4 ± 5506351.51 | 11686084.23 ± 3499530.67 | Sham vs. CPR 6 h, 0.014 CPR 6 h vs. CPR + TMZ 6 h, 0.038 | | |
| 3-phospho-D-glycerate | 1763595.05 ± 267659.74 | 4636341.47 ± 502118.8 | 2937035.57 ± 474740.75 | Sham vs. CPR 6 h, 0.000 CPR 6 h vs. CPR + TMZ 6 h, 0.005 | | |
| Lactate/pyruvate ratio | 394.19 ± 30.62 | 605.2 ± 80.13 | 509.18 ± 44.22 | Sham vs. CPR 6 h, 0.000 CPR 6 h vs. CPR + TMZ 6 h, 0.026 | | |
| The key intermediate products of glucose oxidation | | | | | | |
| AKG | 2418330.11 ± 319828.6 | 1673549.55 ± 160275.97 | 2324160.51 ± 245632.42 | Sham vs. CPR 6 h, 0.034 CPR 6 h vs. CPR + TMZ 6 h, 0.006 | | |
| Citrate | 102137.4 ± 9345.74 | 150015.51 ± 13696.5 | 100833 ± 23156.7 | Sham vs. CPR 6 h, 0.003 CPR 6 h vs. CPR + TMZ 6 h, 0.002 | | |
| Succinate | 90700.06 ± 9145.65 | 138561.3 ± 15226.47 | 101777.62 ± 10572.9 | Sham vs. CPR 6 h, 0.009 CPR 6 h vs. CPR + TMZ 6 h, 0.026 | | |
| Energy marker | | | | | | |
| The total ATP | 7953685.05 ± 861412.36 | 6515711.65 ± 600582.21 | 7566185.2 ± 444470.3 | Sham vs. CPR 6 h, 0.001 CPR 6 h vs. CPR + TMZ 6 h, 0.034 | | |
| (¹⁸F)-FDG PET/CT | | | | | | |
| SUV | 1.20 ± 0.06 | 2.51 ± 0.15 | 0.92 ± 0.29 | Sham vs. CPR 6 h, 0.000 CPR 6 h vs. CPR + TMZ 6 h, 0.000 | | |
| Variable | Groups | | | | | |
| Cardiac dysfunction | Sham (Mean ± SD) | CPR 6 h (Mean ± SD) | CPR + TMZ 6 h (Mean ± SD) | CPR 24 h (Mean ± SD) | CPR + TMZ 24 h (Mean ± SD) | P |
| EF | 68.17 ± 5.49 | 23.39 ± 10.35 | 37.19 ± 4.37 | 56.39 ± 10.68 | 73.62 ± 7.6 | Sham vs. CPR 6 h, 0.000 CPR 24 h vs. CPR + TMZ 6 h, 0.026 |
| FS | 38.88 ± 5.04 | 11.15 ± 5.13 | 18.22 ± 2.71 | 29.83 ± 7.65 | 43.91 ± 7.02 | Sham vs. CPR 6 h, 0.000 CPR 24 h vs. CPR + TMZ 6 h, 0.014 |

TMZ, trimetazidine; SD, standard deviation; CTNI, cardiac troponin I; PEP, phosphoenolpyruvate; AKG, alpha-ketoglutarate; SUV, standardized uptake value; EF, ejection fraction; FS, fraction shortening; ATP, adenosine triphosphate; CPR, cardiopulmonary resuscitation; (¹⁸F)-FDG PET/CT, (¹⁸F)-fluoro-D-glucose positron emission tomography/computed tomography

portant energy substrates for myocardial metabolism. Sixty to seventy percent of the energy required for cardiac contraction in myocardial metabolism is mainly generated by the oxidative metabolism of fatty acids.^{7,18,19} The rest of the energy was mainly derived from the supply of aerobic oxidation of glucose. However, the effects of changes in glucose metabolism in the myocardium after CPR remains poorly understood. It is well known that the most important metabolism of glucose is the decomposition into PEP, 3-phospho-D-glycerate, and pyruvate through glycolysis. Then, under aerobic conditions, pyruvate enters the tricarboxylic acid cycle and gradually produces AKG, succinic acid, citrate, etc., producing more ATP in this process. Under anaerobic conditions, pyruvate enters the anaerobic glycolysis pathway to generate lactic acid and less ATP. Studies have also shown that the level of myocardial ATP is closely related to myocardial cell damage and has a positive correlation with myocardial contractile energy.²⁰ Various factors, such as myocardial ischemia-reperfusion injury caused by energy metabolism disorders after CPR, could lead to severe systolic dysfunction,^{21,22} and the severity of this injury directly determines the patient's prognosis.²³ Consistent with the results of these studies, the authors found that the lactate/pyruvate ratio was significantly increased; in contrast, the level of AKG was significantly downregulated, while succinate and citrate were considerably upregulated increased in myocardial tissue after CPR. The increase in succinate and citrate after CPR was also a manifestation of mitochondrial energy metabolism disorder. This disorder was related to the increase in reactive oxygen species generated from myocardial oxidative stress after CPR. This result showed that the role of anaerobic glycolysis in the energy supply of the myocardium might be greatly enhanced and the level of aerobic oxidation of glucose may be significantly reduced in the heart after CPR. The authors also found that PEP and 3-phospho-D-glycerate in the rat myocardium were significantly increased, indicating that glucose uptake in the myocardium was enhanced after CPR. Consistent with Liu et al.²⁴ research results, glucose uptake in myocardial ischemia and hypoxia was also ameliorated, even after the myocardial blood flow was restored. Although the authors test results showed that the total ATP level in the rat myocardium was significantly reduced compared to that in the sham group, myocardial glucose uptake was increased after CPR. This result suggested that the total energy supply to the myocardium was de-

creased, but the metabolism of glucose also underwent adaptive changes after CPR.

Interestingly, the myocardial injury marker CTNI was upregulated significantly, and the left ventricular function of the animal heart also deteriorated significantly with the downregulation in ATP. As mentioned above, myocardial damage and cardiac function changes were closely related to myocardial energy metabolism. After CPR, glucose metabolism in the myocardium also showed significant adaptive changes. These findings suggested that glucose metabolism might play an important role in CPR.

To further clarify the relationship between glucose metabolism and myocardial damage and cardiac function after CPR, TMZ, a regulator to improve the aerobic oxidation of myocardial glucose, was applied in this experiment.^{25,26} TMZ mainly optimized the oxygen utilization process in the cell mitochondrial matrix and inhibited 3-KAT function while enhancing the activity of pyruvate dehydrogenase to amplify the aerobic oxidation of glucose to ultimately optimize the energy supply of cardiomyocytes.²⁷⁻³⁰ The authors' research results showed that the expression levels of intermediates (AKG, succinate, and citrate) of the tricarboxylic acid cycle were very close to those of the sham group, and the anaerobic glycolysis marker (the ratio of lactic acid to pyruvate) was significantly decreased in the TMZ intervention group compared with the CPR group. And the expression of ATP in the TMZ + CPR group was significantly upregulated. Surprisingly, with the increase in ATP expression levels, myocardial damage and cardiac function were also significantly improved. There was a negative correlation between energy metabolism and myocardial injury. Hence, enhanced anaerobic glycolysis after CPR played a role in protecting the myocardium.

In addition, it was interesting that the authors' study revealed that the expression levels of PEP and 3-phospho-D-glycerate in the TMZ + CPR group were significantly lower than those in the CPR group. This result suggested that myocardial glucose uptake was reduced in the TMZ + CPR group. Hence, the authors found that the myocardial glucose uptake rate could be used to predict or assist in monitoring the changes in myocardial injury and cardiac function after CPR. Furthermore, the laboratory and cardiac ultrasound data collected in this study also supported this hypothesis.

The authors realized the importance of glucose metabolism to the myocardium af-

ter CPR through the above series of experiments. Then, the authors further explored the possibility of basic theoretical research that could be applied to the clinic. (¹⁸F)-FDG PET/CT technology was used to track the footprint of glucose metabolism in cardiomyocytes. (¹⁸F)-FDG is a radionuclide fluorine-labeled deoxyglucose that can track the initial processes involved in glucose metabolism, including glucose transmembrane transport and hexokinase-regulated phosphorylation in the heart.³¹ In myocardial cells, (¹⁸F)-FDG is phosphorylated into (¹⁸F)-FDG-6-phosphate, and the dephosphorylation process of FDG-6-phosphate is very slow. It does not easily pass through the cell membrane and is not further metabolized through glycogen synthesis and catabolism to stay in cardiomyocytes.¹³ Therefore, the glucose metabolism of the myocardium could be measured by FDG PET imaging. In the authors' experiment, the (¹⁸F)-FDG PET/CT results showed that the SUV value and FDG uptake after CPR were significantly higher than those of the control group. At the same time, the experimental group treated with TMZ had the opposite result.

In clinical diagnosis and treatment, the prognosis for patients after CPR is closely related to the location, scope, and degree of myocardial injury. The traditional blood test is affected by many factors and can only evaluate the degree of myocardial injury, while the location and scope of myocardial injury cannot be accurately evaluated. (¹⁸F)-FDG PET/CT a non-invasive technology, can directly determine the location and scope of myocardial injury by monitoring glucose metabolism changes in the myocardium to more accurately evaluate the prognosis and risk of patients after CPR. It is also possible that the changes in myocardial metabolism may be earlier than the abnormalities of myocardial blood perfusion. In this case, an earlier warning can be achieved through (¹⁸F)-FDG PET/CT technology before traditional examinations find myocardial damage and changes in cardiac function, thereby enabling early treatment and possibly improving prognosis.

There were some limitations to the authors' study. First, the myocardial glucose uptake can be affected by the levels of insulin, fatty acids, and other substances. Any follow-up study needs to increase the number of samples and evaluate the factors affecting the (¹⁸F)-FDG uptake. Second, there was a certain proportion of CPR patients with diabetes. Such samples were not included in this study. Follow-up studies are needed to establish a CPR model with diabetes and

analyze the myocardial (¹⁸F)-FDG uptake of diabetes patients. Last, most medical institutions do not have the conditions for PET/CT. Therefore, the authors can explore the relationship between magnetic resonance imaging or Doppler echocardiography and myocardial energy metabolism.

In conclusion, the present study confirms that anaerobic glycolysis acted as a protector in the heart after CPR, and the improvement in aerobic metabolism of glucose could attenuate myocardial damage after CPR. Glucose metabolism plays an important role in myocardial tissue repair after CPR. As a non-invasive imaging technique, (¹⁸F)-FDG PET/CT can track the footprint of glucose metabolism to evaluate the functional status of cardiomyocytes after CPR, which helps to better guide clinical treatment and prognostic evaluation.

Conflict of interest disclosure

The authors declared no conflicts of interest.

Funding



National Natural Science Youth Foundation of China (no: 81701871).

References

- Mehaffey JH, Money D, Charles EJ, et al. Adenosine 2A receptor activation attenuates ischemia reperfusion injury during extracorporeal cardiopulmonary resuscitation. *Ann Surg.* 2019;269(6):1176-1183. [\[CrossRef\]](#)
- Matsuura TR, Bartos JA, Tsangaris A, et al. Early effects of prolonged cardiac arrest and ischemic postconditioning during cardiopulmonary resuscitation on cardiac and brain mitochondrial function in pigs. *Resuscitation.* 2017;116:8-15. [\[CrossRef\]](#)
- Zhang Y, Song Y, Shu T, Liang L, Shao W, Guo L, Sun P. Ultrasound improves the outcomes of cardiopulmonary resuscitation in rats by stimulating the cholinergic anti-inflammatory pathway. *Mol Med Rep.* 2019;20(3):2675-2684. [\[CrossRef\]](#)
- Ulmer BM, Stoehr A, Schulze ML, et al. Contractile work contributes to maturation of energy metabolism in hiPSC-derived cardiomyocytes. *Stem Cell Reports.* 2018;10(3):834-847. [\[CrossRef\]](#)
- Ulmer BM, Eschenhagen T. Human pluripotent stem cell-derived cardiomyocytes for studying energy metabolism. *Biochim Biophys Acta Mol Cell Res.* 2020;1867(3):118471. [\[CrossRef\]](#)
- Piquereau J, Ventura-Clapier R. Maturation of cardiac energy metabolism during perinatal development. *Front Physiol.* 2018;9:959. [\[CrossRef\]](#)
- Heather LC, Howell NJ, Emmanuel Y, Cole MA, Frenneaux MP, Pagano D, Clarke K. Changes in cardiac substrate transporters and metabolic proteins mirror the metabolic shift in patients with aortic stenosis. *PLoS One.* 2011;6(10):e26326. [\[CrossRef\]](#)
- Tran DH, Wang ZV. Glucose metabolism in cardiac hypertrophy and heart failure. *J Am Heart Assoc.* 2019;8(12):e012673. [\[CrossRef\]](#)
- Hackenhaar FS, Medeiros TM, Heemann FM, et al. Therapeutic hypothermia reduces oxidative damage and alters antioxidant defenses after cardiac arrest. *Oxid Med Cell Longev.* 2017;2017:8704352. [\[CrossRef\]](#)
- Tournier N, Saba W, Goutal S, et al. Influence of P-glycoprotein inhibition or deficiency at the blood-brain barrier on (18)F-2-fluoro-2-deoxy-D-glucose ((18)F-FDG) brain kinetics. *AAPS J.* 2015;17(3):652-659. [\[CrossRef\]](#)
- Dou KF, Gao XJ, Xie BQ, Li Y, He ZX, Yang MF. Dual-time-point myocardial 18F-FDG imaging in the detection of coronary artery disease. *BMC Cardiovasc Disord.* 2017;17(1):120. [\[CrossRef\]](#)
- Rahman WT, Wale DJ, Viglianti BL, et al. The impact of infection and inflammation in oncologic 18F-FDG PET/CT imaging. *Biomed Pharmacother.* 2019;117:109168. [\[CrossRef\]](#)
- Skali H, Schulman AR, Dorbala S. 18F-FDG PET/CT for the assessment of myocardial sarcoidosis. *Curr Cardiol Rep.* 2013;15(4):352. [\[CrossRef\]](#)
- Chung YH, Lu KY, Chiu SC, et al. early imaging biomarker of myocardial glucose adaptations in high-fat-diet-induced insulin resistance model by using 18F-FDG PET and [U-13C]glucose nuclear magnetic resonance tracer. *Contrast Media Mol Imaging.* 2018;2018:8751267. [\[CrossRef\]](#)
- Wang P, Yao L, Zhou LL, et al. Carbon monoxide improves neurologic outcomes by mitochondrial biogenesis after global cerebral ischemia induced by cardiac arrest in rats. *Int J Biol Sci.* 2016;12(8):1000-1009. [\[CrossRef\]](#)
- Fu ZY, Wu ZJ, Zheng JH, Qin T, Yang YG, Chen MH. The incidence of acute kidney injury following cardiac arrest and cardiopulmonary resuscitation in a rat model. *Ren Fail.* 2019;41(1):278-283. [\[CrossRef\]](#)
- Schroeder DC, Maul AC, Mahabir E, et al. Evaluation of small intestinal damage in a rat model of 6 Minutes cardiac arrest. *BMC Anesthesiol.* 2018;18(1):61. [\[CrossRef\]](#)
- Carolo dos Santos K, Pereira Braga C, Octavio Barbanera P, Seiva FR, Fernandes Junior A, Fernandes AA. Cardiac energy metabolism and oxidative stress biomarkers in diabetic rat treated with resveratrol. *PLoS One.* 2014;9(7):e102775. [\[CrossRef\]](#)
- Li F, Li J, Li S, Guo S, Li P. Modulatory effects of chinese herbal medicines on energy metabolism in ischemic heart diseases. *Front Pharmacol.* 2020;11:995. [\[CrossRef\]](#)
- Mijailovich SM, Nedic D, Svicevic M, et al. Modeling the actin.myosin ATPase cross-bridge cycle for skeletal and cardiac muscle myosin isoforms. *Biophys J.* 2017;112(5):984-996. [\[CrossRef\]](#)
- Anderson RJ, Jinadasa SP, Hsu L, et al. Shock subtypes by left ventricular ejection fraction following out-of-hospital cardiac arrest. *Crit Care.* 2018;22(1):162. [\[CrossRef\]](#)
- Yang CF. Clinical manifestations and basic mechanisms of myocardial ischemia/reperfusion injury. *Ci Ji Yi Xue Za Zhi.* 2018;30(4):209-215. [\[CrossRef\]](#)
- Zhao ZG, Tang ZZ, Zhang WK, Li JG. Protective effects of embelin on myocardial ischemia-reperfusion injury following cardiac arrest in a rabbit model. *Inflammation.* 2015;38(2):527-533. [\[CrossRef\]](#)
- Liu Z, Chen JM, Huang H, et al. The protective effect of trimetazidine on myocardial ischemia/reperfusion injury through activating AMPK and ERK signaling pathway. *Metabolism.* 2016;65(3):122-130. [\[CrossRef\]](#)
- Dehina L, Vaillant F, Tabib A, et al. Trimetazidine demonstrated cardioprotective effects through mitochondrial pathway in a model of acute coronary ischemia. *Naunyn Schmiedebergs Arch Pharmacol.* 2013;386(3):205-215. [\[CrossRef\]](#)
- Chrusciel P, Rysz J, Banach M. Defining the role of trimetazidine in the treatment of cardiovascular disorders: some insights on its role in heart failure and peripheral artery disease. *Drugs.* 2014;74(9):971-980. [\[CrossRef\]](#)
- Kantor PF, Lucien A, Kozak R, Lopaschuk GD. The antianginal drug trimetazidine shifts cardiac energy metabolism from fatty acid oxidation to glucose oxidation by inhibiting mitochondrial long-chain 3-ketoacyl coenzyme A thiolase. *Circ Res.* 2000;86(5):580-588. [\[CrossRef\]](#)
- Fragasso G, Spoladore R, Cuko A, Pallosi A. Modulation of fatty acids oxidation in heart failure by selective pharmacological inhibition of 3-ketoacyl coenzyme-A thiolase. *Curr Clin Pharmacol.* 2007;2(3):190-196. [\[CrossRef\]](#)
- Jain D, He ZX, Lele V, Aronow WS. Direct myocardial ischemia imaging: a new cardiovascular nuclear imaging paradigm. *Clin Cardiol.* 2015;38(2):124-130. [\[CrossRef\]](#)
- Ramezani-Aliakbari F, Badavi M, Dianat M, Mard SA, Ahangarpour A. The effects of trimetazidine on QT-interval prolongation and cardiac hypertrophy in diabetic rats. *Arq Bras Cardiol.* 2019;112(2):173-178. [\[CrossRef\]](#)
- Daly KP, Dearling JL, Seto T, Dunning P, Fahey F, Packard AB, Briscoe DM. Use of [18F]FDG positron emission tomography to monitor the development of cardiac allograft rejection. *Transplantation.* 2015;99(9):e132-e139. [\[CrossRef\]](#)



The effect of breast shielding outside the field of view on breast entrance surface dose in axial X-ray examinations: a phantom study

Lauren Hurley* 
 Yazeed Alashban 
 Salman Albeshan* 
 Andrew England 
 Mark F. McEntee 

*First joint author

PURPOSE

The purpose of this study was to evaluate the effect of outside-field-of-view (FOV) lead shielding on the entrance surface dose (ESD) of the breast on an anthropomorphic X-ray phantom for a variety of axial skeleton X-ray examinations.

METHODS

Using an anthropomorphic phantom and radiation dosimeter, the ESD of the breast was measured with and without outside-FOV shielding in anterior-posterior (AP) abdomen, AP cervical spine, occipitontental 30° (OM30) facial bones, AP lumbar spine, and lateral lumbar spine radiography. The effect of several exposure parameters, including a low milliamperere-seconds technique, grid use, automatic exposure control use, wraparound lead (WAL) use, trolley use, and X-ray table use, on the ESD of the breast with and without outside-FOV shielding was investigated. The mean ESD (μSv) and standard deviation for each radiographic protocol were calculated. A one-tailed Student's t-test was carried out to evaluate whether ESD to the breast was reduced with the use of outside-FOV shielding.

RESULTS

A total of 920 breast ESD measurements were recorded across the different protocol parameters. The largest decrease in mean ESD of the breast with outside-FOV shielding was $0.002 \mu\text{Sv}$ ($P = 0.084$), recorded in the AP abdomen on the table with a grid, OM30 on the table with a grid, OM30 standard protocol on the trolley, and OM30 on the trolley with WAL protocols. This decrease was found to be statistically non-significant.

CONCLUSION

This study found no significant decrease in the ESD of the breast with the use of outside-FOV shielding for the AP abdomen, AP cervical spine, OM30 facial bones, AP lumbar spine, or lateral lumbar spine radiography across a range of protocols.

KEYWORDS

Field of view, shielding, entrance surface dose, anthropomorphic phantom, wraparound lead, radiography

From the Department of Medical Imaging and Radiation Therapy (L.H., A.E., M.F.E.), University College Cork, School of Medicine, Brookfield Health Sciences, Munster, Ireland; Department of Radiological Sciences (Y.A., S.A. [✉ salbeshan@ksu.edu.sa](mailto:salbeshan@ksu.edu.sa)), King Saud University, College of Applied Medical Sciences, Riyadh, Saudi Arabia.

Received 20 January 2023; revision requested 06 March 2023; accepted 03 April 2023.



Epub: 02.05.2023

Publication date: 30.05.2023

DOI: 10.4274/dir.2023.232126

Protection and optimization of patient radiation doses are key principles in the safe practice of diagnostic radiography.¹ Ionizing radiation can result in deterministic or stochastic effects on biological tissue,² and radiation protection serves to eliminate or reduce deterministic effects and render the probability of stochastic effects as low as possible.³ Lead shielding has been used as a radiation protection tool since low levels of diagnostic radiation became implicated in late radiation responses approximately 80 years ago.⁴ Lead (or equivalent) shielding is a radiation protection apparatus that can be directly applied to the patient either inside the field of view (FOV) to reduce the radiation dose to radiosensitive organs, or outside the FOV to protect the patient against scattered radiation. Despite this, several radiation advisory bodies have recently published position statements advocating the curtailment

You may cite this article as: Hurley L, Alashban Y, Albeshan S, England A, McEntee MF. The effect of breast shielding outside the field of view on breast entrance surface dose in axial X-ray examinations: a phantom study. *Diagn Interv Radiol.* 2023;29(3):555-560.

of the practice of using lead protection in diagnostic imaging.⁵⁻⁷

The “as low as reasonably practical (ALARP)” principle is based on the optimization of patient radiation dose by balancing the benefit with the risk of the dose applied to obtain a diagnostically acceptable image.⁸ Factors that can be considered when applying the ALARP principle include decreasing exposure time, increasing the distance between the source and object, and the use of shielding.⁸ The ALARP principle can be applied to both primary and secondary radiation. The radiation dose in the primary beam is relatively high, 2% of which is directly absorbed by the patient.⁹ It has been suggested that lead shielding within the primary beam may increase the patient radiation dose in some instances by interfering with the automatic exposure control (AEC) and by misplacement or movement that may obscure pathology, potentially leading to overexposure and repeat exposures.^{5,10-12} However, this current study focuses on secondary radiation and so these factors were not of concern.

Secondary radiation originates from the attenuation of primary radiation, including scatter and extra-focal radiation.¹³ Lead shielding outside the FOV has been advocated by many studies, with scatter radiation reduced by more than 20% when lead shielding was used in mobile pediatric chest radiographs and breast dose reduced up to 80% by breast shielding in anterior-posterior (AP) and lateral lumbar spine X-ray projections.^{14,15} While the later study included 100 patients and 40 phantom measurements, only five pediatric patients were included in the former study, possibly limiting its generalizability. The International Commission of Radiological Protection (ICRP) is of the consensus that shielding more than 5 cm from the primary beam has a negligible effect on additional patient dose from secondary

radiation.¹⁶ Furthermore, for the anatomy outside the FOV, radiation exposure results largely from internal scattering, which lead shielding cannot protect against.¹⁶ The British Institute of Radiology has reported that scattered radiation in projection radiography often amounts to no more than 0.2% of overall patient radiation dose.⁵ This has led to the argument that radiographers should focus on the main source of patient radiation dose—the primary beam—by improving collimation, increasing the distance, and individualizing doses by using the AEC.

Breast tissue and the gonads have a tissue weighting (wT) factor of 0.12 and 0.08, respectively, meaning that the relative risk of stochastic effects occurring in the breast is relatively high.¹⁷ The linear threshold model is used to estimate the risk from low-dose radiation exposure, which is endorsed by the United States National Academy of Sciences and the ICRP. According to this model, even the smallest dose of radiation can increase the risk of harmful effects proportionally, and there is no safe level of exposure.¹⁸ In a laboratory setting, it was found that the number of double-strand breaks increased linearly with doses ranging from 1 mGy to 1 Gy in cultured cells.¹⁸ Another investigation reported that exposure to a chest X-ray increases the risk of breast cancer by a factor of two, irrespective of age, at first exposure and by up to five times when carrying three or more rare variants in a deoxyribonucleic acid (DNA) repair gene.¹⁹ However, it is probable that the tissue and cellular response to radiation, including damage and repair, is influenced by specific trigger thresholds, hormesis, and hypersensitivity of a particular tissue.¹⁸ Both studies indicated that further research is required to identify subpopulations that are vulnerable to ionizing radiation, which in turn would be useful in a clinical setting.

When considering the radiosensitivity of breast tissue, the well-known breast cancer-carrying gene (BRCA1) and breast cancer gene 2 (BRCA2) mutations put some individuals, particularly those exposed before the age of 30 years, at an increased risk of breast cancer development from diagnostic levels of radiation.²⁰ Due to the generation of an abnormal protein in individuals carrying a BRCA1 or BRCA2 gene mutation, they may not be able to fix this DNA damage, with 72% of BRCA1 and 50% of BRCA2 healthy mutation carriers displaying a radiosensitive phenotype.^{21,22} A cohort study of 1,601 women carrying BRCA1 and BRCA2 mutations reported an association between increased risk of breast cancer and exposure to chest

X-rays [hazard ratio (HR): 1.54; $P = 0.007$]. This risk was higher in women aged 40 years and younger (HR: 1.97; $P < 0.001$).²³

Although the cancer risk of any tissue reduces significantly with increased age, it should be noted that a single dose of 0.1 Gy results in approximately 914 cases and 70 cases of breast cancer per 100,000 when exposed at 5 years and 50 years, respectively.²⁴ Outside-FOV breast shielding in AP cervical spine radiography was shown to reduce breast dose by 99.9% in a phantom study.²⁵ Additionally, Foley et al.²⁶ demonstrated that breast displacement combined with lead shielding outside the FOV in computed tomography (CT) angiography reduced breast dose by 36%. However, a 23% reduction may be a result of displacement alone, with no data reported for shielding alone.²⁶ It has been suggested that with the advancement in radiographic technology in the past 70 years, fixed exposure systems have turned into modern, efficient direct digital systems that can use the AEC to control exposure level.^{27,28} This has resulted in a substantial decrease in entrance doses, from 12 mGy in the 1950s to now below 1 mGy.⁵ Therefore, it has been questioned whether other mechanisms of dose optimization such as primary beam collimation and AEC use are more important.^{5,6}

It has been reported that overall patient radiation dose for a standard AP pelvis radiograph has reduced by a factor of 60 between 1900 and 2012.^{5,29-31} However, the number of diagnostic imaging examinations patients undergo has increased, leading to an increased cumulative dose with two patients per 1,000 receiving a cumulative effective dose greater than 100 mSv in a 5-year period being reported in an international study on CT examinations.³² Therefore, despite the dose reduction for individual examinations, cumulative doses are increasing. As a result, low doses of scattered radiation outside the FOV are also increasing, contributing to the argument that outside-FOV lead shielding should still be considered in radiographic examinations, particularly for those known to be sensitive to radiation such as children and those with BRCA1/2 mutations. Currently, the state of practice concerning the use of lead shielding differs throughout Europe, individual countries, and local departments. Due to recent publications, many radiographers are opting to use or not use lead shielding in X-ray examinations,^{5,6} and this inconsistency has the potential to create confusion and patient fear in a radiographer's practice. It is generally agreed that a united,

Main points

- The largest decrease in mean entrance surface dose (ESD) of the breast with outside-field of view (FOV) shielding was 0.002 μ Sv ($P = 0.084$).
- This phantom-based study suggests that outside-FOV lead shielding of the breast does not significantly reduce ESD to the breast in anterior-posterior (AP) abdomen, AP cervical spine, occipitontal 30° facial bone, AP lumbar spine, and lateral lumbar spine radiography.
- Further studies are required to support the complete discontinuation of this radiation protection tool.

definitive statement from regulatory bodies throughout Europe regarding the use of lead shielding would be useful to limit confusion and differing practices by radiographers.³³

The current study aimed to investigate whether there is a reduction in the entrance surface dose (ESD) of the breast with the use of outside-FOV shielding for AP abdomen, AP cervical spine, occipitontal 30° (OM30) facial bones, AP lumbar spine, and lateral lumbar spine radiography across a range of parameters.

Methods

Experimental design

This study was conducted in the X-ray laboratory in the Assert Building at University College Cork (UCC). The approval of the UCC Ethics Committee was not required for this research. All experiments were conducted using the Carestream Health Inc. DRX-Evolution Plus X-ray unit and the DRX Plus 3543C detector. A dosimeter (Quarta, RADEX ONE) was used to obtain the ESD of the breast on a whole-body anthropomorphic X-ray phantom (PBU-50., Kyoto Kagaku) with dimensions of 165 cm and 50 kg. Detailed phantom information can be found in the reference section.³⁴ In the current experiment, the X-ray energy used in abdominal radiography was 75 kVp, lumbar spine and facial bone was 80 kVp, cervical spine was 70 kVp, and lateral lumbar spine was 90 kVp.

Quality control

Quality control tests on the lead shielding, X-ray tube output, and X-ray equipment were carried out before the study. The entire surface area of the lead shielding apron (0.35 mm Pb/150 kV) and the WAL (0.25 mm Pb/150 kV) were placed on the detector and screened, and no defects were detected. Tube output variability was assessed by securing the dosimeter to the breast region of the phantom 5 cm from the FOV, setting a fixed exposure, and irradiating the phantom 10 times. All QA tests fell within expected tolerances.

Pilot study

A pilot study was conducted to assess dosimeter placement stability, parameter selection, dosimeter reading variability, and phantom positioning issues. It was found that the dosimeter required fixation to the phantom. Dosimeter reading variability fell within acceptable tolerances. It was established that the variable parameters would include a low

milliamperes-seconds (mAs) technique and the use of a grid, AEC, WAL, a trolley, and an X-ray table. The phantom could not be supported when erect or on its side; therefore, all projections were conducted in the supine position.

Entrance surface dose measurements

The dosimeter was secured to the breast of the phantom in the midline. Outside-FOV shielding was placed on top of the dosimeter, or, in the case of WAL, wrapped around the phantom and dosimeter 5 cm or more from the FOV in all projections, as shown in Figure 1. The phantom underwent AP abdominal, AP cervical spine, OM30 facial bone, AP lumbar spine, and lateral lumbar spine radiography. A standard set of exposure parameters, adapted from Bontrager's Handbook of Radiographic Positioning and Techniques, were set for each projection.³⁵ Based on the standard, a low mAs technique and the use of a grid, AEC, combined grid and AEC, WAL, a trolley, and an X-ray table were explored for each projection. The phantom was exposed 10 times under each protocol, and the ESD of the breast and deviation index (DI) with and without outside-FOV shielding was recorded for each exposure.

Statistical analysis

The collected data underwent statistical analysis using Microsoft Excel 2019 (Microsoft Corp., Redmond, WA). The mean ESD of the breast with and without outside-FOV shielding for each projection was calculated. The standard deviation (SD) for each data set

was also computed. A one-tailed Student's t-test was conducted to determine whether a statistically significant difference was present between the ESD of the breast with and without outside-FOV shielding for each projection. Statistical significance was defined as $P < 0.05$.

Results

The ESD of the breast for each protocol with and without outside-FOV shielding was collected and expressed as the mean and SD. A paired one-tailed t-test revealed that the use of outside-FOV shielding was not found to significantly reduce the ESD of the breast when compared with no shielding for any X-ray projection or parameter ($P < 0.05$). The SD of the mean ESD was considered low for all protocols, at between 0–0.006 μSv . Many of the deviation indices indicated overexposure of the phantom. A summary of the mean ESD data can be found in Table 1. For AP abdominal radiography, the largest decrease (0.002 μSv) in mean ESD of the breast was observed in the grid X-ray table protocol ($P = 0.084$). In AP cervical spine radiography, the greatest reduction in mean ESD was reported in the AEC X-ray table, WAL X-ray table, and grid trolley protocols, with a decrease of 0.001 μSv ($P = 0.172$). For OM30 facial bone radiography, a 0.002 μSv decrease in mean ESD with the use of outside-FOV shielding was recorded in the grid X-ray table, standard trolley, and the WAL trolley protocols ($P = 0.084$). For the AP lumbar spine, the greatest reduction in mean ESD was 0.001 μSv , observed in the grid X-ray table, standard trolley, low mAs trolley, grid trolley, and WAL

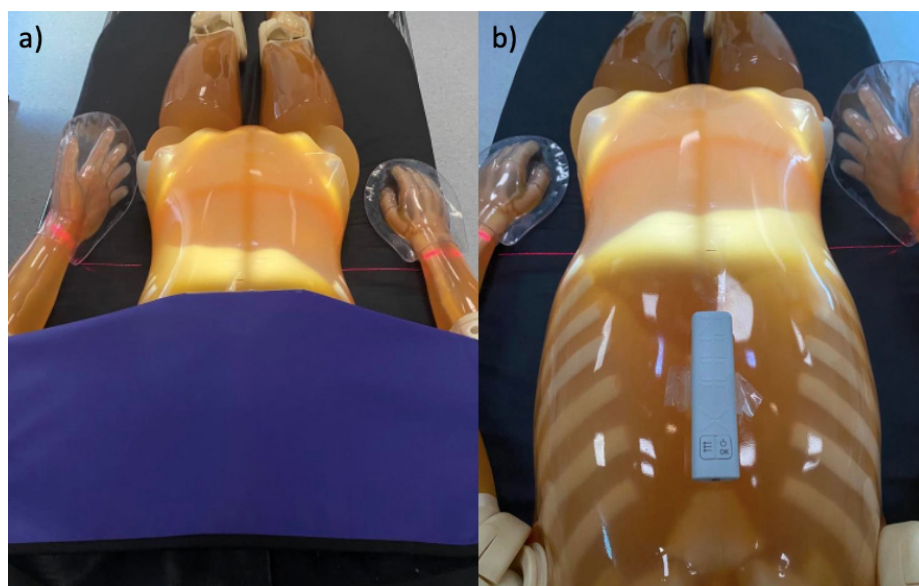


Figure 1. The anthropomorphic phantom displaying the dosimeter placement and collimation for anterior-posterior abdominal imaging (a) with the gonadal shield placed outside the field of view and (b) with no shielding.

Table 1. Summary of the data for each projection protocol

| Protocol | Lead | AP abdomen | Cervical spine | OM30 facial bones | AP lumbar spine | Lateral lumbar spine |
|-------------------------|------|------------|----------------|-------------------|-----------------|----------------------|
| Standard table | No | 0.031 | 0.021 | 0.031 | 0.030 | |
| | Yes | 0.030 | 0.021 | 0.030 | 0.031 | |
| Low mAs table | No | 0.022 | 0.016 | 0.021 | 0.021 | |
| | Yes | 0.021 | 0.016 | 0.020 | 0.021 | |
| Grid table | No | 0.032 | 0.021 | 0.032 | 0.031 | |
| | Yes | 0.030 | 0.021 | 0.030 | 0.030 | |
| AEC table | No | 0.004 | 0.006 | 0.009 | 0.003 | 0.010* |
| | Yes | 0.004 | 0.005 | 0.009 | 0.004 | 0.010* |
| Grid and AEC table | No | 0.012 | 0.009 | 0.029 | 0.010 | 0.024* |
| | Yes | 0.012 | 0.009 | 0.028 | 0.010 | 0.022* |
| Wraparound lead table | No | 0.031 | 0.021 | 0.031 | 0.030 | |
| | Yes | 0.030 | 0.020 | 0.030 | 0.031 | |
| Standard trolley | No | 0.032 | 0.021 | 0.032 | 0.032 | 0.056 |
| | Yes | 0.031 | 0.022 | 0.030 | 0.031 | 0.055 |
| Low mAs trolley | No | 0.022 | 0.016 | 0.021 | 0.023 | 0.046 |
| | Yes | 0.022 | 0.016 | 0.020 | 0.022 | 0.046 |
| Grid trolley | No | 0.031 | 0.022 | 0.031 | 0.032 | 0.055 |
| | Yes | 0.031 | 0.021 | 0.030 | 0.031 | 0.056 |
| Wraparound lead trolley | No | 0.032 | 0.021 | 0.032 | 0.032 | 0.056 |
| | Yes | 0.031 | 0.021 | 0.030 | 0.031 | 0.056 |

*Measurements were conducted on the trolley using the upright bucky. No data were found to be statistically significant ($P < 0.05$). AP, anterior-posterior; OM30, occipitomeatal 30°; mAs, milliamperere-seconds; AEC, automatic exposure control.

trolley protocols ($P = 0.172$). The trolley grid and AEC protocol demonstrated the greatest decrease in mean ESD of $0.002 \mu\text{Sv}$ for lateral lumbar spine radiography ($P = 0.222$).

Discussion

The use of outside-FOV shielding has long been employed as a radiation protection tool in diagnostic radiography.^{5,36} Numerous regulatory bodies have recently advocated the curtailment of its use, citing issues with efficacy, efficiency, patient comfort, and infection control.⁵⁻⁷ This phantom-based study set out to examine whether breast shielding outside the FOV for AP abdomen, AP cervical spine, OM30 facial bones, AP lumbar spine, and lateral lumbar spine radiography reduced the ESD of the breast.

In 2017, it was reported that radiology services in Ireland and internationally experience an annual 8%–10% increase in demand.³⁷ Although radiation doses for individual examinations have decreased dramatically in the last century due to the advent of modern technology, the population as a whole undergo more radiological examinations, thereby increasing an individ-

ual's cumulative radiation dose.^{38,39} Children are particularly at an increased risk of radiation-induced cancer development due to the increased rate at which their cells divide and their life expectancy post-exposure when compared to the adult population.^{40,41} Breast tissue is considered the most radiosensitive organ of the human body, with a wT of 0.12 reported by the ICRP 103.^{16,42} Ionizing radiation can lead to breaks in DNA, leading to cancer, thereby imposing an additional risk, on top of the intrinsic risk, of breast cancer development in individuals carrying *BRCA1/2* gene mutations.⁴³ Therefore, the importance of radiation protection and dose reduction to the breast in all patients, especially in children and *BRCA1/2* carriers, cannot be ignored.

However, the present study reports no significant reduction in the ESD of the breast with the use of outside-FOV shielding for AP abdomen, AP cervical spine, OM30 facial bones, AP lumbar spine, or lateral lumbar spine radiography across all examined protocols. The SD calculated for the protocols was considered acceptably low. Although the mean DI recorded in most protocols indicated overexposure, it must be considered that a

55 kg phantom may not accurately represent the DI recorded for a standard-sized adult patient under the same parameters. Multiple studies and radiation advisory boards report that the dose to organs outside the FOV is almost entirely from internal scatter generated within the patient, which lead shielding cannot protect against.^{5,6,16,44-47} This research supports the view that shielding anatomy outside the primary beam provides negligible additional radiation protection in terms of breast ESD to the patient. Therefore, this study recommends alternative methods of reducing patient radiation doses, such as primary beam collimation, increasing distance, and the use of the AEC or patient-adapted exposure factors.

Interestingly, a study that reported a 99.9% decrease in absorbed dose to the breast using outside-FOV shielding in AP cervical spine radiography utilized 2.5 mm Al filtration and 70 kVp.²⁵ The present study utilized no additional filtration with 70 kVp, implying that more scatter was generated per exposure in the current study. This suggests that beam filtration was not a contributing factor to breast ESD in the current study. Due to the differing conclusions and no definitive

reasons as to why this current study saw no significant reduction in ESD to the breast using outside-FOV shielding, one must also question if tube housing comes into play. This study utilized a Varex Imaging B-130H housing model type which has a permanent filtration of 0.7 mm Al/77 kV. This modern equipment may not be available due to a lack of resources in many parts of the world. Therefore, the relevance of this study's findings for worldwide consideration is questionable. Furthermore, many of the studies reporting a decrease in radiation dose with the use of outside-FOV shielding are almost a decade old and may not represent the most recent advancements in technology and its effect on patient radiation dose.^{14,15,26} One study has proposed that shielding outside the FOV may contribute to increased patient radiation dose as a result of shielding backscatter that reduces with distance from the primary beam.⁴⁴ In contrast, additional radiation dose due to the backscatter from lead shielding was not found in this study, as the addition of outside-FOV shielding or WAL did not significantly increase patient breast ESD for any protocol. However, it must be considered that in the present study, all shielding was placed 5 cm or more from the primary beam.

While the present study examined multiple parameters across 920 exposures, further studies could explore the effect of varying kVp, shielding placement 0–5 cm from the primary beam, and the effects of outside-FOV breast shielding on other organs such as the lungs. Furthermore, infection control, patient discomfort, and manual handling issues have been cited as reasons to abandon shielding use. The recent severe acute respiratory syndrome-coronavirus-2 pandemic has increased radiographer awareness and has shown that infection prevention and control measures can be achieved in a busy hospital environment. Despite this, Yu et al.⁴⁸ reported that the risk of infection due to outside-FOV lead shielding outweighed the 0.7% dose reduction it provided in pediatric chest CT examinations. Of note, this study only examined one phantom the size of a 5-year-old child, and the potential infection risk due to shielding contamination was not quantified. Additionally, an international survey found that lead shielding led to 25% of patients reporting discomfort due to shielding weight or position.⁴⁹ Undoubtedly, more studies are required in these areas. Finally, as breast shielding outside the FOV has the potential to induce a sense of security or imply that radiation doses outside the area of

interest are high, the psychological effects of breast shielding should also be explored.

Limitations to this research include sampling bias associated with the use of a 55 kg anthropomorphic phantom rather than human patients. Therefore, the results of this study may not accurately represent the X-ray attenuation and resulting ESD of the breast in patients of different weights (e.g., obese or pediatric patients) and densities (e.g., fibrous and glandular breast tissue). Future work should include a population study to validate or conflict with this study's findings. Furthermore, unlike a similar study, this study did not involve placing radiation dosimeters in the four quadrants of the breast.²⁶ Rather, the dosimeter was placed in the midline, at the level of the breasts. This may result in a loss of data regarding the ESD received in all regions of the breast. Additionally, only the ESD of the breast was measured. An organ dose measured by thermoluminescent dosimeters inside the phantom may provide greater insight into the effects of outside-FOV shielding of the breasts. Combined, these limitations may limit the generalizability to the human population.

In conclusion, this phantom-based study suggests that outside-FOV lead shielding of the breast does not significantly reduce ESD to the breast in AP abdomen, AP cervical spine, OM30 facial bone, AP lumbar spine, and lateral lumbar spine radiography. Further studies are required to support the complete discontinuation of this radiation protection tool.

Conflict of interest disclosure

The authors declared no conflicts of interest.

Funding

The authors would like to extend their sincere appreciation to the researchers supporting program for funding this work under Researchers Supporting project number (RSPD2023R780), King Saud University, P.O. box 145111, Riyadh 4545, Saudi Arabia.

References

1. Strauss KJ, Kaste SC. The ALARA (as low as reasonably achievable) concept in pediatric interventional and fluoroscopic imaging: striving to keep radiation doses as low as possible during fluoroscopy of pediatric patients—a white paper executive summary. *Pediatr Radiol*. 2006;36(Suppl 2):110-112. [\[CrossRef\]](#)

2. Choudhary S. Deterministic and stochastic effects of radiation. *Cancer Ther Oncol Int J*. 2018;12(2):31-32. [\[CrossRef\]](#)
3. Hamada N, Fujimichi Y. Classification of radiation effects for dose limitation purposes: history, current situation and future prospects. *J Radiat Res*. 2014;55(4):629-640. [\[CrossRef\]](#)
4. Engel-Hills P. Radiation protection in medical imaging. *Radiography*. 2006;12(2):153-160. [\[CrossRef\]](#)
5. The British Institute of Radiology. Guidance on using shielding on patients for diagnostic radiology applications. 2020. [\[CrossRef\]](#)
6. American Association of Physicists in Medicine. AAPM position statement on the use of patient gonadal and fetal shielding. *Policy Statement PP-32A*. 2019. [\[CrossRef\]](#)
7. The Society of Radiographers. Contact Shielding for Patients No Longer Required. 2020. [\[CrossRef\]](#)
8. Lakhwani OP, Dalal V, Jindal M, Nagala A. Radiation protection and standardization. *J Clin Orthop Trauma*. 2019;10(4):738-743. Erratum in: *J Clin Orthop Trauma*. 2020;11(6):1176. [\[CrossRef\]](#)
9. Pizzutiello RJ, Cullinan JE. Introduction to medical radiographic imaging: Health Sciences Division, Eastman Kodak Company; 1993. [\[CrossRef\]](#)
10. Davies BH, Manning-Stanley AS, Hughes VJ, Ward AJ. The impact of gonad shielding in anteroposterior (AP) pelvis projections in an adult: a phantom study utilising digital radiography (DR). *Radiography (Lond)*. 2020;26(3):240-247. [\[CrossRef\]](#)
11. Frantzen MJ, Robben S, Postma AA, Zoetelief J, Wildberger JE, Kemerink GJ. Gonad shielding in paediatric pelvic radiography: disadvantages prevail over benefit. *Insights Imaging*. 2012;3(1):23-32. [\[CrossRef\]](#)
12. Fawcett SL, Barter SJ. The use of gonad shielding in paediatric hip and pelvis radiographs. *Br J Radiol*. 2009;82(977):363-370. [\[CrossRef\]](#)
13. Brateman L. Radiation safety considerations for diagnostic radiology personnel. *Radiographics*. 1999;19(4):1037-1055. [\[CrossRef\]](#)
14. Hawking NG, Sharp TD. Decreasing radiation exposure on pediatric portable chest radiographs. *Radiol Technol*. 2013;85(1):9-16. [\[CrossRef\]](#)
15. Mekis N, Zontar D, Skrk D. The effect of breast shielding during lumbar spine radiography. *Radiol Oncol*. 2013;47(1):26-31. [\[CrossRef\]](#)
16. ICRP; Khong PL, Ringertz H, et al. ICRP publication 121: radiological protection in paediatric diagnostic and interventional radiology. *Ann ICRP*. 2013;42(2):1-63. Erratum in: *Ann ICRP*. 2020;146645320966413. Erratum in: *Ann ICRP*. 2021;1466453211000254. [\[CrossRef\]](#)

17. The 2007 Recommendations of the International Commission on Radiological Protection. ICRP publication 103. *Ann ICRP*. 2007;37(2-4):1-332. [\[CrossRef\]](#)
18. Nguyen PK, Wu JC. Radiation exposure from imaging tests: is there an increased cancer risk? *Expert Rev Cardiovasc Ther*. 2011;9(2):177-183. [\[CrossRef\]](#)
19. Ribeiro Guerra M, Coignard J, Eon-Marchais S, et al. Diagnostic chest X-rays and breast cancer risk among women with a hereditary predisposition to breast cancer unexplained by a BRCA1 or BRCA2 mutation. *Breast Cancer Res*. 2021;23(1):79. [\[CrossRef\]](#)
20. Pijpe A, Andrieu N, Easton DF, et al. Exposure to diagnostic radiation and risk of breast cancer among carriers of BRCA1/2 mutations: retrospective cohort study (GENE-RAD-RISK). *BMJ*. 2012;345:e5660. [\[CrossRef\]](#)
21. Baert A, Depuydt J, Van Maerken T, et al. Increased chromosomal radiosensitivity in asymptomatic carriers of a heterozygous BRCA1 mutation. *Breast Cancer Res*. 2016;18(1):52. [\[CrossRef\]](#)
22. Baert A, Depuydt J, Van Maerken T, et al. Analysis of chromosomal radiosensitivity of healthy BRCA2 mutation carriers and non-carriers in BRCA families with the G2 micronucleus assay. *Oncol Rep*. 2017;37(3):1379-1386. [\[CrossRef\]](#)
23. Andrieu N, Easton DF, Chang-Claude J, et al. Effect of chest X-rays on the risk of breast cancer among BRCA1/2 mutation carriers in the international BRCA1/2 carrier cohort study: a report from the EMBRACE, GENEPSO, GEO-HEBON, and IBCCS Collaborators' Group. *J Clin Oncol*. 2006;24(21):3361-3366. [\[CrossRef\]](#)
24. National Research Council. Health risks from exposure to low levels of ionizing radiation: BEIR VII phase 2. 2006. [\[CrossRef\]](#)
25. Elshami W, Abuzaid MM, Tekin HO. Effectiveness of breast and eye shielding during cervical spine radiography: an experimental study. *Risk Manag Healthc Policy*. 2020;13:697-704. [\[CrossRef\]](#)
26. Foley SJ, McEntee MF, Achenbach S, Brennan PC, Rainford LS, Dodd JD. Breast surface radiation dose during coronary CT angiography: reduction by breast displacement and lead shielding. *AJR Am J Roentgenol*. 2011;197(2):367-373. [\[CrossRef\]](#)
27. Jeukens CRLPN, Kütterer G, Kicken PJ, et al. Gonad shielding in pelvic radiography: modern optimised X-ray systems might allow its discontinuation. *Insights Imaging*. 2020;11(1):15. [\[CrossRef\]](#)
28. Marsh RM, Silosky M. Patient shielding in diagnostic imaging: discontinuing a legacy practice. *AJR Am J Roentgenol*. 2019;212(4):755-757. [\[CrossRef\]](#)
29. Kotre CJ, Little BG. Patient and staff radiation doses from early radiological examinations (1899-1902). *Br J Radiol*. 2006;79(946):837-842. [\[CrossRef\]](#)
30. Lord A. Radiological hazards to patients: final report of the committee: great Britain. Ministry of Health. Committee on Radiological Hazards to Patients: Free Download, Borrow, and Streaming: Internet Archive. 1966. [\[CrossRef\]](#)
31. Hart D, Hillier M, Shrimpton P. Doses to patients from radiographic and fluoroscopic X-ray imaging procedures in the UK-2010 review HPA-CRCE-034. *Chilton HPA*. 2012. [\[CrossRef\]](#)
32. Rehani MM, Hauptmann M. Estimates of the number of patients with high cumulative doses through recurrent CT exams in 35 OECD countries. *Phys Med*. 2020;76:173-176. [\[CrossRef\]](#)
33. Gilligan P, Damilakis J. Patient shielding: The need for a European consensus statement. *Phys Med*. 2021;82:266-268. [\[CrossRef\]](#)
34. Kagaku K. Whole Body Phantom "PBU-50". [\[CrossRef\]](#)
35. Lampignano J, Kendrick LE. Bontrager's textbook of radiographic positioning and related anatomy-E-book: Elsevier Health Sciences; 2017. [\[CrossRef\]](#)
36. Hiles P, Gilligan P, Damilakis J, et al. European consensus on patient contact shielding. *Insights Imaging*. 2021;12(1):194. [\[CrossRef\]](#)
37. Health Service Executive. Review of the clinical radiology medical workforce in Ireland. 2017. [\[CrossRef\]](#)
38. Schaefer-Prokop C, Neitzel U, Venema HW, Uffmann M, Prokop M. Digital chest radiography: an update on modern technology, dose containment and control of image quality. *Eur Radiol*. 2008;18(9):1818-1830. [\[CrossRef\]](#)
39. Bansal GJ. Digital radiography. A comparison with modern conventional imaging. *Postgrad Med J*. 2006;82(969):425-428. [\[CrossRef\]](#)
40. Kutanzi KR, Lumen A, Koturbash I, Miousse IR. Pediatric exposures to ionizing radiation: carcinogenic considerations. *Int J Environ Res Public Health*. 2016;13(11):1057. [\[CrossRef\]](#)
41. Tomasetti C, Poling J, Roberts NJ, et al. Cell division rates decrease with age, providing a potential explanation for the age-dependent deceleration in cancer incidence. *Proc Natl Acad Sci U S A*. 2019;116(41):20482-20488. [\[CrossRef\]](#)
42. Authors on behalf of ICRP; Stewart FA, Akleyev AV, et al. ICRP publication 118: ICRP statement on tissue reactions and early and late effects of radiation in normal tissues and organs—threshold doses for tissue reactions in a radiation protection context. *Ann ICRP*. 2012;41(1-2):1-322. [\[CrossRef\]](#)
43. Hutchinson L. Breast cancer: radiation risk in BRCA carriers. *Nat Rev Clin Oncol*. 2012;9(11):611. [\[CrossRef\]](#)
44. Matyagin YV, Collins PJ. Effectiveness of abdominal shields in chest radiography: a Monte Carlo evaluation. *Br J Radiol*. 2016;89(1066):20160465. [\[CrossRef\]](#)
45. Daniels C, Furey E. The effectiveness of surface lead shielding of gonads outside the primary X-ray beam. *J Med Imaging Radiat Sci*. 2008;39(4):189-191. [\[CrossRef\]](#)
46. Sidhu M, Strauss KJ, Connolly B, et al. Radiation safety in pediatric interventional radiology. *Tech Vasc Interv Radiol*. 2010;13(3):158-166. [\[CrossRef\]](#)
47. Samara ET, Saltybaeva N, Sans Merce M, Gianolini S, Ith M. Systematic literature review on the benefit of patient protection shielding during medical X-ray imaging: towards a discontinuation of the current practice. *Phys Med*. 2022;94:102-109. [\[CrossRef\]](#)
48. Yu L, Bruesewitz MR, Vrieze TJ, McCollough CH. Lead shielding in pediatric Chest CT: effect of apron placement outside the scan volume on radiation dose reduction. *AJR Am J Roentgenol*. 2019;212(1):151-156. [\[CrossRef\]](#)
49. Iball GR, Brettle DS. Use of lead shielding on pregnant patients undergoing CT scans: results of an international survey. *Radiography*. 2011;17(2):102-108. [\[CrossRef\]](#)



Letter to the Editor: Indeterminate pulmonary subsolid nodules in patients with no history of cancer

Furkan Ufuk

Dear Editor,

I read with interest the original article entitled "Indeterminate pulmonary subsolid nodules in patients with no history of cancer: growing prediction, CT pattern, and pathological diagnosis" by Guo et al.¹ In this retrospective study, the authors assessed the growth patterns of indeterminate subsolid pulmonary nodules on computed tomography in patients without a history of malignancy. The authors reported that the risk of pulmonary subsolid nodule growth increases by 4% each year in patients without a history of malignancy. They further stated that partial solid nodules have a three-fold greater risk of growth than non-solid nodules, and that subsolid nodules with aggressive pathological features grow faster. Although these results are remarkable and make an essential contribution to the literature, I suggest a few points need to be clarified to ensure the reproducibility of this study and the reliability of the data.

First, the authors reported that 80 subsolid nodules in 77 patients were resected. However, they have specified only 77 pathological diagnoses, including 29 adenocarcinomas *in situ*, 29 minimally invasive adenocarcinomas, 18 invasive adenocarcinomas, and one atypical adenomatous hyperplasia.¹ There is a discrepancy in the number of resected and histopathologically reported nodules in the study.

Second, Guo et al.¹ reported that all indeterminate subsolid nodules in their study were pre-malignant or had malignant histopathology. However, according to the literature, the incidence of malignancy in subsolid lung nodules is much lower than in the study of Guo et al.¹ It is known that the presence and size of the solid component and the size of the subsolid nodule increase the risk of malignancy. The malignancy rate of non-solid nodules smaller than 1 cm is approximately 1%, whereas the malignancy rate of partial solid nodules with a solid component of ≥ 6 mm is around 20%.²⁻⁴ The frequency of malignancy in indeterminate subsolid lung nodules in the current study is inconsistent with that reported in the literature.

KEYWORDS

Computed tomography, diagnosis, lung, neoplasm, nodule

From the Department of Radiology (F.U. ✉ furkan.ufuk@hotmail.com), Pamukkale University Faculty of Medicine, Denizli, Turkey.

Received 20 Apr 2022; revision requested 10 Jun 2022; accepted 08 July 2022.



Epub: 21.12.2022

Publication date: 30.05.2023

DOI: 10.4274/dir.2022.221590

References

1. Guo X, Jia X, Zhang D, Feng H, Dou Y, Shi G. Indeterminate pulmonary subsolid nodules in patients with no history of cancer: growing prediction, CT pattern, and pathological diagnosis. *Diagn Interv Radiol.* 2022;28(3):230-238. [\[CrossRef\]](#)
2. Hammer MM, Palazzo LL, Kong CY, Hunsaker AR. Cancer risk in subsolid nodules in the national lung screening trial. *Radiology.* 2019;293(2):441-448. [\[CrossRef\]](#)
3. Robbins HA, Katki HA, Cheung LC, Landy R, Berg CD. Insights for management of ground-glass opacities from the national lung screening trial. *J Thorac Oncol.* 2019;14(9):1662-1665. [\[CrossRef\]](#)
4. Baldwin DR, Callister ME; Guideline Development Group. The British Thoracic Society guidelines on the investigation and management of pulmonary nodules. *Thorax.* 2015;70(8):794-798. [\[CrossRef\]](#)

You may cite this article as: Ufuk F. Letter to the Editor: Indeterminate pulmonary subsolid nodules in patients with no history of cancer. *Diagn Interv Radiol.* 2023;29(3):561.



Copyright@Author(s) - Available online at dirjournal.org.
Content of this journal is licensed under a Creative Commons
Attribution-NonCommercial 4.0 International License.

Li C, Liu H, Wang J, et al. Multiparametric MRI combined with liver volume for quantitative evaluation of liver function in patients with cirrhosis. *Diagn Interv Radiol.* 2022;28(6):547-554.

The mistake have been made inadvertently by the author.

In the article titled "Multiparametric MRI combined with liver volume for quantitative evaluation of liver function in patients with cirrhosis" with the DOI number 10.5152/dir.2022.211325, an Acknowledgements paragraph has been added after the Conclusion section on page 553, before the Conflict of Interest Disclosure information. The added Acknowledgements paragraph is below:

Acknowledgements

We are grateful to Professor Jie Zheng from the Clinical Research Center of the First Affiliated Hospital of Xi'an Jiaotong University for kindly statistical advice for this manuscript. This study has received funding from General Project of Key Research and Development Programs of Shaanxi Province [2019SF-007] and Academy Fund from The First Affiliated Hospital of Xi'an Jiaotong University [2019ZYTS-16].



DOI: 10.4274/dir.2023.0001